

ACCEPTED MANUSCRIPT • OPEN ACCESS

Fluctuations and pairing in Fe-based superconductors: light scattering experiments

To cite this article before publication: Nenad Lazarevic *et al* 2020 *J. Phys.: Condens. Matter* in press <https://doi.org/10.1088/1361-648X/ab8849>

Manuscript version: Accepted Manuscript

Accepted Manuscript is “the version of the article accepted for publication including all changes made as a result of the peer review process, and which may also include the addition to the article by IOP Publishing of a header, an article ID, a cover sheet and/or an ‘Accepted Manuscript’ watermark, but excluding any other editing, typesetting or other changes made by IOP Publishing and/or its licensors”

This Accepted Manuscript is © 2020 IOP Publishing Ltd.

As the Version of Record of this article is going to be / has been published on a gold open access basis under a CC BY 3.0 licence, this Accepted Manuscript is available for reuse under a CC BY 3.0 licence immediately.

Everyone is permitted to use all or part of the original content in this article, provided that they adhere to all the terms of the licence <https://creativecommons.org/licenses/by/3.0>

Although reasonable endeavours have been taken to obtain all necessary permissions from third parties to include their copyrighted content within this article, their full citation and copyright line may not be present in this Accepted Manuscript version. Before using any content from this article, please refer to the Version of Record on IOPscience once published for full citation and copyright details, as permissions may be required. All third party content is fully copyright protected and is not published on a gold open access basis under a CC BY licence, unless that is specifically stated in the figure caption in the Version of Record.

View the [article online](#) for updates and enhancements.

Fluctuations and pairing in Fe-based superconductors: Light scattering experiments

N Lazarević

Center for Solid State Physics and New Materials, Institute of Physics Belgrade,
University of Belgrade, Pregrevica 118, 11080 Belgrade, Serbia

E-mail: nenadl@ipb.ac.rs

R Hackl

Walther Meissner Institut, Bayerische Akademie der Wissenschaften, 85748
Garching, Germany

E-mail: hackl@wmi.badw.de

21 March 2020

Abstract. Inelastic scattering of visible light (Raman effect) offers a window into properties of correlated metals such as spin, electron and lattice dynamics as well as their mutual interactions. In this review we focus on electronic and spin excitations in Fe-based pnictides and chalcogenides, in particular but not exclusively superconductors. After a general introduction to the basic theory including the selection rules for the various scattering processes we provide an overview over the major results. In the superconducting state below the transition temperature T_c the pair-breaking effect can be observed, and the gap energies may be derived and associated with the gaps on the electron and hole bands. In spite of the similarities of the overall band structures the results are strongly dependent on the family and may even change qualitatively within one family. In some of the compounds strong collective modes appear below T_c . In $\text{Ba}_{1-x}\text{K}_x\text{Fe}_2\text{As}_2$, which has the most isotropic gap of all Fe-based superconductors, there are indications that these modes are exciton-like states appearing in the presence of a hierarchy of pairing tendencies. The strong in-gap modes observed in Co-doped NaFeAs are interpreted in terms of quadrupolar orbital excitations which become undamped in the superconducting state. The doping dependence of the scattering intensity in $\text{Ba}(\text{Fe}_{1-x}\text{Co}_x)_2\text{As}_2$ is associated with a nematic resonance above a quantum critical point and interpreted in terms of a critical enhancement at the maximal T_c . In the normal state the response from particle-hole excitations reflects the resistivity. In addition, there are strongly temperature-dependent contributions from presumably critical fluctuations in the energy range of $k_B T$ which can be compared to the elastic properties. Currently it is not settled whether the fluctuations observed by light scattering are related to spin or charge. Another controversy relates to putative two-magnon excitations, typically in the energy range below 0.5 eV. Whereas this response presumably originates from charge excitations in most of the Fe-based compounds theory and experiment suggest that the excitations in the 60 meV range in FeSe are from localized spins in a nearly frustrated system.

1. Introduction

Superconductivity in iron-based compounds (FeBCs) came as a big surprise when first reported by Kamihara and coworkers [1, 2]. The FeBCs consist of quadratically coordinated Fe planes sandwiched between layers of pnictogen (As, P) or chalcogen (S, Se, Te) atoms as shown in Fig. 1(a). The rest of the structure is rather variable as can be seen from the sum formulae in Table 1. For this variability and the relative change in the band structures the FeBCs are a laboratory for studying the interrelation of magnetism, fluctuations and superconductivity or strong *versus* weak-coupling effects as summarized in excellent reviews including [3, 4, 5, 6, 7, 8].

FeBCs typically have a magnetically ordered phase at zero nominal doping. Upon elemental substitution or application of pressure, magnetism can be suppressed and superconductivity (SC) may appear [Fig. 1(b)]. In contrast to the cuprates, all phases are metallic. The order at zero doping is a stripe-like antiferromagnetic spin-density wave (SDW) and widely believed to originate from the nesting properties of the hole- and electron-like Fermi surfaces encircling the (0, 0) (Γ) and the $(\pm\pi, 0)/ (0, \pm\pi)$ (X/Y) points in the idealized 1Fe Brillouin zone. Similarly, the topology of the Fermi surface is considered important for superconductivity [9]. Although the Fermi surfaces are always centered at Γ and X/Y there are substantial variations in shape and character across the families and as a function of doping [10]. However, this variation is not necessarily and exclusively at the origin of the differences in the superconducting ground states. Already on the level of local-density approximation (LDA) [11] a variety of nearly degenerate superconducting ground states is expected [6, 12].

In addition to the SDW and SC phase transitions, nematic order, with the rotational symmetry broken but the translational symmetry preserved, and wide temperature ranges with fluctuations are observed [14]. For studying this plethora of instabilities, a wide variety of experimental methods has been applied. Inelastic light scattering is a useful technique, since relevant information on practically all phases and their fluctuations can be obtained.

It will be the purpose of this review to present typical results, provide a snapshot of the current status of the field and outline possible future developments.

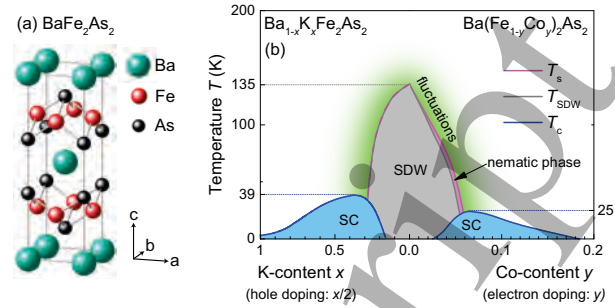


Figure 1. Crystal structure and phase diagram. (a) Crystal structure of BaFe₂As₂. Thin grey lines indicate the edges of the unit cell (2 Fe per layer, I4/mmm). Grey connecting lines between Fe and As illustrate covalent Fe-As bonds. (b) Phase diagram. The spin density wave (SDW) and the superconducting (SC) ranges are indicated in grey and blue, respectively. The dashed magenta-grey line indicates a simultaneous structural transition at T_s and SDW transition at T_{SDW}. The nematic phase is shaded magenta. The green shaded area indicates the existence of fluctuations next to the SDW transition. Note that the scales in x (hole doping) and y (electron doping) differ. From [13] with permission.

First, we briefly describe the experiment and the theoretical background and then summarize the most relevant results obtained from light scattering with the focus placed on electronic and spin excitations.

2. Raman experiment

Shown in Fig. 2 is a schematic view of the experimental setup of a typical macro Raman experiment *in vacuo* and in a diamond anvil cell (inset) on opaque samples. In the macro setup the incident light with polarization \hat{e}_I impinges on the surface at an angle of incidence $\vartheta_I \sim 70^\circ$ in order to prevent the directly reflected light from entering the optics and the spectrometer. For this “pseudo-Brewster” angle the reflection is minimal for \hat{e}_I parallel to the plane of incidence. The scattered light is collected along the surface normal. Photons having a selected polarization state \hat{e}_S enter the spectrometer. A charge-coupled device (CCD) detector registers the number of transmitted photons per unit time $\dot{N}_{I,S}(\Omega)$ (“Raman spectrum”) for a given energy shift $\Omega = \omega_I - \omega_S$ and polarization combination (\hat{e}_I, \hat{e}_S) , where $\omega_{I,S}$ are the energies of the photons. The differential light scattering cross-section is proportional to the Raman spectrum,

$$\frac{d^2\sigma_{I,S}}{d\Omega_S d\omega_S} = \hbar r_0^2 \frac{\omega_S}{\omega_I} \frac{1}{\pi} \{1 + n(\Omega, T)\} R_{I,S} \chi''_{I,S}(\mathbf{q}, \Omega, T). \quad (1)$$

Here Ω_S is the solid angle into which the photons are

Raman scattering in Fe-based systems

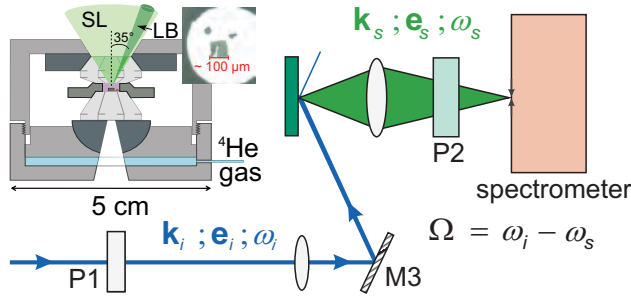


Figure 2. Schematic representation of a Raman experiment. The polarized monochromatic photons hit the sample at a large angle of incidence. The scattered photons are collected along the surface normal and pass the analyzer before entering the spectrometer. Inset: Side view of a Raman pressure cell. The laser beam (LB) enters from the right, the scattered light (SL) is collected along the normal of the sample surface. From [15].

scattered, and $R_{I,S}$ absorbs matrix element effects and experimental factors, $\chi_{I,S}(\mathbf{q}, \Omega, T) = \chi'_{I,S} + i\chi''_{I,S}$ is the typically non-resonant response function, $n(\Omega, T) = [\exp(\hbar\Omega/k_B T) - 1]^{-1}$ is the Bose-Einstein occupation number and $r_0 = e^2/(4\pi\epsilon_0 mc^2)$ the Thompson electron radius, thus Eq. (1) describes the cross section per electron. From linear combinations of the spectra, pure symmetries μ can be derived (for details see Section 4.9).

3. Materials

Most of the existing FeBCs were studied by Raman scattering. In the beginning the phonons were in the main focus [16, 17, 18, 19, 20, 21, 22]. With the advent of high-quality single crystals of the 122 family [23], being a result of FeAs self-flux growth [24], the study of electronic properties by light scattering became promising, and the superconducting gap was studied successfully in $\text{Ba}(\text{Fe}_{1-x}\text{Co}_x)_2\text{As}_2$ for two doping levels [25]. Soon thereafter the redistribution of spectral weight in the SDW state of BaFe_2As_2 was reported [26, 27]. Finally, the fluctuations above the magneto-structural transformation, inferred from transport [28], were observed [29, 30]. Although there are reports on spectra in the range 1000 cm^{-1} to 4000 cm^{-1} (the energy range of two-magnon excitations) [31], their interpretation remains controversial.

The materials for which data on the spin, charge and orbital response exist are compiled in Table 1.

4. Theoretical background

The analysis of the results in the FeBCs requires insight into the theoretical background, including both standard knowledge and modern developments. We give a brief historical summary and sketch the

underlying theory with the emphasis placed on metallic systems.

4.1. Historical remarks

Raman scattering studies of excitations of localized spins started in the 1960s on insulating antiferromagnets [60] and experienced a renaissance with the advent of the cuprates [61]. The theoretical framework was set by the seminal work of Elliot, Fleury and Loudon [62] which still represents the basis of contemporary analyses [63] even in the case of metallic systems such as the FeBCs [31, 64, 65].

Light scattering from conduction electrons was first discussed in the context of superconductors [66]. It took almost 20 years to observe the effect experimentally in the layered compound 2H-NbSe_2 [67]. In NbSe_2 superconductivity competes with a charge density wave (CDW) for area on the Fermi surface (FS), and the spectral features observed below T_c cannot directly be traced back to the superconducting energy gap in contrast to those for selected symmetries in the A15 compounds V_3Si and Nb_3Sn [68, 69] or in the cuprates [63, 70, 71]. Hence, only in special cases the Raman spectra of superconductors can be described satisfactorily in terms of lowest order weak coupling theory as developed between 1961 and 1984 [66, 72, 73]. In all other cases, including the FeBCs, lowest order is insufficient, although it still captures the plain vanilla such as the strong momentum dependence of the gap if the symmetries of the response are properly taken into account [74].

In normal metals, contributions from particle-hole excitations were observed and discussed for doped semiconductors [75, 76], but in-depth studies started only in the cuprates [77, 78, 79, 80, 81]. Similarly as in the superconducting state, the major contribution from Raman scattering, in addition to what was known from optical spectroscopy, was the observation of a polarization dependent relaxation of the carriers which could be mapped on the electronic momentum [74, 82].

Important new developments include the observation and analysis of critical fluctuations in both cuprates [83, 84] and FeBCs [29, 30, 49, 85, 86, 87]. In the superconducting state an anisotropic pairing potential [73, 88, 89, 90, 91, 92], amplitude (“Higgs”) fluctuations of the superconducting order parameter [93, 94], number-phase fluctuations in multiband systems (Leggett modes [95]) [96, 97, 98, 99, 100] or a nematic resonance [39] need to be included. Whereas the interpretation of the results in NbSe_2 in terms of coupled gap excitations and amplitude fluctuations in a coupled SC-CDW system seems to converge [101, 102] the discussion of the E_g symmetry contributions in the A15 materials [68, 69, 103, 89, 102], the B_{1g} response in

Table 1. Materials studied by Raman scattering. The table includes only materials for which electronic properties (spin, charge, fluctuations) were studied. In the second column typical acronyms are listed which will be used occasionally in the text. The main subject of the respective experiments are listed in the second to last column.

material	acronym	substitution	subject	reference
BaFe ₂ As ₂	BFA/Ba122	no	SDW	[27, 32]
SrFe ₂ As ₂	Sr122	no	SDW, fluctuations	[29, 33]
EuFe ₂ As ₂	Eu122	no	SDW, fluctuation	[33, 34]
CaFe ₂ As ₂	Ca122	no	SDW	[34]
LaFeAsO	1111	no	SDW	[35]
Ba(Fe _{1-x} Co _x) ₂ As ₂	BFCA	$x = 0.061, 0.085$	SC gap	[25]
Ba(Fe _{1-x} Co _x) ₂ As ₂	BFCA	$x = 0.061$	gap, vertex	[36]
Ba(Fe _{1-x} Co _x) ₂ As ₂	BFCA	$x = 0.08$	gap	[37]
Ba(Fe _{1-x} Co _x) ₂ As ₂	BFCA	$0 \leq x \leq 0.045$	SDW	[26]
Ba(Fe _{1-x} Co _x) ₂ As ₂	BFCA	$0 \leq x \leq 0.20$	fluctuations	[30]
Ba(Fe _{1-x} Co _x) ₂ As ₂	BFCA	$0.055 \leq x \leq 0.10$	SC gap	[38]
Ba(Fe _{1-x} Co _x) ₂ As ₂	BFCA	$0 \leq x \leq 0.10$	SC gap-nematicity	[39]
Ba(Fe _{1-x} Co _x) ₂ As ₂	BFCA	$x = 0, 0.025, 0.051$	fluctuations	[40]
Ba(Fe _{1-x} Co _x) ₂ As ₂	BFCA	$0.045 \leq x \leq 0.085$	fluctuations and SC gap	[41]
Ca(Fe _{1-x} Co _x) ₂ As ₂		$x = 0.03$	crystal field	[42]
Sr(Fe _{1-x} Co _x) ₂ As ₂		$x = 0, 0.04, 0.20$	SDW	[43, 44]
Ba(Fe _{1-x} Au _x) ₂ As ₂		$x = 0, 0.012, 0.014, 0.031$	fluctuations	[45]
Ba _{1-x} K _x Fe ₂ As ₂	BKFA	$x = 0.4$	SC gap and pairing	[46]
Ba _{1-x} K _x Fe ₂ As ₂	BKFA	$x = 0.4$	SC gap and pairing	[47]
Ba _{1-x} K _x Fe ₂ As ₂	BKFA	$0.22 \leq x \leq 0.70$	fluctuations and SC gap	[41, 41]
Ba _{1-x} K _x Fe ₂ As ₂	BKFA	$x = 0.25, 0.4, 0.6$	fluctuations and SC gap	[48]
BaFe ₂ (As _{1-x} P _x) ₂	BFAP	$x = 0.5$	fluctuations and SC gap	[48]
NaFe _{1-x} Co _x As	Na111	$0 \leq x \leq 0.08$	fluctuations and SC gap	[49]
CaKFe ₄ As ₄	CKFA/1144	no	SC gap and pairing	[50, 51]
Fe _{1+δ} Te _{1-x} Se _x		$x = 0, 0.4$	SC gap, phonon, magnon	[52]
FeSe	11	no	fluctuations	[15, 53, 54]
FeSe	11	no	2-magnon	[55]
FeSe _{0.82}	11	no	crystal field	[56]
FeSe _{1-x} S _x		$x = 0, 0.04, 0.08, 0.15, 0.20$	fluctuations	[57]
K _{0.75} Fe _{1.75} Se ₂		no	gap	[58]
Rb _{0.8} Fe _{1.6} Se ₂		no	gap	[46]
A _{0.8} Fe _{1.6} Se ₂		$A = \text{K, Rb, Cs, Tl}$	2-magnon	[59]

the cuprates [104, 105, 106, 107, 108, 109] or the in-gap modes in the FeBCs [39, 41, 46, 47, 49] remains controversial. In addition to the weak-coupling description of the superconducting state at $T = 0$ a lot more work is needed to arrive at a coherent picture for the normal and superconducting states in the presence of collisions, fluctuations and strong coupling. Only a few special cases have been studied theoretically so far [77, 85, 86, 87, 110, 111, 112, 113, 83, 114, 115, 116]. More details can be found in Refs. [63] and [82] and, for recent developments, in [41, 64, 65, 85, 86, 87, 91, 92, 99, 100, 115, 116, 117, 118].

4.2. Light scattering

Photons in the visible or x-ray range do not directly scatter off low-energy excitations. Rather, high-energy electron-hole pairs having energies of the incoming photons ($1.6 \leq \hbar\omega_I \leq 3.5$ eV for the visible) are

created and couple to excitations in the range $\hbar\Omega = 1 \dots 200$ meV such as phonons, fluctuations, particle-hole, gap or spin excitations [119]. After scattering, the electron-hole pairs recombine and emit photons with energies $\hbar\omega_S = \hbar\omega_I \mp \hbar\Omega$. The mechanism works whether or not the intermediate electronic states are eigenstates. If they are eigenstates the cross-section is resonantly enhanced, but most of the results were successfully analysed in terms of non-resonant scattering. In systems with a high correlation energy $U = \mathcal{O}(\hbar\omega_I)$ there are no well-defined eigenstates, and the resonances are in fact found to be mild in most of the cases.

Given these considerations, Eq. (1) is most naturally derived from scattering matrix elements in third order perturbation theory such as in the case of phonons or spin excitations [62, 119]. For electrons the Raman susceptibility or response function $\chi(\Omega, T)$ is almost always derived in the non-resonant limit

using either diagrammatic techniques [66, 73, 77, 63] or the kinetic equation [82, 120]. Since $\chi(\Omega, T)$ is not a pure density or current correlation function there is no general sum rule such as the f -sum rule in optical conductivity [121].[‡] Usually For this reason, the Raman cross section may be a superposition of independent contributions, for example particle-hole excitations (electronic continuum) and magnons or phonons. Occasionally, some of the excitations may be interrelated, for instance phonons and particle-hole excitations leading to the Fano effect (not discussed in this review) or gap formation and excitations in density-wave or superconducting states and the continuum playing an important role below.

The Raman response of all types of excitations is causal implying that $\chi_{I,S}^*(-\Omega) = \chi_{I,S}(\Omega)$ where $*$ denotes the conjugate complex. Thus $\chi_{I,S}''(\Omega)$ is anti-symmetric with respect to the origin, and its expansion contains only odd powers of Ω .

In Fig. 3, Feynman diagrams for Raman scattering are displayed. γ and Γ are the bare and the renormalized vertices, respectively, for the interaction between light and electrons [63]. They depend on the light polarizations and on momentum and determine the selection rules. In panel (a) particle-hole excitations are described. The bare vertex γ is an approximation where properties of the intermediate states are neglected assuming that all photon energies are smaller than any band gap, $\hbar\omega_{I,S} < |\epsilon_c - \epsilon_\nu|$, where the subscripts c and ν refer to electrons in the conduction bands and those in other bands, respectively. Γ is a renormalized vertex in the spirit of the Bethe-Salpeter equation [123]. In panel (b) scattering from bosons *via* electrons is described. f is the vertex for the interaction between electrons and other excitations.

4.3. Charged systems

In general, visible light cannot transfer substantial momentum to a crystal since the lattice constant a is much smaller than the wavelengths $\lambda_{I,S}$ of the incoming and outgoing photons, and all unit cells are excited in phase. This is usually called the $q = 0$ selection rule of Raman scattering in crystals. In the case of (resonant) inelastic x-ray scattering [(R)IXS] with $\lambda = \mathcal{O}(a)$, most of the Brillouin zone can be accessed [124]. Metals have a small penetration depth for light $a < \delta_0 < \lambda_{I,S}$. As a consequence, the momentum transfer in a metal is bigger than in an insulator, $|\mathbf{q}| = q \sim \delta_0^{-1}$, where $100 \text{ \AA} < \delta_0 < 1000 \text{ \AA}$ for typical metals, as pointed out first by Abrikosov and Fal'kovskii [66]. Yet, the available momentum is still much smaller than π/a , and for exciting a

[‡] Special cases [107, 122] are beyond the scope of this review.

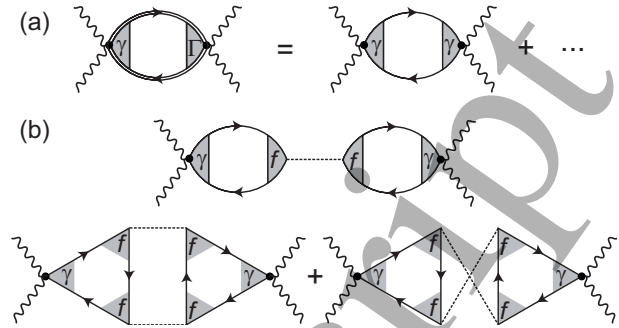


Figure 3. Feynman diagrams for (non-resonant) light scattering. (a) Raman response of particle-hole excitations in the presence of interactions and (b) scattering processes involving one and two bosonic excitations. Wavy lines represent incident and scattered photons whereas solid lines are electronic propagators. The bosonic excitation or fluctuation propagators are represented by dashed lines. The bare and renormalized Raman vertices γ and Γ describe the interaction of light and electrons and f describes the interaction of electrons and other excitations, e.g. bosons.

non-interacting conduction electron from an occupied (i) to an unoccupied (f) state the maximal energy is limited by $\hbar\Omega_{\max} = \epsilon_{\mathbf{k}}^{(f)} - \epsilon_{\mathbf{k}}^{(i)} \approx \hbar v_F \delta_0^{-1}$ where $\epsilon_{\mathbf{k}}$ is the electronic dispersion. In the FeBCs the relevant in-plane Fermi velocity is of order 10^6 cm/s , and the penetration depth is close to 1000 \AA yielding $\hbar\Omega_{\max} \lesssim 1 \text{ meV} \equiv 8 \text{ cm}^{-1}$.

Due to charge conservation and screening all isotropic charge excitations are pushed up to the plasma frequency Ω_{pl} [125], and there is no scattering in the range of $k_B T$ in non-interacting systems with a strictly quadratic electron dispersion. What looks like a disadvantage at first glance is the origin of the selection rules for electronic Raman scattering [72]. Loosely speaking, one cannot move charges from one unit cell to another one but the charges can only be redistributed in phase inside all unit cells (quadrupolar-type of excitations). This is the origin of the form factors, and the light does not scatter from the charge density but from a weighted charge density [72, 73, 89],

$$\tilde{\rho}_{\mathbf{q}} = \frac{1}{N} \sum_n \sum_{\mathbf{k}, \sigma} \gamma_n(\mathbf{k}, \mathbf{q}) c_{n, \mathbf{k}+\mathbf{q}, \sigma}^\dagger c_{n, \mathbf{k}, \sigma}. \quad (2)$$

n is the band index, and $\gamma_n(\mathbf{k}, \mathbf{q})$ is a form factor which is related to the Raman vertex $\gamma_{\alpha, \beta}(\mathbf{k}, \mathbf{q})$ through the polarization directions $\hat{\mathbf{e}}_{I,S}$,

$$\gamma_n(\mathbf{k}, \mathbf{q}) = \sum_{\alpha, \beta} e_I^\alpha \gamma_{n, \alpha, \beta}(\mathbf{k}, \mathbf{q}) e_S^\beta. \quad (3)$$

The bare response $\tilde{\chi}(\mathbf{q}, \Omega)$ is the commutator of $\tilde{\rho}_{\mathbf{q}}$,

$$\tilde{\chi}(\mathbf{q}, \Omega) = \langle \langle [\tilde{\rho}_{\mathbf{q}}(t), \tilde{\rho}_{-\mathbf{q}}(0)] \rangle \rangle_\Omega = \tilde{\chi}' + i\tilde{\chi}'', \quad (4)$$

where $\langle \langle \dots \rangle \rangle_\Omega$ denotes the thermodynamic average and the Fourier transformation, and $\tilde{\chi}'$ and $\tilde{\chi}''$ are the real

and imaginary part of $\tilde{\chi}$, respectively. Eq. (4) includes a sum over the Brillouin zone and the bands through Eq. (2), and can be recast as [82],

$$\tilde{\chi}_{a,b}(\mathbf{q}, \Omega) = \frac{1}{N} \sum_n \sum_{\mathbf{k}} a_{\mathbf{k}} b_{\mathbf{k}} \Theta_n(\mathbf{k}, \Omega). \quad (5)$$

$a = a_{\mathbf{k}}$ and $b = b_{\mathbf{k}}$ are generalized vertices that stand for either an isotropic (1) or Raman $[\gamma(\mathbf{k}, \mathbf{q})]$ or renormalized Raman $[\Gamma(\mathbf{k}, \mathbf{q})]$ vertex. $\Theta_n(\mathbf{k}, \Omega)$ is the response kernel, examples of which will be presented below.

The bare response is not gauge invariant, and charge conservation and screening lead to the final - exact and gauge-invariant - result for the response [89, 120, 126],

$$\chi_{\gamma,\gamma} = \tilde{\chi}_{\gamma,\gamma} - \frac{\tilde{\chi}_{1,\gamma} \tilde{\chi}_{\gamma,1}}{\tilde{\chi}_{1,1}} \left(1 - \frac{1}{\varepsilon} \right). \quad (6)$$

The projected structure of the first two terms is a result of charge conservation. The polarization-dependent vertex is written down explicitly as a subscript in Eq. (6), and ε in the third term is the dielectric function which originates from screening alone. Since a constant vertex can be pulled in front of the sum of Eq. (2) the first two terms of Eq. (6) cancel for constant γ (corresponding to lowest order A_{1g} symmetry and/or strictly parabolic dispersion), and only the last term survives but is suppressed as q^2/Ω_{pl}^2 in a charged system. In the fully symmetric channel having A_{1g} symmetry in the D_{4h} space group, applicable for most of the FeBCs, the response is at least partially screened.

4.4. Weakly interacting systems

The scattering from free electrons cuts off at $\hbar\Omega_{\text{max}}$ [127]. In a realistic normal metal with a single conduction band either impurities or interactions can maintain the $q = 0$ selection rule and facilitate the occurrence of broad continua extending to energies well above $\hbar\Omega_{\text{max}}$ [77, 128]. Obviously this is the case in all materials of interest with interactions including the FeBCs, the cuprates, the A15 compounds, MgB₂ and many others. However, only in the cuprates the argumentation is straightforward since in the single-layer compounds with only one CuO₂ plane per unit cell, for instance La_{2-x}Sr_xCuO₄, there is a single conduction band. Somewhat surprisingly, the response in the double-layer compounds (two neighboring CuO₂ planes) such as YBa₂Cu₃O_{6+y} is nearly identical to that in materials with just one CuO₂ plane. It was in fact shown that the contributions from individual bands in multi-band systems just add up to a good approximation not only in the cuprates [129] but also in the FeBC [117] allowing one, as a starting point, to treat the response in a band basis and neglect inter-band transition.

If we disregard spurious contributions to the cross section such as luminescence (being a good approximation at low energies; see, however, Ref. [57]) only (dynamic) interactions can produce the broad continua observed [81, 130]. Impurities are present but irrelevant in high-quality single crystals as can be seen directly below T_c since impurities reduce the effect of pair breaking in the Raman spectra. As shown by Klein and Dierker [73] the response of a clean isotropic superconductor has a square root singularity at the gap edge 2Δ in the limit $q = 0$. In the presence of impurities (and similarly for finite q [73]) the singularity disappears and the response at 2Δ becomes finite and scales as $\Delta\tau_0$, where τ_0 is the impurity scattering time [110, 111, 112]. In all realistic cases the difference between the normal and superconducting spectra cannot be observed any further for $\hbar\tau_0^{-1} \rightarrow \Delta$. Therefore, the continuum in superconductors essentially comes from dynamical interactions between the conduction electrons and other excitations which are gapped out below T_c for $\hbar\Omega \lesssim 2\Delta$. In nearly all superconductors which have been studied by light scattering this conclusion holds. The only exception is the A_{1g} response in A15 compounds where the normal state intensity vanishes [103, 131].

Although the normal state continuum generally signals the presence of strong interactions, it is impossible to describe the superconducting response in terms of strong-coupling theory so long as the microscopic origin of the relevant interactions is unknown. Only in the case of spin fluctuations both the normal and the superconducting spectra have been modelled microscopically on equal footing [113]. In a few cases phenomenological descriptions on the basis of Eliashberg theory were applied [112, 132, 133, 134].

In the majority of cases, the weak-coupling result [73] is used since it is sufficient to capture the generic properties of the superconducting state. The response kernel is given by the Tsuneto-Maki (TM) function [135],

$$\Theta''_{\mathbf{k},\text{TM}}(\Omega, T) = \frac{\pi}{2} \frac{|2\Delta_{\mathbf{k}}|^2}{\Omega \sqrt{\Omega^2 - |2\Delta_{\mathbf{k}}|^2}}; \quad \Omega > |2\Delta_{\mathbf{k}}|. \quad (7)$$

It is the result of a superposition of particle excitations across the gap from an occupied into an unoccupied state and pair breaking. Both contributions have a square-root singularity at $|2\Delta_{\mathbf{k}}|$ and, because of the coherence factors, add constructively in the case of light scattering and destructively in the case of the (real part of the) optical (IR) conductivity $\sigma'(\Omega)$ [136].

In the case of a charge or spin density wave the functional form of the response close to the density-wave gap $|2\Delta_{\text{DW}}|$ is also described by Eq. (7) [137] if the material is insulating below the transition. In a metal the best way of describing the response is the superposition of a normal metallic response (see

next section) and a condensate in the spirit of a two-fluid model [82]. In all metallic cases there is an incomplete redistribution of spectral weight from low to high energies starting abruptly at the transition temperature. The line shape is comparable to that of a superconductor having an anisotropic gap with BaFe_2As_2 being a prototypical example for SDW formation in the pnictides [38].

4.5. Collision limited regime

The simplest type of response in the normal state in systems with vanishingly small $\hbar v_F q$ results from the presence of (heavy) impurities. Here the electrons change only their momentum but not their energy (Drude model). The gauge-invariant kernel was derived by Zawadowski and Cardona [77],

$$\Theta''_{\mathbf{k},D}(\Omega) = \frac{\pi}{2} \frac{\hbar \Omega \Gamma_{\mathbf{k}}^*}{(\hbar \Omega)^2 + (\Gamma_{\mathbf{k}}^*)^2}, \quad (8)$$

where $\Gamma_{\mathbf{k}}^* = \hbar(\tau_{\mathbf{k}}^*)^{-1}$. $\tau_{\mathbf{k}}^*$ is not identical to the electronic relaxation time but is renormalized by a (presumably small) channel-dependent vertex correction, similarly as in ordinary transport where the vertex corrections ensure (among other things) that forward scattering does not contribute to the resistivity. $\Gamma_{\mathbf{k}}^*$ is temperature and energy independent.

If the electrons scatter from excitations in the energy range of $k_B T$ such as phonons, spin fluctuations or among themselves they transfer both momentum and energy. As a consequence they become dressed quasi-particles, and the relaxation rate depends now on energy, momentum and temperature. Due to these interaction effects, the electron velocity gets reduced and the mass increases by the same factor $1 + \lambda_{\mathbf{k}}(\Omega, T)$, and the extended Drude response reads [81]

$$\Theta''_{\mathbf{k},eD}(\Omega, T) = \frac{\pi}{2} \frac{\hbar \Omega \Gamma_{\mathbf{k}}^*(\Omega, T)}{(\hbar \Omega [1 + \lambda_{\mathbf{k}}(\Omega, T)])^2 + [\Gamma_{\mathbf{k}}^*(\Omega, T)]^2}. \quad (9)$$

The energy and temperature dependent projected parameters $\Gamma_{\mathbf{k}}^*(\Omega, T)$ and $1 + \lambda_{\mathbf{k}}(\Omega, T)$ can be derived if $\Theta''_{\mathbf{k},eD}(\Omega, T)$ is known for a sufficiently wide energy interval [81]. The zero-energy extrapolation value of $\Gamma_0(T) = \Gamma_{\mathbf{k}}^*(\Omega \rightarrow 0, T)$ can be compared with ordinary or optical transport, for instance. Shastri and Shraiman [138] noticed that the relation between the Raman response and the real part of the optical conductivity, $\Theta''_{\mathbf{k},(e)D}(\Omega, T) \propto \Omega \sigma'(\Omega, T)$, is a good approximation in many cases, in particular if the momentum dependence is weak.[§] In this sense $\Theta''_{\mathbf{k},(e)D}(\Omega, T)/\Omega$ is a momentum dependent ‘‘Raman conductivity’’.

An expression equivalent to Eq. (9) can be derived for the superconducting or a density-wave state

[§] The reason is that σ' is always an average over the entire Fermi surface whereas $\Theta''_{\mathbf{k},(e)D}$ is not (see below).

in terms of Eliashberg theory. It is considerably more complicated, and the normal state continuum and the gap excitations are closely interrelated [113]. Since this analysis was not used in the case of for the FeBCs so far we do not reproduce it here. The interested reader can consult Refs. [132] and [134]. Qualitatively, the continuum is gapped out below 2Δ for zero temperature and increases continuously for $0 < T \leq T_{c(DW)}$ due to the presence of thermal excitations. In the zero-energy limit $\chi'' \propto \Omega$, and the initial slope reflects the anomalous (Nambu) Raman relaxation rate $\Gamma_{0,\mu}^{SC(DW)}$ inside the gap being similarly difficult to analyze as the relaxation rates in NMR, microwave or ultrasound absorption experiments, in particular in unconventional systems.

All results summarized here are essentially lowest-order response theory. However, the experiments in $\text{Ba}_{1-x}\text{K}_x\text{Fe}_2\text{As}_2$ and $\text{Na}(\text{Fe}_{1-x}\text{Co}_x)\text{As}_2$ show [41, 46, 47, 49] that higher order corrections may be necessary for the proper interpretation and for extracting relevant information on the pairing in the superconducting state [47, 90, 91, 115, 118].

4.6. Beyond lowest order

Eq. (7) is the lowest-order approximation of the response and is not gauge invariant as already pointed out by Klein and Dierker [73]. The controversy as to whether or not the resulting vertex corrections are relevant for the interpretation in the A15 materials is still not settled [73, 89, 94, 103, 139]. A similar narrow in-gap mode as in the E_g response of the A15s was observed recently in BKFA where it is well separated from the pair-breaking peak [46]. A mode in the $d_{x^2-y^2}$ channel (1 Fe unit cell) with this property was predicted by Scalapino and Devereaux [91] for a two-band model applicable to the FeBCs. Chubukov and coworkers predicted an A_{1g} mode originating from the same type of mechanism for a different hierarchy of pairing instabilities.

The existence of in-gap modes in a superconductor was first noticed by Bardasis and Schrieffer (BS) [140]. They studied the effect of final state interaction in the presence of an anisotropic pairing potential $V_{\mathbf{k},\mathbf{k}'}$ and found undamped modes below the gap edge, $\hbar \Omega_{L,M} < 2\Delta$, which are characterized by quantum numbers L and M corresponding to the expansion of $V_{\mathbf{k},\mathbf{k}'}$ into spherical harmonics. These collective excitations, usually called BS modes, are similar to excitons in semiconductors with binding energy $E_{b,L,M} = 2\Delta - \hbar \Omega_{L,M}$. For simplicity they may be referred to as $E_{BS,\alpha}$ labelled by α in consecutive order. The result was adopted for light scattering in superconductors [89] and is formally similar to light scattering from roton pairs in superfluid ^4He [88, 141]. The predictions include symmetry selection rules and the dependence of $E_{BS,\alpha}$

and the strength of the pole $Z_{BS,\alpha}$ on the relative coupling strength of the sub-leading channels $\alpha > 1$ with respect to the ground state $\alpha = 1$, λ_α/λ_1 . As pointed out in Refs. [90] and [91] the analysis of these excitons would help in clarifying the so far elusive pairing mechanism in the FeBCs.

The functional form of the response additional to lowest order [Eq. (7)] reads [91],

$$\Delta\tilde{\chi}''(\Omega) = \frac{8}{\Omega^2} \Im \left\{ \frac{\langle \gamma(\mathbf{k})g(\mathbf{k})\Delta(\mathbf{k})\bar{P}(\Omega, \mathbf{k}) \rangle^2}{(\lambda_d^{-1} - \lambda_s^{-1}) - \langle g^2\bar{P}(\Omega, \mathbf{k}) \rangle} \right\}, \quad (10)$$

where $\gamma(\mathbf{k})$ is the usual Raman vertex, $g(\mathbf{k})$ is the d -wave-like formfactor on the electron bands for making the interaction between them separable, and $\bar{P}(\Omega, \mathbf{k})$ is the complex superconducting response kernel the imaginary part of which is given in Eq. (7). Eq. (10) was used in Ref. [47] for estimating the value of the sub-leading $d_{x^2-y^2}$ coupling parameter λ_d from the electronic Raman spectra of BKFA for a given s -wave coupling strength λ_s . Identical expressions with redefined coupling parameters were derived for explaining the nematic resonance [39]. Similarly as in the case of excitons, there may be more than one BS mode in the presence of several sub-leading coupling channels. This possibility was considered recently in a theoretical study [92].

In a system with more than one band there is an additional contribution to the response from number-phase oscillations between the bands in momentum space comparable to the Josephson effect in real space [95]. It must be included to make the response gauge invariant, as pointed out recently by Cea and Benfatto [99]. Usually, for instance in the cases studied theoretically by Suhl and coworkers [142], which is possibly realized in MgB₂, the main contribution to superconductivity comes from coupling in the individual bands having strength $\lambda_{i,i}$. The inter-band coupling $\lambda_{i,j}$ is weaker but leads to an increase of T_c to values above the maximum of the individual bands. It is widely believed that the main contribution to pairing in the FeBC has its origin in inter-band [9] or inter-orbital [143] coupling and that the intra-band pairing is weak. The effect of weak inter-band coupling was investigated already earlier in the context of MgB₂ [96, 97] whereas strong inter-band coupling was addressed only recently in the context of the FeBCs [98, 99, 100]. The symmetry properties of the Leggett modes depend sensitively on the orbital content [98, 100].

For weak inter-band coupling, the mode related to the number-phase fluctuations is below the gap energy and increases essentially linearly with $\lambda_{i,j}$. For $\lambda_{i,i} \ll \lambda_{i,j}$ the Leggett mode is in the continuum above 2Δ and is therefore overdamped. Figure 4 shows the transition between the two coupling regimes and demonstrates

Figure 4. Response from Leggett modes in a two-gap system. N_i is the density of states on band i . η encodes the ratio of intra- to inter-band coupling with $\eta = -1$ and $\eta = 1$ representing pure intra- and inter-band coupling, respectively. The mode's energy saturates at the maximal gap. The damping starts above the smaller gap. From [99] with permission.

the damping effect. In addition, it could be shown that the energy saturates at the maximal gap energy.

4.7. Spin excitations

For spin excitations the Elliot-Fleury-Loudon Hamiltonian [62] is the simplest nonresonant interaction operator which describes scattering in a Heisenberg model with nearest-neighbour exchange coupling J ,

$$\hat{H}_{\text{EFL}} = J \sum_{\langle i, \hat{\delta} \rangle} (\hat{\delta} \cdot \hat{\mathbf{e}}_I)(\hat{\delta} \cdot \hat{\mathbf{e}}_S)(\mathbf{S}_{\mathbf{r}(i)} \cdot \mathbf{S}_{\mathbf{r}(i)+\hat{\delta}a}). \quad (11)$$

$\mathbf{S}_{\mathbf{r}(i)}$ is a spin at site $\mathbf{r}(i)$, a is the distance between the sites and $\hat{\delta}$ is a unit vector pointing towards one of the nearest neighbors. $\langle i, \hat{\delta} \rangle$ is a restricted sum to avoid double counting. The spectral shape can either be determined in terms of spin-wave theory [62], by numerical [64] or field theoretical methods [144]. In the thermodynamic limit (infinitely large systems) of a spin-only model the low-energy limit is characterized by an Ω^3 variation of the response [145, 146, 144, 147]. If there exist itinerant electrons in addition to localized spins, such as proposed for FeSe for instance [148, 149, 150], the spin response may be superimposed on an electronic continuum. Possible interrelation effects have not been explored yet.

In anisotropic systems two-magnon excitations may be observed well above T_N . Then the evolution of the two-magnon line is continuous over large temperature ranges below and above T_N [151]. Thus the line shape and the temperature dependence of the response allows one to clearly distinguish the scattering from localized and itinerant spins as described at the end of section 4.4.

Screening may become relevant in metallic systems such as the FeBCs in which the spins forming the SDW are itinerant as opposed to the cuprates which are Mott insulators at low doping. However, there is no analytic treatment yet dealing with the problem of light scattering from spin polarized conduction electrons beyond SDW formation or the

Raman scattering in Fe-based systems

nearly antiferromagnetic Fermi liquid [152]. Doped cuprates were studied using Quantum Monte Carlo methods [153, 154]. Considerations along these lines may surface when analyzing the differences between the pnictides and chalcogenides where the magnetism is believed to be predominantly itinerant and localized, respectively, at least for some orbitals [149, 155, 156, 157, 158]. However, this rather general problem cannot be solved here although the controversial discussion on spin excitations in the FeBCs requires additional work.

4.8. Fluctuations

In the case of fluctuations, there are three possibilities to deal with the $q = 0$ selection rule. (i) A fluctuation can have zero momentum. This case applies if all unit cells have the same excitation pattern as for the case of ferro-orbital fluctuations [49]. (ii) A fluctuation with finite critical wave vector such as $\mathbf{q}_c = (\pi, \pi)$ or $\mathbf{q}_c = (\pi, 0)$ for incipient Néel type or stripe-like antiferromagnetic order, respectively, can exchange momentum with another excitation or a defect. The case of moderately high defect concentrations was studied by Gallais and Paul [116]. The momentum transferred by the photons is certainly insufficient for large critical momenta (see section 4.3). (iii) Two fluctuations with opposite momenta are exchanged. It is exactly what happens in the case of two-magnon excitations in a system with long-ranged order [62, 159]. The same type of scattering may also occur in partially ordered systems [160] or in the presence of critical fluctuations [83]. This type of diagrams were first studied by Aslamazov and Larkin in the context of paraconductivity above the superconduction transition [161].

For the FeBCs there are various theoretical studies on the Raman response of fluctuations [118, 115, 85, 86, 87]. Although spin, orbital, and charge degrees of freedom are not independent, the question as to the leading instability remains relevant and crucial for the understanding of the FeBCs [40, 49, 115, 116, 118, 162, 163, 164, 165, 166].

4.9. Selection rules

In an inelastic light scattering experiment, all selection rules must be compatible with the direct product of two dipole transitions in the relevant crystal structure [119]. Figure 5 shows the main scattering geometries and the related sums of projected symmetries μ of the D_{4h} point group relevant for FeBCs (and cuprates). The pure symmetries can only be obtained by linear combinations of the spectra measured in appropriate geometries. The symmetry selection rules are generally valid and well known for, e.g., phonons. We now consider those for spin and charge excitations.

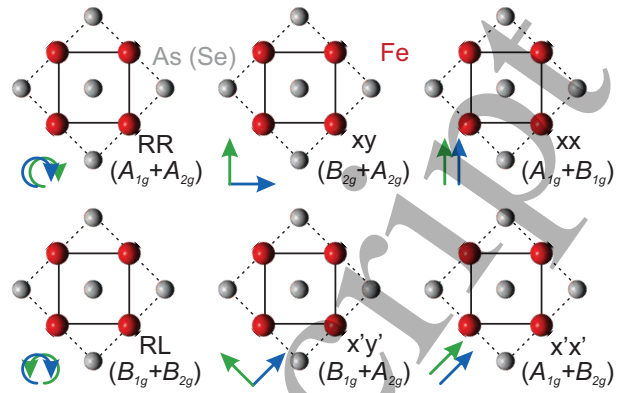


Figure 5. Scattering geometry and symmetries for the ab plane of FeBCs. Incoming and scattered photon polarizations are indicated as blue and green arrows. In backscattering configuration, the arrows corresponding to R and L polarization of the scattered light should be interchanged. The symmetries refer to the 1Fe unit cell (full line) which is relevant (and frequently used) for electronic and spin excitations. Phonons have the right symmetry in the crystallographic or 2Fe unit cell (broken line) where B_{1g} and B_{2g} are interchanged with respect to the 1Fe cell.

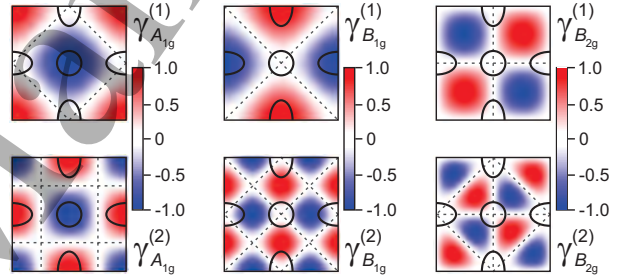


Figure 6. Symmetry properties and momentum dependences of the Raman vertices γ_μ . Shown are the first and second order vertices (form factors) for the symmetries $\mu = A_{1g}, B_{1g}$ and B_{2g} of the D_{4h} point group. The zeroth order A_{1g} vertex is just a constant and is entirely screened. Higher order A_{1g} vertices are only partially screened. The solid lines represent an idealized two-band Fermi surface of FeSCs in the 1Fe unit cell. For the symmetry properties of the band structure in the FeBCs the screening in A_{1g} symmetry is almost negligible [117].

4.9.1. Particle-hole and gap excitations In the simplest approximation the vertices relevant for the projections in the Brillouin zone can be expanded into crystal harmonics of the respective point group [167]. Figure 6 shows the related symmetry form factors μ .

In first order approximation selection rules can be derived on the basis of symmetry alone since $\gamma_\mu(\mathbf{k}, \mathbf{q} \rightarrow \mathbf{0})$ can be expanded into the set of basis functions $\Phi_\mu(\mathbf{k})$ [82]. Figure 6 shows schematic representations of the first and second order basis functions (crystal harmonics) of each symmetry to which the Raman vertices γ_μ are proportional. For particle-hole excitations, symmetry-resolved Raman vertices can be derived from the band structure within

the effective mass approximation,

$$\gamma_{n,A_{1g}}(\mathbf{k}, \mathbf{q} \rightarrow 0) \propto \frac{1}{2} \left(\frac{\partial^2 \varepsilon_n(\mathbf{k})}{\partial k_x \partial k_x} + \frac{\partial^2 \varepsilon_n(\mathbf{k})}{\partial k_y \partial k_y} \right) \quad (12)$$

$$\gamma_{n,B_{1g}}(\mathbf{k}, \mathbf{q} \rightarrow 0) \propto \frac{1}{2} \left(\frac{\partial^2 \varepsilon_n(\mathbf{k})}{\partial k_x \partial k_x} - \frac{\partial^2 \varepsilon_n(\mathbf{k})}{\partial k_y \partial k_y} \right) \quad (13)$$

$$\gamma_{n,B_{2g}}(\mathbf{k}, \mathbf{q} \rightarrow 0) \propto \left(\frac{\partial^2 \varepsilon_n(\mathbf{k})}{\partial k_x \partial k_y} \right), \quad (14)$$

where n is the band index. The vertex for each symmetry μ is obtained by summing over all bands crossing E_F .

The first-order diagram on the right hand side of Fig. 3(a) describes particle-hole excitations above and below T_c upon using the propagators for either the normal or the superconducting state. The evaluation yields the Raman response which depends quadratically on $\gamma_\mu(\mathbf{k})$. The vertices for $\text{Ba}(\text{Fe}_{1-x}\text{Co}_x)_2\text{As}_2$ and $\text{Ba}_{1-x}\text{K}_x\text{Fe}_2\text{As}_2$ were calculated in Refs. [36] and [47] yielding $\gamma_{A_{1g}}^{(1)}$ rather than $\gamma_{A_{1g}}^{(1)}$ to be relevant for presumably most of the FeBCs. As can be seen from Fig. 6, in the B_{1g} symmetry ($\gamma_{B_{1g}}^{(1)}$) one may expect to probe electron pockets, whereas both electron and hole pockets may be probed in A_{1g} symmetry ($\gamma_{A_{1g}}^{(2)}$). The dependence of the Raman response on $\gamma_\mu^2(\mathbf{k})$ directly explains the selectivity in k -space.

4.9.2. Bardasis Schrieffer modes The selection rules for BS modes depend on the symmetry of the sub-leading interaction. The first proposals considered a ground state being driven by spin fluctuations thus having an s_\pm -wave gap with opposite sign on the electron and hole bands. Then, if the sub-leading channel originates from orbital fluctuations, predominantly along the $(\pi, 0)$ direction [143], the BS mode is expected in the A_{1g} channel [90]. Alternatively, the next strongest pairing interactions can have the same origin as the ground state resulting from spin fluctuations between the electron bands along (π, π) thus entailing a BS mode in B_{1g} symmetry.

4.9.3. Leggett modes The symmetry selection rules for the Leggett modes depend on the interactions included and thus on the band structure and the coupling. If two concentric bands or interactions with wave-vector $(\pi, 0)$ are included the Leggett mode appears in the fully symmetric A_{1g} channel [99]. In the case when (π, π) interactions have to be considered, in particular if the central hole band is missing, the Leggett modes appear in B_{1g} symmetry [100]. In the case of fluctuations between the d_{xz} and d_{yz} orbitals Leggett modes may also appear in B_{1g} symmetry so long as they are not overdamped [98].

4.9.4. Fluctuations Fluctuation contributions to the Raman response may arise from one and/or two fluctuations [see Fig. 3(b)]. As can be seen from the diagrams, the first order term is non-vanishing only if the symmetry of the fluctuation is that of the Raman vertex. On the other hand, second order diagrams include electronic loops $\Lambda_\mu^0(\mathbf{q})$ which depend linearly on γ and quadratically on f . Consequently, for a given critical vector \mathbf{q}_c and a set of FS hot spots \mathbf{k}_0 which are connected by \mathbf{q}_c , the selection rules for the second order term read $\Lambda_\mu^0(\mathbf{q}_c) \propto \sum_{\mathbf{k}_0} \gamma_\mu(\mathbf{q}_c)$ [83]. It states that a finite response in symmetry channel μ is expected only if \mathbf{q}_c connects hot-spots in which γ_μ does not change sign. As opposed to the first order term, γ_μ does not necessarily reflect the symmetry of the fluctuation for second order processes.

5. Instabilities beyond superconductivity

The phase diagram (Fig. 1) shows that the FeBCs have a multitude of instabilities beyond superconductivity. Their interrelation amongst each other and with superconductivity is a main focus of research. For certain ranges of doping and/or applied pressure all FeBCs exhibit long range magnetism while remaining metallic in contrast to undoped cuprates. Some of the FeBCs like FeSe display only short-ranged magnetic order at finite temperature [157, 168]. Not surprisingly, the nature of the magnetism is still under discussion. It was shown recently that the degree of localization of electrons and thus spins may depend on the orbital and varies between the materials [149].

Above the magnetic ordering temperature there are various structural transitions which typically go along with electronic anisotropies such as substantial differences in the resistivities measured along inequivalent directions [28] or orbital order, specifically of the d_{xz} and d_{yz} orbitals [169]. Yet, how can the origin of these differences be pinned down?

5.1. Excitations from localized spins

While itinerant and localized magnetism cannot easily be distinguished by neutron scattering, Raman scattering offers clear criteria [55] which are outlined in sections 4.4 and 4.7. The main arguments are the temperature, doping and symmetry dependences and line shapes.

Early experiments on Fe chalcogenides and pnictides reported excitations in the range 2000 to 4000 cm^{-1} in all symmetries. The results were interpreted in terms of local spins [27, 31], and the energies are in fact compatible with the exchange coupling $J \approx 120 \text{ meV}$ found by neutron scattering or density functional theory (DFT) [170]. With the improvement of the sample quality, the peaks in

this range faded away and may be traced back to luminescence with high probability [43].

Recent experiments in FeSe support scattering from localized spins. The B_{1g} spectra at high (300 K) and low (20 K) temperature are dominated by a broad peak centred at approximately 500 cm^{-1} , whereas near T_S an additional sharp peak appears in the range $100\text{--}200 \text{ cm}^{-1}$ [53, 57, 55] which we disregard here but discuss in detail below in the context of fluctuations. The main peak in B_{1g} symmetry at 500 cm^{-1} depends continuously on temperature [55] and survives low doping with sulfur [57]. For FeS the excitation is completely gone. In contrast to Massat *et al.* [53] and Zhang *et al.* [57], Baum and coworkers [55] assign this peak to a two-magnon excitation of nearly frustrated spins.

There are experimental and theoretical arguments for this assessment. Very generally, antiferromagnetically ordered local spins give rise to two-magnon excitations close to $3J$ [62] whereas SDW order in a metallic system leads to instantaneously appearing coherence effects close to the gap energy in the electronic excitation spectrum similar to those in a superconductor (see section 4.4). In FeSe, the pronounced excitation in B_{1g} symmetry on top of the particle-hole continuum builds up gradually [53, 55]. Thus the temperature dependence of the scattering intensity is compatible with that of a quasi two-dimensional Néel antiferromagnet, e.g., $\text{YBa}_2\text{Cu}_3\text{O}_6$ [151]. However, the energy of the B_{1g} peak is too small by approximately a factor of five, suggesting frustrated magnetism, as studied theoretically already in pnictides and chalcogenides [64], expected from LDA results [170], and explored recently for FeSe using exact diagonalization [171].

On a square lattice, frustration can occur in the presence of interactions beyond nearest-neighbour coupling. In this case, a variety of ordering patterns or wave vectors may be realized. A possible model is the $J_1 - J_2 - J_3 - K$ Heisenberg model [170] where nearest, next-nearest and next-next-nearest neighbour exchange couplings are taken into account. K is the coefficient of the bilinear interaction proportional to $(\mathbf{S}_i \cdot \mathbf{S}_j)^2$ which, depending on the sign (de)stabilizes long-range order. For $J_2 \approx 0.5J_1$ Néel (π, π) and stripe $(\pi, 0)$ order occur with similar probability for $J_3 \rightarrow 0$ and are separated by a $(\pi, \pi/2)$ phase for $J_3 > 0$ [170]. In all cases, little energy is required for flipping a spin, and the maximum of the two-magnon excitation moves to zero energy in the classical limit ($S \rightarrow \infty$) and to approximately $0.5J_1$ for $S = 1/2$ as opposed to $2.84J_1$ when J_1 dominates [144]. The near degeneracy of the Néel and the stripe state going along with short range order in FeSe was not only predicted by LDA studies [170] but also observed recently by neutron scattering [157].

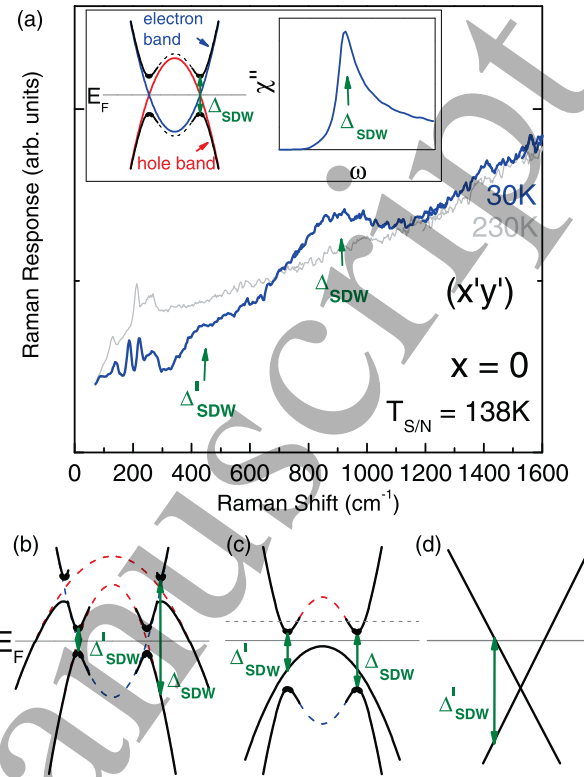


Figure 7. (Color online) Effect of SDW formation on the Raman response of BFA. (a) High- and low-temperature Raman response in $x'y'$ configuration. The spectra show two spectral features at Δ_{SDW} and Δ'_{SDW} . The inset shows the anti-crossing of the hole and electron band and the related opening of Δ_{SDW} . The Raman response (right) is given by Eq. (7). (b) If one electron band and two hole bands anti-cross Δ_{SDW} is much larger than Δ'_{SDW} . (c) If one of the hole bands does not reach the Fermi level the two gaps are expected to have similar magnitude. For phase-space reasons the response at Δ_{SDW} has higher spectral weight than that at Δ'_{SDW} in case (b) in comparison to case (c). (d) In the presence of a Dirac cone (non-interacting bands) Δ'_{SDW} should be characterized by very small spectral weight, and Δ_{SDW} is not expected to be observable. From [26] with permission.

The B_{1g} response in FeSe was studied theoretically for zero and finite temperature by diagonalizing a 4×4 cluster carrying spin 1 using $J_2 = 0.528J_1$ and $J_3 = 0$ [55, 171]. The observed agreement between theory and experiment is semi-quantitative for all symmetries. The conclusions are in agreement with those of the neutron scattering experiments [157] and support the existence of local spins. How are local spins compatible with metallic transport in FeSe and why is FeSe different from the pnictides? Before discussing this question in section 5.4 the SDW systems and fluctuations will be reviewed.

5.2. Spin density wave order

Signatures of the SDW in the Raman spectra of BFA were first discussed by Chauvière *et al.* [26].

Figure 7 compares the low and high temperature B_{1g} Raman response. Spectral weight is redistributed from energies below to above the SDW gap upon entering the SDW state. The Raman spectra exhibit two distinct features: A peak at about 900 cm^{-1} appearing only in B_{1g} symmetry and a step-like increase at about 400 cm^{-1} in all channels [26].

The B_{1g} selection rules for inter-orbital transitions would be compatible with a transition $d_{x^2-y^2} \leftrightarrow d_{z^2}$ to correspond to the peak at 900 cm^{-1} . Yet, this straightforward explanation is in conflict with band-structure calculations which find the dominant contribution to the states at the Fermi surface to originate from d_{xz} , d_{yz} , and d_{xy} orbitals. Thus intensity can only be redistributed among these orbitals. Consequently, a band-folding picture was suggested with two types of electronic transitions in the SDW state: (i) a high-energy transition between electron and hole bands anti-crossing after back-folding and (ii) a low-energy transition involving either interacting or noninteracting bands. Upon Co substitution, the peak observed in B_{1g} symmetry disappears due to the increase of the Fermi energy and the related filling of the unoccupied states at the anti-crossing points [26].

A much more pronounced redistribution of spectral weight was reported for Sr122 [43] with a suppression at low energies and three distinct peaks at 820 cm^{-1} , 1140 cm^{-1} and 1420 cm^{-1} appearing in B_{1g} symmetry. The peak at 820 cm^{-1} is also present in B_{2g} symmetry. In A_{1g} symmetry no peaks can be resolved. On the basis of the symmetry selection rules the authors argue that the peaks at 1140 cm^{-1} and 1420 cm^{-1} originate from anti-crossing bands in the presence of imperfect nesting rendering the X and Y points inequivalent. The peak at 1420 cm^{-1} appears only well below T_{SDW} and was explained in terms of a temperature dependent Fermi surface topology and the disappearance of a hole-like Fermi surface pocket very close to the chemical potential in the reconstructed SDW electronic structure. The peak at 820 cm^{-1} is assigned to an optical transition between folded bands away from the $\Gamma - X$ and $\Gamma - Y$ directions which are probed in xy configuration.

Recently Zhang *et al.* [34] reported spectral weight redistribution in twinned Eu122 and detwinned mono-domain Ca122 single-crystals in the SDW phase, as shown in Fig. 8. In the $x'y'$ [$\equiv XY$] configuration, spectral weight is transferred from low energy to above 800 cm^{-1} with the development of a peak at 1220 cm^{-1} and 1060 cm^{-1} for Ca122 and Eu122, respectively [see panels (a2) and (b2) in Fig. 8]. For de-twinned Ca122 a large intensity anisotropy of the 1220 cm^{-1} peak is observed in xx and yy scattering configurations [see panel (a3) in Fig. 8]. In addition, a weak spectral

feature is observed at 830 cm^{-1} in $x'x'$ [$\equiv XX$] and xy scattering configurations as indicated by arrows. The authors derive the selection rules for inter- and intra-orbital transitions on the basis of the D_{2h} group for the high symmetry points in the Brillouin zone. The symmetry analysis, augmented by an orbital-resolved DFT+DMFT study [34], suggests that the peak at 1200 cm^{-1} in the A_g symmetry channel originates from an intra-orbital transition at the Z point induced by the SDW band folding, whereas the peak at 830 cm^{-1} in the B_{1g} channel arises from the $d_{xz} \leftrightarrow d_{yz}$ transition at the Γ point.

The analysis of the Raman spectra in the SDW state shows that the typical gaps induced by ordering of the magnetic moments of itinerant electrons are in the range of $100\text{--}150\text{ meV}$ or $8k_B T_{\text{SDW}}$. This ratio is in the same range as that of the superconducting gap, and one cannot conclude that T_{SDW} is suppressed by fluctuations as, for instance, in the tritellurides [137]. Rather, the large value may indicate strong coupling. Whether or not the $a - b$ anisotropy of the gap energy found in Ca122 [34] is a generic feature of all pnictides cannot be decided on the basis of the material at hand. However, a strong electronic anisotropy was also found in the energy range of $2\text{--}3\text{ eV}$ in Ba122 below T_{SDW} when studying resonance effects of the A_g arsenic phonon [172]. Thus, anisotropies in the electronic structure were identified by Raman scattering at low and high energies in the magnetically ordered phase.

5.3. Fluctuations above the ordering transitions

There are various types of instabilities in the FeSCs which can drive the phase transitions. While some groups consider magnetic ordering the dominant interaction [9, 173], Kontani *et al.* see orbital ordering in the driver's seat [174]. These basic considerations were studied in some detail and refined recently. A tendency towards charge-driven or Pomeranchuk-type order was found for FeSe using either Hubbard models with strong coupling between spin and orbitals [163] or renormalization group (RG) schemes on model band structures [164, 165] or orbital-dependent nesting properties [166]. For the pnictides these studies favor spin-driven nematicity and explain, on a qualitative basis, the proximity of the nematic and the magnetic transitions and the absence of magnetism in the chalcogenides. This rather incomplete selection of theoretical work already highlights the importance of experimental studies for clarifying the issue.

Since strong fluctuations precede the structural transitions in many compounds, experimental access to the fluctuations is highly desirable. Raman spectroscopy is among the handful of techniques available but does not probe the fluctuations alone. Rather, since the FeBCs are metals the contribution

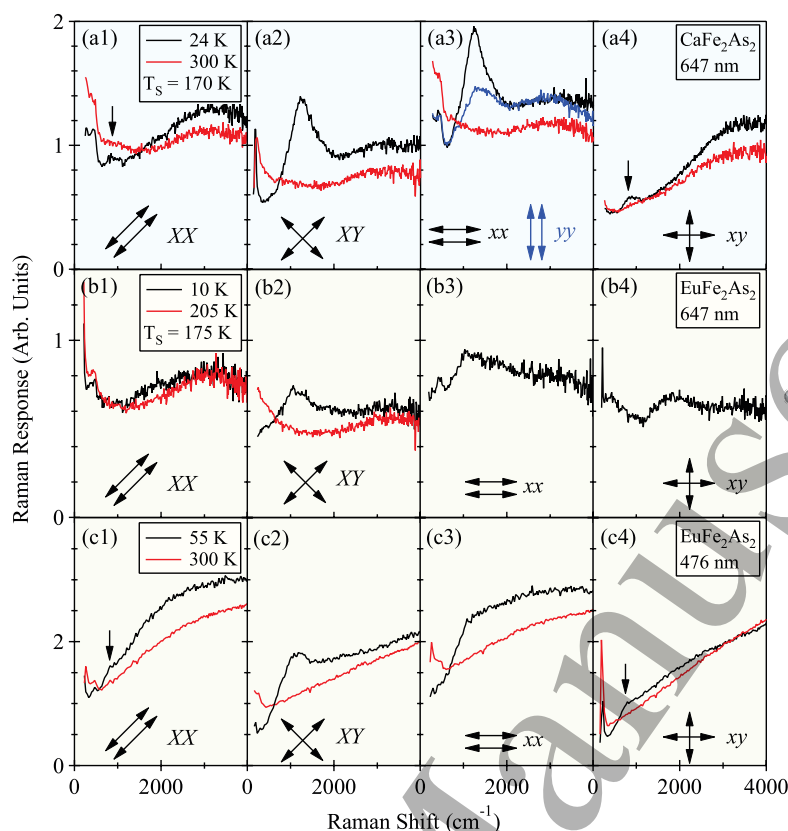


Figure 8. (Color online) Effect of SDW order in the Raman spectra of CaFe_2As_2 and EuFe_2As_2 . The unit cell on the right which the polarizations in the panels refer to is added to the original figure for clarity. Note the notations $X \equiv x'$ and $Y \equiv y'$. (a1)-(a4) Spectra of CaFe_2As_2 measured with 647 nm laser excitation in the normal state (300 K, red) and in the SDW phase (24 K, black/blue) of a twin-free sample. (b1)-(b4) Raman response of EuFe_2As_2 in the normal state (205 K, red) and the SDW state (10 K, black) of a twinned sample. (c1)-(c4) Same as (b1)-(b4) with 476 nm laser excitation. From [34] with permission.

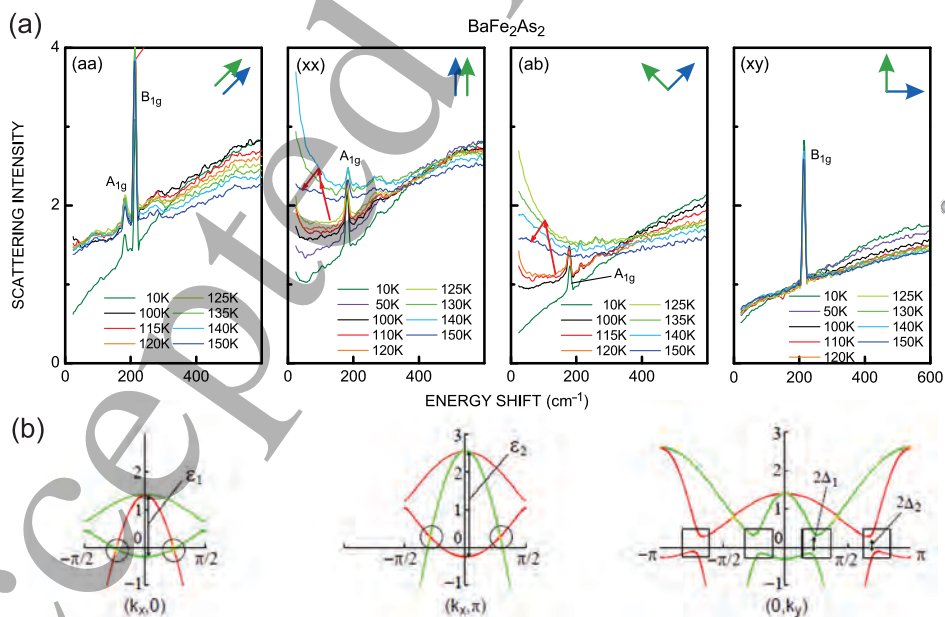


Figure 9. (Color online) (a) Low-energy Raman spectra of BaFe_2As_2 at temperatures as indicated. The pictograms displaying the unit cell and the polarizations are added to the original figure for clarity. The two central panels (xx) and (ab) $\equiv x'y'$ show contributions from fluctuations at low energy and the redistribution of spectral weight from below to above 350 cm^{-1} upon cooling through $T_{\text{SDW}} \approx 135 \text{ K}$ as indicated by red arrows. (b) Electron dispersions in $(k_x, 0)$, (k_x, π) , and $(0, k_y)$ direction. The circles denote the Dirac nodes, and the squares denote the “anti-nodes” where the electrons interact. From [27, 32] with permission.

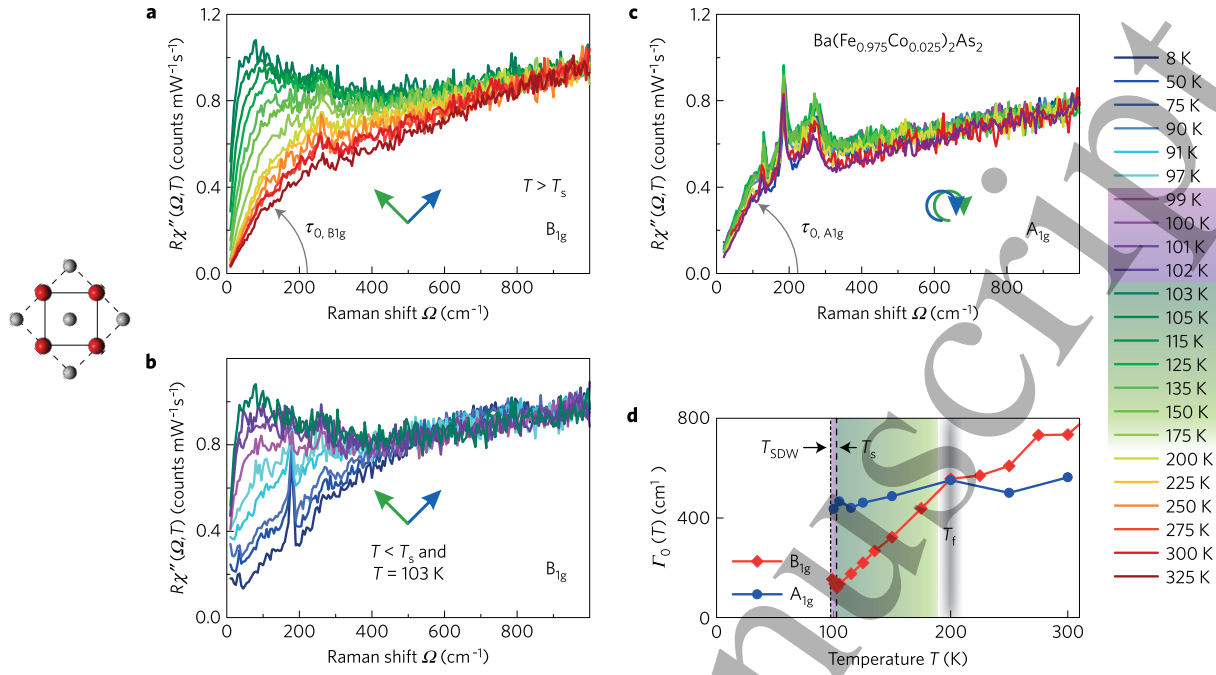


Figure 10. (Color online) Polarization-resolved Raman results for $\text{Ba}(\text{Fe}_{0.975}\text{Co}_{0.025})_2\text{As}_2$. (a)–(c) Response $R\chi''(\Omega, T)$ at temperatures as indicated. The pictograms for the polarizations were added. (a) B_{1g} spectra above and (b) below T_S . (c) A_{1g} response. The initial slopes defined in (a) and (c) by grey arrows are proportional to the static two-particle lifetime $\tau_{0,\mu}$ in symmetry $\mu = A_{1g}, B_{1g}$. (d) Raman relaxation rates $\Gamma_{0,\mu}(T) = \hbar/\tau_{0,\mu}(T)$, in A_{1g} (blue circles) and B_{1g} (red diamonds) symmetry as a function of temperature. The A_{1g} and B_{1g} data above T_f closely follow the resistivity. The fluctuation range $T_S < T < T_f$ and the nematic phase $T_{SDW} < T < T_S$ are shaded green and magenta, respectively. From [40] with permission.

is always superimposed on the particle-hole continuum which needs to be taken into account for quantitative analyses.

A contribution from fluctuations to the Raman spectra of FeBCs were first reported by Choi *et al.* [29]. They observed a pronounced build up of the low energy Raman response in Sr122 upon cooling towards T_S and suggested a magnetic nature of the fluctuations. The similar build up of the low-energy signal in the B_{1g} channel was also observed for Ba122 by Sugai *et al.* [27, 32] as presented in Figure 9. The authors attributed the low-energy $x'x'$ [$\equiv aa$] and xy spectra to excitations near Dirac nodes where the bands intersect without interacting [circles in Fig. 9(b)] and the xx and $x'y'$ [$\equiv ab$] spectra to the “anti-nodal” excitations where the back-folded bands interact [squares in Fig. 9(b)]. The increase of the low-energy scattering intensity was interpreted in terms of critical fluctuations related to the opening of the anti-nodal gap.

Several detailed studies of fluctuations in both pnictides and chalcogenides were presented more recently in Refs. [30, 33, 35, 40, 44, 49, 53, 116, 175, 176]. As discussed in section 4.8, one and/or two fluctuations may contribute to the Raman spectra via distinct scattering processes. Gallais and Paul [116] and Thorsmølle *et al.* [49] point out that the first order term has a non-zero contribution only in the presence

of momentum scattering processes (or, equivalently, finite $v_F q$). On the other hand, the second order AL diagrams may include contributions having $q \gg 0$.

Gallais and coworkers suggested to use the static limit of the real part of the response, $\chi'_{B_{1g}}(\Omega = 0, T)$, for analyzing the Raman data and comparing them to the results of other quasi-static methods such as NMR or elasticity. $\chi'_{B_{1g}}(\Omega = 0, T)$ was directly extracted from $\chi''_{B_{1g}}(\Omega, T)$ via Kramers-Kronig transformation, $\chi'_{B_{1g}}(\Omega = 0, T) = \pi^{-1} \int d\Omega \chi''_{B_{1g}}(\Omega, T)/\Omega$, where $\chi''_{\mu}(\Omega, T)/\Omega$ has the meaning of a channel dependent Raman conductivity. This procedure requires an extrapolation of $\chi''_{B_{1g}}(\Omega, T)$ to zero energy and the selection of a high-energy cutoff since $\chi''_{B_{1g}}(\Omega \rightarrow \infty, T) \approx c$ where c is a constant. The method was applied to the analysis of the data of BFCA [30, 116] (see next paragraph) and subsequently of Eu/Sr122 [33, 44], BKFA [176], and Na111 [49]. Thorsmølle *et al.* demonstrated the scaling of the static susceptibility obtained from Raman scattering and NMR data for Na111. Consequently, low energy quasielastic scattering was related to d^{\pm} quadrupolar nematic fluctuations which became critical on approaching a Pomeranchuk instability with a deformation of the Fermi surface [177, 178].

The low-energy Raman response in differently doped BFCA was extensively studied by Gallais *et al.* [30, 116]. The authors argue that the

nematic susceptibility is observable in the B_{1g} channel and originates from charge fluctuations for symmetry reasons since inelastic light scattering couples preferably to the charge. They observe a strong enhancement of the B_{1g} response $\chi''_{B_{1g}}(\Omega \approx k_B T, T)$ upon cooling towards T_S and a collapse thereof in the orthorhombic/SDW state, whereas the B_{2g} response is essentially temperature independent. First, $\chi'_{B_{1g}}(\Omega = 0, T)$ was determined. Second, it is shown that this quantity is equal to the quasi-static nematic susceptibility and, in fact, compares well to the Young modulus $c_{66}(T)$ derived from thermal expansion [116, 179]. Interestingly, neither $c_{66}(T)$ nor $\chi'_{B_{1g}}(\Omega = 0, T)$ diverge at T_S due to the coupling of the electronic/spin degrees of freedom to the lattice [30, 116, 180]. As a consequence, the divergence of $\chi'_{B_{1g}}(\Omega = 0, T)$ derived from a Curie-Weiss fit occurs always below the structural transition, $T_0 < T_S$.

Kretzschmar *et al.* [40] focused their attention on BFCA at finite doping where the magnetic ordering temperature and the structural transition are separated ($T_{SDW} < T_S$) as shown in Figure 10. The memory function method [81] was used for extracting the static Raman relaxation rates $\Gamma_0(T)$ in A_{1g} and B_{1g} symmetry and for facilitating the identification of the cross-over temperature T_f below which the contributions from fluctuations become detectable in the B_{1g} channel.

The fluctuations and the particle-hole continuum can only be considered additive if they get excited through independent scattering channels such as, e.g., phonons and charge excitations. If two fluctuations are excited simultaneously (AL mechanism) the response from fluctuations exists independent of other excitations, otherwise the excitations are entangled. In order to separate the fluctuation contribution, the high temperature particle-hole continuum ($T > T_f$) was extrapolated down to low temperatures by varying $\Gamma_0(T)$ in a way that the initial slope of the spectra matches the transport results and was subtracted from the respective total Raman response.

It is considered the key observation of that paper that the fluctuations do not disappear directly below T_S but continuously lose spectral weight with the peak maximum staying pinned. This indicates a nearly constant correlation length between T_S and T_{SDW} . The persistence of the fluctuations down to T_{SDW} and their immediate disappearance below T_{SDW} favours their magnetic origin.

For LaFeAsO and $\text{Sr}(\text{Fe}_{1-x}\text{Co}_x)_2\text{As}_2$ the analysis arrives at slightly different conclusions for the temperature dependence but similar ones for the origin of the fluctuations [35, 44]. In both compounds the maxima of the fluctuation response do not coincide with the structural transition temperature, and in

$\text{Sr}(\text{Fe}_{0.8}\text{Co}_{0.2})_2\text{As}_2$ the fluctuations do not disappear right below the magnetic ordering temperature. Some of the discrepancies may be related to the time scale of the fluctuations relative to that of the phonons. In fact, the peak positions indicate much slower dynamics in $\text{Sr}(\text{Fe}_{0.8}\text{Co}_{0.2})_2\text{As}_2$ than in the other materials. In addition, inhomogeneities in the Co content may contribute. It is certainly necessary to study more doping levels before concluding finally.

The spectral shape of the fluctuations can be described quantitatively in terms AL-type of diagrams if electron-phonon interaction is included [83]. Otherwise the decay on the high-energy side is too slow [118, 115]. The corresponding selection rules (see section 4.9) yield $\mathbf{q}_c = (\pi, 0)$ as the wave vector of the critical fluctuations. Furthermore, it was demonstrated that the initial slope of the fluctuation response χ''_{fluct} exhibits qualitative agreement with the temperature dependence of the nematic susceptibility in the tetragonal and the nematic phase, as expected from a Ginzburg-Landau type of consideration. A comparison of BFCA and BKFA and details of the analysis are further discussed in Ref. [181].

In FeSe, having a structural transition at $T_S \approx 90\text{ K}$ and short-ranged but no long-ranged magnetic order above 4 K [157, 168], the fluctuations survive down to temperatures right above $T_c \approx 9\text{ K}$ [53, 57, 55]. The experimental results, of the three groups of authors agree with each other in the energy and temperature range where they can be compared. We show the results of Massat *et al.* in Figure 11 and describe those in B_{1g} symmetry in detail. At 295 K [upper part of panel (a)] a broad peak at 50 meV is observed which is unique for FeSe (and $\text{FeSe}_{1-x}\text{S}_x$ for $x \leq 0.2$). In the pnictides or in pure FeS it is absent, the spectra are nearly flat and the overall intensity in all symmetry projections is similar. Upon cooling, this peak first gains intensity. Below 200 K an additional structure starts to appear at some 20 meV which becomes clearly discernible in the yellow spectrum at 142 K [see also and panel (b)]. At $T_S = 90\text{ K}$ (black) it peaks at 4-5 meV and has maximal intensity. The peak at 50 meV stays nearly pinned and has now almost twice the intensity as at 295 K. Below 90 K [panel (c)] the low energy peak survives down to at least 45 K (Baum *et al.* [55] can resolve it even at 20 K) and moves to lower energies reaching some 2 meV directly above T_c while losing most of its intensity. The redistribution of spectral weight in the superconducting state shows directly that the remaining intensity below 15 meV originates from particle-hole excitations as in the pnictides. Concomitantly, the peak at 50 meV hardens slightly and increases further. Baum *et al.* [55] argue that the persistence of the fluctuations well below T_S is supportive of spin fluctuations similar to

those in BFCA, whereas Massat *et al.* [53] assign the fluctuations to charge and/or orbital physics and the peak at 50 meV to interband transitions. Zhang *et al.* [57] interpret the quasi-elastic peak at low-energy in terms of ferro-quadrupole fluctuations of a d -wave Pomeranchuk instability at $q = 0$ and the assign the reduction of the intensity below 50 meV and T_S to the opening of a gap in the electronic excitation spectrum following the lattice distortion.

In a recent preprint [87] Udina *et al.* present a detailed gauge-invariant study of the charge part of the low-energy Raman response in FeSe and assign the temperature dependence of the spectra to the relative shift of the Fe $3d_{xz}$ and $3d_{yz}$ orbitals in the nematic phase. The authors predict the variation of the spectral shape below T_S and find that the energy of the quasi-elastic peak increases with decreasing temperature if an order-parameter-like variation of the orbital splitting is assumed (see Fig. 3 of Ref. [87]). This variation leads to a gap-like suppression of the intensity at low energies and resembles the temperature dependent intensity of the fluctuation peak, whereas the energy of the quasi-elastic peak increases below T_S at variance with the experimental findings (see last preceding paragraph).

Massat and coworkers apply an analysis similar to that in BFCA for studying FeSe at ambient [53] and applied pressure [15], as shown in Figure 11. The spectra for $P = 0$ exhibit a pronounced temperature dependence in the B_{1g} channel [Figure 11(a)-(c)]. The real part of the static Raman susceptibility $\chi'_{B_{1g}}(\Omega = 0, T)$, as derived from the “Raman conductivity” $\chi''_{B_{1g}}(\Omega, T)/\Omega$, follows a Curie-Weiss law with T_0 significantly lower than T_S for reasons discussed above in agreement with the stiffness data. With increasing pressure [Fig. 11(e)] T_S decreases, and above 2 GPa the SDW is the dominating phase with T_{SDW} reaching 45 K at approximately 5 GPa [Figure 11(d)] [182]. With the appearance of the SDW phase above 2 GPa the Curie-Weiss-type variation of $\chi'_{B_{1g}}(\Omega = 0, T)$, as determined from the spectra in Fig. 11(f), disappears as opposed to the observations in BFCA. Apparently, the magnetism in FeSe has aspects different from those in the pnictides.

5.4. Origin of the excitations: spin or charge?

There is no consensus yet on the leading instability in the FeBCs, and there are arguments in favor of both orbital and spin ordering. This controversy characterizes also the interpretation of the Raman data, in particular those of the fluctuation response. It is true that photons couple to the charge, and if the vertex has the same symmetry as the fluctuations, there is coupling. However, this does not exclude other types of fluctuations to couple to the light; in other words, the selection rules and the coupling

argument are not sufficient for deciding between spin and charge.

Selection rules similar to those of charge excitations can also be derived for spin fluctuations owing to the specific band structure of the FeBCs [40, 83]. Given the issue with the selection rules, the temperature dependence may be used as another criterion, since critical fluctuations are expected to disappear immediately at the corresponding ordering temperature. This disappearance is observed directly at $T_S \approx T_{SDW}$ in BFA [39, 40], at $T_{SDW} < T_S$ in BFCA [40], and not at all in FeSe without long-ranged order [53, 55]. $\chi'_{B_{1g}}(\Omega = 0, T)$ as an energy-integrated quantity possibly obscures this important detail to some extent. Therefore, we argue that spin fluctuations dominate the low-energy Raman spectra in most of the FeBCs but would not go so far as to say that there is evidence beyond reasonable doubt. However, we believe that the issue can be settled, presumably by light scattering, using a wide range of excitation energies in the visible range for tracking the resonance behaviour or by resonant inelastic x-ray scattering (RIXS) [183].

The second open question pertains to the nature of the short- or long-ranged spin ordering (which exists beyond any doubt): In the pnictides the spins of itinerant electrons order because of a Fermi surface instability [9, 184, 185], whereas the spins or at least some of the spins in the chalcogenides are more localized than in the pnictides [149, 186]. The signatures of these different types of order in the Raman spectra are relatively clear as can be directly seen by comparing the Raman response in cuprates to that in Ba122, for instance. However, it was argued that the band at 500 cm⁻¹ in FeSe originates from incoherent intra-band scattering [53] rather than spin excitations [55]. Yet, there are two considerations which are hard to reconcile with charge (particle-hole) excitations: (i) Since the energy of the band does not vary significantly upon cooling from 300 to 4 K, only momentum scattering having a scattering rate of approximately 500 cm⁻¹ and a temperature independent intensity [77] can be at its origin. (ii) With the scattering rate being an order of magnitude larger than the superconducting gap the gap excitations would be entirely suppressed [110, 111] as opposed to the experimental results [53, 55, 57].

On the other hand, the semi-quantitative agreement of the spectra in all symmetries with simulations

|| Coupling to the charge does not mean that the photons couple directly to low-energy charge excitations. Rather, the effective scattering Hamiltonian for particle-hole excitations close to E_F is an approximation derived for photon energies much smaller than the gaps in the band structure [63]. Why this approximation works quite well in the FeBCs and in the cuprates in the presence of low-lying bands is not entirely clear. It may have its origin in strong correlation effects which broaden all electronic states away from E_F and thus reduce resonances.

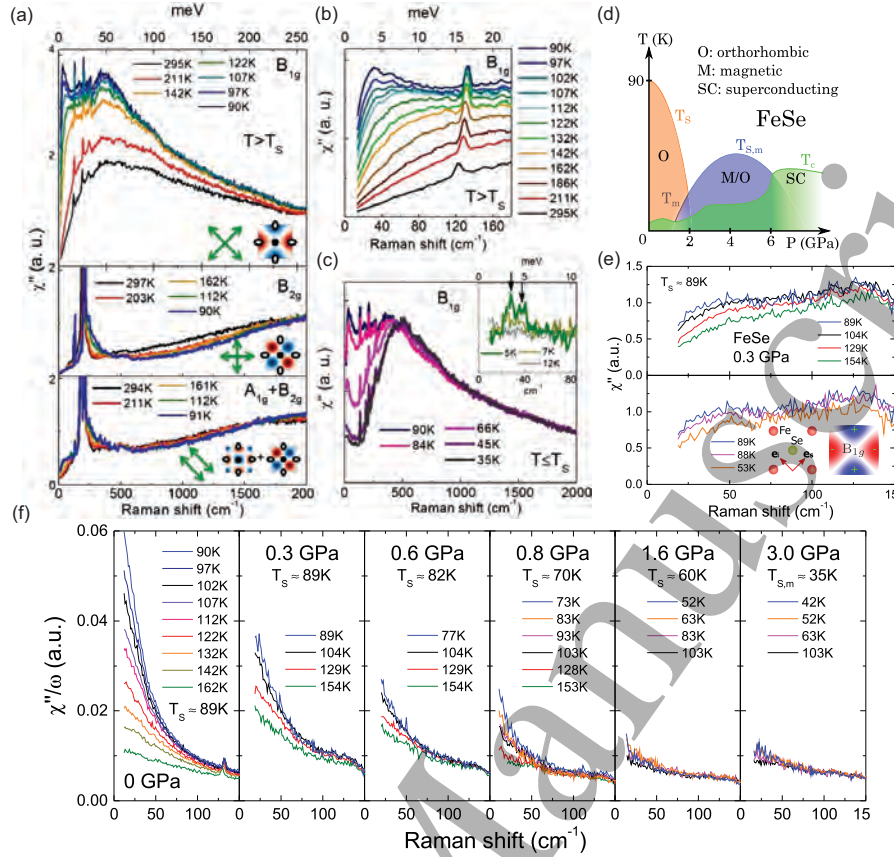


Figure 11. (Color online) Light scattering in FeSe. (a)-(c) Symmetry-dependent Raman spectra of FeSe above $T_S = 87$ K using photons at 2.33 eV. The sharp peaks superimposed on the electronic continuum are due to Raman active optical phonons. The insets display the Raman form factors in different symmetries (blue and red colors indicate positive and negative amplitudes, respectively), and the polarization configurations used to select them. (b) Temperature dependence of the low energy B_{1g} spectra above T_S . (c) Evolution of the B_{1g} spectra across T_S . The inset shows the spectra across the superconducting transition at $T_c = 8.5$ K. The arrows indicate the peaks associated with 2Δ . From [53] with permission. (d) Pressure-temperature phase diagram of FeSe. (e) B_{1g} response at $P = 0.3$ GPa and temperatures as indicated. (f) $\chi''(\omega)/\omega$ in B_{1g} symmetry for pressure values and temperatures as indicated. Panels (d)-(f) from [15] with permission.

[55, 171] provides an attractive explanation for the observed spectra. While the dependence (or independence) of the B_{1g} peak on S substitution [57] still needs to be clarified it does not seem to be a killer argument [187]. The orbital dependent localization [149, 156] provides the necessary explanation for the differences between the pnictides and chalcogenides, including the experimentally observed near localization of the electrons in the d_{xy} orbitals in FeSe as opposed to the by and large orbital-independent itineracy of the electrons in all bands in the pnictides [188]. RIXS as a rapidly developing technique may help to pin down the orbital character of the differently localized electrons [189].

In spite of all these arguments the problem is not settled, and the type of fluctuations and the leading instability may be different in the pnictides and chalcogenides as outlined in the beginning of sec. 5.3. Thus further criteria for the analysis of the B_{1g} Raman data were proposed recently including scaling arguments for the slope of the spectra in the zero-energy limit and for the real part of the static

susceptibility [86]. Klein *et al.* analyzed data of FeSe, Ba122 and $\text{NaFe}_{1-x}\text{Co}_x\text{As}$ and found support for a Pomeranchuk-type charge instability in FeSe and for spin fluctuations in the pnictides. Close to a quantum critical point being ubiquitous in the pnictides and chalcogenides energy power laws for the response were derived but were not tested yet against experiments [85].

6. Superconductivity

The identification of the pairing mechanism remains one of the major challenges in all unconventional superconductors. The momentum dependence of the gap magnitude (and phase, if possible) is among the important observables for addressing this question since $\Delta_{\mathbf{k}}$ and the pairing potential $V_{\mathbf{k},\mathbf{k}'}$ are interrelated via the BCS gap equation [190]. Therefore, a large variety of methods has been applied to derive properties of the energy gap in the iron-based materials with the goal to understand $V_{\mathbf{k},\mathbf{k}'}$ and the coupling [7].

Raman spectroscopy allows access to the magnitude of the gap [66, 73, 74], its number-phase fluctuations [95, 96, 97] and bound in-gap states encoding the anisotropy of $V_{\mathbf{k},\mathbf{k}'}$ [89, 90, 91, 140].

6.1. Gap spectroscopy

6.1.1. Results from canonical methods From the beginning, a substantial band and momentum dependence of the energy gap was observed. Yet, sign changes of the gap on individual bands or between the bands could not be pinned down unambiguously although tunneling experiments with an applied magnetic field [191] and neutron scattering experiments [192] supported unconventional order parameters in Fe(Se,Te) and BKFA, respectively. More pieces need to be added to solve the puzzle and clarify the type of pairing in the ground state.

Further complication arises since the gaps vary strongly between the families and with elemental substitution [12, 210, 211]. In BKFA at optimal doping band dependent gaps with little variation on the individual Fermi surfaces are observed by angle-resolved photoemission spectroscopy (ARPES) [201, 212], while the gaps vary rather strongly around the electron and hole pockets and along the k_z reciprocal axis in BFCA and overdoped BKFA [196, 199, 213, 214]. As a general feature, the maximal gaps observed across the families are in the range 6-8 in units of $k_B T_c$ similar to those in cuprates.

In Table 2 we compile characteristic results found by ARPES, specific heat (c_{el}), neutron scattering (INS) and tunneling spectroscopy (STS) and compare them to Raman results. It is instructive to have this overview in addition to the light scattering results which are usually more subject to controversy than the canonical methods, since data analysis is more difficult due to the appearance of additional electronic excitations close to or below the gap energy (cf. section 4.6).

6.1.2. Raman results Momentum- and band-resolved Raman results for the energy gap were first presented and discussed by Muschler *et al.* [25] and are shown in Fig. 12. They reported data of a complete symmetry analysis in the normal and superconducting states of optimally doped $\text{Ba}(\text{Fe}_{1-x}\text{Co}_x)_2\text{As}_2$ ($x = 0.061$). For the symmetry analysis the 2Fe unit cell was used, and the related projections in the Brillouin zone were discussed subsequently on the basis of an LDA band structure [36]. For comparison with Fig. 5 the B_{1g} and B_{2g} symmetries must be interchanged. The effect of superconductivity is best seen by comparing spectra taken well below and slightly above T_c similarly as in the case of an SDW (see Fig. 7).

In $\text{Ba}(\text{Fe}_{1-x}\text{Co}_x)_2\text{As}_2$, differences between the spectra above and below T_c which are associated with

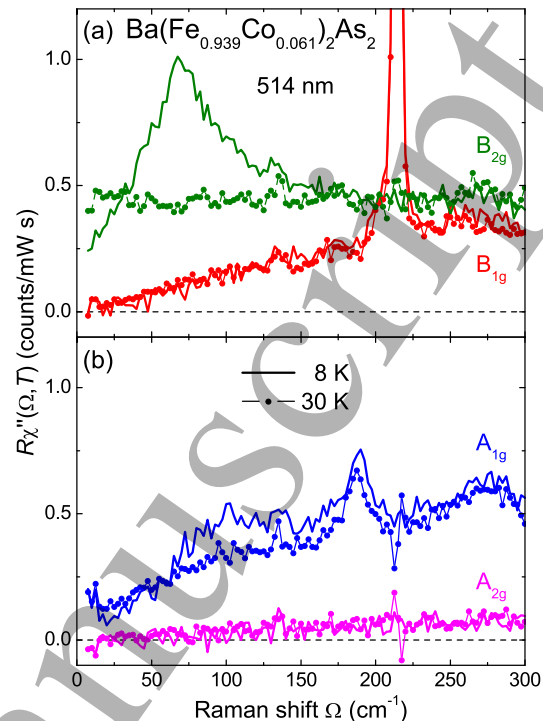


Figure 12. (Color online) Symmetry-resolved Raman response of $\text{Ba}(\text{Fe}_{1-x}\text{Co}_x)_2\text{As}_2$ ($x = 0.061$) for in-plane light polarizations right above (points) and well below T_c (full lines). The redistribution of intensity typical for superconductivity is observed only in (a) B_{2g} and (b) A_{1g} symmetry. (a) In this study, the 2Fe unit cell was used for the symmetry assignment implying that the out-of-phase Fe phonon at 214cm^{-1} is observed in the proper B_{1g} symmetry. (b) In A_{1g} symmetry there is a small increase for $\Omega \rightarrow 0$ from insufficient rejection of the laser light. The A_{2g} signal can safely be neglected at low energies. From [25] with permission.

the opening of the superconducting gap are observed only in A_{1g} and B_{1g} symmetry. In A_{2g} the intensity is generally low for the absence of excitations having the right symmetry. In B_{2g} symmetry little spectral weight is expected since the vertices are small close to the Fermi surface crossings of the bands. Surprisingly, the intensity becomes comparable to that in A_{1g} and B_{1g} symmetry at approximately 300cm^{-1} but there are no indications of an energy gap. There are essentially three explanations for the absence of gap structures: (i) The intensity originates from excitations other than electron-hole pairs such as spins. The slow increase of the B_{2g} intensity indicates either that (ii) states far away from the Fermi surface are projected consistent with the vertices or that (iii) the relaxation rate is much higher than expected from transport. Such an anisotropy may occur if the quasi-particle relaxation is strongly momentum dependent for the presence of Co scatterers in the Fe plane. Then the gap excitations are suppressed for specific symmetry projections [112]. We consider (iii) the most likely explanation since spin excitations are already very weak at optimal doping

Table 2. Compilation of gap energies in Fe-based superconductors as observed by angle-resolved photoemission (ARPES), tunneling (STS), optical (IR) and Raman spectroscopy. For selected cases we show also the results of thermodynamic measurements (c_{el}) and neutron scattering (INS) revealing local gap minima and, respectively, the spin resonance energy which are typically below the maximal gap. In the third last column the maximal gap of each method is given in units of $k_B T_c$. A similar compilation of the results and a discussion may be found in Refs. [8] and [193]. In particular in the case of ARPES but also for some of the thermodynamic and Raman measurements the entries are not exhaustive and display only typical values. In some Raman studies the data of B_{1g} symmetry were fitted using one, two or three gap scenarios as indicated. For four samples of BKFA the data of all symmetries were fitted simultaneously using a phenomenology including collective modes [41, 47]. In some cases the peak frequencies alone are reproduced. For the analysis of the IR spectra the theory by Mattis and Bardeen [136] was applied. The BFCA sample used for STS [194] had a nominal doping of $x = 0.10$ but the T_c is more compatible with optimal doping.

Material	T_c [K]	Method	$2\Delta_i$ [meV]	$2\Delta_i$ [cm^{-1}]	$2\Delta_{\text{max}}$ [$k_B T_c$]	Ref.	comment
Ba(Fe_{1-x}Co_x)₂As₂							
$x = 0.051$	19	ARPES	8.0/11.6		7.1	[195]	el/h band
$x = 0.051$	18	Raman	3.7...7.4/9.9	40...60/80	6.4	[181]	B_{1g}/A_{1g} peaks
$x = 0.052$	20	c_{el}	3.1/7.1		4.1	[196]	min/max gap
$x = 0.055$	20.5	Raman	5.0	41		[38]	B_{1g} ; 1-gap
$x = 0.055$	23	Raman	8.7/12.4	65/105	5.9	[181]	B_{1g}/A_{1g} peaks
$x = 0.060$	24	Raman	4.1/9.3	33/75	4.5	[38]	B_{1g} ; 2-gaps
$x = 0.061$	24	Raman	8.7/12.4	70/100	5.9	[25]	B_{1g}/A_{1g} ; aniso.
$x = 0.060$	25	c_{el}	4.3/10.8		5.0	[196]	min/max gap
$x = 0.065$	24.5	Raman	1.9/8.9	15/72	4.2	[38]	B_{1g} ; 2-gaps
$x = 0.067$	25	INS	8.0 \pm 1			[195]	spin resonance
$x = 0.067$	25	ARPES	9.2/13.0		6.0	[195]	el/h band
$x = 0.075$	25.5	ARPES	10/13.8		6.2	[197]	el/h band; isotropic
$x = 0.075$	23.5	Raman	9.7	78	4.8	[38]	B_{1g} ; 1-gap
$x = 0.085$	23	c_{el}	4.0/8.7		4.4	[196]	min/max gap
$x = 0.085$	22	Raman	9.3/11.8	75/95	6.2	[25]	B_{1g}/A_{1g} peaks
$x = 0.095$	19	ARPES	9.2/11.2		6.8	[195]	el/h band
$x = 0.100$	25.3	STS	12.5 \pm 3.0		5.7	[194]	average; OPT?
$x = 0.100$	20	Raman	9.8	79	5.7	[38]	B_{1g} ; 1-gap
Ba_{1-x}K_xFe₂As₂							
$x = 0.22$	24.6	Raman	3.1...13.7	25...110	6.5	[41]	only B_{1g} peaks
$x = 0.25$	26	ARPES	7.8/15.7		7.0	[198]	el/h bands
$x = 0.25$	31	c_{el}	1.9/16.0		6.0	[199]	min/max gap
$x = 0.25$	31	Raman	6.0, 20.0	48, 161	7.5	[48]	B_{1g} peaks
$x = 0.25$	30.9	Raman	7.4, 18.6	60, 150 \pm 20	7.0	[41]	B_{1g} peaks
$x = 0.27$	31	IR	13.7/27.1	110/218	10.1	[200]	Mattis-Bardeen
$x = 0.35$	38.9	Raman	9.9...31.8	80...256	9.5	[41]	phenomenology
$x = 0.40$	38	INS	14			[192]	spin resonance
$x = 0.40$	38	ARPES	12/24		7.5	[201]	min/max gap
$x = 0.40$	38	ARPES	8/24		7.5	[202]	min/max gap; k_z
$x = 0.40$	38	ARPES	7.2/20.4		6.2	[203]	min/max gap; k_z
$x = 0.40$	37	STS	30		\approx 9.4	[204]	
$x = 0.40$	39.0	IR	18.6/31.0	157/263	9.7	[200]	Mattis-Bardeen
$x = 0.40$	38.5	Raman	8.4...32.0	68...258	9.6	[46, 47]	phenomenology
$x = 0.42$	38.5	c_{el}	2.3/24.2		7.3	[199]	min/max gap
$x = 0.43$	36.7	Raman	6.2...31.0	50...250	9.8	[41]	phenomenology
$x = 0.48$	34.3	Raman	4.0...20.0	32...161	6.8	[41]	phenomenology
$x = 0.51$	34.2	c_{el}	2.1/17.7		6.0	[199]	min/max gap
$x = 0.62$	26.6	Raman	7.4...13.7	60...110 \pm 10	6.0	[41]	peak energies
$x = 0.70$	22	c_{el}	2.1/9.1		4.8	[199]	min/max gap
$x = 0.70$	21.6	Raman	6.2...11.2	50...90 \pm 10	6.0	[41]	peak energies
CaKFe ₄ As ₄	35	ARPES	16/24		8.0	[205]	el/h band
CaKFe ₄ As ₄	35	Raman	15.5/26.7	125/215	8.8	[50]	all symmetries
CaKFe ₄ As ₄	35	Raman	13.6/16.8/20.2	110/135/162	6.7	[51]	B_{1g} ; 3-gaps
BaFe₂(As_{0.65}P_{0.35})₂							
BaFe ₂ (As _{0.7} P _{0.3}) ₂	30	ARPES	12/15.2		5.9	[207]	nodal gap
BaFe ₂ (As _{0.5} P _{0.5}) ₂	18.2	c_{el}	4.8		3.1	[208]	average gap
BaFe ₂ (P _{0.5} As _{0.5}) ₂	16	Raman	6.7	54	4.9	[176]	B_{1g}
FeSe							
FeSe	9	STS	5.0/7.0		9.0	[209]	
FeSe	8.5	Raman	3.6/4.7	29...38	6.4	[53]	B_{1g}
FeSe	8.9	Raman	3.0...4.6	24...37	6.0	[57, 55]	B_{1g}

and B_{2g} gap features indeed appear in $\text{Ba}_{1-x}\text{K}_x\text{Fe}_2\text{As}_2$ where the substitution generates only out-of-plane defects [46].

In superconducting BFCA [25], the broad maximum close to 100 cm^{-1} and the well-defined peak at around 70 cm^{-1} in A_{1g} and B_{1g} symmetry, respectively, correspond to gap excitations in the hole and the electron band. Finite spectral weight observed down to very small energies indicates vanishingly small gaps. The $\sqrt{\Omega}$ dependence in B_{1g} symmetry suggests accidental nodes [215].

Similar spectra were reported for doping levels in the range $0.045 \leq x \leq 0.10$ [37, 38, 181, 216] where broad pair-breaking peaks appear in A_{1g} symmetry between 50 cm^{-1} and 160 cm^{-1} . The B_{1g} spectra generally peak at lower energy than those in A_{1g} symmetry. In both symmetries the spectral changes upon entering the superconducting state become less pronounced below and above optimal doping [38, 181, 216]. In A_{1g} symmetry the peak maxima scale approximately as $6k_B T_c$ in agreement with $2\Delta_{\max}$ from other methods. The B_{1g} spectra peak at $4k_B T_c$ at optimal doping and at $3k_B T_c$ for $x < 0.055$.

The discussion about the details of the interpretation of the spectral shape in superconducting BFCA is not finally settled although the data agree and the basic features are clear. Chauvière *et al.* [38] interpret their B_{1g} results for optimally doped and underdoped samples in terms of a two-gap scenario with a maximal gap $2\Delta_{\max} \approx 75\text{ cm}^{-1}$ and a small but finite gap $2\Delta_{\min} \approx 15\text{ cm}^{-1}$ (see Table 2). The maximal superconducting gap appears in the same location in momentum space as the SDW gap and is thus suppressed rapidly below optimal doping by the opening of the larger SDW gap, $2\Delta_{\text{SDW}} > 2\Delta_{\max}$, and only the feature related to $2\Delta_{\min}$ survives. The spectral shape in B_{1g} symmetry may also be reproduced with a strong k_z dependence of $\Delta_{\mathbf{k}}$ but the disappearance of the structure at $2\Delta_{\max}$ in underdoped samples can only be explained with an in-plane anisotropy.

Muschler *et al.* [25] argue that the $\sqrt{\Omega}$ variation of the low-energy B_{1g} spectra can be explained with accidental nodes or near-nodes on the outer electron band. This would be in agreement with the results from heat transport [217] and theoretical considerations [36]. Sugai *et al.* find support from band structure calculations for the B_{1g} intensity (1 Fe cell) to originate from the hole bands [37]. The latter conclusion is at variance with symmetry arguments (cf. Fig. 5) and the LDA results of Mazin *et al.* [36]. As a matter of fact, the gap in BFCA is very anisotropic at all doping levels and may even vanish for certain momenta. The maximum is in the range $2\Delta_{\max} \approx 6k_B T_c$. Below optimal doping there is an interaction with the SDW gap.

The observation of gap features in other pnictides and in chalcogenides was delayed by sample and surface issues. In chalcogenides the observation of pair breaking succeeded first in $\text{Rb}_{0.8}\text{Fe}_{1.6}\text{Se}_2$ after cleaving the sample *in situ* at low temperature [46]. Differences between normal and superconducting spectra were only found in B_{1g} symmetry. Since $\text{Rb}_{0.8}\text{Fe}_{1.6}\text{Se}_2$ has presumably no hole pockets, the B_{1g} selection rule supports the symmetry assignment of Refs. [25] and [36] as reproduced in section 4.9. The observed gap appears to be almost constant on the electron pockets, being compatible with either a simple *s*- or a *d*-wave state without nodes on the Fermi surface and a sign change between the pockets. From what we shall see below *d*-wave symmetry is more likely but cannot be distinguished from an *s*-wave gap on the basis of the light scattering experiment. As in the case of BFCA, it is difficult to explain the intensities in other symmetries which do not show features induced by superconductivity. As a hypothesis which needs to be worked out in more detail we assign the continua in A_{1g} and B_{2g} symmetry to excitations in lower lying bands and/or the tails of the numerous phonon lines.

In $\text{Ba}_{0.6}\text{K}_{0.4}\text{Fe}_2\text{As}_2$ continua and gap structures are observed in all symmetries and are by and large in agreement with the results from other methods [46] as shown in Table 2. Since the hole-like Fermi surfaces are more extended in the Brillouin zone, the relevant electronic states are well sampled by all vertices. Second, the simulations using the effective mass approximation arrive at a semi-quantitative explanation of the spectra [47]. Third, the effect of defects induced by K doping in the Ba layer is expected to be weak. Finally, resonance effects may contribute [41, 49, 65] although they were found to be mild in BFCA [36].

The spectra of $\text{Ba}_{0.6}\text{K}_{0.4}\text{Fe}_2\text{As}_2$ clearly show a small but true gap of approximately 30 cm^{-1} indicating, among other things, that the contributions from luminescence are negligible here. The largest gaps reside on the middle hole band and on the electron bands and are rather sharp as opposed to BFCA. The gap maximum $2\Delta_{\max}$ reaches almost 10 in units of $k_B T_c$ [46, 47]. This large ratio exceeds the ARPES results and, in particular, the gap ratio derived from the electronic specific heat as a typical bulk method [199]. However, thermally activated behaviour is generally sensitive to the small gaps on the individual bands. These minimal gap energies are typically 180 cm^{-1} or 6.8 in units of $k_B T_c$ in the phenomenological analysis [47, 41] thus reconciling Raman scattering and thermodynamic measurements.

In addition to the pair-breaking features, the B_{1g} spectra show unexpected structures below $2\Delta_{\max}$ which, as opposed to the pair-breaking features, have

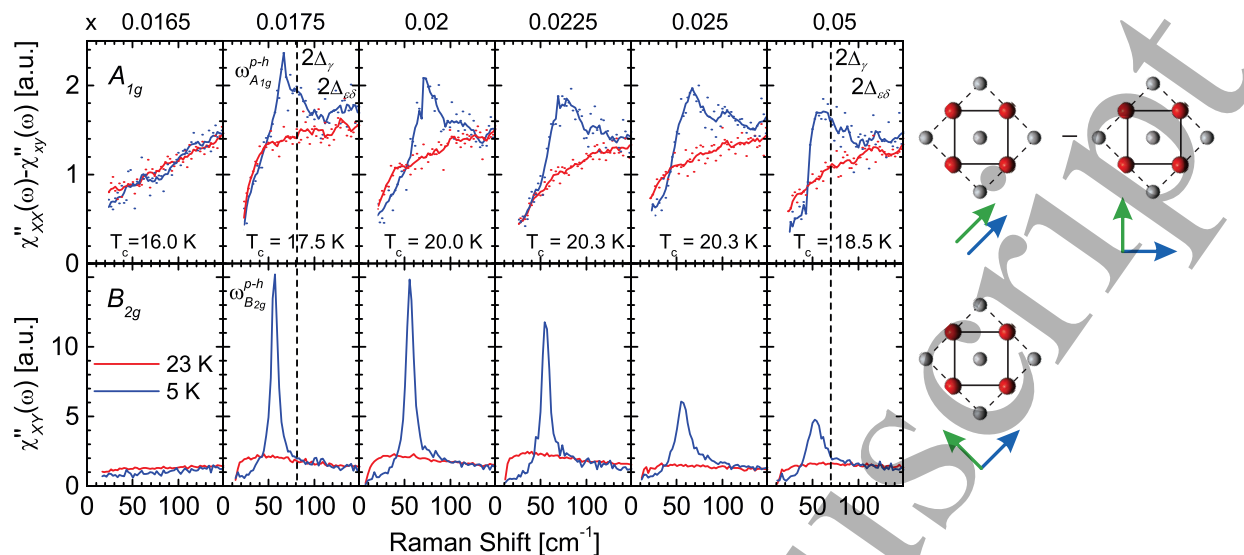


Figure 13. (Color online) Raman susceptibilities of $\text{Na}(\text{Fe}_{1-x}\text{Co}_x)\text{As}_2$ in the normal (red) and superconducting (blue) states for excitation with blue photons (476 nm). From [49] with permission. The pictograms were added by the authors for clarity. (a) $\chi''_{xx}(\omega) - \chi''_{yy}(\omega)$ (top row) and $\chi''_{xy}(\omega)$ (bottom row) in the superconducting (5 K) and normal (23 K) states at doping levels as indicated. The vertical dashed lines, shown for $x = 0.0175$ and 0.05 , indicate the lowest superconducting gaps $2\Delta_\gamma \simeq 10$ meV and 9 meV, respectively, determined by ARPES. B_{2g} symmetry in the figure corresponds to B_{1g} used in this review.

a nearly resolution limited width and will be discussed in detail in the following section. Here we first wrap up observations of the energy gaps by Raman scattering in other compounds.

A pair-breaking peak was also observed in the A_{1g} spectrum of $\text{BaFe}_2(\text{As}_{0.5}\text{P}_{0.5})_2$ [48] with the spectral weight decreasing linearly towards low frequencies indicating the presence of nodes in agreement with recent ARPES results for optimally doped $\text{BaFe}_2(\text{As}_{0.65}\text{P}_{0.35})_2$ [207] but, at first glance, not with thermodynamic results on a material with comparable doping [208] (see Table 2). However, the small value of the thermodynamically derived gap indicates a substantial anisotropy also for $\text{BaFe}_2(\text{As}_{0.5}\text{P}_{0.5})_2$ which may be concealed by the notion of a single (average) gap.

Very recently, pair-breaking features were observed in $\text{CaKFe}_4\text{As}_4$ [50, 51]. Depending on the incoming photon energy, gap features are observed either in all symmetries [50] or only in B_{1g} symmetry (1 Fe unit cell corresponding to B_{2g} in the 2 Fe cell used by Zhang *et al.* [51]). The gap energies derived from the A_{1g} and B_{2g} (1 Fe) Raman data are compatible with those determined by ARPES [205] if the entire energy range given by Mou *et al.* is considered (see also Table 2). The B_{1g} maximum (1 Fe) appears at a substantially smaller energy, has a sharp onset and is clearly peaked [50]. Zhang *et al.* [51] identify all features observed in B_{1g} symmetry with pair breaking while Jost *et al.* [50], based on the results in three symmetries, propose that the B_{1g} peak at 134 cm^{-1} originates from a collective mode similar to that in slightly underdoped

BKFA [41]. This - controversial - point of view would indicate a sub-leading interaction having $d_{x^2-y^2}$ symmetry which is to be discussed in more detail now.

6.2. Collective modes

The lowest order gap excitations in the electronic Raman spectra essentially reflect the magnitude of the energy gap. Yet, some caution is appropriate when numbers are to be derived (see table 2). Similar as in the ARPES or tunneling spectra neither the onset of the enhanced intensity nor the peak maxima are directly related to the gap 2Δ . Only in the clean limit, for $q = 0$, and an isotropic superconductor a square-root singularity is expected at 2Δ [73]. In all other cases the maximum is at higher energies [73, 74, 110, 112], and numbers can only be extracted *via* theoretical models. Specifically in multiband systems, such as the FeBCs or in the presence of higher order corrections (final state interactions), only a model analysis leads to useful conclusions as outlined in paragraph 4.6. Yet, since a host of additional information can in principle be derived from the spectra in general and from higher order contributions specifically it is worth the effort.

There is general consensus that collective modes exist in at least some of the pnictides having sufficiently clean gaps [41, 46, 47, 49, 50]. Indications of collective modes were also reported for the chalcogenide $\text{K}_{0.75}\text{Fe}_{1.75}\text{Se}_2$ and discussed along with a theoretical model [58] but we are not aware of a comprehensive symmetry analysis or an in-depth study. Including this report, collective modes were observed mainly in B_{1g} (1 Fe) or B_{2g} (2 Fe) symmetry (which are equivalent).

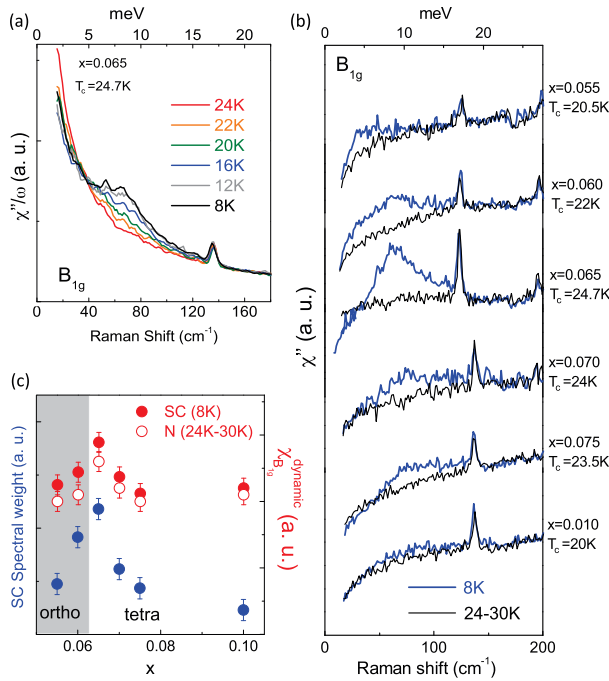


Figure 14. (Color online) Doping dependence of the Raman spectra of $\text{Ba}(\text{Fe}_{1-x}\text{Co}_x)_2\text{As}_2$. (a) Evolution of the B_{1g} Raman conductivity χ''/ω across T_c for $x = 0.065$. (b) B_{1g} Raman response well below (blue) and right above T_c (black) as a function of Co doping as indicated. (c) Integrated SC spectral weight of the Raman response χ'' (blue) as a function of Co doping. The corresponding nematic susceptibilities $\chi_{B1g}^{dynamic}$ both slightly above T_c (N) and well below T_c (SC) are also shown (open and, respectively, full red symbols). From [116] with permission.

An A_{1g} collective mode, as predicted by Chubukov *et al.* [90], was observed as part of a broad spectrum but not as an isolated line [49].

There is a lively discussion on how the collective modes are to be explained in terms of one of the essentially four possibilities (see also section 6.4): (i) amplitude (Higgs) fluctuations of the order parameter (ii) Leggett modes, (iii) fluctuation modes which become undamped in the presence of a gap and (vi) BS modes. Here, the distinction between particle-particle and particle-hole modes [49] was introduced only recently, and both of them were actually coined excitons in the original paper of Bardasis and Schrieffer [140]. We adopt this nomenclature in the following. The essential difference is that particle-particle and particle-hole bound states are expected for attractive and, respectively, repulsive contributions to an attractive pairing potential and *vice versa*. From an experimental point of view a distinction is difficult or impossible.

6.2.1. Amplitude fluctuations of the order parameter

were discussed mainly for systems where superconduc-

tivity competes with other ordering phenomena such as a CDW [67, 94, 101] which break the particle-hole symmetry. Otherwise the coupling to the amplitude mode is weak [218]. Currently it is not clear whether or not amplitude fluctuations can be observed in the FeSCs. The only chance would be in $\text{Ba}_{1-x}\text{K}_x\text{Fe}_2\text{As}_2$ below $x < 0.25$ where the gap is sufficiently clean and $T_{SDW} > T_c$. So far we are not aware of related reports.

6.2.2. Leggett modes [95] were first discussed for MgB_2 [96, 97] where the intra-band interaction dominates and the Leggett modes are below the gap edge. In FeBCs there is a wide agreement that the intra-band interaction is weaker than the inter-band interaction [9, 219], and the Leggett modes are expected to be pushed towards the continuum and overdamped. They may contribute to the Raman intensity at the gap edge and are thus indistinguishable from the pair-breaking effect [98, 99]. Consequently, they are unlikely to augment the information derived from gap spectroscopies, although interesting conclusions about the pairing symmetry could be derived in special cases of chalcogenides without a central Fermi surface [100]. Here the Leggett modes are predicted to appear in B_{1g} symmetry, whereas, in the presence of a Fermi surface encircling the Γ point, as in all pnictides and in bulk FeSe, the Leggett modes are expected to be observed in A_{1g} symmetry [99]. This argument needs to be qualified if the orbital content of the bands is taken into account [98]. An experimental study thereof does not exist and seems difficult. Only resonance effects may be a viable approach.

6.2.3. Quadrupole modes In $\text{NaFe}_{1-x}\text{Co}_x\text{As}$, when excited with blue light (476 nm), a very strong and narrow B_{2g} mode (B_{1g} in the 1 Fe unit cell) appears below T_c at approximately 56 cm^{-1} close to the gap edge derived from ARPES [49]. As shown in Figure 13, 56 cm^{-1} is close to the maximum of the fluctuation peak observed above T_c . The continuous temperature dependence across T_c , the narrowing below T_c and the independence of the mode energy of T_c support the interpretation in terms of a quadrupole fluctuation of charges between the electron and hole bands which becomes undamped inside the superconducting gap.

In A_{1g} symmetry a broad peak is observed which cuts off softly below the maximum located at approximately 70 cm^{-1} thus indicating a finite density of states inside the gap. The maximum - as an integral part of the peak - is interpreted in terms of the particle-hole collective Bardasis-Schrieffer mode predicted by Chubukov, Eremin, and Korshunov [90] for the case of an s_{\pm} ground state, where the gap has opposite sign on the electron and hole bands and an s_{++} subleading

instability without a sign change induced by orbital fluctuations [143]. Since the relatively broad peak includes several excitations, the gap energy can be extracted only with difficulties from the smoothed A_{1g} spectra. For $x = 0.0175$ and 0.05 the humps on the high-energy side are close to the ARPES gaps.

The authors also used red photons (646 nm) for excitation but show only B_{2g} spectra, making a comparison with the spectra obtained for blue light less stringent. For 646 nm, the B_{2g} excitation at 56 cm^{-1} becomes much weaker in the underdoped range, $x \leq 0.0175$, and two new modes appear. These modes are compared to the BS mode in the A_{1g} spectrum measured with excitation at 476 nm and are tentatively assigned to p-h and p-p collective modes without experimental substantiation or a phenomenological theory. Therefore, more work is needed to disentangle the complex but very interesting Raman spectra of $\text{NaFe}_{1-x}\text{Co}_x\text{As}$.

Whereas the normal-state data of $\text{NaFe}_{1-x}\text{Co}_x\text{As}$ are rather similar to those of BFCA several differences are observed below T_c . For instance, the gap anisotropy on the individual bands is larger in BFCA than in $\text{NaFe}_{1-x}\text{Co}_x\text{As}$ as can be inferred from the Raman spectra [25, 38, 49] or, similarly, from other experiments [213, 220, 221]. Given the rather anisotropic gap in BFCA, it is not surprising that no sharp in-gap modes comparable to those in $\text{NaFe}_{1-x}\text{Co}_x\text{As}$ are observed. On the other hand, the peak maximum in B_{1g} symmetry is quite sharp in optimally doped BFCA and may be interpreted alternatively in terms of a nematic resonance near a quantum critical point [39, 116]. In BFCA, both the enhancement of the spectral weight of the B_{1g} pair-breaking peak upon approaching optimal doping, $x \approx 0.065$, and its scaling with the nematic response above T_c (Figure 14) argue in favour of the nematic resonance. Yet, a similar doping dependence is also observed in A_{1g} symmetry and qualifies this conclusion [181].

Na111 and BFCA seem to be the two material classes with the strongest interaction between superconductivity and nematic fluctuations. In contrast, the fluctuations can hardly be observed in BKFA [48, 181] or CKFA [222], and a detailed comparison of these material classes seems highly desirable.

6.2.4. BS modes Finally, we discuss the possibility of sub-leading pairing interactions having $d_{x^2-y^2}$ symmetry and the related BS modes inside the gap in the B_{1g} Raman spectra. The BS modes display various properties which distinguish them from other collective modes [see Eq. (10)].

(a) In a clean gap the BS modes are resolution limited. The energy, $\Omega_{\text{BS}}(T)$, is directly linked to the gap

parameter [89], as opposed to the maximum of the pair-breaking peak $\Omega_{\text{pb}}(T)$ which depends on both the gap $\Delta_{\text{max}}(T)$ and the quasi-particle relaxation rate $\Gamma_{\text{qp}}(T)$ as $\Omega_{\text{pb}}(T) \approx 2\sqrt{|\Delta_{\text{max}}(T)|^2 + \Gamma_{\text{qp}}^2(T)}$ [110, 111, 112, 113]. Thus the temperature dependence of the BS modes rather than that of $\Omega_{\text{pb}}(T)$ is expected to be determined by that of the single particle gap, $\Omega_{\text{BS}} \propto \Delta_{\text{max}}(T)$.

(b) The BS mode drains spectral weight from the pair-breaking peak, but there is no sum rule. Rather, the intensity in the pair-breaking maximum is reduced rapidly, whereas the spectral weight in the BS mode increases first with increasing interaction strength λ_α , with α indexing the eigenvalues (see section 6.3), and then decreases towards zero [41]. In isotropic systems the intensity in the pair-breaking maximum is reduced in the entire energy range. In systems with anisotropic interactions $V_{\mathbf{k},\mathbf{k}'}$ only parts of the pair-breaking peak are depleted depending on the channel-specific components of $V_{\mathbf{k},\mathbf{k}'}$. This behavior can be modeled phenomenologically [47] or on the basis of the eigenvectors $g_\alpha(\mathbf{k})$ which determine the momentum dependence of the gap $\Delta_\alpha(\mathbf{k})$ and, to some extent, reflect the variation of $V_{\mathbf{k},\mathbf{k}'}$ by virtue of the BCS gap equation [92, 41].

(c) The binding energies of the BS modes, $E_{\text{BS},\alpha} = 2\Delta_{\text{max}} - \Omega_{\text{BS},\alpha}$, are related to the coupling strengths of the sub-leading channels λ_α ($\alpha > 1$) with respect to that of the ground state λ_1 . For $\lambda_1 \approx 1$ the relationship is given by $\sqrt{E_{\text{BS},\alpha}/2\Delta_{\text{max}}} \approx \lambda_\alpha/\lambda_1$ and is thus much simpler than that of the intensities [41].

All B_{1g} peaks observed in $\text{Ba}_{0.6}\text{K}_{0.4}\text{Fe}_2\text{As}_2$ were suggested to be BS modes [46] following the phenomenology for anisotropic gaps proposed by Scalapino and Devereaux [91]. The detailed study of the temperature dependence performed later [47] is shown in Fig. 15 and requires this assignment to be revisited. The inset demonstrates the scaling of $\Omega_{\text{BS}}(T)$ at 140 cm^{-1} and $\Delta_{\text{max}}(T)$ as directly observed by ARPES [212], while the maximum at 170 cm^{-1} stays pinned. Apparently, the two strongest modes depend distinctly differently on temperature suggesting the mode at 170 cm^{-1} to be related to pair breaking and that at 140 cm^{-1} to a sub-leading channel. The comparison of all symmetries shows that intensity is in fact drained from the B_{1g} pair-breaking maximum although part of the peak survives indicating highly anisotropic interactions.

Maiti *et al.* [92] pointed out that there may be more than one BS mode in the presence of a hierarchy of sub-leading coupling channels in addition to the s_{\pm} -wave ground state. Although there is a candidate peak at 70 cm^{-1} (see Fig. 15), this proposal can only be addressed by studying differently doped samples.

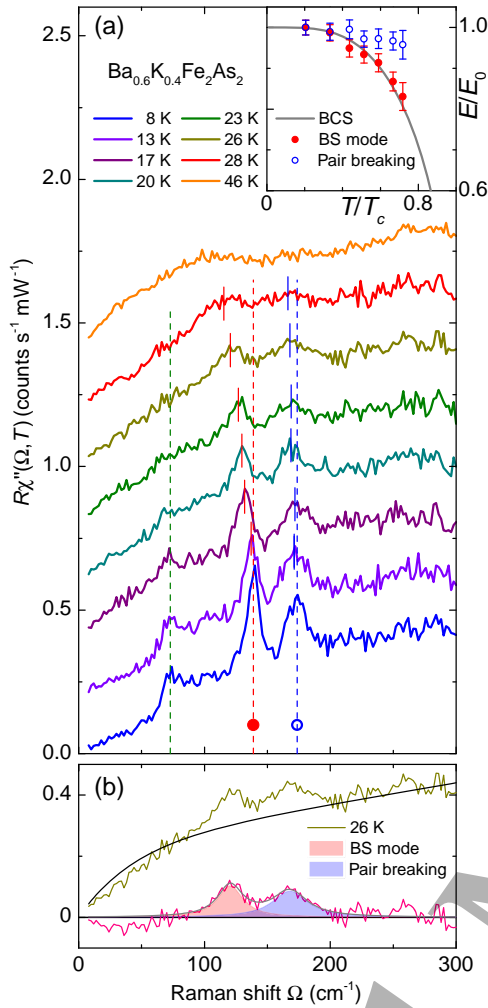


Figure 15. (Color online) Temperature dependence of the Raman spectra of $\text{Ba}_{0.6}\text{K}_{0.4}\text{Fe}_2\text{As}_2$ in B_{1g} symmetry. (a) The spectra measured above 8 K are consecutively shifted up by 0.2 units. The pair-breaking features (open symbols) and the collective mode (full circles) depend differently on temperature, as shown in the inset (where zero energy is suppressed). The pair-breaking maximum exhibits a temperature dependence which is different from the BCS prediction due to interaction effects. (b) The peak energies are determined by fitting the spectra with two Lorentzians and a smooth phenomenological background (black curve). From [47] with permission.

6.3. Doping

Doping x or pressure P can be used as non-thermal control parameters in the context of quantum phase transitions. Here, doping x proves useful for the assignment of the in-gap modes and for scrutinizing the anisotropy of the pairing potential $V_{\mathbf{k},\mathbf{k}'}$ through the evolution with x of the related in-gap modes in BKFA. This will be the main focus of this subsection, but prior to this discussion the results on BFCA and BFAP will be summarized. For Na111 the reader is referred to section 6.2.

The parent compound Ba122 can be driven

superconducting in various ways. Both chemical substitution, using isovalent phosphorus substitution for arsenic, and applied pressure lead to T_c values in the 30 K range [223, 224]. Currently there are no Raman studies of pressure-induced superconductivity in BFA. However, BFAP can be considered to fill this gap at least as a proxy [176]. For $x = 0.5$ BFAP has a T_c of 16 K and displays a broad pair-breaking peak in A_{1g} symmetry having a maximum at $\Omega_{\text{pb}}(T) \approx 2\Delta_{\text{max}} = 6.7 \text{ meV}$ or $4.9 k_B T_c$ (see Table 2 and section 6.1). The nearly linear energy dependence of the spectra below the peak maximum indicates a much broader gap distribution than in BKFA and suggests line nodes of the gap. If the peak is identified with the gap maximum of $4.9 k_B T_c$, it falls below the ratio in the range of $6\text{--}8 k_B T_c$ for other compounds [8]. There are no gap structures in the other symmetries and no collective modes in any symmetry. Thus from all aspects BFAP is closer to BFCA than BKFA.

Due to the doping dependent changes of the band structure, (π, π) scattering is expected to gain strength in BFCA in comparison to BKFA, and one would expect enhanced sub-dominant coupling channels. Rather, the anisotropy of the gaps grows, and the resulting density of states below the gap maximum leads to overdamping of potential in-gap modes similar to what has theoretically been shown to happen for d -wave gaps [120]. Therefore no collective modes can be resolved in BFCA, and the doping dependence is limited to intensity variations of the pair-breaking features described above. Consequently, only BKFA and the related CKFA [50] facilitate the study of changes of $V_{\mathbf{k},\mathbf{k}'}$ as a function of doping or, more appropriately, of the Fermi surface topology.

In what follows we assume that the modes observed below the maximal gap in BKFA are excitonic in origin [140]. This interpretation is not entirely accepted, although many criteria were tested experimentally (see above) and found to be in agreement with the theoretical prediction whereas counterarguments were not presented yet. The doping dependence adds another piece of evidence to this assignment.

Although BKFA is superconducting for $0.1 < x \leq 1$ the range without magnetic order or changes of the Fermi surface topology is rather small, $0.25 < x < 0.6$. For $x < 0.25$ BKFA develops an SDW which gaps out part of the Fermi surface. For $x > 0.6$ the Fermi energy dives below the bottom of the inner electron band and for $x > 0.7$ hole-like bands appear around the X points [225]. It is still under debate which doping level should be associated with the Lifshitz transition but, as a matter of fact, one electron band is lost at $x \approx 0.6$.

The doping dependence of the Raman spectra in superconducting BKFA was studied by two groups.

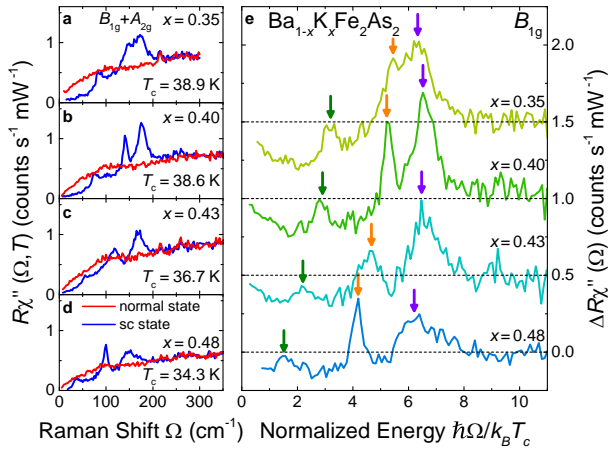


Figure 16. B_{1g} Raman spectra of BKFA for doping levels as indicated. (a)-(d) Raw data (after division by the Bose-Einstein factor) slightly above (red) and well below T_c (blue). (e) Difference spectra $\Delta R\chi''(\Omega) = R\chi''(\Omega, T \approx 8 \text{ K}) - R\chi''(\Omega, T \gtrsim T_c)$. Here all temperature independent features drop out. Apparently, there are no temperature-dependent phonons. As an artifact, the intensity becomes negative inside the gap. Zero-intensity is indicated by horizontal lines (dashes). From [41] with permission.

Wu and coworkers [48] looked at three doping levels, $x = 0.25, 0.4$, and 0.6 and, for $x = 0.4$, reproduced earlier results [46]. Three peaks were observed in B_{1g} symmetry at $50, 120$, and 168 cm^{-1} and at $70, 140$, and 172 cm^{-1} for the first and the second cleave, respectively, of the same crystal. Sample-dependent differences at optimal doping were also observed by Kretzschmar and collaborators [46] but the variations were much smaller, in particular the peak energies were nearly and the overall intensities entirely identical. We find it difficult to explain that the results obtained from two successive cleaves of the same crystal differ substantially, while the local T_c values or doping concentrations x are not reported to be different. For $x = 0.25$ Wu *et al.* observe spectra which are qualitatively different from those at optimal doping and similar to what was found later by Böhm *et al.* [41] in comparable samples. The spectra of Wu's overdoped BKFA, having nominally $x = 0.6$ and $T_c = 25 \text{ K}$, are closer to the results found for $x = 0.43 \dots 0.48$ in Ref. [41] although the T_c values differ by at least 10 K . An explanation of these discrepancies without directly comparing the magnetization measurements of the samples studied cannot be a subject of this review.

Regarding the experiments in the doping range $0.35 \leq x \leq 0.48$ studied in Ref. [41] only samples without indications of secondary transitions and with $\Delta T_c < 1.3 \text{ K}$ were selected. In this relatively small doping range which is sufficiently far away from the SDW and from changes in the Fermi surface topology the Raman spectra of all symmetries depend

continuously on x . The highest peak energies in all symmetries follow T_c to within $\pm 12\%$. In general, the A_{1g} and B_{2g} energies are close to $(8 \pm 1) k_B T_c$ (see Table 2) and thus higher than those in B_{1g} symmetry which scale roughly as $6.2 k_B T_c$ as shown in Fig. 16 which displays raw and difference spectra in B_{1g} symmetry. There are two other maxima in B_{1g} symmetry at lower energy which are clearly resolved in all data sets and scale as $1 - x$ rather than T_c [Fig. 16(e)]. The comparison of all symmetries and doping levels demonstrates that there are only very weak or no maxima in A_{1g} and B_{2g} symmetry in the range of the low-energy B_{1g} peaks. In addition, the low-energy peaks are nearly resolution limited and depend on temperature as $\Delta(T)$ [47].

For $0.35 \leq x \leq 0.48$ the spectra of all symmetries can be described consistently [41] in terms of the phenomenology outlined in Ref. [91] and further elaborated on by Böhm *et al.* [47] for $x = 0.4$. This approach starts from a realistic electronic structure [11], and the doping is accounted for by a shift of the Fermi energy. The Raman vertices are derived from the band structure [see Eqs. (12), (13), and (14)]. The A_{1g} and B_{2g} spectra are used for determining the band and momentum dependent gap values compatible with ARPES studies. After some iterations the bare B_{1g} spectra (without final state interaction) become consistent with the experimental B_{1g} spectra. Here, consistent does not mean that the entire B_{1g} spectra can be reproduced. Rather, there are three features which by no combination of gaps can be explained: the two sharp lines below the gap edge and the missing intensity above the B_{1g} pair-breaking maximum which is expected according to the A_{1g} and B_{2g} spectra. With the final state interaction “switched on” this part of the calculated B_{1g} spectrum is suppressed and reappears in the narrow modes. An explicit calculation was performed only for the stronger mode which was then found to acquire too much spectral weight for the coupling strength λ_d derived from the energy position [see Eq. (10)].

This discrepancy was solved later when theoretical considerations suggested the existence of two sub-leading channels rather than one [92, 41]. The two sub-leading channels ($\alpha = 2, 3$ ordered by strength) were derived from two independent microscopic approaches and were found to have second and first order $d_{x^2-y^2}$ (B_{1g}) symmetry (see Fig. 6 center). Having the higher binding energy $E_{BS(2)} > E_{BS(3)}$ the intensity of the BS mode at lower absolute energy (higher binding energy) is much smaller but still high enough for being the strongest spectral feature in the respective energy range. Unfortunately, the gap energies of the outer hole bands are in the same range [199], motivating Wu *et al.* to assign the mode to that gap at $x = 0.4$ [176]. Yet,

both the phenomenology and the experimental results in A_{1g} and B_{2g} symmetry show that the B_{1g} mode is at least an order of magnitude too strong for justifying an explanation in terms of direct gap excitations [41] thus furnishing further evidence for the excitonic character of the two narrow in-gap modes.

Very recently, CKFA was studied. CKFA is a stoichiometric version of BKFA since the Ca and K layers alternate in a regular fashion for the substantial size difference of the Ca and K ions. From the viewpoint of valence count CKFA should be slightly overdoped, and the T_c values are indeed close to the maximum found for BKFA. The ARPES [205] and Raman experiments [50, 51] find gaps similar to those of BKFA. The features appearing below T_c are relatively strong in B_{1g} symmetry. In A_{1g} and B_{2g} symmetry they are weak and can only be observed for $\hbar\omega_I = 2.16\text{ eV}$ [50] but not for $\hbar\omega_I = 1.92\text{ eV}$ [51]. The weak structures in A_{1g} and B_{2g} symmetry are compatible with the gaps derived from ARPES. The B_{1g} spectra have substructures similar to those found for $x = 0.35$ in BKFA. There is agreement that the mode at 134 cm^{-1} may be a collective excitation and that the hump at 160 cm^{-1} is a remainder from pair breaking. The very weak structure at 50 cm^{-1} , tentatively assigned to a second BS mode in Ref. [50], remains controversial.

Even though there is no full agreement among the experimental groups about the details of the interpretation and, in particular, the doping dependence in BKFA, the question arises as to whether or not the idea of competing pairing channels may be a relevant contribution from Raman scattering to directly support the microscopic considerations. For addressing this question the hierarchy of pairing interactions was studied.

6.4. Possible conclusions for Cooper pairing

In conventional superconductors, the ground state has a much lower energy than potential competing pairing tendencies. Unconventional superconductors have typically various instabilities in close proximity, all of which may be intertwined with Cooper pairing. The ways to study the related phase diagrams include Hubbard-like models [143], the spin-fluctuation scenario which is studied in the random phase approximation (RPA) [9, 226], and the functional renormalization group (fRG) scheme [12, 210, 227, 228] which, as opposed to RPA, treats all possible interactions on equal footing.

In contrast to the Hubbard-Holstein model, which predicts an s_{++} ground state [143], both RPA and fRG find an s_{\pm} ground state for the specific band structure of the FeBCs where the energy gap has the same magnitude on the electron and hole bands but opposite

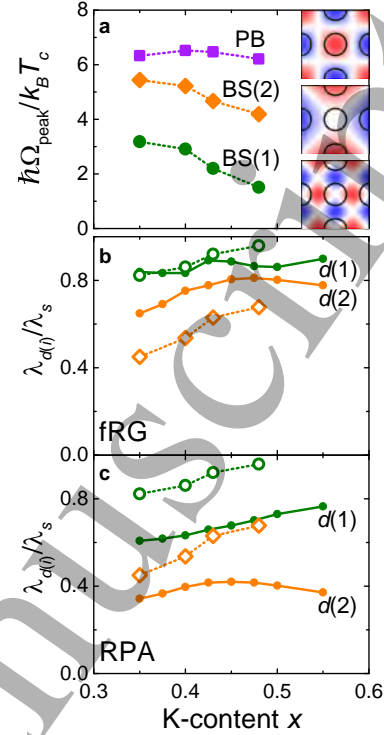


Figure 17. Doping dependence of the pairing strength in BKFA. (a) The positions of the pair-breaking maxima scale approximately as T_c whereas the energies of the BS modes decrease monotonously with increasing doping in the range $0.35 \leq x \leq 0.48$ indicating increasing coupling in the sub-leading channels. The insets show the eigenvectors $g_\alpha(\mathbf{k})$ of the three channels. (b) and (c) The coupling strength of the two sub-leading $d_{x^2-y^2}$ -wave channels relative to the s_{\pm} -wave ground state, $\lambda_{d(i)}/\lambda_s$ (s , $d(1)$, and $d(2)$ correspond to $\alpha = 1, 2$, and 3 , respectively), is predicted to increase with doping (full symbols) in qualitative agreement with experiment (open symbols). $\lambda_{d(i)}/\lambda_s$ is derived from the binding energies in (a) as described in section 6.2. The results on the basis of fRG and RPA are similar. From [41] with permission.

sign [9, 12, 210, 227, 228]. Upon using a realistic band structure [11] and a rigid band model for simulating the doping, the hierarchy of pairing interactions was studied with RPA and fRG schemes. The results are similar in both cases and show that the ground state is s_{\pm} wave followed by two $d_{x^2-y^2}$ pairing tendencies. The solution of the eigenvalue equations yields the eigenvectors $g_\alpha(\mathbf{k})$ and eigenvalues λ_α in channel α . $g_\alpha(\mathbf{k})$ and λ_α describe the variation with \mathbf{k} of the energy gap and, respectively, the coupling strength in channel α . On this basis the positions of the BS modes can be predicted and compared with the experiments as shown in Fig. 17.

The agreement of experiment and theory is remarkable in the case of fRG and still qualitative for RPA. The RPA results are offset to lower coupling strengths by 10 to 20%. Since RPA neglects contributions other than spin-fluctuations, the

observed discrepancy may indicate the existence of weak contributions from other coupling mechanisms such as charge fluctuations [41]. Yet, the similarity of the fRG and RPA results for the hierarchy of pairing channels supports spin-fluctuation-induced superconductivity in BKFA in the doping range studied. CKFA appears to fit into this picture although the weakness of the putative low-energy BS mode, the proximity of the second BS mode to the pair-breaking maximum [50], and the resulting controversy in the interpretation [51] qualify this conclusion and call for further experiments.

Whereas the recent RPA and fRG studies favor spin fluctuations, an s_{\pm} -wave gap and two sub-leading pairing channels having $d_{x^2-y^2}$ symmetry, the Hubbard-Holstein model leads to different conclusions and finds an s_{++} ground state driven by electron-phonon coupling and orbital fluctuations [143]. For the construction of the model sub-leading channels were not identified. However, if the sub-leading interactions in this model would be identified to have $d_{x^2-y^2}$ symmetry the resulting Raman spectra would be indistinguishable from those observed in BKFA and CKFA. Thus the case for spin fluctuation induced pairing depends crucially on the reliability of the hierarchy of pairing tendencies derived from fRG and RPA. Other experimental probes such as the study of quasi-particle interference effects in magnetic fields [191] or in the presence of impurities [229, 230] by scanning tunneling spectroscopy may help to clarify the symmetry of the ground state.

7. Conclusions

Raman scattering in iron pnictides and chalcogenides has provided a host of information on the electronic, magnetic and lattice properties of these systems. We focused on the the spin and charge degrees of freedom in this review.

In all cases the spectra consist of a superposition of several types of excitations. To which extent *luminescence* (as an *a priori* undesired contribution) plays a role is not entirely clear, but the comparison of a large amount of results shows that luminescence decreases substantially with improved sample quality and may be neglected at least at low energies.

Particle-hole excitations are important in all compounds and for all doping levels. They are partially gapped out in the SDW state (section 5.2) where the materials remain metallic and are fully gapped out, for instance, in superconducting BKFA when the surfaces are sufficiently clean (see section 6.1 and Ref. [46]). In the normal state, the particle-hole excitations in A_{1g} symmetry depend on temperature as expected from the static resistivity [cf. Fig. 10 (d)].

In B_{1g} symmetry, a strong contribution from *fluctuations* (see section 5.3) is observed below room temperature at energies of order $k_B T$ which softens with decreasing temperature, has the strongest spectral weight directly at the structural transition T_S , and loses intensity below T_S without, however vanishing so long as the material does not order magnetically. Raman scattering is particularly useful here since other spectroscopies have generic difficulties in observing the fluctuations: In the case of neutron scattering, the fluctuations appear only in the notoriously weak four-particle correlation, and NMR spectroscopy covers only a small energy range well below $k_B T$. The same holds true for thermodynamic methods [231] or transport [232] both of which probe fluctuations only indirectly. We argue that the temperature dependence identifies the Raman response as critical fluctuations which are expected to vanish at the related transition temperature. The persistence of the excitations below T_S is therefore considered an indication of spin rather than charge fluctuations. Yet, there is no consensus in the published literature on this point. However, if the controversy could be settled the driving force behind the phase transitions would be identified.

In all pnictides, the response of the *spin density wave* (SDW) is clearly observed (section 5.2). Although the gap energies are in the range 6-8 $k_B T_{SDW}$, the spectra are by and large described by weak-coupling physics including band reconstruction in the ordered state. This indicates that the magnetism here results from a Fermi surface instability of itinerant electrons. The relevant gap energies are in the range 100-150 meV in the parent compounds and decrease with doping or substitution along with the gradual suppression of the magnetically ordered phase.

In the chalcogenide $\text{Fe}(\text{Se}_{1-x}\text{S}_x)$ the B_{1g} response is distinctly different from that in the pnictides at all temperatures [57, 55]. In the range 60 meV, a broad excitation is observed for $x \lesssim 0.2$ which gains spectral weight by a factor of approximately two upon cooling without moving by more than a few percent. This temperature (and doping) dependence is not expected for quasi-particle scattering from impurities. Rather, the peak was associated with *two-magnon excitations of nearly localized moments in a frustrated magnet* (see sections 5.1 and 5.4) in agreement with neutron scattering experiments [157], LDA predictions for the exchange parameters J_1 and J_2 [170], and simulations using exact diagonalization [55, 171]. The response from fluctuations entirely fills the gap below 60 meV in the temperature range around T_S and persists down to $T \approx 20$ K. Indications of an SDW were not found. It is argued that orbital dependent localization of electrons as expected in Hund's metals with $J \sim U$ may be at

the origin of this dichotomy between the pnictides and chalcogenides [149, 156].

In the *superconducting state gap excitations* are observed in all sufficiently clean systems independent of the concentration of substitutional atoms (see section 6.1). Only Co substitution gradually suppresses the pair-breaking features. In all FeBCs there is a strong band dependence of the gaps. In FeSe the gap can be resolved in the Raman spectra but its small magnitude prevents a reliable analysis. In BFCA, the gaps on the electron bands exhibit a strong modulation with momentum and may even have accidental nodes at optimal doping. Here, Raman scattering and transport measurements arrive at similar conclusions [25, 36, 217]. In BKFA and presumably CKFA, the gaps on the individual bands are nearly constant. This fact, first derived from ARPES [205, 212], manifests itself in sharp gap edges in the Raman spectra.

Below the gap edges narrow, nearly *resolution-limited lines* are observed in the B_{1g} spectra of BKFA [47] (see sections 6.2 and 6.3). These lines display a BCS-like temperature dependence, vary as $1 - x$ with doping and steal spectral weight from the pair-breaking features. The pair-breaking features scale with T_c and barely depend on temperature. These criteria are predicted only for BS modes that result from sub-leading pairing interactions competing with the ground state.

Microscopic model calculations using fRG and RPA (see section 6.4) show that the pnictides have indeed a hierarchy of pairing channels with very similar eigenvalues, an s_{\pm} ground state, and two sub-leading $d_{x^2-y^2}$ instabilities of different order [41]. The Raman experiments agree semi-quantitatively with these predictions concerning doping dependence but cannot pin down the sign change of the ground state. Tunneling experiments in samples with different impurity concentration [233] and with applied field [191] or RIXS [234] may settle this point. Yet, the doping dependence of the sub-leading channels in BKFA and presumably the results in CKFA as well make a strong case for spin fluctuations to contribute partially or predominantly to the Cooper pairing in the pnictides.

In summary, the most significant contributions from light scattering experiments to the physics of the FeBCs pertain to the analysis of fluctuations and of the superconducting pairing states. The fluctuations can be compared to the evolution of the elasticity [116, 181] and of the spin-lattice relaxation as obtained from NMR studies [49]. While the interrelation of the various methods is obvious several aspects of the interpretation remain controversial, in particular the origin of the fluctuations. Concerning superconductivity the derivation of the gap energies is of

specific relevance. Table 2 shows that the results from light scattering fit very well into the concert of the other methods if the data are read properly. Reading properly means, in particular, understanding the respective observables and including collective excitations which reveal details of the pairing potential $V_{\mathbf{k},\mathbf{k}'}$. In many cases the Raman response contributes information which cannot easily or not at all be obtained by other methods. Thus, part of the understanding of the pnictides and chalcogenides may rest on light scattering results, in particular if the remaining challenges in the interpretation can be settled. Additional insight is expected from novel x-ray techniques [124] which may help to settle, e.g., the sign problem of the order parameter [234] and from experiments under extreme conditions, specifically pressure. Here, the problem of the luminescence in the diamond anvils is a particular challenge if continuous spectra rather than narrow phonon lines have to be analyzed quantitatively.

Acknowledgements

We gratefully acknowledge discussions with A. Baum, L. Benfatto, G. Blumberg, A. Chubukov, T.P. Devereaux, Y. Gallais, M. Grilli, W. Hanke, F. Hardy, P. Hirschfeld, D. Jost, M. Khodas, S. Lederer, S. Maiti, C. Meingast, B. Moritz, Z.V. Popović, and R. Thomale, I. Tüttö.

Financial support came from the German Research Foundation (DFG) via the Priority Program SPP 1458 (grant-no. Ha2071/7), the Transregional Collaborative Research Center TRR80 (Project ID 107745057), from the Serbian Ministry of Education, Science and Technological Development under Project III45018 and by the Science Fund of the Republic of Serbia (Project “StrainedFe”). We acknowledge support by the DAAD through the bilateral project between Serbia and Germany (grant numbers 57335339 and 57449106).

- [1] Kamihara Y, Hiramatsu H, Hirano M, Kawamura R, Yanagi H, Kamiya T and Hosono H 2006 *J. Am. Chem. Soc.* **128** 10012
- [2] Kamihara Y, Watanabe T, Hirano M and Hosono H 2008 *J. Am. Chem. Soc.* **130** 3296
- [3] Paglione J and Greene R L 2010 *Nature Phys.* **6** 645
- [4] Johnston D C 2010 *Adv. Phys.* **59** 803
- [5] Stewart G R 2011 *Rev. Mod. Phys.* **83**(4) 1589–1652
- [6] Hirschfeld P J, Korshunov M M and Mazin I I 2011 *Rep. Prog. Phys.* **74** 125508
- [7] Hirschfeld P J 2016 *C. R. Physique* **17** 197 – 231
- [8] Korshunov M M 2018 *Phys. Rev. B* **98**(10) 104510
- [9] Mazin I I, Singh D J, Johannes M D and Du M H 2008 *Phys. Rev. Lett.* **101** 057003
- [10] Kordyuk A A, Zabolotnyy V B, Evtushinsky D V, Yaresko A N, Büchner B and Borisenko S V 2013 *J. Supercond. Nov. Magn.* **26** 2837–2841

- [11] Graser S, Maier T, Hirschfeld P and Scalapino D 2009 *New J. Phys.* **11** 025016
- [12] Thomale R, Platt C, Hanke W and Bernevig B A 2011 *Phys. Rev. Lett.* **106**(18) 187003
- [13] Böhm T 2017 *The case for spin-fluctuation induced pairing in Ba_{1-x}K_xFe₂As₂* Ph.D. thesis Technische Universität München
- [14] Fernandes R M, Chubukov A V and Schmalian J 2014 *Nature Phys.* **10** 97
- [15] Massat P, Quan Y, Grasset R, Méasson M A, Cazayous M, Sacuto A, Karlsson S, Strobel P, Toulemonde P, Yin Z and Gallais Y 2018 *Phys. Rev. Lett.* **121**(7) 077001
- [16] Hadjiev V G, Iliev M N, Sasmal K, Sun Y Y and Chu C W 2008 *Phys. Rev. B* **77** 220505
- [17] Litvinchuk A P, Hadjiev V G, Iliev M N, Lv B, Guloy A M and Chu C W 2008 *Phys. Rev. B* **78** 060503
- [18] Rahlenbeck M, Sun G L, Sun D L, Lin C T, Keimer B and Ulrich C 2009 *Phys. Rev. B* **80** 064509
- [19] Um Y J, Park J T, Min B H, Song Y J, Kwon Y S, Keimer B and Le Tacon M 2012 *Phys. Rev. B* **85**(1) 012501
- [20] Lazarević N, Popović Z V, Hu R and Petrovic C 2011 *Phys. Rev. B* **83** 024302
- [21] Lazarević N, Abeykoon M, Stephens P W, Lei H, Bozin E S, Petrovic C and Popović Z V 2012 *Phys. Rev. B* **86**(5) 054503
- [22] Zhang A M, Liu K, Xiao J H, He J B, Wang D M, Chen G F, Normand B and Zhang Q M 2012 *Phys. Rev. B* **85**(2) 024518
- [23] Rotter M, Tegel M and Johrendt D 2008 *Phys. Rev. Lett.* **101** 107006 (pages 4)
- [24] Sefat A S, Jin R, McGuire M A, Sales B C, Singh D J and Mandrus D 2008 *Phys. Rev. Lett.* **101** 117004
- [25] Muschler B, Prestel W, Hackl R, Devereaux T P, Analytis J G, Chu J H and Fisher I R 2009 *Phys. Rev. B* **80** 180510
- [26] Chauvière L, Gallais Y, Cazayous M, Méasson M A, Sacuto A, Colson D and Forget A 2011 *Phys. Rev. B* **84**(10) 104508
- [27] Sugai S, Mizuno Y, Watanabe R, Kawaguchi T, Takenaka K, Ikuta H, Takayanagi Y, Hayamizu N and Sone Y 2012 *J. Phys. Soc. Japan* **81** 024718
- [28] Chu J H, Analytis J G, Greve K D, McMahon P L, Islam Z, Yamamoto Y and Fisher I R 2010 *Science* **329** 824
- [29] Choi K Y, Lemmens P, Eremin I, Zwickyagl G, Berger H, Sun G L, Sun D L and Lin C T 2010 *J. Phys.: Condens. Matter* **22** 115802
- [30] Gallais Y, Fernandes R M, Paul I, Chauvière L, Yang Y X, Méasson M A, Cazayous M, Sacuto A, Colson D and Forget A 2013 *Phys. Rev. Lett.* **111**(26) 267001
- [31] Okazaki K, Sugai S, Niitaka S and Takagi H 2011 *Phys. Rev. B* **83**(3) 035103
- [32] Sugai S, Mizuno Y, Watanabe R, Kawaguchi T, Takenaka K, Ikuta H, Kiho K, Nakajima M, Lee C H, Iyo A, Eisaki H and Uchida S 2013 *J. Supercond. Novel Magn.* **26** 1179–1183
- [33] Zhang W L, Richard P, Ding H, Sefat A S, Gillett J, Sebastian S E, Khodas M and Blumberg G 2014 *arXiv e-prints* arXiv:1410.6452
- [34] Zhang W L, Yin Z P, Ignatov A, Bukowski Z, Karpinski J, Sefat A S, Ding H, Richard P and Blumberg G 2016 *Phys. Rev. B* **93**(20) 205106
- [35] Kaneko U F, Gomes P F, García-Flores A F, Yan J Q, Lograsso T A, Barberis G E, Vaknin D and Granado E 2017 *Phys. Rev. B* **96**(1) 014506
- [36] Mazin I I, Devereaux T P, Analytis J G, Chu J H, Fisher I R, Muschler B and Hackl R 2010 *Phys. Rev. B* **82** 180502
- [37] Sugai S, Mizuno Y, Kiho K, Nakajima M, Lee C H, Iyo A, Eisaki H and Uchida S 2010 *Phys. Rev. B* **82** 140504
- [38] Chauvière L, Gallais Y, Cazayous M, Méasson M A, Sacuto A, Colson D and Forget A 2010 *Phys. Rev. B* **82** 180521
- [39] Gallais Y, Paul I, Chauvière L and Schmalian J 2016 *Phys. Rev. Lett.* **116**(1) 017001
- [40] Kretzschmar F, Böhm T, Karahasanović U, Muschler B, Baum A, Jost D, Schmalian J, Caprara S, Grilli M, Di Castro C, Analytis J H, Chu J H, Fisher I R and Hackl R 2016 *Nature Phys.* **12** 560–563
- [41] Böhm T, Kretzschmar F, Baum A, Rehm M, Jost D, Ahangharnejhad R H, Thomale R, Platt C, Maier T A, Hanke W, Moritz B, Devereaux T P, Scalapino D J, Maiti S, Hirschfeld P J, Adelmann P, Wolf T, Wen H H and Hackl R 2018 *npj Quantum Materials* **3** 48
- [42] Kumar P, Muthu D V S, Harnagea L, Wurmehl S, Buchner B and Sood A K 2014 *J. Phys. Condens. Matter* **26** 305403
- [43] Yang Y X, Gallais Y, Rullier-Albenque F, Méasson M A, Cazayous M, Sacuto A, Shi J, Colson D and Forget A 2014 *Phys. Rev. B* **89**(12) 125130
- [44] Kaneko U F, Piva M M, Jesus C, Saleta M, Urbano R, Pagliuso P G and Granado E 2019 *J. Phys.: Condens. Matter* **31** 495402
- [45] Wu S F, Zhang W L, Li L, Cao H, Kung H H, Sefat A, Ding H, Richard P and Blumberg G 2017 *arXiv preprint arXiv:1712.06066*
- [46] Kretzschmar F, Muschler B, Böhm T, Baum A, Hackl R, Wen H H, Tsurkan V, Deisenhofer J and Loidl A 2013 *Phys. Rev. Lett.* **110**(18) 187002
- [47] Böhm T, Kemper A F, Moritz B, Kretzschmar F, Muschler B, Eiter H M, Hackl R, Devereaux T P, Scalapino D J and Wen H H 2014 *Phys. Rev. X* **4**(4) 041046
- [48] Wu S F, Richard P, Ding H, Wen H H, Tan G, Wang M, Zhang C, Dai P and Blumberg G 2017 *Phys. Rev. B* **95**(8) 085125
- [49] Thorsmølle V K, Khodas M, Yin Z P, Zhang C, Carr S V, Dai P and Blumberg G 2016 *Phys. Rev. B* **93**(5) 054515
- [50] Jost D, Scholz J R, Zweck U, Meier W R, Böhmer A E, Canfield P C, Lazarević N and Hackl R 2018 *Phys. Rev. B* **98**(2) 020504
- [51] Zhang W L, Meier W R, Kong T, Canfield P C and Blumberg G 2018 *Phys. Rev. B* **98**(14) 140501
- [52] Okazaki K, Sugai S, Niitaka S and Takagi H 2011 *Phys. Rev. B* **83** 035103
- [53] Massat P, Farina D, Paul I, Karlsson S, Strobel P, Toulemonde P, Méasson M A, Cazayous M, Sacuto A, Kasahara S, Shibauchi T, Matsuda Y and Gallais Y 2016 *Proc. Natl. Acad. Sci.* **113** 9177–9181
- [54] Glamazda A, Lemmens P, Ok J M, Kim J S and Choi K Y 2019 *Phys. Rev. B* **99**(7) 075142
- [55] Baum A, Ruiz H N, Lazarević N, Wang Y, Böhm T, Hosseinian Ahangharnejhad R, Adelmann P, Wolf T, Popović Z V, Moritz B, Devereaux T P and Hackl R 2019 *Commun. Phys.* **2** 14
- [56] Kumar P, Kumar A, Saha S, Muthu D, Prakash J, Patnaik S, Waghmare U, Ganguli A and Sood A 2010 *Solid State Commun.* **150** 557
- [57] Zhang W L, Wu S F, Kasahara S, Shibauchi T, Matsuda Y and Blumberg G 2017 *arXiv e-prints* arXiv:1710.09892
- [58] Khodas M, Chubukov A V and Blumberg G 2014 *Phys. Rev. B* **89**(24) 245134
- [59] Zhang A M, Xiao J H, Li Y S, He J B, Wang D M, Chen G F, Normand B, Zhang Q M and Xiang T 2012 *Phys. Rev. B* **85**(21) 214508
- [60] Fleury P A, Porto S P S, Cheesman L E and Guggenheim H J 1966 *Phys. Rev. Lett.* **17**(2) 84–87
- [61] Lyons K B, Sulewski P E, Fleury P A, Carter H L, Cooper A S, Espinosa G P, Fisk Z and Cheong S W 1989 *Phys. Rev. B* **39** 9693
- [62] Fleury P A and Loudon R 1968 *Phys. Rev.* **166** 514
- [63] Devereaux T P and Hackl R 2007 *Rev. Mod. Phys.* **79** 175

- [64] Chen C C, Jia C J, Kemper A F, Singh R R P and Devereaux T P 2011 *Phys. Rev. Lett.* **106** 067002
- [65] Baum A, Milosavljević A, Lazarević N, Radonjić M M, Nikolić B, Mitschek M, Maranloo Z I, Šćepanović M, Grujić-Brojin M, Stojilović N, Opel M, Wang A, Petrovic C, Popović Z V and Hackl R 2018 *Phys. Rev. B* **97**(5) 054306
- [66] Abrikosov A A and Fal'kovskii L A 1961 *Zh. Eksp. Teor. Fiz.* **40** 262 [Sov. Phys. JETP **13**, 179 (1961)]
- [67] Sooryakumar R and Klein M V 1980 *Phys. Rev. Lett.* **45**(8) 660–662
- [68] Dierker S B, Klein M V, Webb G W and Fisk Z 1983 *Phys. Rev. Lett.* **50** 853
- [69] Hackl R, Kaiser R and Schick Tanz S 1983 *J. Phys. C: Solid State Phys.* **16** 1729
- [70] Cooper S L, Klein M V, Pazol B G, Rice J P and Ginsberg D M 1988 *Phys. Rev. B* **37**(10) 5920–5923
- [71] Hackl R, Gläser W, Müller P, Einzel D and Andres K 1988 *Phys. Rev. B* **38** 7133
- [72] Abrikosov A and Genkin V 1973 *Zh. Eksp. Teor. Fiz.* **65** 842 [Sov. Phys. JETP **38**, 417 (1974)]
- [73] Klein M V and Dierker S B 1984 *Phys. Rev. B* **29** 4976
- [74] Devereaux T P, Einzel D, Stadlober B, Hackl R, Leach D H and Neumeier J J 1994 *Phys. Rev. Lett.* **72** 396
- [75] Chandrasekhar M, Cardona M and Kane E O 1977 *Phys. Rev. B* **16**(8) 3579–3595
- [76] Ipatova I, Subashiev A and Voitenko V 1981 *Solid State Commun.* **37** 893 – 895
- [77] Zawadowski A and Cardona M 1990 *Phys. Rev. B* **42** 10732
- [78] Staufer T, Hackl R and Müller P 1990 *Solid State Commun.* **75** 975
- [79] Slakey F, Klein M V, Rice J P and Ginsberg D M 1991 *Phys. Rev. B* **43** 3764
- [80] Hackl R, Opel M, Müller P F, Krug G, Stadlober B, Nemetschek R, Berger H and Forró L 1996 *J. Low Temp. Phys.* **105** 733–742 ISSN 1573-7357
- [81] Opel M, Nemetschek R, Hoffmann C, Philipp R, Müller P F, Hackl R, Tüttő I, Erb A, Revaz B, Walker E, Berger H and Forró L 2000 *Phys. Rev. B* **61**(14) 9752–9774
- [82] Einzel D and Hackl R 1996 *J. Raman Spectrosc.* **27** 307–319 ISSN 1097-4555
- [83] Caprara S, Di Castro C, Grilli M and Suppa D 2005 *Phys. Rev. Lett.* **95**(11) 117004
- [84] Tassini L, Venturini F, Zhang Q M, Hackl R, Kikugawa N and Fujita T 2005 *Phys. Rev. Lett.* **95** 117002
- [85] Klein A, Lederer S, Chowdhury D, Berg E and Chubukov A 2018 *Phys. Rev. B* **97**(15) 155115
- [86] Klein A, Lederer S, Chowdhury D, Berg E and Chubukov A 2018 *Phys. Rev. B* **98**(4) 041101
- [87] Udina M, Grilli M, Benfatto L and Chubukov A V 2019 *arXiv e-prints* arXiv:1908.11361
- [88] Zawadowski A, Ruvalds J and Solana J 1972 *Phys. Rev. A* **5** 399–421
- [89] Monien H and Zawadowski A 1990 *Phys. Rev. B* **41**(13) 8798–8810
- [90] Chubukov A V, Eremin I and Korshunov M M 2009 *Phys. Rev. B* **79** 220501
- [91] Scalapino D J and Devereaux T P 2009 *Phys. Rev. B* **80** 140512
- [92] Maiti S, Maier T A, Böhm T, Hackl R and Hirschfeld P J 2016 *Phys. Rev. Lett.* **117**(25) 257001
- [93] Littlewood P B and Varma C M 1981 *Phys. Rev. Lett.* **47** 811–814
- [94] Littlewood P B and Varma C M 1982 *Phys. Rev. B* **26**(9) 4883–4893
- [95] Leggett A J 1966 *Prog. Theor. Phys.* **36** 901
- [96] Blumberg G, Mialitsin A, Dennis B S, Klein M V, Zhigadlo N D and Karpinski J 2007 *Phys. Rev. Lett.* **99** 227002
- [97] Klein M V 2010 *Phys. Rev. B* **82** 014507
- [98] Burnell F J, Hu J, Parish M M and Bernevig B A 2010 *Phys. Rev. B* **82**(14) 144506
- [99] Cea T and Benfatto L 2016 *Phys. Rev. B* **94**(6) 064512
- [100] Huang W, Sigrist M and Weng Z Y 2018 *Phys. Rev. B* **97**(14) 144507
- [101] Méasson M A, Gallais Y, Cazayous M, Clair B, Rodière P, Cario L and Sacuto A 2014 *Phys. Rev. B* **89**(6) 060503
- [102] Pekker D and Varma C 2015 *Annu. Rev. Cond. Mat. Phys.* **6** 269–297
- [103] Hackl R, Kaiser R and Gläser W 1989 *Physica C (Amsterdam)* **162-164** 431
- [104] Kendziora C and Rosenberg A 1995 *Phys. Rev. B* **52** 9867
- [105] Chen X K, Naeini J G, Hewitt K C, Irwin J C, Liang R and Hardy W N 1997 *Phys. Rev. B* **56** R513
- [106] Sugai S and Hosokawa T 2000 *Phys. Rev. Lett.* **85** 1112
- [107] Le Tacon M, Sacuto A, Georges A, Kotliar G, Gallais Y, Colson D and Forget A 2006 *Nature Phys.* **2** 537
- [108] Munnikes N, Muschler B, Venturini F, Tassini L, Prestel W, Ono S, Ando Y, Peets D C, Hardy W N, Liang R, Bonn D A, Damascelli A, Eisaki H, Greven M, Erb A and Hackl R 2011 *Phys. Rev. B* **84**(14) 144523
- [109] Li Y, Le Tacon M, Matiks Y, Boris A V, Loew T, Lin C T, Chen L, Chan M K, Dorow C, Ji L, Barišić N, Zhao X, Greven M and Keimer B 2013 *Phys. Rev. Lett.* **111**(18) 187001
- [110] Devereaux T P 1992 *Phys. Rev. B* **45** 12965
- [111] Devereaux T P 1993 *Phys. Rev. B* **47**(9) 5230–5238
- [112] Devereaux T P 1995 *Phys. Rev. Lett.* **74** 4313
- [113] Manske D 2004 *Theory of Unconventional Superconductors* (Springer Tracts in Modern Physics **202**)
- [114] Caprara S, Colonna M, Di Castro C, Hackl R, Muschler B, Tassini L and Grilli M 2015 *Phys. Rev. B* **91**(20) 205115
- [115] Karahasanovic U, Kretzschmar F, Böhm T, Hackl R, Paul I, Gallais Y and Schmalian J 2015 *Phys. Rev. B* **92**(7) 075134
- [116] Gallais Y and Paul I 2016 *C. R. Physique* **17** 113 – 139
- [117] Boyd G R, Devereaux T P, Hirschfeld P J, Mishra V and Scalapino D J 2009 *Phys. Rev. B* **79** 174521
- [118] Khodas M and Levchenko A 2015 *Phys. Rev. B* **91**(23) 235119
- [119] Hayes W and Loudon R 2005 *Scattering of Light by Crystals* (New York: Dover)
- [120] Devereaux T P and Einzel D 1995 *Phys. Rev. B* **51** 16336
- [121] Kosztin J and Zawadowski A 1991 *Solid State Commun.* **78** 1029–1032 ISSN 0038-1098
- [122] Freericks J K, Devereaux T P, Moraghebi M and L C S 2005 *Phys. Rev. Lett.* **94** 216401
- [123] Salpeter E E and Bethe H A 1951 *Phys. Rev.* **84**(6) 1232–1242
- [124] Ament L J P, van Veenendaal M, Devereaux T P, Hill J P and van den Brink J 2011 *Rev. Mod. Phys.* **83**(2) 705–767
- [125] Pines D and Nozières P 1966 *The Theory of Quantum Liquids: Normal Fermi Liquids* (Benjamin, Reading, MA)
- [126] Maiti S, Chubukov A V and Hirschfeld P J 2017 *Phys. Rev. B* **96**(1) 014503
- [127] Platzman P M 1965 *Phys. Rev.* **139** A379
- [128] Kostur V N 1992 *Z. Phys. B: Condensed Matter* **89** 149–159 ISSN 1431-584X
- [129] Devereaux T P, Virostek A and Zawadowski A 1996 *Phys. Rev. B* **54** 12523
- [130] Muschler B, Prestel W, Tassini L, Hackl R, Lambacher M, Erb A, Komiya S, Ando Y, Peets D, Hardy W, Liang R and Bonn D 2010 *Eur. Phys. J. Special Topics* **188** 131
- [131] Hackl R and Kaiser R 1988 *J. Phys. C: Solid State Physics* **21** L453

- [132] Cuk T, Lu D H, Zhou X J, Shen Z X, Devereaux T P and Nagaosa N 2005 *Phys. Stat. Sol. (b)* **242** 11
- [133] Inosov D S, Borisenko S V, Eremin I, Kordyuk A A, Zabolotnyy V B, Geck J, Koitzsch A, Fink J, Knupfer M, Büchner B, Berger H and Follath R 2007 *Phys. Rev. B* **75** 172505
- [134] Prestel W, Venturini F, Muschler B, Tüttö I, Hackl R, Lambacher M, Erb A, Komiya S, Ono S, Ando Y, Inosov D, Zabolotnyy V B and Borisenko S V 2010 *Eur. Phys. J. Special Topics* **188** 163
- [135] Tsuneto T 1960 *Phys. Rev.* **118**(4) 1029–1035
- [136] Mattis D C and Bardeen J 1958 *Phys. Rev.* **111**(2) 412–417
- [137] Eiter H M, Lavagnini M, Hackl R, Nowadnick E A, Kemper A F, Devereaux T P, Chu J H, Analytis J G, Fisher I R and Degiorgi L 2013 *Proc. Nat. Acad. Sciences* **110** 64–69
- [138] Shastry B S and Shraiman B I 1990 *Phys. Rev. Lett.* **65** 1068
- [139] Varma C M 2002 *J. Low Temp. Phys.* **126**(3/4) 901
- [140] Bardasis A and Schrieffer J R 1961 *Phys. Rev.* **121** 1050–1062
- [141] Greytak T J and Yan J 1969 *Phys. Rev. Lett.* **22**(19) 987–990
- [142] Suhl H, Matthias B T and Walker L R 1959 *Phys. Rev. Lett.* **3**(12) 552–554
- [143] Kontani H and Onari S 2010 *Phys. Rev. Lett.* **104**(15) 157001
- [144] Weidinger S A and Zwerger W 2015 *Eur. Phys. B* **88** 237
- [145] Podolsky D, Auerbach A and Arovas D P 2011 *Phys. Rev. B* **84**(17) 174522
- [146] Gazit S, Podolsky D and Auerbach A 2013 *Phys. Rev. Lett.* **110**(14) 140401
- [147] Chelwani N, Baum A, Böhm T, Opel M, Venturini F, Tassini L, Erb A, Berger H, Forró L and Hackl R 2018 *Phys. Rev. B* **97**(2) 024407
- [148] de' Medici L, Hassan S R, Capone M and Dai X 2009 *Phys. Rev. Lett.* **102**(12) 126401
- [149] Yin Z P, Haule K and Kotliar G 2011 *Nature Mater.* **10** 932–935 ISSN 1476-1122
- [150] Leonov I, Skornyakov S L, Anisimov V I and Vollhardt D 2015 *Phys. Rev. Lett.* **115**(10) 106402
- [151] Knoll P, Thomsen C, Cardona M and Murugaraj P 1990 *Phys. Rev. B* **42**(7) 4842–4845
- [152] Devereaux T P and Kampf A P 1999 *Phys. Rev. B* **59**(9) 6411–6420
- [153] Moritz B, Johnston S, Devereaux T P, Muschler B, Prestel W, Hackl R, Lambacher M, Erb A, Komiya S and Ando Y 2011 *Phys. Rev. B* **84**(23) 235114
- [154] Jia C J, Nowadnick E A, Wohlfeld K, Kung Y F, Chen C C, Johnston S, Tohyama T, Moritz B and Devereaux T P 2014 *Nature Commun.* **5** 3314 ISSN 2041-1723
- [155] Georges A, de' Medici L and Mravlje J 2013 *Annu. Rev. Cond. Mat. Phys.* **4** 137–178
- [156] Si Q, Yu R and Abrahams E 2016 *Nat. Rev. Mater.* **1** 16017
- [157] Wang Q, Shen Y, Pan B, Zhang X, Ikeuchi K, Iida K, Christianson A D, Walker H C, Adroja D T, Abdel-Hafiez M, Chen X, Chareev D A, Vasiliev A N and Zhao J 2016 *Nature Commun.* **7** 12182
- [158] Skornyakov S L, Anisimov V I, Vollhardt D and Leonov I 2017 *Phys. Rev. B* **96**(3) 035137
- [159] Sulewski P E, Fleury P A, Lyons K B and Cheong S W 1991 *Phys. Rev. Lett.* **67** 3864
- [160] Venturini F, Michelucci U, Devereaux T P and Kampf A P 2000 *Phys. Rev. B* **62** 15204–15207
- [161] Aslamasov L G and Larkin A I 1968 *Sov. Phys. Solid State* **10** 875
- [162] Fernandes R M and Schmalian J 2012 *Supercond. Sci. Technol.* **25** 084005
- [163] Yamakawa Y, Onari S and Kontani H 2016 *Phys. Rev. X* **6**(2) 021032
- [164] Chubukov A V, Khodas M and Fernandes R M 2016 *Phys. Rev. X* **6**(4) 041045
- [165] Classen L, Xing R Q, Khodas M and Chubukov A V 2017 *Phys. Rev. Lett.* **118**(3) 037001
- [166] Fanfarillo L, Benfatto L and Valenzuela B 2018 *Phys. Rev. B* **97**(12) 121109
- [167] Allen P B 1976 *Phys. Rev. B* **13**(4) 1416–1427
- [168] Baek S H, Efremov D V, Ok J M, Kim J S, van den Brink J and Büchner B 2014 *Nature Mater.* **14** 210–214
- [169] Yi M, Lu D, Chu J H, Analytis J G, Sorini A P, Kemper A F, Moritz B, Mo S K, Moore R G, Hashimoto M, Lee W S, Hussain Z, Devereaux T P, Fisher I R and Shen Z X 2011 *Proc. Nat. Acad. Sci.* **108** 6878–6883
- [170] Glasbrenner J K, Mazin I I, Jeschke H O, Hirschfeld P J, Fernandes R M and Valentí R 2015 *Nature Phys.* **11** 953–958
- [171] Ruiz H, Wang Y, Moritz B, Baum A, Hackl R and Devereaux T P 2019 *Phys. Rev. B* **99**(12) 125130
- [172] Baum A, Li Y, Tomić M, Lazarević N, Jost D, Löffler F, Muschler B, Böhm T, Chu J H, Fisher I R, Valentí R, Mazin I I and Hackl R 2018 *Phys. Rev. B* **98**(7) 075113
- [173] Fernandes R M, Chubukov A V, Knolle J, Eremin I and Schmalian J 2012 *Phys. Rev. B* **85**(2) 024534
- [174] Kontani H, Saitō T and Onari S 2011 *Phys. Rev. B* **84**(2) 024528
- [175] Gnezdilov V, Pashkevich Y G, Lemmens P, Wulferding D, Shevtsova T, Gusev A, Chareev D and Vasiliev A 2013 *Phys. Rev. B* **87**(14) 144508
- [176] Wu S F, Zhang W L, Hu D, Kung H H, Lee A, Mao H C, Dai P C, Ding H, Richard P and Blumberg G 2016 *arXiv preprint arXiv:1607.06575*
- [177] Yamase H and Zeyher R 2011 *Phys. Rev. B* **83** 115116
- [178] Yamase H and Zeyher R 2013 *Phys. Rev. B* **88**(12) 125120
- [179] Yoshizawa M, Kimura D, Chiba T, Simayi S, Nakanishi Y, Kihou K, Lee C H, Iyo A, Eisaki H, Nakajima M and Uchida S i 2012 *J. Phys. Soc. Japan* **81** 024604
- [180] Kontani H and Yamakawa Y 2014 *Phys. Rev. Lett.* **113**(4) 047001
- [181] Böhm T, Ahangharnejhad R H, Jost D, Baum A, Muschler B, Kretzschmar F, Adelman P, Wolf T, Wen H H, Chu J H, Fisher I R and Hackl R 2017 *phys. status solidi (b)* **254** 1600308
- [182] Sun J P, Matsuura K, Ye G Z, Mizukami Y, Shimozaawa M, Matsubayashi K, Yamashita M, Watashige T, Kasahara S, Matsuda Y, Yan J Q, Sales B C, Uwatoko Y, Cheng J G and Shibauchi T 2016 *Nature Commun.* **7** 12146
- [183] Jia C, Wohlfeld K, Wang Y, Moritz B and Devereaux T P 2016 *Phys. Rev. X* **6**(2) 021020
- [184] de la Cruz C, Huang Q, Lynn J, Li J, II W R, Zarestky J, Mook H, Chen G, Luo J, Wang N and Dai P 2008 *Nature* **453** 899
- [185] Chu J H, Analytis J G, Kucharczyk C and Fisher I R 2009 *Phys. Rev. B* **79** 014506
- [186] Yi M, Liu Z K, Zhang Y, Yu R, Zhu J X, Lee J, Moore R, Schmitt F, Li W, Riggs S, Chu J H, Lv B, Hu J, Hashimoto M, Mo S K, Hussain Z, Mao Z, Chu C, Fisher I, Si Q, Shen Z X and Lu D 2015 *Nature Commun.* **6** 7777
- [187] Coldea A I, Blake S F, Kasahara S, Haghighirad A A, Watson M D, Knafo W, Choi E S, McCollam A, Reiss P, Yamashita T, Bruma M, Speller S C, Matsuda Y, Wolf T, Shibauchi T and Schofield A J 2019 *npj Quantum Mater.* **4** 2
- [188] Yi M, Zhang Y, Shen Z X and Lu D 2017 *npj Quantum Mater.* **2** 57
- [189] Yao D W and Li T 2019 *EPL (Europhysics Letters)* **125** 37002
- [190] Bardeen J, Cooper L N and Schrieffer J R 1957 *Phys. Rev.*

- 106** 162
- [191] Hanaguri T, Niitaka S, Kuroki K and Takagi H 2010 *Science* **328** 474
- [192] Christianson A D, Lumsden M D, Malliakas C D, Todorov I S, Claus H, Chung D Y, Kanatzidis M G, Bewley R I and Guidi T 2008 *Nature* **456** 930
- [193] Korshunov M M, Shestakov V A and N T Y 2017 *J. Magn. Mater.* **440** 133 – 135
- [194] Yin Y, Zech M, Williams T L, Wang X F, Wu G, Chen X H and Hoffman J E 2009 *Phys. Rev. Lett.* **102** 097002
- [195] Wang M, Yi M, Sun H L, Valdivia P, Kim M G, Xu Z J, Berlijn T, Christianson A D, Chi S, Hashimoto M, Lu D H, Li X D, Bourret-Courchesne E, Dai P, Lee D H, Maier T A and Birgeneau R J 2016 *Phys. Rev. B* **93**(20) 205149
- [196] Hardy F, Burger P, Wolf T, Fisher R A, Schweiss P, Adelmann P, Heid R, Fromknecht R, Eder R, Ernst D, von Löhneysen H and Meingast C 2010 *Europhys. Lett.* **91** 47008
- [197] Terashima K, Sekiba Y, Bowen J H, Nakayama K, Kawahara T, Sato T, Richard P, Xu Y M, Li L J, Cao G H, Xu Z A, Ding H and Takahashi T 2009 *Proc. Natl. Acad. Sci.* **106** 7330
- [198] Nakayama K, Sato T, Richard P, Xu Y M, Kawahara T, Umezawa K, Qian T, Neupane M, Chen G F, Ding H and Takahashi T 2011 *Phys. Rev. B* **83** 020501
- [199] Hardy F, Böhmer A E, de' Medici L, Capone M, Giovannetti G, Eder R, Wang L, He M, Wolf T, Schweiss P, Heid R, Herbig A, Adelmann P, Fisher R A and Meingast C 2016 *Phys. Rev. B* **94**(20) 205113
- [200] Xu B, Dai Y M, Xiao H, Shen B, Wen H H, Qiu X G and Lobo R P S M 2017 *Phys. Rev. B* **96**(11) 115125
- [201] Ding H, Richard P, Nakayama K, Sugawara K, Arakane T, Sekiba Y, Takayama A, Souma S, Sato T, Takahashi T, Wang Z, Dai X, Fang Z, Chen G F, Luo J L and Wang N L 2008 *Europhys. Lett.* **83** 47001
- [202] Zhang Y, Yang L X, Chen F, Zhou B, Wang X F, Chen X H, Arita M, Shimada K, Namatame H, Taniguchi M, Hu J P, Xie B P and Feng D L 2010 *Phys. Rev. Lett.* **105** 117003
- [203] Evtushinsky D V, Zabolotnyy V B, Kim T K, Kordyuk A A, Yaresko A N, Maletz J, Aswartham S, Wüfmehl S, Boris A V, Sun D L, Lin C T, Shen B, Wen H H, Varykhalov A, Follath R, Büchner B and Borisenko S V 2014 *Phys. Rev. B* **89**(6) 064514
- [204] Wray L, Qian D, Hsieh D, Xia Y, Li L, Checkelsky J G, Pasupathy A, Gomes K K, Parker C V, Fedorov A V, Chen G F, Luo J L, Yazdani A, Ong N P, Wang N L and Hasan M Z 2008 *Phys. Rev. B* **78** 184508
- [205] Mou D, Kong T, Meier W R, Lochner F, Wang L L, Lin Q, Wu Y, Bud'ko S L, Eremin I, Johnson D D, Canfield P C and Kaminski A 2016 *Phys. Rev. Lett.* **117**(27) 277001
- [206] Shimojima T, Sakaguchi F, Ishizaka K, Ishida Y, Kiss T, Okawa M, Togashi T, Chen C T, Watanabe S, Arita M, Shimada K, Namatame H, Taniguchi M, Ohgushi K, Kasahara S, Terashima T, Shibauchi T, Matsuda Y, Chainani A and Shin S 2011 *Science* **332** 564–567
- [207] Zhang Y, Ye Z R, Ge Q Q, Chen F, Jiang J, Xu M, Xie B P and Feng D L 2012 *Nat. Physics* **8** 371
- [208] Diao Z, Campanini D, Fang L, Kwok W K, Welp U and Rydh A 2016 *Phys. Rev. B* **93**(1) 014509
- [209] Kasahara S, Watashige T, Hanaguri T, Kohsaka Y, Yamashita T, Shimoyama Y, Mizukami Y, Endo R, Ikeda H, Aoyama K, Terashima T, Uji S, Wolf T, von Löhneysen H, Shibauchi T and Matsuda Y 2014 *Proc. Nat. Acad. Sci.* **111** 16309–16313
- [210] Thomale R, Platt C, Hu J, Honerkamp C and Bernevig B A 2009 *Phys. Rev. B* **80** 180505
- [211] Thomale R, Platt C, Hanke W, Hu J and Bernevig B A 2011 *Phys. Rev. Lett.* **107**(11) 117001
- [212] Evtushinsky D V, Inosov D S, Zabolotnyy V B, Koitzsch A, Knapfer M, Büchner B, Viazovska M S, Sun G L, Hinkov V, Boris A V, Lin C T, Keimer B, Varykhalov A, Kordyuk A A and Borisenko S V 2009 *Phys. Rev. B* **79** 054517
- [213] Tanatar M A, Ni N, Martin C, Gordon R T, Kim H, Kogan V G, Samolyuk G D, Bud'ko S L, Canfield P C and Prozorov R 2009 *Phys. Rev. B* **79** 094507
- [214] Tanatar M A, Ni N, Thaler A, Bud'ko S L, Canfield P C and Prozorov R 2010 *Phys. Rev. B* **82** 134528
- [215] Hirschfeld P J 2009 *Physics* **2** 100
- [216] Muschler B 2012 *Carrier dynamics of Ba(Fe_{1-x}Co_x)₂As₂ as a function of doping* Dissertation Technical University Munich
- [217] Tanatar M A, Reid J P, Shakeripour H, Luo X G, Doiron-Leyraud N, Ni N, Bud'ko S L, Canfield P C, Prozorov R and Taillefer L 2010 *Phys. Rev. Lett.* **104** 067002
- [218] Cea T, Castellani C and Benfatto L 2016 *Phys. Rev. B* **93**(18) 180507
- [219] Boeri L, Dolgov O V and Golubov A A 2008 *Phys. Rev. Lett.* **101** 026403
- [220] Liu C, Palczewski A D, Dhaka R S, Kondo T, Fernandes R M, Mun E D, Hodovanets H, Thaler A N, Schmalian J, Bud'ko S L, Canfield P C and Kaminski A 2011 *Phys. Rev. B* **84**(2) 020509
- [221] Ge Q Q, Ye Z R, Xu M, Zhang Y, Jiang J, Xie B P, Song Y, Zhang C L, Dai P and Feng D L 2013 *Phys. Rev. X* **3**(1) 011020
- [222] Zhang W L, Meier W R, Kong T, Canfield P C and Blumberg G 2018 *Phys. Rev. B* **98**(14) 140501
- [223] Colombier E, Bud'ko S L, Ni N and Canfield P C 2009 *Phys. Rev. B* **79** 224518 (pages 9)
- [224] Analytis J G, Kuo H H, McDonald R D, Wartenbe M, Rourke P M C, Hussey N E and Fisher I R 2014 *Nature Phys.* **10** 194
- [225] Xu N, Richard P, Shi X, van Roekeghem A, Qian T, Razzoli E, Rienks E, Chen G F, Ieki E, Nakayama K, Sato T, Takahashi T, Shi M and Ding H 2013 *Phys. Rev. B* **88**(22) 220508
- [226] Maier T A, Graser S, Scalapino D J and Hirschfeld P J 2009 *Phys. Rev. B* **79** 224510
- [227] Chubukov A V, Efremov D V and Eremin I 2008 *Phys. Rev. B* **78**(13) 134512
- [228] Platt C, Hanke W and Thomale R 2014 *Adv. Phys.* **62**(4-6) 453–562
- [229] Hirschfeld P J, Altenfeld D, Eremin I and Mazin I I 2015 *Phys. Rev. B* **92**(18) 184513
- [230] Böker J, Volkov P A, Hirschfeld P J and Eremin I 2019 *New J. Phys.* **21** 083021
- [231] Böhmer A E and Meingast C 2016 *C. R. Phys.* **17** 90 – 112
- [232] Chu J H, Kuo H H, Analytis J G and Fisher I R 2012 *Science* **337** 710–712
- [233] Martiny J H J, Kreisel A, Hirschfeld P J and Andersen B M 2017 *Phys. Rev. B* **95**(18) 184507
- [234] Marra P, van den Brink J and Sykora S 2016 *Sci. Reports* **6** 25386

Evidence of spin-phonon coupling in CrSiTe₃A. Milosavljević,¹ A. Šolajić,¹ J. Pešić,¹ Yu Liu (刘育),² C. Petrovic,² N. Lazarević,^{1,*} and Z. V. Popović^{1,3}¹Center for Solid State Physics and New Materials, Institute of Physics Belgrade, University of Belgrade, Pregrevica 118, 11080 Belgrade, Serbia²Condensed Matter Physics and Materials Science Department, Brookhaven National Laboratory, Upton, New York 11973-5000, USA³Serbian Academy of Sciences and Arts, Knez Mihailova 35, 11000 Belgrade, Serbia

(Received 12 July 2018; published 18 September 2018)

We present Raman scattering results on the layered semiconducting ferromagnetic compound CrSiTe₃. Four Raman-active modes, predicted by symmetry, are observed and assigned. The experimental results are supported by density functional theory calculations. The self-energies of the A_g^3 and the E_g^3 symmetry modes exhibit unconventional temperature evolution around 180 K. In addition, the doubly degenerate E_g^3 mode shows a clear change of asymmetry in the same temperature region. The observed behavior is consistent with the presence of the previously reported short-range magnetic order and strong spin-phonon coupling.

DOI: [10.1103/PhysRevB.98.104306](https://doi.org/10.1103/PhysRevB.98.104306)

I. INTRODUCTION

Trichalcogenides CrXTe₃ ($X = \text{Si, Ge}$) belong to a rare class of quasi-two-dimensional semiconducting materials with a ferromagnetic order, band gaps of 0.4 eV for Si and 0.7 eV for Ge compounds, and Curie temperatures (T_C) of 32 and 61 K, respectively [1–6]. Because of their layered structure, due to van der Waals bonding, they can be exfoliated to mono- and few-layer nanosheets, which, together with their semiconducting and magnetic properties, make an ideal combination for applications in optoelectronics and nanospintronics [7–11]. This was further supported by the observation of giant resistivity modulation of CrGeTe₃-based devices [12].

From an x-ray diffraction study [1], it was revealed that CrSiTe₃ crystals are twinned along c axes, the thermal expansion is negative at low temperatures, and the thermal conductivity shows strong magnon-phonon scattering effects. A very small single-ion anisotropy favoring magnetic order along c axes and spin waves was found in CrSiTe₃ by elastic and inelastic neutron scattering [13]. Spin-wave measurements suggest the absence of three-dimensional correlations above T_C , whereas in-plane dynamic correlations are present up to 300 K. First-principles calculations suggested the possibility of graphenelike mechanical exfoliation for CrXTe₃ ($X = \text{Si, Ge}$) single crystals with conserved semiconducting and ferromagnetic properties [14]. The exfoliation of CrSiTe₃ bulk to mono- and few-layer two-dimensional crystals onto a Si/SiO₂ substrate has been achieved [15] with a resistivity between 80 and 120 K, depending on the number of layers. Critical exponents for CrSiTe₃ were also determined from theoretical analysis [16].

Spin-phonon coupling in CrGeTe₃ was investigated in Raman scattering experiments [17]. Splitting of the two lowest-energy E_g modes in the ferromagnetic phase has been observed and ascribed to time-reversal symmetry breaking by

the spin ordering. Furthermore, the significant renormalization of the three higher-energy modes' self-energies below T_C provided additional evidence of spin-phonon coupling [17]. The external pressure-induced effect on lattice dynamics and magnetization in CrGeTe₃ has also been studied [18].

The Raman spectrum of CrSiTe₃ single crystals was reported in Ref. [1], where three Raman-active modes have been observed. Similar results have also been presented in Ref. [15] for ultrathin nanosheets of CrSiTe₃. Here, we report a Raman scattering study of CrSiTe₃ single crystals, with the main focus on phonon properties in the temperature range between 100 and 300 K. Our experimental results are qualitatively different from those previously reported [1,15] but consistent with the results obtained for CrGeTe₃ [17,18]. Furthermore, our data reveal the asymmetry of the E_g^3 mode, which is suppressed at higher temperatures. The A_g^3 and E_g^3 symmetry modes exhibit nonanharmonic self-energy temperature dependence in the region around 180 K, related to the strong spin-lattice interaction due to short-range magnetic order [1]. Energies and symmetries of the observed Raman-active modes are in good agreement with theoretical calculations.

II. EXPERIMENT AND NUMERICAL METHOD

Single crystals of CrSiTe₃ and CrGeTe₃ were grown as described previously [19]. For a Raman scattering experiment, a Tri Vista 557 spectrometer was used in the backscattering micro-Raman configuration with a 1800/1800/2400 grooves/mm diffraction grating combination. A coherent Verdi G solid-state laser with a 532-nm line was used as the excitation source. The direction of the incident (scattered) light coincides with a crystallographic c axis. Right before being placed in the vacuum, the samples were cleaved in the air. All measurements were performed in a high vacuum (10^{-6} mbar) using a KONTI CryoVac continuous-helium-flow cryostat with a 0.5-mm-thick window. Laser-beam focusing was achieved through a microscope objective with $\times 50$ magnification, a spot size of approximately 8 μm , and a power

*nenadl@ipb.ac.rs

TABLE I. Calculated and experimental crystallographic lattice parameters for CrSiTe₃ ($|a| = |b|$), bond lengths, interlayer distance (d), and van der Waals (vdW) gap.

CrSiTe ₃	Calculation (Å)	Experiment (Å) [20]
a	6.87	6.76
c	19.81	20.67
Si-Si	2.27	2.27
Si-Te	2.52	2.51
Cr-Te	2.77	2.78
d	6.86	6.91
vdW gap	3.42	3.42

<2 mW on the surface of a sample. All spectra were corrected for the Bose factor.

Density functional theory calculations were performed in the Quantum Espresso software package [21], using the PBE exchange-correlation functional [22], PAW pseudopotentials [23,24], and energy cutoffs for wave functions and the charge density of 85 and 425 Ry, respectively. For k -point sampling, the Monkhorst-Pack scheme was used, with a Γ -centered $8 \times 8 \times 8$ grid. Optimization of the atomic positions in the unit cell was performed until the interatomic forces were minimized down to 10^{-6} Ry/Å. In order to obtain the parameters accurately, treatment of the van der Waals interactions was included using the Grimme-D2 correction [25]. Phonon frequencies were calculated at the Γ point

within the linear response method implemented in Quantum Espresso. Calculated crystallographic properties obtained by relaxing the structures are in good agreement with x-ray diffraction measurements [20]. A comparison between our, calculated, and experimental results is presented in Table I.

III. RESULTS AND DISCUSSION

A. Polarization dependence

CrSiTe₃ crystallizes in the rhombohedral crystal structure, described by $R\bar{3}$ (C_{3i}^2) [26]. Wyckoff positions of atoms, together with each site's contribution to phonons at the Γ point and corresponding Raman tensors, are listed in Table II. The phonon mode distribution obtained by factor-group analysis for the $R\bar{3}$ space group is as follows:

$$\Gamma_{\text{Raman}} = 5A_g + 5E_g,$$

$$\Gamma_{\text{IR}} = 4A_u + 4E_u,$$

$$\Gamma_{\text{Acoustic}} = A_u + E_u.$$

Since the plane of incidence is ab , where $|a| = |b|$ [$\angle(a, b) = 120^\circ$], and the direction of light propagation is along c axes, from the selection rules, it is possible to observe all Raman-active modes, i.e., five A_g modes and five doubly degenerate E_g modes. According to the Raman tensors presented in Table II, A_g symmetry modes are observable only in the parallel polarization configuration, whereas E_g symmetry

TABLE II. (a) Type of atoms, Wyckoff positions, each site's contribution to the phonons at the Γ point, and corresponding Raman tensors for the $R\bar{3}$ space group of CrSiTe₃. (b) Phonon symmetry, calculated optical phonon frequencies at 0 K, and experimental values for Raman-active (at 100 K) and infrared (IR)-active (at 110 K) [1] CrSiTe₃ phonons.

(a) Space group $R\bar{3}$ (No. 148)					
Atom(s) (Wyckoff positions)			Irreducible representations		
Cr, Si (6 <i>c</i>)			$A_g + E_g + A_u + E_u$		
Te (18 <i>f</i>)			$3A_g + 3E_g + 3A_u + 3E_u$		
(b) Raman tensors					
$A_g = \begin{pmatrix} a & 0 & 0 \\ 0 & b & 0 \\ 0 & 0 & c \end{pmatrix}$		$E_g^1 = \begin{pmatrix} c & d & e \\ d & -c & f \\ e & f & 0 \end{pmatrix}$		$E_g^2 = \begin{pmatrix} d & -c & -f \\ -c & -d & e \\ -f & e & 0 \end{pmatrix}$	
Raman active			IR active [1]		
Symmetry	Calc. (cm ⁻¹)	Expt. (cm ⁻¹)	Symmetry	Calc. (cm ⁻¹)	Expt. (cm ⁻¹)
A_g^1	88.2	—	A_u^1	91.8	91.0
E_g^1	93.5	88.9	E_u^1	93.7	—
E_g^2	96.9	—	A_u^2	116.8	—
E_g^3	118.3	118.2	E_u^2	117.1	—
A_g^2	122.0	—	A_u^3	202.4	—
A_g^3	148.0	147.4	E_u^3	206.2	207.9
A_g^4	208.7	—	A_u^4	243.7	—
E_g^4	219.5	217.2	E_u^4	365.8	370.4
E_g^5	357.4	—			
A_g^5	508.8	—			

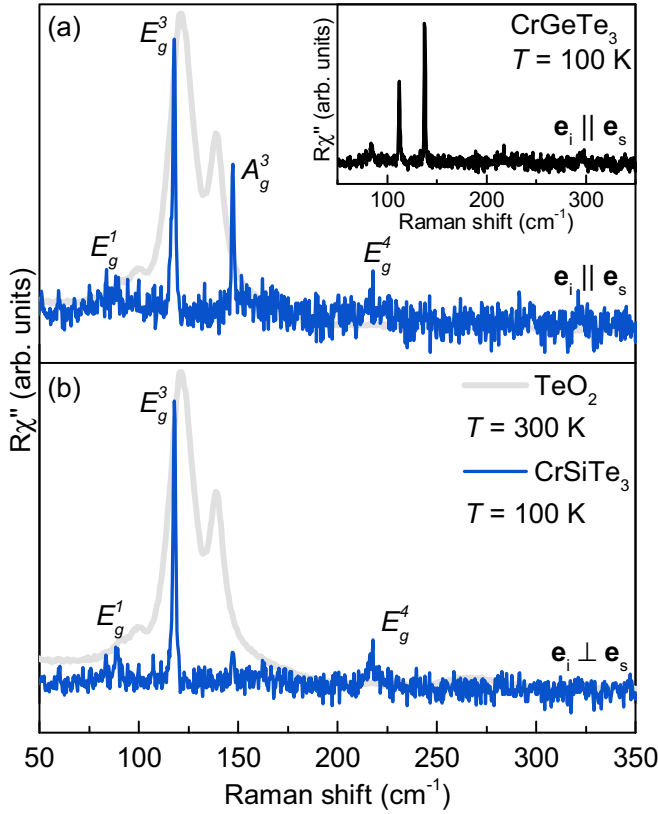


FIG. 1. Raman spectra of CrSiTe₃ single crystals measured at 100 K in (a) parallel and (b) cross polarization configurations. The gray line represents the TeO₂ spectrum measured at 300 K. Inset: Raman spectrum of CrGeTe₃ in the parallel polarization configuration measured at 100 K.

modes can be expected to appear for both in-parallel and cross polarization configurations.

The Raman spectra of CrSiTe₃ for two main linear polarization configurations, at 100 K, are shown in Fig. 1. Four peaks can be observed in the spectra, at energies of 88.9, 118.2, 147.4, and 217.2 cm⁻¹. Since only the peak at 147.4 cm⁻¹ vanishes in the cross polarization configuration, it corresponds to the A_g symmetry mode. The other three modes appear in both parallel and cross polarization configurations and, thereby, can be assigned as E_g symmetry modes (Fig. 1).

In order to exclude the possibility that any of the observed features originate from the TeO₂ [17,27], its Raman spectrum is also presented in Fig. 1. It can be noted that no TeO₂ contribution is present in our CrSiTe₃ data. Furthermore, the observed CrSiTe₃ Raman spectra are also consistent with the CrGeTe₃ Raman spectra (see inset in Fig. 1), isostructural to CrSiTe₃. Five Raman-active modes have been observed for CrGeTe₃, two A_g modes, at 137.9 and 296.6 cm⁻¹, and three E_g modes, at 83.5, 112.2, and 217.5 cm⁻¹, in agreement with the previously published data [17,18]. The main difference in the spectra of CrSiTe₃ and CrGeTe₃ arises from the change in mass and lattice parameter effects that cause the peaks to shift.

Calculated and observed Raman-active phonon energies are compiled in Table II, together with the experimental energies of the infrared (IR)-active phonons [1], and are found to be in good agreement. Displacement patterns of the A_g

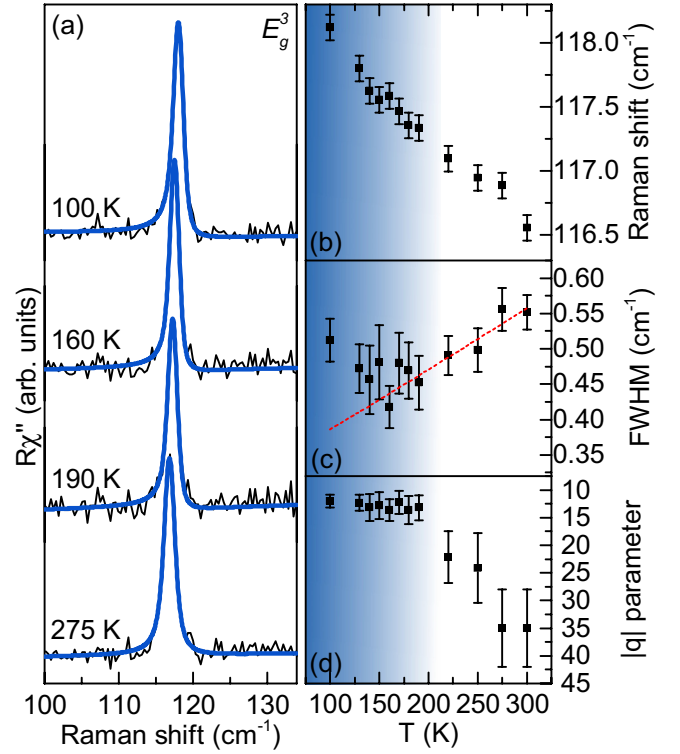


FIG. 2. (a) The E_g^3 mode Raman spectra of CrSiTe₃ at four temperatures measured in the cross polarization configuration. Blue lines represent line shapes obtained as a convolution of the Fano line shape and Gaussian, calculated to fit the experimental data. Temperature dependence of (b) the energy, (c) the line width, and (d) the Fano parameter q of the E_g^3 mode. The dashed red line represents standard anharmonic behavior [28,29]. All the parameters show a change in tendency around 180 K.

and E_g symmetry modes are presented in Fig. 4, in the Appendix.

B. Temperature dependence

After proper assignment of all the observed CrSiTe₃ Raman-active modes we proceeded with temperature evolution of their properties, focusing on the most prominent ones, E_g³ and A_g³. Figure 2(a) shows the spectral region of the doubly degenerate E_g³ mode at an energy of 118.2 cm⁻¹, at four temperatures. Closer inspection of the 100 K spectra revealed clear asymmetry of the peak on the low-energy side. The presence of defects may result in the appearance of the mode asymmetry [30], however, they would also contribute to the mode line width and, possibly, the appearance of phonons from the edge of the Brillouin zone in the Raman spectra [29]. The very narrow lines and absence of additional features in the Raman spectra of CrSiTe₃ do not support this scenario. The asymmetry may also arise when the phonon is coupled to a continuum [31]. Such a coupling of the E_g³ phonon mode would result in a line shape given by the convolution of a Fano function and a Gaussian, the latter representing the resolution of the spectrometer [29]. Comparison between the Fano line shape convoluted with a Gaussian, the Voigt line shape, and the experimental data at 100 K is presented in Fig. 5, in the

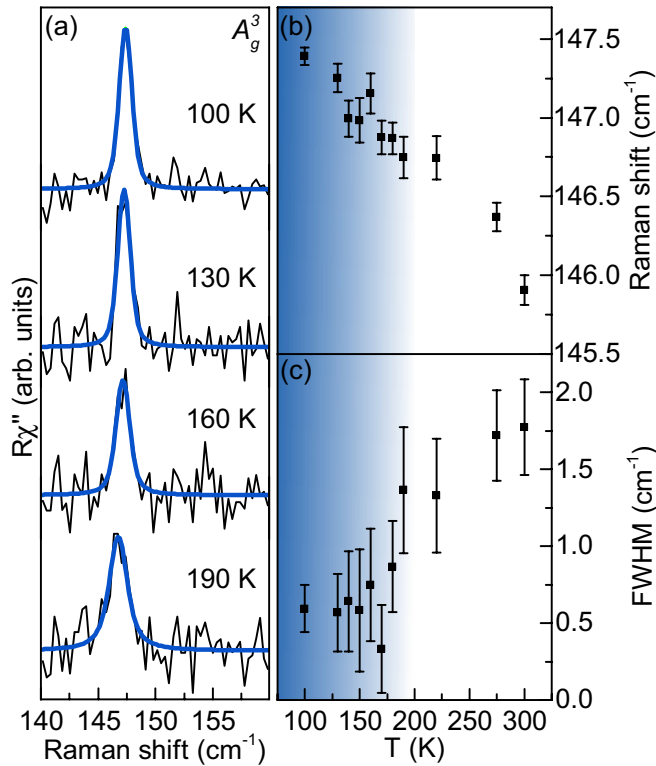


FIG. 3. (a) A_g^3 mode Raman spectra of CrSiTe_3 at four temperatures measured in the parallel polarization configuration. Blue lines represent Voigt line shapes. (b) Energy and (c) line-width temperature dependence of the A_g^3 mode.

Appendix, with the former yielding better agreement with the experimental data. Furthermore, it fully captures the E_g^3 mode line shape at all temperatures under investigation [Figs. 2(a) and 6].

Upon cooling of the sample, the E_g^3 mode energy hardens [Fig. 2(b)] with a very small discontinuity in the temperature range around 180 K. Down to the same temperature, the line width monotonically narrows in line with the standard anharmonic behavior [dashed red line in Fig. 2(c)]. Upon further cooling, the line width increased, deviating from the expected anharmonic tendency. This indicates activation of an additional scattering mechanism, e.g., spin-phonon interaction. Figure 2(d) shows the evolution of the Fano parameter, $|q|$. Whereas in the region below 180 K, it increases slightly but continuously, at higher temperatures it promptly goes to lower values and the mode recovers a symmetric line shape. We believe that the observed behavior of the E_g^3 mode can be traced back to the short-range magnetic correlations, which, according to Ref. [1], persist up to 150 K, and the strong spin-phonon coupling in CrSiTe_3 . Similar behavior of the energy and line width, which differs from the conventional anharmonic, as well as the E_g mode Fano-type line shape, was recently reported in $\alpha\text{-RuCl}_3$ and was interpreted as a consequence of the spin-phonon interaction [32].

Unlike the E_g^3 mode, no pronounced asymmetry was observed for the A_g^3 mode. As can be seen from Figs. 3(b) and 3(c) both the energy and the line width of the A_g^3 mode showed

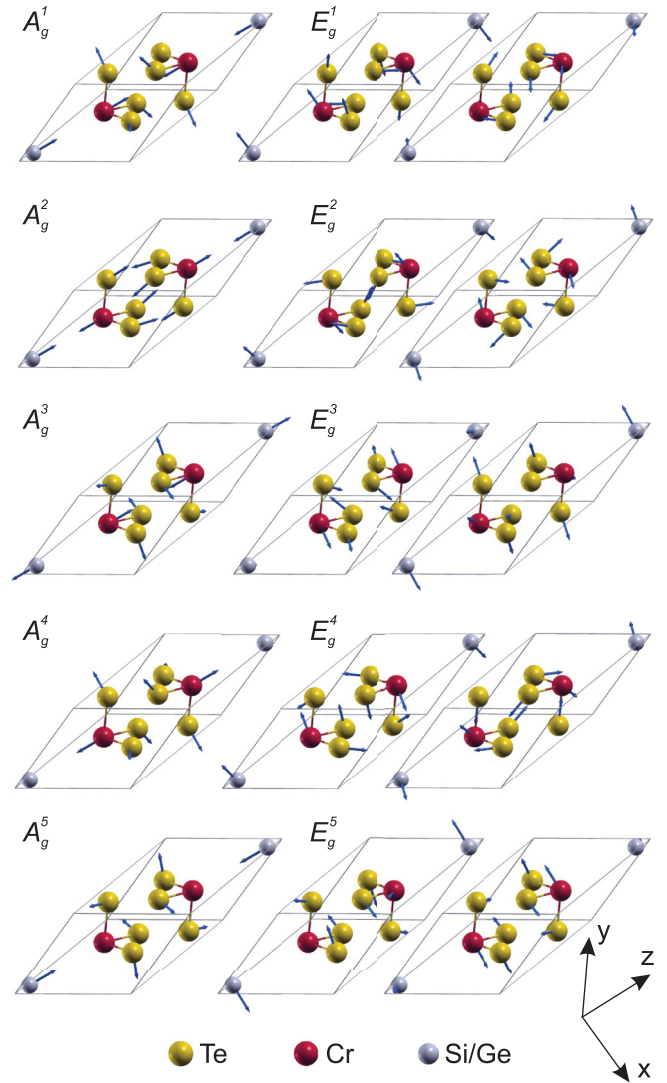


FIG. 4. Unit cell of a CrSiTe_3 single crystal (solid lines) with the displacement patterns of the A_g and E_g symmetry modes. Arrow lengths are proportional to the square root of the interatomic forces.

a similar change in tendency in the same temperature region as the E_g^3 mode, most likely due to the spin-phonon coupling.

IV. CONCLUSION

The lattice dynamics of CrSiTe_3 , a compound isostructural to CrGeTe_3 , is presented. An A_g and three E_g modes were observed and assigned. The experimental results are well supported by theoretical calculations. The temperature dependences of the energies and line widths of the A_g^3 and E_g^3 modes deviate from the conventional anharmonic model in the temperature range around 180 K. In addition, the E_g^3 mode shows clear Fano resonance at lower temperatures. This can be related to the previously reported short-range magnetic correlations at temperatures up to 150 K [1] and the strong spin-phonon coupling.

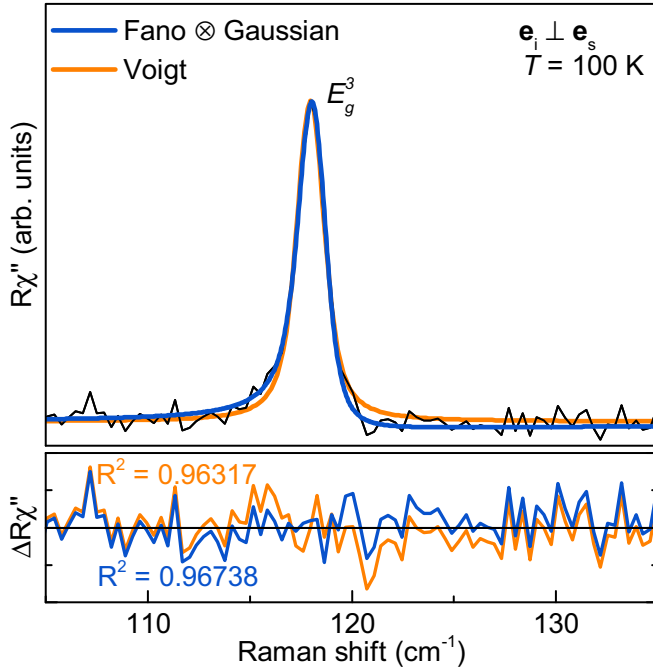


FIG. 5. Analysis of the E_g^3 asymmetry. Measured data are shown as the black line. The solid blue line represents the line shape obtained as a convolution of the Fano line shape and a Gaussian, whereas the orange line represents a Voigt line shape, both calculated to fit the experimental data. The Voigt profile deviates from the experimental data at the peak flanks.

ACKNOWLEDGMENTS

The work was supported by the Serbian Ministry of Education, Science and Technological Development under Projects III45018 and OI171005. DFT calculations were performed using computational resources at Johannes Kepler University, Linz, Austria. Work at Brookhaven is supported by the U.S. DOE under Contract No. DE-SC0012704.

A.M. and N.L. conceived and performed the experiment, analyzed and discussed data, and wrote the paper; A.S. and J.P. calculated phonon energies, analyzed and discussed data, and wrote the paper; Y.L. and C.P. synthesized and characterized the samples; Z.V.P. analyzed and discussed data and wrote the paper. All authors commented on the manuscript.

APPENDIX

1. Eigenvectors of Raman-active modes

Figure 4 summarizes the A_g and E_g symmetry mode displacement patterns of a CrSiTe₃ single crystal ($R\bar{3}$ space group). Arrow lengths are proportional to the square root of the interatomic forces.

2. Asymmetry of the E_g^3 line

The peak at 118.2 cm^{-1} , which we assigned as the E_g^3 symmetry mode, at low temperatures shows a significant asymmetry towards lower energies. The possibility of additional defect-induced features in Raman spectra can be excluded, since the modes are very narrow, suggesting high crystallinity

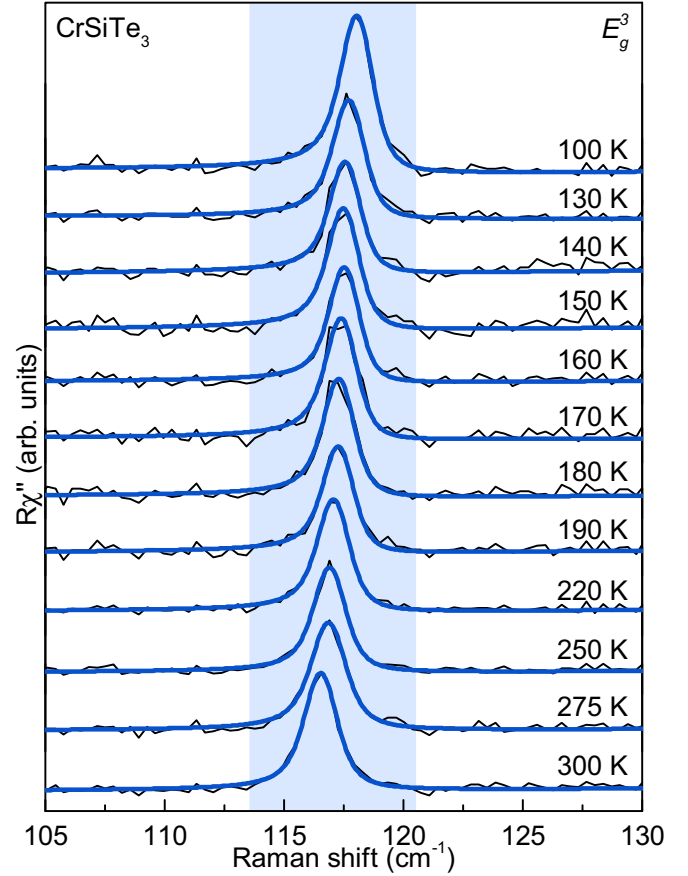


FIG. 6. The E_g^3 mode Raman spectra of CrSiTe₃ at all temperatures measured in the cross polarization configuration. Blue lines represent calculated spectra obtained as the convolution of the Fano line shape and Gaussian.

of the sample. Also, the theoretical calculations do not predict additional Raman-active modes in this energy region. On the other hand, coupling of the phonon mode to a continuum may result in an asymmetric line shape described with the Fano function. Due to the finite resolution of the spectrometer it has to be convoluted with a Gaussian ($\Gamma_G = 1 \text{ cm}^{-1}$). In Fig. 5 we present a comparison of the line obtained as a convolution of the Fano line shape and a Gaussian (blue line) and a Voigt line shape (orange line) fitted to the experimental data. Whereas the Voigt line shape deviates at the peak flanks, excellent agreement has been achieved for convolution of the Fano line shape and a Gaussian.

3. E_g^3 mode temperature dependence

Figure 6 shows Raman spectra of CrSiTe₃ in the region of the E_g^3 mode in the cross polarization configuration at various temperatures. Solid blue lines represent the convolution of the Fano line shape and Gaussian fitted to the experimental data. The asymmetry is the most pronounced below 190 K. Above this temperature, the asymmetry is decreasing, and at high temperatures the peak recovers the fully symmetric line shape.

- [1] L. D. Casto, A. J. Clune, M. O. Yokosuk, J. L. Musfeldt, T. J. Williams, H. L. Zhuang, M.-W. Lin, K. Xiao, R. G. Hennig, B. C. Sales, J.-Q. Yan, and D. Mandrus, Strong spin-lattice coupling in CrSiTe₃, *APL Mater.* **3**, 041515 (2015).
- [2] X. Zhang, Y. Zhao, Q. Song, S. Jia, J. Shi, and W. Han, Magnetic anisotropy of the single-crystalline ferromagnetic insulator Cr₂Ge₂Te₆, *Jpn. J. Appl. Phys.* **55**, 033001 (2016).
- [3] T. Leineweber and H. Kronmüller, Micromagnetic examination of exchange coupled ferromagnetic nanolayers, *J. Magn. Magn. Mater.* **176**, 145 (1997).
- [4] G. Ouvrard, E. Sandre, and R. Brec, Synthesis and crystal structure of a new layered phase: The chromium hexatellurosilicate Cr₂Si₂Te₆, *J. Solid State Chem.* **73**, 27 (1988).
- [5] B. Siberchicot, S. Jobic, V. Carteaux, P. Gressier, and G. Ouvrard, Band structure calculations of ferromagnetic chromium tellurides CrSiTe₃ and CrGeTe₃, *J. Phys. Chem.* **100**, 5863 (1996).
- [6] V. Carteaux, F. Moussa, and M. Spiesser, 2D Ising-like ferromagnetic behaviour for the lamellar Cr₂Si₂Te₆ compound: A neutron scattering investigation, *Europhys. Lett.* **29**, 251 (1995).
- [7] N. Sivasdas, M. W. Daniels, R. H. Swendsen, S. Okamoto, and D. Xiao, Magnetic ground state of semiconducting transition-metal trichalcogenide monolayers, *Phys. Rev. B* **91**, 235425 (2015).
- [8] K. S. Novoselov, A. K. Geim, S. V. Morozov, D. Jiang, Y. Zhang, S. V. Dubonos, I. V. Grigorieva, and A. A. Firsov, Electric field effect in atomically thin carbon films, *Science* **306**, 666 (2004).
- [9] Q. H. Wang, K. Kalantar-Zadeh, A. Kis, J. N. Coleman, and M. S. Strano, Electronics and optoelectronics of two-dimensional transition metal dichalcogenides, *Nat. Nanotechnol.* **7**, 699 (2012), review Article.
- [10] C. Gong, L. Li, Z. Li, H. Ji, A. Stern, Y. Xia, T. Cao, W. Bao, C. Wang, Y. Wang, Z. Q. Qiu, R. J. Cava, S. G. Louie, J. Xia, and X. Zhang, Discovery of intrinsic ferromagnetism in two-dimensional van der Waals crystals, *Nature* **546**, 265 (2017).
- [11] B. Huang, G. Clark, E. Navarro-Moratalla, D. R. Klein, R. Cheng, K. L. Seyler, D. Zhong, E. Schmidgall, M. A. McGuire, D. H. Cobden, W. Yao, D. Xiao, P. Jarillo-Herrero, and X. Xu, Layer-dependent ferromagnetism in a van der Waals crystal down to the monolayer limit, *Nature* **546**, 270 (2017).
- [12] W. Xing, Y. Chen, P. M. Odenthal, X. Zhang, W. Yuan, T. Su, Q. Song, T. Wang, J. Zhong, S. Jia, X. C. Xie, Y. Li, and W. Han, Electric field effect in multilayer Cr₂Ge₂Te₆: A ferromagnetic 2D material, *2D Mater.* **4**, 024009 (2017).
- [13] T. J. Williams, A. A. Aczel, M. D. Lumsden, S. E. Nagler, M. B. Stone, J.-Q. Yan, and D. Mandrus, Magnetic correlations in the quasi-two-dimensional semiconducting ferromagnet CrSiTe₃, *Phys. Rev. B* **92**, 144404 (2015).
- [14] X. Li and J. Yang, CrXTe₃ (X = Si, Ge) nanosheets: Two dimensional intrinsic ferromagnetic semiconductors, *J. Mater. Chem. C* **2**, 7071 (2014).
- [15] M.-W. Lin, H. L. Zhuang, J. Yan, T. Z. Ward, A. A. Piretzky, C. M. Rouleau, Z. Gai, L. Liang, V. Meunier, B. G. Sumpter, P. Ganesh, P. R. C. Kent, D. B. Geohegan, D. G. Mandrus, and K. Xiao, Ultrathin nanosheets of CrSiTe₃: A semiconducting two-dimensional ferromagnetic material, *J. Mater. Chem. C* **4**, 315 (2016).
- [16] B. Liu, Y. Zou, S. Zhou, L. Zhang, Z. Wang, H. Li, Z. Qu, and Y. Zhang, Critical behavior of the van der Waals bonded high T_C ferromagnet Fe₃GeTe₂, *Sci. Rep.* **7**, 6184 (2017).
- [17] Y. Tian, M. J. Gray, H. Ji, R. J. Cava, and K. S. Burch, Magneto-elastic coupling in a potential ferromagnetic 2D atomic crystal, *2D Mater.* **3**, 025035 (2016).
- [18] Y. Sun, R. C. Xiao, G. T. Lin, R. R. Zhang, L. S. Ling, Z. W. Ma, X. Luo, W. J. Lu, Y. P. Sun, and Z. G. Sheng, Effects of hydrostatic pressure on spin-lattice coupling in two-dimensional ferromagnetic Cr₂Ge₂Te₆, *Appl. Phys. Lett.* **112**, 072409 (2018).
- [19] Y. Liu and C. Petrovic, Critical behavior of quasi-two-dimensional semiconducting ferromagnet Cr₂Ge₂Te₆, *Phys. Rev. B* **96**, 054406 (2017).
- [20] G. T. Lin, H. L. Zhuang, X. Luo, B. J. Liu, F. C. Chen, J. Yan, Y. Sun, J. Zhou, W. J. Lu, P. Tong, Z. G. Sheng, Z. Qu, W. H. Song, X. B. Zhu, and Y. P. Sun, Tricritical behavior of the two-dimensional intrinsically ferromagnetic semiconductor CrGeTe₃, *Phys. Rev. B* **95**, 245212 (2017).
- [21] P. Giannozzi, S. Baroni, N. Bonini, M. Calandra, R. Car, C. Cavazzoni, D. Ceresoli, G. L. Chiarotti, M. Cococcioni, I. Dabo, A. D. Corso, S. de Gironcoli, S. Fabris, G. Fratesi, R. Gebauer, U. Gerstmann, C. Gougoussis, A. Kokalj, M. Lazzeri, L. Martin-Samos, N. Marzari, F. Mauri, R. Mazzarello, S. Paolini, A. Pasquarello, L. Paulatto, C. Sbraccia, S. Scandolo, G. Sclauzero, A. P. Seitsonen, A. Smogunov, P. Umari, and R. M. Wentzcovitch, Quantum espresso: A modular and open-source software project for quantum simulations of materials, *J. Phys.: Condens. Matter* **21**, 395502 (2009).
- [22] J. P. Perdew, K. Burke, and M. Ernzerhof, Generalized Gradient Approximation Made Simple, *Phys. Rev. Lett.* **77**, 3865 (1996).
- [23] P. E. Blöchl, Projector augmented-wave method, *Phys. Rev. B* **50**, 17953 (1994).
- [24] G. Kresse and D. Joubert, From ultrasoft pseudopotentials to the projector augmented-wave method, *Phys. Rev. B* **59**, 1758 (1999).
- [25] G. Stefan, Semiempirical GGA-type density functional constructed with a long-range dispersion correction, *J. Comput. Chem.* **27**, 1787 (2006).
- [26] R. E. Marsh, The crystal structure of Cr₂Si₂Te₆: Corrigendum, *J. Solid State Chem.* **77**, 190 (1988).
- [27] N. Lazarević, E. S. Bozin, M. Šćepanović, M. Opačić, Hechang Lei, C. Petrovic, and Z. V. Popović, Probing IrTe₂ crystal symmetry by polarized Raman scattering, *Phys. Rev. B* **89**, 224301 (2014).
- [28] M. Opačić, N. Lazarević, M. Šćepanović, H. Ryu, H. Lei, C. Petrovic, and Z. V. Popović, Evidence of superconductivity-induced phonon spectra renormalization in alkali-doped iron selenides, *J. Phys.: Condens. Matter* **27**, 485701 (2015).
- [29] A. Baum, A. Milosavljević, N. Lazarević, M. M. Radonjić, B. Nikolić, M. Mitschek, Z. Inanloo Maranloo, M. Šćepanović, M. Grujić-Brožćin, N. Stojilović, M. Opel, Aifeng Wang, C. Petrovic, Z. V. Popović, and R. Hackl, Phonon anomalies in FeS, *Phys. Rev. B* **97**, 054306 (2018).
- [30] N. Lazarević, M. Radonjić, M. Šćepanović, Hechang Lei, D. Tanasković, C. Petrovic, and Z. V. Popović, Lattice dynamics of KNi₂Se₂, *Phys. Rev. B* **87**, 144305 (2013).

- [31] N. Lazarević, Z. V. Popović, Rongwei Hu, and C. Petrovic, Evidence for electron-phonon interaction in $\text{Fe}_{1-x}\text{M}_x\text{Sb}_2$ ($M = \text{Co}$ and Cr ; $0 \leq x \leq 0.5$) single crystals, *Phys. Rev. B* **81**, 144302 (2010).
- [32] L. J. Sandilands, Y. Tian, K. W. Plumb, Y.-J. Kim, and K. S. Burch, Scattering Continuum and Possible Fractionalized Excitations in $\alpha\text{-RuCl}_3$, *Phys. Rev. Lett.* **114**, 147201 (2015).

ARTICLE

<https://doi.org/10.1038/s42005-019-0107-y>

OPEN

Frustrated spin order and stripe fluctuations in FeSe

A. Baum^{1,2}, H.N. Ruiz^{3,4}, N. Lazarević⁵, Yao Wang^{3,6,10}, T. Böhm^{1,2,11}, R. Hosseinian Ahangharnejhad^{1,2,12}, P. Adelman⁷, T. Wolf⁷, Z.V. Popović^{5,8}, B. Moritz³, T.P. Devereaux^{3,9} & R. Hackl¹

The charge and spin dynamics of the structurally simplest iron-based superconductor, FeSe, may hold the key to understanding the physics of high temperature superconductors in general. Unlike the iron pnictides, FeSe lacks long range magnetic order in spite of a similar structural transition around 90 K. Here, we report results of Raman scattering experiments as a function of temperature and polarization and simulations based on exact diagonalization of a frustrated spin model. Both experiment and theory find a persistent low energy peak close to 500 cm⁻¹ in B_{1g} symmetry, which softens slightly around 100 K, that we assign to spin excitations. By comparing with results from neutron scattering, this study provides evidence for nearly frustrated stripe order in FeSe.

¹Walther Meissner Institut, Bayerische Akademie der Wissenschaften, 85748 Garching, Germany. ²Fakultät für Physik E23, Technische Universität München, 85748 Garching, Germany. ³Stanford Institute for Materials and Energy Sciences, SLAC National Accelerator Laboratory, 2575 Sand Hill Road, Menlo Park, CA 94025, USA. ⁴Department of Physics, Stanford University, Stanford, CA 94305, USA. ⁵Center for Solid State Physics and New Materials, Institute of Physics Belgrade, University of Belgrade, Pregrevica 118, 11080 Belgrade, Serbia. ⁶Department of Applied Physics, Stanford University, Stanford, CA 94305, USA. ⁷Karlsruher Institut für Technologie, Institut für Festkörperphysik, 76021 Karlsruhe, Germany. ⁸Serbian Academy of Sciences and Arts, Knez Mihailova 35, 11000 Belgrade, Serbia. ⁹Geballe Laboratory for Advanced Materials, Stanford University, Stanford, CA 94305, USA. ¹⁰Present address: Lyman Laboratory 336, Harvard University, 17 Oxford St. Cambridge, 02138 MA, USA. ¹¹Present address: TNG Technology Consulting GmbH, Beta-Straße, 85774 Unterföhring, Germany. ¹²Present address: School of Solar and Advanced Renewable Energy, Department of Physics and Astronomy, University of Toledo, Toledo, OH 43606, USA. Correspondence and requests for materials should be addressed to R.H. (email: hackl@wmi.badw.de)

Fe-based pnictides and chalcogenides, similar to cuprates, manganites or some heavy fermion compounds, are characterized by the proximity and competition of various phases including magnetism, charge order, and superconductivity. Specifically the magnetism of Fe-based systems has various puzzling aspects which do not straightforwardly follow from the Fe valence or changes in the Fermi surface topology^{1–4}. Some systems have a nearly ordered localized moment close to $2\mu_B$ ⁵, such as FeTe or rare-earth iron selenides, whereas the moments of AFe_2As_2 -based compounds ($A = Ba, Sr, Eu$ or Ca) are slightly below $1\mu_B$ ⁶ and display aspects of itinerant spin-density-wave (SDW) magnetism with a gap in the electronic excitation spectrum⁷. In contrast others do not order down to the lowest temperatures, such as FeSe⁸ or LaFePO⁹.

The material specific differences are a matter of intense discussion, and low- as well as high-energy electronic and structural properties determine the properties^{1,2,4,10–13}. At the Fermi energy E_F , the main fraction of the electronic density of states originates from t_{2g} Fe orbitals, but a substantial part of the Fe–Fe hopping occurs via the pnictogen or chalcogen atoms, hence via the xz , yz , and p_z orbitals. For geometrical reasons, the resulting exchange coupling energies between nearest (J_1) and next nearest neighbor (J_2) iron atoms have the same order of magnitude, and small changes in the pnictogen (chalcogen) height above the Fe plane influence the ratio J_2/J_1 , such that various orders are energetically very close¹².

The reduced overlap of the in-plane xy orbitals decreases the hopping integral t and increases the influence of the Hund's rule interactions and the correlation energy U , even though they are only in the range of 1–2 eV. Thus the electrons in the xy orbitals have a considerably higher effective mass m^* and smaller quasi-particle weight Z than those of the xz and yz orbitals. This effect was coined orbital selective Mottness^{14–16} and was observed by photoemission spectroscopy (ARPES) in Fe-based chalcogenides¹⁷. It is similar in spirit to what was found by Raman scattering in the cuprates as a function of momentum¹⁸. In either case some of the electron wave functions are more localized than others. This paradigm may explain why the description remains difficult and controversial in all cases.

Therefore we address the question as to whether systematic trends can be found across the families of the Fe-based superconductors, how the spin excitations are related to other highly correlated systems, and how they can be described appropriately.

As an experimental tool we use Raman scattering since the differences expected theoretically^{1,3} and indicated experimentally in the electronic structure⁷ can be tracked in both the charge and the spin channel. Another advantage is the large energy range of approximately 1 meV to 1 eV (8–8000 cm^{-1}) accessible by light scattering¹⁹.

Early theoretical work on Fe-based systems considered the Heisenberg model the most appropriate approach²⁰, and the high-energy maxima observed by Raman scattering in $BaFe_2As_2$ were interpreted in terms of localized spins^{21,22}. On the other hand, the low-energy spectra are reminiscent of charge density wave (CDW) or SDW formation^{22–25}. In principle, both effects can coexist if the strength of the correlations varies for electrons from different orbitals, where itinerant electrons form a SDW, while those on localized orbitals give rise to a Heisenberg-like response.

In contrast to the AFe_2As_2 -based compounds, FeSe seems to be closer to localized order with a larger mass renormalization than in the iron pnictides¹. Apart from low lying charge excitations, the remaining, presumably spin, degrees of freedom in FeSe may be adequately described by a spin-1 J_1 – J_2 – J_3 – K Heisenberg model¹² which provides also a consistent description of our results shown in this work and allows for the presence of different

spin orders. Since various types of spin order are energetically in close proximity^{12,26,27}, frustration may quench long-range order down to the lowest temperatures⁸, even though neutron scattering experiments in FeSe find large values for the exchange energies^{27,28}.

Recent experiments on FeSe focused on low-energies and B_{1g} ($x^2 - y^2$) symmetry, and the response was associated with particle-hole excitations and critical fluctuations²⁹. Here, we obtain similar experimental results below 1500 cm^{-1} . Those in the range 50–200 cm^{-1} show similarities with the other Fe-based systems while those above 200 cm^{-1} are distinctly different but display similarities with the cuprates^{30,31}. In addition to previous work, we analyze all symmetries at higher energies up to 3500 cm^{-1} , to uncover crucial information about the behavior of the spin degrees of freedom.

By comparing experimental and simulated Raman data we find a persistent low-energy peak at roughly 500 cm^{-1} in B_{1g} symmetry, which softens slightly around 100 K. We assign the B_{1g} maximum and the related structures in A_{1g} and B_{2g} symmetry to spin excitations. The theoretical simulations also aim at establishing a link between light and neutron scattering data with respect to the spin degrees of freedom and to furnish evidence for nearly frustrated stripe order at low temperature. We arrive at the conclusion that frustrated order of localized spins dominates the physics in FeSe, while critical spin and/or charge fluctuations are not the main focus of the paper.

Results

Experiments. Symmetry-resolved Raman spectra of single-crystalline FeSe (see Methods) in the energy range up to 0.45 eV (3600 cm^{-1}) are shown in Fig. 1. The spectra are linear combinations of the polarization dependent raw data (see Methods and Supplementary Fig. 1 in Supplementary Note 1). For B_{1g} symmetry (Fig. 1a) we plot only two temperatures, 40 and 300 K, to highlight the persistence of the peak at ~ 500 cm^{-1} . The full temperature dependence will be shown below. For A_{1g} , A_{2g} , and B_{2g} symmetry we show spectra at 40, 90, and 300 K (Fig. 1b–d). Out of the four symmetries, the A_{1g} , B_{1g} , and B_{2g} spectra display Raman active phonons, magnons or electron-hole excitations, while the A_{2g} spectra are weak and vanish below 500–1000 cm^{-1} . As intensity in A_{2g} symmetry appears only under certain conditions not satisfied in the present study, we ignore it here.

In the high-energy limit the intensities are smaller in all symmetries than those in other Fe-based systems such as $BaFe_2As_2$ (see Supplementary Fig. 2 in Supplementary Note 2). However, in the energy range up to ~ 3000 cm^{-1} there is a huge additional contribution to the B_{1g} cross section in FeSe (Fig. 1a). The response is strongly temperature dependent and peaks at 530 cm^{-1} in the low-temperature limit. Between 90 and 40 K the A_{1g} and B_{2g} spectra increase slightly in the range around 700 and 3000 cm^{-1} , respectively (indicated as blue shaded areas in Fig. 1b, d). The overall intensity gain in the A_{1g} and B_{2g} spectra in the shaded range is a fraction of $\sim 5\%$ of that in B_{1g} symmetry. The B_{2g} spectra exhibit a reduction in spectral weight in the range from 600 to 1900 cm^{-1} (shaded red) which is already fully developed at the structural transition at $T_s = 89.1$ K in agreement with earlier work²⁹. In contrast to A_{1g} and B_{2g} symmetry, the temperature dependence of the B_{1g} intensity is strong, whereas the peak energy changes only weakly, displaying some similarity with the cuprates³². This similarity, along with the considerations of Glasbrenner et al.¹², motivated us to explore a spin-only, Heisenberg-like model for describing the temperature evolution of the Raman scattering data.

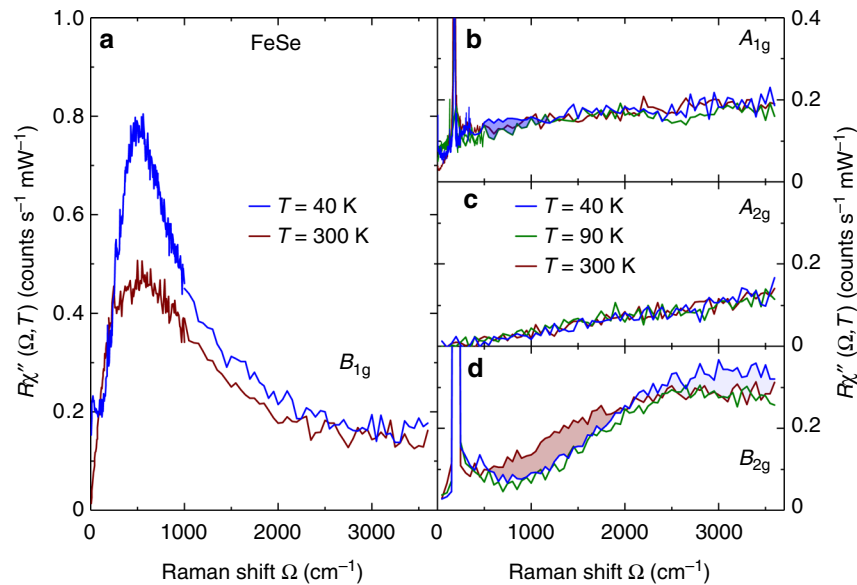


Fig. 1 Symmetry-resolved Raman spectra of FeSe at various temperatures for large energy transfers. **a** B_{1g} spectra at temperatures as indicated. The spectrum at 90 K is omitted here for clarity but is displayed in a separate figure below. The weak structure at $T = 40$ K in the range 20–25 cm^{-1} is left over from the fluctuation peak which is most pronounced right above T_s as shown below. **b** A_{1g} , **c** A_{2g} , and **d** B_{2g} spectra at temperatures as indicated. In A_{1g} and B_{2g} symmetry particle-hole excitations dominate the response. In agreement with the simulations weak additional peaks from spin excitations appear at low temperature (blue shaded areas). B_{2g} shows a loss of spectral weight (shaded red). The narrow lines close to 200 cm^{-1} are the A_{1g} and B_{1g} phonons. In the 1 Fe unit cell used here the B_{1g} phonon appears in B_{2g} symmetry since the axes are rotated by 45° with respect to the crystallographic (2 Fe) cell. The A_{2g} intensity vanishes below 500 cm^{-1} and the cross section is completely temperature independent

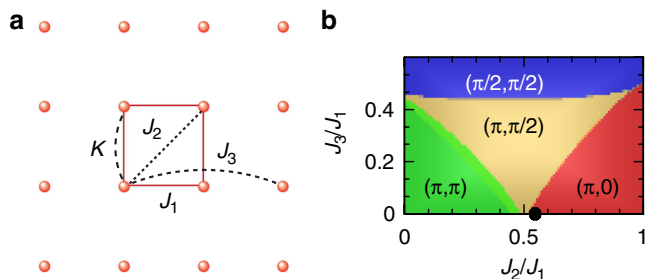


Fig. 2 Model and resulting phase diagram. **a** A 4×4 cluster was used for the simulations. The red spheres represent the Fe atoms, each of which carries localized spin \mathbf{S}_i , with $S = 1$. The nearest, next-nearest, and next-next-nearest neighbor interactions J_1 , J_2 , and J_3 , respectively, are indicated. K is the coefficient of the biquadratic term proportional to $(\mathbf{S}_i \cdot \mathbf{S}_j)^2$. **b** $J_2 - J_3$ phase diagram as obtained from our simulations at $T = 0$ and for $K = 0.1$. The black dot shows the parameters at which temperature-dependent simulations have been performed

Simulations at zero temperature. We performed numerical simulations at zero temperature for a frustrated spin-1 system on the basis of a J_1 - J_2 - J_3 - K Heisenberg model¹² on a 16-points cluster as shown in Fig. 2a and described in the Methods section. Figure 2b shows the resulting phase diagram as a function of J_2 and J_3 . K was set at 0.1 (repulsive) in order to suppress ordering tendencies on the small cluster. The parameter set for the simulations of the Raman and neutron data at finite temperature is indicated as a black dot.

In Fig. 3 we show the low-temperature data (Fig. 3a) along with the simulations (Fig. 3b). The energy scale for the simulations is given in units of J_1 which has been derived¹² to be 123 meV or 990 cm^{-1} , allowing a semi-quantitative comparison with the experiment. As already mentioned, the experimental A_{1g} and B_{2g} spectra are not dominated by spin excitations and we do not attempt to further analyze the continua extending to energies in

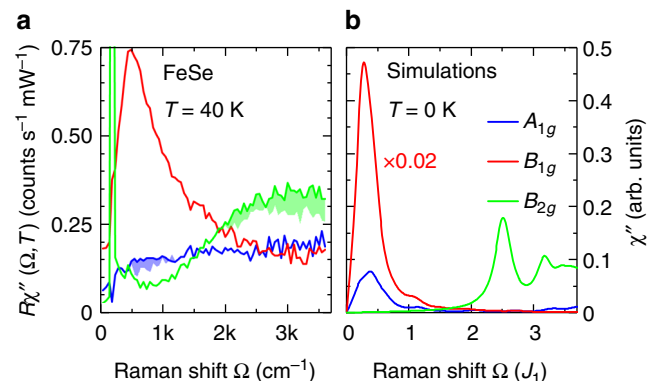


Fig. 3 Symmetry-resolved Raman spectra of FeSe for large energy shifts at low temperature. **a** Experimental results for symmetries as indicated at 40 K. The B_{1g} peak at 500 cm^{-1} dominates the spectrum. In A_{1g} and B_{2g} symmetry the electron-hole continua dominate the response, and the magnetic excitations yield only small additional contributions at approximately 700 and 3000 cm^{-1} , respectively. **b** Simulated Raman spectra at $T = 0$ K including only magnetic contributions. The A_{1g} and B_{1g} symmetries have peaks solely at low energies whereas the B_{2g} contributions are at high energies only. The B_{1g} response is multiplied by a factor of 0.02

excess of 1 eV, considering them a background. The opposite is true for B_{1g} symmetry, also borne out in the simulations. For the selected values of $J_1 = 123$ meV, $J_2 = 0.528J_1$, $J_3 = 0$, and $K = 0.1J_1$, the positions of the spin excitations in the three symmetries and the relative intensities are qualitatively reproduced. The choice of parameters is motivated by the previous use of the J_1 - J_2 Heisenberg model, with $J_1 = J_2$ to describe the stripe phase of iron pnictides²⁰. Here we use a value of J_2 smaller than J_1 to enhance competition between Néel and stripe orders when describing

FeSe. This approach and choice of parameters is strongly supported in a recent neutron scattering study²⁷.

The comparison of the different scattering symmetries, the temperature dependence, and our simulations indicate that the excitation at 500 cm^{-1} is an additional scattering channel superimposed on the particle-hole continuum and fluctuation response, as shown in Supplementary Note 3 with Supplementary Figs. 3 and 4. Here we focus on the peak centered at $\sim 500\text{ cm}^{-1}$ which, in agreement with the simulations, originates from two-magnon excitations in a highly frustrated spin system, although the features below 500 cm^{-1} also are interesting and were interpreted in terms of quadrupolar orbital fluctuations²⁹.

Temperature dependence. It is enlightening to look at the B_{1g} spectra across the whole temperature range as plotted in Fig. 4. The well-defined two-magnon peak centered at $\sim 500\text{ cm}^{-1}$ in the low temperature limit loses intensity, and becomes less well-defined with increasing temperature up to the structural transition $T_s = 89.1\text{ K}$. Above the structural transition, the spectral weight continues to decrease and the width of the two-magnon feature grows, while the peak again becomes well-defined and the energy increases slightly approaching the high temperature limit of the study. What may appear as a gap opening at low temperature is presumably just the reduction of spectral weight in a low-energy feature at $\sim 22\text{ cm}^{-1}$. The intensity of this lower energy response increases with temperature, leading to a well-formed peak at an energy around 50 cm^{-1} near the structural transition. Above the structural transition this feature rapidly loses spectral weight, hardens, and becomes indistinguishable from the two-magnon response in the high temperature limit. This low-energy feature develops in a fashion very similar to that found in $\text{Ba}(\text{Fe}_{1-x}\text{Co}_x)_2\text{As}_2$ for $x > 0$ ^{33–35}.

Now we compare the measurements with numerical simulations for the temperature dependence of the Raman B_{1g} susceptibility in Fig. 5a, b, respectively. For the simulations (Fig. 5b) we use the same parameters as at $T = 0$ (black dot in Fig. 3). At zero temperature the simulations show a single low energy B_{1g} peak around $0.3J_1$. As temperature increases, a weak shoulder forms on the low-energy side of the peak, and the whole peak softens slightly and broadens over the simulated temperature range. Except for the additional intensity at low energies, $\Omega < 200\text{ cm}^{-1}$ (Fig. 5a), there is good qualitative agreement between

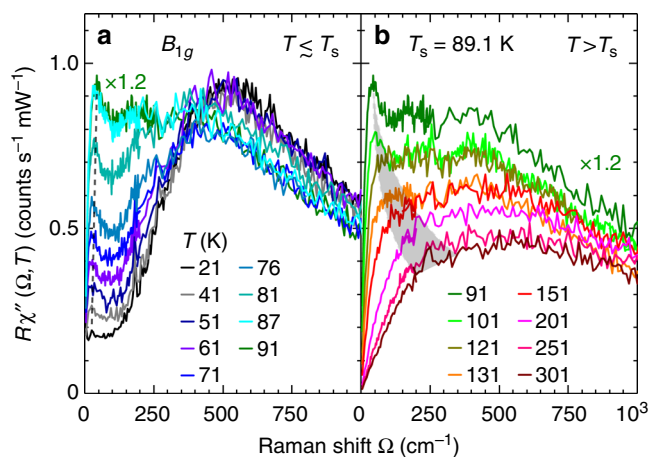


Fig. 4 Raman spectra in B_{1g} symmetry at temperatures **a** below and **b** above $T_s = 89.1\text{ K}$. The spectrum at 91 K appears in both panels for better comparison. The black dashed line in **a** and the gray shaded area in **b** indicate the approximate positions of the low-energy peak resulting from critical fluctuations. The peak centered close to 500 cm^{-1} results from excitations of neighboring spins which are studied here. A tentative decomposition is shown in Supplementary Fig. 4

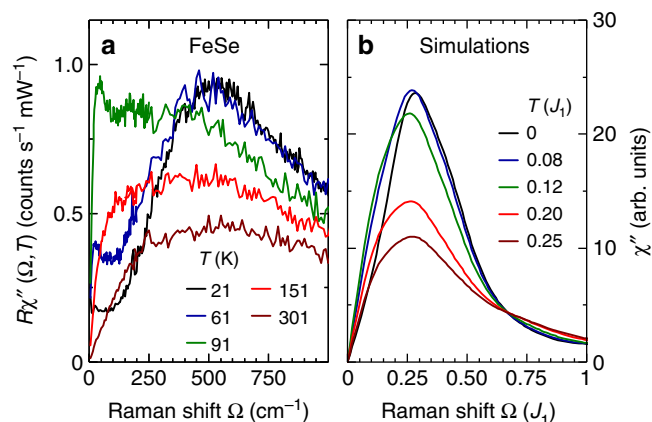


Fig. 5 Temperature dependence of the B_{1g} response. **a** Experimental spectra at selected temperatures as indicated. The spectra include several excitations the decomposition of which is shown in Supplementary Fig. 4. **b** Simulated Raman response at temperatures as indicated. Only magnetic excitations are included. The coupling constant was derived as $J_1 = 123\text{ meV}$ in ref. ¹²

theory and experiment. As shown in Supplementary Fig. 5 in Supplementary Note 4, a similar agreement between experiment and simulations is obtained for the temperature dependence in A_{1g} and B_{2g} symmetries, indicating that both the gain in intensity (blue shaded areas in Fig. 1) as well as the reduction in spectral weight in B_{2g} from 600 to 1900 cm^{-1} (shaded red in Fig. 1d) can be attributed to the frustrated localized magnetism.

Connection to the spin structure factor. To support our explanation of the Raman data, we simulated the dynamical spin structure factor $S(\mathbf{q}, \omega)$ and compared the findings to results of neutron scattering experiments²⁷. While clearly not observing long-range order, above the structural transition neutron scattering finds similar intensity at finite energy for several wave vectors along the line $(\pi, 0) - (\pi, \pi)$. Upon cooling, the spectral weight at these wave vectors shifts away from (π, π) to directions along $(\pi, 0)$, although the respective peaks remain relatively broad. In Fig. 6a, b we show the results of the simulations for two characteristic temperatures. As the temperature decreases, spectral weight shifts from (π, π) toward $(\pi, 0)$ in agreement with the experiment²⁷. In Fig. 6c we show the evolution of the spectral weights around (π, π) and $(\pi, 0)$ in an energy window of $(0.4 \pm 0.1)J_1$ as a function of temperature, similar to the results shown in ref. ²⁷. In the experiment, the temperature where the integrated dynamical spin structure factor changes most dramatically is close to the structural transition. From our simulations, the temperature where similar changes occur in comparison to neutron scattering corresponds to the temperature at which the simulated B_{1g} response (Fig. 5) shows the most pronounced shoulder, and the overall intensity begins to decrease. Not surprisingly, the low-energy peak in the Raman scattering experiment is also strongest near the structural transition.

Discussion

The agreement of experiment with theory in both neutron and Raman scattering suggests that a dominant contribution to the FeSe spectra comes from frustrated magnetism of essentially local spins. The differences between the classes of ferro-pnictides and -chalcogenides, in particular the different degrees of itineracy, may then originate in a subtle orbital differentiation across the families¹.

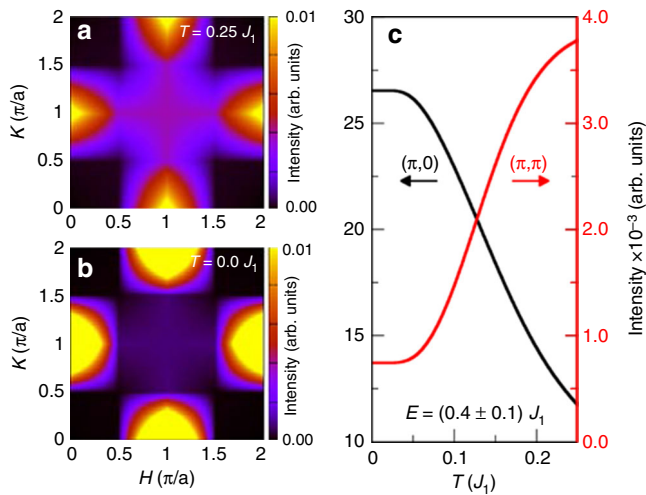


Fig. 6 Simulations of the dynamical structure factor $S(\mathbf{q}, \omega)$ of localized spin excitations integrated over an energy window of $(0.4 \pm 0.1)J_1$. **a, b** display cuts through the first Brillouin zone at $T = 0.25$ and $0J_1$, respectively. At high temperature there is intensity at (π, π) indicating a tendency toward Néel order. At low temperature the intensity at (π, π) is reduced and the stripe-like antiferromagnetism with $(\pi, 0)$ ordering wave vector becomes stronger. **c** $S(\mathbf{q}, \omega)$ integrated over an energy window $(0.4 \pm 0.1)J_1$ for fixed momenta (π, π) and $(\pi, 0)$ intensities as a function of temperature

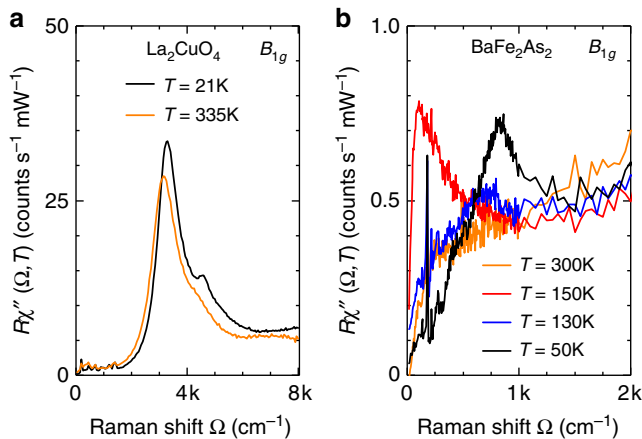


Fig. 7 Examples of localized and itinerant magnets. **a** B_{1g} Raman spectra of La_2CuO_4 . From ref. ³¹. **b** B_{1g} spectra of BaFe_2As_2 at four characteristic temperatures as indicated

If FeSe were frustrated, near such a phase boundary between magnetic states, then its behavior would be consistent with the observed sensitivity to intercalation^{36,37}, layer thickness³⁸, and pressure³⁹, which could affect the exchange interactions through the hopping. Relative to the theoretical results below 200 cm^{-1} , critical fluctuations of any origin, which are characterized by a diverging correlation length close to the transition, can neither be described nor distinguished in such a small cluster calculation. Here, only experimental arguments can be applied similar to those in ref. ³⁵, but will not be further discussed, since they are not the primary focus of the analysis. A brief summary may be found in the Supplementary Note 3.

It is remarkable how clearly the Raman spectra of an SDW state originating from a Fermi surface instability and a magnet with local moments can be distinguished. For comparison, Fig. 7

shows B_{1g} Raman spectra for La_2CuO_4 and BaFe_2As_2 at characteristic temperatures. La_2CuO_4 (Fig. 7a) is an example of a material with local moments on the Cu sites^{30,31} having a Néel temperature of $T_N = 325 \text{ K}$. The well-defined peak at $\sim 2.84J_1$ ^{40,41} possesses a weak and continuous temperature dependence across T_N ³². The origin of the scattering in La_2CuO_4 and other insulating cuprates⁴² can thus be traced back to Heisenberg-type physics of local moments⁴³, which, for simplicity, need only include the nearest-neighbor exchange interaction J_1 .

In contrast, most iron-based superconductors are metallic antiferromagnets in the parent state exhibiting rather different Raman signatures. In BaFe_2As_2 (Fig. 7b) abrupt changes are observed in B_{1g} symmetry upon entering the SDW state: the fluctuation peak below 100 cm^{-1} vanishes, a gap develops below some $500\text{--}600 \text{ cm}^{-1}$, and intensity piles up in the range $600\text{--}1500 \text{ cm}^{-1}$ (ref. ^{22,44}), the typical behavior of an SDW or CDW²⁴ in weak-coupling, resulting from Fermi surface nesting. Yet, even for itinerant systems such as these, longer range exchange interactions can become relevant and lead to magnetic frustration⁴⁵.

In summary, the Raman response of FeSe was measured in all symmetries and compared to simulations of a frustrated spin-1 system. The experimental data were decomposed in order to determine which parts of the spectra originate from particle-hole excitations, fluctuations of local spins, and low energy critical fluctuations. Comparison of the decomposed experimental data with the simulations gives evidence that the dominant contribution of the Raman spectra comes from magnetic competition between $(\pi, 0)$ and (π, π) ordering vectors. These features of the Raman spectra, which agree qualitatively with a spin-only model, consist of a dominant peak in B_{1g} symmetry around 500 cm^{-1} along with a peak at similar energy but lower intensity in A_{1g} and at higher energy in B_{2g} symmetry. These results will likely help to unravel the mechanism behind the superconducting phase found in FeSe.

Methods

Experiment. The FeSe crystals were prepared by the vapor transport technique. Details of the crystal growth and characterization are described elsewhere⁴⁶. Before the experiment the samples were cleaved in air and the exposure time was minimized. The surfaces obtained in this way have several atomically flat regions allowing us to measure spectra down to 5 cm^{-1} . At the tetragonal-to-orthorhombic transition T_s twin boundaries appear and become clearly visible in the observation optics. As described in detail by Kretzschmar et al.³⁵ the appearance of stripes can be used to determine the laser heating ΔT_L and T_s to be $(0.5 \pm 0.1) \text{ K mW}^{-1}$ and $(89.1 \pm 0.2) \text{ K}$, respectively.

Calibrated Raman scattering equipment was used for the experiment. The samples were attached to the cold finger of a He-flow cryostat having a vacuum of $\sim 5 \times 10^{-5} \text{ Pa}$ ($5 \times 10^{-7} \text{ mbar}$). For excitation we used a diode-pumped solid state laser emitting at 575 nm (Coherent GENESIS MX-SLM 577-500) and various lines of an Ar ion laser (Coherent Innova 304). The angle of incidence was close to 66° for reducing the elastic stray light entering the collection optics. Polarization and power of the incoming light were adjusted in a way that the light inside the sample had the proper polarization state and, respectively, a power of typically $P_a = 4 \text{ mW}$ independent of polarization. For the symmetry assignment we use the 1 Fe unit cell (axes x and y parallel to the Fe-Fe bonds) which has the same orientation as the magnetic unit cell in the cases of Néel or single-stripe order (4 Fe cell). The orthorhombic distortion is along these axes whereas the crystallographic cell assumes a diamond shape with the length of the tetragonal axes preserved. Because of the rotated axes in the 1 Fe unit cell the B_{1g} phonon appears in the B_{2g} spectra. Spectra at low to medium energies were measured with a resolution $\sigma \approx 5 \text{ cm}^{-1}$ in steps of $\Delta\Omega = 2.5$ or 5 cm^{-1} below 250 cm^{-1} and steps of 10 cm^{-1} above where no sharp peaks need to be resolved. Spectra covering the energy range up to $0.5\text{--}1 \text{ eV}$ were measured with a resolution $\sigma \approx 20 \text{ cm}^{-1}$ in steps of $\Delta\Omega = 50 \text{ cm}^{-1}$.

Simulations. We use exact diagonalization to study a Heisenberg-like model on a 16-site square lattice, which contains the necessary momentum points and is small enough that exact diagonalization can reach high enough temperatures to find agreement with the temperature dependence in the experiment. This was solved

using the parallel Arnoldi method⁴⁷. The Hamiltonian is given by

$$\mathcal{H} = \sum_{nn} \left[J_1 \mathbf{S}_i \cdot \mathbf{S}_j + K (\mathbf{S}_i \cdot \mathbf{S}_j)^2 \right] + \sum_{2nn} J_2 \mathbf{S}_i \cdot \mathbf{S}_j + \sum_{3nn} J_3 \mathbf{S}_i \cdot \mathbf{S}_j \quad (1)$$

where \mathbf{S}_i is a spin-1 operator reflecting the observation that the local moments of iron chalcogenides are close to $2\mu_B$ ⁴⁸. The sum over nn is over nearest neighbors, the sum over $2nn$ is over next nearest neighbors, and the sum over $3nn$ is over next next nearest neighbors.

We determine the dominant order according to the largest static spin structure factor, given by

$$S(\mathbf{q}) = \frac{1}{N} \sum_i e^{i\mathbf{q} \cdot \mathbf{R}_i} \sum_j \langle \mathbf{S}_{\mathbf{R}_i + \mathbf{R}_j} \cdot \mathbf{S}_{\mathbf{R}_i} \rangle. \quad (2)$$

Due to the possible spontaneous symmetry breaking we adjust the structure factor by the degeneracy of the momentum. To characterize the relative strength of the dominant fluctuations we project the relative intensity of the dominant static structure factor onto the range [0, 1] using the following

$$\text{Intensity} = 1 - \frac{d_{\mathbf{q}_{\text{sub}}} S(\mathbf{q}_{\text{sub}})}{d_{\mathbf{q}_{\text{max}}} S(\mathbf{q}_{\text{max}})} \quad (3)$$

where $d_{\mathbf{q}}$ is the degeneracy of momentum \mathbf{q} , \mathbf{q}_{max} is the momentum with the largest $d_{\mathbf{q}} S_{\mathbf{q}}$ and \mathbf{q}_{sub} is the momentum with the second largest (subdominant) $d_{\mathbf{q}} S_{\mathbf{q}}$.

The Raman susceptibilities for B_{1g} , B_{2g} and A_{1g} symmetries for non-zero temperatures were calculated using the Fleury-Loudon scattering operator²⁰ given by

$$\mathcal{O} = \sum_{ij} J_{ij} (\hat{\mathbf{e}}_{\text{in}} \cdot \hat{\mathbf{d}}_{ij}) (\hat{\mathbf{e}}_{\text{out}} \cdot \hat{\mathbf{d}}_{ij}) \mathbf{S}_i \cdot \mathbf{S}_j \quad (4)$$

where J_{ij} are the exchange interaction values used in the Hamiltonian, $\hat{\mathbf{d}}_{ij}$ is a unit vector connecting sites i and j and $\hat{\mathbf{e}}_{\text{in/out}}$ are the polarization vectors. For the symmetries calculated we use the polarization vectors

$$\begin{aligned} \hat{\mathbf{e}}_{\text{in}} &= \frac{1}{\sqrt{2}} (\hat{\mathbf{x}} + \hat{\mathbf{y}}), \quad \hat{\mathbf{e}}_{\text{out}} = \frac{1}{\sqrt{2}} (\hat{\mathbf{x}} - \hat{\mathbf{y}}) \text{ for } A_{1g} \oplus B_{2g}, \\ \hat{\mathbf{e}}_{\text{in}} &= \hat{\mathbf{x}}, \quad \hat{\mathbf{e}}_{\text{out}} = \hat{\mathbf{y}} \text{ for } B_{2g}, \\ \hat{\mathbf{e}}_{\text{in}} &= \frac{1}{\sqrt{2}} (\hat{\mathbf{x}} + \hat{\mathbf{y}}), \quad \hat{\mathbf{e}}_{\text{out}} = \frac{1}{\sqrt{2}} (\hat{\mathbf{x}} - \hat{\mathbf{y}}) \text{ for } B_{1g}, \end{aligned} \quad (5)$$

(where $\hat{\mathbf{x}}$ and $\hat{\mathbf{y}}$ point along the Fe-Fe directions). We use this operator to calculate the Raman response $R(\omega)$ using the continued fraction expansion⁴⁹, where $R(\omega)$ is given by

$$R(\omega) = -\frac{1}{\pi Z} \sum_n e^{-\beta E_n} \text{Im} \left(\langle \Psi_n | \mathcal{O}^\dagger \frac{1}{\omega + E_n + i\epsilon - \mathcal{H}} \mathcal{O} | \Psi_n \rangle \right) \quad (6)$$

with Z the partition function. The sum traverses over all eigenstates Ψ_n of the Hamiltonian \mathcal{H} having eigenenergies $E_n < E_0 + 2J_1$ where E_0 is the ground state energy. The Raman susceptibility is given by $\chi''(\omega) = \frac{1}{2} [R(\omega) - R(-\omega)]$. The dynamical spin structure factor was calculated using the same method with \mathcal{O} replaced with $\mathbf{S}_q^z = \frac{1}{\sqrt{N}} \sum_i e^{i\mathbf{q} \cdot \mathbf{R}_i} S_i^z$. **Note added in proof:** More details about the numerical study of the model can be found in ref. ⁵⁰.

Data availability

Data are available upon reasonable request from the corresponding author.

Received: 18 June 2018 Accepted: 21 December 2018

Published online: 04 February 2019

References

- Yin, Z. P., Haule, K. & Kotliar, G. Kinetic frustration and the nature of the magnetic and paramagnetic states in iron pnictides and iron chalcogenides. *Nat. Mater.* **10**, 932–935 (2011).
- Georges, A., de' Medici, L. & Mravlje, J. Strong correlations from Hund's coupling. *Annu. Rev. Cond. Mat. Phys.* **4**, 137–178 (2013).
- Si, Q., Yu, R. & Abrahams, E. High-temperature superconductivity in iron pnictides and chalcogenides. *Nat. Rev. Mater.* **1**, 16017 (2016).
- Skornyakov, S. L., Anisimov, V. I., Vollhardt, D. & Leonov, I. Effect of electron correlations on the electronic structure and phase stability of FeSe upon lattice expansion. *Phys. Rev. B* **96**, 035137 (2017).
- Li, S. et al. First-order magnetic and structural phase transitions in $\text{Fe}_{1+y}\text{Se}_x\text{Te}_{1-x}$. *Phys. Rev. B* **79**, 054503 (2009).
- Johnston, D. C. The puzzle of high temperature superconductivity in layered iron pnictides and chalcogenides. *Adv. Phys.* **59**, 803 (2010).
- Yi, M., Zhang, Y., Shen, Z.-X. & Lu, D. Role of the orbital degree of freedom in iron-based superconductors. *npj Quantum Mater.* **2**, 57 (2017).
- Baek, S.-H. et al. Orbital-driven nematicity in FeSe. *Nat. Mater.* **14**, 210–214 (2014).
- Taylor, A. E. et al. Absence of strong magnetic fluctuations in FeP-based systems LaFePO and $\text{Sr}_2\text{ScO}_3\text{FeP}$. *J. Phys. Condens. Matter* **25**, 425701 (2013).
- Mazin, I. I. & Johannes, M. D. A key role for unusual spin dynamics in ferropnictides. *Nat. Phys.* **5**, 141 (2009).
- Stadler, K. M., Yin, Z. P., von Delft, J., Kotliar, G. & Weichselbaum, A. Dynamical mean-field theory plus numerical renormalization-group study of spin-orbital separation in a three-band Hund metal. *Phys. Rev. Lett.* **115**, 136401 (2015).
- Glasbrenner, J. K. et al. Effect of magnetic frustration on nematicity and superconductivity in iron chalcogenides. *Nat. Phys.* **11**, 953–958 (2015).
- Baum, A. et al. Interplay of lattice, electronic, and spin degrees of freedom in detwinned BaFe_2As_2 : a Raman scattering study. *Phys. Rev. B* **98**, 075113 (2018).
- Anisimov, V. I., Nekrasov, I. A., Kondakov, D. E., Rice, T. M. & Sigrist, M. Orbital-selective Mott-insulator transition in $\text{Ca}_{2-x}\text{Sr}_x\text{RuO}_4$. *Eur. Phys. J. B* **25**, 191–201 (2002).
- de' Medici, L., Hassan, S. R., Capone, M. & Dai, X. Orbital-selective Mott transition out of band degeneracy lifting. *Phys. Rev. Lett.* **102**, 126401 (2009).
- de' Medici, L. Hund's induced fermi-liquid instabilities and enhanced quasiparticle interactions. *Phys. Rev. Lett.* **118**, 167003 (2017).
- Yi, M. et al. Observation of universal strong orbital-dependent correlation effects in iron chalcogenides. *Nat. Commun.* **6**, 7777 (2015).
- Venturini, F. et al. Observation of an unconventional metal-insulator transition in overdoped CuO_2 compounds. *Phys. Rev. Lett.* **89**, 107003 (2002).
- Devereaux, T. P. & Hackl, R. Inelastic light scattering from correlated electrons. *Rev. Mod. Phys.* **79**, 175 (2007).
- Chen, C.-C., Jia, C. J., Kemper, A. F., Singh, R. R. P. & Devereaux, T. P. Theory of Two-Magnon Raman Scattering in Iron Pnictides and Chalcogenides. *Phys. Rev. Lett.* **106**, 067002 (2011).
- Okazaki, K., Sugai, S., Niitaka, S. & Takagi, H. Phonon, two-magnon, and electronic Raman scattering of $\text{Fe}_{1+y}\text{Te}_{1-x}\text{Se}_x$. *Phys. Rev. B* **83**, 035103 (2011).
- Sugai, S. et al. Spin-density-wave gap with Dirac nodes and two-magnon Raman scattering in BaFe_2As_2 . *J. Phys. Soc. Jpn.* **81**, 024718 (2012).
- Chauvière, L. et al. Raman scattering study of spin-density-wave order and electron-phonon coupling in $\text{Ba}(\text{Fe}_{1-x}\text{Co}_x)_2\text{As}_2$. *Phys. Rev. B* **84**, 104508 (2011).
- Eiter, H.-M. et al. Alternative route to charge density wave formation in multiband systems. *Proc. Natl Acad. Sci. USA* **110**, 64–69 (2013).
- Yang, Y.-X. et al. Temperature-induced change in the Fermi surface topology in the spin density wave phase of $\text{Sr}(\text{Fe}_{1-x}\text{Co}_x)_2\text{As}_2$. *Phys. Rev. B* **89**, 125130 (2014).
- Wang, F., Kivelson, S. A. & Lee, D.-H. Nematicity and quantum paramagnetism in FeSe. *Nat. Phys.* **11**, 959–963 (2015).
- Wang, Q. et al. Magnetic ground state of FeSe. *Nat. Commun.* **7**, 12182 (2016).
- Rahn, M. C., Ewings, R. A., Sedlmaier, S. J., Clarke, S. J. & Boothroyd, A. T. Strong $(\pi, 0)$ spin fluctuations in β -FeSe observed by neutron spectroscopy. *Phys. Rev. B* **91**, 180501 (2015).
- Massat, P. et al. Charge-induced nematicity in FeSe. *Proc. Natl Acad. Sci. USA* **113**, 9177–9181 (2016).
- Sulewski, P. E., Fleury, P. A., Lyons, K. B. & Cheong, S.-W. Observation of chiral spin fluctuations in insulating planar cuprates. *Phys. Rev. Lett.* **67**, 3864 (1991).
- Muschler, B. et al. Electron interactions and charge ordering in CuO_2 compounds. *Eur. Phys. J. Spec. Top.* **188**, 131 (2010).
- Knoll, P., Thomsen, C., Cardona, M. & Murugaraj, P. Temperature-dependent lifetime of spin excitations in $\text{RBa}_2\text{Cu}_3\text{O}_6$ ($R = \text{Eu}, \text{Y}$). *Phys. Rev. B* **42**, 4842–4845 (1990).
- Choi, K.-Y. et al. Lattice and electronic anomalies of CaFe_2As_2 studied by Raman spectroscopy. *Phys. Rev. B* **78**, 212503 (2008).
- Gallais, Y. et al. Observation of incipient charge nematicity in $\text{Ba}(\text{Fe}_{1-x}\text{Co}_x)_2\text{As}_2$. *Phys. Rev. Lett.* **111**, 267001 (2013).
- Kretzschmar, F. et al. Critical spin fluctuations and the origin of nematic order in $\text{Ba}(\text{Fe}_{1-x}\text{Co}_x)_2\text{As}_2$. *Nat. Phys.* **12**, 560–563 (2016).
- Burrard-Lucas, M. et al. Enhancement of the superconducting transition temperature of fese by intercalation of a molecular spacer layer. *Nat. Mater.* **12**, 15–19 (2013).
- Zhang, A.-M. et al. Superconductivity at 44 K in K intercalated FeSe system with excess Fe. *Sci. Rep.* **3**, 1216 (2013).
- Ge, J.-F. et al. Superconductivity above 100 K in single-layer FeSe films on doped SrTiO_3 . *Nat. Mater.* **14**, 285–289 (2015).

39. Medvedev, S. et al. Electronic and magnetic phase diagram of β -Fe_{1.01}Se with superconductivity at 36.7 K under pressure. *Nat. Mater.* **8**, 630 (2009).
40. Canali, C. M. & Girvin, S. M. Theory of Raman scattering in layered cuprate materials. *Phys. Rev. B* **45**, 7127–7160 (1992).
41. Weidinger, S. A. & Zwerger, W. Higgs mode and magnon interactions in 2D quantum antiferromagnets from Raman scattering. *Eur. Phys. J. B* **88**, 237 (2015).
42. Chelwani, N. et al. Magnetic excitations and amplitude fluctuations in insulating cuprates. *Phys. Rev. B* **97**, 024407 (2018).
43. Fleury, P. A. & Loudon, R. Scattering of light by one- and two-magnon excitations. *Phys. Rev.* **166**, 514 (1968).
44. Chauvière, L. et al. Impact of the spin-density-wave order on the superconducting gap of Ba(Fe_{1-x}Co_x)₂As₂. *Phys. Rev. B* **82**, 180521 (2010).
45. Yildirim, T. Frustrated magnetic interactions, giant magneto-elastic coupling, and magnetic phonons in iron-pnictides. *Phys. C* **469**, 425 (2009).
46. Böhrer, A. E. et al. Lack of coupling between superconductivity and orthorhombic distortion in stoichiometric single-crystalline FeSe. *Phys. Rev. B* **87**, 180505 (2013).
47. Sorensen, D., Lehoucq, R. & Yang, C. *ARPACK Users' Guide: Solution of Large-Scale Eigenvalue Problems with Implicitly Restarted Arnoldi Methods*. (SIAM, Philadelphia, 1998).
48. Gretarsson, H. et al. Revealing the dual nature of magnetism in iron pnictides and iron chalcogenides using x-ray emission spectroscopy. *Phys. Rev. B* **84**, 100509 (2011).
49. Dagotto, E. Correlated electrons in high-temperature superconductors. *Rev. Mod. Phys.* **66**, 763 (1994).
50. Ruiz, H., Wang, Y., Moritz, B. & Devereaux, T. P. Frustrated magnetism from local moments in FeSe. Preprint at <https://arxiv.org/abs/1812.09609> (2018).

Acknowledgements

The work was supported by the German Research Foundation (DFG) via the Priority Program SPP 1458 (grant-no. Ha2071/7) and the Transregional Collaborative Research Center TRR80 and by the Serbian Ministry of Education, Science and Technological Development under Project III45018. We acknowledge support by the DAAD through the bilateral project between Serbia and Germany (grant numbers 57142964 and 57335339). The collaboration with Stanford University was supported by the Bavaria California Technology Center BaCaTeC (grant-no. A5 [2012-2]). Work in the SIMES at Stanford University and SLAC was supported by the U.S. Department of Energy, Office of Basic Energy Sciences, Division of Materials Sciences and Engineering, under Contract No. DE-AC02-76SF00515. Computational work was performed using the resources of

the National Energy Research Scientific Computing Center supported by the U.S. Department of Energy, Office of Science, under Contract No. DE-AC02-05CH11231.

Author contributions

A.B., T.B. and R.H. conceived the experiment. B.M. and T.P.D. conceived the ED analysis. P.A. and T.W. synthesized and characterized the samples. A.B., N.L., T.B. and R.H. A. performed the Raman scattering experiment. H.N.R. and Y.W. coded and performed the ED calculations. A.B., H.N.R., N.L., B.M. and R.H. analyzed and discussed the data. A.B., H.N.R., N.L., Z.P., B.M., T.P.D. and R.H. wrote the paper. All authors commented on the manuscript.

Additional information

Supplementary information accompanies this paper at <https://doi.org/10.1038/s42005-019-0107-y>.

Competing interests: The authors declare no competing interests.

Reprints and permission information is available online at <http://npg.nature.com/reprintsandpermissions/>

Publisher's note: Springer Nature remains neutral with regard to jurisdictional claims in published maps and institutional affiliations.



Open Access This article is licensed under a Creative Commons Attribution 4.0 International License, which permits use, sharing, adaptation, distribution and reproduction in any medium or format, as long as you give appropriate credit to the original author(s) and the source, provide a link to the Creative Commons license, and indicate if changes were made. The images or other third party material in this article are included in the article's Creative Commons license, unless indicated otherwise in a credit line to the material. If material is not included in the article's Creative Commons license and your intended use is not permitted by statutory regulation or exceeds the permitted use, you will need to obtain permission directly from the copyright holder. To view a copy of this license, visit <http://creativecommons.org/licenses/by/4.0/>.

© The Author(s) 2019

Indication of subdominant d -wave interaction in superconducting $\text{CaKFe}_4\text{As}_4$ D. Jost,^{1,2} J.-R. Scholz,^{1,2} U. Zweck,^{1,2} W. R. Meier,^{3,4} A. E. Böhmer,^{4,*} P. C. Canfield,^{4,3} N. Lazarević,⁵ and R. Hackl¹¹*Walther Meissner Institut, Bayerische Akademie der Wissenschaften, 85748 Garching, Germany*²*Fakultät für Physik E23, Technische Universität München, 85748 Garching, Germany*³*Department of Physics and Astronomy, Iowa State University, Ames, Iowa 50011, USA*⁴*Division of Materials Science and Engineering, Ames Laboratory, Ames, Iowa 50011, USA*⁵*Center for Solid State Physics and New Materials, Institute of Physics Belgrade, University of Belgrade, Pregrevica 118, 11080 Belgrade, Serbia*

(Received 31 May 2018; revised manuscript received 26 June 2018; published 13 July 2018)

We report inelastic light scattering results on the stoichiometric and fully ordered superconductor $\text{CaKFe}_4\text{As}_4$ as a function of temperature and light polarization. In the energy range between 10 and 315 cm^{-1} (1.24 and 39.1 meV) we observe the particle-hole continuum above and below the superconducting transition temperature T_c and seven of the eight Raman active phonons. The main focus is placed on the analysis of the electronic excitations. Below T_c all three symmetries projected with in-plane polarizations display a redistribution of spectral weight characteristic for superconductivity. The energies of the pair-breaking peaks in A_{1g} and B_{2g} symmetry are in approximate agreement with the results from photoemission studies. In B_{1g} symmetry the difference between the normal and superconducting state is most pronounced, and the feature is shifted downwards with respect to those in A_{1g} and B_{2g} symmetry. The maximum peaking at 134 cm^{-1} (16.6 meV) has a substructure on the high-energy side. We interpret the peak at 134 cm^{-1} in terms of a collective Bardasis-Schrieffer (BS) mode and the substructure as a remainder of the pair-breaking feature on the electron bands. There is a very weak peak at 50 cm^{-1} (6.2 meV) which is tentatively assigned to another BS mode.

DOI: [10.1103/PhysRevB.98.020504](https://doi.org/10.1103/PhysRevB.98.020504)

$\text{CaKFe}_4\text{As}_4$ is among the few iron-based compounds which are superconducting at a high transition temperature T_c at stoichiometry [1] since the Ca and K atoms form alternating intact layers, as shown in Fig. 1. The high degree of order allows one to get as close to the intrinsic properties of the material class as possible since the effects of disorder are expected to be negligible or at least significantly smaller than in solid solutions such as $\text{Ba}_{1-x}\text{K}_x\text{Fe}_2\text{As}_2$ or $\text{Ba}(\text{Fe}_{1-x}\text{Co}_x)_2\text{As}_2$. For instance, the residual resistivity ratio (RRR) reaches 15 and is much higher than for $\text{Ba}(\text{Fe}_{1-x}\text{Co}_x)_2\text{As}_2$ and is comparable to or better than that for $\text{Ba}_{1-x}\text{K}_x\text{Fe}_2\text{As}_2$ [2]. Other transport and thermodynamic properties [2] highlight the similarities to optimally or overdoped $\text{Ba}_{1-x}\text{K}_x\text{Fe}_2\text{As}_2$.

These similarities include the electronic structure, in particular, the Fermi surfaces [Fig. 1(c)] and the superconducting energy gaps [3]. The gaps were found to be rather isotropic on the individual bands having values of $2\Delta_\alpha = 21\text{ meV}$, $2\Delta_\beta = 24\text{ meV}$, $2\Delta_\gamma = 16\text{ meV}$, and $2\Delta_\delta = 24\text{ meV}$ on the three hole bands (α, β, γ) and the electron band (δ), respectively. The good nesting observed between the β and δ bands was considered to support s -wave interband pairing [3–5], as proposed earlier for the iron-based materials in general [6].

Since there is also nesting among the electron bands, one can expect a competing pairing interaction with d -wave symmetry as a subleading instability [7]. Indications thereof were found recently in Raman scattering experiments on

$\text{Ba}_{1-x}\text{K}_x\text{Fe}_2\text{As}_2$ [8–10]. The subleading channel manifests itself as a narrow line below the gap edge given that the gap is as clean as, e.g., in $\text{Ba}_{1-x}\text{K}_x\text{Fe}_2\text{As}_2$ [11–13]. The bound state has its origin in a phase fluctuation of the condensate of Cooper pairs. The experimental identification of this excitation as a Bardasis-Schrieffer (BS) exciton rests on the shape of the line, its temperature dependence, and the spectral weight transfer from the pair-breaking feature to the in-gap mode, as described in detail in Refs. [9,10].

Given its nearly clean gap and high crystal quality, $\text{CaKFe}_4\text{As}_4$ is an excellent candidate for scrutinizing the superconducting properties of hole-doped 122 systems. We aim at answering the question as to whether or not subleading channels can also be observed in systems other than $\text{Ba}_{1-x}\text{K}_x\text{Fe}_2\text{As}_2$ and whether they can be identified as generic.

Calibrated Raman scattering equipment was used for the experiments. The sample was attached to the cold finger of a He-flow cryostat. For excitation, a diode-pumped solid state laser emitting at 575 nm (Coherent GENESIS MX-SLM 577-500) was used. The polarization of the incoming light was adjusted in such a way that the light inside the sample had the proper polarization state. The absorbed power (inside the sample) was set at typically $P_a = 2\text{ mW}$, independent of polarization. By setting the polarizations of the incident and scattered photons, the four symmetries A_{1g} , A_{2g} , B_{1g} , and B_{2g} of the D_{4h} space group can be accessed. For the symmetry assignment we use the 1-Fe unit cell [see Figs. 1(b) and 1(c)] since the density of states at the Fermi energy E_F is nearly entirely derived from Fe orbitals. The related projections in the first Brillouin zone (BZ) are visualized in Fig. S1 of the

*Present address: Karlsruher Institut für Technologie, Institut für Festkörperphysik, 76021 Karlsruhe, Germany.

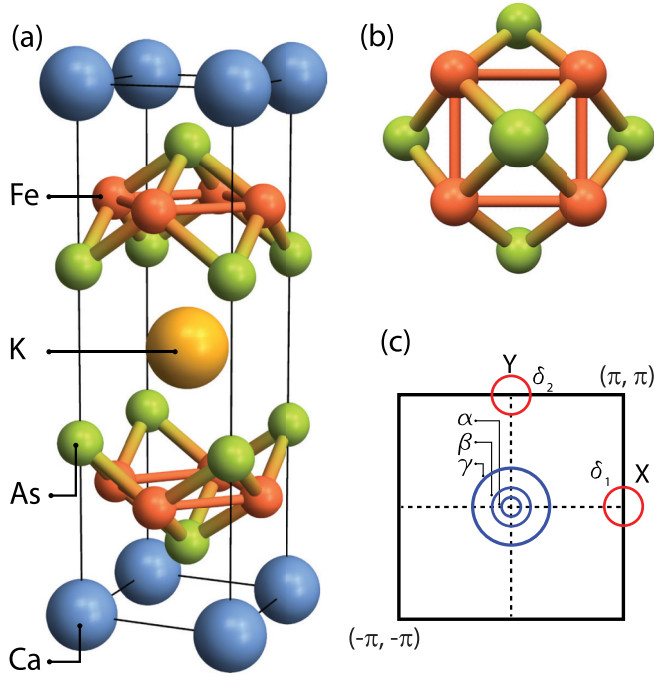


FIG. 1. Structure and Fermi surface of $\text{CaKFe}_4\text{As}_4$. (a) Tetragonal unit cell with the Ca, K, Fe, and As atoms shown in blue, gold, red, and green, respectively [1]. (b) Quasi-two-dimensional (2D) Fe_2As_2 layer with the solid orange line depicting the 1-Fe unit cell. (c) Brillouin zone of the 1-Fe cell. The three hole bands labeled α , β , and γ (blue) encircle the Γ point. The electron bands δ_1 and δ_2 (red) are centered at the X and Y points, respectively (adopted from Mou *et al.* [3]).

Supplemental Material [14]. In this Rapid Communication, the focus is placed on low energies, where A_{2g} is negligibly small. The polarization combinations RR , xy , and $x'y'$ almost exclusively project the A_{1g} , B_{2g} , and B_{1g} symmetries, as desired. Here, x and y are horizontal and vertical, respectively, in the laboratory system. Note that the out-of-phase vibration of the Fe atoms appears in B_{2g} symmetry in the 1-Fe unit cell rather than in B_{1g} symmetry of the crystallographic unit cell hosting two Fe atoms per Fe_2As_2 plane [14]. The spectra are represented as response functions $R\chi''(T, \Omega)$ which are obtained by dividing the measured cross section by the thermal Bose factor $\{1 + n(\Omega, T)\} = \{1 + [\exp(\hbar\omega/k_B T) - 1]^{-1}\}$. R is an experimental constant.

The $\text{CaKFe}_4\text{As}_4$ single crystals were grown from the FeAs flux and characterized thoroughly as described by Meier and co-workers [2,15]. The T_c value of 35.21 ± 0.10 K we found here is in the range 35.0 ± 0.2 K determined by Meier *et al.* (see Fig. S3 in the Supplemental Material [14]). The crystal structure of $\text{CaKFe}_4\text{As}_4$ is very similar to that of AFe_2As_2 systems [cf. Fig. 1(a)] and belongs to the tetragonal D_{4h} space group. Since $\text{CaKFe}_4\text{As}_4$ has alternating Ca and K planes between the Fe_2As_2 layers, the point group is simple tetragonal ($P4/mmm$) [1] rather than the body-centered tetragonal ($I4/mmm$) as BaFe_2As_2 [16].

Figure 2 shows the normal (red) and superconducting (blue) Raman spectra of $\text{CaKFe}_4\text{As}_4$ at the three polarization configurations (a) RR , (b) xy , and (c) $x'y'$. The sample is rotated by 45° with respect to the orientation in Fig. 1 in

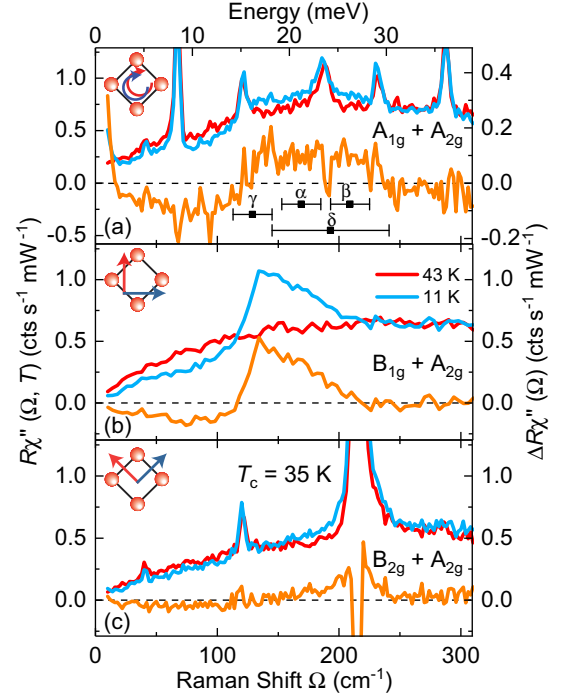


FIG. 2. Raman response in $\text{CaKFe}_4\text{As}_4$ at symmetries and polarizations as indicated. Shown are raw data for $T \ll T_c$ (blue), $T > T_c$ (red), and difference spectra (orange). Phonon modes are present in the A_{1g} and B_{2g} spectra. (a) The pair-breaking maximum extends from $\Omega_0^{(A_{1g})} = 120 \pm 5 \text{ cm}^{-1}$ to $\Omega_m \approx 230 \text{ cm}^{-1}$. The gap energies $2\Delta_i$ for the four bands i observed by ARPES [3] are reproduced as horizontal bars. Note that the right vertical axis is expanded by a factor of 2.5 with respect to the left one. (b) The B_{1g} pair-breaking peak is well defined and sets on at $\Omega_0^{(B_{1g})} = 116 \pm 5 \text{ cm}^{-1}$. (c) The weak B_{2g} pair-breaking peak is located slightly above $2\Delta_\beta$. The intersection of the normal and superconducting spectra is close to $\Omega_0^{(B_{2g})} = 130 \pm 5 \text{ cm}^{-1}$.

order to suppress any c -axis projection in the B_{1g} spectra (xy in the laboratory system). Superimposed on the particle-hole continua we observe six and four phonons in RR and $x'y'$ polarization, respectively [17], which will be discussed in the Supplemental Material [14]. As intended, there are no phonons in the xy configuration, and the spectrum in the normal state is completely smooth to within the experimental error. The structureless shape indicates that there is no polarization leakage and, more importantly, that there is no defect-induced scattering from phonons, highlighting the high crystal quality.

We focus now exclusively on the electronic continua. To this end we also plot the difference spectra,

$$\Delta R\chi''(\Omega) = R\chi''(T = 11 \text{ K}, \Omega) - R\chi''(T = 43 \text{ K}) \quad (1)$$

(orange in Fig. 2), along with the raw data of each polarization configuration. In the difference spectra $\Delta R\chi''(\Omega)$ temperature-independent structures such as (most of) the phonons and the presumably weak and temperature-independent luminescence contributions are eliminated. In this way the changes induced by superconductivity are highlighted.

All spectra show the typical changes upon entering the superconducting state: (i) The opening of the gap induces a suppression of the intensity below a crossover energy of

$\Omega_0 = 125, 115$, and 130 cm^{-1} for A_{1g} , B_{1g} , and B_{2g} symmetry, respectively. In this range, $\Delta R\chi''(\Omega)$ (orange) is negative. (ii) The intensity piles up above Ω_0 due to a coherent superposition of pair-breaking and Bogoliubov quasiparticle excitations across the gap 2Δ . The amplitude of the redistribution is small in A_{1g} and B_{2g} symmetry (Figs. 2(a) and 2(c) and Figs. S4 and S6 of Ref. [14]) but pronounced in B_{1g} symmetry. (Fig. 2(b) and Fig. S5 of Ref. [14]). In the A_{1g} response [Fig. 2(a)] the signal at $\Omega \rightarrow 0$ is enhanced because of the surface layers of accumulating residual gas molecules at low temperature (see Fig. S4 of Ref. [14]) and the insufficient suppression of the elastically scattered light in the case of parallel light polarizations (RR here).

The first striking observation is the nearly symmetry-independent crossover energy Ω_0 where the normal (red) and superconducting (blue) spectra intersect each other or where $\Delta R\chi''(\Omega)$ changes sign. Yet, the intensity for $\Omega < \Omega_0$ does not vanish entirely as expected for a clean gap, but is only reduced. No additional structures are observed in the A_{1g} and B_{2g} spectra while a weak hump appears at approximately 50 cm^{-1} [see Fig. 2(b) and asterisks in Figs. 3(c)–3(e)] in B_{1g} symmetry, as can also be seen in Fig. S5 of Ref. [14].

Second, whereas the normal and the superconducting spectra merge at similar energies close to $\Omega_m = 230 \text{ cm}^{-1}$ in all symmetries the distribution of spectral weight in the range $\Omega_0 < \Omega < \Omega_m$ varies substantially. In none of the symmetries do the pair-breaking features display the typical shape. The pair-breaking maximum in B_{2g} symmetry is found at approximately 215 cm^{-1} right underneath the Fe phonon. The negative intensity at 215 cm^{-1} shows that the phonon is renormalized below T_c , and an influence of this renormalization on the electronic features cannot be excluded. However, the gap below 130 cm^{-1} indicates the presence of an intensity redistribution below T_c . In A_{1g} symmetry a wide plateau is observed between Ω_0 and Ω_m . Finally, in B_{1g} symmetry, a pronounced peak is found at 135 cm^{-1} , above which the intensity decays. Upon studying various temperatures, a secondary maximum at about 165 cm^{-1} can be resolved, as shown in Fig. S5 of Ref. [14].

For the discussion below we additionally plot in Fig. 2(a) the gap energies $2\Delta_i$ as horizontal bars, according to a recent photoemission study [3], where i is the band index [cf. Fig. 1(c)]. The width of the bars corresponds to the error bars of order $\pm 10\%$ indicated there.

We now discuss the possible interpretations of the electronic Raman spectra presented above. Can the spectra be interpreted exclusively in terms of pair breaking, or are collective modes, similarly as in $\text{Ba}_{1-x}\text{K}_x\text{Fe}_2\text{As}_2$, necessary for a more consistent explanation?

Using yellow excitation we find a strong redistribution of spectral weight in B_{1g} symmetry, similarly as in a simultaneous Raman study using red photons [18]. (Note that B_{1g} and B_{2g} are interchanged in the two studies.) With yellow photons we observe the redistribution in all three symmetry channels. As already noticed earlier, this difference in the experimental results may be traced back to orbital-dependent resonance effects [10]. In contrast to Zhang and co-workers [18], we find finite intensity in the range below the maximal gap at approximately 215 cm^{-1} , similar as in $\text{Ba}_{1-x}\text{K}_x\text{Fe}_2\text{As}_2$. We attribute this intensity predominantly to the multigap structure in both compounds. Since there is an intensity redistribution

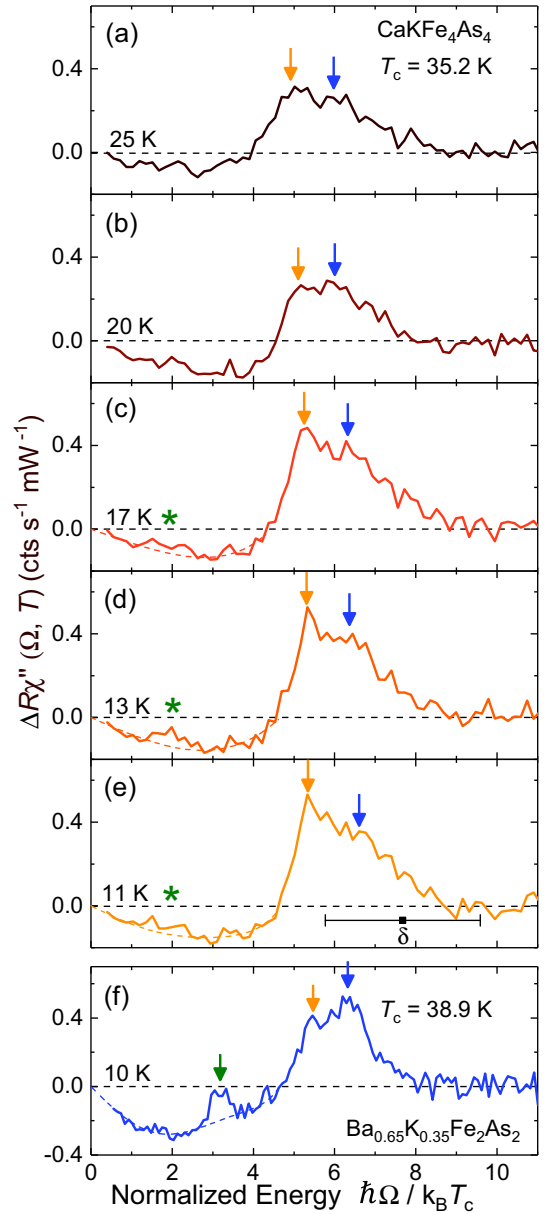


FIG. 3. Difference spectra of the B_{1g} Raman response in $\text{CaKFe}_4\text{As}_4$ and $\text{Ba}_{1-x}\text{K}_x\text{Fe}_2\text{As}_2$ for temperatures as indicated. For raw data, cf. Fig. 2 and S5 of Ref. [14]. The main peak exhibits a double structure (orange and blue arrows). A second hump is visible in the spectra at 11, 13, and 17 K (asterisks) above the spectral shape expected for a clean gap (colored dashes). (f) Difference spectrum of $\text{Ba}_{0.65}\text{K}_{0.35}\text{Fe}_2\text{As}_2$. From Ref. [10]. The arrows show two Bardasis-Schrieffer modes at $3.1k_B T_c$ (green arrow) and $5.2k_B T_c$ (orange arrow). The remainder of the pair-breaking peak is located at $6.2k_B T_c$ (blue arrow) since the high-energy part is drained into the BS modes.

below T_c in all channels we do not believe that there is a strong background at low energies from, e.g., luminescence, which has an intensity comparable to that of particle-hole excitations.

The highest pair-breaking energy in our study is observed in B_{2g} symmetry, implying a maximal gap energy of $2\Delta_{\max} \approx 215 \text{ cm}^{-1}$. This energy corresponds to $\Delta_{\max} = 13.3 \text{ meV}$, which is slightly higher than the largest gaps derived for the β

and δ bands, $\Delta_{\beta,\delta} = 12$ meV, using angle-resolved photoemission spectroscopy (ARPES) [3]. The value 215 cm^{-1} coincides with the edge of the A_{1g} pair-breaking feature (see Fig. 2), and we conclude that the ARPES data slightly underestimate the gap energies found by Raman scattering, as already observed for $\text{Ba}_{1-x}\text{K}_x\text{Fe}_2\text{As}_2$ [8,9]. Similarly, the lowest gap energy of $\Delta_\gamma = 8$ meV is below 9.3 meV, as expected from the lower edge in the A_{1g} spectra. There are no structures in the A_{1g} and B_{2g} spectra which one could associate with the gap energy on the α band, $\Delta_\alpha = 10.5$ meV, obtained from ARPES. On this basis we conclude that the maximal gap energies derived from the A_{1g} and B_{2g} Raman spectra are in the same range of approximately $9k_B T_c$ as in $\text{Ba}_{1-x}\text{K}_x\text{Fe}_2\text{As}_2$ close to optimal doping [9].

The question arises whether ARPES and Raman results are compatible with the selection rules. As shown in Fig. S1 of Ref. [14], all bands should be visible in A_{1g} symmetry with comparable weight upon neglecting the resonance effects. In fact, all energies are represented in the spectra shown in Fig. 2(a). Even if a Leggett mode contributes to the A_{1g} spectra, as suggested recently [19], this conclusion survives since the Leggett modes are expected to be close to the maximal gap energies in the Fe-based systems. The B_{2g} spectra are less easily reconciled with this scenario since the gaps on the hole bands should be projected with a similar spectral weight as that of the electron band. Yet, we find only a contribution from the largest gap. Although the overall intensity is very weak, here the absence of contributions from the γ band cannot be explained by the variation of the peak height with $|\Delta|^2$ [20] or by applying the symmetry selection rules. Either a phenomenological treatment as for $\text{Ba}_{1-x}\text{K}_x\text{Fe}_2\text{As}_2$ [9] or a detailed resonance study needs to be performed which, however, is beyond the scope of this work.

Given that the single-particle gap energies are by and large reproduced in the A_{1g} and B_{2g} spectra, it is important to understand the B_{1g} spectra. As shown in Fig. 2(c), the energies appearing there are well below those of the A_{1g} and B_{2g} spectra. This is particularly surprising as the δ bands are expected to be projected fully (and not marginally) in B_{1g} symmetry (see Fig. S1 of Ref. [14]) as opposed to all hole bands. Thus, the argument that the strongest peak in the B_{1g} spectra results from the γ band can be discarded. Since in contrast to $\text{Ba}(\text{Fe}_{1-x}\text{Co}_x)_2\text{As}_2$ [21,22], $\text{NaFe}_{1-x}\text{Co}_x\text{As}$ [23], or FeSe [24,25] there is no nematic phase and related fluctuations in $\text{CaKFe}_4\text{As}_4$, an interpretation of the observation in B_{1g} symmetry in terms of nematic fluctuations would be far fetched.

As a consequence, there remains only one scenario which reconciles the results observed in the three Raman active symmetries and the ARPES results: The B_{1g} spectra do not directly reflect gap energies but rather are shifted downward by a final state interaction, as discussed for $\text{Ba}_{1-x}\text{K}_x\text{Fe}_2\text{As}_2$ in earlier work [8–10]. The similarity can be observed directly by comparing the data in Fig. 3. The difference spectra as a function of temperature indicate that the B_{1g} peak has a robust shoulder on the high-energy side. The overall shape is surprisingly similar to the spectra of $\text{Ba}_{0.65}\text{K}_{0.35}\text{Fe}_2\text{As}_2$.

Following this reasoning we identify the maximum of the B_{1g} spectra at 134 cm^{-1} with a collective mode pulled off of the

maximal gap energy on the δ band due to a $d_{x^2-y^2}$ -wave subleading interaction among the two electron bands, as predicted theoretically [13] and observed in $\text{Ba}_{1-x}\text{K}_x\text{Fe}_2\text{As}_2$. The hump at approximately 165 cm^{-1} is then the remaining intensity of the pair-breaking peak on the δ band after switching on the final state interaction, which induces a transfer of intensity from the pair-breaking peak into the bound state [9,12,13]. The missing intensity in the range of $2\Delta_\delta$ can only be explained consistently in this way.

It is tempting, yet a bit speculative, to explain the faint peak close to 50 cm^{-1} ($2k_B T_c$) in terms of a second BS mode in a similar fashion as in $\text{Ba}_{1-x}\text{K}_x\text{Fe}_2\text{As}_2$ [10]. This would mean that the subdominant coupling is already very strong, and $\text{CaKFe}_4\text{As}_4$ is on the brink of a d -wave instability. The very weak intensity of the peak argues in this direction since the BS mode is expected to vanish when d -wave pairing wins [10]. Yet, the vanishingly small intensity is also the Achilles' heel of the argument, and we refrain from going beyond pointing out this possibility. A robust statement is possible only on the basis of improved counting statistics and a microscopic model, which includes the derivation of the eigenvectors of the subdominant pairing channels, as proposed for $\text{Ba}_{1-x}\text{K}_x\text{Fe}_2\text{As}_2$ [10]. Such an expensive theoretical treatment is beyond the scope of this experimental study.

In summary, we investigated the recently discovered superconductor $\text{CaKFe}_4\text{As}_4$ with inelastic light scattering as a function of photon polarization and temperature. Using yellow light (575 nm), superconducting features were found in A_{1g} , B_{1g} , and B_{2g} symmetry.

A weak but well-defined pair-breaking feature is found at 215 cm^{-1} (corresponding to $\Delta = 13.3$ meV) in B_{2g} symmetry, which is slightly above the largest gaps observed by ARPES for the β and the δ bands [3] and close to the energy Ω_m where the normal and the superconducting spectra merge in all symmetry projections. This feature is also present in the A_{1g} spectra. In addition to the high-energy feature, the A_{1g} intensity displays a plateaulike shape down to $\Omega_0^{(A_{1g})} = 125 \text{ cm}^{-1}$. Given the small discrepancies between the gap energies derived from the ARPES data and the Raman spectra, one can conclude that the A_{1g} spectra reflect the entire range of gap energies of $\text{CaKFe}_4\text{As}_4$ even though the individual gap energies cannot be resolved.

In B_{1g} symmetry, the superconducting feature is centered at a lower energy than in the two other symmetries. We interpret the sharp maximum at 134 cm^{-1} as a collective Bardasis-Schrieffer mode pulled off of the maximal gap on the δ band, similarly as in the sister compound $\text{Ba}_{0.65}\text{K}_{0.35}\text{Fe}_2\text{As}_2$. The shoulder at approximately 165 cm^{-1} is a remainder of the pair-breaking peak losing most of its intensity to the collective mode [9,13]. Whether or not the weak structure at 50 cm^{-1} is another BS mode with even stronger coupling cannot be decided with certainty because of the fading intensity. If this interpretation could be supported further, $\text{CaKFe}_4\text{As}_4$ would be closer to a d -wave instability than $\text{Ba}_{1-x}\text{K}_x\text{Fe}_2\text{As}_2$. The smaller T_c of $\text{CaKFe}_4\text{As}_4$ argues in this direction since a strong d -pairing channel frustrates the s -wave ground state and reduces T_c . Even without dwelling on the peak at 50 cm^{-1} , we may conclude that $\text{CaKFe}_4\text{As}_4$ is a true sibling of $\text{Ba}_{1-x}\text{K}_x\text{Fe}_2\text{As}_2$ [10], thus demonstrating that

pairing fingerprints can be observed preferably in materials with clean gaps.

We acknowledge valuable discussions with G. Blumberg. The work was supported by the Friedrich-Ebert-Stiftung, the Deutsche Forschungsgemeinschaft (DFG) via the Trans-regional Collaborative Research Center TRR 80, and the Serbian Ministry of Education, Science and Technological Development under Project No. III45018. We acknowledge

support by the Deutscher Akademischer Austauschdienst (DAAD) through the bilateral project between Serbia and Germany (Grants No. 56267076 and No. 57142964). Work at Ames Laboratory was supported by the U.S. Department of Energy, Office of Basic Energy Sciences, Division of Materials Sciences and Engineering under Contract No. DE-AC02-07CH11358. W.R.M. was supported by the Gordon and Betty Moore Foundation's EPIQS Initiative through Grant No. GBMF4411.

- [1] A. Iyo, K. Kawashima, T. Kinjo, T. Nishio, S. Ishida, H. Fujihisa, Y. Gotoh, K. Kihou, H. Eisaki, and Y. Yoshida, New-structure-type Fe-based superconductors: CaFe_4As_4 ($A = \text{K, Rb, Cs}$) and SrFe_4As_4 ($A = \text{Rb, Cs}$), *J. Am. Chem. Soc.* **138**, 3410 (2016).
- [2] W. R. Meier, T. Kong, U. S. Kaluarachchi, V. Taufour, N. H. Jo, G. Drachuck, A. E. Böhm, S. M. Saunders, A. Sapkota, A. Kreyssig, M. A. Tanatar, R. Prozorov, A. I. Goldman, F. F. Balakirev, A. Gurevich, S. L. Bud'ko, and P. C. Canfield, Anisotropic thermodynamic and transport properties of single-crystalline $\text{CaKFe}_4\text{As}_4$, *Phys. Rev. B* **94**, 064501 (2016).
- [3] D. Mou, T. Kong, W. R. Meier, F. Lochner, L.-L. Wang, Q. Lin, Y. Wu, S. L. Bud'ko, I. Eremin, D. D. Johnson, P. C. Canfield, and A. Kaminski, Enhancement of the Superconducting Gap by Nesting in $\text{CaKFe}_4\text{As}_4$: A New High Temperature Superconductor, *Phys. Rev. Lett.* **117**, 277001 (2016).
- [4] P. K. Biswas, A. Iyo, Y. Yoshida, H. Eisaki, K. Kawashima, and A. D. Hillier, Signature of multigap nodeless superconductivity in $\text{CaKFe}_4\text{As}_4$, *Phys. Rev. B* **95**, 140505 (2017).
- [5] R. Yang, Y. Dai, B. Xu, W. Zhang, Z. Qiu, Q. Sui, C. C. Homes, and X. Qiu, Anomalous phonon behavior in superconducting $\text{CaKFe}_4\text{As}_4$: An optical study, *Phys. Rev. B* **95**, 064506 (2017).
- [6] I. I. Mazin, D. J. Singh, M. D. Johannes, and M. H. Du, Unconventional Superconductivity with a Sign Reversal in the Order Parameter of $\text{LaFeAsO}_{1-x}\text{F}_x$, *Phys. Rev. Lett.* **101**, 057003 (2008).
- [7] P. J. Hirschfeld, Using gap symmetry and structure to reveal the pairing mechanism in Fe-based superconductors, *C. R. Phys.* **17**, 197 (2016).
- [8] F. Kretschmar, B. Muschler, T. Böhm, A. Baum, R. Hackl, H.-H. Wen, V. Tsurkan, J. Deisenhofer, and A. Loidl, Raman-Scattering Detection of Nearly Degenerate s -Wave and d -Wave Pairing Channels in Iron-Based $\text{Ba}_{0.6}\text{K}_{0.4}\text{Fe}_2\text{As}_2$ and $\text{Rb}_{0.8}\text{Fe}_{1.6}\text{As}_2$ Superconductors, *Phys. Rev. Lett.* **110**, 187002 (2013).
- [9] T. Böhm, A. F. Kemper, B. Moritz, F. Kretschmar, B. Muschler, H.-M. Eiter, R. Hackl, T. P. Devereaux, D. J. Scalapino, and H.-H. Wen, Balancing Act: Evidence for a Strong Subdominant d -Wave Pairing Channel in $\text{Ba}_{0.6}\text{K}_{0.4}\text{Fe}_2\text{As}_2$, *Phys. Rev. X* **4**, 041046 (2014).
- [10] T. Böhm, F. Kretschmar, A. Baum, M. Rehm, D. Jost, R. Hosseinian Ahangharnejhad, R. Thomale, C. Platt, T. A. Maier, W. Hanke, B. Moritz, T. P. Devereaux, D. J. Scalapino, S. Maiti, P. J. Hirschfeld, P. Adelman, T. Wolf, H.-H. Wen, and R. Hackl, Microscopic pairing fingerprint of the iron-based superconductor $\text{Ba}_{1-x}\text{K}_x\text{Fe}_2\text{As}_2$, *arXiv:1703.07749*.
- [11] A. Bardasis and J. R. Schrieffer, Excitons and plasmons in superconductors, *Phys. Rev.* **121**, 1050 (1961).
- [12] H. Monien and A. Zawadowski, Theory of Raman scattering with final-state interaction in high- T_c BCS superconductors: Collective modes, *Phys. Rev. B* **41**, 8798 (1990).
- [13] D. J. Scalapino and T. P. Devereaux, Collective d -wave exciton modes in the calculated Raman spectrum of Fe-based superconductors, *Phys. Rev. B* **80**, 140512 (2009).
- [14] See Supplemental Material at <http://link.aps.org/supplemental/10.1103/PhysRevB.98.020504> for details on selection rules, phonons, samples, and for additional raw data.
- [15] W. R. Meier, T. Kong, S. L. Bud'ko, and P. C. Canfield, Optimization of the crystal growth of the superconductor $\text{CaKFe}_4\text{As}_4$ from solution in the $\text{FeAs-CaFe}_2\text{As}_2\text{-KFe}_2\text{As}_2$ system, *Phys. Rev. Mater.* **1**, 013401 (2017).
- [16] M. Rotter, M. Tegel, and D. Johrendt, Superconductivity at 38 K in the Iron Arsenide $(\text{Ba}_{1-x}\text{K}_x)\text{Fe}_2\text{As}_2$, *Phys. Rev. Lett.* **101**, 107006 (2008).
- [17] J.-R. Scholz, Raman scattering study of the superconducting pairing in $\text{CaKFe}_4\text{As}_4$, Master's thesis, Technische Universität München, 2017.
- [18] W.-L. Zhang, W. R. Meier, T. Kong, P. C. Canfield, and G. Blumberg, High T_c superconductivity in $\text{CaKFe}_4\text{As}_4$ in absence of nematic fluctuations, *arXiv:1804.06963*.
- [19] T. Cea and L. Benfatto, Signature of the Leggett mode in the A_{1g} Raman response: From MgB_2 to iron-based superconductors, *Phys. Rev. B* **94**, 064512 (2016).
- [20] T. P. Devereaux and R. Hackl, Inelastic light scattering from correlated electrons, *Rev. Mod. Phys.* **79**, 175 (2007).
- [21] Y. Gallais, R. M. Fernandes, I. Paul, L. Chauvière, Y.-X. Yang, M.-A. Méasson, M. Cazayous, A. Sacuto, D. Colson, and A. Forget, Observation of Incipient Charge Nematicity in $\text{Ba}(\text{Fe}_{1-x}\text{Co}_x)_2\text{As}_2$, *Phys. Rev. Lett.* **111**, 267001 (2013).
- [22] F. Kretschmar, T. Böhm, U. Karahasanović, B. Muschler, A. Baum, D. Jost, J. Schmalian, S. Caprara, M. Grilli, C. Di Castro, J. H. Analytis, J.-H. Chu, I. R. Fisher, and R. Hackl, Critical spin fluctuations and the origin of nematic order in $\text{Ba}(\text{Fe}_{1-x}\text{Co}_x)_2\text{As}_2$, *Nat. Phys.* **12**, 560 (2016).
- [23] V. K. Thorsmølle, M. Khodas, Z. P. Yin, C. Zhang, S. V. Carr, P. Dai, and G. Blumberg, Critical quadrupole fluctuations and collective modes in iron pnictide superconductors, *Phys. Rev. B* **93**, 054515 (2016).
- [24] P. Massat, D. Farina, I. Paul, S. Karlsson, P. Strobel, P. Toulemonde, M.-A. Méasson, M. Cazayous, A. Sacuto, S. Kasahara, T. Shibauchi, Y. Matsuda, and Y. Gallais, Charge-induced nematicity in FeSe, *Proc. Natl. Acad. Sci. USA* **113**, 9177 (2016).
- [25] A. Baum, H. N. Ruiz, N. Lazarević, Y. Wang, T. Böhm, R. Hosseinian Ahangharnejhad, P. Adelman, T. Wolf, Z. V. Popović, B. Moritz, T. P. Devereaux, and R. Hackl, Frustrated spin order and stripe fluctuations in FeSe, *arXiv:1709.08998*.



Influence of chemical fixation process on primary mesenchymal stem cells evidenced by Raman spectroscopy

J.J. Lazarević^a, U. Ralević^a, T. Kukolj^b, D. Bugarski^b, N. Lazarević^{a,*}, B. Bugarski^c, Z.V. Popović^{a,d}

^aCenter for Solid State Physics and New Materials, Institute of Physics Belgrade, University of Belgrade, Pregrevica 118, Belgrade 11080, Serbia

^bLaboratory for Experimental Hematology and Stem Cells, Institute for Medical Research, University of Belgrade, Belgrade 11000, Serbia

^cDepartment of Chemical Engineering, Faculty of Technology and Metallurgy, University of Belgrade, Karnegijeva 4, Belgrade 11060, Serbia

^dSerbian Academy of Sciences and Arts, Knez Mihailova 35, Belgrade 11000, Serbia

ARTICLE INFO

Article history:

Received 7 December 2018

Received in revised form 6 March 2019

Accepted 6 March 2019

Available online 9 March 2019

Keywords:

Raman spectroscopy

Stem cells

Chemical fixation

ABSTRACT

In investigation of (patho)physiological processes, cells represent frequently used analyte as an exceptional source of information. However, spectroscopic analysis of live cells is still very seldom in clinics, as well as in research studies. Among others, the reasons are long acquisition time during which autolysis process is activated, necessity of specified technical equipment, and inability to perform analysis in a moment of sample preparation. Hence, an optimal method of preserving cells in the existing state is of extreme importance, having in mind that selection of fixative is cell lineage dependent. In this study, two commonly used chemical fixatives, formaldehyde and methanol, are used for preserving primary mesenchymal stem cells extracted from periodontal ligament, which are valuable cell source for reconstructive dentistry. By means of Raman spectroscopy, cell samples were probed and the impact of these fixatives on their Raman response was analyzed and compared. Different chemical mechanisms are the core processes of formaldehyde and methanol fixation and certain Raman bands are shifted and/or of changed intensity when Raman spectra of cells fixed in that manner are compared. In order to get clearer picture, comprehensive statistical analysis was performed.

© 2019 Elsevier B.V. All rights reserved.

1. Introduction

Mesenchymal stem cells (MSCs) are heterogenous group of adult stem cells originally discovered in bone marrow, but present in all tissues and organs, with the purpose to keep tissue homeostasis, regeneration and renewal. These acts are performed not only through multipotent differentiation potential (toward chondrogenic, adipogenic, and osteogenic lineages), but also through their ability to modulate immune response (directly or indirectly) [1–5]. Although MSCs possess common cellular features, it is overall accepted that these cells still exhibit variable regenerative capacity due to different tissue origin, donor diversity, and variations in culture conditions [6,7]. Human MSCs investigated in this study originate from periodontal ligament, a fibrous, cellular, and vascular soft connective tissue. The main role of periodontal ligament is to anchor tooth to the alveolar bone, maintain mineralisation level and alleviate mechanical forces associated with the process of mastication [8–10]. Previously, it was demonstrated that human periodontal ligament

stem cells (hPDLSCs) investigated in this experiment fulfill criteria for MSCs identification and characterization, set by The International Society for Cell Therapy (ISCT) [11,12]. Minimal criteria for characterization of human MSCs, set by ISCT, include plastic adhesion, with expression of CD73, CD90, CD105 surface markers and lack of hematopoietic markers CD34–, CD45–, CD14–, CD79α–, HLA-DR–; and multilineage differentiation potential into osteoblasts, adipocytes, and chondroblasts [13]. However, MSCs nature, including hPDLSCs, is still elusive. Therefore, the exploration of hPDLSCs, as a cell source for reconstructive dentistry, is of great importance for the novel therapeutic strategies related to recovery of periodontium and curing dental defects [14].

Taking into account the heterogeneity of MSCs, it is crucial for these cells to be adequately characterized during the lifespan, before further manipulation. Although many techniques are available in this field, including mass spectroscopy, flow cytometry, and immunocytochemistry, most of them are destructive, invasive, time consuming or require expensive cell-specific labels [15,16]. However, a light scattering technique, Raman spectroscopy, is able to overrun these issues due to its unique properties: it is non-invasive, non-destructive, fast, label-free, and complex sample preparation is not required. It operates with low sample volume even in aqueous

* Corresponding author.

E-mail address: nenadl@ipb.ac.rs (N. Lazarević).

solutions and provide a plenty of biochemical information as an outcome. Raman spectroscopy is a type of vibrational spectroscopy, based on Raman effect [17], in which an inelastically scattered component of the visible light bears the information of the analyte. Raman scattering experiment results in vibrational spectrum, a fingerprint of a sample, which carries the information about chemical composition and structure of a sample, on a submolecular level. Typically, it comprises vibrational modes of the highest Raman scattering cross section [16, 18–20].

Spectroscopic analysis of live cells is still very seldom, both in clinical and research conditions, particularly due to the longevity of the processes, when autolysis is inevitable. On the other hand, it is not always possible to investigate a sample in a moment of acquiring. The crucial and fundamental step in cell biology, for obtaining sensitive and reproducible results, is a process called fixation, which maintain the localization of biomolecules. It is used for preserving a cell in a physiological state, by preventing cell shrinkage or swelling caused by osmotic pressure initiated with air-drying, as well as autolysis by activating lysosomal enzymes, which includes denaturation of proteins, dephosphorylation of mononucleotides, phospholipids and proteins, chromatin compaction, nuclear fragmentation, and cytoplasmic condensation and fragmentation [21]. However, it is known that selection of a fixative is very much dependent on a cell nature when it comes to Raman spectroscopy and can significantly distort experimental data [22]. In the past decade, investigations of different fixatives' influence on Raman spectra of numerous cell lineages were reported, with an aim to clarify the best option for each cell lineage. One of the studies investigated the effect of formaldehyde and ethanol fixation on CARS (Coherent Anti-Stokes Raman Spectroscopy) signal of proteins and lipids in different cellular compartments of glial and neuronal cells, concluding that formaldehyde fixation is preferable method of preservation of these cells [22]. Also, the effect of chemical fixation procedures on the Raman spectra of normal and leukemia cells was characterized [23]. When compared to the spectra of unfixed cells, the fixed cell spectra showed changes in the intensity of specific Raman markers, and latter statistical analysis suggested that methanol provokes greater changes in Raman spectra when compared to paraformaldehyde. Further, micro-Raman spectroscopy was employed for chemical fixation mechanism study in three cell lines (normal skin, normal bronchial epithelium, and lung adenocarcinoma) [24]. Nucleic acid degradation, protein denaturation, and lipid leaching was observed with all fixatives (formalin, Carnoy's fixative, and methanol-acetic acid) and for all cell lines, but to varying degrees. Also, the authors suggested that formalin best preserves cellular integrity and gives the closest spectral content to that in live cells. The next study monitored the impact of fixation by formalin, desiccation, and air-drying on *in vitro* cell culture lines [25]. The results indicate that the choice of fixation methodology significantly influences the quality and reproducibility of the resulting spectral data. Formalin showed inconsistency in sample preservation and a loss of signal intensity, while air-drying appears to be inconsistent in terms of spectral reproducibility. Desiccation showed good spectral reproducibility and good signal-to-noise ratio [25].

Although numerous Raman studies of fixative process' spectral influence have been performed [22–25], according to our knowledge, no such research has been performed on primary mesenchymal stem cells originating from periodontal ligament. We used micro-Raman spectroscopy in order to probe fixed hPDLSCs and investigate the effects of two most frequently used chemical fixatives which have different chemical mechanisms of preservation (formaldehyde and methanol), and then compared those effects. Formaldehyde reacts extensively with amino groups to form methylene bridges and cross-links molecules, which alters, but stabilizes them [26]. Further, formaldehyde does not appear to perturb tertiary structure very much. On the other hand, methanol replaces water in cell environment, disrupts hydrophobic and hydrogen bonding, and

consequently alters tertiary structure of proteins [27,28]. Although fixation substantially alters composition and appearance, it is possible to produce consistent chemical and physical properties by selection of suitable preparation conditions. Nevertheless, standardization of Raman spectroscopy regarding fixative selection could provide valuable additional information in many biological tests that require cell fixation and also indicate the existence of fine differences in the fixative effect that are necessary to be taken into consideration during standard biological protocols.

2. Experiment

2.1. Isolation and Cultivation of Human Periodontal Ligament Stem Cells

After getting the informed consent from healthy patients (age 18), subjected to the procedure of tooth extraction for orthodontic reasons, at the Department of Oral Surgery of the Faculty of Dental Medicine, the University of Belgrade, human periodontal ligament tissues from normal impacted third molars were collected. Immediately after, tissues were placed in sterile cell culturing conditions. As previously reported [11], human PDLSCs were isolated, characterized and expanded. For hPDLSCs isolation, periodontal tissues were carefully detached from the mid-third of the root surface, cut into small pieces and placed in a 25 cm² flask with Dulbecco's modified Eagle's medium (DMEM; Sigma-Aldrich St. Louis, MO, USA) supplemented with 10% fetal bovine serum (FBS; Capricorn-Scientific, Germany), 100 U/ml penicillin and 100 mg/ml streptomycin (Gibco, Thermo Fisher Scientific, USA). Standard cultivation conditions included 37 °C temperature, humidified atmosphere containing 5% CO₂, while medium was exchanged two times per week. After reaching 80% to 90% confluence, cells were detached regularly in growth medium (GM-DMEM with 10% FBS) using 0.05% trypsin with 1 mM EDTA (Gibco, Thermo Fisher Scientific, USA). In order to demonstrate the universality of experimental results for MSCs, cells from third and sixth passages were used, divided into two batches. Moreover, hPDLSCs were characterized based on immunophenotype and multipotent differentiation potential toward osteogenic, chondrogenic and adipogenic lineages as it has been described before [11]. All treatments were performed according to the approved ethical guidelines set by Ethics Committee of the Faculty of Dental Medicine, University of Belgrade and Declaration of Helsinki.

2.2. Sample Preparation

For the Raman experiment, hPDLSCs were seeded on rounded CaF₂ slides in 24-well plate (5 × 10³ cells per slide) and cultivated in GM in standard cultivation conditions during 24 h. Following the adhesion, hPDLSCs were washed with saline buffer and fixed with 3.7% formaldehyde or methanol for 10 min at room temperature. Right before Raman spectroscopy was performed, samples were washed with distilled water.

2.3. μ -Raman Spectroscopy

In most of the cases, the Raman spectroscopy independently probes single vibrations within a molecule or a crystal, but in a complex biological systems composed of various types of macromolecules, only vibrational bands consisting of numerous vibrations of the same type, rather than a single vibration, could be distinguished. Consequently, the changes of biological system composition may result with a change of certain Raman bands line-shapes and/or intensities.

The Raman scattering experiment was performed using NTegra Spectra from NTMDT. The 532 nm line of a semiconductor laser was used as an excitation source. The laser power was set to 2 mW

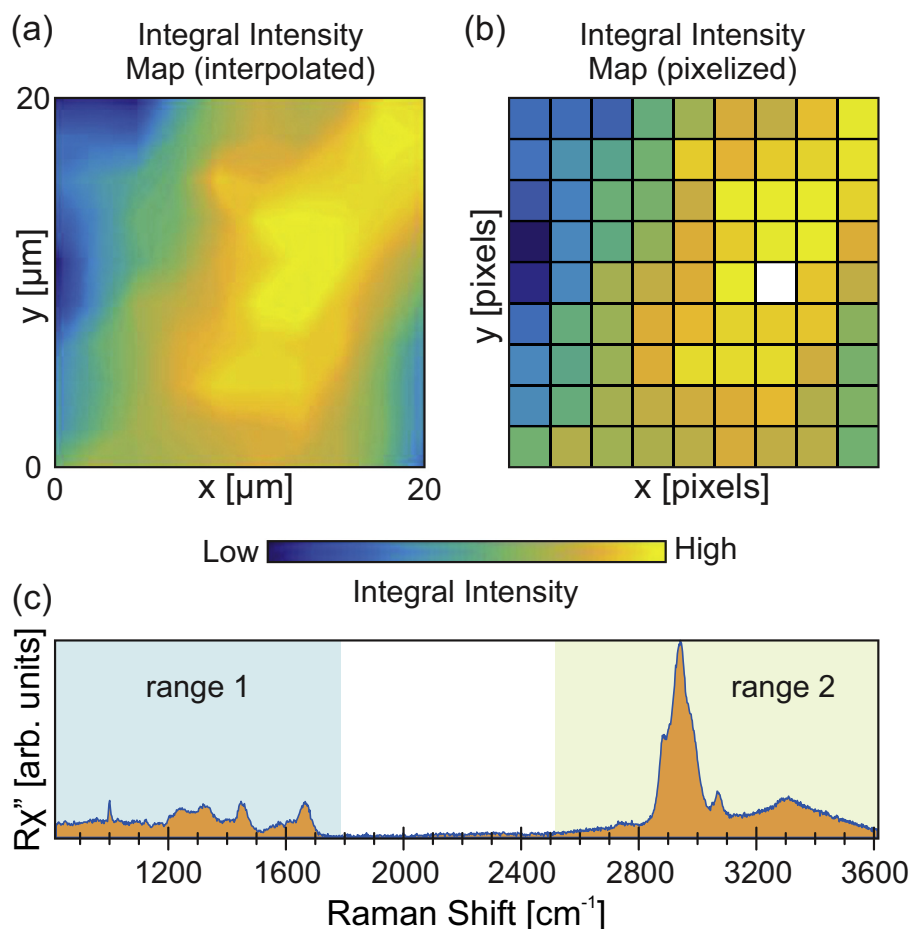


Fig. 1. A single PDLSC Raman (a) interpolated integral intensity map, and (b) pixelized integral intensity map. (c) Human PDLSC Raman scattering spectrum acquired on a pixel marked in white.

and focused on the area of about $1\ \mu\text{m}$, in order to provide a reasonable Raman intensity for a 60 s long acquisition. Under these conditions, the sample associated Raman bands, acquired sequentially at the same position, were found to be stable in terms of both the band intensity and spectral position. In other words, no visible laser induced modifications of the cells were observed upon repeating the signal acquisition for a few times at any of the acquisition points.

Due to very complex inner structure of a cell, there may be small variations in Raman spectra for the data collected at different positions. Consequently, suitable methodology must be applied in order to achieve the needed level of sample representation. In other words, the applied method has to be robust. Here, two batches of cells treated with methanol and formaldehyde were examined by spatially mapping the Raman scattering signal on 20 cells per batch. The spectra were collected at 10×10 or 11×11 matrices of spatial points separated by a distance larger than the estimated focus diameter of $\approx 1\ \mu\text{m}$. The distance between adjacent spatial points, or the spatial resolution, was varied between $2\ \mu\text{m}$ and $3\ \mu\text{m}$ depending on the cell size. The example of an interpolated spectral map of a single methanol fixed cell is presented in Fig. 1(a). Fig. 1(b) shows the same map with the actual pixels omitting the interpolation for clarity. The x and y represent spatial coordinates in which a spectrum is acquired. The intensity of a pixel, labeled white in Fig. 1(b), is obtained by integrating the Raman spectra collected at that pixel. The value of the integral is equal to the area below the acquired signal as illustrated by shaded (orange) area below the typical hPDLSC

Raman spectra in Fig. 1(c). It is characterized by clearly visible Raman bands in two spectral regions marked in Fig. 1(c). The first spectral region spans from $800\ \text{cm}^{-1}$ to $1770\ \text{cm}^{-1}$, whereas the second starts at $2500\ \text{cm}^{-1}$ and ends at $3600\ \text{cm}^{-1}$.

2.4. Data Processing and Analysis

In addition to typical PDLSCs Raman spectra [Fig. 1(c)], a few (in total) significantly different spectra, having an extremely high

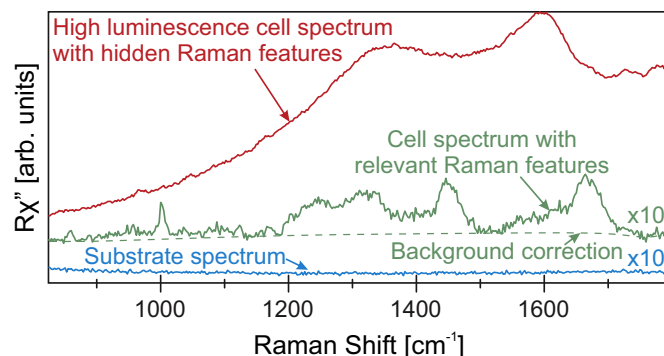


Fig. 2. A typical PDLSCs, substrate, and high luminescence points Raman spectra in the range from $800\ \text{cm}^{-1}$ to $1800\ \text{cm}^{-1}$, depicting spectral selection and preprocessing.

luminescence contribution, were observed as well. The example of such a spectrum truncated to the spectral region from 800 cm^{-1} to 1770 cm^{-1} is shown in Fig. 2. Clearly, extremely strong luminescence masks the relevant Raman bands, making them misleading. Consequently, the high luminescence spectra were omitted from the analysis. The relevant Raman spectra were preprocessed before further manipulation. In the initial step, the background, modelled as a polynomial function of the fourth degree, was subtracted (see Fig. 2). Upon background removal, the spectra were normalized to the value of the integral intensity, calculated within the considered spectral region and then subjected to the analysis.

Besides the direct comparison of the Raman spectra of the cells fixed with formaldehyde and methanol, a multivariate statistical method, principal component analysis (PCA), was applied [15,18,29,30]. Thereby, the dimensionality of the experimental data set is reduced, by transforming to a new set of variables, the principal components, which are uncorrelated and ordered in a way that the first few retain most of the variation present in all of the original variables [31]. The outcome of this analysis is distinct grouping of Raman spectra based on their mutual features [18,29].

3. Results and Discussion

Regarding biological background of our samples, it is well known that primary mesenchymal stem cell cultures represent heterogenic cellular populations, thus the intrinsic heterogeneity of primary cells should be taken into consideration. Moreover, cellular features of

these cells are highly prone to modifications during standard cultivation process [32,33]. Therefore, in order to get reproducible results, we analyzed cells from different passages (passage 3 in Batch 1 and passage 6 in Batch 2).

It is known that the effect of fixation process is cell type and fixative dependent [25]. Different chemical mechanisms may result in variations of the respective Raman spectra. Whereas depletion of certain component will result in reduction of corresponding Raman bands' intensities, various perturbations of the electronic cloud will lead to the changes of bands energy and linewidth. The second does not exclude the possibility of variations of the Raman intensities since the change in electronic structure may impact probability of the inelastic light scattering processes. In our data, the most pronounced changes are occurring in two spectral regions [Fig. 1], ranging from 800 cm^{-1} to 1770 cm^{-1} and from 2500 cm^{-1} to 3600 cm^{-1} . In the statistical treatment, these regions were analyzed independently due to the intrinsic imperfections of the spectrometer.

In Fig. 3, 2D Raman spectra map, averaged spectra, their difference and PCA of Batch 1 and Batch 2 of formaldehyde and methanol fixed PDLSCs, are presented respectively, for spectral region between 800 cm^{-1} and 1770 cm^{-1} . Closer inspection of formaldehyde and methanol fixed PDLSCs 2D Raman spectra map [Fig. 3(a) and (c)] already reveals significant difference between two groups. Relative change of intensity and/or energy shift can be clearly observed for multiple Raman bands. This is even more evident in the difference of formaldehyde and methanol fixed PDLSCs average Raman spectra [Fig. 3(a) and (c)]. It can be seen that phenylalanine peaks at 1002 cm^{-1} and 1030 cm^{-1} are of higher intensity in methanol fixed PDLSCs Raman spectra compared to formaldehyde fixed ones.

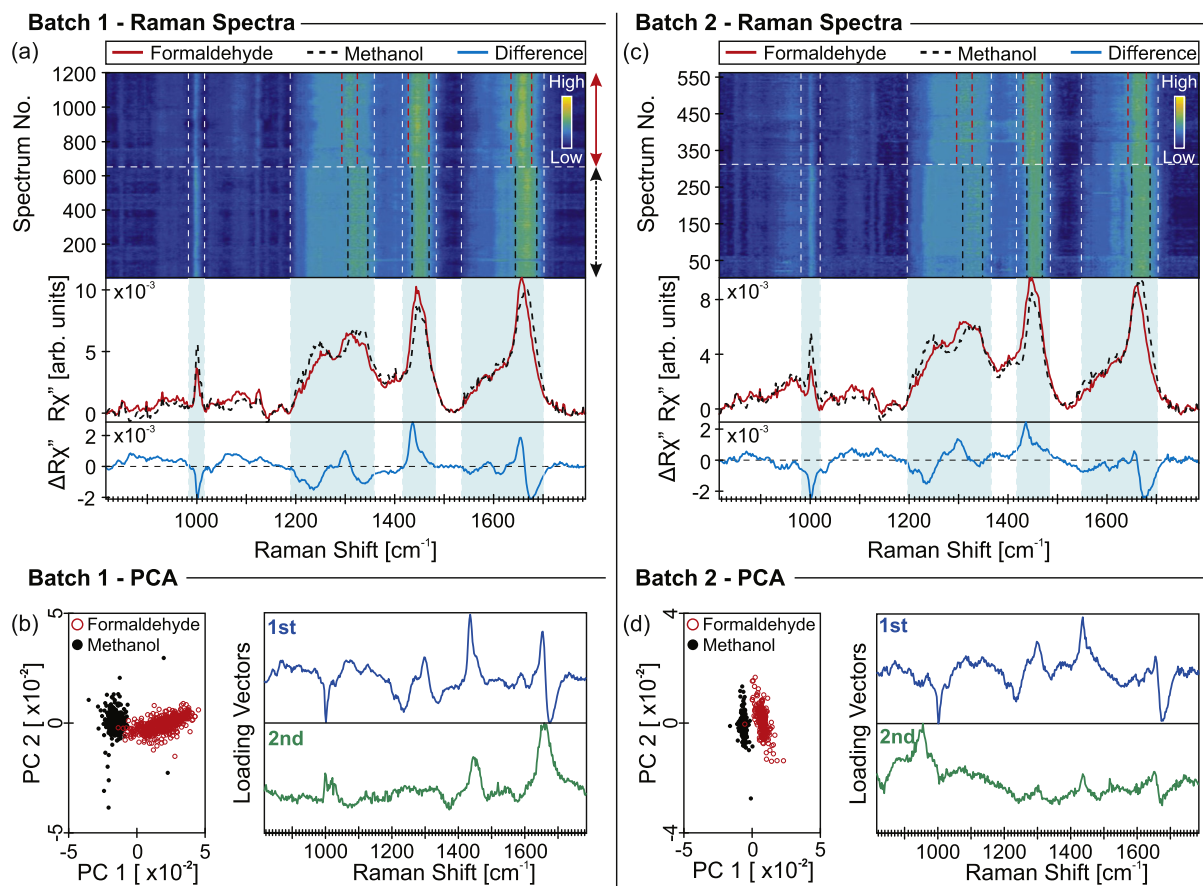


Fig. 3. 2D Raman spectra map obtained from PDLSCs (see Supplementary information), fixed with formaldehyde and methanol, their mean spectra, as well as their difference for the spectral region from 800 cm^{-1} to 1770 cm^{-1} ; PCA score plots calculated for these two groups of cells, and PCA loading vectors for (a)–(b) Batch 1 and (c)–(d) Batch 2, respectively. Percentage of variance PC1–PC2: for Batch 1 19.85%–5.76%; for Batch 2 17.95%–7.43%.

The DNA bands at 1095 cm^{-1} , 1130 cm^{-1} , and 1330 cm^{-1} are of higher intensity in formaldehyde fixed PDLSCs spectra whereas the band at about 1330 cm^{-1} is also slightly shifted. Amide III band at about 1260 cm^{-1} is significantly shifted and of higher intensity in methanol fixed spectra. When it comes to lipid band at 1450 cm^{-1} , it is of noticeable higher intensity and shifted in formaldehyde fixed spectra, as well as the Amide I band at about 1660 cm^{-1} .

The observed behaviour is consistent with the biochemical picture in which the protein content is larger in methanol fixed cells. This is evidenced by more pronounced phenylalanine peak. On the other hand, the secondary structure is more preserved in formaldehyde fixed samples (Amide I band). Modification of native proteins by formaldehyde does not perturb the secondary structure very much. Lipid content is maintained greatly in formaldehyde fixed sample, which is in a good agreement with the literature, due to methanol-caused leaching of lipids through deteriorated cell membrane. As a consequence of cross-linking mechanism of fixation, DNA level is maintained in greater moiety in formaldehyde fixed PDLSCs Raman spectrum [27,28,34].

Spectra of averaged formaldehyde and methanol fixed PDLSCs spectra, and their difference spectrum, from Batch 2 are given in Fig. 3(c). The only observable difference, in comparison to Batch 1, is lower intensity of Amide I band at 1660 cm^{-1} in formaldehyde fixed PDLSCs Raman spectrum, relative to methanol fixed PDLSCs spectrum.

The same procedure is repeated for spectral region from 2500 cm^{-1} to 3600 cm^{-1} . In Fig. 4, 2D Raman spectra map, averaged

spectra, their difference, and PCA of Batch 1 and Batch 2 of formaldehyde and methanol fixed PDLSCs, are presented respectively. Again, formaldehyde and methanol fixed PDLSCs Raman spectra are compared in this spectral region which reflects protein, lipid, and water content. In Fig. 4(a) and (c), it is observable from averaged spectra of difference that the bands at 2860 cm^{-1} and 2890 cm^{-1} , are more intense in formaldehyde fixed PDLSCs Raman spectra. These two bands present CH_2 and CH_3 symmetric stretch in lipids and proteins [35]. Raman band at 2940 cm^{-1} is assigned to CH vibrations in lipids and proteins and is more pronounced in methanol fixed PDLSCs Raman spectra. This confirms above-mentioned statements that formaldehyde better maintains the level of lipids with regard to methanol. On the other hand, methanol keeps protein levels.

Further, PCA is applied for the treatment of the spectral data, and the outcome is presented in Figs. 3 (b), (d) and 4(b), (d) for Batch 1 and Batch 2, respectively. Analyzing PCA score plots, clear assemblage of cells fixed with the same fixative is observable and, as expected, in all cases, PC1 is the component that makes the difference [Figs. 3(b), (d), and 4(b), (d)]. Only a few overlapping points have been observed due to the heterogeneity of the samples and/or variable signal-to-noise ratio. For illustration, PC2s and corresponding loading vectors are also presented. They represent intra- and inter-cellular variations, within the group of cells fixed with the same fixative. PC1 loading vectors are consistent with discrepancies directly observable in Raman spectra of differences, as discussed above. This is not surprising, having in mind the nature of this principal component and the algorithms applied.

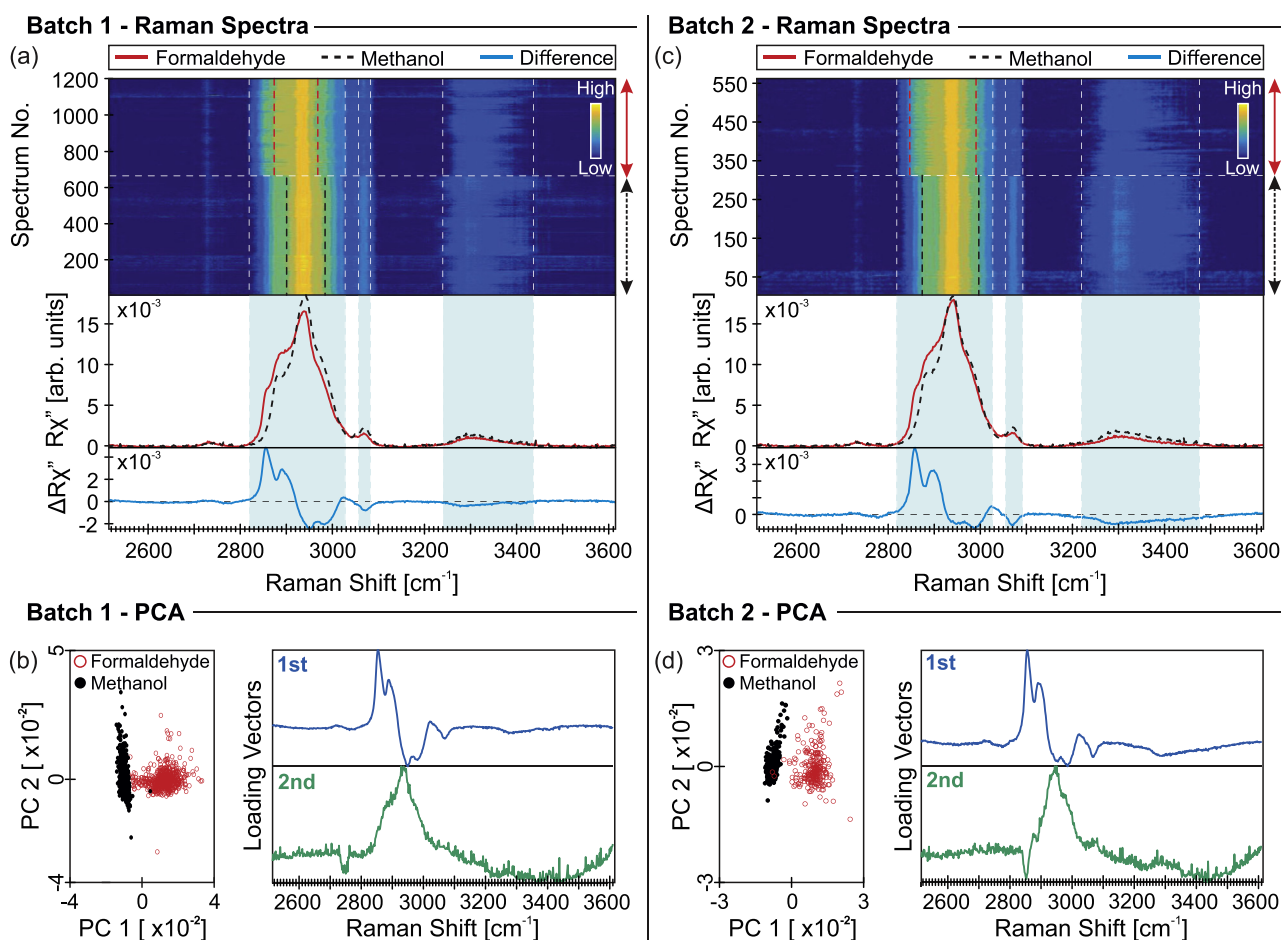


Fig. 4. 2D Raman spectra map obtained from PDLSCs (see Supplementary information), fixed with formaldehyde and methanol, their mean spectra, as well as their difference for spectral region from 2500 cm^{-1} to 3600 cm^{-1} ; PCA score plots calculated for these two groups of cells, and PCA loading vectors for (a)–(b) Batch 1 and (c)–(d) Batch 2, respectively. Percentage of variance PC1–PC2: for Batch 1 64.09%–12.59%; for Batch 2 60.08%–14.64%.

Closer inspection of PCA score plots [Figs. 3(b), (d), and 4(b), (d)] reveals greater spread along PC1 for Batch 1, in particular for the spectral region from 800 cm^{-1} to 1770 cm^{-1} of formaldehyde fixed cells. This is most likely a consequence of heterogeneity of these primary cells. Depending on the nature of the inter-/intracellular variations, fixation process may enhance and/or suppress their Raman spectra signatures [22–26]. Detailed comparison between batches for both fixatives is presented in the Supplementary information.

4. Conclusion

Fixatives cause dramatic changes for all cell types but to varying extent. It is crucial to have a clear idea of what is expected from the sample when choosing the fixative agent. Preservation of cells by formaldehyde and methanol treatment represents standard procedures in most laboratory protocols. In this study, we investigated the effects of these two chemicals on Raman spectra of primary cell lineage, PDLSCs. Both procedures provided quantitatively and qualitatively close Raman spectra that can be considered as fingerprint spectra for this cell lineage. Through the direct comparison of the Raman spectra, as well as the statistical treatment, subtle differences have been observed between two groups that can be traced back to the variations in lipid and protein content. Consequently, when choosing the fixation method, the purpose of investigation has to be kept in mind. When it comes to Raman spectroscopy of hPDLSCs, both formaldehyde and methanol are acceptable choices, but with unlike sensitivity for tracing different biochemical composition.

Acknowledgments

We gratefully acknowledge M. Miletić and M. Andrić for supplying the periodontal ligament tissue. This work was supported by the Ministry of Education, Science, and Technological Development of the Republic of Serbia under Projects Nos. III46010, III45018, ON175062, and OI171005.

Appendix A. Supplementary Data

Supplementary data to this article can be found online at <https://doi.org/10.1016/j.saa.2019.03.012>.

References

- [1] M. Gazdic, V. Volarevic, N. Arsenijevic, M. Stojkovic, Mesenchymal stem cells: a friend or foe in immune-mediated diseases, *Stem Cell Rev. Rep.* 11 (2) (2015) 280–287.
- [2] Y. Sato, H. Araki, J. Kato, K. Nakamura, Y. Kawano, M. Kobune, T. Sato, K. Miyaniishi, T. Takayama, M. Takahashi, et al. Human mesenchymal stem cells xenografted directly to rat liver are differentiated into human hepatocytes without fusion, *Blood* 106 (2) (2005) 756–763.
- [3] R.O. Oreffo, C. Cooper, C. Mason, M. Clements, Mesenchymal stem cells, *Stem Cell Rev.* 1 (2) (2005) 169–178.
- [4] A.R. Williams, J.M. Hare, Mesenchymal stem cells biology, pathophysiology, translational findings, and therapeutic implications for cardiac disease, *Circ. Res.* 109 (8) (2011) 923–940.
- [5] J. Lazarević, T. Kukolj, D. Bugarski, N. Lazarević, B. Bugarski, Z. Popović, Probing primary mesenchymal stem cells differentiation status by micro-Raman spectroscopy, *Spectrochim. Acta A Mol. Biomol. Spectrosc.* 213, 384–390.
- [6] R. Hass, C. Kasper, S. Böhm, R. Jacobs, Different populations and sources of human mesenchymal stem cells (msc): a comparison of adult and neonatal tissue-derived msc, *Cell Commun. Signal* 9 (1) (2011) 12.
- [7] D.G. Phinney, Functional heterogeneity of mesenchymal stem cells: implications for cell therapy, *J. Cell. Biochem.* 113 (9) (2012) 2806–2812.
- [8] I.C. Gay, S. Chen, M. MacDougall, Isolation and characterization of multipotent human periodontal ligament stem cells, *Orthod. Craniofacial Res.* 10 (3) (2007) 149–160.
- [9] S. Ivanovski, S. Gronthos, S. Shi, P. Bartold, Stem cells in the periodontal ligament, *Oral Dis.* 12 (4) (2006) 358–363.
- [10] M. Shimono, T. Ishikawa, H. Ishikawa, H. Matsuzaki, S. Hashimoto, T. Muramatsu, K. Shima, K.I. Matsuzaka, T. Inoue, Regulatory mechanisms of periodontal regeneration, *Microsc. Res. Tech.* 60 (5) (2003) 491–502.
- [11] A. Miletić, S. Mojsilović, I. Okić-Djordjević, T. Kukolj, A. Jauković, J. Santibanez, G. Jovčić, D. Bugarski, Mesenchymal stem cells isolated from human periodontal ligament, *Arch. Biol. Sci.* 66 (1) (2014) 261–271.
- [12] T. Kukolj, D. Trivanović, I.O. Djordjević, J. Mojsilović, J. Krstić, H. Obradović, S. Janković, J.F. Santibanez, A. Jauković, D. Bugarski, Lipopolysaccharide can modify differentiation and immunomodulatory potential of periodontal ligament stem cells via ERK1, 2 signaling, *J. Cell. Physiol.* 233 (1) (2018) 447–462.
- [13] A. Klimczak, U. Kozłowska, Mesenchymal stromal cells and tissue-specific progenitor cells: their role in tissue homeostasis, *Stem Cells Int.* 2016 (2016) 1–11.
- [14] H. Egusa, W. Sonoyama, M. Nishimura, I. Atsuta, K. Akiyama, Stem cells in dentistry—part II: clinical applications, *J. Prosthodont. Res.* 56 (4) (2012) 229–248.
- [15] A. Downes, R. Mouras, A. Elfick, Optical spectroscopy for noninvasive monitoring of stem cell differentiation, *BioMed Res. Int.* 2010 (2010) 1–10.
- [16] A. Downes, R. Mouras, P. Bagnaninchi, A. Elfick, Raman spectroscopy and CARS microscopy of stem cells and their derivatives, *J. Raman Spectrosc.* 42 (10) (2011) 1864–1870.
- [17] C.V. Raman, K.S. Krishnan, A new type of secondary radiation, *Nature* 121 (3048) (1928) 501.
- [18] J.W. Chan, D.K. Lieu, Label-free biochemical characterization of stem cells using vibrational spectroscopy, *J. Biophotonics* 2 (11) (2009) 656–668.
- [19] A.F. Palonpon, J. Ando, H. Yamakoshi, K. Dodo, M. Sodeoka, S. Kawata, K. Fujita, Raman and SERS microscopy for molecular imaging of live cells, *Nat. Protoc.* 8 (4) (2013) 677–692.
- [20] I. Nottingher, I. Bisson, A.E. Bishop, W.L. Randle, J.M. Polak, L.L. Hench, In situ spectral monitoring of mRNA translation in embryonic stem cells during differentiation in vitro, *Anal. Chem.* 76 (11) (2004) 3185–3193.
- [21] F. Lyng, E. Gazi, P. Gardner, Preparation of Tissues and Cells for Infrared and Raman Spectroscopy and Imaging, *Biomedical Applications of Synchrotron Infrared Microspectroscopy: A Practical Approach*, Royal Society of Chemistry, Cambridge, 2010, 147–191.
- [22] S.M. Levchenko, X. Peng, L. Liu, J. Qu, The impact of cell fixation on CARS signal intensity in neuronal and glial cell lines, *J. Biophotonics* (2018) e201800203.
- [23] J.W. Chan, D.S. Taylor, D.L. Thompson, The effect of cell fixation on the discrimination of normal and leukemia cells with laser tweezers Raman spectroscopy, *Biopolymers Original Res. Biomol.* 91 (2) (2009) 132–139.
- [24] A.D. Meade, C. Clarke, F. Draux, G.D. Sockalingum, M. Manfait, F.M. Lyng, H.J. Byrne, Studies of chemical fixation effects in human cell lines using Raman microspectroscopy, *Anal. Bioanal. Chem.* 396 (5) (2010) 1781–1791.
- [25] M.M. Mariani, P. Lampen, J. Popp, B.R. Wood, V. Deckert, Impact of fixation on in vitro cell culture lines monitored with Raman spectroscopy, *Analyst* 134 (6) (2009) 1154–1161.
- [26] E.A. Hoffman, B.L. Frey, L.M. Smith, D.T. Auble, Formaldehyde crosslinking: a tool for the study of chromatin complexes, *J. Biol. Chem.* (2015) jbc-R115.
- [27] M. Noguchi, J.S. Furuya, T. Takeuchi, S. Hirohashi, Modified formalin and methanol fixation methods for molecular biological and morphological analyses, *Pathol. Int.* 47 (10) (1997) 685–691.
- [28] J. Shaham, Y. Bomstein, A. Meltzer, Z. Kaufman, E. Palma, J. Ribak, DNA-protein crosslinks, a biomarker of exposure to formaldehyde in vitro and in vivo studies, *Carcinogenesis* 17 (1) (1996) 121–126.
- [29] T. Ichimura, K.F. Liang-da Chiu, S. Kawata, T.M. Watanabe, T. Yanagida, H. Fujita, Visualizing cell state transition using Raman spectroscopy, *PLoS One* 9 (1) (2014) 1–8.
- [30] E. Brauchle, K. Schenke-Layland, Raman spectroscopy in biomedicine—non-invasive in vitro analysis of cells and extracellular matrix components in tissues, *Biotechnol. J.* 8 (3) (2013) 288–297.
- [31] I. Jolliffe, Principal component analysis, *International Encyclopedia of Statistical Science*, Springer, 2011, pp. 1094–1096.
- [32] W. Wagner, P. Horn, M. Castoldi, A. Diehlmann, S. Bork, R. Saffrich, V. Benes, J. Blake, S. Pfister, V. Eckstein, et al. Replicative senescence of mesenchymal stem cells: a continuous and organized process, *PLoS One* 3 (5) (2008) e2213.
- [33] Y.H.K. Yang, C.R. Ogando, C.W. See, T.Y. Chang, G.A. Barabino, Changes in phenotype and differentiation potential of human mesenchymal stem cells aging in vitro, *Stem Cell Res. Ther.* 9 (1) (2018) 131.
- [34] E. Gazi, J. Dwyer, N.P. Lockyer, J. Miyan, P. Gardner, C. Hart, M. Brown, N.W. Clarke, Fixation protocols for subcellular imaging by synchrotron-based Fourier transform infrared microspectroscopy, *Biopolymers Original Res. Biomol.* 77 (1) (2005) 18–30.
- [35] A.C.S. Talari, Z. Movasaghi, S. Rehman, I.U. Rehman, Raman spectroscopy of biological tissues, *Appl. Spectrosc. Rev.* 50 (1) (2015) 46–111.

Interplay of lattice, electronic, and spin degrees of freedom in detwinned BaFe₂As₂: A Raman scattering study

A. Baum,^{1,2} Ying Li,³ M. Tomić,³ N. Lazarević,⁴ D. Jost,^{1,2} F. Löffler,^{1,2,*} B. Muschler,^{1,2,*} T. Böhm,^{1,2,†} J.-H. Chu,^{5,6,7}
I. R. Fisher,^{5,6} R. Valentí,³ I. I. Mazin,⁸ and R. Hackl^{1,‡}

¹Walther Meissner Institut, Bayerische Akademie der Wissenschaften, 85748 Garching, Germany

²Fakultät für Physik E23, Technische Universität München, 85748 Garching, Germany

³Institut für Theoretische Physik, Goethe-Universität Frankfurt, Max-von-Laue-Straße 1, 60438 Frankfurt am Main, Germany

⁴Center for Solid State Physics and New Materials, Institute of Physics Belgrade, University of Belgrade,
Pregrevica 118, 11080 Belgrade, Serbia

⁵Stanford Institute for Materials and Energy Sciences, SLAC National Accelerator Laboratory, 2575 Sand Hill Road,
Menlo Park, California 94025, USA

⁶Geballe Laboratory for Advanced Materials & Dept. of Applied Physics, Stanford University, California 94305, USA

⁷Department of Physics, University of Washington, Seattle, Washington 98195, USA

⁸Code 6393, Naval Research Laboratory, Washington, DC 20375, USA



(Received 13 June 2018; revised manuscript received 18 July 2018; published 7 August 2018)

We report results of Raman scattering experiments on twin-free BaFe₂As₂ with the main focus placed on understanding the influence of electronic and spin degrees of freedom on the lattice dynamics. In particular, we scrutinize the E_g modes and the As A_{1g} mode. Each of the two E_g phonons in the tetragonal phase is observed to split into a B_{2g} and a B_{3g} mode upon entering the orthorhombic stripe-magnetic phase. The splitting amounts to approximately 10 cm⁻¹ and less than 5 cm⁻¹ for the low- and the high-energy E_g mode, respectively. The detailed study of the fully symmetric As mode using parallel incident and outgoing photon polarizations along either the antiferromagnetic or the ferromagnetic Fe-Fe direction reveals an anisotropic variation of the spectral weight with the energy of the exciting laser indicating a polarization-dependent resonance effect. Along with the experiments we present results from density functional theory calculations of the phonon eigenvectors, the dielectric function, and the Raman tensor elements. The comparison of theory and experiment indicates that (i) orbital-selective electronic correlations are crucial to understand the lattice dynamics and (ii) all phonon anomalies originate predominantly from the magnetic ordering and the corresponding reconstruction of the electronic bands at all energies.

DOI: [10.1103/PhysRevB.98.075113](https://doi.org/10.1103/PhysRevB.98.075113)

I. INTRODUCTION

One of the most debated issues in Fe-based superconductors is the interplay of spin, orbital, and lattice degrees of freedom at the onset of magnetism, nematicity, and superconductivity [1–5], particularly interplay between phonons and magnetic degrees of freedom. For instance, soon after the discovery of Fe-based superconductors, the magnetic moment was predicted to couple to the As position [6]. Zbiri *et al.* found a modulation of the electronic density of states (DOS) at the Fermi energy E_F by the two E_g and the A_{1g} modes [7]. Various anomalies were observed experimentally using neutron, Raman, and optical spectroscopy [8–15] but are not fully understood yet.

One particular effect is the observation of substantial Raman scattering intensity of the As phonon below the magnetostruc-

tural transition in crossed polarizations with the electric fields oriented along the axes of the pseudo-tetragonal 2 Fe unit cell [9] [for the definition of the axes see Fig. 1(a)]. From the weak coupling point of view, it has been argued that the formation of a spin-density wave (SDW) modifies the low-energy electronic structure near the Fermi level, and this modification leads to the anomalous intensity [16]. On the other hand, recent experiments were interpreted by introducing a phenomenological coupling between the phonon and the particle-hole continuum scaling with the amplitude of ordered magnetic moment [17] being on the order of 1 μ_B . This approach is clearly beyond the weak-coupling regime. Density functional (DFT) calculations and general considerations suggest that substantial modifications of the electronic structure occur in a broad energy range of order $J_{\text{Hund}} \gtrsim 1$ eV, corresponding to the Raman *photon* (as opposed to phonon) energy scale. This raises suspicion that a quantitative description of the modifications in the Raman spectra upon magnetic ordering should take into account the broad energy range covering the entire d – electron band widths. Unfortunately, previous studies were done either in twinned samples or using only a single excitation energy, which limited the scope of experimental data being, as

*Present address: Zoller & Fröhlich GmbH, Simoniustrasse 22, 88239 Wangen im Allgäu, Germany

†Present address: TNG Technology Consulting GmbH, Beta-Straße, 85774 Unterföhring, Germany

‡hackl@wmi.badw.de

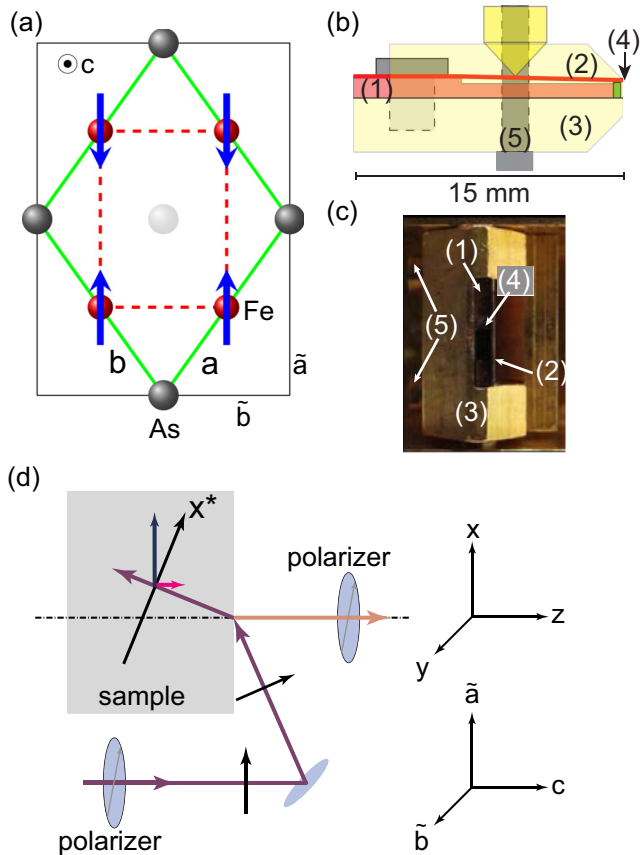


FIG. 1. FeAs layer of BaFe_2As_2 and detwinning clamp. (a) The As-atoms (grey) in the center and at the edges are below and, respectively, above the Fe plane (red). For this reason, the 2 Fe unit cell with the axes a and b (green) is determined by the As atoms. In the orthorhombic phase, the Fe-Fe distances become inequivalent with the distortion strongly exaggerated here. The magnetic unit cell is twice as large as the 2 Fe unit cell and has the axes \tilde{a} and \tilde{b} . (b) Schematic sketch and (c) photograph of the detwinning clamp. The sample (4) is glued on the copper plate (1), which is in good thermal contact with the sample holder (3). Upon tightening the screws (5), the force exerted by the copper-beryllium cantilever (2) can be adjusted. (d) Schematic representation of the geometry of our Raman scattering experiment. All incoming light polarizations \mathbf{e}_i which are not parallel to y have finite projections on the c axis (red arrow).

a result, not sufficiently restrictive to different, maybe even contradictory, interpretations.

In this paper, we systematically address this issue experimentally, using detwinned samples and resonant Raman scattering, and interpret the results quantitatively, not on a phenomenological or model level, but using DFT calculations. Our two most vital conclusions are that (i) magnetism affects *all* Fe bands in an essential way and that has to be accounted for in explaining Raman efficiencies and (ii) the fact that Fe d states are correlated on a moderate, but considerable level, while As p states are not, is not just quantitatively, but qualitatively important in understanding the resonant behavior.

A key issue hindering straightforward DFT calculations is the fact that the *high-temperature tetragonal* phase is paramagnetically disordered, and cannot be simulated by calculations with suppressed local magnetism [18]. As explained

in detail below, we circumvented this problem by assuming a magnetic order that preserves the large (albeit probably still somewhat underestimated) magnetic moment but respects the tetragonal symmetry. Yet another issue was to account for the correlation-driven renormalization of the d – band width. To this end, we separated the energy bands into two windows, a high-energy one dominated by As and a low-energy one derived predominantly from Fe. The Fe states were then uniformly renormalized. With these two assumptions, we could reproduce (i) the positions of the Raman-active phonons and their splitting and evolution in the detwinned orthorhombic antiferromagnetic state and (ii) Raman intensities, including the $\tilde{a} - \tilde{b}$ anisotropy as well as the complex resonant evolution with the laser light energy $\hbar\omega_l$. While it is not clear *a priori* that the two computational tricks described above are sufficiently accurate, even being physically motivated, the results provide an experimental justification and convincingly substantiate the underlying physical concepts: the pivotal role of local moments in the lattice dynamics of Fe-based superconductors, and the importance of band renormalizations for d -electrons. This said, further calculations avoiding these approximations, such as full-scale dynamical mean-field theory (DMFT) computations, are quite desirable but are beyond the scope of this work.

II. METHODS

A. Samples

The BaFe_2As_2 crystal was prepared using a self-flux technique. Details of the crystal growth and characterization are described elsewhere [19]. BaFe_2As_2 is a parent compound of double-layer iron-based superconductors and orders in a stripelike SDW below $T_{\text{SDW}} \approx 135$ K. Superconductivity can be obtained by substituting any of the ions or by pressure [20]. In $\text{Ba}(\text{Fe}_{1-x}\text{Co}_x)_2\text{As}_2$ ($0 < x \lesssim 0.06$), the SDW is preceded by a structural phase transition from a tetragonal ($I4/mmm$) to an orthorhombic ($Fmmm$) lattice at $T_s > T_{\text{SDW}}$ [19]. It remains a matter of debate as to whether or not T_{SDW} and T_s coincide in BaFe_2As_2 [19,21].

Figure 1(a) shows the relation of the various axes. The axes of the tetragonal crystal ($T > T_s$, green lines) are denoted a and b with $a = b$. The axes of the magnetically ordered structure (4 Fe per unit cell, black lines), \tilde{a} and \tilde{b} , differ by approximately 0.7% below T_{SDW} [22] and the Fe-Fe distance along the \tilde{b} axis becomes shorter than along the \tilde{a} axis as sketched in Fig. 1(a). As a result, the angle between a and b differs from 90° by approximately 0.4° .

Below T_{SDW} , the spins order ferromagnetically along \tilde{b} and antiferromagnetically along \tilde{a} . Due to the small difference between \tilde{a} and \tilde{b} , the crystals are twinned below T_s , and the orthogonal \tilde{a} and \tilde{b} axes change roles at twin boundaries running along the directions of the tetragonal a and b axes. The orthorhombic distortion makes the proper definition of the axes important as has been shown for twin-free crystals by longitudinal and optical transport as well as by ARPES [23–28]. To obtain a single-domain orthorhombic crystal, we constructed a sample holder for applying uniaxial pressure parallel to the Fe-Fe direction.

B. Detwinning clamp

The detwinning clamp is similar to that used by Chu *et al.* [23]. Figures 1(b) and 1(c) show, respectively, a schematic drawing and a photograph of the clamp. The sample is attached to a thermally sunk copper block (1) with GE varnish, which remains sufficiently elastic at low temperatures and maintains good thermal contact between the holder (3) and the sample (4). The stress is applied using a copper-beryllium cantilever (2), which presses the sample against the body of the clamp. Upon tightening the screws (5), the force on the sample can be adjusted. In our experiment, the pressure is applied along the Fe-Fe bonds. The c axis of the sample is perpendicular to the force and parallel to the optical axis. The uniaxial pressure can be estimated from the rate of change of the tetragonal-to-orthorhombic phase transition at T_s . Using the experimentally derived rate of 1 K per 7 MPa [29,30], we find approximately 35 MPa for our experiment to be sufficient to detwin the sample.

C. Light scattering

The experiment was performed with a standard light scattering setup. We used two ion lasers (Ar⁺ Coherent Innova 304C and Kr⁺ Coherent Innova 400) and two diode pumped solid state lasers (Coherent Genesis MX SLM, Laser Quantum Ignis) providing a total of 14 lines ranging from 407 nm to 676 nm, corresponding to incident energies $\hbar\omega_I$ between 3.1 and 1.8 eV. Due to this wide range, the raw data have to be corrected. The quantity of interest is the response function $R\chi''(\Omega)$ where $\Omega = \omega_I - \omega_S$ is the Raman shift, ω_S is the energy of the scattered photons and R is an experimental constant. Details of the calibration are described in Appendix A.

Application of the Raman selection rules requires well-defined polarizations for the exciting and scattered photons. The polarizations are given in Porto notation with the first and the second symbol indicating the directions of the incoming and scattered photons' electric fields \mathbf{e}_I and \mathbf{e}_S , respectively. We use xyz for the laboratory system [see Fig. 1(d)]. The xz plane is vertical and defines the plane of incidence, yz is horizontal, xy is the sample surface, and the z axis is parallel to the optical axis and to the crystallographic c axis. For the sample orientation used here (see Fig. 1), the Fe-Fe bonds are parallel to x and y , specifically $\tilde{a} = (1, 0, 0) \parallel x$ and $\tilde{b} = (0, 1, 0) \parallel y$. Since the orthorhombicity below T_s is small, the angle between a and \tilde{a} deviates only by 0.2° from 45° . It is therefore an excellent approximation to use $a \parallel x' = 1/\sqrt{2}(x + y) \equiv 1/\sqrt{2}(1, 1, 0)$ and $b \parallel y' = 1/\sqrt{2}(y - x) \equiv 1/\sqrt{2}(1, \bar{1}, 0)$.

As the angle of incidence of the exciting photons is as large as 66° in our setup [see Fig. 1(d)], the orientations of \mathbf{e}_I parallel and perpendicular to the xz plane are inequivalent. In particular, \mathbf{e}_I has a projection on the c axis for $\mathbf{e}_I \parallel xz$. This effect was used before [8] and allows one to project out the E_g phonons in the x^*x and x^*y configurations, where $x^* \parallel (x + \alpha z)$ inside the crystal [see Fig. 1(d)]. For BaFe₂As₂, the index of refraction is $n' = 2.2 + 2.1i$ at 514 nm, resulting in $\alpha \approx 0.4$ for an angle of incidence of 66° . The corresponding intensity contribution is then 0.16. As a consequence, x^*x and yy are inequivalent whereas $\mathbf{e}_I = x'^* \parallel (x' + \alpha z/\sqrt{2})$ and $\mathbf{e}_I = y'^* \parallel (y' + \alpha z/\sqrt{2})$ are equivalent for having the same projection on the c direction. Upon comparing x^*y and yx , the

leakage of the c -axis polarized contributions to the electronic continuum can be tested. In the case here, they are below the experimental sensitivity. The effect of the finite angle of acceptance of the collection optics ($\pm 15^\circ$ corresponding to a solid angle $\tilde{\Omega}$ of 0.21 sr) on the projections of the scattered photons can be neglected.

D. Theoretical calculations

The phonon eigenvectors $Q^{(\nu)}$ (displacement patterns of the vibrating atoms in the branch ν) and the energies of all Raman-active phonons of BaFe₂As₂ in the tetragonal ($I4/mmm$) and the orthorhombic ($Fmmm$) phases were obtained from *ab initio* DFT calculations within the Perdew-Burke-Ernzerhof parametrization [31] of the generalized gradient approximation. The phonon frequencies were calculated by diagonalizing the dynamical matrices using the *phonopy* package [32,33]. The dynamical matrices were constructed from the force constants determined from the finite displacements in $2 \times 2 \times 1$ supercells [34]. We used the projector augmented wave approximation [35], as implemented in the Vienna package (VASP) [36–38]. The Brillouin zone for one unit cell was sampled with a $10 \times 10 \times 10$ \mathbf{k} point mesh, and the plane wave cutoff was set at 520 eV. For the tetragonal phase, we used a Néel-type magnetic order to relax the structure and to obtain the experimental lattice parameters.¹ For the orthorhombic phase, we used the stripe-like magnetic order shown in Fig. 1(a).

We have then calculated the complex Raman tensor $\alpha_{jk}^{(\nu)}(\omega_I) = \alpha_{jk}^{(\nu')}(\omega_I) + i\alpha_{jk}^{(\nu'')}(\omega_I)$, defined as the derivative of the dielectric tensor elements $\epsilon_{jk}(\omega_I) = \epsilon'_{jk}(\omega_I) + i\epsilon''_{jk}(\omega_I)$ with respect to the normal coordinate of the respective phonon, $Q^{(\nu)}$. Since we are interested only in the resonance behavior of the As phonon, we only needed the derivatives with respect to $Q^{(\text{As})}$,

$$\alpha_{ll}^{(\text{As})}(\omega_I) = \frac{\partial \epsilon'_{ll}(\omega_I)}{\partial Q^{(\text{As})}} + i \frac{\partial \epsilon''_{ll}(\omega_I)}{\partial Q^{(\text{As})}}. \quad (1)$$

To calculate the dielectric (tensor) function $\hat{\epsilon}$ we used the *optics* code package [39] implemented in WIEN2k [40] with the full-potential linearized augmented plane-wave basis. The Perdew-Burke-Ernzerhof generalized gradient approximation [31] was employed as the exchange correlation functional and the basis-size controlling parameter RK_{max} was set to 8.5. A mesh of 400 \mathbf{k} points in the first Brillouin zone for the self-consistency cycle was used. The DOS and dielectric tensors were computed using a $10 \times 10 \times 10$ \mathbf{k} mesh. For the dielectric tensor, a Lorentzian broadening of 0.1 eV was introduced.

III. RESULTS AND DISCUSSION

A. Lattice dynamics

The energies and symmetries as obtained from lattice dynamical calculations for tetragonal and orthorhombic

¹The local correlations in the tetragonal phase are of the stripe type; however, we had to use a pattern that does not break the symmetry, and it is known [18] that the difference in the elastic properties calculated within different magnetic orders is much smaller than between magnetic and nonmagnetic calculations.

TABLE I. Raman-active phonons in BaFe₂As₂. The experimental and theoretically determined energies are given in cm⁻¹. In addition, the symmetry correlations between the tetragonal (*I4/mmm*) and orthorhombic (*Fmmm*) structures are shown.

	<i>I4/mmm</i>			<i>Fmmm</i>	
	Exp. (140 K)	Theory		Exp. (60 K)	Theory
A_{1g}	180	168	→	A_g	180
B_{1g}	215	218	→	B_{1g}	215
$E_g^{(1)}$	130	140	↗	$B_{2g}^{(1)}$	125
			↘	$B_{3g}^{(1)}$	135
$E_g^{(2)}$	268	290	↗	$B_{2g}^{(2)}$	270
			↘	$B_{3g}^{(2)}$	273

BaFe₂As₂ are compiled in Table I. The four modes in tetragonal *I4/mmm* symmetry obey $A_{1g} + B_{1g} + 2 E_g$ selection rules. The eigenvectors are depicted in Fig. 2. In the orthorhombic *Fmmm* phase, the two E_g modes are expected to split into B_{2g} and B_{3g} modes. Thus, there are six nondegenerate modes in the orthorhombic phase, $A_g + B_{1g} + 2 B_{2g} + 2 B_{3g}$. Table I shows the symmetry relations between the tetragonal and orthorhombic phonons.

Since the A_g and B_{1g} eigenvectors remain unchanged upon entering the orthorhombic phase, only those of the B_{2g} and B_{3g} phonons are shown in Fig. 3. For the B_{2g} and B_{3g} phonons, the As and Fe atoms move perpendicular to the *c* axis and perpendicular to each other. The calculated phonon vibrations agree with previous results for BaFe₂As₂ [7], however our energies differ slightly from those reported by Zbiri *et al.* [7]. In particular, we find a splitting between the $B_{2g}^{(1)}$ and $B_{3g}^{(1)}$ phonons.

B. E_g phonons

Table I displays the experimental phonon energies above and below the magneto-structural transition, along with the theoretical values. The $E_g^{(1)}$ phonon found at 130 cm⁻¹ above T_s splits into two well-separated lines as predicted (Table I) and shown in Fig. 4. The splitting of the $E_g^{(2)}$ mode at 268 cm⁻¹ is small, and the $B_{2g}^{(2)}$ and $B_{3g}^{(2)}$ modes are shifted to higher energies by 2 cm⁻¹ and 5 cm⁻¹, respectively.

The theoretical and experimental phonon energies are in agreement to within 14% for both crystal symmetries. The

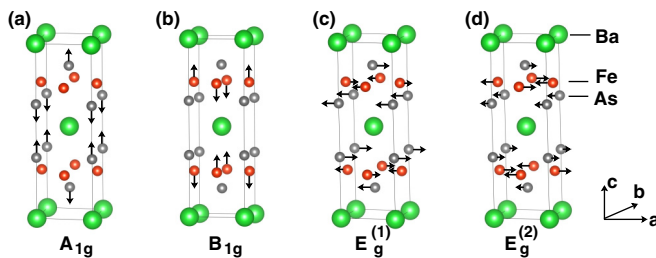


FIG. 2. Raman-active phonons in BaFe₂As₂ with the symmetry assignments in the tetragonal crystallographic unit cell *abc*.

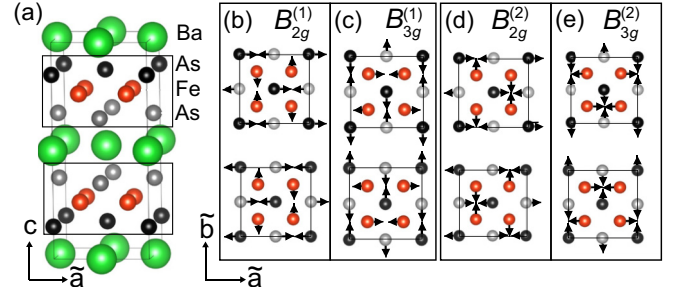


FIG. 3. B_{2g} and B_{3g} phonon modes in BaFe₂As₂ with the symmetry assignments in the orthorhombic crystallographic unit cell $\tilde{a}\tilde{b}\tilde{c}$.

splitting between the B_{2g} and B_{3g} modes is overestimated in the calculations.

Previous experiments were performed on twinned crystals [8,41,42] and the B_{2g} and B_{3g} modes were observed next to each other in a single spectrum. An equivalent result can be obtained in detwinned samples by using x'^*y' , x'^*x' , or RR polarizations where the x and y axes are simultaneously projected (along with the z axis). In neither case can the symmetry of the B_{2g} and B_{3g} phonons be pinned down. Only in a detwinned sample where the xz and yz configurations are projected separately, the B_{2g} and B_{3g} modes can be accessed independently.

Uniaxial pressure along the Fe-Fe direction, as shown by the black arrows in the insets of Fig. 4, determines the orientation of the shorter \tilde{b} axis. This configuration enables us to observe the $B_{2g}^{(1)}$ mode at 125 cm⁻¹ and the $B_{3g}^{(1)}$ mode at 135 cm⁻¹ in x^*x and, respectively, x^*y polarization configurations, thus augmenting earlier work. With the shorter axis determined by

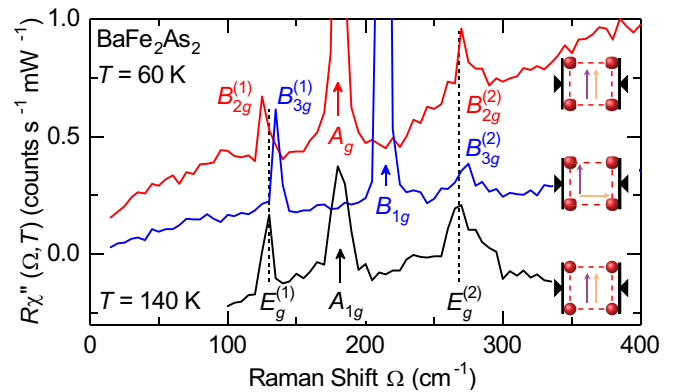


FIG. 4. Phonons in detwinned BaFe₂As₂. The spectra at 60 K (red and blue) are displayed with the experimental intensity. The spectrum at 140 K (black) is downshifted by 1.4 counts s⁻¹ mW⁻¹ for clarity. Each of the two tetragonal E_g phonons (vertical dashed lines) splits into two lines below T_s . The $B_{2g}^{(1)}$ and $B_{3g}^{(1)}$ lines appear at distinct positions for polarizations of the scattered light parallel (blue) and perpendicular (red) to the applied pressure as indicated in the insets. The $B_{2g}^{(2)}$ and $B_{3g}^{(2)}$ phonons are shifted only slightly upward with respect to the $E_g^{(2)}$ mode. Violet and orange arrows indicate the polarizations of the incident and scattered photons, respectively. The black triangles indicate the direction of the applied pressure. The shorter \tilde{b} axis is parallel to the stress.

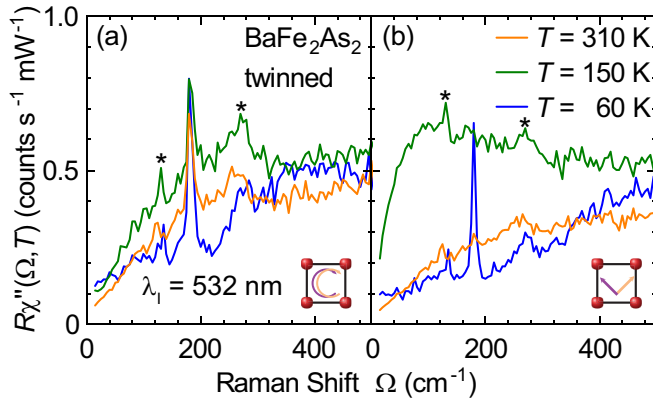


FIG. 5. Raman spectra of twinned BaFe_2As_2 at temperatures as indicated. The spectra were measured using $\hbar\omega_1 = 2.33$ eV (532 nm). (a) In parallel RR polarization configuration (see inset), the As phonon appears at all temperatures. (b) For crossed light polarizations (ab), the As phonon is present only below the magnetostructural transition at $T_s = 135$ K as reported before [8]. Asterisks mark the E_g modes discussed in Sec. III B.

the direction of the stress (insets of Fig. 4) the assignment of the B_{2g} and B_{3g} modes is unambiguous. Since the x^*x spectrum (red) comprises $\tilde{a}\tilde{a}$ and $\tilde{c}\tilde{a}$ polarizations both the A_g and the B_{2g} phonons appear. The x^*y spectrum (blue) includes the B_{1g} ($\tilde{a}\tilde{b}$) and B_{3g} ($\tilde{c}\tilde{b}$) symmetries.

The calculated splitting between the B_{2g} and B_{3g} modes is smaller for the $E_g^{(2)}$ than for the $E_g^{(1)}$ mode, qualitatively agreeing with the experiment. However, in the calculations this difference is entirely due to the different reduced masses for these modes since the $E_g^{(1)}$ and $E_g^{(2)}$ phonon are dominated by As and Fe motions, respectively. In the experiment the splitting for the $E_g^{(2)}$ mode is close to the spectral resolution, indicating an additional reduction of the splitting below that obtained in the calculation. The source of this additional reduction is unclear at the moment.

C. As phonon line intensity

Figure 5 shows low-energy spectra of twinned BaFe_2As_2 for (a) RR and (b) ab polarization configurations at 310 (orange), 150 (green), and 60 K (blue). The As phonon at 180 cm^{-1} is the strongest line in the RR spectra at all temperatures as expected and gains intensity upon cooling. In ab polarizations, there is no contribution from the As mode above T_s . Below T_s (blue spectrum), the As phonon assumes a similar intensity as in the RR polarization as reported earlier [8,17]. Due to a finite projection of the incident light polarizations onto the c axis [see Fig. 1(d)] in both RR and ab configurations, the E_g phonons appear in all spectra (asterisks). The electronic continuum has been extensively discussed in previous works [43–47] and is not a subject of the study here.

To understand the appearance of the As line in the crossed ab polarizations, it is sufficient to consider the in-plane components of the A_g Raman tensor,

$$\hat{\alpha}^{(Ag)} = \begin{pmatrix} \alpha_{11} & 0 \\ 0 & \alpha_{22} \end{pmatrix}. \quad (2)$$

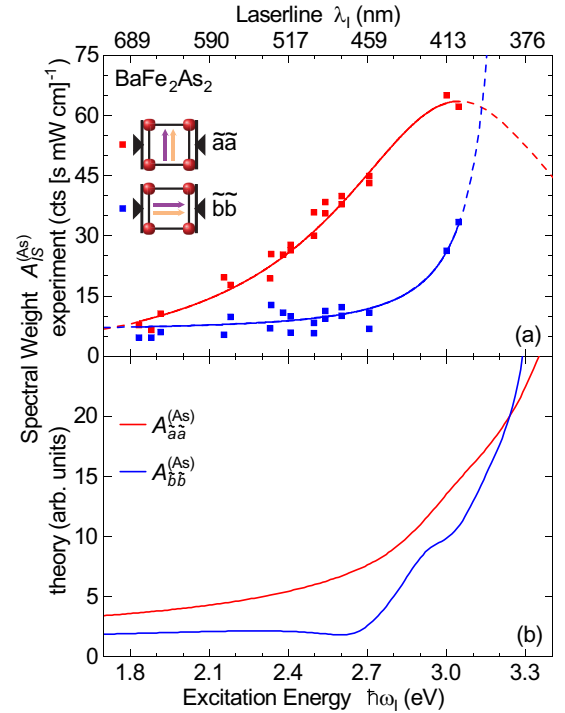


FIG. 6. Spectral weight $A_{IS}^{(As)}(\omega_1)$ of the As phonon as a function of excitation energy and polarization. The top axis shows the corresponding wavelength of the exciting photons. (a) Experimental data. The intensity for parallel light polarizations along the ferromagnetic axis ($\tilde{b}\tilde{b}$, blue squares) is virtually constant for $\hbar\omega_1 < 2.7$ eV and increases rapidly for $\hbar\omega_1 > 2.7$ eV. For light polarizations along the antiferromagnetic axis ($\tilde{a}\tilde{a}$, red squares), the phonon intensity increases monotonically over the entire range studied. The solid lines are Lorentzian functions whose extrapolations beyond the measured energy interval are shown as dashed lines. (b) Theoretical prediction of $A_{aa}^{(As)}$ (red) and $A_{bb}^{(As)}$ (blue). The curves qualitatively reproduce the experimental data shown in panel (a).

The response of this phonon for the polarization configuration $(\mathbf{e}_l, \mathbf{e}_s)$ is given by $\chi_{IS}^{(As)} \propto |\mathbf{e}_s^* \cdot \hat{\alpha}^{(Ag)} \cdot \mathbf{e}_l|^2$ (where $*$ means conjugate transposed). In the tetragonal (A_{1g}) case, the two elements are equal, $\alpha_{11} = \alpha_{22}$, and the phonon appears only for $\mathbf{e}_s \parallel \mathbf{e}_l$. In the orthorhombic phase the tensor elements are different, and one can expect the phonon to appear for $\mathbf{e}_s \perp \mathbf{e}_l$ since then the intensity depends on the difference between α_{11} and α_{22} .

In detwinned samples, α_{11} and α_{22} can be accessed independently by using parallel polarizations for the incident and scattered light oriented along either the \tilde{a} or the \tilde{b} axis. In addition, putative imaginary parts of α_{ii} may be detected by analyzing more than two polarization combinations as discussed in Appendix C. Spectra for $\tilde{a}\tilde{a}$ and $\tilde{b}\tilde{b}$ configurations are shown in Fig. 7 of Appendix B and we proceed here directly with the analysis of the phonon spectral weight $A_{IS}^{(As)}(\omega_1)$ as a function of the incident photon excitation energy ($\hbar\omega_1$) and polarization.

Figure 6(a) shows $A_{IS}^{(As)}(\omega_1)$ as derived by fitting the peak with a Voigt function, after subtracting a linear background. Measurements were repeated several times to check the reproducibility. The variation of the spectral weight between

different measurements can be taken as an estimate of the experimental error. For light polarizations parallel to the antiferromagnetic \tilde{a} axis, $A_{\tilde{a}\tilde{a}}^{(\text{As})}(\omega_1)$ (red squares) increases continuously with increasing $\hbar\omega_1$ whereas $A_{\tilde{b}\tilde{b}}^{(\text{As})}$ (blue squares) stays virtually constant for incident photons in the red and green spectral range, $\hbar\omega_1 < 2.7$ eV, and increases rapidly for $\hbar\omega_1 > 2.7$ eV. For all wavelengths, the spectral weight is higher for the $\tilde{a}\tilde{a}$ than for the $\tilde{b}\tilde{b}$ configuration.

The variations of $A_{\tilde{a}\tilde{a}}^{(\text{As})}(\omega_1)$ and $A_{\tilde{b}\tilde{b}}^{(\text{As})}(\omega_1)$ display a typical resonance behavior [48], which is expected when the intermediate state of the Raman scattering process is an eigenstate of the electronic system. Then, in second-order perturbation theory, the intensity diverges as $|\hbar\omega_1 - E_0|^{-2}$, where E_0 is the energy difference between an occupied and an unoccupied electronic Bloch state. In real systems having a finite electronic lifetime, a Lorentzian profile is expected. We therefore approximated $A_{IS}^{(\text{As})}(\omega_1)$ with Lorentzians centered at $E_{0,IS}$ as shown by solid lines in Fig. 6(a). From these model functions we determine $E_{0,\tilde{a}\tilde{a}} = 3.1$ eV and $E_{0,\tilde{b}\tilde{b}} = 3.3$ eV.

As discussed in the Introduction, the band structure needs to be renormalized so as to account for correlation effects (for details, see Appendix D). To this end, we differentiated three regions: (i) the unoccupied Fe 3d bands near the Fermi energy that we rescale uniformly, (ii) the occupied bands below -2.7 eV of predominantly As 4p character that remain unchanged, and (iii) the occupied bands between -2.7 eV and the Fermi level derived from hybridized Fe 3d and As 4p orbitals. Due to this hybridization, the renormalization of the latter bands cannot be performed by simple rescaling. One can anticipate that the optical absorption would set in at energies below 1.8 eV, smaller than our minimal laser energy, if the occupied Fe bands would have been renormalized prior to hybridization with the As bands. Due to the small DOS of the As bands in the range from -2.7 eV to E_F , their contribution to the dielectric function would be small. With this in mind, we simply excluded all occupied bands in this range from the calculations. The effect of these bands, although small, could be accounted for using the DMFT method, which, however, is beyond the scope of our present work.

The results obtained as described above are presented in Fig. 6(b). One can see that the resonances lie in the range $\hbar\omega_1 > 2.7$ eV, and our calculations capture both the intensities and the $\tilde{a} - \tilde{b}$ anisotropy in this range rather well. Note that the antiferromagnetic ordering along the \tilde{a} axis entails a backfolding of the electronic bands; we tentatively ascribe the much larger width of the resonance in the $\tilde{a}\tilde{a}$ configuration to this backfolding.

A corollary of our analysis is that resonance effects are the main source of the anomalous intensity of the As phonon in crossed polarizations. The main experimental argument is based on the anisotropic variation of the phonon intensities with $\hbar\omega_1$ in $\tilde{a}\tilde{a}$ and $\tilde{b}\tilde{b}$ polarization configurations that comes about because of band reconstruction at higher energies. As proposed previously [16], magnetism appears to be the origin of the anisotropy. However, the intensity anisotropy cannot be explained without taking into account the high-energy electronic states.

Finally, we briefly look into the cross-polarization anomaly and find further support for its magnetic origin.

In $\text{Ba}(\text{Fe}_{1-x}\text{Co}_x)_2\text{As}_2$, the transition temperature T_{SDW} is several degrees below T_s for a finite x , and one observes that the anomaly of the As phonon does not appear at T_s , but rather at the magnetic transition. For $x = 0.025$, the phonon assumes intensity in crossed polarizations only below T_{SDW} (see supplementary information of Ref. [46]). For $x = 0.051$, the anomaly appears at T_s , as displayed in Fig. 10 in the Appendix but the spectral weight does not show an order-parameter-like temperature dependence. The increase is nearly linear and saturates below T_{SDW} at a value which is smaller by approximately a factor of 7 than that in the RR polarization projecting A_g/A_{1g} symmetry. In FeSe, with a structural transition at $T_s = 89.1$ K but no long-range magnetism [49], the anomalous intensity can also be observed below T_s but the intensity relative to that in the A_g projection is only 1%, as shown in Fig. 11. Similar to $\text{Ba}(\text{Fe}_{0.949}\text{Co}_{0.051})_2\text{As}_2$, the spectral weight increases approximately linearly but does not saturate, presumably because FeSe does not develop a long-ranged magnetic order.

IV. CONCLUSION

We studied the Raman scattering for three As phonons, the two E_g , and the one fully symmetric modes, in twin-free BaFe_2As_2 , accompanied by DFT calculations of Raman intensities, with the goal of clarifying the impact of magnetism on electrons and phonons.

The tetragonal E_g phonons at 130 cm^{-1} ($E_g^{(1)}$) and 268 cm^{-1} ($E_g^{(2)}$) were studied with the laser line at 532 nm and found to split into two modes in the orthorhombic phase. The detwinning allows us to identify the modes at 125 cm^{-1} and 135 cm^{-1} as the $B_{2g}^{(1)}$ and $B_{3g}^{(1)}$ phonons, respectively. DFT calculations predict the symmetries correctly and show that the splitting occurs because of the stripe magnetic order (and not because of the orthorhombic distortion).

The As A_g phonon was studied for various laser lines in the range 1.8 to 3.1 eV. In the ordered phase, the spectral weight of the phonon resonates for an excitation energy of (3.2 ± 0.1) eV. The resonance energy is almost the same for the light polarized along the ferro- or antiferromagnetic directions \tilde{b} and \tilde{a} [for the definition of the axes see Fig. 1(a)], whereas the variation of the spectral weight with the energy of the incident photon is rather different for the $\tilde{b}\tilde{b}$ and $\tilde{a}\tilde{a}$ configurations. The larger width of the resonance in $\tilde{a}\tilde{a}$ configuration can be understood qualitatively in terms of band backfolding along the antiferromagnetic direction.

Our DFT calculations reproduce the anisotropy and the resonance very well for energies above 2.7 eV if we include both the effects of the magnetism and of the correlations-induced renormalization of Fe 3d bands. Due to DFT limitations, for energies below 2.7 eV, where correlated Fe 3d bands are strongly hybridized with the As bands, our approximation is only semiquantitative. Further studies based, for instance, on DMFT or other many-body methods are needed to test this approximation, apart from experimental verification. As in the case of the E_g phonons, all effects are strongly linked to magnetism. However, in the case of the As phonon, the inclusion of electronic states at high energies is essential because of the observed resonance behavior. Weak-coupling, low-energy physics with magnetism-induced anisotropic electron-phonon

coupling [16] appears insufficient for explaining the anomalous intensity in crossed polarizations.

More generally, our experimental observations and theoretical studies indicate the importance of orbital-dependent band renormalizations and of (nearly) localized ordered spins on the electronic properties at all energy scales.

ACKNOWLEDGMENTS

We gratefully acknowledge discussions with L. Degiorgi and thank him for providing us with raw and analyzed IR data of BaFe₂As₂. The work was supported by the Deutsche Forschungsgemeinschaft (DFG) via the Priority Program No. SPP 1458, the Transregional Collaborative Research Centers TRR 80 and TRR 49, and by the Serbian Ministry of Education, Science and Technological Development under Project No. III45018. We acknowledge support by the DAAD through the bilateral project between Serbia and Germany (Grants No. 56267076 and No. 57142964). The collaboration with Stanford University was supported by the Bavaria California Technology Center BaCaTeC (Grant No. A5 [2012-2]). Work in the SIMES at Stanford University and SLAC was supported by the U.S. Department of Energy, Office of Basic Energy Sciences, Division of Materials Sciences and Engineering, under Contract No. DE-AC02-76SF00515. Y.L. and R.V. acknowledge the allotment of computer time at the Centre for Scientific Computing (CSC) in Frankfurt. I.I.M. was supported by ONR through the NRL basic research program and by the Alexander von Humboldt-Stiftung.

APPENDIX A: CALIBRATION OF THE SENSITIVITY

Scattering experiments performed over a wide energy range necessitate an appropriate correction of the data. The quantity of interest is the response function $R\chi''_{IS}(\Omega)$ where $\Omega = \omega_I - \omega_S$ is the Raman shift, and ω_S is the energy of the scattered photons. R includes all experimental constants and units in a way that $R\chi''_{IS}(\Omega)$ is as close as possible to the count rate \dot{N}_{IS}^* , measured for a given laser power $P_I = I_I \hbar \omega_I$ absorbed by the sample. I_I is the number of incoming photons per unit time and I, S refer to both photon energies and polarizations. With A_f , the (nearly) energy-independent area of the laser focus the cross section is given by [50]

$$\frac{\dot{N}_{IS}^*(\Delta\omega_S, \Delta\tilde{\Omega})}{P_I} \hbar \omega_I A_f = R^* r(\omega_S) \frac{d^2\sigma}{d\omega_S d\tilde{\Omega}} \Delta\omega_S \Delta\tilde{\Omega}. \quad (\text{A1})$$

R^* and $r(\omega_S)$ are a constant and the relative sensitivity, respectively. $r(\omega_S)$ is assumed to be dimensionless and includes energy-dependent factors such as surface losses, penetration depth, and the monochromatic efficiency of the setup. $\Delta\omega_S$ and $\Delta\tilde{\Omega}$ are the bandwidth and the solid angle of acceptance, respectively, and depend both on ω_S . $r(\omega_S)\Delta\omega_S\Delta\tilde{\Omega}$ is determined by calibration and used for correcting the raw data. The resulting rate \dot{N}_{IS} is close to \dot{N}_{IS}^* in the range $\Omega \leq 1,000 \text{ cm}^{-1}$ but increasingly different for larger energy transfers mainly for the strong variation of $\Delta\omega_S$. Applying the

fluctuation-dissipation theorem, one obtains

$$\begin{aligned} \frac{\dot{N}_{IS}}{P_I} \hbar \omega_I A_f &= R' \frac{d^2\sigma}{d\omega_S d\tilde{\Omega}} \\ &= R' \frac{\hbar}{\pi} r_0^2 \frac{\omega_S}{\omega_I} \{1 + n(\Omega, T)\} \chi''(\Omega), \quad (\text{A2}) \end{aligned}$$

where R' is another constant, which is proportional to $\Delta\omega_S(\omega_0)\Delta\tilde{\Omega}(\omega_0)$, $n(\Omega, T) = [\exp(\frac{\hbar\Omega}{k_B T}) - 1]^{-1}$ is the thermal Bose factor and r_0 is the classical electron radius. Finally, after collecting all energy-independent factors in R we obtain

$$R\chi''_{IS}(\Omega) = \frac{\dot{N}_{IS}}{P_I} \frac{\omega_I^2}{\omega_0 \omega_S} \left\{ 1 - \exp\left(-\frac{\hbar\Omega}{k_B T}\right) \right\}. \quad (\text{A3})$$

Here, $\omega_0 = 20,000 \text{ cm}^{-1}$ is inserted for convenience to get a correction close to unity. Therefore, the spectra shown reflect the measured number of photon counts per second and mW absorbed power as closely as possible, thus approximately obeying counting statistics as intended. Since the spectra are taken with constant slit width the spectral resolution depends on energy, and narrow structures such as phonons may change their shapes but the spectral weight is energy independent.

APPENDIX B: A_g SPECTRA

Figure 7 shows the complete set of the A_g spectra we measured for detwinned BaFe₂As₂ and used for deriving the spectral weights $A_{\bar{a}\bar{a}}^{(As)}(\omega_I)$ and $A_{\bar{b}\bar{b}}^{(As)}(\omega_I)$ displayed in Fig. 6(a). All spectra were corrected as described in Appendix A. For all spectra, the same constant width of $550 \mu\text{m}$ of the intermediate slit of the spectrometer was used. This results in an energy-dependent resolution varying between approximately 12 cm^{-1} at $24,630 \text{ cm}^{-1}$ (3.05 eV or 406 nm) and 3 cm^{-1} at $14,793 \text{ cm}^{-1}$ (1.83 eV or 676 nm). Accordingly, the width of the peak changes as a function of the excitation wavelength and does not reflect the intrinsic line width of the phonon, in particular

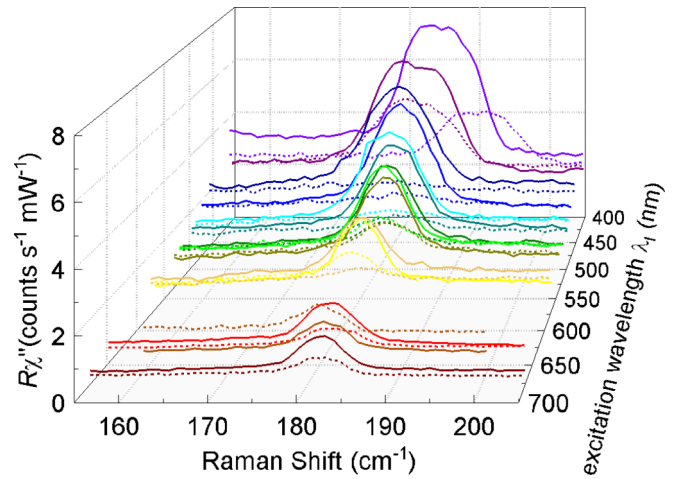


FIG. 7. (Color online.) A_g spectra of detwinned BaFe₂As₂ at various laser wavelengths λ_I . We used laser lines between 406 and 676 nm and parallel polarizations of incoming and outgoing photons along the antiferromagnetic ($\bar{a}\bar{a}$, solid lines) and the ferromagnetic ($\bar{b}\bar{b}$, dashed lines) direction.

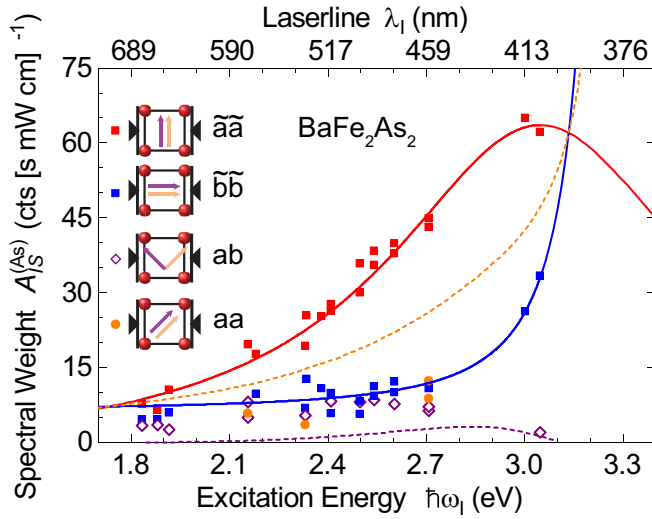


FIG. 8. Spectral weight $A_{IS}^{(As)}(\omega_1)$ of the As phonon as a function of excitation energy and polarization. The top axis shows the corresponding wavelength of the exciting photons. The data for $\tilde{a}\tilde{a}$ (red squares) and $\tilde{b}\tilde{b}$ (blue squares) polarizations as well as the Lorentzian model functions (red and blue solid lines) are identical to Fig. 6(a). The intensity for crossed (ab , purple diamonds) and for aa polarizations (orange dots) is comparable to the intensity found for $\tilde{b}\tilde{b}$ polarization. The purple dashed line is the intensity for ab polarization calculated from the fitted resonance profiles (solid lines) assuming a Raman tensor with real elements. The orange dashed line shows the same calculation for aa polarization.

not for blue photons. The intensity of the peak monotonically increases towards short wavelengths for the $\tilde{a}\tilde{a}$ spectra (solid lines). For light polarized parallel to the ferromagnetic axis ($\tilde{b}\tilde{b}$, dashed lines), the intensity is low for $\lambda_1 > 450$ nm, but strongly increases for $\lambda_1 < 450$ nm. The underlying electronic continuum, which is not a subject of this paper, also changes in intensity as a function of the excitation wavelength. From the spectra, the spectral weight $A_{IS}^{(As)}(\omega_1)$ of the phonon can be derived by fitting a Voigt function to the phonon peak after subtracting a linear background. The width of the Gaussian part of the Voigt function is given by the known resolution of the spectrometer while that of the Lorentzian part reflects the line width of the phonon.

APPENDIX C: SPECTRAL WEIGHT FOR aa AND ab POLARIZATIONS

Since the ratio $A_{ab}^{(As)}/A_{aa}^{(As)}$ was not in the main focus of our work, Fig. 6(a) displays only part of the data we collected. We also measured spectra in aa and ab configurations (cf. Figs. 1(a) and 8 for the definitions) and find them instructive for two reasons. The aa and ab data (i) can be compared directly with results presented recently [17] and (ii) indicate that the Raman tensor has large imaginary parts which can result only from absorption processes. Figure 8 shows the spectral weights of the As phonon mode for aa and ab polarizations, $A_{aa}^{(As)}(\omega_1)$ (orange circles) and $A_{ab}^{(As)}(\omega_1)$ (open purple diamonds), respectively, for selected wavelengths together with the data and model functions from Fig. 6(a) of the main text. Given the experimental error, the respective intensities for aa and

ab polarizations are rather similar and are also comparable to $A_{\tilde{b}\tilde{b}}^{(As)}(\omega_1)$ (blue squares) in the range $1.9 < \hbar\omega_1 \leq 2.7$ eV. For $\hbar\omega_1 = 3.05$ eV (406 nm), $A_{ab}^{(As)}(\omega_1)$ is very small, for the yellow-green spectral range $A_{ab}^{(As)}(\omega_1)$ may be even larger than $A_{aa}^{(As)}(\omega_1)$ in qualitative agreement with Ref. [17].

If the elements of the Raman tensor $\hat{\alpha}^{(Ag)}$ [Eq. (2) of the main text] would be strictly real, they could be derived directly from the experimental data as $\alpha_{11} = \sqrt{A_{\tilde{a}\tilde{a}}^{(As)}}$ and $\alpha_{22} = \sqrt{A_{\tilde{b}\tilde{b}}^{(As)}}$. Then, the phonon's spectral weight expected for all other polarizations could be calculated right away, and $A_{aa}^{(As)}$ is just the average of $A_{\tilde{a}\tilde{a}}^{(As)}$ and $A_{\tilde{b}\tilde{b}}^{(As)}$ (dashed orange line in Fig. 8). Obviously, there is no agreement with the experimental values for $A_{aa}^{(As)}$ (orange circles).

$A_{ab}^{(As)}$ can be determined in a similar fashion. In Fig. 8, we show the expected spectral weight as purple dashed line. The dependence on ω_1 is again derived from the model functions describing the resonance (full red and blue lines). Also for $A_{ab}^{(As)}$, the mismatch between experiment (open purple diamonds) and expectation (purple dashed line) is statistically significant, and one has to conclude that the assumption of real tensor elements in the orthorhombic phase is not valid.

This effect is not particularly surprising in an absorbing material and was in fact discussed earlier for the cuprates [51,52]. For the Fe-based systems, the possibility of complex Raman tensor elements for the As phonon was not considered yet. Our experimental observations show that the complex nature of $\hat{\alpha}^{(Ag)}$ is crucially important and that the imaginary parts of α_{11} and α_{22} must have opposite sign to explain the observed enhancement of $A_{ab}^{(As)}(\omega_1)$ and the suppression of $A_{aa}^{(As)}(\omega_1)$ with respect to the values expected for real tensor elements (dashed orange and purple lines in Fig. 8).

In summary, the results for $A_{aa}^{(As)}(\omega_1)$ and $A_{ab}^{(As)}(\omega_1)$ along with those for $A_{\tilde{a}\tilde{a}}^{(As)}(\omega_1)$ and $A_{\tilde{b}\tilde{b}}^{(As)}(\omega_1)$ support our point of view that absorption processes are important for the proper interpretation of the Raman data. Currently, we cannot imagine anything else but resonance effects due to interband transitions as the source.

APPENDIX D: BAND STRUCTURE

The DFT band structure is shown in Fig. 9. Bands above E_F stem predominantly from Fe $3d$ orbitals (brown) while for $E < -2.7$ eV As $4p$ orbitals prevail (black). For a suitable comparison to the experiment these Fe bands are renormalized by a factor between 2 and 3 [53–56] while no renormalization is needed for the As bands. The bands between -2.7 eV and E_F are of mixed Fe/As character and are left out when calculating the dielectric tensor as is illustrated by the grey shade in Fig. 9. Only transitions between the ranges $[-5.5$ eV, -2.7 eV] and $[0, 2.6$ eV], highlighted by turquoise rectangles, are taken into account. Thus for photon energies below 2.7 eV, the absorption in our calculations originates predominantly from the Drude response whereas for $\hbar\omega_1 > 2.7$ eV the results become increasingly realistic since they include interband absorption. In either case, we use a phenomenological damping of 0.1 eV. We determine the dielectric tensor and the Raman tensor as described in Sec. IID on the basis of this renormalized

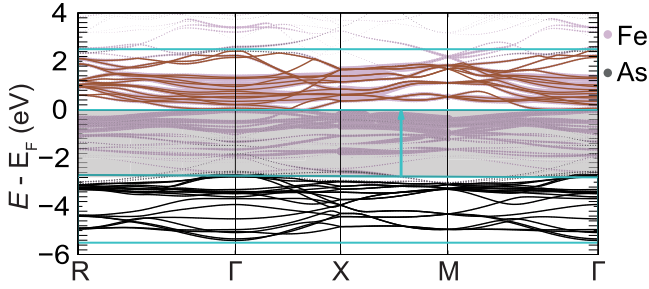


FIG. 9. DFT band structure. Bands predominantly from Fe states are shown in brown, bands predominantly from As states in black. The shaded region from -2.7 eV to E_F contains bands of mixed character and is blacked out for the calculation of the dielectric tensor. Only transitions between the bands within the turquoise frames are included.

band structure. While the $\tilde{a} - \tilde{b}$ anisotropy is qualitatively reproduced for all energies ω_l as shown in Fig. 6(b) of the main text, the two other experimental quantities, $A_{ab}^{(As)}(\omega_l)$ (purple) and $A_{aa}^{(As)}(\omega_l)$ (orange) shown in Fig. 8 here, are not captured properly simply because the imaginary parts of the theoretically determined tensor elements $\alpha_{ii}^{(As)''}$ become very small below 2.7 eV. To describe $A_{aa}^{(As)}(\omega_l)$ and $A_{ab}^{(As)}(\omega_l)$, absorption processes which lead to imaginary parts of the Raman tensor are necessary. Upon phenomenologically introducing imaginary parts of $\hat{\alpha}$ for low energies, which cut off at 2.7 eV where the correct absorption takes over, full agreement can be achieved. However, a solution on a microscopic basis becomes possible only by using schemes that include many-body effects beyond DFT.

APPENDIX E: INTERRELATION OF THE A_g PHONON ANOMALY AND MAGNETISM IN $\text{Ba}(\text{Fe}_{1-x}\text{Co}_x)_2\text{As}_2$ AND FeSe

Similarly as in BaFe_2As_2 , the anomalous intensity of the A_g phonon in crossed polarizations is also linked to magnetic order in other Fe-based systems as shown for $\text{Ba}(\text{Fe}_{1-x}\text{Co}_x)_2\text{As}_2$ at $x = 0.025$ a while ago [46] and more recently for EuFe_2As_2 , NaFeAs , LaFeAsO , and FeSe [17]. Here, we add a few more results which support our interpretation. Figure 10(a) shows Raman spectra in ab polarization of $\text{Ba}(\text{Fe}_{1-x}\text{Co}_x)_2\text{As}_2$ with $x = 5.1\%$ having $T_s = 60.9$ K and $T_{\text{SDW}} = 50.0$ K. The As mode appears below T_s and gains strength upon cooling. Figure 10(b) shows the corresponding spectral weight as a function of temperature. In the nematic phase $T_{\text{SDW}} < T < T_s$, the phonon spectral weight increases almost linearly upon cooling (rather than order-parameter-like), becomes constant in the magnetic phase for $T < T_{\text{SDW}}$ and reaches approximately 15% of that in the fully symmetric channel (A_g/A_{1g}).

In FeSe, the Se phonon appears also in the ab spectra as shown in Fig. 11(a) when the temperature is lowered below the structural phase transition at $T_s \approx 90$ K. Upon cooling [Fig. 11(b)], the spectral weight of the phonon increases almost linearly for crossed polarizations (ab , black squares), but stays virtually constant across the phase transition for parallel light polarizations [RR , orange circles in Fig. 11(b)]. As opposed to $\text{Ba}(\text{Fe}_{1-x}\text{Co}_x)_2\text{As}_2$, no saturation of the spectral weight

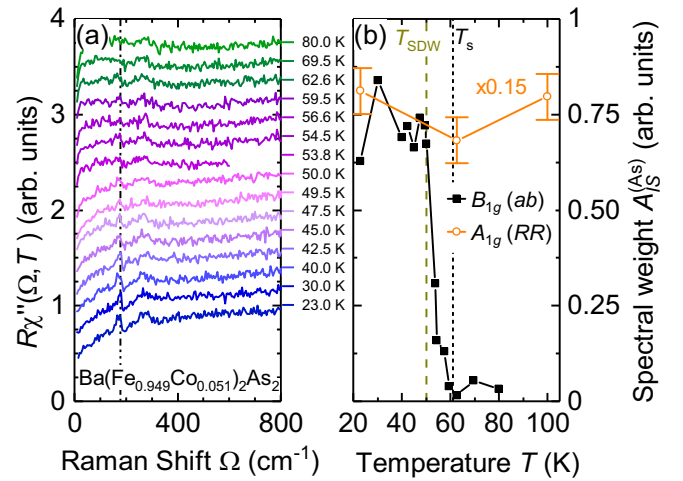


FIG. 10. As phonon in crossed polarizations for $\text{Ba}(\text{Fe}_{1-x}\text{Co}_x)_2\text{As}_2$ at $x = 0.051$. (a) Raw data for temperatures as indicated. The phonon position is shown as a vertical dash-dotted line. The spectra are shifted vertically for clarity. (b) Temperature dependence of the spectral weight. The spectral weight in A_{1g} symmetry (orange circles) was multiplied by 0.15. T_s and T_{SDW} are indicated as vertical dashed lines.

in ab polarizations is found, likely because FeSe shows no long-range magnetic order down to the lowest temperatures [49]. Only about 1% of the spectral weight of the A_{1g} spectra (RR) is found in crossed polarizations here, in contrast to BaFe_2As_2 and $\text{Ba}(\text{Fe}_{1-x}\text{Co}_x)_2\text{As}_2$, where the spectral weight of the phonon is larger (Figs. 5 and 10).

The nearly linear temperature dependence in both FeSe and $\text{Ba}(\text{Fe}_{1-x}\text{Co}_x)_2\text{As}_2$ and the larger saturation value in magnetically ordered $\text{Ba}(\text{Fe}_{1-x}\text{Co}_x)_2\text{As}_2$ indicate that the anomalous intensity is more likely related to magnetism than to the orthorhombic distortion.

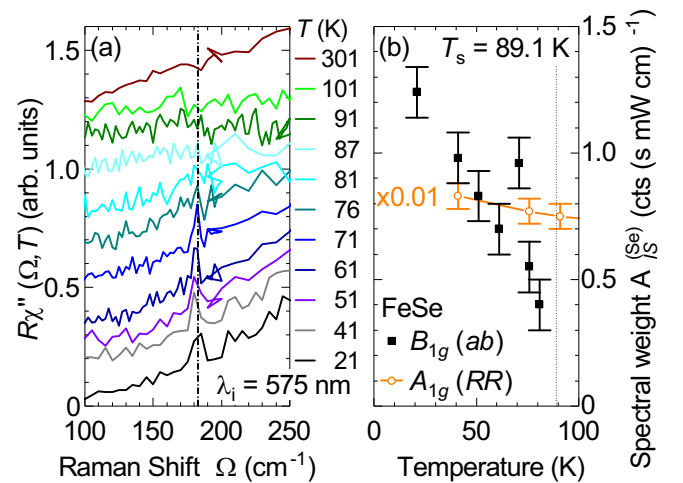


FIG. 11. Se phonon in crossed polarization for FeSe. (a) Raw data for temperatures as indicated. The phonon position is shown as dash-dotted line. The spectra are shifted vertically for clarity. (b) Temperature dependence of the spectral weight. The spectral weight in A_{1g} symmetry (orange circles) was multiplied by 0.01. T_s is indicated as vertical dotted line.

- [1] A. S. Sefat and D. J. Singh, Chemistry and electronic structure of iron-based superconductors, *MRS Bull.* **36**, 614 (2011).
- [2] F. Wang, S. A. Kivelson, and D.-H. Lee, Nematicity and quantum paramagnetism in FeSe, *Nat. Phys.* **11**, 959 (2015).
- [3] Y. Gallais and I. Paul, Charge nematicity and electronic Raman scattering in iron-based superconductors, *C. R. Phys.* **17**, 113 (2016).
- [4] M. Yi, Y. Zhang, Z.-X. Shen, and D. Lu, Role of the orbital degree of freedom in iron-based superconductors, *npj Quantum Mater.* **2**, 57 (2017).
- [5] A. E. Böhmer and A. Kreisel, Nematicity, magnetism and superconductivity in FeSe, *J. Phys.: Condens. Matter* **30**, 023001 (2018).
- [6] T. Yildirim, Strong Coupling of the Fe-Spin State and the As-As Hybridization in Iron-Pnictide Superconductors from First-Principle Calculations, *Phys. Rev. Lett.* **102**, 037003 (2009).
- [7] M. Zbiri, H. Schober, M. R. Johnson, S. Rols, R. Mittal, Y. Su, M. Rotter, and D. Johrendt, Ab initio lattice dynamics simulations and inelastic neutron scattering spectra for studying phonons in BaFe₂As₂: Effect of structural phase transition, structural relaxation, and magnetic ordering, *Phys. Rev. B* **79**, 064511 (2009).
- [8] L. Chauvière, Y. Gallais, M. Cazayous, A. Sacuto, M. A. Méasson, D. Colson, and A. Forget, Doping dependence of the lattice dynamics in Ba(Fe_{1-x}Co_x)₂As₂ studied by Raman spectroscopy, *Phys. Rev. B* **80**, 094504 (2009).
- [9] L. Chauvière, Y. Gallais, M. Cazayous, M. A. Méasson, A. Sacuto, D. Colson, and A. Forget, Raman scattering study of spin-density-wave order and electron-phonon coupling in Ba(Fe_{1-x}Co_x)₂As₂, *Phys. Rev. B* **84**, 104508 (2011).
- [10] M. Rahlenbeck, G. L. Sun, D. L. Sun, C. T. Lin, B. Keimer, and C. Ulrich, Phonon anomalies in pure and underdoped R_{1-x}K_xFe₂As₂ (R = Ba, Sr) investigated by Raman light scattering, *Phys. Rev. B* **80**, 064509 (2009).
- [11] P. Kumar, A. Kumar, S. Saha, D. V. S. Muthu, J. Prakash, S. Patnaik, U. V. Waghmare, A. K. Ganguli, and A. K. Sood, Anomalous Raman scattering from phonons and electrons of superconducting FeSe_{0.82}, *Solid State Commun.* **150**, 557 (2010).
- [12] R. Mittal, L. Pintschovius, D. Lamago, R. Heid, K.-P. Bohnen, D. Reznik, S. L. Chaplot, Y. Su, N. Kumar, S. K. Dhar, A. Thamizhavel, and T. Brueckel, Measurement of Anomalous Phonon Dispersion of CaFe₂As₂ Single Crystals Using Inelastic Neutron Scattering, *Phys. Rev. Lett.* **102**, 217001 (2009).
- [13] V. Gnezdilov, Y. G. Pashkevich, P. Lemmens, D. Wulferding, T. Shevtsova, A. Gusev, D. Chareev, and A. Vasiliev, Interplay between lattice and spin states degree of freedom in the FeSe superconductor: Dynamic spin state instabilities, *Phys. Rev. B* **87**, 144508 (2013).
- [14] V. Gnezdilov, Y. Pashkevich, P. Lemmens, A. Gusev, K. Lam-onova, T. Shevtsova, I. Vitebskiy, O. Afanasiev, S. Gnatchenko, V. Tsurkan, J. Deisenhofer, and A. Loidl, Anomalous optical phonons in FeTe chalcogenides: Spin state, magnetic order, and lattice anharmonicity, *Phys. Rev. B* **83**, 245127 (2011).
- [15] A. Akrap, J. J. Tu, L. J. Li, G. H. Cao, Z. A. Xu, and C. C. Homes, Infrared phonon anomaly in BaFe₂As₂, *Phys. Rev. B* **80**, 180502 (2009).
- [16] N. A. García-Martínez, B. Valenzuela, S. Ciuchi, E. Cappelluti, M. J. Calderón, and E. Bascones, Coupling of the As A_{1g} phonon to magnetism in iron pnictides, *Phys. Rev. B* **88**, 165106 (2013).
- [17] S.-F. Wu, W.-L. Zhang, V. K. Thorsmølle, G. F. Chen, G. T. Tan, P. C. Dai, Y. G. Shi, C. Q. Jin, T. Shibauchi, S. Kasahara, Y. Matsuda, A. S. Sefat, H. Ding, P. Richard, and G. Blumberg, Magneto-elastic coupling in Fe-based superconductors (2017), [arXiv:1712.01896](https://arxiv.org/abs/1712.01896) [cond-mat.supr-con].
- [18] I. I. Mazin, M. D. Johannes, L. Boeri, K. Koepernik, and D. J. Singh, Problems with reconciling density functional theory calculations with experiment in ferropnictides, *Phys. Rev. B* **78**, 085104 (2008).
- [19] J.-H. Chu, J. G. Analytis, C. Kucharczyk, and I. R. Fisher, Determination of the phase diagram of the electron-doped superconductor Ba(Fe_{1-x}Co_x)₂As₂, *Phys. Rev. B* **79**, 014506 (2009).
- [20] S. A. J. Kimber, A. Kreyssig, Y.-Z. Zhang, H. O. Jeschke, R. Valentí, F. Yokaichiya, E. Colombier, J. Yan, T. C. Hansen, T. Chatterji, R. J. McQueeney, P. C. Canfield, A. I. Goldman, and D. N. Argyriou, Similarities between structural distortions under pressure and chemical doping in superconducting BaFe₂As₂, *Nat. Mater.* **8**, 471 (2009).
- [21] M. G. Kim, R. M. Fernandes, A. Kreyssig, J. W. Kim, A. Thaler, S. L. Bud'ko, P. C. Canfield, R. J. McQueeney, J. Schmalian, and A. I. Goldman, Character of the structural and magnetic phase transitions in the parent and electron-doped BaFe₂As₂ compounds, *Phys. Rev. B* **83**, 134522 (2011).
- [22] M. Rotter, M. Tegel, and D. Johrendt, Superconductivity at 38 K in the Iron Arsenide (Ba_{1-x}K_x)Fe₂As₂, *Phys. Rev. Lett.* **101**, 107006 (2008).
- [23] J.-H. Chu, J. G. Analytis, K. D. Greve, P. L. McMahon, Z. Islam, Y. Yamamoto, and I. R. Fisher, In-plane resistivity anisotropy in an underdoped iron arsenide superconductor, *Science* **329**, 824 (2010).
- [24] J. J. Ying, X. F. Wang, T. Wu, Z. J. Xiang, R. H. Liu, Y. J. Yan, A. F. Wang, M. Zhang, G. J. Ye, P. Cheng, J. P. Hu, and X. H. Chen, Measurements of the Anisotropic in-Plane Resistivity of Underdoped FeAs-Based Pnictide Superconductors, *Phys. Rev. Lett.* **107**, 067001 (2011).
- [25] A. Dusza, A. Lucarelli, F. Pfner, J.-H. Chu, I. R. Fisher, and L. Degiorgi, Anisotropic charge dynamics in detwinned Ba(Fe_{1-x}Co_x)₂As₂, *Europhys. Lett.* **93**, 37002 (2011).
- [26] A. Dusza, A. Lucarelli, A. Sanna, S. Massidda, J.-H. Chu, I. R. Fisher, and L. Degiorgi, Anisotropic in-plane optical conductivity in detwinned Ba(Fe_{1-x}Co_x)₂As₂, *New J. Phys.* **14**, 023020 (2012).
- [27] M. Nakajima, T. Liang, S. Ishida, Y. Tomioka, K. Kihou, C. H. Lee, A. Iyo, H. Eisaki, T. Kakeshita, T. Ito, and S. Uchida, Unprecedented anisotropic metallic state in undoped iron arsenide BaFe₂As₂ revealed by optical spectroscopy, *Proc. Natl. Acad. Sci. USA* **108**, 12238 (2011).
- [28] M. Yi, D. Lu, J.-H. Chu, J. G. Analytis, A. P. Sorini, A. F. Kemper, B. Moritz, S.-K. Mo, R. G. Moore, M. Hashimoto, W.-S. Lee, Z. Hussain, T. P. Devereaux, I. R. Fisher, and Z.-X. Shen, Symmetry-breaking orbital anisotropy observed for detwinned Ba(Fe_{1-x}Co_x)₂As₂ above the spin density wave transition, *Proc. Natl. Acad. Sci. USA* **108**, 6878 (2011).
- [29] T. Liang, M. Nakajima, K. Kihou, Y. Tomioka, T. Ito, C. H. Lee, H. Kito, A. Iyo, H. Eisaki, T. Kakeshita, and S. Uchida, Effects of uniaxial pressure and annealing on the resistivity of Ba(Fe_{1-x}Co_x)₂As₂, *J. Phys. Chem. Solids* **72**, 418 (2011).
- [30] E. C. Blomberg, A. Kreyssig, M. A. Tanatar, R. M. Fernandes, M. G. Kim, A. Thaler, J. Schmalian, S. L. Bud'ko, P. C. Canfield,

- A. I. Goldman, and R. Prozorov, Effect of tensile stress on the in-plane resistivity anisotropy in BaFe_2As_2 , *Phys. Rev. B* **85**, 144509 (2012).
- [31] J. P. Perdew, K. Burke, and M. Ernzerhof, Generalized Gradient Approximation Made Simple, *Phys. Rev. Lett.* **77**, 3865 (1996).
- [32] A. Togo, F. Oba, and I. Tanaka, First-principles calculations of the ferroelastic transition between rutile-type and CaCl_2 -type SiO_2 at high pressures, *Phys. Rev. B* **78**, 134106 (2008).
- [33] A. Togo and I. Tanaka, First principles phonon calculations in materials science, *Scr. Mater.* **108**, 1 (2015).
- [34] K. Parlinski, Z. Q. Li, and Y. Kawazoe, First-Principles Determination of the Soft Mode in Cubic ZrO_2 , *Phys. Rev. Lett.* **78**, 4063 (1997).
- [35] P. E. Blöchl, Projector augmented-wave method, *Phys. Rev. B* **50**, 17953 (1994).
- [36] G. Kresse and J. Hafner, Ab initio molecular dynamics for liquid metals, *Phys. Rev. B* **47**, 558 (1993).
- [37] G. Kresse and J. Furthmüller, Efficient iterative schemes for ab initio total-energy calculations using a plane-wave basis set, *Phys. Rev. B* **54**, 11169 (1996).
- [38] G. Kresse and J. Furthmüller, Efficiency of ab-initio total energy calculations for metals and semiconductors using a plane-wave basis set, *Comput. Mater. Sci.* **6**, 15 (1996).
- [39] C. Ambrosch-Draxl and J. O. Sofo, Linear optical properties of solids within the full-potential linearized augmented planewave method, *Comput. Phys. Commun.* **175**, 1 (2006).
- [40] P. Blaha, K. Schwarz, G. K. H. Madsen, D. Kvasnicka, and J. Luitz, *WIEN2k: An Augmented Plane Wave Plus Local Orbitals Program for Calculating Crystal Properties* (Technische Universität Wien, Wien, 2001).
- [41] X. Ren, L. Duan, Y. Hu, J. Li, R. Zhang, H. Luo, P. Dai, and Y. Li, Nematic Crossover in BaFe_2As_2 under Uniaxial Stress, *Phys. Rev. Lett.* **115**, 197002 (2015).
- [42] W.-L. Zhang, A. S. Sefat, H. Ding, P. Richard, and G. Blumberg, Stress-induced nematicity in EuFe_2As_2 studied by Raman spectroscopy, *Phys. Rev. B* **94**, 014513 (2016).
- [43] K.-Y. Choi, D. Wulferding, P. Lemmens, N. Ni, S. L. Bud'ko, and P. C. Canfield, Lattice and electronic anomalies of CaFe_2As_2 studied by Raman spectroscopy, *Phys. Rev. B* **78**, 212503 (2008).
- [44] L. Chauvière, Y. Gallais, M. Cazayous, M. A. Méasson, A. Sacuto, D. Colson, and A. Forget, Impact of the spin-density-wave order on the superconducting gap of $\text{Ba}(\text{Fe}_{1-x}\text{Co}_x)_2\text{As}_2$, *Phys. Rev. B* **82**, 180521 (2010).
- [45] S. Sugai, Y. Mizuno, R. Watanabe, T. Kawaguchi, K. Takenaka, H. Ikuta, Y. Takayanagi, N. Hayamizu, and Y. Sone, Spin-density-wave gap with Dirac nodes and two-magnon Raman scattering in BaFe_2As_2 , *J. Phys. Soc. Jpn.* **81**, 024718 (2012).
- [46] F. Kretzschmar, T. Böhm, U. Karahasanović, B. Muschler, A. Baum, D. Jost, J. Schmalian, S. Caprara, M. Grilli, C. Di Castro, J. H. Analytis, J.-H. Chu, I. R. Fisher, and R. Hackl, Critical spin fluctuations and the origin of nematic order in $\text{Ba}(\text{Fe}_{1-x}\text{Co}_x)_2\text{As}_2$, *Nat. Phys.* **12**, 560 (2016).
- [47] V. K. Thorsmølle, M. Khodas, Z. P. Yin, C. Zhang, S. V. Carr, P. Dai, and G. Blumberg, Critical quadrupole fluctuations and collective modes in iron pnictide superconductors, *Phys. Rev. B* **93**, 054515 (2016).
- [48] M. Cardona, *Resonance Phenomena*, 1st ed. (Springer-Verlag, Berlin, Heidelberg, 1982) Chap. 2, pp. 19–178.
- [49] S.-H. Baek, D. V. Efremov, J. M. Ok, J. S. Kim, J. van den Brink, and B. Büchner, Orbital-driven nematicity in FeSe , *Nat. Mater.* **14**, 210 (2014).
- [50] B. Muschler, W. Prestel, L. Tassini, R. Hackl, M. Lambacher, A. Erb, S. Komiya, Y. Ando, D. C. Peets, W. N. Hardy, R. Liang, and D. A. Bonn, Electron interactions and charge ordering in CuO_2 compounds, *Eur. Phys. J. Special Topics* **188**, 131 (2010).
- [51] T. Strach, J. Brunen, B. Lederle, J. Zegenhagen, and M. Cardona, Determination of the phase difference between the Raman tensor elements of the A_{1g} -like phonons in $\text{SmBa}_2\text{Cu}_3\text{O}_{7-\delta}$, *Phys. Rev. B* **57**, 1292 (1998).
- [52] C. Ambrosch-Draxl, H. Auer, R. Kouba, E. Y. Sherman, P. Knoll, and M. Mayer, Raman scattering in $\text{YBa}_2\text{Cu}_3\text{O}_7$: A comprehensive theoretical study in comparison with experiments, *Phys. Rev. B* **65**, 064501 (2002).
- [53] S. L. Skornyakov, A. V. Efremov, N. A. Skorikov, M. A. Korotin, Y. A. Izyumov, V. I. Anisimov, A. V. Kozhevnikov, and D. Vollhardt, Classification of the electronic correlation strength in the iron pnictides: The case of the parent compound BaFe_2As_2 , *Phys. Rev. B* **80**, 092501 (2009).
- [54] Y. X. Yao, J. Schmalian, C. Z. Wang, K. M. Ho, and G. Kotliar, Comparative study of the electronic and magnetic properties of BaFe_2As_2 and BaMn_2As_2 using the Gutzwiller approximation, *Phys. Rev. B* **84**, 245112 (2011).
- [55] J. Ferber, K. Foyevtsova, R. Valentí, and H. O. Jeschke, LDA + DMFT study of the effects of correlation in LiFeAs , *Phys. Rev. B* **85**, 094505 (2012).
- [56] S. Backes, H. O. Jeschke, and R. Valentí, Microscopic nature of correlations in multiorbital AFe_2As_2 ($A = \text{K}, \text{Rb}, \text{Cs}$): Hund's coupling versus Coulomb repulsion, *Phys. Rev. B* **92**, 195128 (2015).

Lattice dynamics and phase transition in CrI₃ single crystals

S. Djurdjic-Mijin,¹ A. Šolajić,¹ J. Pešić,¹ M. Šćepanović,¹ Y. Liu (刘育),² A. Baum,^{3,4} C. Petrovic,²
N. Lazarević,¹ and Z. V. Popović^{1,5}

¹Center for Solid State Physics and New Materials, Institute of Physics Belgrade, University of Belgrade,
Pregrevica 118, 11080 Belgrade, Serbia

²Condensed Matter Physics and Materials Science Department, Brookhaven National Laboratory, Upton, New York 11973-5000, USA

³Walther Meissner Institut, Bayerische Akademie der Wissenschaften, 85748 Garching, Germany

⁴Fakultät für Physik E23, Technische Universität München, 85748 Garching, Germany

⁵Serbian Academy of Sciences and Arts, Knez Mihailova 35, 11000 Belgrade, Serbia



(Received 9 July 2018; published 18 September 2018)

The vibrational properties of CrI₃ single crystals were investigated using Raman spectroscopy and were analyzed with respect to the changes of the crystal structure. All but one mode are observed for both the low-temperature $R\bar{3}$ and the high-temperature $C2/m$ phase. For all observed modes the energies and symmetries are in good agreement with DFT calculations. The symmetry of a single layer was identified as $p\bar{3}1/m$. In contrast to previous studies we observe the transition from the $R\bar{3}$ to the $C2/m$ phase at 180 K and find no evidence for coexistence of both phases over a wide temperature range.

DOI: [10.1103/PhysRevB.98.104307](https://doi.org/10.1103/PhysRevB.98.104307)

I. INTRODUCTION

Two-dimensional layered materials have gained attention due to their unique properties, the potential for a wide spectrum of applications, and the opportunity for the development of functional van der Waals heterostructures. CrI₃ is a member of the chromium-trihalide family which are ferromagnetic semiconductors [1]. Recently they have received significant attention as candidates for the study of magnetic monolayers. The experimental realization of CrI₃ ferromagnetic monolayers [1] motivated further efforts towards their understanding. CrI₃ features electric field controlled magnetism [2] as well as a strong magnetic anisotropy [3,4]. With the main absorption peaks lying in the visible part of the spectrum, it is a great candidate for low-dimensional semiconductor spintronics [5]. In its ground state, CrI₃ is a ferromagnetic semiconductor with a Curie temperature of 61 K [1,6] and a band gap of 1.2 eV [6]. It was demonstrated that the magnetic properties of CrI₃ mono- and bilayers can be controlled by electrostatic doping [2]. Upon cooling, CrI₃ undergoes a phase transition around 220 K from the high-temperature monoclinic ($C2/m$) to the low-temperature rhombohedral ($R\bar{3}$) phase [3,7]. Although the structural phase transition is reported to be first order, it was suggested that the phases may coexist over a wide temperature range [3]. Raman spectroscopy can be of use here due to its capability to simultaneously probe both phases in a phase-separated system [8–10].

A recent theoretical study predicted the energies of all Raman active modes in the low-temperature and high-temperature structure of CrI₃ suggesting a near degeneracy between the A_g and B_g modes in the monoclinic ($C2/m$) structure. Their energies match the energies of E_g modes in the rhombohedral ($R\bar{3}$) structure [7].

In this article we present an experimental and theoretical Raman scattering study of CrI₃ lattice dynamics. In both phases all but one of the respective modes predicted by

symmetry were observed. The energies for all modes are in good agreement with the theoretical predictions for the assumed crystal symmetry. Our data suggest that the first-order transition occurs at $T_s \approx 180$ K without evidence for phase coexistence over a wide temperature range.

II. EXPERIMENT AND NUMERICAL METHOD

The preparation of the single crystal CrI₃ sample used in this study is described elsewhere [11]. The Raman scattering experiment was performed using a Tri Vista 557 spectrometer in backscattering micro-Raman configuration with a 1800/1800/2400 grooves/mm diffraction grating combination. The 532 nm line of a Coherent Verdi G solid state laser was used for excitation. The direction of the incident light coincides with the crystallographic c axis. The sample was oriented so that its principal axis of the $R\bar{3}$ phase coincides with the x axis of the laboratory system. A KONTI CryoVac continuous helium flow cryostat with a 0.5-mm-thick window was used for measurements at all temperatures under high vacuum (10^{-6} mbar). The sample was cleaved in air before being placed into the cryostat. The obtained Raman spectra were corrected by the Bose factor and analyzed quantitatively by fitting Voigt profiles to the data whereby the Gaussian width $\Gamma_{\text{Gauss}} = 1 \text{ cm}^{-1}$ reflects the resolution of the spectrometer.

The spin polarized density functional theory (DFT) calculations have been performed in the Quantum Espresso (QE) software package [12] using the Perdew-Burke-Ernzerhof (PBE) exchange-correlation functional [13] and PAW pseudopotentials [14,15]. The energy cutoffs for the wave functions and the charge density were set to be 85 and 425 Ry, respectively, after convergence tests. For k -point sampling, the Monkhorst-Pack scheme was used with a $8 \times 8 \times 8$ grid centered around the Γ point. Optimization of the atomic positions in the unit cell was performed until the interatomic forces

were smaller than 10^{-6} Ry/Å. To treat the van der Waals (vdW) interactions a Grimme-D2 correction [16] is used in order to include long-ranged forces between the layers, which are not properly captured within LDA or GGA functionals. This way, the parameters are obtained more accurately, especially the interlayer distances. Phonon frequencies were calculated at the Γ point using the linear response method implemented in QE. The phonon energies are compiled in Table III together with the experimental values. The eigenvectors of the Raman active modes for both the low- and high-temperature phase are depicted in Fig. 5 of the Appendix.

III. RESULTS AND DISCUSSION

CrI₃ adopts a rhombohedral $R\bar{3}$ (C_{3i}^2) crystal structure at low temperatures and a monoclinic $C2/m$ (C_{2h}^3) crystal structure at room temperature [3], as shown in Fig. 1. The main difference between the high- and low-temperature crystallographic space groups arises from different stacking sequences with the CrI₃ layers being almost identical. In the rhombohedral structure the Cr atoms in one layer are placed above the center of a hole in the Cr honeycomb net of the two adjacent layers. When crossing the structural phase transition at T_s to the monoclinic structure the layers are displaced along the a direction so that every fourth layer is at the same place as the first one. The interatomic distances, mainly the interlayer distance, and the vdW gap, are slightly changed by the structural transition. The crystallographic parameters for both phases are presented in Table I. The numerically obtained values are in good agreement with reported x-ray diffraction data [11].

The vibrational properties of layered materials are typically dominated by the properties of the single layers composing the crystal. The symmetry of a single layer can be described by one of the 80 diperiodic space groups (DG) obtained by

TABLE I. Calculated and experimental [11] parameters of the crystallographic unit cell for the low-temperature $R\bar{3}$ and high-temperature $C2/m$ phase of CrI₃.

T (K)	Space group $R\bar{3}$		Space group $C2/m$	
	Calc.	Expt. [11]	Calc.	Expt. [11]
a (Å)	6.87	6.85	6.866	6.6866
b (Å)	6.87	6.85	11.886	11.856
c (Å)	19.81	19.85	6.984	6.966
α (deg)	90	90	90	90
β (deg)	90	90	108.51	108.68
γ (deg)	120	120	90	90

lifting translational invariance in the direction perpendicular to the layer [17]. In the case of CrI₃, the symmetry analysis revealed that the single layer structure is fully captured by the $p\bar{3}1/m$ (D_{3d}^1) diperiodic space group DG71, rather than by $R\bar{3}2/m$ as proposed in Ref. [7].

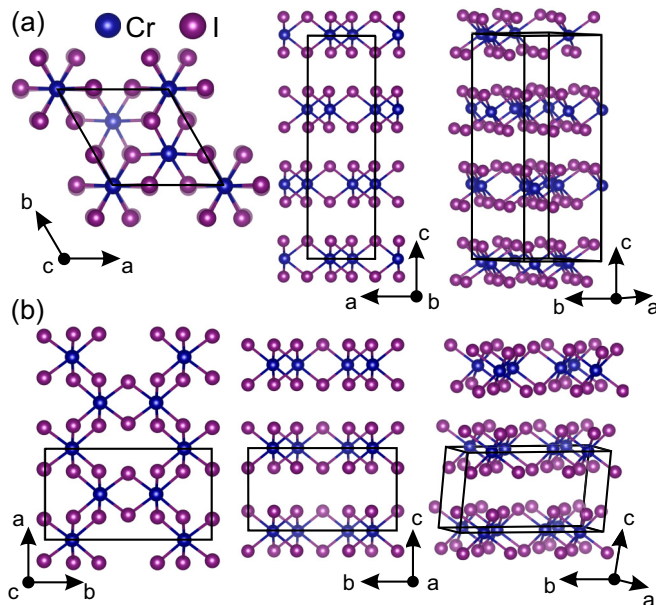


FIG. 1. Schematic representation of (a) the low-temperature $R\bar{3}$ and (b) the high-temperature $C2/m$ crystal structure of CrI₃. Black lines represent unit cells.

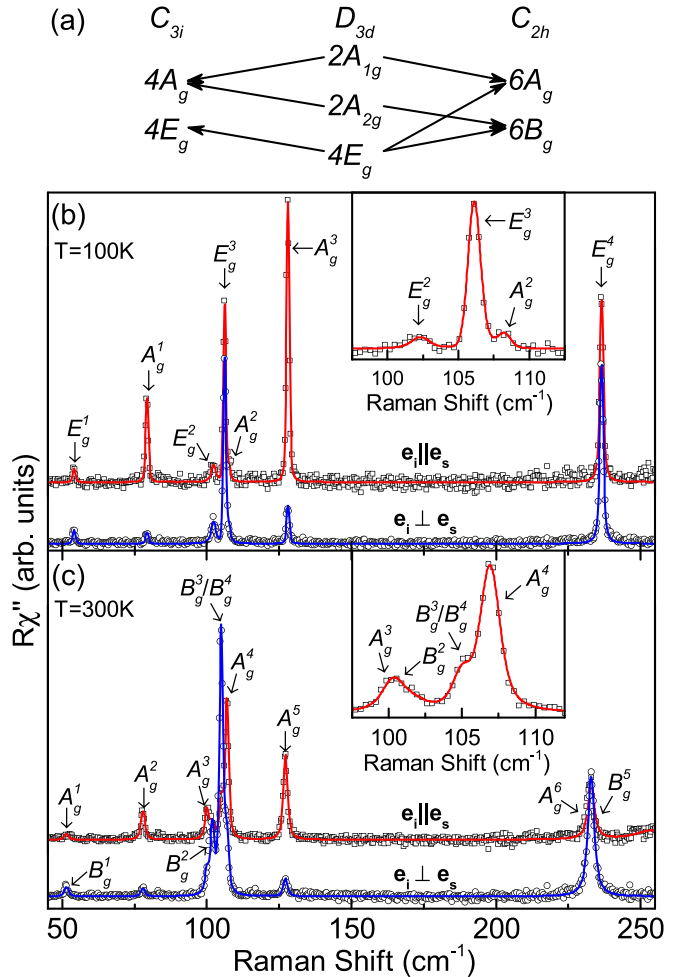


FIG. 2. (a) Compatibility relations for the CrI₃ layer and the crystal symmetries. Raman spectra of (b) the low-temperature $R\bar{3}$ and (c) the high-temperature $C2/m$ crystal structure measured in parallel (open squares) and crossed (open circles) polarization configurations at 100 and 300 K, respectively. Red and blue solid lines represent fits of Voigt profiles to the experimental data.

TABLE II. Wyckoff positions of the two types of atoms and their contributions to the Γ -point phonons for the $R\bar{3}$ and $C2/m$ as well as the $p\bar{3}1/m$ diperiodic space group. The second row shows the Raman tensors for the corresponding space groups.

Space group $R\bar{3}$		Diperiodic space group $p\bar{3}1/m$		Space group: $C2/m$	
Atoms	Irreducible representations	Atoms	Irreducible representations	Atoms	Irreducible representations
Cr (6c)	$A_g + A_u + E_g + E_u$	Cr (2c)	$A_{2g} + A_{2u} + E_g + E_u$	Cr (4g)	$A_g + A_u + 2B_g + 2B_u$
I (18f)	$3A_g + 3A_u + 3E_g + 3E_u$	I (6k)	$2A_{1g} + A_{1u} + A_{2g} + 2A_{2u} + 3E_g + 3E_u$	I (4i)	$2A_g + 2A_u + B_g + B_u$
				I (8j)	$3A_g + 3A_u + 3B_g + 3B_u$
$A_g = \begin{pmatrix} a & & \\ & a & \\ & & b \end{pmatrix}$		$A_{1g} = \begin{pmatrix} a & & \\ & a & \\ & & b \end{pmatrix}$		$A_g = \begin{pmatrix} a & d \\ & c \\ d & b \end{pmatrix}$	
${}^1E_g = \begin{pmatrix} c & d & e \\ d & -c & f \\ e & f & \end{pmatrix}$		${}^1E_g = \begin{pmatrix} c & & \\ -c & d & \\ d & & \end{pmatrix}$		$B_g = \begin{pmatrix} e & \\ e & f \\ f & \end{pmatrix}$	
${}^2E_g = \begin{pmatrix} d & -c & -f \\ -c & -d & e \\ -f & e & \end{pmatrix}$		${}^2E_g = \begin{pmatrix} & -c & -d \\ -c & & \\ -d & e & \end{pmatrix}$			

According to the factor group analysis (FGA) for a single CrI_3 layer, six modes ($2A_{1g} + 4E_g$) are expected to be observed in the Raman scattering experiment (see Table II). By stacking the layers the symmetry is reduced and, depending on the stacking sequence, FGA yields a total of eight Raman active modes ($4A_g + 4E_g$) for the $R\bar{3}$ and 12 Raman active modes ($6A_g + 6B_g$) for the $C2/m$ crystal symmetry. The correlation between layer and crystal symmetries for both cases is shown in Fig. 2(a) [18,19].

Figure 2(b) shows the CrI_3 single crystal Raman spectra measured at 100 K in two scattering channels. According to the selection rules for the rhombohedral crystal structure (Table II) the A_g modes can be observed only in the parallel polarization configuration, whereas the E_g modes appear in both parallel and crossed polarization configurations. Based on the selection rules the peaks at about 78, 108, and 128 cm^{-1} were identified as A_g symmetry modes, whereas the peaks at about 54, 102, 106, and 235 cm^{-1} are assigned as E_g symmetry. The weak observation of the most pronounced A_g modes in crossed polarizations [Fig. 2(b)] is attributed to

the leakage due to a slight sample misalignment and/or the presence of defects in the crystal. The energies of all observed modes are compiled in Table III together with the energies predicted by our calculations and by Ref. [7], and are found to be in good agreement for the E_g modes. The discrepancy is slightly larger for the low energy A_g modes. Our calculations in general agree with those from Ref. [7]. The A_g^4 mode of the rhombohedral phase, predicted by calculation to appear at about 195 cm^{-1} , was not observed in the experiment, most likely due to its low intensity.

When the symmetry is lowered in the high-temperature monoclinic $C2/m$ phase [Fig. 2(c)] the E_g modes split into an A_g and a B_g mode each, whereas the rhombohedral A_g^2 and A_g^4 modes are predicted to switch to the monoclinic B_g symmetry. The correspondence of the phonon modes across the phase transition is indicated by the arrows in Table III. The selection rules for $C2/m$ (see Table II) predict that A_g and B_g modes can be observed in both parallel and crossed polarization configurations. Additionally, the sample forms three types of domains which are rotated with respect to each other. We

TABLE III. Phonon symmetries and phonon energies for the low-temperature $R\bar{3}$ and high-temperature $C2/m$ phase of CrI_3 . The experimental values were determined at 100 and 300 K, respectively. All calculations were performed at zero temperature. Arrows indicate the correspondence of the phonon modes across the phase transition.

Space group $R\bar{3}$					Space group C2/ m			
Symm.	Expt. (cm ⁻¹)	Calc. (cm ⁻¹)	Calc. (cm ⁻¹) [7]		Symm.	Expt. (cm ⁻¹)	Calc. (cm ⁻¹)	Calc. [7] (cm ⁻¹)
E_g^1	54.1	59.7	53	$\begin{smallmatrix} \rightarrow \\ \rightarrow \end{smallmatrix}$	B_g^1	52.0	57.0	52
					A_g^1	53.6	59.8	51
A_g^1	73.33	89.6	79	\longrightarrow	A_g^2	78.6	88.4	79
E_g^2	102.3	99.8	98	$\begin{smallmatrix} \rightarrow \\ \rightarrow \end{smallmatrix}$	A_g^3	101.8	101.9	99
					B_g^2	102.4	101.8	99
E_g^3	106.2	112.2	102	$\begin{smallmatrix} \rightarrow \\ \rightarrow \end{smallmatrix}$	B_g^3	106.4 ^a	108.9	101
					A_g^4	108.3	109.3	102
A_g^2	108.3	98.8	88	\longrightarrow	B_g^4	106.4 ^a	97.8	86
A_g^3	128.1	131.1	125	\longrightarrow	A_g^5	128.2	131.7	125
A_g^4	—	195.2	195	\longrightarrow	B_g^5	—	198.8	195
E_g^4	236.6	234.4	225	$\begin{smallmatrix} \rightarrow \\ \rightarrow \end{smallmatrix}$	A_g^6	234.6	220.1	224
					B_g^6	235.5	221.1	225

^aObserved as two peak structure.

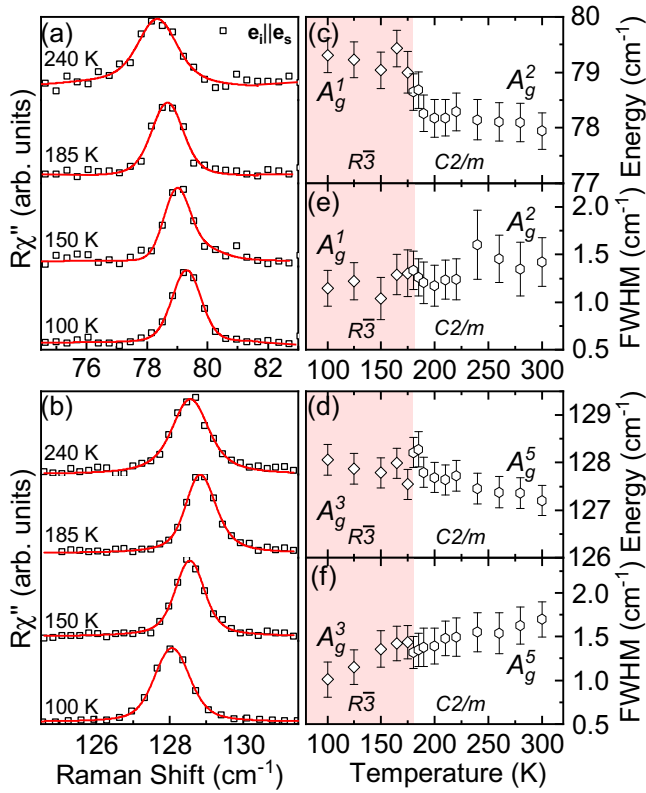


FIG. 3. Temperature dependence of the A_g^1 and A_g^3 phonon modes of the rhombohedral structure and the corresponding A_g^2 and A_g^5 modes of the monoclinic structure, respectively. (a) and (b) Raman spectra at temperatures as indicated. The spectra are shifted for clarity. Solid red lines represent Voigt profiles fitted to the data. (c) and (d) and (e) and (f) Temperature dependence of the phonon energies and linewidths, respectively. Both modes show an abrupt change in energy at the phase transition at 180 K.

therefore identify the phonons in the $C2/m$ phase in relation to the calculations and find again good agreement of the energies. The B_g^3 and B_g^4 modes overlap and therefore cannot be resolved separately. As can be seen from the temperature dependence shown below [Fig. 4(b)] the peak at 106 cm^{-1} broadens and gains spectral weight in the monoclinic phase in line with the expectation that two modes overlap. The missing rhombohedral A_g^4 mode corresponds to the monoclinic B_g^5 mode, which is likewise absent in the spectra.

The temperature dependence of the observed phonons is shown in Figs. 3 and 4. In the low-temperature rhombohedral phase all four E_g modes as well as A_g^1 and A_g^2 soften upon warming, whereas A_g^3 hardens up to $T \approx 180\text{ K}$ before softening again. Crossing the first-order phase transition from $R\bar{3}$ to $C2/m$ crystal symmetry is reflected in the spectra as a symmetry change and/or renormalization for the non-degenerate modes and lifting of the degeneracy of the E_g modes as shown in Table II. In our samples, this transition is observed at $T_s \approx 180\text{ K}$. The splitting of the E_g phonons into A_g and B_g modes at the phase transition is sharp (Fig. 4). The rhombohedral A_g^1 and A_g^3 phonons show a jump in energy and a small discontinuity in the linewidth at T_s (Fig. 3). Our spectra were taken during warming in multiple runs after

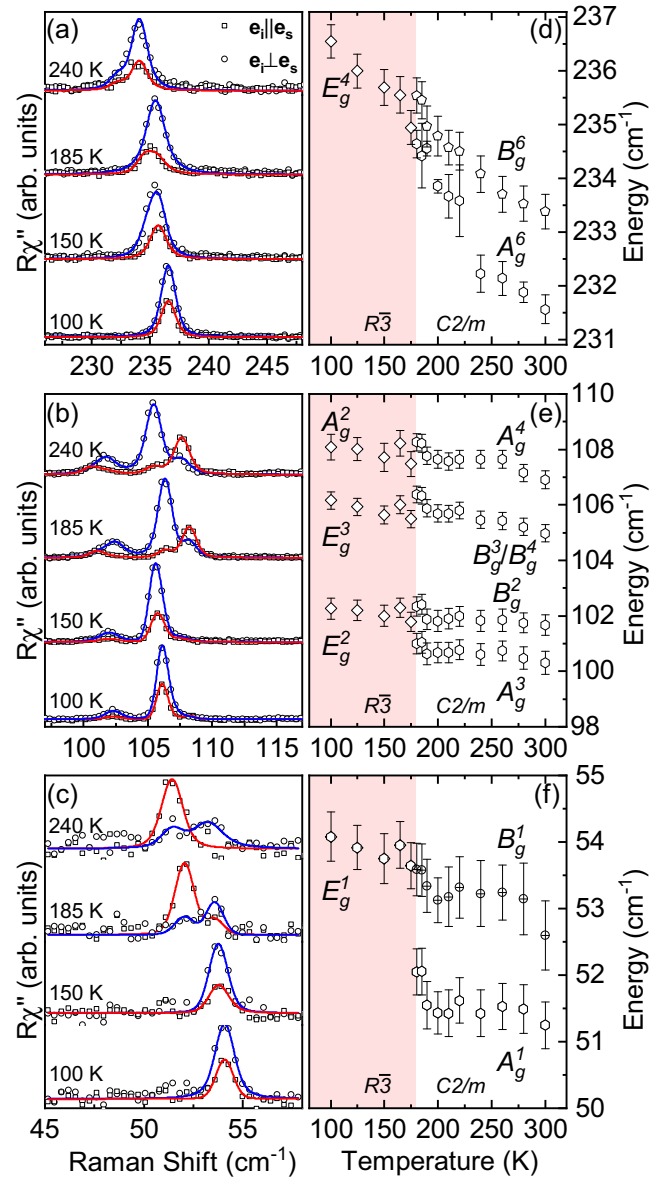


FIG. 4. Temperature dependence of the rhombohedral A_g^4 and E_g modes. (a)–(c) Raman spectra in parallel (open squares) and crossed (open circles) light polarizations at temperatures as indicated. The spectra are shifted for clarity. Blue and red solid lines are fits of Voigt profiles to the data. Two spectra were analyzed simultaneously in two scattering channels with the integrated intensity as the only independent parameter. (d)–(f) Phonon energies obtained from the Voigt profiles. Each E_g mode splits into an A_g and a B_g mode above 180 K.

cooling to 100 K each time. We found that the temperature dependence for the phonon modes obtained this way was smooth in each phase. McGuire *et al.* [3,20] reported T_s in the range of 220 K, a coexistence of both phases and a large thermal hysteresis. However, they also noted that the first and second warming cycle showed identical behavior and only found a shift of the transition temperature to higher values for cooling cycles. We therefore consider the difference between the reported transition around 220 K and our $T_s \approx 180\text{ K}$ significant. To some extent this difference may be attributed

to local heating by the laser. More importantly, we find no signs of phase coexistence in the observed temperature range. The spectra for the low-temperature and high-temperature phases are distinctly different (Fig. 2) and the E_g modes exhibit a clearly resolved splitting which occurs abruptly at T_S . We performed measurements in small temperature steps (see Figs. 3 and 4). This limits the maximum temperature interval where the phase coexistence could occur in our samples to approximately 5 K, much less than the roughly 30 to 80 K reported earlier [3,20]. We cannot exclude the possibility that a small fraction of the low-temperature phase could still

coexist with the high-temperature phase over a wider temperature range, whereby weak peaks corresponding to the remains of the low-temperature $R\bar{3}$ phase might be hidden under the strong peaks of the $C2/m$ phase.

IV. CONCLUSION

We studied the lattice dynamics in single crystalline CrI_3 using Raman spectroscopy supported by numerical calculations. For both the low-temperature $R\bar{3}$ and the high-temperature $C2/m$ phase, all except one of the predicted

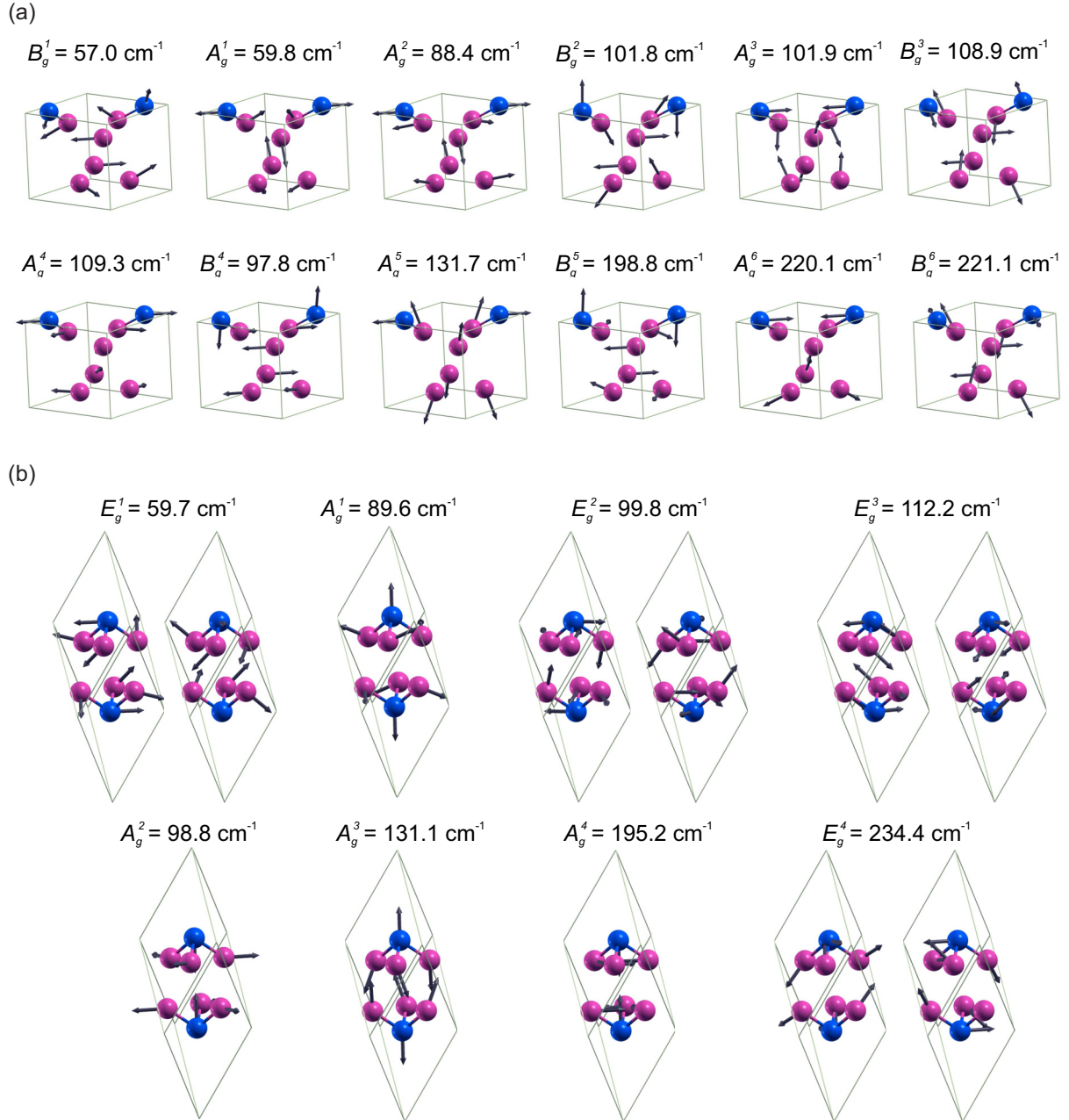


FIG. 5. Raman-active phonons in CrI_3 for (a) the monoclinic phase hosting A_g and B_g modes and for (b) the rhombohedral phase hosting A_g and E_g modes. Blue and violet spheres denote Cr and I atoms, respectively. Solid lines represent primitive unit cells. Arrow lengths are proportional to the square root of the interatomic forces. The given energies are calculated for zero temperature.

phonon modes were identified and the calculated and experimental phonon energies were found to be in good agreement. We determined that the symmetry of the single CrI_3 layers is $p\bar{3}1/m$. Abrupt changes to the spectra were found at the first-order phase transition which was located at $T_s \approx 180$ K, lower than in previous studies. In contrast to the prior reports we found no sign of phase coexistence over temperature ranges exceeding 5 K.

ACKNOWLEDGMENTS

The work was supported by the Serbian Ministry of Education, Science and Technological Development under Projects No. III45018 and No. OI171005. DFT calculations were performed using computational resources at Johannes Kepler University, Linz, Austria. Work at Brookhaven is supported by the U.S. DOE under Contract No. DE-SC0012704.

S.Dj.M. and N.L. conceived the experiment, performed the experiment, analyzed and discussed the data, and wrote the paper. A.Š. and J.P. calculated the phonon energies, analyzed and discussed the data, and wrote the paper. Y.L. and C.P. synthesized and characterized the samples. M.Š. performed the experiment and analyzed and discussed the data. A.B. and Z.V.P. analyzed and discussed the data and wrote the paper. All authors commented on the manuscript.

APPENDIX: EIGENVECTORS

In addition to the phonon energies we also calculated the phonon eigenvectors which are shown in Fig. 5(a) for the high-temperature monoclinic phase and in Fig. 5(b) for the low-temperature rhombohedral phase. The energies, as given, are calculated for zero temperature. The relative displacement of the atoms is denoted by the length of the arrows.

-
- [1] E. Navarro-Moratalla, B. Huang, G. Clark *et al.*, Layer-dependent ferromagnetism in a van der Waals crystal down to the monolayer limit, *Nature (London)* **546**, 270 (2017).
 - [2] S. Jiang, L. Li, Z. Wang, K. F. Mak, and J. Shan, Controlling magnetism in 2D CrI_3 by electrostatic doping, *Nat. Nanotechnol.* **13**, 549 (2018).
 - [3] M. A. McGuire, H. Dixit, V. R. Cooper, and B. C. Sales, Coupling of crystal structure and magnetism in the layered, ferromagnetic insulator CrI_3 , *Chem. Mater.* **27**, 612 (2015).
 - [4] J. L. Ladno and J. Fernández-Rossier, On the origin of magnetic anisotropy in two dimensional CrI_3 , *2D Mater.* **4**, 035002 (2017).
 - [5] W.-B. Zhang, Q. Qu, P. Zhu, and C.-H. Lam, Robust intrinsic ferromagnetism and half semiconductivity in stable two-dimensional single-layer chromium trihalides, *J. Mater. Chem. C* **3**, 12457 (2015).
 - [6] J. F. Dillon, Jr. and C. E. Olson, Magnetization, resonance, and optical properties of the ferromagnet CrI_3 , *J. Appl. Phys.* **36**, 1259 (1965).
 - [7] D. T. Larson and E. Kaxiras, Raman Spectrum of CrI_3 : An *ab initio* study, *Phys. Rev. B* **98**, 085406 (2018).
 - [8] N. Lazarević, M. Abeykoon, P. W. Stephens, H. Lei, E. S. Bozin, C. Petrovic, and Z. V. Popović, Vacancy-induced nanoscale phase separation in $\text{K}_x\text{Fe}_{2-y}\text{Se}_2$ single crystals evidenced by Raman scattering and powder x-ray diffraction, *Phys. Rev. B* **86**, 054503 (2012).
 - [9] H. Ryu, M. Abeykoon, K. Wang, H. Lei, N. Lazarevic, J. B. Warren, E. S. Bozin, Z. V. Popovic, and C. Petrovic, Insulating and metallic spin glass in Ni-doped $\text{K}_x\text{Fe}_{2-y}\text{Se}_2$ single crystals, *Phys. Rev. B* **91**, 184503 (2015).
 - [10] H. Ryu, K. Wang, M. Opacic, N. Lazarevic, J. B. Warren, Z. V. Popovic, E. S. Bozin, and C. Petrovic, Sustained phase separation and spin glass in Co-doped $\text{K}_x\text{Fe}_{2-y}\text{Se}_2$ single crystals, *Phys. Rev. B* **92**, 174522 (2015).
 - [11] Y. Liu and C. Petrovic, Three-dimensional magnetic critical behavior in CrI_3 , *Phys. Rev. B* **97**, 014420 (2018).
 - [12] P. Giannozzi, S. Baroni, N. Bonini, M. Calandra, R. Car, C. Cavazzoni, D. Ceresoli, G. L. Chiarotti, M. Cococcioni, I. Dabo, A. D. Corso, S. de Gironcoli, S. Fabris, G. Fratesi, R. Gebauer, U. Gerstmann, C. Gougoussis, A. Kokalj, M. Lazzeri, L. Martin-Samos, N. Marzari, F. Mauri, R. Mazzarello, S. Paolini, A. Pasquarello, L. Paulatto, C. Sbraccia, S. Scandolo, G. Sclauzero, A. P. Seitsonen, A. Smogunov, P. Umari, and R. M. Wentzcovitch, Quantum espresso: A modular and open-source software project for quantum simulations of materials, *J. Phys. Condens. Matter* **21**, 395502 (2009).
 - [13] J. P. Perdew, K. Burke, and M. Ernzerhof, Generalized Gradient Approximation Made Simple, *Phys. Rev. Lett.* **77**, 3865 (1996).
 - [14] P. E. Blöchl, Projector augmented-wave method, *Phys. Rev. B* **50**, 17953 (1994).
 - [15] G. Kresse and D. Joubert, From ultrasoft pseudopotentials to the projector augmented-wave method, *Phys. Rev. B* **59**, 1758 (1999).
 - [16] S. Grimme, Semiempirical GGA-type density functional constructed with a long-range dispersion correction, *J. Comput. Chem.* **27**, 1787 (2006).
 - [17] E. A. Wood, The 80 diperiodic groups in three dimensions, *Bell Syst. Tech. J.* **43**, 541 (1964).
 - [18] W. G. Fateley, N. T. McDevitt, and F. F. Bentley, Infrared and raman selection rules for lattice vibrations: The correlation method, *Appl. Spectrosc.* **25**, 155 (1971).
 - [19] N. Lazarević, Z. V. Popović, R. Hu, and C. Petrovic, Evidence of coupling between phonons and charge-density waves in ErTe_3 , *Phys. Rev. B* **83**, 024302 (2011).
 - [20] M. A. McGuire, G. Clark, S. KC, W. M. Chance, G. E. Jellison, V. R. Cooper, X. Xu, and B. C. Sales, Magnetic behavior and spin-lattice coupling in cleavable van der Waals layered CrCl_3 crystals, *Phys. Rev. Mater.* **1**, 014001 (2017).

Lattice dynamics and phase transitions in $\text{Fe}_{3-x}\text{GeTe}_2$

A. Milosavljević,¹ A. Šolajić,¹ S. Djurdjić-Mijin,¹ J. Pešić,¹ B. Višić,¹ Yu Liu (刘育),² C. Petrovic,²
N. Lazarević,¹ and Z. V. Popović^{1,3}

¹*Center for Solid State Physics and New Materials, Institute of Physics Belgrade,
University of Belgrade, Pregrevica 118, 11080 Belgrade, Serbia*

²*Condensed Matter Physics and Materials Science Department, Brookhaven National Laboratory, Upton, New York 11973-5000, USA*

³*Serbian Academy of Sciences and Arts, Knez Mihailova 35, 11000 Belgrade, Serbia*



(Received 23 April 2019; published 17 June 2019)

We present Raman spectroscopy measurements of the van der Waals bonded ferromagnet $\text{Fe}_{3-x}\text{GeTe}_2$, together with lattice dynamics. Four out of eight Raman active modes are observed and assigned, in agreement with numerical calculations. The energies and linewidths of the observed modes display an unconventional temperature dependence at about 150 and 220 K, followed by the nonmonotonic evolution of the Raman continuum. Whereas the former can be related to the magnetic phase transition, the origin of the latter anomaly remains an open question.

DOI: [10.1103/PhysRevB.99.214304](https://doi.org/10.1103/PhysRevB.99.214304)

I. INTRODUCTION

A novel class of magnetism hosting van der Waals bonded materials has recently become of great interest, since the materials are suitable candidates for numbers of technical applications [1–5]. Whereas CrXTe_3 ($X = \text{Si, Ge, Sn}$) and CrX_3 ($X = \text{Cl, Br, I}$) classes maintain low phase transition temperatures [1,6–9] even in a monolayer regime [10], $\text{Fe}_{3-x}\text{GeTe}_2$ has a high bulk transition temperature, between 220 and 230 K [11,12], making it a promising applicant.

The $\text{Fe}_{3-x}\text{GeTe}_2$ crystal structure consists of Fe_{3-x}Ge sublayers stacked between two sheets of Te atoms, and a van der Waals gap between neighboring Te layers [13,14]. Although the structure contains two different types of Fe atoms, it is revealed that vacancies take place only in the Fe2 sites [13,15].

Neutron diffraction, thermodynamic and transport measurements, and Mössbauer spectroscopy were used to analyze the magnetic and functional properties of $\text{Fe}_{3-x}\text{GeTe}_2$, with an Fe atom deficiency of $x \approx 0.1$ and $T_C = 225$ K. It is revealed that at a temperature of 1.5 K, magnetic moments of $1.95(5)\mu_B$ and $1.56(4)\mu_B$ are directed along the easy magnetic c axes [16]. In chemical vapor transport (CVT) grown Fe_3GeTe_2 single crystals, besides the ferromagnetic (FM)-paramagnetic (PM) transition at a temperature of 214 K, FM layers order antiferromagnetically at 152 K [17]. Close to a ferromagnetic transition temperature of 230 K, a possible Kondo lattice behavior, i.e., coupling of traveling electrons and periodically localized spins, is indicated at $T_K = 190 \pm 20$ K, which is in good agreement with theoretical predictions of 222 K [18].

Lattice parameters, as well as the magnetic transition temperature, vary with Fe ion concentration. Lattice parameters a and c follow the opposite trend, whereas the Curie temperature T_C decreases with an increase of Fe ion concentration [15]. For flux-grown crystals, the critical behavior was investigated by bulk dc magnetization around the ferromagnetic phase transition temperature of 152 K [13]. The anomalous Hall effect was also studied, where a significant amount of defects produces bad metallic behavior [19].

Theoretical calculations predict a dynamical stability of Fe_3GeTe_2 single-layer, uniaxial magnetocrystalline anisotropy that originates from spin-orbit coupling [20]. Recently, anomalous Hall effect measurements on single-crystalline metallic Fe_3GeTe_2 nanoflakes with different thicknesses are reported, with a T_C near 200 K and strong perpendicular magnetic anisotropy [21].

We report $\text{Fe}_{3-x}\text{GeTe}_2$ single-crystal lattice dynamic calculations, together with Raman spectroscopy measurements. Four out of eight Raman active modes were observed and assigned. Phonon energies are in a good agreement with theoretical predictions. Analyzed phonon energies and linewidths reveal fingerprint of a ferromagnetic phase transition at a temperature around 150 K. Moreover, discontinuities in the phonon properties are found at temperatures around 220 K. Consistently, in the same temperature range, the Raman continuum displays nonmonotonic behavior.

II. EXPERIMENT AND NUMERICAL METHOD

$\text{Fe}_{3-x}\text{GeTe}_2$ single crystals were grown by the self-flux method as previously described [13]. Samples for scanning electron microscopy (SEM) were cleaved and deposited on graphite tape. Energy dispersive spectroscopy (EDS) maps were collected using a FEI Helios NanoLab 650 instrument equipped with an Oxford Instruments EDS system, equipped with an X-max SSD detector operating at 20 kV. The surface of the as-cleaved $\text{Fe}_{3-x}\text{GeTe}_2$ crystal appears to be uniform for several tens of microns in both directions, as shown in Fig. 4 of Appendix A. Additionally, the elemental composition maps of Fe, Ge, and Te show a distinctive homogeneity of all the three elements (Fig. 5 of Appendix A).

For Raman scattering experiments, a Tri Vista 557 spectrometer was used in the backscattering micro-Raman configuration. As an excitation source, a solid state laser with a 532 nm line was used. In our scattering configuration, the plane of incidence is the ab plane, where $|a| = |b|$ ($\angle(a, b) = 120^\circ$), with the incident (scattered) light propagation direction

TABLE I. Top panel: The type of atoms, Wyckoff positions, each site's contribution to the phonons in the Γ point, and corresponding Raman tensors for the $P6_3/mmc$ space group of $\text{Fe}_{3-x}\text{GeTe}_2$. Bottom panel: Phonon symmetry, calculated optical Raman active phonon frequencies (in cm^{-1}) for the magnetic (M) phase, and experimental values for Raman active phonons at 80 K.

Space group $P6_3/mmc$ (No. 194)		
Fe1 (4e)	$A_{1g} + E_{1g} + E_{2g} + A_{2u} + E_{1u}$	
Fe2 (2c)	$E_{2g} + A_{2u} + E_{1u}$	
Ge (2d)	$E_{2g} + A_{2u} + E_{1u}$	
Te (2c)	$A_{1g} + E_{1g} + E_{2g} + A_{2u} + E_{1u}$	
Raman tensors		
$A_{1g} = \begin{pmatrix} a & 0 & 0 \\ 0 & a & 0 \\ 0 & 0 & b \end{pmatrix}$	$E_{1g} = \begin{pmatrix} 0 & 0 & -c \\ 0 & 0 & c \\ -c & c & 0 \end{pmatrix}$	$E_{2g} = \begin{pmatrix} d & -d & 0 \\ -d & -d & 0 \\ 0 & 0 & 0 \end{pmatrix}$
Raman active modes		
Symmetry	Calculations (M)	Experiment (M)
E_{2g}^1	50.2	
E_{1g}^1	70.3	
E_{2g}^2	122.2	89.2
A_{1g}^1	137.2	121.1
E_{1g}^2	209.5	
E_{2g}^3	228.6	214.8
A_{1g}^2	233.4	239.6
E_{2g}^4	334.3	

along the c axes. Samples were cleaved in the air, right before being placed in the vacuum. All the measurements were performed in the high vacuum (10^{-6} mbar) using a KONTE CryoVac continuous helium flow cryostat with a 0.5 mm thick window. To achieve laser beam focusing, a microscope objective with $\times 50$ magnification was used. A Bose factor correction of all spectra was performed. More details can be found in Appendix C.

Density functional theory (DFT) calculations were performed with the QUANTUM ESPRESSO (QE) software package [22]. We used the projector augmented-wave (PAW) pseudopotentials [23,24] with the Perdew-Burke-Ernzerhof (PBE) exchange-correlation functional [25]. The electron wave function and charge density cutoffs of 64 and 782 Ry were chosen, respectively. The k points were sampled using the Monkhorst-Pack scheme, with an $8 \times 8 \times 4$ Γ -centered grid. Both magnetic and nonmagnetic calculations were performed, using the experimentally obtained lattice parameters and the calculated values obtained by relaxing the theoretically proposed structure. In order to obtain the lattice parameters accurately, a treatment of the van der Waals interactions is introduced. The van der Waals interaction was included in all calculations using the Grimme-D2 correction [26]. Phonon frequencies in the Γ point are calculated within the linear response method implemented in QE.

III. RESULTS AND DISCUSSION

$\text{Fe}_{3-x}\text{GeTe}_2$ crystallizes in a hexagonal crystal structure, described with the $P6_3/mmc$ (D_{6h}^4) space group. The atom type, site symmetry, each site's contribution to the phonons

in the Γ point, and corresponding Raman tensors for the $P6_3/mmc$ space group are presented in Table I.

Calculated displacement patterns of Raman active modes, which can be observed in our scattering configuration, are presented in Fig. 1(a). Since the Raman tensor of the E_{1g} mode contains only the z component (Table I), by selection rules, it cannot be detected when measuring from the ab plane in the backscattering configuration. Whereas A_{1g} modes include vibrations of Fe and Te ions along the c axis, E_{2g} modes include in-plane vibrations of all four atoms. The Raman spectra of $\text{Fe}_{3-x}\text{GeTe}_2$ in the magnetic phase (M), at 80 K, and nonmagnetic phase (NM), at 280 K, in a parallel scattering configuration ($\mathbf{e}_i \parallel \mathbf{e}_s$), are presented in Fig. 1 (b). As it can be seen, four peaks at 89.2, 121.1, 214.8, and 239.6 cm^{-1} can be clearly observed at 80 K. According to numerical calculations (see Table I), peaks at 89.2 and 239.6 cm^{-1} correspond to two out of four E_{2g} modes, whereas peaks at 121.1 and 239.6 cm^{-1} can be assigned as two A_{1g} symmetry modes. One should note that numerical calculations performed by using experimentally obtained lattice parameters in the magnetic phase yield a better agreement with experimental values. This is not surprising since the calculations are performed for the stoichiometric compound as opposed to the nonstoichiometry of the sample. Furthermore, it is known that lattice parameters strongly depend on the Fe atom deficiency [15]. All calculated Raman and infrared phonon frequencies, for the magnetic and nonmagnetic phase of $\text{Fe}_{3-x}\text{GeTe}_2$, using relaxed and experimental lattice parameters, together with experimentally observed Raman active modes, are summarized in Table II of Appendix D.

After assigning all observed modes we focused on their temperature evolution. Having in mind finite instrumental

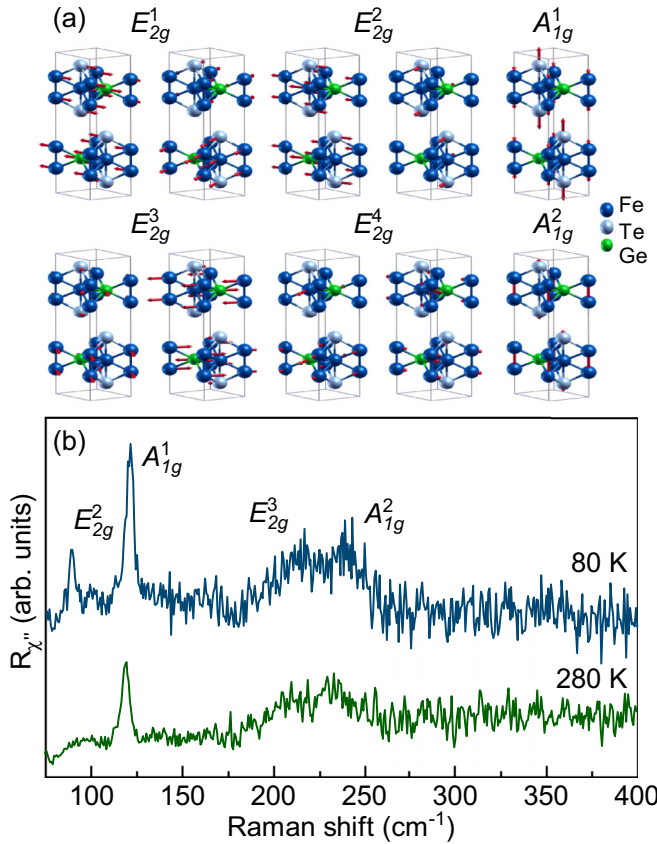


FIG. 1. (a) Displacement patterns of A_{1g} and E_{2g} symmetry modes. (b) Raman spectra of Fe_{3-x}GeTe₂ single crystal measured at different temperatures in a parallel polarization configuration.

broadening, the Voigt line shape was used for the data analysis [27,28]. The modeling procedure is described in detail in Appendix B and presented in Fig. 6. Figure 2 shows the temperature evolution of the energy and linewidth of the A_{1g}^1 , E_{2g}^3 , and A_{1g}^2 modes between 80 and 300 K. Upon heating the sample, both the energy and linewidth of A_{1g}^1 and A_{1g}^2 symmetry modes exhibit a small but sudden discontinuity at about 150 K [Figs. 2(a) and 2(e)]. An apparent discontinuity in energy of all analyzed Raman modes is again present at temperatures around 220 K. In the same temperature range the linewidths of these Raman modes show a clear deviation from the standard anharmonic behavior [27–31].

Apart from the anomalies in the phonon spectra, a closer inspection of the temperature-dependent Raman spectra measured in the parallel polarization configuration reveals a pronounced evolution of the Raman continuum [Fig. 3(a)]. For the analysis we have used a simple model including a damped Lorentzian and linear term, $\chi''_{\text{cont}} \propto a\Gamma\omega/(\omega^2 + \Gamma^2) + b\omega$ [32], where a , b , and Γ are temperature-dependent parameters. Figure 3(b) summarizes the results of the analysis with the linear term omitted (most likely originating from a luminescence). At approximately the same temperatures, where phonon properties exhibit discontinuities, the continuum temperature dependence manifests nonmonotonic behavior. The maximum positions of the curve were obtained by integrating

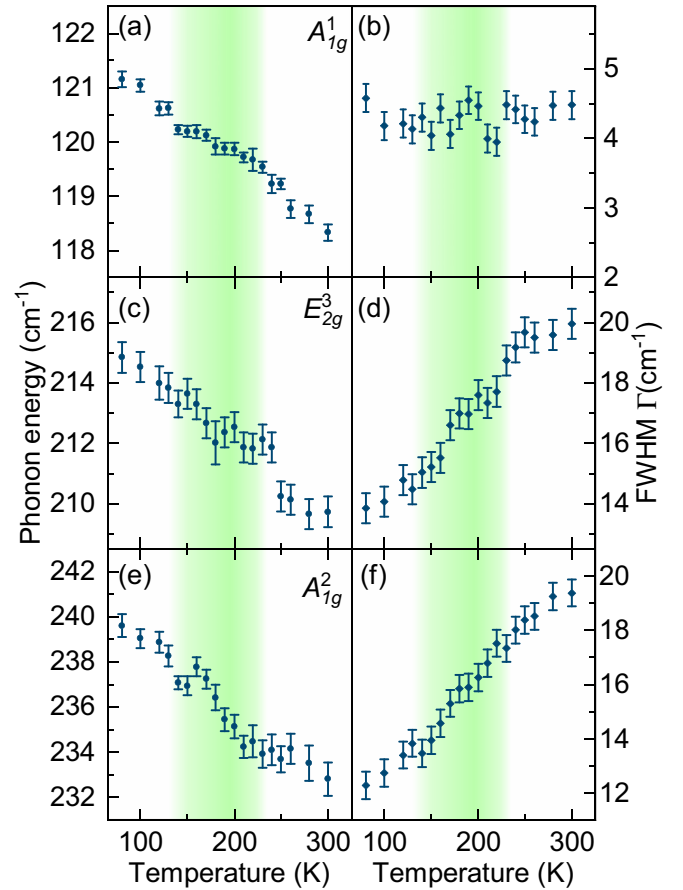


FIG. 2. Energy and linewidth temperature dependence of A_{1g}^1 [(a) and (b)], E_{2g}^3 [(c) and (d)], and A_{1g}^2 [(e) and (f)] phonon modes in Fe_{3-x}GeTe₂.

those shown in Fig. 3(b). The inset of Fig. 3(b) shows the temperature evolution of their displacements. This analysis confirms the presence of discontinuities in the electronic continuum at temperatures around 150 and 220 K, which leaves a trace in the phonon behavior around these temperatures (Fig. 2). While we do not have evidence for the Kondo effect in the Fe_{3-x}GeTe₂ crystals we measured, a modification of the electronic background at FM ordering due to localization or the Kondo effect cannot be excluded.

The temperature evolutions of the phonon self-energies and the continuum observed in the Raman spectra of Fe_{3-x}GeTe₂ suggest the presence of phase transition(s). Magnetization measurements of the samples were performed as described in Ref. [13], revealing a FM-PM transition at 150 K. Thus, the discontinuity in the observed phonon properties around this temperature can be traced back to the weak to moderate spin-phonon coupling. The question remains open regarding the anomaly observed at about 220 K. As previously reported, the Curie temperature of the Fe_{3-x}GeTe₂ single crystals grown by the CVT method is between 220 and 230 K [11,12,14], varying with the vacancy concentration, i.e., a decrease in the vacancy content will result an increment of T_C [15]. On the other hand, the Fe_{3-x}GeTe₂ crystals grown by the self-flux method usually have a lower Curie temperature, since the

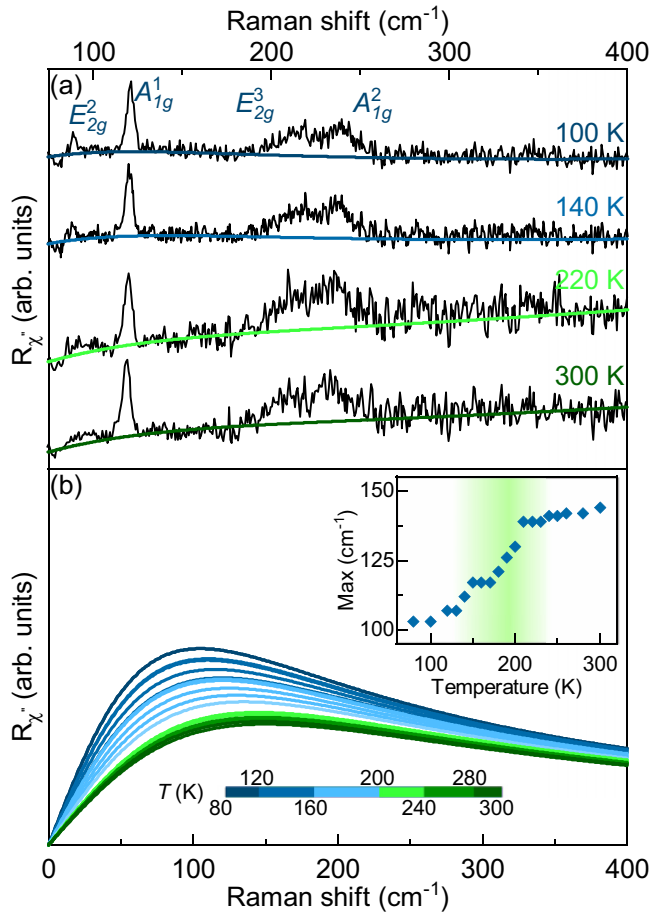


FIG. 3. (a) Raman spectra of $\text{Fe}_{3-x}\text{GeTe}_2$ at four temperatures measured in a parallel polarization configuration. Solid lines represent the theoretical fit to the experimental data. (b) Temperature evolution of the electronic continuum after omitting the linear term. Inset: Displacement of the maximum of fitted curves.

vacancy content is higher [13,15]. Crystals used in the Raman scattering experiment presented here were grown by the self-flux method with a Fe vacancy content of $x \approx 0.36$ [13]. This is in good agreement with our EDS results of $x = 0.4 \pm 0.1$, giving rise to the FM-PM transition at 150 K. Nevertheless,

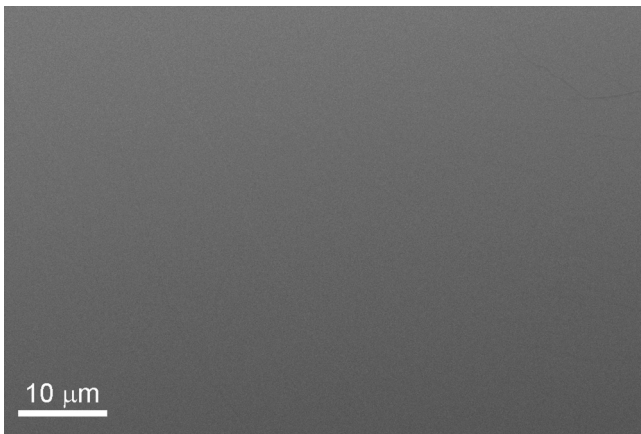


FIG. 4. SEM image of a $\text{Fe}_{3-x}\text{GeTe}_2$ single crystal.

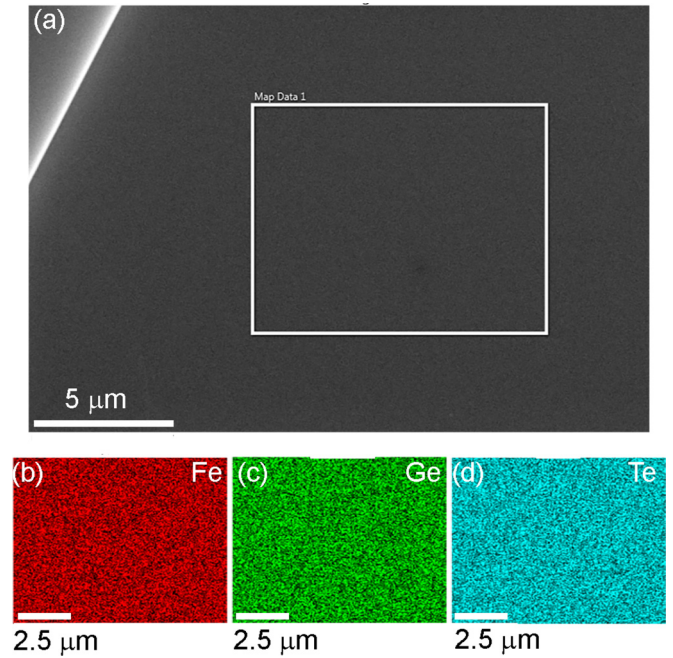


FIG. 5. EDS mapping on a $\text{Fe}_{3-x}\text{GeTe}_2$ single crystal. (a) Secondary electron image of the crystal with the mapping performed within the rectangle. (b)–(d) Associated EDS maps for Fe, Ge, and Te, respectively.

an inhomogeneous distribution of vacancies may result the formation of vacancy depleted “islands” which in turn would result in an anomaly at 220 K similar to the one observed in our Raman data. However, the EDS data (see Fig. 5) do not support this possibility. At this point we can only speculate that while the long-range order temperature is shifted to a lower temperature by the introduction of vacancies, short-range correlations may develop at 220 K.

IV. CONCLUSION

We have studied the lattice dynamics of flux-grown $\text{Fe}_{3-x}\text{GeTe}_2$ single crystals by means of Raman spectroscopy and DFT. Four out of eight Raman active modes, two A_{1g} and two E_{2g} , have been observed and assigned. DFT calculations are in good agreement with experimental results. The temperature dependence of the A_{1g}^1 , E_{2g}^3 , and A_{1g}^2 mode properties reveals a clear fingerprint of spin-phonon coupling, at a temperature of around 150 K. Furthermore, the anomalous behavior in the energies and linewidths of the observed phonon modes is present in the Raman spectra at temperatures around 220 K with the discontinuity also present in the electronic continuum. Its origin still remains an open question, and requires further analysis.

ACKNOWLEDGMENTS

The work was supported by the Serbian Ministry of Education, Science and Technological Development under Projects No. III45018 and No. OI171005. DFT calculations were performed using computational resources at Johannes Kepler University, Linz, Austria. Materials synthesis was supported

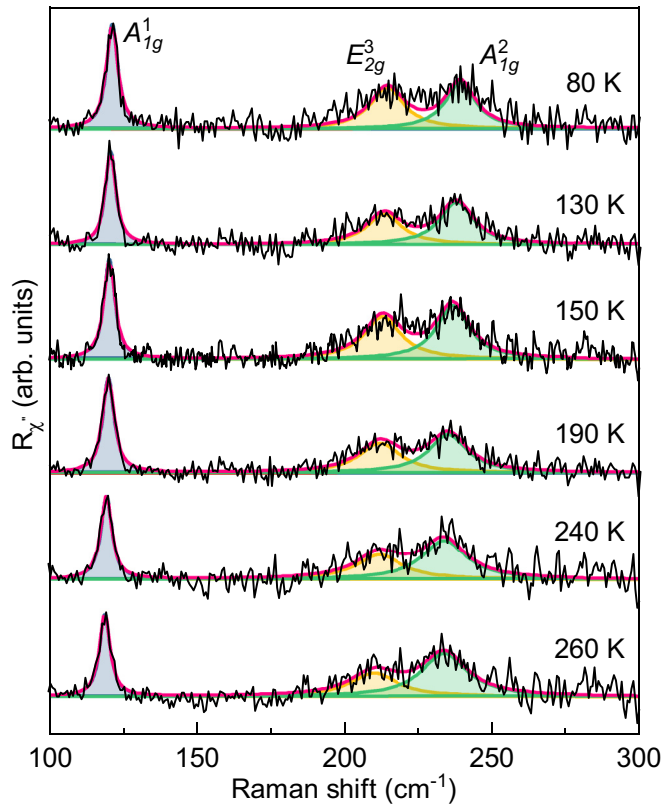


FIG. 6. Modeled Raman spectra of $\text{Fe}_{3-x}\text{GeTe}_2$ single crystal, after subtracting continuum contributions, obtained at various temperatures. For experimental data modeling, the Voigt line shape was used.

by the US Department of Energy, Office of Basic Energy Sciences as part of the Computation Material Science Program (Y.L. and C.P.). Electron microscopy was performed at Jozef Stefan Institute, Ljubljana, Slovenia under Slovenian Research Agency Contract No. P1-0099 (B.V.). This work has received funding from the European Union's Horizon 2020 research and innovation program under the Marie Skłodowska-Curie Grant Agreement No. 645658 (DAFNEOX Project).

APPENDIX A: ELECTRON MICROSCOPY

In order to examine the uniformity of $\text{Fe}_{3-x}\text{GeTe}_2$, Scanning electron microscopy (SEM) was performed on as-cleaved crystals. It can be seen from Fig. 4 that the crystals maintain uniformity for several tens of microns. Furthermore, the elemental composition was obtained using EDS mapping, as shown in Fig. 5. The atomic percentage, averaged over ten measurements, is 47%, 17%, and 36% ($\pm 2\%$) for Fe, Ge, and Te, respectively, with the vacancy content $x = 0.4 \pm 0.1$. The maps associated with the selected elements appear homogeneous, as they are all present uniformly with no apparent islands or vacancies.

APPENDIX B: DATA MODELING

In order to obtain the temperature dependence of the energies and linewidths of the observed $\text{Fe}_{3-x}\text{GeTe}_2$ phonon modes, the Raman continuum, shown in colored lines in

TABLE II. Top panel: Comparison of calculated energies of Raman active phonons using relaxed (R) and experimental [non-relaxed (NR)] lattice parameters for the magnetic (M) and nonmagnetic phase (NM), given in cm^{-1} . Obtained experimental values in the magnetic phase at a temperature of 80 K are given in the last column. Bottom panel: Comparison of calculated energies of infrared optical phonons of $\text{Fe}_{3-x}\text{GeTe}_2$.

Raman active modes					
Calculations					Experiment (M)
Sym.	NM-R	M-R	NM-NR	M-NR	
E_{2g}^1	28.4	49.6	33.9	50.2	
E_{1g}^1	79.2	70.2	71.7	70.3	
E_{2g}^2	115.5	121.0	100.0	122.2	89.2
A_{1g}^1	151.7	139.2	131.7	137.2	121.1
E_{1g}^2	225.5	206.0	194.3	209.5	
E_{2g}^3	238.0	232.6	204.9	228.6	214.8
A_{1g}^2	272.0	262.6	235.7	233.4	239.6
E_{2g}^4	362.0	337.6	315.4	334.7	
Infrared active modes					
A_{2u}^1	70.7	96.6	73.5	92.7	
E_{1u}^1	112.5	121.2	89.4	121.6	
A_{2u}^2	206.0	162.5	183.1	153.7	
E_{1u}^2	226.4	233.6	192.1	231.3	
A_{2u}^3	271.8	248.6	240.8	241.0	
E_{1u}^3	361.1	336.6	314.7	334.7	

Fig. 3(a), was subtracted for simplicity from the raw Raman susceptibility data (black line). The spectra obtained after the subtraction procedure are presented in Fig. 6 (black line) for various temperatures. Because of the finite resolution of the spectrometer and the fact that line shapes of all the observed phonons are symmetric, the Voigt line shape ($\Gamma_G = 0.8 \text{ cm}^{-1}$) was used for data modeling. Blue, yellow, and green lines in Fig. 6 represent fitting curves for A_{1g}^1 , E_{2g}^3 , and A_{2g}^2 phonon modes, respectively, whereas the overall spectral shape is shown in the red line.

APPENDIX C: EXPERIMENTAL DETAILS

Before being placed in a vacuum and being cleaved, the sample was glued to a copper plate with GE varnish in order to achieve good thermal conductivity and prevent strain effects. Silver paste, as a material with high thermal conductivity, was used to attach the copper plate with the sample to the cryostat. The laser beam spot, focused through an Olympus long-range objective of $\times 50$ magnification, was approximately $6 \mu\text{m}$ in size, with a power less than 1 mW at the sample surface. A TriVista 557 triple spectrometer was used in the subtractive mode, with a diffraction grating combination of 1800/1800/2400 grooves/mm and the entrance and second intermediate slit set to $80 \mu\text{m}$, in order to enhance stray light rejection and attain good resolution.

APPENDIX D: CALCULATIONS

In Table II the results of DFT calculations are presented for magnetic (M) and nonmagnetic (NM) relaxed and experimental lattice parameters. For comparison, the

experimental results are shown in the last column. Since the lattice parameters strongly depend on the Fe atom deficiency, the best agreement with experimental results gives the magnetic nonrelaxed solution.

- [1] N. Sivadas, M. W. Daniels, R. H. Swendsen, S. Okamoto, and D. Xiao, Magnetic ground state of semiconducting transition-metal trichalcogenide monolayers, *Phys. Rev. B* **91**, 235425 (2015).
- [2] K. S. Novoselov, A. K. Geim, S. V. Morozov, D. Jiang, Y. Zhang, S. V. Dubonos, I. V. Grigorieva, and A. A. Firsov, Electric field effect in atomically thin carbon films, *Science* **306**, 666 (2004).
- [3] Q. H. Wang, K. Kalantar-Zadeh, A. Kis, J. N. Coleman, and M. S. Strano, Electronics and optoelectronics of two-dimensional transition metal dichalcogenides, *Nat. Nanotechnol.* **7**, 699 (2012).
- [4] C. Gong, L. Li, Z. Li, H. Ji, A. Stern, Y. Xia, T. Cao, W. Bao, C. Wang, Y. Wang, Z. Q. Qiu, R. J. Cava, S. G. Louie, J. Xia, and X. Zhang, Discovery of intrinsic ferromagnetism in two-dimensional van der Waals crystals, *Nature (London)* **546**, 265 (2017).
- [5] B. Huang, G. Clark, E. Navarro-Moratalla, D. R. Klein, R. Cheng, K. L. Seyler, D. Zhong, E. Schmidgall, M. A. McGuire, D. H. Cobden, W. Yao, D. Xiao, P. Jarillo-Herrero, and X. Xu, Layer-dependent ferromagnetism in a van der Waals crystal down to the monolayer limit, *Nature (London)* **546**, 270 (2017).
- [6] M. A. McGuire, H. Dixit, V. R. Cooper, and B. C. Sales, Coupling of crystal structure and magnetism in the layered, ferromagnetic insulator CrI_3 , *Chem. Mater.* **27**, 612 (2015).
- [7] H. L. Zhuang, Y. Xie, P. R. C. Kent, and P. Ganesh, Computational discovery of ferromagnetic semiconducting single-layer CrSnTe_3 , *Phys. Rev. B* **92**, 035407 (2015).
- [8] G. T. Lin, H. L. Zhuang, X. Luo, B. J. Liu, F. C. Chen, J. Yan, Y. Sun, J. Zhou, W. J. Lu, P. Tong, Z. G. Sheng, Z. Qu, W. H. Song, X. B. Zhu, and Y. P. Sun, Tricritical behavior of the two-dimensional intrinsically ferromagnetic semiconductor CrGeTe_3 , *Phys. Rev. B* **95**, 245212 (2017).
- [9] L. D. Casto, A. J. Clune, M. O. Yokosuk, J. L. Musfeldt, T. J. Williams, H. L. Zhuang, M.-W. Lin, K. Xiao, R. G. Hennig, B. C. Sales, J.-Q. Yan, and D. Mandrus, Strong spin-lattice coupling in CrSiTe_3 , *APL Mater.* **3**, 041515 (2015).
- [10] M.-W. Lin, H. L. Zhuang, J. Yan, T. Z. Ward, A. A. Puretzy, C. M. Rouleau, Z. Gai, L. Liang, V. Meunier, B. G. Sumpter, P. Ganesh, P. R. C. Kent, D. B. Geohegan, D. G. Mandrus, and K. Xiao, Ultrathin nanosheets of CrSiTe_3 : A semiconducting two-dimensional ferromagnetic material, *J. Mater. Chem. C* **4**, 315 (2016).
- [11] J.-X. Zhu, M. Janoschek, D. S. Chaves, J. C. Cezar, T. Durakiewicz, F. Ronning, Y. Sassa, M. Mansson, B. L. Scott, N. Wakeham, E. D. Bauer, and J. D. Thompson, Electronic correlation and magnetism in the ferromagnetic metal Fe_3GeTe_2 , *Phys. Rev. B* **93**, 144404 (2016).
- [12] B. Chen, J. H. Yang, H. D. Wang, M. Imai, H. Ohta, C. Michioka, K. Yoshimura, and M. H. Fang, Magnetic properties of layered itinerant electron ferromagnet Fe_3GeTe_2 , *J. Phys. Soc. Jpn.* **82**, 124711 (2013).
- [13] Y. Liu, V. N. Ivanovski, and C. Petrovic, Critical behavior of the van der Waals bonded ferromagnet $\text{Fe}_{3-x}\text{GeTe}_2$, *Phys. Rev. B* **96**, 144429 (2017).
- [14] H.-J. Deiseroth, K. Aleksandrov, C. Reiner, L. Kienle, and R. K. Kremer, Fe_3GeTe_2 and Ni_3GeTe_2 - Two new layered transition-metal compounds: Crystal structures, HRTEM investigations, and magnetic and electrical properties, *Eur. J. Inorg. Chem.* **2006**, 1561 (2006).
- [15] A. F. May, S. Calder, C. Cantoni, H. Cao, and M. A. McGuire, Magnetic structure and phase stability of the van der Waals bonded ferromagnet $\text{Fe}_{3-x}\text{GeTe}_2$, *Phys. Rev. B* **93**, 014411 (2016).
- [16] V. Yu. Verchenko, A. A. Tsirlin, A. V. Sobolev, I. A. Presniakov, and A. V. Shevelkov, Ferromagnetic order, strong magnetocrystalline anisotropy, and magnetocaloric effect in the layered telluride $\text{Fe}_{3-\delta}\text{GeTe}_2$, *Inorg. Chem.* **54**, 8598 (2015).
- [17] J. Yi, H. Zhuang, Q. Zou, Z. Wu, G. Cao, S. Tang, S. A. Calder, P. R. C. Kent, D. Mandrus, and Z. Gai, Competing antiferromagnetism in a quasi-2D itinerant ferromagnet: Fe_3GeTe_2 , *2D Mater.* **4**, 011005 (2016).
- [18] Y. Zhang, H. Lu, X. Zhu, S. Tan, W. Feng, Q. Liu, W. Zhang, Q. Chen, Y. Liu, X. Luo, D. Xie, L. Luo, Z. Zhang, and X. Lai, Emergence of Kondo lattice behavior in a van der Waals itinerant ferromagnet, Fe_3GeTe_2 , *Sci. Adv.* **4**, eaao6791 (2018).
- [19] Y. Liu, E. Stavitski, K. Attenkofer, and C. Petrovic, Anomalous Hall effect in the van der Waals bonded ferromagnet $\text{Fe}_{3-x}\text{GeTe}_2$, *Phys. Rev. B* **97**, 165415 (2018).
- [20] H. L. Zhuang, P. R. C. Kent, and R. G. Hennig, Strong anisotropy and magnetostriction in the two-dimensional Stoner ferromagnet Fe_3GeTe_2 , *Phys. Rev. B* **93**, 134407 (2016).
- [21] C. Tan, J. Lee, S.-G. Jung, T. Park, S. Albarakati, J. Partridge, M. R. Field, D. G. McCulloch, L. Wang, and C. Lee, Hard magnetic properties in nanoflake van der Waals Fe_3GeTe_2 , *Nat. Commun.* **9**, 1554 (2018).
- [22] P. Giannozzi *et al.*, QUANTUM ESPRESSO: A modular and open-source software project for quantum simulations of materials, *J. Phys.: Condens. Matter* **21**, 395502 (2009).
- [23] P. E. Blöchl, Projector augmented-wave method, *Phys. Rev. B* **50**, 17953 (1994).
- [24] G. Kresse and D. Joubert, From ultrasoft pseudopotentials to the projector augmented-wave method, *Phys. Rev. B* **59**, 1758 (1999).
- [25] J. P. Perdew, K. Burke, and M. Ernzerhof, Generalized Gradient Approximation Made Simple, *Phys. Rev. Lett.* **77**, 3865 (1996).
- [26] S. Grimme, Semiempirical GGA-type density functional constructed with a long-range dispersion correction, *J. Comput. Chem.* **27**, 1787 (2006).
- [27] A. Milosavljević, A. Šolajić, J. Pešić, Y. Liu, C. Petrovic, N. Lazarević, and Z. V. Popović, Evidence of spin-phonon coupling in CrSiTe_3 , *Phys. Rev. B* **98**, 104306 (2018).
- [28] A. Baum, A. Milosavljević, N. Lazarević, M. M. Radonjić, B. Nikolić, M. Mitschek, Z. I. Maranloo, M. Šćepanović, M. Grujić-Brožćin, N. Stojilović, M. Opel, A. Wang,

- C. Petrovic, Z. V. Popović, and R. Hackl, Phonon anomalies in FeS, *Phys. Rev. B* **97**, 054306 (2018).
- [29] M. Opačić, N. Lazarević, M. M. Radonjić, M. Šćepanović, H. Ryu, A. Wang, D. Tanasković, C. Petrovic, and Z. V. Popović, Raman spectroscopy of $K_xK_{2-y}Se_2$ single crystals near the ferromagnet–paramagnet transition, *J. Phys.: Condens. Matter* **28**, 485401 (2016).
- [30] Z. V. Popović, N. Lazarević, S. Bogdanović, M. M. Radonjić, D. Tanasković, R. Hu, H. Lei, and C. Petrovic, Signatures of the spin-phonon coupling in $Fe_{1+y}Te_{1-x}Se_x$ alloys, *Solid State Commun.* **193**, 51 (2014).
- [31] Z. V. Popović, M. Šćepanović, N. Lazarević, M. Opačić, M. M. Radonjić, D. Tanasković, H. Lei, and C. Petrovic, Lattice dynamics of $BaFe_2X_3$ ($X = S, Se$) compounds, *Phys. Rev. B* **91**, 064303 (2015).
- [32] T. P. Devereaux and R. Hackl, Inelastic light scattering from correlated electrons, *Rev. Mod. Phys.* **79**, 175 (2007).

Phonon anomalies and magnetic excitations in BaFe₂Se₂O

Feng Jin,¹ Nenad Lazarević,² Changle Liu,³ Jianting Ji,⁴ Yimeng Wang,¹ Shuna He,¹ Hechang Lei,¹ Cedimir Petrovic,⁵ Rong Yu,¹ Zoran V. Popović,^{2,6} and Qingming Zhang^{4,7,*}

¹*Department of Physics and Beijing Key Laboratory of Opto-electronic Functional Materials & Micro-nano Devices, Renmin University of China, Beijing 100872, China*

²*Center for Solid State Physics and New Materials, Institute of Physics Belgrade, University of Belgrade, Pregrevica 118, 11080 Belgrade, Serbia*

³*State Key Laboratory of Surface Physics and Department of Physics, Fudan University, Shanghai 200433, China*

⁴*Beijing National Laboratory for Condensed Matter Physics, Institute of Physics, Chinese Academy of Sciences, Beijing 100190, China*

⁵*Condensed Matter Physics and Materials Science Department, Brookhaven National Laboratory, Upton, New York 11973-5000, USA*

⁶*Serbian Academy of Sciences and Arts, Knez Mihailova 35, Belgrade 11000, Serbia*

⁷*School of Physical Science and Technology, Lanzhou University, Lanzhou 730000, China*



(Received 6 March 2019; revised manuscript received 4 April 2019; published 22 April 2019)

We report a temperature- and magnetic-field-dependent Raman-scattering study of the spin-ladder compound BaFe₂Se₂O. Temperature evolution of the B_{1g} mode self-energies revealed anomalous behavior at about 100 and 240 K with strong temperature-dependent Fano asymmetry. Furthermore, the A_g modes integrated intensity exhibits an additional change in tendency at about 50 K. All the observed anomalies can be traced back to spin-phonon interaction contributions as well as multiple magnetic phase transitions present in BaFe₂Se₂O also detected in the Raman continuum induced by the spin fluctuations. Moreover, the absence of magnetic-field dependence of the magnetic mode observed at 436 cm⁻¹ and the small linewidth and high intensity are different from the magnetic modes at about 650 cm⁻¹. This suggests a two-magnon continuum and a two-magnon bound state resonance for this mode.

DOI: [10.1103/PhysRevB.99.144419](https://doi.org/10.1103/PhysRevB.99.144419)

I. INTRODUCTION

Quantum spin ladders have attracted much interest because of their fascinating properties and their possible relevance to the phase diagram of high-temperature superconducting cuprates [1–4]. The ground-state properties and the quasiparticle spectrum of the two-leg spin ladder have been studied theoretically [5–9] and experimentally [10–14]. Generally these systems may host various competing magnetic phases that are in close proximity.

Raman scattering offers a unique and powerful tool for probing lattice, spin, and charge excitations as well as interplay between them [4]. In the undoped spin ladder compound La₆Ca₈Cu₂₄O₄₁, the ladders contribute to a very broad triplet Raman line shape whose position is slightly different for leg-leg and rung-rung polarizations [15] in accordance with theoretical models [16]. However, in the spin-ladder and charge-ordered compound Sr₁₄Cu₂₄O₄₁, only a particularly sharp peak is observed at the same frequency for both polarizations [12,15]. Here, the spin-ladder (antiferromagnetic dimer) structure magnon related modes appear in the form of singularities of one-dimensional density of two-magnon states [11].

The iron-based compound BaFe₂Se₂O is an experimental realization of a two-leg ladder structure [17–19]. In this compound, all iron ions are in the Fe²⁺ oxidation state with

a high spin $S = 2$. The Fe₂Se₂O planes containing weakly coupled ladders are stacked along the c crystallographic axis. The ladder legs and rungs are along the b and a crystallographic axis, respectively. The basic magnetic properties of BaFe₂Se₂O have been characterized by magnetic susceptibility and specific-heat measurements [17,18]. The magnetic susceptibility shows a broad maximum at $T_{\max} \approx 450$ K and three successive magnetic phase transitions at $T \approx 240$, 115, and 43 K with T_{\max} explained as due to the short-range correlation of the local moments [17] and the three magnetic phase transitions explained as either due to the antiferromagnetic phase transition (240 K) or due to the formation of spin-singlet dimers (115 and 43 K) [18]. Surprisingly, the specific-heat measurements indicate that the magnetic entropy up to 300 K is much smaller than the expected value. Local-spin-density-approximation calculations [17] suggest that the interaction along the rungs J is more than three times stronger than the interladder interaction J' , whereas the interaction along the legs J'' can be neglected. A lattice dynamics study of BaFe₂Se₂O was recently reported by Popović *et al.* [19]. They also observed a magnetic excitation related structure in the form of a magnon continuum with peaks corresponding to the singularities in the one-dimensional density of magnon states. In order to clarify the unusually large intensity of the lower-energy (magnon) peak and the origin of the B_{1g} modes line-shape asymmetry, a systematic Raman study, particularly in magnetic fields, is highly required.

In this paper, we report temperature- and field-dependent Raman-scattering measurements on BaFe₂Se₂O. The

*Corresponding author: qmzhang@ruc.edu.cn

temperature-dependent Raman spectra indicate the absence of a structural phase transition between 10 and 300 K, consistent with a moderate spin-phonon coupling. The Raman continuum observed only in the parallel polarization suggests strong spin fluctuations, and allows us to identify magnetic phase transitions at about 50, 100, and 240 K. The intensity of the sharp magnetic mode at 436 cm^{-1} exhibits a strong nonmonotonic field-dependent behavior with no observable energy shift with external magnetic fields up to 9 T. It is interpreted in terms of the two-magnon continuum and a two-magnon bound state resonance. The present study provides the fundamental lattice and spin dynamics information on $\text{BaFe}_2\text{Se}_2\text{O}$ and deepens the understanding of magnetic excitations in low-dimensional spin systems.

II. EXPERIMENTS

The $\text{BaFe}_2\text{Se}_2\text{O}$ single crystals used in this study were grown using the self-flux method. The details of crystal growth can be found elsewhere [18]. The average stoichiometry was checked using energy-dispersive x-ray spectroscopy (EDS; Oxford X-Max 50). The average atomic ratios determined from EDS are $\text{Ba:Fe:Se} = 1.0:1.9(2):2.0(2)$, close to the ratio of stoichiometric $\text{BaFe}_2\text{Se}_2\text{O}$. The presence of oxygen was confirmed for $\text{BaFe}_2\text{Se}_2\text{O}$, but the exact amount could not be quantified because of experimental limitations.

Freshly cleaved samples of (001) orientation were transferred into a UHV cryostat with a vacuum of better than 10^{-8} mbar. Temperature-dependent Raman spectra were collected with a Jobin Yvon LabRam HR800 spectrometer equipped with a volume Bragg grating low-wave-number suite, a liquid-nitrogen-cooled back-illuminated charge-coupled device detector, and a 633-nm laser (Melles Griot) with $\Gamma_\sigma < 0.1 \text{ cm}^{-1}$. The laser was focused into a spot of $\sim 5 \text{ }\mu\text{m}$ in diameter on the sample surface, with a power $< 100 \text{ }\mu\text{W}$, to avoid overheating. Magnetic-field-dependent Raman spectra were collected with a Jobin Yvon T64000 spectrometer also equipped with a liquid-nitrogen-cooled back-illuminated CCD. A 532-nm diode-pumped solid-state laser (Torus 532; Laser Quantum) was used as an excitation source. The laser was focused onto the samples with a spot size of $5\text{--}10 \text{ }\mu\text{m}$ in diameter. The laser power was maintained at a level of $300 \text{ }\mu\text{W}$ and monitored with a power meter (Coherent Inc.). Magnetic fields were generated up to 9 T using a superconducting magnet (Cryomagnetics) that has a room-temperature bore that is suitable for a microscope lens. The magnetic-field direction was perpendicular to the (001) plane of the sample.

In this paper, the Porto notation $i(jk)l$ is used for the scattering geometry, where i and l denote the direction and j and k the polarization of the incident and scattered light, respectively, and u stands for unpolarized light.

III. RESULTS AND DISCUSSION

A. Lattice dynamics and spin-phonon coupling

$\text{BaFe}_2\text{Se}_2\text{O}$ crystallizes in the orthorhombic crystal structure, described with space group $Pmmm$, with Ba and O atoms having C_{2v} site symmetry, whereas Fe and Se atoms have C_s site symmetry [19]. The symmetry analysis yields a total of 18 Raman-active modes $\Gamma_{\text{Raman}} = 6A_g + 2B_{1g} + 6B_{2g} +$

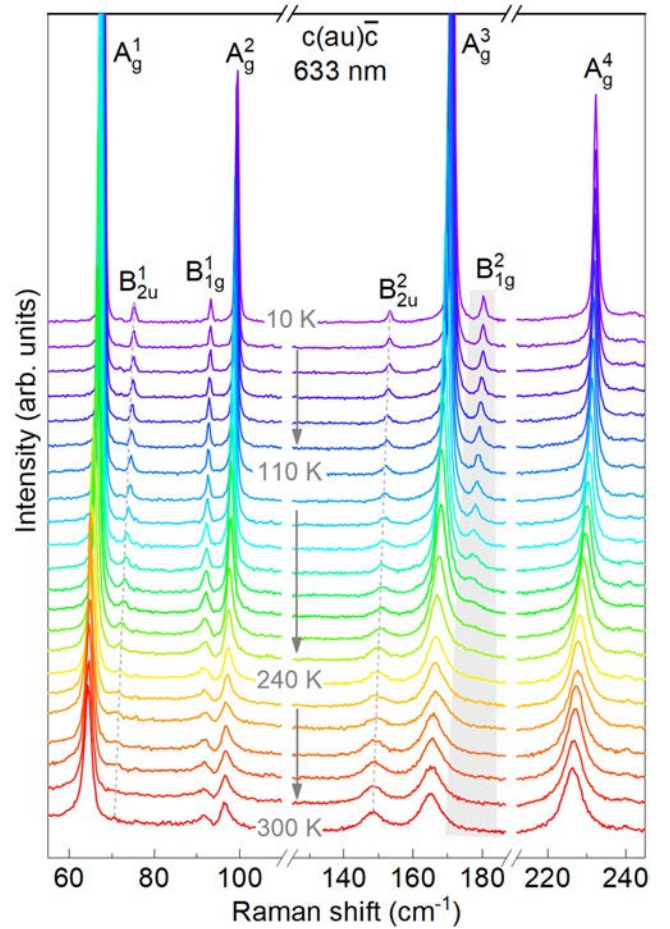


FIG. 1. Identification and temperature dependence of phonon modes in $\text{BaFe}_2\text{Se}_2\text{O}$. No change of crystal structure fingerprint was observed in the phonon spectra down to 10 K.

$4B_{3g}$, out of which, according to the Raman tensors below and the selection rules, only eight ($6A_g + 2B_{1g}$) are observable for our scattering geometry.

$$A_g = \begin{pmatrix} a & 0 & 0 \\ 0 & b & 0 \\ 0 & 0 & c \end{pmatrix}, \quad B_{1g} = \begin{pmatrix} 0 & d & 0 \\ d & 0 & 0 \\ 0 & 0 & 0 \end{pmatrix},$$

$$B_{2g} = \begin{pmatrix} 0 & 0 & e \\ 0 & 0 & 0 \\ e & 0 & 0 \end{pmatrix}, \quad B_{3g} = \begin{pmatrix} 0 & 0 & 0 \\ 0 & 0 & f \\ 0 & f & 0 \end{pmatrix}.$$

Figure 1 shows the temperature evolution of the $\text{BaFe}_2\text{Se}_2\text{O}$ Raman spectra in the temperature range between 10 and 300 K, in which eight phonon modes are observed. According to the lattice dynamical calculations [19], four A_g and two B_{1g} modes can be well assigned, as shown in Fig. 1. In addition to the A_g and B_{1g} symmetry modes, two peaks at about 75.2 and 153.3 cm^{-1} were also observed, which we previously attributed to new phonon modes due to the possible change of crystal symmetry accompanying the magnetic phase transition at $T_N = 240 \text{ K}$ [19]. As can be seen in Fig. 1, these peaks are also observable in our data even above T_N , indicating different origin. Energies are consistent with B_{2u}^1 and B_{2u}^2 infrared-active phonon modes, theoretically

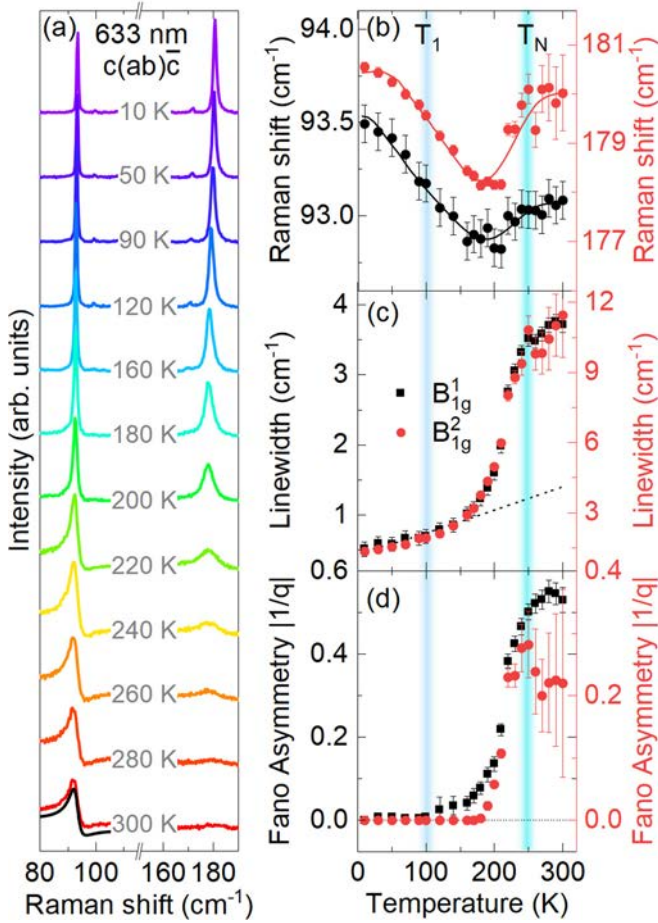


FIG. 2. Anomalies of B_{1g} modes induced by spin-lattice coupling. (a) Temperature dependence of Raman spectra for the $c(ab)\bar{c}$ polarization configuration, in which only the B_{1g} modes can be observed. The solid black line is a fit to a Fano line shape. Temperature dependence of the (b) frequency shift, (c) linewidth, and (d) Fano asymmetry parameters $|1/q|$ of B_{1g} (left axis, black) and B_{2g} (right axis, red) modes. The solid lines in (b) represent a fit to Eq. (1) and the dotted line in (c) represents the behavior expected from anharmonicity.

predicted by density functional theory calculations [19], and we assign them accordingly. Their observability in Raman data may stem from the release of symmetry selection rule by the structural imperfections. In our previous paper [18], Mössbauer data suggested oxygen deficiency, i.e., O_{1-x} composition for $\text{BaFe}_2\text{Se}_2\text{O}$. This might be the source of structural imperfections.

First, we focus on B_{1g} phonon modes, which display a pronounced asymmetry at high temperatures ($T > T_N$) that is suppressed at low temperatures ($T \ll T_N$), as can be seen in Fig. 2(a). Having in mind small instrumental broadening, the analysis of the line shape was preformed by using Fano function alone [20,21]: $I(\omega) = I_0(q + \varepsilon)^2 / (1 + \varepsilon^2)$, where $\varepsilon = (\omega - \omega_0) / \Gamma$, ω_0 is the bare phonon frequency, Γ is the linewidth, and q is the asymmetry parameter [22]. Frequency shift, linewidth, and Fano asymmetry parameter $|1/q|$ for both modes as a function of temperature are presented in Figs. 2(b), 2(c), and 2(d), respectively. Whereas they exhibit very similar

temperature dependence, upon heating from 10 K a small deviation from the “standard” anharmonic type of behavior can be noticed at about $T_1 = 100$ K accompanied by the appearance of the line-shape asymmetry. Further heating results in a significant renormalization of the phonon self-energies around T_N with the Fano asymmetry parameters reaching maximum value in the same temperature region.

The pronounced Fano asymmetry observed for the B_{1g} modes above T_N [Fig. 2(d)] indicates strong coupling to a continuum of excitations. Here we attribute the continuum to the magnetic scattering stemming from the spin fluctuation, which will be further discussed below. In comparison, an electronic mechanism for the continuum is unlikely as $\text{BaFe}_2\text{Se}_2\text{O}$ is electrically insulating with a transport gap of 1.86 eV [17]. According to the lattice dynamical calculations [19], the B_{1g} modes are mainly due to the vibration of Fe and Se atoms along the b axis which mediate the magnetic interaction. Therefore, one could expect B_{1g} modes to couple to the magnetic scattering.

The coupling of B_{1g} modes to the spin system is also reflected in the abnormal behaviors of their linewidth. To demonstrate this, we have included in Fig. 2(c) plots of the behavior expected from anharmonicity, $\Gamma(T) = \Gamma_0[1 + 2/(e^{\hbar\omega/2k_B T} - 1)]$. The fit strongly deviates already around 170 K, implying an additional relaxation mechanism which we ascribe to spin-phonon coupling. Such coupling is very pronounced in low-dimensional spin dimer systems, as well as in two- and three-dimensional frustrated spin systems [23–25].

In order to estimate the spin-phonon coupling constant in $\text{BaFe}_2\text{Se}_2\text{O}$, we may approximate phonon frequency temperature dependence as

$$\omega(T) = \omega(0) - C \left(1 + \frac{2}{e^x - 1} \right) + \lambda \langle S_i S_j \rangle, \quad (1)$$

where $\omega(0)$ is the harmonic frequency of an optical mode at zero temperature, $x = \hbar\omega(0)/2k_B T$, λ is the spin-phonon coupling constant, $\langle S_i S_j \rangle$ represents the spin-spin correlation function, and C is an anharmonic constant. The second term in Eq. (1) describes the anharmonic phonon contribution based on symmetrical optical phonon decay into acoustic phonons [26], whereas the third term represents the contribution from the spin-phonon coupling based on the Baltensperger and Helman model [27,28]. If we take into account only the nearest-neighbor interactions, the spin-spin correlation function $\langle S_i S_j \rangle_\chi$ can be written as [25]

$$\langle S_i S_j \rangle_\chi = \frac{k_B T \chi_m(T)}{N_A g^2 \mu_B^2} - \frac{S(S+1)}{3}, \quad (2)$$

where $g = 2$, $S = 2$, and the magnetic susceptibility $\chi_m(T)$ is given in Ref. [18]. We can now analyze the B_{1g} symmetry modes frequency temperature dependence within Eq. (1) [see solid lines in Fig. 2(b)]. This yields the spin-phonon coupling constants $\lambda(B_{1g}^1) = 1.8 \text{ cm}^{-1}$, $\lambda(B_{1g}^2) = 12.8 \text{ cm}^{-1}$, and the anharmonic constant $C(B_{1g}^1) = 0.33 \text{ cm}^{-1}$, $C(B_{1g}^2) = 4.76 \text{ cm}^{-1}$. The individual contribution due to anharmonic and spin-phonon coupling can be found in Fig. 5 in Appendix A. Obtained spin-phonon coupling constants are smaller than those in the spin-Peierls system CuGeO_3 , where spin-phonon

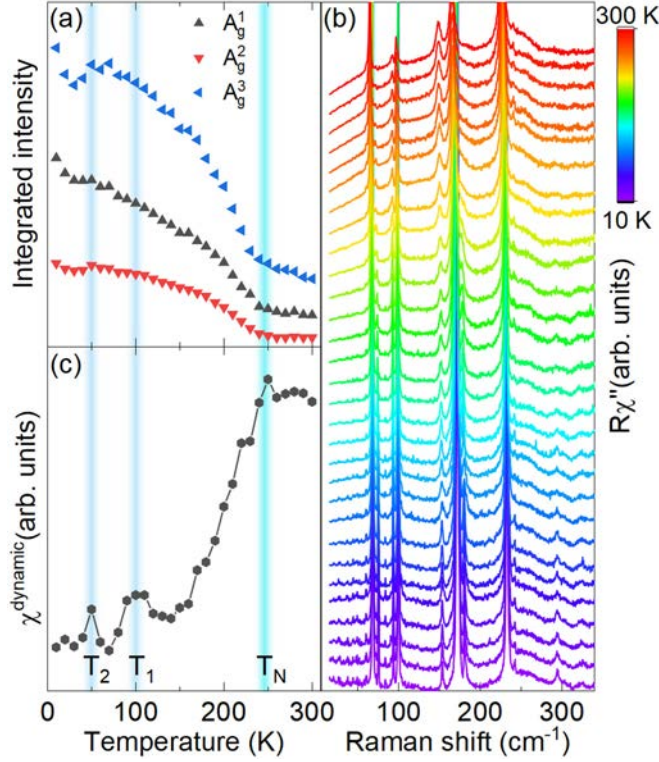


FIG. 3. (a) Integrated intensity of the A_g^1 , A_g^2 , and A_g^3 symmetry modes as a function of temperature. (b) Temperature evolution of Raman susceptibility data for BaFe₂Se₂O obtained in parallel scattering configuration. The pronounced Raman continuum evolution is observable only in parallel [i.e., (aa) or (bb)] and absent in cross polarization configurations [i.e., (ab) or (ba)] (not shown). (c) Temperature dependence of dynamical susceptibility $\chi^{\text{dynamic}}(T)$ obtained from the Raman data.

coupling constants of $\lambda_{103} = -10 \text{ cm}^{-1}$, $\lambda_{215} = 40 \text{ cm}^{-1}$, $\lambda_{366} = -21 \text{ cm}^{-1}$, and $\lambda_{812} = -8 \text{ cm}^{-1}$ were found [29]. Thus moderate spin-phonon coupling constants in BaFe₂Se₂O may account for the absence of a structural phase transition at the magnetic phase transition.

Now we turn our attention to the A_g symmetry modes. As can be seen from Fig. 3(a), the integrated intensity temperature dependence of the analyzed A_g modes exhibits clear discontinuity at T_N . In addition, another change in tendency has been observed at about $T_2 = 50 \text{ K}$.

Whereas the phonon anomalies at T_N can be directly traced back to the spin dynamics, the origin of the phonon anomalies at T_1 and T_2 is not clear. To clarify this, we analyze the Raman continuum that nonmonotonically develops in the A_{1g} channel with temperature [see Fig. 3(a)], as expected for the (quasi-) one-dimensional spin systems [30–32]. Directly from the Raman data, dynamic Raman susceptibility [33] can be calculated using the Kramers-Kronig relation $\chi^{\text{dynamic}} = \lim_{\omega \rightarrow 0} \chi(q=0, \omega) \propto \int_0^\infty \frac{\chi''}{\omega} d\omega$. Since we do not attempt to quantitatively analyze the spin-fluctuation contributions, which falls beyond the scope of our work, but to pinpoint possible magnetic phase transition, we approximate $\chi^{\text{dynamic}}(T)$ as an integral of the Raman conductivity data after excluding the contributions from phonons. As can be seen in Fig. 3(c),

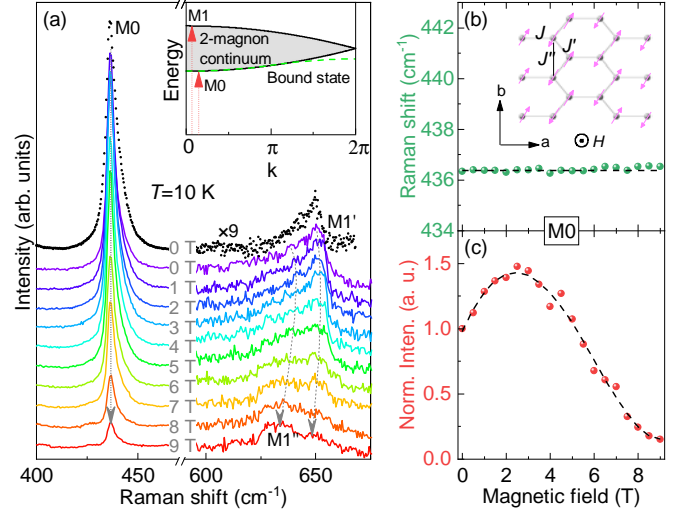


FIG. 4. Identification of magnetic excitations in BaFe₂Se₂O. (a) Field-dependent Raman spectra, measured at 10 K with 532-nm laser line (solid lines). The spectrum (dotted line) collected at 0 T with a 633-nm laser are also shown for comparison. Inset: Schematic spin excitation spectrum of BaFe₂Se₂O. The green dashed line represents a possible two-magnon bound state. Field dependence of the (b) energy and (c) intensity of the $M0$ mode. Inset of (b): Schematic representation of the periodic magnetic structure in the (ab) plane. J represents Fe-O-Fe antiferromagnetic (AFM) exchange interaction along the rungs; J' is the interladder Fe-Se-Fe AFM exchange interaction. J'' is the ferromagnetic Fe-Se-Fe exchange interaction along the ladder legs and can be neglected.

$\chi^{\text{dynamic}}(T)$ strongly increases upon approaching T_N after which it saturates in the paramagnetic phase where the spins are not correlated. At low temperatures it develops two peak-like features coinciding with observed anomalies in the lattice dynamic thus indicating their spin dynamics related origin. Furthermore, $\chi^{\text{dynamic}}(T)$ exhibits good agreement with the previously reported magnetic susceptibility data [18], indicating additional magnetic phase transitions in BaFe₂Se₂O at low temperatures.

B. Two-magnon Raman scattering

The two asymmetric peaks at 436 and 653 cm⁻¹ (see Fig. 4) have been reported before and assigned as a magnetic excitation related structure due to their special polarization and temperature-dependent characterizations [19]. However, the extremely high intensity of the 436 cm⁻¹ ($M0$) mode suggests an additional mechanism that comes into play, other than those manifested with the 653 cm⁻¹ mode. In particular, compared with the linewidth of two-magnon modes in other two-dimensional (2D) spin systems, the $M0$ linewidth of only $\sim 5 \text{ cm}^{-1}$ at 15 K is quite unusual for a 2D spin-ladder system. For example, the linewidth of the two-magnon mode is $\sim 800 \text{ cm}^{-1}$ for Sr₂Cu₂O₂Cl₂ [34], whereas it is $\sim 500 \text{ cm}^{-1}$ in La₆Ca₈Cu₂₄O₄₁ [13]. To the best of our knowledge, the sharpest two-magnon mode so far was found in CaV₂O₅ with a width of more than 50 cm⁻¹ [10], still one order of magnitude larger than that in BaFe₂Se₂O.

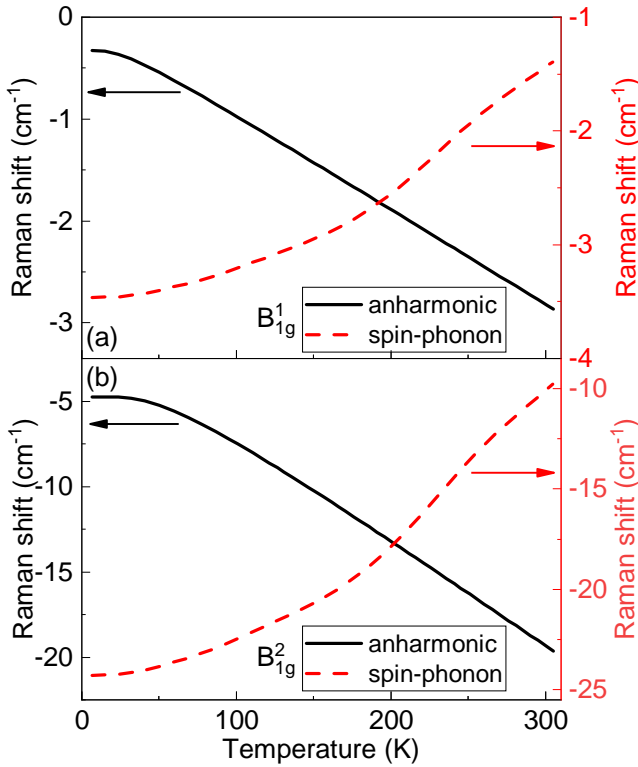


FIG. 5. Anharmonic (solid line) and spin-phonon (dashed line) contribution to the temperature dependence of the energy of (a) B_{1g} and (b) B_{2g} phonon modes obtained by fitting Eq. (1) to the experimental data.

To clarify the origin of the unusual $M0$ mode, the magnetic-field- and temperature-dependent Raman experiments have been performed on $\text{BaFe}_2\text{Se}_2\text{O}$ crystals [Fig. 4(a) and Fig. 6 in Appendix B]. The field dependence of the energy and intensity of the $M0$ mode are summarized in Figs. 4(b) and 4(c). It can be seen that both the $M0$ energy and the linewidth are nearly field independent, whereas the intensity exhibits a strong nonmonotonic field dependence. The intensity slightly increases with magnetic fields below 3 T, but quickly drops down above 3 T and almost vanishes for $B = 9$ T. A closer inspection of the 653-cm^{-1} peak magnetic-field-dependent spectra reveals its two-peak nature ($M1'$ and $M1''$; see Fig. 4). Both peaks harden up to 3 T after which they soften. Whereas the $M1'$ intensity follows the $M0$ mode behavior, $M1''$ experiences a constant gain of intensity. The strong field dependence of $M0$, $M1'$, and $M1''$ as well as their special polarization and temperature-dependent characterizations [19] confirms that these modes are indeed magnon related, but not due to some structural imperfections.

In general, several theoretical scenarios can be considered to account for the strength and sharpness of the magnon modes in the 2D system: (i) backfolding of the triplet dispersion due to charge ordering [13]; (ii) large anisotropy of the magnetic exchanges along rung and leg directions [35]; and (iii) the resonance between the two-magnon continuum and a two-magnon bound state [16,36]. In $\text{BaFe}_2\text{Se}_2\text{O}$, the origin of dispersion backfolding can be excluded because of its electrically insulating nature. Although the large anisotropy between J'' and J explains the observation of the $M0$ mode

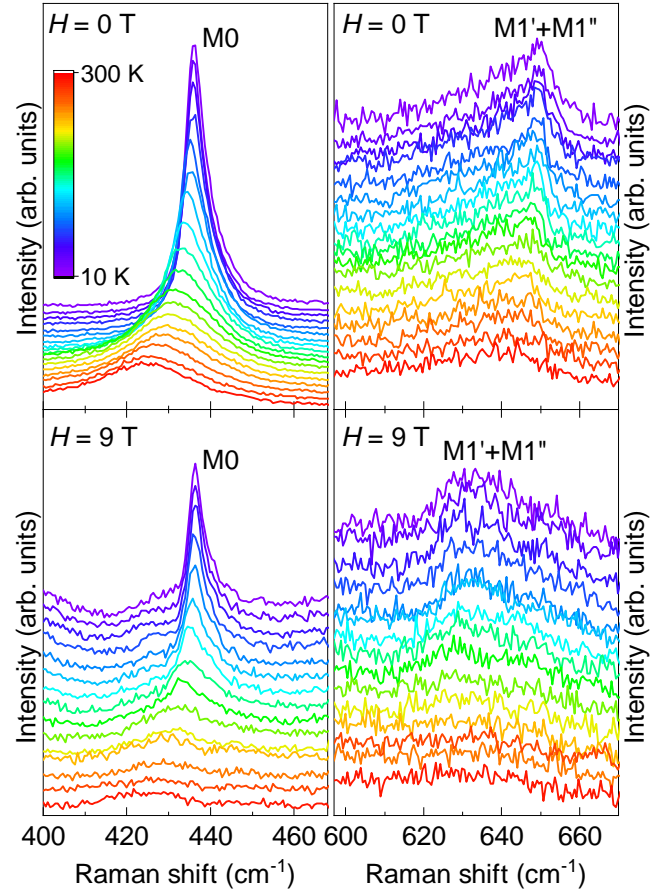


FIG. 6. Temperature-dependent spectra of the $M0$, $M1'$, and $M1''$ modes at 0 and 9 T.

at the given energy, it alone cannot account for the intensity and its magnetic-field dependence. This kind of behavior can be observed in the presence of the resonance between the two-magnon continuum and a two-magnon bound state.

In low-dimensional antiferromagnets, a strong magnon-magnon interaction induces a magnetic bound state [31,37–40] that merges with the two-magnon continuum at zero momentum (schematically shown in Fig. 4). This allows a resonance at the bottom of the continuum and contributes to the asymmetric line shape [36]. Such a resonance can well explain the strength, sharpness, and asymmetry of the $M0$ mode. The field dependence of the $M0$ mode intensity provides further support for the picture. External magnetic fields usually lead to a spin canting or even a spin flop/flip transition [41] and consequently modulate the magnon excitation spectrum. In $\text{BaFe}_2\text{Se}_2\text{O}$, the modulation of the magnon excitation spectrum is evidenced by the energy shift of the $M1'$ and $M1''$ modes (Fig. 4). A quantitative understanding of the $M0$, $M1'$, and $M1''$ modes magnetic-field dependence requires more theoretical work in the future and goes beyond the scope of this paper.

IV. SUMMARY

In summary, a $\text{BaFe}_2\text{Se}_2\text{O}$ temperature- and field-dependent Raman-scattering study has been performed. The

temperature evolution of the Raman-active modes indicates that there is no structural phase transition accompanying the magnetic phase transitions. Observed anomalies in the phonon spectra can be traced back to moderate spin-phonon interaction contributions as well as multiple magnetic phase transitions present in $\text{BaFe}_2\text{Se}_2\text{O}$ also detected in the Raman continuum induced by the spin fluctuations. The anomalous intensity of the $M0$ peak is attributed to the contribution from the two-magnon continuum and a two-magnon bound state resonance. The present study provides the fundamental lattice and spin dynamics information on $\text{BaFe}_2\text{Se}_2\text{O}$ and is of significance for the understanding of magnetic excitations in low-dimensional spin systems.

ACKNOWLEDGMENTS

This work was supported by the National Natural Science Foundation of China, the Ministry of Science and Technology of China, the Fundamental Research Funds for the Central Universities, the Research Funds of Renmin University of China and Serbian Ministry of Education, Science and Technological Development under Project III45018. The work at Brookhaven National Laboratory was supported by the

U.S. DOE under Contract No. DE-SC0012704 (material synthesis).

APPENDIX A: ANHARMONIC AND SPIN-PHONON CONTRIBUTIONS TO PHONON MODE ENERGIES

In this Appendix, we show the individual contribution of anharmonic and spin-phonon terms to the temperature dependence of the energy of the two B1g modes (Fig. 5), which are obtained by fitting Eq. (1) to the experimental data.

APPENDIX B: TEMPERATURE- AND FIELD-DEPENDENT RAMAN SPECTRA

To explore the origin of the magnetic scattering modes, we performed temperature-dependent Raman experiments and the collected spectra of the $M0$ $M1'$ and $M1''$ modes at 0 and 9 T are shown in Fig. 6. One can see that these modes exhibit distinctive temperature dependent behaviors, namely, a characteristic decrease in energy and intensity, and an increase in linewidth, with increasing temperature, reflecting the renormalization of magnon energies and lifetimes by thermally excited carriers.

-
- [1] P. W. Anderson, *Science* **235**, 1196 (1987).
 - [2] E. Dagotto and T. M. Rice, *Science* **271**, 618 (1996).
 - [3] E. Dagotto, *Rep. Prog. Phys.* **62**, 1525 (1999).
 - [4] P. Lemmens, G. Güntherodt, and C. Gros, *Phys. Rep.* **375**, 1 (2003).
 - [5] T. Barnes, E. Dagotto, J. Riera, and E. S. Swanson, *Phys. Rev. B* **47**, 3196 (1993).
 - [6] T. Barnes and J. Riera, *Phys. Rev. B* **50**, 6817 (1994).
 - [7] S. R. White, R. M. Noack, and D. J. Scalapino, *Phys. Rev. Lett.* **73**, 886 (1994).
 - [8] S. Gopalan, T. M. Rice, and M. Sigrist, *Phys. Rev. B* **49**, 8901 (1994).
 - [9] D. G. Shelton, A. A. Nersisyan, and A. M. Tsvelik, *Phys. Rev. B* **53**, 8521 (1996).
 - [10] M. J. Konstantinović, Z. V. Popović, M. Isobe, and Y. Ueda, *Phys. Rev. B* **61**, 15185 (2000).
 - [11] Z. V. Popović, M. J. Konstantinović, V. A. Ivanov, O. P. Khuong, R. Gajić, A. Vietkin, and V. V. Moshchalkov, *Phys. Rev. B* **62**, 4963 (2000).
 - [12] A. Gozar, G. Blumberg, B. S. Dennis, B. S. Shastry, N. Motoyama, H. Eisaki, and S. Uchida, *Phys. Rev. Lett.* **87**, 197202 (2001).
 - [13] K. P. Schmidt, C. Knetter, M. Grüninger, and G. S. Uhrig, *Phys. Rev. Lett.* **90**, 167201 (2003).
 - [14] A. Gößling, U. Kuhlmann, C. Thomsen, A. Löffert, C. Gross, and W. Assmus, *Phys. Rev. B* **67**, 052403 (2003).
 - [15] S. Sugai and M. Suzuki, *Phys. Status Solidi B* **215**, 653 (1999).
 - [16] K. P. Schmidt, C. Knetter, and G. S. Uhrig, *Europhys. Lett.* **56**, 877 (2001).
 - [17] F. Han, X. Wan, B. Shen, and H.-H. Wen, *Phys. Rev. B* **86**, 014411 (2012).
 - [18] H. Lei, H. Ryu, V. Ivanovski, J. B. Warren, A. I. Frenkel, B. Cekic, W.-G. Yin, and C. Petrovic, *Phys. Rev. B* **86**, 195133 (2012).
 - [19] Z. V. Popović, M. Šćepanović, N. Lazarević, M. M. Radonjić, D. Tanasković, H. Lei, and C. Petrovic, *Phys. Rev. B* **89**, 014301 (2014).
 - [20] A. Baum, A. Milosavljević, N. Lazarević, M. M. Radonjić, B. Nikolić, M. Mitschek, Z. I. Maranloo, M. Šćepanović, M. Grujić-Brojčin, N. Stojilović, M. Opel, A. Wang, C. Petrovic, Z. V. Popović, and R. Hackl, *Phys. Rev. B* **97**, 054306 (2018).
 - [21] A. Milosavljević, A. Šolajić, J. Pešić, Y. Liu, C. Petrovic, N. Lazarević, and Z. V. Popović, *Phys. Rev. B* **98**, 104306 (2018).
 - [22] U. Fano, *Phys. Rev.* **124**, 1866 (1961).
 - [23] M. Braden, B. Hennion, W. Reichardt, G. Dhalenne, and A. Revcolevschi, *Phys. Rev. Lett.* **80**, 3634 (1998).
 - [24] K.-Y. Choi, Y. G. Pashkevich, K. V. Lamonova, H. Kageyama, Y. Ueda, and P. Lemmens, *Phys. Rev. B* **68**, 104418 (2003).
 - [25] C. Kant, J. Deisenhofer, T. Rudolf, F. Mayr, F. Schrettle, A. Loidl, V. Gnezdilov, D. Wulferding, P. Lemmens, and V. Tsurkan, *Phys. Rev. B* **80**, 214417 (2009).
 - [26] J. Menéndez and M. Cardona, *Phys. Rev. B* **29**, 2051 (1984).
 - [27] W. Baltensperger and J. S. Helman, *Helv. Phys. Acta* **41**, 668 (1968).
 - [28] W. Baltensperger, *J. Appl. Phys.* **41**, 1052 (1970).
 - [29] R. Werner, C. Gros, and M. Braden, *Phys. Rev. B* **59**, 14356 (1999).
 - [30] T. Sekine, M. Jouanne, C. Julien, and M. Balkanski, *Phys. Rev. B* **42**, 8382 (1990).
 - [31] P. Lemmens, M. Grove, M. Fischer, G. Güntherodt, V. N. Kotov, H. Kageyama, K. Onizuka, and Y. Ueda, *Phys. Rev. Lett.* **85**, 2605 (2000).

- [32] K. Y. Choi, J. W. Hwang, P. Lemmens, D. Wulferding, G. J. Shu, and F. C. Chou, [Phys. Rev. Lett. **110**, 117204 \(2013\)](#).
- [33] A. Glamazda, P. Lemmens, S. H. Do, Y. S. Choi, and K. Y. Choi, [Nat. Commun. **7**, 12286 \(2016\)](#).
- [34] G. Blumberg, P. Abbamonte, M. V. Klein, W. C. Lee, D. M. Ginsberg, L. L. Miller, and A. Zibold, [Phys. Rev. B **53**, R11930 \(1996\)](#).
- [35] K. P. Schmidt, A. Gössling, U. Kuhlmann, C. Thomsen, A. Löffert, C. Gross, and W. Assmus, [Phys. Rev. B **72**, 094419 \(2005\)](#).
- [36] C. Jurecka, V. Grützun, A. Friedrich, and W. Brenig, [Eur. Phys. J. B **21**, 469 \(2001\)](#).
- [37] O. P. Sushkov and V. N. Kotov, [Phys. Rev. Lett. **81**, 1941 \(1998\)](#).
- [38] G. Bouzerar, A. P. Kampf, and G. I. Japaridze, [Phys. Rev. B **58**, 3117 \(1998\)](#).
- [39] M. Windt, M. Grüninger, T. Nunner, C. Knetter, K. P. Schmidt, G. S. Uhrig, T. Kopp, A. Freimuth, U. Ammerahl, B. Büchner, and A. Revcolevschi, [Phys. Rev. Lett. **87**, 127002 \(2001\)](#).
- [40] C. Knetter, K. P. Schmidt, M. Grüninger, and G. S. Uhrig, [Phys. Rev. Lett. **87**, 167204 \(2001\)](#).
- [41] S. Blundell, in *Magnetism in Condensed Matter* (Oxford University Press, New York, 2001).

Phonon anomalies in FeS

A. Baum,^{1,2} A. Milosavljević,³ N. Lazarević,³ M. M. Radonjić,⁴ B. Nikolić,⁵ M. Mitschek,^{1,2,*} Z. Inanloo Maranloo,^{1,†}
 M. Šćepanović,³ M. Grujić-Brojčin,³ N. Stojilović,^{3,6} M. Opel,¹ Aifeng Wang (王爱峰),⁷ C. Petrovic,⁷
 Z. V. Popović,^{3,8} and R. Hackl¹

¹Walther Meissner Institut, Bayerische Akademie der Wissenschaften, 85748 Garching, Germany

²Fakultät für Physik E23, Technische Universität München, 85748 Garching, Germany

³Center for Solid State Physics and New Materials, Institute of Physics Belgrade, University of Belgrade,
 Pregrevica 118, 11080 Belgrade, Serbia

⁴Scientific Computing Laboratory, Center for the Study of Complex Systems, Institute of Physics Belgrade, University of Belgrade,
 Pregrevica 118, 11080 Belgrade, Serbia

⁵Faculty of Physics, University of Belgrade, Studentski trg 12, Belgrade, Serbia

⁶Department of Physics and Astronomy, University of Wisconsin Oshkosh, Oshkosh, Wisconsin 54901, USA

⁷Condensed Matter Physics and Materials Science Department, Brookhaven National Laboratory, Upton, New York 11973-5000, USA

⁸Serbian Academy of Sciences and Arts, Knez Mihailova 35, 11000 Belgrade, Serbia



(Received 12 December 2017; published 12 February 2018)

We present results from light scattering experiments on tetragonal FeS with the focus placed on lattice dynamics. We identify the Raman active A_{1g} and B_{1g} phonon modes, a second order scattering process involving two acoustic phonons, and contributions from potentially defect-induced scattering. The temperature dependence between 300 and 20 K of all observed phonon energies is governed by the lattice contraction. Below 20 K the phonon energies increase by $0.5\text{--}1\text{ cm}^{-1}$, thus indicating putative short range magnetic order. Along with the experiments we performed lattice-dynamical simulations and a symmetry analysis for the phonons and potential overtones and find good agreement with the experiments. In particular, we argue that the two-phonon excitation observed in a gap between the optical branches becomes observable due to significant electron-phonon interaction.

DOI: [10.1103/PhysRevB.97.054306](https://doi.org/10.1103/PhysRevB.97.054306)

I. INTRODUCTION

In the iron based superconductors (IBS) magnetic order, structure, nematicity, and superconductivity are closely inter-related. Upon substituting atoms in the parent compounds the properties change in a way that the shape of the Fermi surface is generally believed to play a crucial role. Yet, the magnetic properties were found recently to be more complex and to depend also on the degree of correlation in the individual d orbitals contributing to the density of states close to the Fermi surface [1–3].

The influence of correlation effects seems to increase from the 122 systems such as BaFe_2As_2 to the 11 chalcogenides FeTe, FeSe, and FeS [4,5]. Surprisingly, the properties of the 11 class members differ substantially although they are isostructural and isoelectronic [3,6]: FeSe undergoes a structural transition at $T_s \sim 90\text{ K}$ and displays electronic nematicity [7]. While long-range magnetic order cannot be observed down to the lowest temperatures [7–10] the thermodynamic properties and the Raman spectra strongly support the presence of short-ranged magnetism [11,12]. Below $T_c \sim 9\text{ K}$ superconductivity is observed [13] in pristine FeSe. In mono-layer FeSe T_c can reach values close to 100 K [14,15].

The replacement of Se by Te leads to slightly off-stoichiometric Fe_{1+y}Te which exhibits a simultaneous magnetostructural transition near 67 K [16] but is not superconducting [17,18]. Finally, FeS having a superconducting transition at $T_c \sim 5\text{ K}$ [19] remains tetragonal down to the lowest temperatures [20]. It is still an open question whether tetragonal FeS hosts magnetic order. Obviously, the iron-chalcogenides are at the verge of various neighboring phases and very susceptible to small changes in the lattice and electronic structure. Yet direct access to the competing phases is still very difficult in FeTe and FeS because of the variation of the crystal quality across the families.

Here, we choose a slightly different approach and do not look directly at the electronic but rather at the lattice properties in FeS close to potential instabilities and use the Raman-active phonons as probes. We identify the A_{1g} and B_{1g} modes, a two-phonon scattering process, and a fourth mode from either defect-induced scattering or second-order scattering as well. These results are in good agreement with numerical calculations. Furthermore the temperature dependence of all phononic modes supports the results reported in Refs. [21,22], where emerging short range magnetic order at approximately 20 K was reported.

II. EXPERIMENT

Single crystals of FeS were synthesized as described elsewhere [23]. Before the experiment the samples were cleaved in air.

*Present address: Physikalisches Institut, Goethe Universität, 60438 Frankfurt am Main, Germany.

†Present address: Fakultät für Physik E21, Technische Universität München, 85748 Garching, Germany.

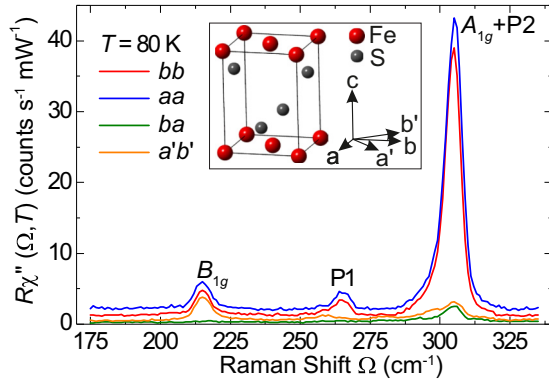


FIG. 1. Raman spectra of FeS at $T = 80$ K measured with light polarizations as indicated. The inset shows the crystal structure of FeS and the polarization directions with respect to the crystal orientation.

Calibrated customized Raman scattering equipment was used for the experiment. The samples were attached to the cold finger of a He-flow cryostat having a vacuum of approximately 5×10^{-5} Pa. For excitation we used a diode-pumped solid state laser emitting at 575 nm (Coherent GENESIS). Polarization and power of the incoming light were adjusted in a way that the light inside the sample had the proper polarization state and, respectively, a power of typically $P_a = 3$ mW independent of polarization. The samples were mounted as shown in the inset of Fig. 1. The crystallographic axes are a and b with $|a| = |b|$. The c axis is parallel to the optical axis. a' and b' are rotated by 45° with respect to a and b . The laser beam reached the sample at an angle of incidence of 66° and was focused to a spot of approximately $50 \mu\text{m}$ diameter. The plane of incidence is the bc plane. By choosing proper in-plane polarizations of the incident and scattered light the four symmetry channels A_{1g} , A_{2g} , B_{1g} , and B_{2g} of the D_{4h} space group can be accessed. Additionally, for the large angle of incidence, exciting photons being polarized along the b axis have a finite c -axis projection and the E_g symmetry can also be accessed. For the symmetry assignment we use the 2 Fe unit cell (crystallographic unit cell).

The observed phonon lines were analyzed quantitatively. Since the phonon lines are symmetric and $\Gamma_L(T) \ll \omega(T)$ the intrinsic line shape can be described by a Lorentz function with a central temperature dependent energy $\omega(T)$ and a width $\Gamma_L(T)$ (FWHM). The widths turn out to be comparable to the resolution σ of the spectrometer. Therefore, the Lorentzian needs to be convoluted with a Gaussian having width $\Gamma_G \equiv \sigma$.

III. THEORY

The electronic structure and the phonon dispersion were calculated using density functional theory (DFT) and density functional perturbation theory (DFPT), respectively, [24] within the QUANTUM ESPRESSO package [25]. The calculations were performed with the experimental unit cell parameters $a = 3.6735 \text{ \AA}$, $c = 5.0328 \text{ \AA}$, and $z = 0.2602$, where z is the height of the sulfur atoms above the Fe plane in units of the c axis [26]. We used the Vanderbilt ultrasoft pseudopotentials with the Becke-Lee-Yang-Parr (BLYP) exchange-correlation functional and s and p semicore states included in the valence for iron. The electron-wave-function and density energy cut-

offs were 70 Ry and 560 Ry, respectively, chosen to ensure stable convergence of the phonon modes. We used a Gaussian smearing of 0.01 Ry. The Brillouin zone was sampled with a $16 \times 16 \times 16$ Monkhorst-Pack k -space mesh. Our electronic structure and phonon calculations are in agreement with previously reported results [27,28].

The experimental positions of the S atoms entail a nonzero z component of the force of $6 \times 10^{-2} \text{ Ry}/a_B$ acting on them with a_B the Bohr radius. However, the relaxation of the z positions of the S atoms would result in a large discrepancy between the calculated and experimental energies of the optical branches [28], whereas the phonon frequencies calculated from experimental structure parameters are in good agreement with the experiment (see Table II). When using the measured lattice parameters, including atomic positions, some of the acoustic phonons are unstable and do not have a linear dispersion at small k . Upon relaxing the atomic positions the acoustic dispersion becomes linear and the energies at the zone boundary decrease slightly. The energies of the optical branches, on the other hand, increase by some 10%. Having all this in mind, we choose to use the experimental lattice parameters stated above. In this sense our calculations should be understood as a compromise.

The phonon dispersion and the density of states were calculated on a $6 \times 6 \times 6$ Monkhorst-Pack k -point mesh, and the dispersion is interpolated along the chosen line. The calculated phonon dispersions of the experimental and relaxed structures qualitatively coincide and display similar shapes and a gap. Discrepancies only appear in the absolute energies.

The selection rules for two-phonon processes were calculated using the modified group projector technique (MGPT) [29], which avoids summing over an infinite set of space group elements.

IV. RESULTS AND DISCUSSION

A. Polarization dependence

Raman spectra of FeS for four linear polarization configurations at a sample temperature of $T = 80$ K are shown in Fig. 1. Three peaks can be identified at 215, 265, and 305 cm^{-1} . The symmetric peak at 215 cm^{-1} shows up for aa , bb , and $a'b'$ polarizations, but vanishes for ba polarization. Hence the excitation obeys B_{1g} selection rules and can be identified as the out-of-phase vibration of iron atoms along the c axis. The strongest slightly asymmetric peak at 305 cm^{-1} obeys A_{1g} selection rules with contributions of order 5% in ba and $a'b'$ polarizations from either leakage or defect-induced scattering. An asymmetric Fano-type line shape can be acquired by coupling a phonon to an electronic continuum. However, as shown in Fig. 6 in the Appendixes, we find that the superposition of two symmetric, yet spectrally unresolved peaks gives a better agreement with the data than the description in terms of a Fano function. The stronger peak at 305 cm^{-1} has A_{1g} symmetry with some remaining leakage. We therefore identify this mode with the in-phase vibration of sulfur atoms along the c axis. The second peak, labeled P2, appears in spectra with parallel light polarizations and vanishes in ba , but has some contribution in $a'b'$ polarizations, suggesting mixed A_{1g} and B_{1g} symmetry. The third peak, labeled P1, is symmetric and appears only in

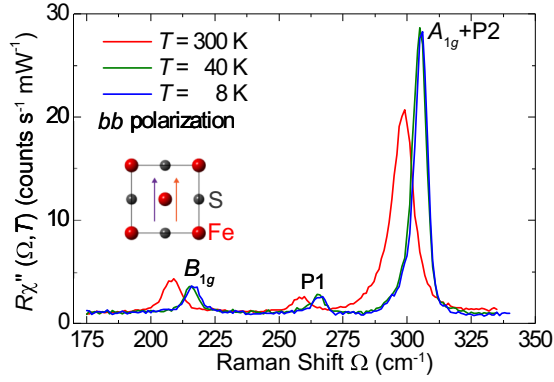


FIG. 2. Raman spectra of FeS in bb polarization projecting $A_{1g} + B_{1g} + E_g$ symmetries measured at temperatures given in the legend. The inset shows the light polarizations with respect to the crystal orientation.

spectra with parallel light polarizations and thus has pure A_{1g} symmetry.

B. Temperature dependence

For properly assigning all observed modes and for getting access to putative phase transitions we studied the temperature dependence. Figure 2 shows Raman spectra in bb polarization at 8, 40, and 300 K. The three peaks shift to higher energies upon cooling. The fourth peak P2 cannot be resolved in the raw data and can only be analyzed after a fitting procedure (see Appendix B). The peak energies $\omega(T)$ and the (intrinsic) linewidths $\Gamma_L(T)$ were determined as described at the end of Sec. II. All four modes show a monotonous increase in energy and decrease in linewidth upon cooling as shown in Fig. 3. Below 20 K the increase in the energies accelerates. We first address this overall behavior and disregard the anomaly around 50 K for the moment.

The shift and narrowing of all modes can be explained in terms of lattice contraction using a constant Grüneisen parameter γ and anharmonic decay into other phonon modes, respectively. The change in the (Lorentzian) linewidth $\Gamma_L(T)$ is given by [30]

$$\Gamma_L(T) = \Gamma_{L,0} \left(1 + \frac{2\lambda_{\text{ph-ph}}}{\exp\left(\frac{\hbar\omega_0}{2k_B T}\right) - 1} \right). \quad (1)$$

The zero temperature limits $\Gamma_{L,0}$ and ω_0 were obtained by extrapolating the respective experimental points of $\Gamma_L(T)$ and $\omega(T)$ in the range $20 \leq T \leq 50$ K to $T = 0$ (Fig. 3). With the phonon-phonon coupling $\lambda_{\text{ph-ph}}$ being the only free parameter the temperature dependence of $\Gamma_L(T)$ can be described as shown by red dashed lines in Fig. 3. The phonon energy $\omega(T)$ contains contributions from both the anharmonic decay and the lattice contraction, which depends essentially on the thermal occupation of the phonons, and can be written as [31]

$$\omega(T) = \omega_0 \left[1 - \gamma \frac{V(T) - V_0}{V_0} - \left(\frac{\Gamma_{L,0}}{\sqrt{2}\omega_0} \right)^2 \left(1 + \frac{4\lambda_{\text{ph-ph}}}{\exp\left(\frac{\hbar\omega_0}{2k_B T}\right) - 1} \right) \right]. \quad (2)$$

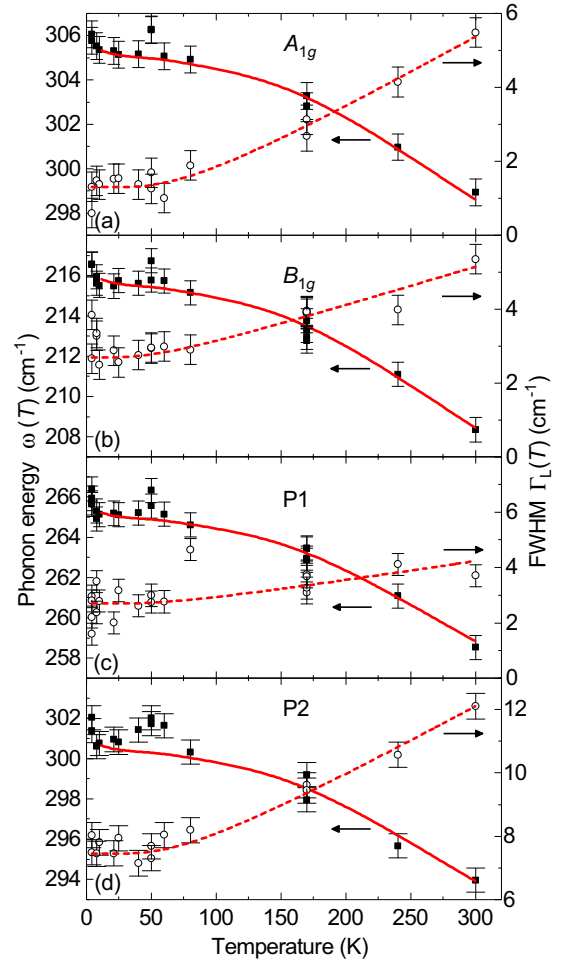


FIG. 3. Temperature dependence of energy and width of the four observed phonon modes in FeS. Black squares show the phonon energies ω ; open circles denote the phonon linewidths Γ_L . The red dashed and solid lines represent the temperature dependencies of the phonon linewidths and energies according to Eqs. (1) and (2), respectively. For better visualizing the low-temperature part, the data of this figure are plotted on a logarithmic temperature scale in Fig. 8 of Appendix D.

$V(T)$ and V_0 are the volumes of the unit cell at temperatures T and $T \rightarrow 0$, respectively. The numbers for the calculations are taken from Ref. [20]. The second term describes the effect of phonon damping on the line position in the harmonic approximation. Using $\lambda_{\text{ph-ph}}$ from Eq. (1), the Grüneisen parameter γ is the only free parameter and is assumed to be constant. The temperature dependencies $\omega(T)$ resulting from the fits are plotted in Fig. 3 as solid red lines. The numerical values for parameters γ and $\lambda_{\text{ph-ph}}$ obtained from the T -dependent energy and linewidth are compiled in Table I.

Below 20 K and around 50 K anomalies are found in the experimental data as follows:

(i) At 50 K the peak energies of all four modes deviate significantly from the otherwise smooth temperature dependence. The nearly discontinuous increase in energy could be reproduced for the A_{1g} phonon and peak P2 in multiple measurements. For the B_{1g} phonon and mode P1 the anomaly is not as clearly reproducible. The energy anomalies do not

TABLE I. Symmetry, Grüneisen constant γ , and phonon-phonon coupling parameter $\lambda_{\text{ph-ph}}$ of the four experimentally observed modes.

Mode	Symmetry	γ	$\lambda_{\text{ph-ph}}$
S	A_{1g}	2.2	1.68
Fe	B_{1g}	3.4	0.31
P1	A_{1g}	2.4	0.25
P2	$A_{1g} + B_{1g}$	2.2	0.31

have a correspondence in the linewidth. As there is neither an abrupt change in the lattice constants [20] nor any other known phase transition close to 50 K the origin of this anomaly remains unexplained although we consider it significant.

(ii) Upon cooling from 20 K to 4 K all four modes exhibit sudden, yet small, increases in energy. The changes in width are heterogeneous in that the A_{1g} mode narrows and the B_{1g} mode broadens. No clear tendencies can be derived for modes P1 and P2. Sudden changes in the temperature dependence typically indicate phase transitions. Yet, no phase transition has been identified so far. However, the anomaly at 20 K coincides with the emergence of short range magnetic order as inferred from two μSR studies [21,22]. Susceptibility measurements on a sample from the same batch were inconclusive. On the other hand, the XRD data show a small anomaly in the lattice parameters and the unit cell volume does not saturate at low temperature but rather decreases faster between 20 K and 10 K than above 20 K [20]. This volume contraction by and large reproduces the change in the phonon energies as can be seen by closely inspecting the low-temperature parts of Fig. 3 (see also Fig. 8). Hence the indications of short-range magnetism in FeS found by μSR have a correspondence in the temperature dependence of the volume and the phonon energies.

Clear phonon anomalies were observed at the onset of the spin density wave (SDW) phases in 122 systems [32–34] and of the more localized magnetic phase in FeTe [35], whereas continuous temperature dependence of the phonons was found in systems without long-range magnetism [36,37]. Upon entering the SDW state in the 122 systems the A_{1g} (As) mode softens abruptly and narrows by a factor of 3, whereas the B_{1g} (Fe) mode stays pinned and narrows only slightly [32]. The strong coupling of the As mode to magnetism was traced back to the interaction of the Fe magnetic moment with the Fe-As tetrahedra angle [38], which goes along with a change of the c -axis parameter. In Fe_{1+y}Te the roles of the B_{1g} and A_{1g} modes are interchanged [35,39,40]. In contrast, all four modes observed here in FeS harden below $T^* \approx 20$ K being indicative of a type of magnetic ordering apparently different from that in the other Fe-based systems.

Very recently, commensurate magnetic order with a wave vector of $\mathbf{q} = (0.25, 0.25, 0)$ was found in FeS below $T_N = 116$ K using neutron powder diffraction [41]. In the Raman spectra no anomalies can be seen around 120 K even if the range is studied with fine temperature increments of 10 K as shown in Appendix C. However, a small change in the temperature dependence of the c -axis parameter is observed around 100 K by XRD [20], which could be related to this type of magnetic order. Since the influence on the volume is small there is no detectable impact on the phonons.

TABLE II. Raman active phonon modes in t-FeS. Shown are the symmetries, the theoretical predictions for the experimental parameters at $T = 0$, and the atoms involved in the respective vibrations. The experimental energies in the third column are extrapolations to $T = 0$ of the points measured between 20 K and 50 K.

Symmetry	Phonon energy (cm^{-1})		Atomic displacement
	Calculation	Experiment	
A_{1g}	316.1	305.3	S
B_{1g}	220.4	215.8	Fe
E_g	231.6		Fe, S
E_g	324.8		Fe, S

C. Analysis of the modes P1 and P2

Based on the energies, the selection rules, and the temperature dependence we first clarify the phononic nature of the two lines P1 and P2, which cannot as straightforwardly be identified as lattice vibrations as the in-phase sulfur and out-of-phase iron vibrations at 305.3 and 215.8 cm^{-1} . Second we derive their origin from the phonon density of states (PDOS) calculated for the zero-temperature limit.

All experimental energies for $T \rightarrow 0$ were derived from the points at low temperature as described in Sec. IV B (see also Fig. 3). The results for the modes at the Γ point are summarized in Table II and can be directly compared to the results of the calculations. The discrepancies between the experimental and theoretical energies for the Raman-active phonons are smaller than 4%. The price for this accuracy in the optical energies is an instability and possibly too high energies in the acoustical branches at small and, respectively, large momentum (see Sec. III).

The unidentified peaks P1 and P2 appear in the spectra measured with aa polarization, where none of the electric fields has a projection on the c axis. Thus they cannot have E_g symmetry obeying ca and cb selection rules. In addition, the observed energies would be relatively far off of the calculated energies (see Table II). Both peaks exhibit temperature dependencies similar to those of the two Raman-active phonons and the Grüneisen parameters are close to the typical value [42] of 2 and similar to those of the Raman-active phonons. The phonon-phonon coupling parameters $\lambda_{\text{ph-ph}}$ derived from the temperature dependence of the linewidths are close to 0.3 similar to that of the B_{1g} phonon. $\lambda_{\text{ph-ph}}$ of the A_{1g} phonon is roughly five times bigger for reasons we address later. Yet, because of the small prefactor $(\Gamma_{L,0}/\sqrt{2}\omega_0)^2 = O(10^{-3})$, the contribution of phonon-phonon coupling to the temperature dependence of $\omega(T)$ remains negligible in all cases and the phonon energies are essentially governed by the lattice contraction. These considerations demonstrate the phononic origin of the peaks P1 and P2.

In the second step we try to identify the phonon branches to which P1 and P2 can be related. To this end the full phonon dispersion and density of states (PDOS) were derived as described in Sec. III and are plotted in Fig. 4.

Independent of using the relaxed or experimental structure, P1 is located in the gap of the (theoretical) PDOS and cannot result from first order defect-induced Raman scattering. What

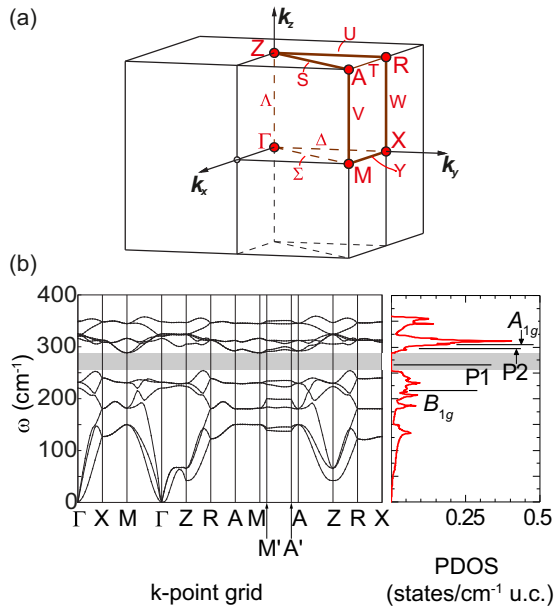


FIG. 4. Phonon dispersion of t-FeS. (a) Brillouin zone with high symmetry points and lines [43]. (b) Phonon dispersion along the directions as indicated and phonon density of states (PDOS). The gray-shaded area marks the gap in the phonon dispersion. The dispersion shown here is derived using experimental lattice parameters. For this reason some of the acoustic phonons are unstable and do not have a linear dispersion around the Γ point. Upon relaxing the structure the acoustic dispersion becomes linear at Γ , and the energies at the zone boundary decrease slightly. The energies of the optical branches, on the other hand, increase by some 10%. $M' = (0.4, 0.4, 0.0)$ and $A' = (0.4, 0.4, 0.5)$. The experimental energies of the four observed modes are shown as black lines.

alternatives exist for explaining P1? If we exclude exotic explanations such as a collective mode for the reasons given above the energy of $\omega_{P1} = 265 \text{ cm}^{-1}$ can only be obtained by the sum of two phonon modes having equal energy $\omega_{P1}/2$ and momenta \mathbf{k} and $-\mathbf{k}$ (for maintaining the $q \approx 0$ selection rule). As shown for various transition metal compounds including TiN, ZrN, or NbC second-order phonon Raman scattering can occur in the presence of defects [44]. Then first-order scattering being proportional to the PDOS (modulo energy and symmetry dependent weighting factors) is expected to be also substantial if not stronger. Although our crystals are slightly disordered there is no indication of substantial intensity at energies with high PDOS as can be seen by directly comparing Figs. 1 and 4(b). Alternatively, second-order scattering can originate in enhanced electron-phonon coupling [45]. In either case the energies of two phonons add up as they get excited in a single scattering process. Generally, no selection rules apply for second order Raman scattering and the resulting peak would appear in all symmetry channels [46]. Exceptions exist if the phonon wave vectors coincide with high-symmetry points or lines of the Brillouin zone.

From the phonon dispersion alone several phonon branches having \mathbf{k} and $-\mathbf{k}$ and energies in the range around $\omega_{P1}/2$ could add up to yield 265 cm^{-1} (see Fig. 4). However, as explained in Appendix F and shown in Table III for the space group P4/nmm

of t-FeS, the A_{1g} selection rules of P1 exclude all nonsymmetric combinations of branches (right column of Table III). On the other hand, all symmetric combinations include A_{1g} selection rules for the two-phonon peak (left column of Table III) and one has to look essentially for a high PDOS in the range $\omega_{P1}/2$. As shown in Fig. 4(b) the PDOS has a maximum in the right energy range. Since the maximum results from momenta away from the high-symmetry points or lines (see Fig. 4) which alone lead to pure A_{1g} symmetry one expects also intensity in B_{1g} and E_g symmetry as opposed to the experiment. For exclusive A_{1g} selection rules only seven possibilities exist. Since phase space arguments favor modes having a flat dispersion in extended regions of the Brillouin zone the Γ , M , and/or A points are unlikely to give rise to P1, and only the lines $S = A - Z$, $\Sigma = \Gamma - M$, and $V = A - M$ remain. The dispersion along the S or Σ branch contributes very little to the PDOS. On the high-symmetry line V a doubly degenerate branch would have a flat dispersion [see Fig. 4(b)] and contributes substantially to the PDOS but the energy of 150 cm^{-1} differs by 13% from the expected energy of 132.5 cm^{-1} . Instead of arguing about the accuracy of the theoretical phonon energies (see Sec. III) we looked at the dispersion close to but not strictly on V where the contribution to B_{1g} and E_g symmetries is expected to be still very small, e.g., along $M' - A'$ [Fig. 4(b)]. A detailed inspection shows that the maximum of the PDOS between 130 and 140 cm^{-1} comes from there. This explains both the selection rules and the energy of P1 to within a few percent.

Peak P2 cannot be explained in terms of one of the two E_g phonons either. As opposed to P1 it is not inside the gap of the PDOS and thus can originate from either first or second order scattering. If P2 originates in second order scattering in the same fashion as P1 there are five possibilities yielding $A_{1g} + B_{1g}$ but not E_g selection rules. As explained in the last paragraph only the branches $\Delta = \Gamma - X$ and $U = Z - R$ may contribute. For the low PDOS there we consider also first order defect-induced scattering for P2 to originate from. In fact, the PDOS possesses its strongest maximum 5 cm^{-1} below the (theoretical) A_{1g} phonon exactly where P2 is found. In spite of the very high PDOS here, the peak is weak explaining the negligible contributions from first order defect-induced scattering at lower energies. The high PDOS between 300 and 325 cm^{-1} may also be an alternative yet less likely explanation for the weak contributions in crossed polarizations in the energy range of the A_{1g} phonon (Fig. 1).

Finally, we wish to clarify whether the large phonon-phonon coupling $\lambda_{\text{ph-ph}}^{A_{1g}}$ found for the A_{1g} Raman-active mode (see Table I) is related to the appearance of P1. Due to the close proximity of the energies the A_{1g} mode apparently decays into states close to those adding up to yield P1. The decay is less restricted by symmetry leaving more options. For both processes the phonon-phonon coupling has to be substantial with the order of magnitude given by $\lambda_{\text{ph-ph}}^{A_{1g}} \approx 1.7$. Phonon-phonon coupling is present in any type of material because of the anharmonic potential. Defects enhance this effect [44]. Since FeS is a metal the phonon-phonon coupling goes at least partially through electronic states and may be indicative of enhanced electron-phonon coupling, $\lambda_{\text{el-ph}}$, as described, e.g., in Ref. [45]. The related contribution to $\lambda_{\text{ph-ph}}$ is then expected

TABLE III. Two-phonon processes in FeS. The symmetry group of the FeS system is the space group $P4/nmm$. For products of irreducible representations (IRs) in the left column Raman active modes (RM) in decomposition are given in the right one. Raman active modes of FeS are Γ_1^+ (A_{1g}), Γ_2^+ (B_{1g}), and two double degenerate Γ_5^+ (E_g). Γ_1^+ comes from vibrations of S atoms, Γ_2^+ from Fe ones, and both atom types contribute with one pair of Γ_5^+ modes. For complex representations ($V_{1,2,3,4}$ and all W) the double index indicates that the real representation is used, for example, $V_{13} = V_1 \oplus V_1^* = V_1 \oplus V_3$. Irreducible representations of the space group given in Ref. [53] are used.

Overtones		Combinations	
IR products (phonon states)	RM in decomposition	IR products (phonon states)	RM in decomposition
$[(\Gamma_i^\pm)^2] (i = 1, 2, 3, 4)$	A_{1g}	$\Gamma_1^h \otimes \Gamma_2^h, \Gamma_3^h \otimes \Gamma_4^h (h = \pm)$	B_{1g}
$[(\Gamma_5^\pm)^2]$	A_{1g}, B_{1g}	$\Gamma_i^h \otimes \Gamma_5^h (i = 1, 2, 3, 4, h = \pm)$	E_g
$[(X_i)^2] (i = 1, 2)$	A_{1g}, B_{1g}, E_g	$X_1 \otimes X_2$	E_g
$[(M_i)^2] (i = 1, 2, 3, 4)$	A_{1g}	$M_1 \otimes M_2, M_3 \otimes M_4$	B_{1g}
$[(\Sigma_i)^2] (i = 1, 2, 3, 4)$	A_{1g}	$M_1 \otimes M_3, M_1 \otimes M_4, M_2 \otimes M_3, M_2 \otimes M_4$	E_g
$[(\Delta_i)^2] (i = 1, 2, 3, 4)$	A_{1g}, B_{1g}	$\Sigma_1 \otimes \Sigma_2, \Sigma_3 \otimes \Sigma_4$	B_{1g}
$[(V_{13})^2], [(V_{24})^2], [(V_5)^2]$	A_{1g}	$\Sigma_1 \otimes \Sigma_3, \Sigma_1 \otimes \Sigma_4, \Sigma_2 \otimes \Sigma_3, \Sigma_2 \otimes \Sigma_4$	E_g
$[(W_{13})^2], [(W_{24})^2]$	A_{1g}, B_{1g}, E_g	$\Delta_1 \otimes \Delta_2, \Delta_1 \otimes \Delta_3, \Delta_2 \otimes \Delta_4, \Delta_3 \otimes \Delta_4$	E_g
$[(Y_1)^2]$	A_{1g}, B_{1g}, E_g	$V_{13} \otimes V_{24}$	Γ_2^+
$[(Z_i^\pm)^2] (i = 1, 2, 3, 4)$	A_{1g}	$V_{13} \otimes V_5, V_{24} \otimes V_5$	Γ_5^+
$[(Z_5^\pm)^2]$	A_{1g}, B_{1g}	$W_{13} \otimes W_{24}$	Γ_5^+
$[(A_i)^2] (i = 1, 2, 3, 4)$	A_{1g}	$Z_1^h \otimes Z_2^h, Z_3^h \otimes Z_4^h (h = \pm)$	B_{1g}
$[(R_i)^2] (i = 1, 2)$	A_{1g}, B_{1g}, E_g	$Z_i^h \otimes Z_5^h (i = 1, 2, 3, 4, h = \pm)$	E_g
$[(S_i)^2] (i = 1, 2, 3, 4)$	A_{1g}	$A_1 \otimes A_2, A_3 \otimes A_4$	B_{1g}
$[(U_i)^2] (i = 1, 2, 3, 4)$	A_{1g}, B_{1g}	$A_1 \otimes A_3, A_1 \otimes A_4, A_2 \otimes A_3, A_2 \otimes A_4$	E_g
$[(\Lambda_i)^2] (i = 1, 2, 3, 4)$	A_{1g}	$R_1 \otimes R_2$	E_g
$[(\Lambda_5)^2]$	A_{1g}, B_{1g}	$S_1 \otimes S_2, S_3 \otimes S_4$	B_{1g}
$[(T_1)^2]$	A_{1g}, B_{1g}, E_g	$S_1 \otimes S_3, S_1 \otimes S_4, S_2 \otimes S_3, S_2 \otimes S_4$	E_g
		$U_1 \otimes U_2, U_1 \otimes U_3, U_2 \otimes U_4, U_3 \otimes U_4$	E_g
		$\Lambda_1 \otimes \Lambda_2, \Lambda_3 \otimes \Lambda_4$	B_{1g}
		$\Lambda_i \otimes \Lambda_5 (i = 1, 2, 3, 4)$	E_g

to be proportional to $\lambda_{\text{el-ph}}^2$. This conclusion is compatible with early results on the branch-dependent electron-phonon coupling in LaFeAsOF, where the strongest effects are reported for some Γ -point modes and the acoustic branches with intermediate to large momenta [47]. $\lambda_{\text{ph-ph}}^{A_{1g}} > 1$ and the two-phonon peak P1 indicate that the electron-phonon coupling is possibly larger than in the other Fe-based systems and reaches values up to unity. In BaFe₂As₂, as an example from the pnictide family, $\lambda_{\text{el-ph}}^2 \approx (1-4) \times 10^{-2} < \lambda_{\text{ph-ph}} \approx 0.1$ is reported [32,48,49]. On the other hand, one finds $\lambda_{\text{el-ph}}^2 \approx 0.4 < \lambda_{\text{ph-ph}} \approx 0.9$ for the E_g phonon in MgB₂, being generally believed to be a conventional superconductor [50,51]. Thus one may speculate whether $\lambda_{\text{el-ph}}$ might be even large enough in FeS to account for a T_c in the 5 K range.

V. CONCLUSION

We have studied and identified phonons in tetragonal FeS by Raman scattering. For the A_{1g} sulfur and B_{1g} iron mode the DFT and DFPT calculations agree to within a few percent with the experiment. A third observed peak within a gap in the theoretical phonon density of states can be identified as a second order scattering process involving two phonons. Both the selection rules, based on the modified group projector tech-

nique, and the energy are in agreement with the experiment. A fourth mode identified close to the A_{1g} sulfur phonon can be traced back to the biggest maximum of the PDOS and is most likely activated by a small amount of defects.

The temperature dependence of all four modes is governed by the contraction of the lattice, but shows anomalies at 50 K and below 20 K. The anomaly observed at 20 K has a correspondence in the thermal expansion [20] and μ SR experiments [21,22], which indicate short-range magnetic order. The long-range magnetic order observed recently by neutron diffraction experiments [41] below $T_N = 116$ K has no correspondence in the Raman spectra.

The appearance of two-phonon scattering indicates strong phonon-phonon scattering, which is likely to originate from an electron-phonon interaction being enhanced in comparison to other pnictides and chalcogenides. We argue that in FeS the T_c can in principle entirely result from electron-phonon interaction.

ACKNOWLEDGMENTS

We acknowledge valuable discussions with T. Böhm and D. Jost. The work was supported by the German Research Foundation (DFG) via the Priority Program SPP 1458 (Grant No. Ha2071/7) and the Serbian Ministry of Education, Science

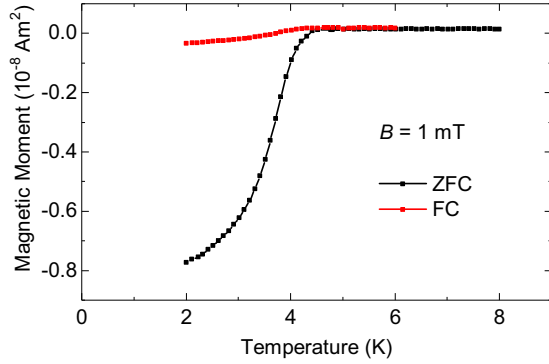


FIG. 5. Magnetization measurements of t-FeS at an applied field of $B = 1$ mT cooled to 2 K with (red curve) and without applied field (black curve).

and Technological Development under Projects No. III45018 and No. ON171017. Numerical simulations were run on the PARADOX supercomputing facility at the Scientific Computing Laboratory of the Institute of Physics Belgrade. We acknowledge support by the DAAD through the bilateral project between Serbia and Germany (Grants No. 56267076 and No. 57142964). Work carried out at the Brookhaven National Laboratory was primarily supported by the Center for Emergent Superconductivity, an Energy Frontier Research Center funded by the U.S. DOE, Office of Basic Energy Sciences (A.W. and C.P.). N.S. was supported by UW Oshkosh FDS498 grant.

A.B. and A.M. have contributed equally to this work.

APPENDIX A: MAGNETIZATION MEASUREMENTS

Figure 5 shows magnetization measurements on a t-FeS sample from the batch studied in small applied fields. Measurements were done on a Quantum Design MPMS XL-7 SQUID magnetometer by cooling the sample to 2 K and sweeping

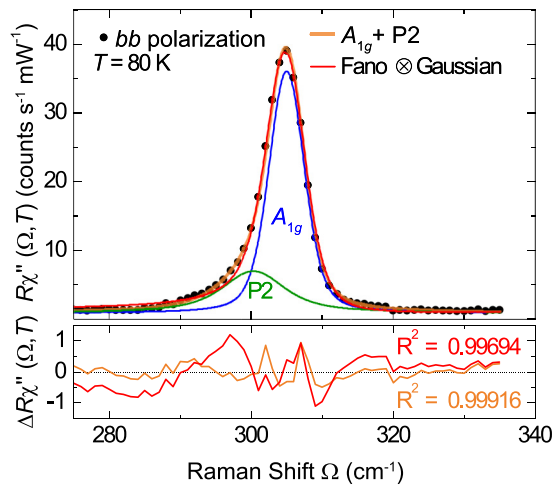


FIG. 6. Decomposition of the asymmetric phonon peak at 305 cm^{-1} . Measured data are shown as black dots. The orange line shows the sum of two Voigt profiles shown as blue and green lines, respectively. The convolution of Fano and Gaussian (red line) deviates in the peak flanks and the nearby continuum.

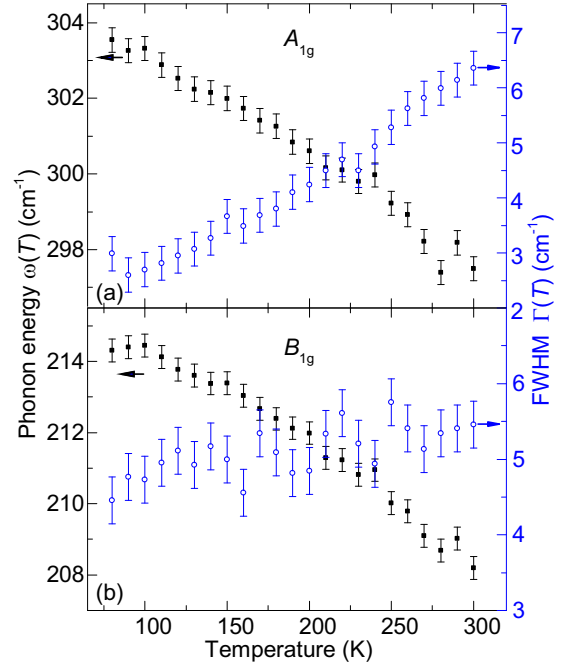


FIG. 7. Temperature dependence of A_{1g} and B_{1g} phonon modes in the temperature range between 80 K and 300 K. Black squares denote the phonon energies; open circles denote the phonon linewidths.

the temperature at 0.1 K/min. When cooled without applied field (ZFC, black curve) the sample shows a superconducting transition with onset at 4.5 K and a center of the transition at 3.6 K. When cooled in an applied field the magnetization decreases only weakly in the superconducting state indicating strong pinning.

APPENDIX B: DECOMPOSITION OF THE LINE AT 305 cm^{-1}

The peak at 305 cm^{-1} at low temperatures shows a significant asymmetry towards lower energies (see also Fig. 1). Coupling of the A_{1g} phonon mode to an electronic continuum by strong electron-phonon coupling would result in a line shape given by the convolution of a Fano function and a Gaussian, the latter representing the resolution of the spectrometer. We find, however, that this does not yield a satisfactory description of the measured line shape as can be seen from the red curve in Fig. 6, and thus conclude that the asymmetry of the peak stems from the overlap of two peaks which cannot be resolved separately. The corresponding line shape is the sum of two Lorentzians convoluted with a Gaussian which governs the resolution of the setup. Due to the distributivity of the convolution this is identical to the sum of two Voigt functions sharing the same width Γ_G of the Gaussian part. The overall spectral shape is shown in Fig. 6 as an orange line and agrees excellently with the data. The two contributing lines are shown in blue and green. From the selection rules (see Fig. 1) we identify the blue curve as the in-phase vibration of sulfur atoms in A_{1g} symmetry. The green line denotes a second mode P2, the origin of which is discussed in the main text.

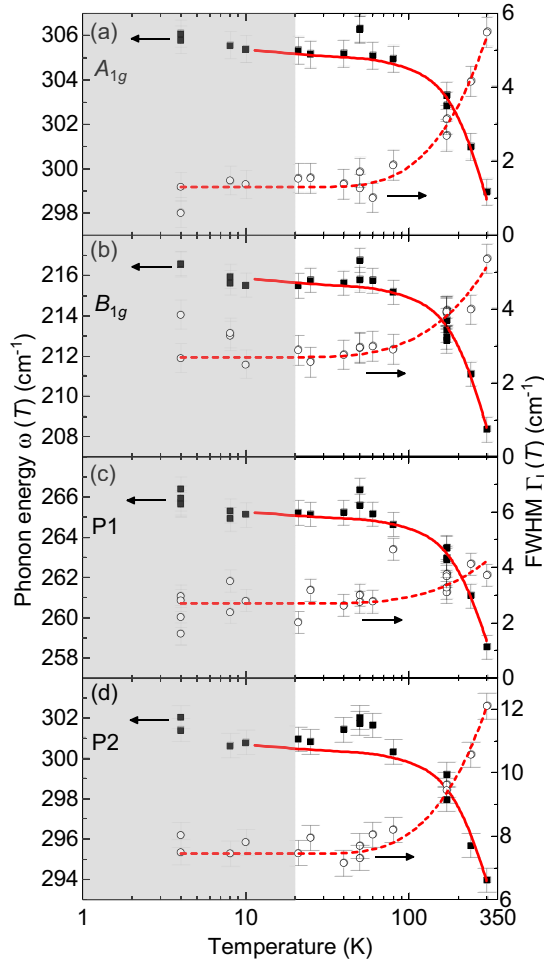


FIG. 8. Temperature dependence of energy and width of the four observed phonon modes in FeS on a logarithmic scale. The data is identical to Fig. 3 of the main text. Black squares show the phonon energies ω ; open circles denote the phonon linewidths Γ_L . The red dashed and full lines represent the temperature dependence of the phonon linewidths and energies according to Eqs. (1) and (2), respectively. The region below 20 K is shaded light gray. Since the data for the volume are limited to the range above 10 K the theoretical curves for the phonon energies (full red lines) end at 10 K.

APPENDIX C: DETAILED TEMPERATURE DEPENDENCE FOR $80 \leq T \leq 300$ K

Figure 7 shows the temperature dependence of the energies ω and linewidths $\Gamma(T)$ (FWHM) from 80 K to 300 K measured in temperature increments of 10 K. Raman scattering measurements were performed using a Jobin Yvon T64000 Raman system in micro-Raman configuration. A solid state laser with 532 nm line was used as an excitation source. Measurements were performed in high vacuum (10^{-6} mbar) using a KONTO CryoVac continuous helium flow cryostat with 0.5 mm thick window. Laser beam focusing was accomplished using a microscope objective with $\times 50$ magnification. The samples were cleaved right before being placed in the vacuum. As can be seen from Fig. 7, there is no deviation from the standard temperature behavior around 120 K.

APPENDIX D: TEMPERATURE DEPENDENCE ON A LOGARITHMIC SCALE

To better illustrate the behavior of the phonons at low temperatures Fig. 8 shows the experimental data and the theoretical curves from Fig. 3 of the main text on a logarithmic temperature scale. The region below 20 K is shaded light gray. As explained in Sec. IV B all four modes show an increase in energy below 20 K instead of the expected saturation, indicative of the putative onset of short range magnetic order. This effect manifests itself also in an incipient decrease of the unit cell volume [20] and is visible in the theoretical results for the phonon energies (full red lines). No clear tendency can be seen for the linewidths. The energy anomaly found around 50 K is discussed in the same section.

APPENDIX E: SECOND SAMPLE BATCH

Figure 9 shows Raman spectra on a t-FeS sample from a different batch (E256) taken at $T = 310$ K. The sample was oriented the same way as described in the main text. All three modes are visible for parallel light polarizations (*bb*), but vanish for crossed polarizations (*ba*), confirming the selection rules observed in the sample described in the main text. The inset shows magnetization measurements on a sample from batch E256 similar to the ones described in Appendix A. The superconducting transition sets in at 4.1 K.

APPENDIX F: SELECTION RULES FOR TWO-PHONON PROCESSES AND MGPT

In the multiphonon scattering process the system goes from an initial vibrational state (ground vibrational state) $|0,0,\dots\rangle$ to a final multiphonon state $|n_\mu, n_{\mu'}, \dots\rangle$, where n_μ is the number of phonons in the same state μ and μ stands for the entire set of quantum numbers (quasimomentum k , angular momentum quantum number m , etc.). For two-phonon processes the final vibrational state is the state with two phonons in the same quantum state (double-phonon or the first overtone state) or with two phonons in different states (combination state). The corresponding matrix element for

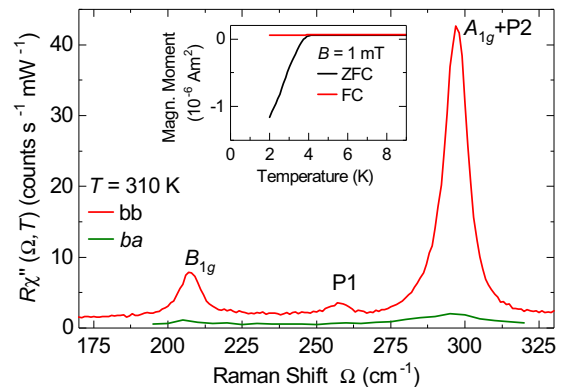


FIG. 9. Raman spectra of a t-FeS sample from a different batch taken at $T = 310$ K in polarizations as given in the legend. The inset shows magnetization measurements on a sample from this batch similar to Appendix A.

two-phonon Raman scattering is

$$\begin{aligned} &\langle 0, \dots, n_\mu, 0, \dots | \mathcal{R} | 0, 0, \dots \rangle, n_\mu = 2, \text{overtones}, \\ &\langle 0, \dots, n_\mu, 0, \dots, n_{\mu'}, \dots | \mathcal{R} | 0, 0, \dots \rangle, \\ &n_\mu = n_{\mu'} = 1, \text{combinations}, \end{aligned} \quad (\text{F1})$$

where \mathcal{R} is the Raman tensor. This matrix element should be a scalar or should transform as unit representation of the system space group \mathcal{S} . The standard approximation for the Raman tensor in infinite wavelength-light approximation for the non-resonant case is the polarizability tensor, which transforms as the (symmetrized) square of the vector representation, $D^{\mathcal{R}}(\mathcal{S})$. Decomposition of $D^{\mathcal{R}}(\mathcal{S})$ gives irreducible representations of the Raman active modes. The ground vibrational state transforms as unit representation, whereas the final two-phonon state transforms as symmetrized square, $[(D^\mu(\mathcal{S}))^2]$, of the corresponding irreducible representation $D^\mu(\mathcal{S})$ (overtones) or the direct product of two irreducible representations $D^\mu(\mathcal{S}) \otimes D^{\mu'}(\mathcal{S})$ (combinations). Symmetrization in the case of overtones comes from the bosonic nature of phonons. The matrix element [Eq. (F1)] transforms as reducible representation

$$\begin{aligned} &[(D^\mu(\mathcal{S}))^2] \otimes D^{\mathcal{R}}(\mathcal{S}), \text{ for overtones, or} \\ &D^\mu(\mathcal{S}) \otimes D^{\mu'}(\mathcal{S}) \otimes D^{\mathcal{R}}(\mathcal{S}), \text{ for combinations.} \end{aligned} \quad (\text{F2})$$

It is a scalar if the decomposition of the representations shown above contains the unit representation or, equivalently, if the intersection of decompositions of $[(D^\mu(\mathcal{S}))^2]$ or $D^\mu(\mathcal{S}) \otimes D^{\mu'}(\mathcal{S})$ and $D^{\mathcal{R}}(\mathcal{S})$ is a nonempty set. To obtain selection rules for two-phonon processes, following Birman's original method [52], it is enough to find the decomposition of $[(D^\mu(\mathcal{S}))^2]$ (for overtones) and $D^\mu(\mathcal{S}) \otimes D^{\mu'}(\mathcal{S})$ (for combinations) for all irreducible representations. If there is any representation

of the Raman active mode in those decompositions then that overtone or two-phonon combination is symmetrically allowed in the Raman scattering process. The decomposition of the (symmetrized) square of the vector representation is straightforward and is actually a finite dimensional point group problem. On the other hand, decomposition of $[(D^\mu(\mathcal{S}))^2]$ or $D^\mu(\mathcal{S}) \otimes D^{\mu'}(\mathcal{S})$ for any irreducible representation could be a difficult task because space groups are infinite. In the standard method based on character theory summation over all group elements is used and it is a problem in the infinite case. Therefore, it is necessary to apply a method which avoids summation over group elements. As is proven in Ref. [29] the modified group projector technique (MGPT) uses only group generators and finite dimensional matrices. Actually, the decomposition $D(\mathcal{S}) = \oplus_\mu f_D^\mu D^{(\mu)}(\mathcal{S})$ of the arbitrary reducible representation $D(\mathcal{S})$ into irreducible representations is effectively a determination of the frequency numbers f_D^μ . The MGPT expression for frequency numbers involves group generators s_i only:

$$f_D^\mu = \text{Tr} F \left(\prod_{i=1}^S F(D(s_i) \otimes D^{(\mu)*}(s_i)) \right). \quad (\text{F3})$$

Here S is the number of group generators, $F(X)$ is the projector on the subspace of the fixed points of the operator X , and Tr is the matrix trace (sum of the diagonal matrix elements). Consequently, the problem is reduced to calculation of the $S + 1$ projector to the fixed points. Technically, one looks for the eigenspaces for the eigenvalue 1 of each of the operators $D(s_i) \otimes D^{(\mu)*}(s_i)$, finding projectors on them, then multiplies the corresponding projectors, and repeats the procedure for the whole product from Eq. (F3). The trace of the final projector gives the corresponding frequency number.

-
- [1] Z. P. Yin, K. Haule, and G. Kotliar, Magnetism and charge dynamics in iron pnictides, *Nat. Phys.* **7**, 294 (2011).
 - [2] Q. Si, R. Yu, and E. Abrahams, High-temperature superconductivity in iron pnictides and chalcogenides, *Nat. Rev. Mater.* **1**, 16017 (2016).
 - [3] I. Leonov, S. L. Skornyakov, V. I. Anisimov, and D. Vollhardt, Correlation-Driven Topological Fermi Surface Transition in FeSe, *Phys. Rev. Lett.* **115**, 106402 (2015).
 - [4] C. Tresca, G. Giovannetti, M. Capone, and G. Profeta, Electronic properties of superconducting FeS, *Phys. Rev. B* **95**, 205117 (2017).
 - [5] J. Miao, X. H. Niu, D. F. Xu, Q. Yao, Q. Y. Chen, T. P. Ying, S. Y. Li, Y. F. Fang, J. C. Zhang, S. Ideta, K. Tanaka, B. P. Xie, D. L. Feng, and F. Chen, Electronic structure of FeS, *Phys. Rev. B* **95**, 205127 (2017).
 - [6] S. L. Skornyakov, V. I. Anisimov, D. Vollhardt, and I. Leonov, Effect of electron correlations on the electronic structure and phase stability of FeSe upon lattice expansion, *Phys. Rev. B* **96**, 035137 (2017).
 - [7] T. M. McQueen, A. J. Williams, P. W. Stephens, J. Tao, Y. Zhu, V. Ksenofontov, F. Casper, C. Felser, and R. J. Cava, Tetragonal-to-Orthorhombic Structural Phase Transition at 90 K in the Superconductor Fe_{1.01}Se, *Phys. Rev. Lett.* **103**, 057002 (2009).
 - [8] Y. Mizuguchi, T. Furubayashi, K. Deguchi, S. Tsuda, T. Yamaguchi, and Y. Takano, Mössbauer studies on FeSe and FeTe, *Physica C (Amsterdam)* **470**, S338 (2010).
 - [9] M. Bendele, A. Amato, K. Conder, M. Elender, H. Keller, H.-H. Klauss, H. Luetkens, E. Pomjakushina, A. Raselli, and R. Khasanov, Pressure Induced Static Magnetic Order in Superconducting FeSe_{1-x}, *Phys. Rev. Lett.* **104**, 087003 (2010).
 - [10] S.-H. Baek, D. V. Efremov, J. M. Ok, J. S. Kim, J. van den Brink, and B. Büchner, Orbital-driven nematicity in FeSe, *Nat. Mater.* **14**, 210 (2015).
 - [11] M. He, L. Wang, F. Hardy, L. Xu, T. Wolf, P. Adelmann, and C. Meingast, Evidence for short-range magnetic order in the nematic phase of FeSe from anisotropic in-plane magnetostriiction and susceptibility measurements, [arXiv:1709.03861](https://arxiv.org/abs/1709.03861) [cond-mat.supr-con].
 - [12] A. Baum, H. N. Ruiz, N. Lazarević, Y. Wang, T. Böhm, R. Hosseinian Ahangharnejhad, P. Adelmann, T. Wolf, Z. V. Popović, B. Moritz, T. P. Devereaux, and R. Hackl, Frustrated spin order and stripe fluctuations in FeSe, [arXiv:1709.08998](https://arxiv.org/abs/1709.08998) [cond-mat.str-el].
 - [13] F.-C. Hsu, J.-Y. Luo, K.-W. Yeh, T.-K. Chen, T.-W. Huang, P. M. Wu, Y.-C. Lee, Y.-L. Huang, Y.-Y. Chu, D.-C. Yan, and M.-K.

- Wu, Superconductivity in the PbO-type structure α -FeSe, *Proc. Natl. Acad. Sci. U.S.A.* **105**, 14262 (2008).
- [14] S. He, J. He, W. Zhang, L. Zhao, D. Liu, X. Liu, D. Mou, Y.-B. Ou, Q.-Y. Wang, Z. Li, L. Wang, Y. Peng, Y. Liu, C. Chen, L. Yu, G. Liu, X. Dong, J. Zhang, C. Chen, Z. Xu, X. Chen, X. Ma, Q. Xue, and X. J. Zhou, Phase diagram and electronic indication of high-temperature superconductivity at 65 K in single-layer FeSe films, *Nat. Mater.* **12**, 605 (2013).
- [15] J.-F. Ge, Z.-L. Liu, C. Liu, C.-L. Gao, D. Qian, Q.-K. Xue, Y. Liu, and J.-F. Jia, Superconductivity above 100 K in single-layer FeSe films on doped SrTiO₃, *Nat. Mater.* **14**, 285 (2014).
- [16] S. Li, C. de la Cruz, Q. Huang, Y. Chen, J. W. Lynn, J. Hu, Y.-L. Huang, F.-C. Hsu, K.-W. Yeh, M.-K. Wu, and P. Dai, First-order magnetic and structural phase transitions in Fe_{1+y}Se_xTe_{1-x}, *Phys. Rev. B* **79**, 054503 (2009).
- [17] M. H. Fang, H. M. Pham, B. Qian, T. J. Liu, E. K. Vehstedt, Y. Liu, L. Spinu, and Z. Q. Mao, Superconductivity close to magnetic instability in Fe(Se_{1-x}Te_x)_{0.82}, *Phys. Rev. B* **78**, 224503 (2008).
- [18] K.-W. Yeh, T.-W. Huang, Y.-I. Huang, T.-K. Chen, F.-C. Hsu, P. M. Wu, Y.-C. Lee, Y.-Y. Chu, C.-L. Chen, J.-Y. Luo, D.-C. Yan, and M.-K. Wu, Tellurium substitution effect on superconductivity of the α -phase iron selenide, *Europhys. Lett.* **84**, 37002 (2008).
- [19] X. Lai, H. Zhang, Y. Wang, X. Wang, X. Zhang, J. Lin, and F. Huang, Observation of superconductivity in tetragonal FeS, *J. Am. Chem. Soc.* **137**, 10148 (2015).
- [20] U. Pachmayr, N. Fehn, and D. Johrendt, Structural transition and superconductivity in hydrothermally synthesized FeX (X = S, Se), *Chem. Commun.* **52**, 194 (2016).
- [21] S. Holenstein, U. Pachmayr, Z. Guguchia, S. Kamusella, R. Khasanov, A. Amato, C. Baines, H.-H. Klauss, E. Morenzoni, D. Johrendt, and H. Luetkens, Coexistence of low-moment magnetism and superconductivity in tetragonal FeS and suppression of T_c under pressure, *Phys. Rev. B* **93**, 140506 (2016).
- [22] F. K. K. Kirschner, F. Lang, C. V. Topping, P. J. Baker, F. L. Pratt, S. E. Wright, D. N. Woodruff, S. J. Clarke, and S. J. Blundell, Robustness of superconductivity to competing magnetic phases in tetragonal FeS, *Phys. Rev. B* **94**, 134509 (2016).
- [23] A. Wang, L. Wu, V. N. Ivanovski, J. B. Warren, J. Tian, Y. Zhu, and C. Petrovic, Critical current density and vortex pinning in tetragonal FeS_{1-x}Se_x (x = 0, 0.06), *Phys. Rev. B* **94**, 094506 (2016).
- [24] S. Baroni, S. de Gironcoli, A. Dal Corso, and P. Giannozzi, Phonons and related crystal properties from density-functional perturbation theory, *Rev. Mod. Phys.* **73**, 515 (2001).
- [25] P. Giannozzi, S. Baroni, N. Bonini, M. Calandra, R. Car, C. Cavazzoni, D. Ceresoli, G. L. Chiarotti, M. Cococcioni, I. Dabo, A. D. Corso, S. de Gironcoli, S. Fabris, G. Fratesi, R. Gebauer, U. Gerstmann, C. Gougousis, A. Kokalj, M. Lazzeri, L. Martin-Samos, N. Marzari, F. Mauri, R. Mazzarello, S. Paolini, A. Pasquarello, L. Paulatto, C. Sbraccia, S. Scandolo, G. Sclauzero, A. P. Seitsonen, A. Smogunov, P. Umari, and R. M. Wentzcovitch, QUANTUM ESPRESSO: a modular and open-source software project for quantum simulations of materials, *J. Phys.: Condens. Matter* **21**, 395502 (2009).
- [26] A. R. Lennie, S. A. T. Redfern, P. F. Schofield, and D. J. Vaughan, Synthesis and Rietveld crystal structure refinement of mackinawite, tetragonal FeS, *Mineral. Mag.* **59**, 677 (1995).
- [27] A. Subedi, L. Zhang, D. J. Singh, and M. H. Du, Density functional study of FeS, FeSe, and FeTe: Electronic structure, magnetism, phonons, and superconductivity, *Phys. Rev. B* **78**, 134514 (2008).
- [28] Y. El Mendili, B. Minisini, A. Abdelouas, and J.-F. Bardeau, Assignment of Raman-active vibrational modes of tetragonal mackinawite: Raman investigations and *ab initio* calculations, *RSC Adv.* **4**, 25827 (2014).
- [29] M. Damnjanović and I. Milošević, Full symmetry implementation in condensed matter and molecular physics—Modified group projector technique, *Phys. Rep.* **581**, 1 (2015).
- [30] P. G. Klemens, Anharmonic decay of optical phonons, *Phys. Rev.* **148**, 845 (1966).
- [31] H.-M. Eiter, P. Jaschke, R. Hackl, A. Bauer, M. Gangl, and C. Pfleiderer, Raman study of the temperature and magnetic-field dependence of the electronic and lattice properties of MnSi, *Phys. Rev. B* **90**, 024411 (2014).
- [32] M. Rahlenbeck, G. L. Sun, D. L. Sun, C. T. Lin, B. Keimer, and C. Ulrich, Phonon anomalies in pure and underdoped R_{1-x}K_xFe₂As₂ (R = Ba, Sr) investigated by Raman light scattering, *Phys. Rev. B* **80**, 064509 (2009).
- [33] L. Chauvière, Y. Gallais, M. Cazayous, A. Sacuto, M. A. Measson, D. Colson, and A. Forget, Doping dependence of the lattice dynamics in Ba(Fe_{1-x}Co_x)₂As₂ studied by Raman spectroscopy, *Phys. Rev. B* **80**, 094504 (2009).
- [34] L. Chauvière, Y. Gallais, M. Cazayous, M. A. Méasson, A. Sacuto, D. Colson, and A. Forget, Raman scattering study of spin-density-wave order and electron-phonon coupling in Ba(Fe_{1-x}Co_x)₂As₂, *Phys. Rev. B* **84**, 104508 (2011).
- [35] Y. J. Um, A. Subedi, P. Toulemonde, A. Y. Ganin, L. Boeri, M. Rahlenbeck, Y. Liu, C. T. Lin, S. J. E. Carlsson, A. Sulpice, M. J. Rosseinsky, B. Keimer, and M. Le Tacon, Anomalous dependence of *c*-axis polarized Fe B_{1g} phonon mode with Fe and Se concentrations in Fe_{1+y}Te_{1-x}Se_x, *Phys. Rev. B* **85**, 064519 (2012).
- [36] Y. J. Um, J. T. Park, B. H. Min, Y. J. Song, Y. S. Kwon, B. Keimer, and M. Le Tacon, Raman scattering study of the lattice dynamics of superconducting LiFeAs, *Phys. Rev. B* **85**, 012501 (2012).
- [37] V. Gnezdilov, Y. G. Pashkevich, P. Lemmens, D. Wulferding, T. Shevtsova, A. Gusev, D. Chareev, and A. Vasiliev, Interplay between lattice and spin states degree of freedom in the FeSe superconductor: Dynamic spin state instabilities, *Phys. Rev. B* **87**, 144508 (2013).
- [38] T. Yildirim, Strong Coupling of the Fe-Spin State and the As-As Hybridization in Iron-Pnictide Superconductors from First-Principle Calculations, *Phys. Rev. Lett.* **102**, 037003 (2009).
- [39] V. Gnezdilov, Yu. Pashkevich, P. Lemmens, A. Gusev, K. Lamonova, T. Shevtsova, I. Vitebskiy, O. Afanasiev, S. Gnatchenko, V. Tsurkan, J. Deisenhofer, and A. Loidl, Anomalous optical phonons in FeTe chalcogenides: Spin state, magnetic order, and lattice anharmonicity, *Phys. Rev. B* **83**, 245127 (2011).
- [40] Z. V. Popović, N. Lazarević, S. Bogdanović, M. M. Radonjić, D. Tanasković, R. Hu, H. Lei, and C. Petrovic, Signatures of the spin-phonon coupling in Fe_{1+y}Te_{1-x}Se_x alloys, *Solid State Commun.* **193**, 51 (2014).
- [41] S. J. Kuhn, M. K. Kidder, D. S. Parker, C. dela Cruz, M. A. McGuire, W. M. Chance, L. Li, L. Debeer-Schmitt, J. Ermen-trout, K. C. Littrell, M. R. Eskildsen, and A. S. Sefat, Structure and property correlations in FeS, *Physica C (Amsterdam)* **534**, 29 (2017).

- [42] R. A. MacDonald and W. M. MacDonald, Thermodynamic properties of fcc metals at high temperatures, *Phys. Rev. B* **24**, 1715 (1981).
- [43] M. I. Aroyo, D. Orobengoa, G. de la Flor, E. S. Tasci, J. M. Perez-Mato, and H. Wondratschek, Brillouin-zone database on the Bilbao Crystallographic Server, *Acta Crystallogr. A* **70**, 126 (2014).
- [44] W. Spengler and R. Kaiser, First and second order Raman scattering in transition metal compounds, *Solid State Commun.* **18**, 881 (1976).
- [45] W. Spengler, R. Kaiser, A. N. Christensen, and G. Müller-Vogt, Raman scattering, superconductivity, and phonon density of states of stoichiometric and nonstoichiometric TiN, *Phys. Rev. B* **17**, 1095 (1978).
- [46] W. Hayes and R. Loudon, *Scattering of Light by Crystals* (John Wiley and Sons, New York, 1978).
- [47] L. Boeri, O. V. Dolgov, and A. A. Golubov, Is LaFeAsO_{1-x}F_x an Electron-Phonon Superconductor? *Phys. Rev. Lett.* **101**, 026403 (2008).
- [48] B. Mansart, D. Boschetto, A. Savoia, F. Rullier-Albenque, F. Bouquet, E. Papalazarou, A. Forget, D. Colson, A. Rousse, and M. Marsi, Ultrafast transient response and electron-phonon coupling in the iron-pnictide superconductor Ba(Fe_{1-x}Co_x)₂As₂, *Phys. Rev. B* **82**, 024513 (2010).
- [49] L. Rettig, R. Cortés, H. S. Jeevan, P. Gegenwart, T. Wolf, J. Fink, and U. Bovensiepen, Electron-phonon coupling in 122 Fe pnictides analyzed by femtosecond time-resolved photoemission, *New J. Phys.* **15**, 083023 (2013).
- [50] H. Martinho, C. Rettori, P. G. Pagliuso, A. A. Martin, N. O. Moreno, and J. L. Sarrao, Role of the E_{2g} phonon in the superconductivity of MgB₂: a Raman scattering study, *Solid State Commun.* **125**, 499 (2003).
- [51] Y. Wang, T. Plackowski, and A. Junod, Specific heat in the superconducting and normal state (2–300 K, 0–16 T), and magnetic susceptibility of the 38 K superconductor MgB₂: evidence for a multicomponent gap, *Physica C (Amsterdam)* **355**, 179 (2001).
- [52] J. L. Birman, Theory of infrared and Raman processes in crystals: Selection rules in diamond and zincblende, *Phys. Rev.* **131**, 1489 (1963).
- [53] M. I. Aroyo, A. Kirov, C. Capillas, J. M. Perez-Mato, and H. Wondratschek, Bilbao Crystallographic Server. II. Representations of crystallographic point groups and space groups, *Acta Crystallogr. A* **62**, 115 (2006).



Probing primary mesenchymal stem cells differentiation status by micro-Raman spectroscopy

J.J. Lazarević^a, T. Kukolj^b, D. Bugarski^b, N. Lazarević^{a,*}, B. Bugarski^c, Z.V. Popović^{a,d}

^aCenter for Solid State Physics and New Materials, Institute of Physics Belgrade, University of Belgrade, Pregrevica 118, Belgrade 11080, Serbia

^bLaboratory for Experimental Hematology and Stem Cells, Institute for Medical Research, University of Belgrade, Belgrade 11000, Serbia

^cDepartment of Chemical Engineering, Faculty of Technology and Metallurgy, University of Belgrade, Karnegijeva 4, Belgrade 11060, Serbia

^dSerbian Academy of Sciences and Arts, Knez Mihailova 35, Belgrade 11000, Serbia

ARTICLE INFO

Article history:

Received 17 September 2018

Accepted 21 January 2019

Available online 29 January 2019

Keywords:

Raman spectroscopy

Stem cells

Differentiation

ABSTRACT

We have employed micro-Raman spectroscopy to get insight into intrinsic biomolecular profile of individual mesenchymal stem cell isolated from periodontal ligament. Furthermore, these cells were stimulated towards adipogenic, chondrogenic, and osteogenic lineages and their status of differentiation was assessed using micro-Raman spectroscopy. In both cases, glass coverslips were used as substrates, due to their wide availability and cost effectiveness. In all sample groups, the same type of behavior was observed, manifested as changes in Raman spectra: the increase of relative intensity of protein/lipid bands and decrease of nucleic acid bands. Comprehensive statistical analysis in the form of principal component analysis was performed, which revealed noticeable grouping of cells with the similar features. Despite the inhomogeneity of primary stem cells and their differentiated lineages, we demonstrated that micro-Raman spectroscopy is sufficient for distinguishing cells' status, which can be valuable for medical and clinical application.

© 2019 Published by Elsevier B.V.

1. Introduction

In the era of regenerative medicine development, stem cells are in the center of attention, bringing hope for treating conditions and diseases presently incurable. In general, these expectations arise from unique qualities of these cells, which include self-renewal and multilineage differentiation potential *in vitro*. When it comes to potential clinical application of stem cells, from the aspect of differentiation capacity, embryonic stem cells (ESCs) and induced pluripotent stem cells (iPSCs) provide the greatest possibilities. However, it is well documented that both ESCs and iPSCs can form teratoma which directly restricts their therapeutic application. On the other hand, considering relatively simple isolation procedures, without ethical issues that follow manipulation of ESCs, mesenchymal stem cells (MSCs) have advantage over ESCs and iPSCs. Therefore, MSCs are promising agents in cell therapy and tissue engineering [1,2]. More than forty years ago, MSCs were discovered in bone marrow, but today it is known that this heterogeneous population of cells resides in tissues and organs throughout the adult organism, where their primary role

is maintenance of tissue regeneration and tissue homeostasis [3,4]. According to The International Society for Cellular Therapy, minimal criteria for characterisation of human MSCs are plastic adhesion with expression of CD73, CD90, and CD105 surface markers and lack of hematopoietic markers CD34-, CD45-, CD14-, CD79α-, HLA-DR-, and multilineage differentiation potential into osteoblasts, adipocytes, and chondroblasts [5]. Even though MSCs possess common cellular features, it is generally accepted that, due to tissue origin, donor age, culture conditions, these cells exhibit variable regenerative capacity [6,7]. Along with differentiation potential, an important part in considering MSCs as possible new therapeutic agents is their ability of immune response modulation (directly, through cell-to-cell contact or indirectly, by secretion of soluble factors) [8]. Originally, it was reported that MSCs can alter immune response in hypoinflammatory manner, but their role in immunity is still the subject of extensive research [9].

Within regenerative dentistry, there is a great interest in development of novel therapeutic strategies related to the recovery of periodontium. As tooth supportive tissue, periodontium is directly responsible for appropriate incorporation of synthetic implants which today represents one of the main methods of medical treatment for curing dental defects. However, damaged periodontal tissue has limited capacity for regeneration and is often influenced by inflammation that can severely hamper periodontal structure,

* Corresponding author.

E-mail address: nenadl@ipb.ac.rs.

disabling implantation and tooth restoration. Periodontal ligament is a soft connective tissue which anchors tooth to the alveolar bone. Hence, the exploration of human periodontal ligament stem cells (hPDLSCs), as potential cell source for reconstructive dentistry, strongly contributes to the improvement of periodontal therapies [10–12]. Previously is demonstrated that PDLSCs fulfill criteria for MSCs identification and characterisation [13,14], set by International Society for Cellular Therapy [5,15]. Keeping in mind that the origin tissue of PDLSCs is periodontal ligament and that the main role of cells within this tissue is maintenance of mineralization level [16,17], it is expected for PDLSCs to be more osteogenic than adipogenic committed when compared to MSCs derived from other sources [18,19].

Regarding heterogeneity of MSCs, carefully performed characterisation of these cells and thoroughly monitored process of their differentiation, before further manipulation, is of great significance for their usage [20]. Various techniques are available in this field, such as immunocytochemistry, flow cytometry, mass spectrometry or gene expression analyses. However, these methods mostly imply disruption of cell integrity and, at the same time, they can be time consuming and require expensive biomarkers for each cell type [21]. Destructiveness comes out as the dominant drawback of these techniques. This gives rise to a need for non-invasive, non-destructive and fast technique, which would be able to monitor stem cells behavior, including differentiation process [20,21]. Owing to its features, Raman spectroscopy appears to be a promising candidate. Regarding clinical applicability, no sample preparation or a minimal preparation, is important feature of Raman spectroscopy. It is also suitable for measurements in aqueous solutions. The outcome of Raman scattering measurement is a vibrational spectrum in which macromolecules, such as proteins, nucleic acids, carbohydrates, and lipids, are presented with the most pronounced vibration modes of different chemical bonds. Interactions of molecules are also visible. Accordingly, Raman spectrum is a fingerprint of the analysed sample. In past decade, the interest in performing this type of analysis on stem cells is well documented [21–30].

Currently, advanced Raman setups are used in biomedical researches [31]. Most of the studies in the field of stem cells biology were performed with more experimentally demanding Raman spectroscopy experiments, such as Coherent anti-Stokes Raman spectroscopy (CARS), Raman tweezers, Tip enhanced Raman spectroscopy (TERS), or Surface enhanced Raman spectroscopy (SARS), due to their higher sensitivity. As far as we know, great number of these studies were focused on live murine and human ESCs [22–26], and spectral mapping of live and apoptotic ESCs [27], but the interest in mesenchymal stem cells is also noticeable [28,29,21]. One of the Raman studies on MSCs was performed to characterise the Raman spectra of bone marrow-derived MSCs and to study the effect of different inducers on their differentiation towards osteogenic lineage [30]. Further, Raman spectroscopy was assessed as the analytical tool which could be used for characterisation and identification of rhesus monkey mesenchymal stem cells from different age groups (fetal to juvenile) [32]. Moreover, Raman spectroscopy was used to map the distribution of different biomolecules within two types of stem cells: adult human bone marrow-derived MSCs and human ESCs, and to identify Raman spectral characteristics which distinguish genetically abnormal and transformed stem cell from normal ones [33]. Another study was dedicated to viability transitions detection of umbilical cord mesenchymal stem cells (hUC-MSCs) by micro-Raman spectroscopy, where the authors proposed that the viability of hUC-MSCs can be described with three peaks of certain energies [28].

Although numerous Raman studies of different stem cell lineages have been performed [22–26], it is still unclear whether Raman spectroscopy can unambiguously distinguish differentiation status of primary stem cells such as hPDLSCs. In order to

address this matter, Raman scattering study of undifferentiated and differentiated hPDLSCs (osteogenic, chondrogenic, and adipogenic cells) has been performed. To assure multilineage mesenchymal differentiation capacity of hPDLSCs, standard biological detection of adipogenesis, chondrogenesis, and osteogenesis was conducted.

In general, the widespread applicability of this technique demands simplicity of the experimental setup and the availability of used substrates. In medicine, the most commonly used substrates are made of glass, which may be challenging for Raman spectroscopy, due to contributions to the sample spectrum. Besides limiting the spectral region that can be probed in the light scattering experiment it also hinders signal to noise ratio. The aim of this work was to determine the analytical ability of micro-Raman spectroscopy in commonly available experimental configuration, in order to assess differentiation status of hPDLSCs, with minimal sample processing, on glass substrates. Direct comparison of the primary hPDLSCs and differentiated hPDLSCs Raman spectra, as well as statistical analysis, revealed clear distinction between these groups. This approach could vastly simplify diagnostics and promote clinical application of MSCs.

2. Experiment

2.1. Isolation and Cultivation of Human Periodontal Ligament Stem Cells

Human PDLSCs were isolated from normal impacted third molars, as described elsewhere [14]. In brief, following the informed consent, tissues were collected from healthy patients aging 18–25 years, subjected to the procedure of tooth extraction for orthodontic reasons, at the Department of Oral Surgery of the Faculty of Dental Medicine, the University of Belgrade. All treatments were performed according to the approved ethical guidelines set by Ethics Committee of the Faculty of Dental Medicine, the University of Belgrade and Declaration of Helsinki. Directly after tooth extraction, periodontal tissues were carefully detached from the mid-third of the root surface, minced into small pieces and placed in a 25 cm² flask with Dulbecco's modified Eagle's medium (DMEM; PAA Laboratories, Pasching, Austria) supplemented with 10% fetal bovine serum (FBS; PAA Laboratories), 100 U/ml penicillin and 100 µg/ml streptomycin (PAA Laboratories), and cultured at 37 °C in a humidified atmosphere containing 5% CO₂, with medium exchange every third day. When the 80% to 90% confluence was reached, the cells were passaged regularly in growth medium (GM-DMEM with 10% FBS) using 0.05% trypsin with 1 mM EDTA (PAA Laboratories) and for this study cells from third to sixth passages were used. Further on, considering the minimal criteria for characterisation of MSC [5] immunophenotype of hPDLSCs and their multipotent differentiation capacity towards osteogenic, chondrogenic, and adipogenic lineages were confirmed as previously reported [14].

2.2. Sample Preparation

For Raman measurements, hPDLSCs were seeded on rounded glass coverslips in 24-well plate (2×10^4 cells per well) and grown in standard cultivation conditions. Simultaneously, cells were seeded in 24-well plate (2×10^4 cells per well) to follow differentiation by regular *in vitro* staining. When the confluence was reached, cells were induced to differentiate into osteogenic, chondrogenic and adipogenic lineages by specific differentiation medium. Osteogenic differentiation medium contained DMEM supplemented with 5% FBS, 100 U/ml penicillin/streptomycin, 50 µM ascorbic acid-2-phosphate and 10 mM β -glycerophosphate (both from Sigma-Aldrich). Chondrogenic medium contained DMEM with 5% FBS, 2 ng/ml of transforming growth

factor- β 1 (TGF- β ; R&D Systems, Minneapolis, MN, USA), 50 μ M ascorbic acid-2-phosphate, 10 nM dexamethasone, 100 U/ml penicillin/streptomycin. Adipogenic medium contained 5% FBS in DMEM, 100 U/ml penicillin/streptomycin, 100 μ g/ml isobutyl-methyl xanthine (IBMX; Sigma-Aldrich), 1 μ M dexamethasone and 10 μ g/ml insulin (Sigma-Aldrich). With regular medium exchange, osteogenesis and chondrogenesis were evaluated after three weeks of cultivation, whereas adipogenesis was induced during four weeks. As for the control samples, cells were cultivated in GM with 5% FBS during the corresponding time. After this period, hPDLSCs were washed with saline buffer, fixed with methanol for 10 min at room temperature and washed with distilled water just before Raman spectroscopy was performed. Standard *in vitro* examination of differentiation process was performed after cells had been fixed and stained with specific dye. Intracellular lipid droplets were observed by Oil Red O (Merck Chemicals, Darmstadt, Germany) staining, while Safranin O confirmed cartilage-specific proteoglycan formation. Alizarin red was used to visualize calcium deposition and mineralization of extracellular matrix (see Fig. 1). Optical microscope with digital camera was used for cell morphology analysis and imaging.

2.3. μ -Raman Spectroscopy

Raman scattering measurements were performed using TriVista 557 Raman system in backscattering μ -Raman configuration. As an excitation source, 532 nm laser line of the Coherent VerdiG laser was used. The focusing on the sample was achieved by using $\times 100$ microscope objective, $NA = 0.80$. The laser spot diameter in our experimental configuration was $\approx 4 \mu$ m. In order to avoid any possible sample damage and/or temperature related effect, the laser power at the sample plain was kept at low levels, ≈ 1 mW. Acquisition time was 900 s. More details on Raman scattering experiment can be found in the Section S1 of the Supplementary Information.

From the aspects of vibrational spectroscopy, which can independently probe a single vibration within a molecule or a crystal, biological samples consisting of various types of macro-molecules, represent rather complicated systems. In these systems, only vibrational bands, consisting of numerous vibrations of the same type, can be taken into consideration, rather than a single vibration. Consequently, the changes of biological system (e.g. single cell) composition, may result in a change of certain Raman bands intensities.

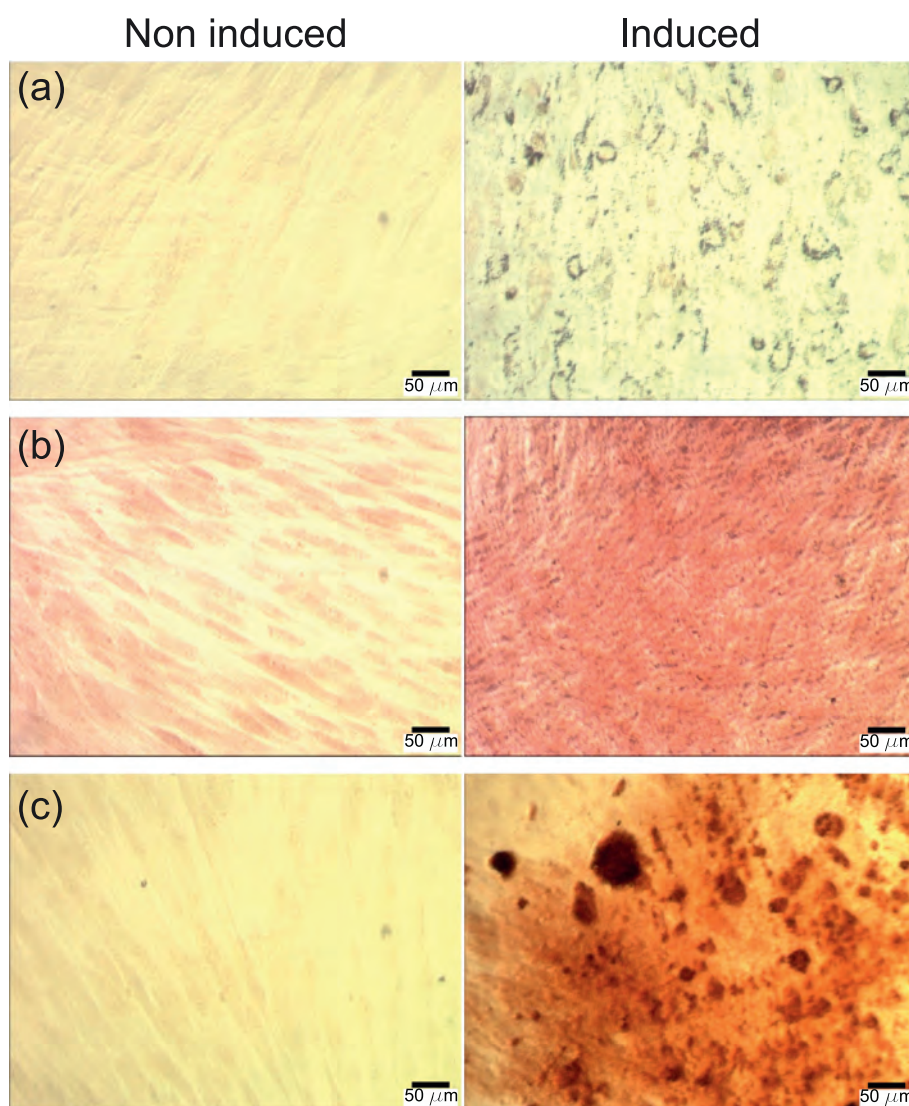


Fig. 1. Multilineage differentiation potential of hPDLSCs. (a) Oil Red O staining showed presence of intracytoplasmatic lipid droplets confirming adipogenic differentiation. (b) Chondrogenic differentiation was demonstrated by positive staining of proteoglycans with Safranin O. (c) Positive Alizarin red staining of extracellular matrix mineralization confirmed osteogenic differentiation.

It should be taken into account that when probing a single cell, due to its complex inner structure, there might be small variations in Raman spectra for the data collected at different positions. To obtain single spectra representative for each of the cells, recorded spectra were averaged. The preliminary experiment involved investigation of 54 cells of Batch 1. For every cell lineage, 9 hPDLSCs and 9 differentiated cells were analysed by probing each cell at 10 randomly chosen positions. The results of the analysis performed on the full set of data as well as on the sub-set including three random positions, revealed no qualitative difference. This implies that for our experimental configuration and for the samples under investigation, three randomly chosen positions are sufficient to make qualitative conclusions. Having in mind statistical treatment of the results, a total of 1080 spectra from 360 cells were recorded and analysed in the main experiment.

2.4. Data Processing and Analysis

Prior to the analysis, all Raman spectra were processed by subtracting the contributions from substrate (see Fig. 2 (a)), as well as biological fluorescence. No spectral smoothing of the samples spectra has been performed. On the other hand, the substrate spectrum was obtained separately with greater acquisition time and statistics and post-processed by Savitzky–Golay filter. Right inset on Fig. 2 (a) compares the substrate and the mean of 540 hPDLSCs Raman spectra. Significantly smaller noise level of the (glass) substrate spectrum indicates absence of its contribution to hPDLSCs spectra statistics. Due to the substantial increase of the substrate spectral weight at lower energies, our analysis was limited to the region above 1000 cm^{-1} .

The absolute value of Raman intensity is not usually a reliable quantity. Even small variations in the experimental conditions may

produce the “artificial” variations of Raman intensity. In order to exclude this possible uncertainty, all spectra were normalised onto the peak at about 1660 cm^{-1} , which is present with high intensity in all obtained spectra.

Besides the direct comparison of spectra obtained from stem cells and differentiated cells, a multivariate statistical method, principal component analysis (PCA), was employed [40,20,25,22]. The main goal of PCA is to reduce the effective dimensionality of the experimental data set by determining the orthonormal basis of loading vectors in a way that the greatest variance is projected onto the first coordinate, the second greatest variance is projected onto the second coordinate, and so on. The outcome of this analysis is clear grouping of Raman spectra according to their mutual features. Prior to performing PCA, the spectral data were subtracted by the mean spectrum and divided by its standard deviation [40,22].

3. Results and Discussion

To get insight on how hPDLSCs differentiation status reflects on Raman spectra, three sets of Raman experiments were performed. The samples were set in two batches. For every lineage, spectra were obtained for 30 hPDLSCs and 30 differentiated cells (hPDLSC grown in standard cultivation medium for the corresponding time for each differentiation). The spectrum of every cell was measured three times on each of three randomly chosen positions within the cell in order to incorporate possible variations within a single cell and test the approach sufficiency for observing the difference between cell lineages.

Fig. 2 (b) shows Raman spectrum of hPDLSCs obtained by averaging spectra of all control samples. The main contribution to the hPDLSCs Raman spectrum for the region under consideration comes from nucleic acids, proteins and lipids [24,28,41,23,37–39]. Spectral features of nucleic acids originate from the individual purine and pyrimidine bases (adenine, thymine, guanine, cytosine, and uracil), as well as from backbone structure of DNA and RNA, whereas protein spectral features include contributions from aromatic amino acids (phenylalanine, tryptophan, and tyrosine), amide groups of secondary protein structures (α -helices, β -sheets, and random coils), and various vibrations of carbon atoms bonded with nitrogen and/or other carbon atoms [38]. Different vibrations within the hydrocarbon chain (e.g. C–C stretching, CH_2 and CH_3 scissoring and twisting) present specific features of lipids in Raman spectra [35]. Principally, various contributions may overlap, making the determination of the potential changes in Raman spectra of undifferentiated and differentiated hPDLSCs a formidable task. As can be seen from Fig. 2 (b), numerous vibrational bands have been observed in hPDLSCs Raman spectrum. The most pronounced bands are assigned according to the literature [24,28,41,23, 34–39] and summarized in Table 1.

Fig. 3 (a)–(c) shows averaged hPDLSCs Raman spectra of control samples, differentiated cells (adipocytes, chondroblasts, and osteoblasts, respectively) of both batches, as well as corresponding pairs' differences. Although the overall spectral features in these pairs of spectra look almost the same, after the subtraction, the difference is more pronounced. General conclusion, consistent with the literature data [22,25], is that relative intensities (with regard to 1660 cm^{-1} peak structure intensity) of nucleic acids and proteins, are able to distinguish stem cells from more mature cells. In the case of adipogenic differentiation, a slight decrease of the relative intensity of the band at 1100 cm^{-1} and increase of the relative intensity of peaks at about 1353 cm^{-1} , 1447 cm^{-1} , and 1590 cm^{-1} (see Fig. 3 (a)) is observed. According to Table 1, this might be understood as slight reduction of nucleic acids and enhancement of proteins and lipids. On the other hand, the possible increase of the band at 1735 cm^{-1} , assigned to lipids (esters), is absent. Explanation for this lies in the fact that these cells do not originate from

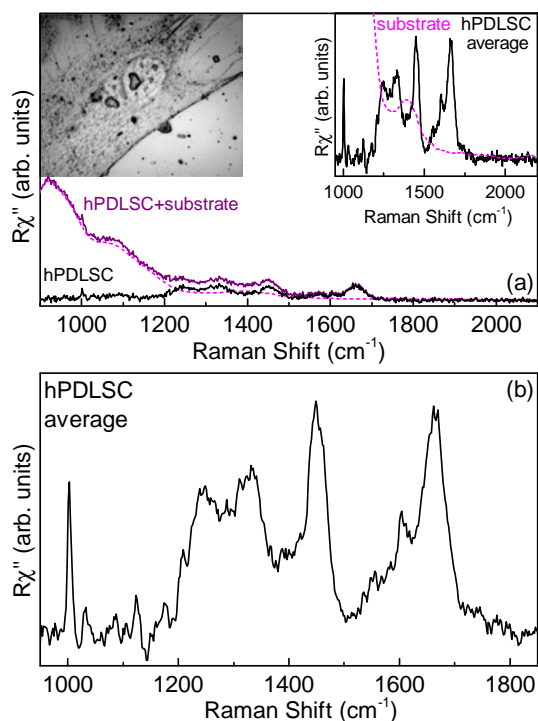


Fig. 2. (a) Raman scattering spectra of hPDLSCs on glass, glass substrate and their difference. Left inset: Image of hPDLSCs. Right inset: Comparison between the substrate and the mean of 540 hPDLSCs Raman spectra. (b) The mean of 540 hPDLSCs Raman spectra.

Table 1

Vibrations in hPDLSCs and their energies noticed in Raman spectrum. (A) adenine, (U) uracil, (C) cytosine, (T) thymine, (G) guanine, (Phe) phenylalanine, (Trp) tryptophan, (Tyr) tyrosine, (vib) vibration, (bg) bending, (br) breathing, (bk) backbone, (def) deformation, (tw) twist, (sym) symmetric, (asym) asymmetric, and (str) stretch [28,23,34–39].

Energy (cm ⁻¹)	Assignment
1004	Phe
1032	Phe
1061	C—N and C—C str
1080	PO ₂ ⁻ sym str
1085	C—O str
1105	PO ₂ ⁻ str (sym)
1130	C—N and C—C asym str
1155	C—C and C—N str of proteins
1165	C—O str, COH bg
1172	G ring str
1178	CH ben Tyr
1209	C—C ₆ H ₅ str, Phe, Trp
1228	Asym phosphate str
1250	T, amide III _β
1260	N—H and C—H bg (amide III/distorted)
1265	Amide III _α
1315	G, CH def.
1332	DNA purine bases (CH ₃ CH ₂ wagging mode of polynucleotide chain)
1450	CH ₂ str def of methylene group in lipids
1456	CH def.
1556	Amide II
1604	Phe, Tyr
1654	Amide I, α helix
1670	Amide I, β sheet

adipose tissue [18,19]. When it comes to the case of chondrogenic differentiation, higher relative intensities of the peaks at 1065 cm⁻¹, 1250–1450 cm⁻¹, and 1630 cm⁻¹ are exhibited (Fig. 3 (b)). These

changes arise from higher content of proteins and proteoglycans [42,43]. Regarding the osteogenic differentiation, spectral changes between hPDLSCs and their differentiated pairs (Fig. 3 (c)) originate from the lower relative intensities of the bands in the region from 1170 cm⁻¹ to 1220 cm⁻¹ and from 1450 cm⁻¹ to 1490 cm⁻¹, and higher relative intensities at about 1045 cm⁻¹, 1070 cm⁻¹, and 1600 cm⁻¹. These changes are caused by decrease in amino acids and likely lipids, and increase in carbonates and phosphates, as expected. This decrease of the band intensity in the region that most likely correspond to lipids, might be understood as a change in proteins to lipids ratio. Typical spectral marker for this type of cells is hydroxyapatite, but due to spectral interference from the substrate (glass), it is out of spectral range of interest in this study [43]. Consistently observed spectral changes during the differentiation process (the increase of protein bands and decrease of nucleic acid bands in differentiated cells) are in accordance with the literature [22,25]. The possible explanation for this behavior is that, as cells differentiate, they gradually begin to use up the pool of mRNA to support the synthesis of new, cell lineage specific proteins [22].

Although the direct comparison between hPDLSCs and their differentiated lineages Raman spectra gave us means to distinguish cell differentiation status, it is demanding and require detailed analysis of the spectra. However, if we utilize the Raman spectra as characteristic fingerprints of the cells under investigation, PCA can be employed for pattern recognition and grouping. Fig. S1 of the Supplementary information summarizes loading vectors for the main PCs. It is noticeable that a certain loading vector or their linear combination fully describe corresponding difference spectra shown in Fig. 3 (a)–(c). Consequently, the same conclusions can be made as in previous paragraph. Fig. 3 (d)–(f) shows score plots calculated independently using PCA for three groups of control hPDLSCs samples and their differentiated lineages'

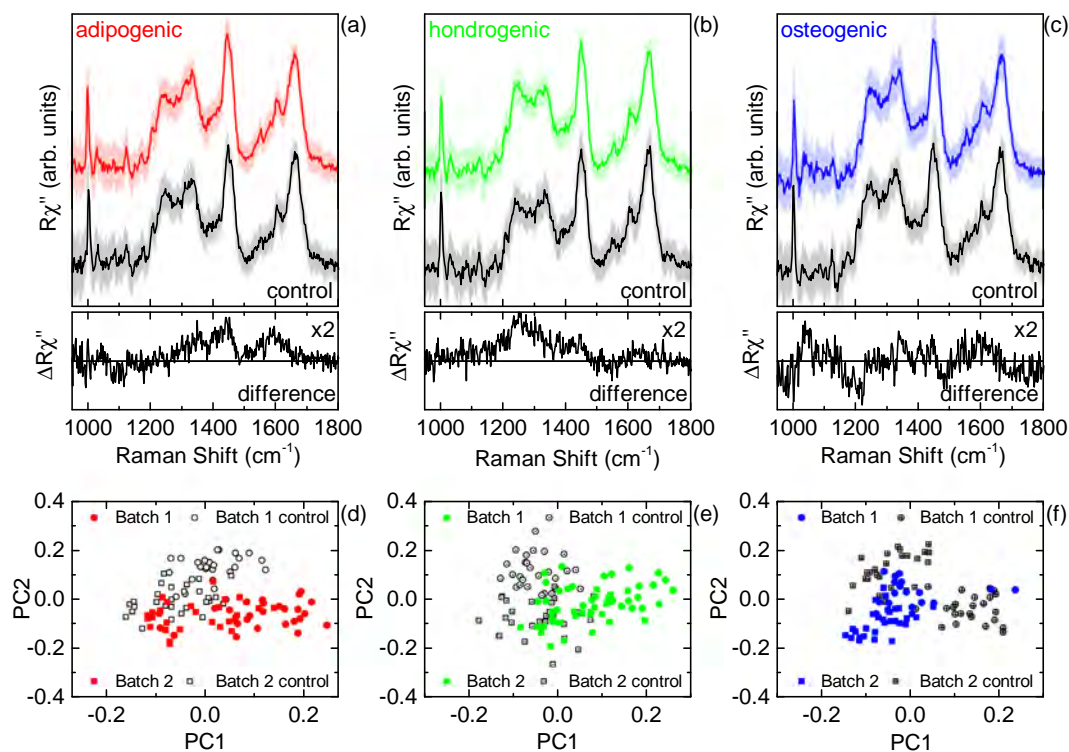


Fig. 3. (a)–(c) Averaged Raman spectra (black lines) of hPDLSCs (control samples), differentiated hPDLSCs (adipogenic, chondrogenic, and osteogenic lineages) and difference spectrum between these two groups of cells. Standard deviation for each lineage and control group is presented with the colored areas. (d)–(f) Score plots calculated independently using PCA for three groups of control hPDLSCs and differentiated hPDLSCs Raman spectra.

Raman spectra. In all three cases, two groups can be observed, with each grouping corresponding to a particular cell lineage. Furthermore, within each grouping, sub-groupings are noticed, indicating variations and inhomogeneity between the batches. In fact, this is not surprising since these are primary cells and the higher level of inhomogeneity is expected. In the following paragraphs, the attention will be focused on the analysis within the batches.

Fig. 4 summarizes adipogenic, chondrogenic, and osteogenic lineages score plots for Batches 1 and 2. Although the separation between data point groupings can be observed for both batches, it is more pronounced for Batch 1. Most likely, this is a consequence of higher inhomogeneity within the Batch 2.

In the next step, we wanted to test whether the same approach can be used to distinguish different types of differentiated cells (adipocytes, chondroblasts, and osteoblasts). For this purpose, the data from all three sets of experiments had been combined and PCA performed, for both batches. The obtained score plots are presented in Fig. 5. Shaded areas represent 1σ 2D confidence level. Remarkably, very good grouping of the different cell lineages has been observed for Batch 1. Less separation of different cell groups was observed for Batch 2, in agreement with the results presented in Fig. 4. Additionally, PCA indicates the variations within hPDLSCs (in particular for Batch 2) although this was not so obvious in direct comparison. When PCA was applied on hPDLSCs from all three control groups and compared with differentiated hPDLSCs data, it could be noticed that even though small variations are present, control hPDLSCs retain characteristics of stem cells, suggesting these cell populations are not homogeneous. Keeping that in mind, spectral analyses of hPDLSCs are in accordance with data obtained by traditional MSCs characterisation methods that also emphasize heterogeneity of MSCs population. As being primary cells, cellular diversity of MSCs is a result of isolation methods and culture conditions. Further, the absence of unique MSCs biomarkers makes these cells still highly difficult for molecular identification

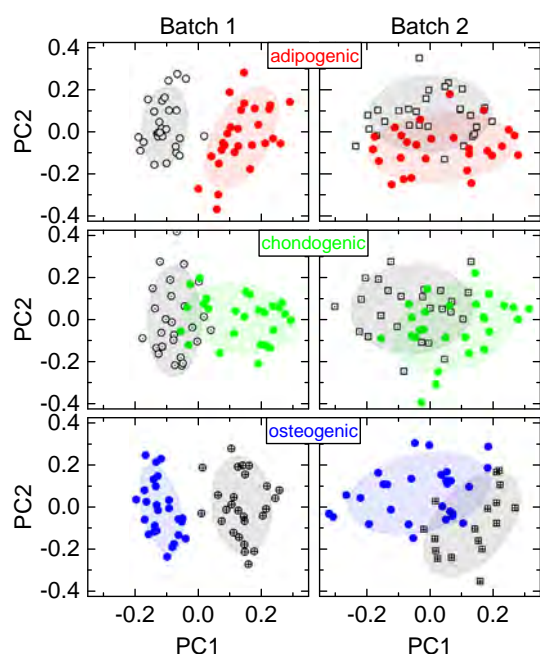


Fig. 4. Score plots calculated independently using PCA for three groups of control (black) and differentiated (adipogenic, chondrogenic, and osteogenic lineages) hPDLSCs samples Raman spectra in two batches. Shaded areas represent 1σ 2D confidence level.

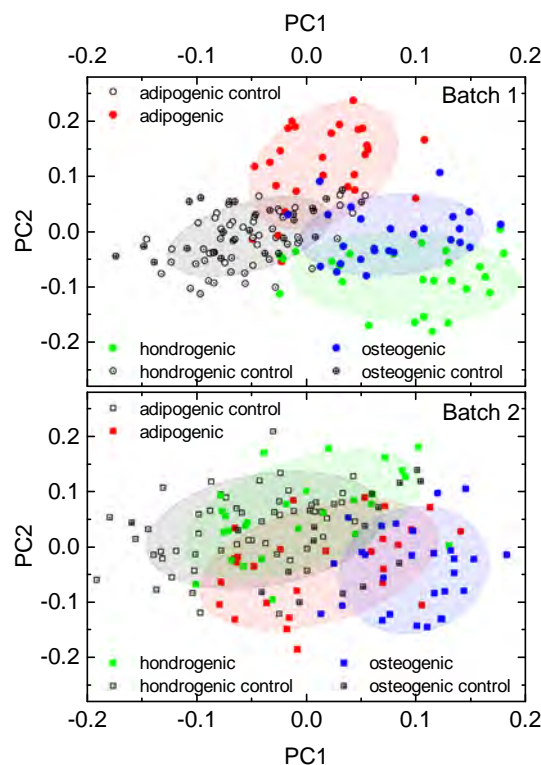


Fig. 5. PCA performed on all obtained Raman spectra of four groups of cells including nondifferentiated hPDLSCs (control) and differentiated hPDLSCs (osteogenic, chondrogenic and adipogenic lineages) for different batches. Shaded areas represent 1σ 2D confidence level.

and characterisation [5,44]. Thus, our results suggest the possibility of the Raman spectroscopy application in characterisation of MSCs.

4. Conclusion

In this study, the applicability of micro-Raman spectroscopy for probing primary hPDLSCs differentiation status on glass substrate was demonstrated. In direct comparison of hPDLSCs and differentiated cells Raman spectra, the difference in the relative intensities of certain marker bands has been observed. Additionally, statistical analysis of fingerprint Raman spectra of the cells using PCA, revealed distinct groupings based on the similar features. This gives a possibility of devising the procedure not only for fast and simple detection of different mesenchymal stem cell lineages, but also for the variations within. Furthermore, due to minimal preparation requirements and independency on the reagents that are necessary in standard biological techniques, Raman spectroscopy can be used as an additional method in MSCs characterisation. From the standpoint of MSCs utilization in biomedicine, simplification of the procedures in cell identification could significantly facilitate research in the field of stem cell biology.

Acknowledgments

We gratefully acknowledge M. Miletić and M. Andrić for supplying the periodontal ligament tissue and Dr. N. Paunović for constructive discussions on the subject. This work was supported by the Ministry of Education, Science, and Technological Development of the Republic of Serbia, Serbia under Projects No. III46010, III45018, and ON175062.

Appendix A. Supplementary data

Supplementary data to this article can be found online at <https://doi.org/10.1016/j.saa.2019.01.069>.

References

- [1] X. Wei, X. Yang, Z. p. Han, F. f. Qu, L. Shao, Y. f. Shi, Mesenchymal stem cells: a new trend for cell therapy, *Acta Pharmacol. Sin.* 34 (6) (2013) 747–754.
- [2] D. Howard, L.D. Buttery, K.M. Shakesheff, S.J. Roberts, Tissue engineering: strategies, stem cells and scaffolds, *J. Anat.* 213 (1) (2008) 66–72.
- [3] Y. Sato, H. Araki, J. Kato, K. Nakamura, Y. Kawano, M. Kobune, T. Sato, K. Miyaniishi, T. Takayama, M. Takahashi, et al. Human mesenchymal stem cells xenografted directly to rat liver are differentiated into human hepatocytes without fusion, *Blood* 106 (2) (2005) 756–763.
- [4] C. Toma, M.F. Pittenger, K.S. Cahill, B.J. Byrne, P.D. Kessler, Human mesenchymal stem cells differentiate to a cardiomyocyte phenotype in the adult murine heart, *Circulation* 105 (1) (2002) 93–98.
- [5] M. Dominici, K. Le Blanc, I. Mueller, I. Slaper-Cortenbach, F. Marini, D. Krause, R. Deans, A. Keating, D. Prockop, E. Horwitz, Minimal criteria for defining multipotent mesenchymal stromal cells. The International Society for Cellular Therapy position statement, *Cytotherapy* 8 (4) (2006) 315–317.
- [6] R. Hass, C. Kasper, S. Böhm, R. Jacobs, D. Populations, Sources of human mesenchymal stem cells (msc). A comparison of adult and neonatal tissue-derived msc, *Cell Commun. Signal* 9 (1) (2011) 12.
- [7] D.G. Phinney, Functional heterogeneity of mesenchymal stem cells: implications for cell therapy, *J. Cell. Biochem.* 113 (9) (2012) 2806–2812.
- [8] M. Gazdic, V. Volarevic, N. Arsenijevic, M. Stojkovic, Mesenchymal stem cells: a friend or foe in immune-mediated diseases, *Stem Cell Rev. Rep.* 11 (2) (2015) 280–287.
- [9] R. Abdi, P. Fiorina, C.N. Adra, M. Atkinson, M.H. Sayegh, Immunomodulation by mesenchymal stem cells: a potential therapeutic strategy for type 1 diabetes, *Diabetes* 57 (7) (2008) 1759–1767.
- [10] S. Shi, P. Bartold, M. Miura, B. Seo, P. Robey, S. Gronthos, The efficacy of mesenchymal stem cells to regenerate and repair dental structures, *Orthod. Craniofac. Res.* 8 (3) (2005) 191–199.
- [11] E.A.A. Neel, W. Chrzanowski, V.M. Salih, H.W. Kim, J.C. Knowles, Tissue engineering in dentistry, *J. Dent.* 42 (8) (2014) 915–928.
- [12] H. Egusa, W. Sonoyama, M. Nishimura, I. Atsuta, K. Akiyama, Stem cells in dentistry-part ii: clinical applications, *J. Prosthodont. Res.* 56 (4) (2012) 229–248.
- [13] T. Kukolj, D. Trivanović, I.O. Djordjević, S. Mojsilović, J. Krstić, H. Obradović, S. Janković, J.F. Santibanez, A. Jauković, D. Bugarski, Lipopolysaccharide can modify differentiation and immunomodulatory potential of periodontal ligament stem cells via erk1,2 signaling, *J. Cell. Physiol.* 233 (1) (2018) 447–462.
- [14] M. Miletić, S. Mojsilović, I. Okić-Djordjević, T. Kukolj, A. Jauković, J. Santibanez, G. Jovčić, D. Bugarski, Mesenchymal stem cells isolated from human periodontal ligament, *Arch. Biol. Sci.* 66 (1) (2014) 261–271.
- [15] A. Klimczak, U. Kozłowska, Mesenchymal stromal cells and tissue-specific progenitor cells: their role in tissue homeostasis, *Stem Cells Int.* 2016 (2016) 1–11.
- [16] M. Shimono, T. Ishikawa, H. Ishikawa, H. Matsuzaki, S. Hashimoto, T. Muramatsu, K. Shima, K.I. Matsuzaka, T. Inoue, Regulatory mechanisms of periodontal regeneration, *Microsc. Res. Tech.* 60 (5) (2003) 491–502.
- [17] A. Nanci, D.D. Bosshardt, Structure of periodontal tissues in health and disease, *Periodontol.* 2000 40 (1) (2006) 11–28.
- [18] T. Iwata, M. Yamato, Z. Zhang, S. Mukobata, K. Washio, T. Ando, J. Feijen, T. Okano, I. Ishikawa, Validation of human periodontal ligament-derived cells as a reliable source for cytotherapeutic use, *J. Clin. Periodontol.* 37 (12) (2010) 1088–1099.
- [19] D. Trivanović, A. Jauković, B. Popović, J. Krstić, S. Mojsilović, I. Okić-Djordjević, T. Kukolj, H. Obradović, J.F. Santibanez, D. Bugarski, Mesenchymal stem cells of different origin: comparative evaluation of proliferative capacity, telomere length and pluripotency marker expression, *Life Sci.* 141 (2015) 61–73.
- [20] A. Downes, R. Mouras, A. Elfick, Optical spectroscopy for noninvasive monitoring of stem cell differentiation, *Biomed. Res. Int.* 2010 (2010) 1–10.
- [21] A. Downes, R. Mouras, P. Bagnaninchi, A. Elfick, Raman spectroscopy and cars microscopy of stem cells and their derivatives, *J. Raman Spectrosc.* 42 (10) (2011) 1864–1870.
- [22] J.W. Chan, D.K. Lieu, Label-free biochemical characterization of stem cells using vibrational spectroscopy, *J. Biophotonics* 2 (11) (2009) 656–668.
- [23] I. Nottingher, I. Bisson, A.E. Bishop, W.L. Randle, J.M. Polak, L.L. Hensch, In situ spectral monitoring of mrna translation in embryonic stem cells during differentiation in vitro, *Anal. Chem.* 76 (11) (2004) 3185–3193.
- [24] C. Aksoy, F. Severcan, Role of vibrational spectroscopy in stem cell research, *J. Spectrosc.* 27 (3) (2012) 167–184.
- [25] E. Brauchle, K. Schenke-Layland, Raman spectroscopy in biomedicine-non-invasive in vitro analysis of cells and extracellular matrix components in tissues, *Biotechnol. J.* 8 (3) (2013) 288–297.
- [26] H.G. Schulze, S.O. Konorov, N.J. Caron, J.M. Piret, M.W. Blades, R.F. Turner, Assessing differentiation status of human embryonic stem cells noninvasively using Raman microspectroscopy, *Anal. Chem.* 82 (12) (2010) 5020–5027.
- [27] A. Ghita, F.C. Pascut, V. Sottile, C. Denning, I. Nottingher, Applications of Raman micro-spectroscopy to stem cell technology: label-free molecular discrimination and monitoring cell differentiation, *EPJ Techniques Instrum.* 2 (1) (2015) 1–14.
- [28] H. Bai, P. Chen, H. Fang, L. Lin, G. Tang, G. Mu, W. Gong, Z. Liu, H. Wu, H. Zhao, et al. Detecting viability transitions of umbilical cord mesenchymal stem cells by Raman micro-spectroscopy, *Laser Phys. Lett.* 8 (1) (2011) 78–84.
- [29] H.K. Chiang, F.Y. Peng, S.C. Hung, Y.C. Feng, In situ Raman spectroscopic monitoring of hydroxyapatite as human mesenchymal stem cells differentiate into osteoblasts, *J. Raman Spectrosc.* 40 (5) (2009) 546–549.
- [30] E. Azrad, D. Zahor, R. Vago, Z. Nevo, R. Doron, D. Robinson, L.A. Gheber, S. Rosenwaks, I. Bar, Probing the effect of an extract of elk velvet antler powder on mesenchymal stem cells using Raman microspectroscopy: enhanced differentiation toward osteogenic fate, *J. Raman Spectrosc.* 37 (4) (2006) 480–486.
- [31] C. Krafft, J. Popp, The many facets of Raman spectroscopy for biomedical analysis, *Anal. Bioanal. Chem.* 407 (3) (2015) 699–717.
- [32] B.S. Kim, C.C.I. Lee, J.E. Christensen, T.R. Huser, J.W. Chan, A.F. Tarantal, Growth, differentiation, and biochemical signatures of rhesus monkey mesenchymal stem cells, *Stem Cells Dev.* 17 (1) (2008) 185–198.
- [33] L. Harkness, S.M. Novikov, J. Beermann, S.I. Bozhevolnyi, M. Kassem, Identification of abnormal stem cells using Raman spectroscopy, *Stem Cells Dev.* 21 (12) (2012) 2152–2159.
- [34] A. Rygula, K. Majzner, K.M. Marzec, A. Kaczor, M. Pilarczyk, M. Baranska, Raman spectroscopy of proteins: a review, *J. Raman Spectrosc.* 44 (8) (2013) 1061–1076.
- [35] K. Czamara, K. Majzner, M. Pacia, K. Kochan, A. Kaczor, M. Baranska, Raman spectroscopy of lipids: a review, *J. Raman Spectrosc.* 46 (1) (2015) 4–20.
- [36] K. Maquelin, C. Kirschner, L.-P. Choo-Smith, N. van den Braak, H. Endtz, D. Naumann, G. Puppels, Identification of medically relevant microorganisms by vibrational spectroscopy, *J. Microbiol. Methods* 51 (3) (2002) 255–271.
- [37] G. Clemens, J.R. Hands, K.M. Dorling, M.J. Baker, Vibrational spectroscopic methods for cytology and cellular research, *Analyst* 139 (18) (2014) 4411–4444.
- [38] Q. Matthews, A. Jirasek, J. Lum, X. Duan, A.G. Brolo, Variability in Raman spectra of single human tumor cells cultured in vitro: correlation with cell cycle and culture confluency, *Appl. Spectrosc.* 64 (8) (2010) 871–887.
- [39] Z. Movasaghi, S. Rehman, I.U. Rehman, Raman spectroscopy of biological tissues, *Appl. Spectrosc. Rev.* 42 (5) (2007) 493–541.
- [40] T. Ichimura, K.F. Liang-da Chiu, S. Kawata, T.M. Watanabe, T. Yanagida, H. Fujita, Visualizing cell state transition using Raman spectroscopy, *PLoS one* 9 (1) (2014) 1–8.
- [41] E. Brauchle, S. Noor, E. Holtorf, C. Garbe, K. Schenke-Layland, C. Busch, Raman spectroscopy as an analytical tool for melanoma research, *Clin. Exp. Dermatol.* 39 (5) (2014) 636–645.
- [42] M. Pudlas, E. Brauchle, T.J. Klein, D.W. Huttmacher, K. Schenke-Layland, Non-invasive identification of proteoglycans and chondrocyte differentiation state by Raman microspectroscopy, *J. Biophotonics* 6 (2) (2013) 205–211.
- [43] G.S. Mandair, M.D. Morris, Contributions of Raman spectroscopy to the understanding of bone strength, *BoneKey Reports* 4 (620) (2015) 1–8.
- [44] J. Kobolak, A. Dinnyes, A. Memic, A. Khademhosseini, A. Mobasheri, Mesenchymal stem cells: identification, phenotypic characterization, biological properties and potential for regenerative medicine through biomaterial micro-engineering of their niche, *Methods* 99 (2016) 62–68.

Čvrste disperzije sa karbamazepinom: optimizacija formulacija, karakterizacija i ispitivanje dugoročne stabilnosti

Marko Krstić¹, Igor Lukić², Alma Bušatlić³, Nenad Lazarević⁴, Dragana Vasiljević¹

¹Farmaceutski fakultet, Katedra za farmaceutsku tehnologiju i kozmetologiju, Univerzitet u Beogradu, Vojvode Stepe 450, 11221 Beograd, Srbija

²ASV Beograd d.o.o., Kumodraška 380, 11221 Beograd, Srbija

³Adoc d. o. o., Milorada Jovanovića 11, 11030 Beograd, Srbija

⁴Centar za fiziku čvrstog stanje i nove materijale, Institut za fiziku, Univerzitet u Beogradu, Pregrevica 118, 11080 Beograd, Srbija

Izvod

U ovom radu je izvršena optimizacija formulacija čvrstih disperzija sa karbamazepinom, primenom metode D-optimalnog eksperimentalnog dizajna smeše, u cilju povećanja brzine rastvaranja navedene teško rastvorljive aktivne supstance. Primenom metode eksperimentalnog dizajna smeše, formulisane su čvrste disperzije variranjem udela karbamazepina (30-50 %), *Gelucire*® 44/14 (20-40 %) i polimera *Soluplus*® (30-50 %) (ulazni parametri). Izrađeno je 16 formulacija, iz kojih je ispitana *in vitro* brzina rastvaranja karbamazepina. Kao izlazni parametri praćeni su procenti rastvorenog karbamazepina, nakon 10, 20, 30, 45 i 60 minuta. Najveći udeo oslobođenog karbamazepina iz čvrstih disperzija (preko 80 % za 30 minuta) se postiže pri udelima aktivne supstance od oko 40 %, *Soluplus*® oko 45 % i *Gelucire*® 44/14 oko 25%. Nakon obrade podataka i optimizacije, iz različitih delova optimizacione oblasti odabrane su 3 formulacije za dalja ispitivanja. Rezultati ispitivanja odabranih optimizovanih uzoraka čvrstih disperzija nakon izrade, kao i nakon skladištenja 24 meseca pod ambijentalnim uslovima (25 °C, 40 % RH), dobijeni primenom metoda diferencijalne skenirajuće kalorimetrije (DSC), infracrvene spektroskopije sa Furijeovom transformacijom (FT-IR) i Ramanske spektroskopije potvrdili su njihovu stabilnost i očuvanje karbamazepina u polimrnom obliku III, jedinom farmakološki aktivnom obliku. Primenom PAMPA (*eng.* Parallel Artificial-Membrane Permeability Assay) testa pokazano je da je u dve, od tri ispitivane optimizovane čvrste disperzije očuvana, odnosno blago povećana permeabilnost karbamazepina.

Ključne reči: čvrste disperzije, karbamazepin, optimizacija formulacija, eksperimentalni dizajn, *in vitro* oslobađanje, fizička stabilnost.

Dostupno na Internetu sa adrese časopisa: <http://www.ache.org.rs/HI/>

NAUČNI RAD

UDC 615.015.14:004.896(043.3)

Hem. Ind. **72** (4) 191–204 (2018)

1. UVOD

Čvrste disperzije se definišu kao disperzije jedne ili više lekovitih supstanci u inernom nosaču (matriksu), u čvrstom stanju, dobijene metodom topljenja, metodom rastvaranja ili kombinacijom ove dve metode. Lekovite supstance u čvrstim disperzijama mogu biti dispergovane kao odvojene molekule, amorfne ili kristalne čestice, dok nosač može biti u kristalnom ili amorfnom stanju. Glavni razlog izrade čvrstih disperzija je povećanje rastvorljivosti/brzine rastvaranja teško rastvorljivih lekovitih supstanci, a sledstveno tome i njihova biološka raspoloživost [1]. Mehanizmi, kojima se to postiže su: rastvaranje lekovite supstance u inernom matriksu, smanjenje veličine čestica i smanjenje aglomeracije, poboljšano kvašenje i solubilizacija lekovite supstance molekulima nosača, povećana poroznost sistema, kao i prelazak lekovite supstance iz kristalnog u amorfni oblik [2 - 4].

Uprkos brojnim prednostima čvrstih disperzija sa teško rastvorljivim lekovitim supstancama, broj komercijalnih preparata tipa čvrstih disperzija na tržištu je mali, zbog problema koji se mogu javiti tokom procesa izrade/proizvodnje i skladištenja. Ovi problemi uključuju termičku nestabilnost lekovitih supstanci i nosača pri izradi čvrstih disperzija

Korespondencija: Marko Krstić, Farmaceutski fakultet, Katedra za farmaceutsku tehnologiju i kozmetologiju, Univerzitet u Beogradu, Vojvode Stepe 450, 11221 Beograd, Srbija

E-mail: mkrstic109@gmail.com; telefon : +381 11 3951-356

Rad primljen: 25. oktobra 2017.

Rad prihvaćen: 25. juna 2018.

<https://doi.org/10.2298/HEMIND171025013K>



metodom topljenja, ostatke rastvarača, primenom metode rastvaranja, rekristalizaciju lekovitih supstanci pri očvršćavanju, taloženje lekovite supstance posle rastvaranja u vodi zbog prezasićenja [2]. Takođe, može doći do razdvajanja lekovite supstance od matriksa, što ima za posledicu njenu neravnomernu raspodelu u čvrstoj disperziji, što se može odraziti na nepravilno doziranje lekovite supstance. Takođe, u toku procesa usitnjavanja izrađene čvrste disperzije može doći do prelaska amornog oblika lekovite supstance u kristalni. Veliki broj tehnoloških operacija u farmaceutskoj industriji, koji se sprovodi u toku proizvodnje čvrstih disperzija je takođe ograničavajući faktor za njihovu širu proizvodnju i primenu [5].

Razvoj formulacije predstavlja složen proces i često se između sastava formulacija i njenih karakteristika ne može uspostaviti jasna, a gotovo nikada linearna korelacija. Iz tog razloga, sve češće se u razvoju formulacija koriste tehnike eksperimentalnog dizajna, kako bi se uz što manji broj eksperimenata došlo do optimalne formulacije. Dizajn smeše predstavlja vrstu eksperimentalnog dizajna, koji se koristi kada se optimizuju formulacije koje imaju više različitih sastojaka, čiji je zbir udela stalan. Jedna od često korišćenih metoda eksperimentalnog dizajna smeše je D-optimalni dizajn, koji omogućava da se na osnovu najmanjeg broja eksperimenata sa velikom pouzdanošću dođe do formulacije željenih karakteristika. Poslednjih godina je uspešno korišćen u razvoju tečnih i čvrstih samo-emulgujućih sistema, kao i čvrstih disperzija [6 - 8].

Tokom izrade formulacija u kojima se povećava rastvorljivost teško rastvorljive lekovite supstance, njena permeabilnost se može smanjiti, povećati ili ostati nepromenjena [9]. Sa ciljem da se proceni uticaj različitih faktora na resorpciju lekovite supstance, kao i da se smanji broj ispitivanja na ljudima i životinjama, stalno se razvijaju i unapređuju *in vitro* metode za procenu resorpcije lekovite supstance [10,11]. PAMPA (*eng.* Parallel Artificial-Membrane Permeability Assay) test je brz, jeftin i jednostavan metod, kojim se može ispitati permeabilnost lekovitih supstanci pasivnom difuzijom. Simulacija bioloških membrana postiže se odgovarajućim odabirom rastvarača i supstanci od kojih se formira veštačka membrana. Dugi niz godina se PAMPA test koristio u proceni permeabilnosti novosintetisanih lekovitih supstanci, a tek poslednjih godina se koristi za ispitivanje permeabilnosti lekovite supstance iz različitih farmaceutskih oblika i savremenih nosača [8,9,12,13].

Cilj rada bio je razvoj i optimizacija formulacija čvrstih disperzija sa karbamazepinom, primenom metode D-optimalnog eksperimentalnog dizajna, radi povećanja brzine rastvaranja navedene lekovite supstance. Takođe, cilj rada je bio i karakterizacija i ispitivanje dugoročne stabilnosti optimizovanih formulacija čvrstih disperzija, nakon skladištenja uzoraka 24 meseca pod ambijentalnim uslovima.

2. MATERIJALI I METODE

2. 1. Materijal

U eksperimentalnom radu korišćen je karbamazepin (Ph. Eur. 8.0), kao model lekovita supstanca. Lauroil makrogol-32 gliceridi (*Gelucire*® 44/14; Gattefosse, Francuska) i makrogol 6000-poli(vinilkaprolaktam)-poli(vinilacetat) kalemljeni (*eng.* graft) polimer (*Soluplus*®; BASF ChemTrade GmbH, Nemačka) su korišćeni kao ekscipijensi za izradu čvrstih disperzija. Za rastvaranje polimera za izradu čvrstih disperzija korišćen je etanol (99,5 % V/V).

Dodekan (Sigma-Aldrich Chemie GmbH, Nemačka) i lecitin jajeta (Lipoid GmbH, Nemačka) korišćeni su u PAMPA testu. Svi drugi reagensi, koji su korišćeni za HPLC analizu, bili su analitičke čistoće.

2. 2. Metode

2. 2. 1. Formulacija čvrstih disperzija

Primenom optimizacione tehnike, uz pomoć kompjuterskog programa *Design Expert*® (version 8.0.7.1, Stat-Ease, SAD), definisan je D-optimalni eksperimentalni dizajn smeše, koju čine tri komponente, sastojci čvrstih disperzija: A –karmabazepin (koncentracija 30 – 50 %), B –*Gelucire*® 44/14 (koncentracija 20-40 %) i C –*Soluplus*® (koncentracija 30-50 %). Ove tri komponente predstavljaju ulazne parametre i njihov ukupan udeo je 100 %. Granične vrednosti udela komponenti postavljene su na osnovu literaturnih podataka i prethodnih ispitivanja. Kao izlazni parametri (odgovori sistema) praćeni su procenti rastvorenog karbamazepina nakon 10, 20, 30, 45 i 60 minuta, označeni sa R₁ - R₅.

Primenom D-optimalnog eksperimentalnog dizajna dobijen je eksperimentalni plan (Tabela 1.), koji se sastojao od 16 formulacija čvrstih disperzija, od kojih su 11 različitih i 5 ponovljenih, radi smanjenja eksperimentalne greške.

2. 2. 2. Izrada čvrstih disperzija

Čvrste disperzije su izrađene kombinacijom metoda topljenja i rastvaranja. *Gelucire*® 44/14 se otopi na temperaturi od 50 °C i dodaje, uz stalno mešanje, u patenu sa karbamazepinom. U disperziju karbamazepina i *Gelucire*® 44/14 dodaje se etanolni rastvor *Soluplus*®, uz neprekidno mešanje. Dobijena smeša se ostavi 72 h na sobnoj temperaturi, da etanol ispari. Izrađene čvrste disperzije su usitnjavane i prosejavane kroz sito 600 (Ph. Eur. 9.0).

Tabela 1. Eksperimentalni plan

Table 1. Experimental plan

Redni broj formulacije	Ulazni parametri		
	A - Sadržaj karbamazepina, %	B - Sadržaj <i>Gelucire</i> ® 44/14, %	C - Sadržaj <i>Soluplus</i> ®, %
F1	34,22	33,59	32,19
F2	33,54	23,93	42,53
F3	50,00	20,00	30,00
F4	30,00	20,01	49,99
F5	41,07	20,00	38,93
F6	30,00	31,48	38,52
F7	43,84	23,32	32,84
F8	30,00	36,08	33,92
F9	40,59	29,41	30,00
F10	36,44	27,30	36,26
F11	30,01	39,99	30,00
F12	50,00	20,00	30,00
F13	41,07	20,00	38,93
F14	30,01	39,99	30,00
F15	40,59	29,41	30,00
F16	30,00	20,01	49,99

2. 2. 3. *In vitro* procena brzine rastvaranja karbamazepina iz čvrstih disperzija

Ispitivanje brzine rastvaranja karbamazepina iz čvrstih disperzija (prašak, veličine čestica $\leq 600 \mu\text{m}$) i komercijalnih tableta sa trenutnim oslobađanjem (ravne površine, prečnika 10 mm), kao i čiste lekovite supstance, izvedeno je u aparaturi sa rotirajućom lopaticom (Erweka DT70, Nemačka). Prilikom ispitivanja, masa čvrstih disperzija je sadržala 200 mg karbamazepina, kao i komercijalne tablete. Kao akceptorski medijum je korišćena prečišćena voda (900 ml), zagrejana na 37°C , a brzina obrtanja rotirajuće lopatice bila je 50 obrtaja/min. Po 4 ml uzorka je uzimano nakon 10, 20, 30, 45 i 60 minuta, uz nadoknađivanje medijuma. U uzorcima je, nakon filtriranja, spektrofotometrijski (spektrofotometar Evolution 300, Termo Fisher Scientific, Engleska) određena količina rastvorenog karbamazepina na 287 nm. Kalibraciona kriva za određivanje karbamazepina data je u prilogu, na slici S1, pri čemu je postignuta visoka vrednost koeficijenta korelacije $r^2 = 0,999$, kao i visoka preciznost metode, pri merenju apsorbancije za svaki standardni rastvor 10 puta RSD nije prelazila 0,61%. Dobijeni rezultati predstavljaju srednju vrednost merenja procenta oslobođenog karbamazepina iz tri uzorka, \pm SD.

2. 2. 4. Modelovanje uticaja ulaznih na izlazne parametre primenom metode dizajna smeše

D-optimalnim eksperimentalnim dizajnom smeše moguće je dobiti odgovarajući regresioni model, koji, u ovom slučaju, opisuje uticaj udela komponenata čvrstih disperzija, kao nezavisno promenljivih, na procenat rastvorenog karbamazepina nakon 10, 20, 30, 45 i 60 minuta, kao zavisno promenljivih. Modeli, koje je najčešće moguće dobiti pri ovakvim ispitivanjima su:

$$\text{specijalni kubni: } Y = b_1A + b_2B + b_3C + b_{12}AB + b_{13}AC + b_{23}BC + b_{123}ABC \quad (1)$$

$$\text{kubni: } Y = b_1A + b_2B + b_3C + b_{12}AB + b_{13}AC + b_{23}BC + b_{123}ABC + \gamma_{12}AB(A - B) + \gamma_{13}AC(A - C) + \gamma_{23}BC(B - C), \quad (2)$$

gde su b_1 - b_{123} i γ_{12} - γ_{23} koeficijenti, koji pokazuju uticaj nezavisno promenljivih, kao i njihovih međusobnih interakcija na vrednost zavisno promenljive. Vrednosti koeficijenata izračunavane su regresionom analizom, korišćenjem programa *Design Expert*®.

Regresioni model, tj. finalna jednačina, razmatra L-Pseudo vrednosti ulaznih parametara (A, B, C), koje se kreću od 0 do 1. Vrednost 0 se dodeljuje donjoj granici, a vrednost 1 gornjoj granici ulaznih parametara, dok se sve ostale vrednosti izračunavaju iz sledećih jednačina:

$$\text{Karbamazepin: } A_{1(L\text{-Pseudo})} = (A_1 - 30)/20 \quad (3)$$

$$\text{Gelucire}^\circledast 44/14: B_{1(L\text{-Pseudo})} = (B_1 - 20)/20 \quad (4)$$

$$\text{Soluplus}^\circledast: C_{1(L\text{-Pseudo})} = (C_1 - 30)/20 \quad (5)$$

gde su A_1 , B_1 i C_1 bilo koje vrednosti koncentracija karbamazepina, *Gelucire*® 44/14 i *Soluplus*®, u okviru postavljenih granica.

Regresioni model, koji najbolje opisuje vezu između ulaznih i izlaznih parametara bira se na osnovu poređenja nekoliko statističkih parametara, uključujući standardnu devijaciju (SD), koeficijent višestruke korelacije (R^2), prilagođen koeficijent višestruke korelacije (prilagođeni R^2) i predvidiv ostatak zbira kvadrata (PRESS). PRESS pokazuje koliko se podaci dobro uklapaju u model i za izabrani model njegova vrednost treba da bude manja, u poređenju sa drugim modelima. Za razliku od vrednosti PRESS, vrednosti za R^2 i prilagođeni R^2 treba da budu veće u odnosu na druge modele, dok vrednost standardne devijacije treba da bude manja. Kompromisom između postavljenih zahteva vrši se odabir najpogodnijeg regresionog modela.

2. 2. 5. Optimizacija formulacija čvrstih disperzija

Nakon dobijanja regresionih modela, izvršena je optimizacija formulacija čvrstih disperzija sa sledećim zahtevima za procenat oslobođenog karbamazepina: $60\% < R_1 < 75\%$, $75\% < R_2 < 85\%$, $85\% < R_3 < 95\%$, $90\% < R_4 < 95\%$, $90\% < R_5 < 100\%$. Iz različitih delova optimizacione oblasti odabrane su 3 formulacije čvrstih disperzija, koje su izrađene i iz kojih je ispitana *in vitro* brzina oslobađanja karbamazepina, na prethodno opisan način. Radi procene uspešnosti predviđanja, predviđeni i eksperimentalno dobijeni profili brzine oslobađanja su upoređeni računanjem faktora sličnosti (f_1) i faktora razlike (f_2) [14].

2. 2. 6. Ispitivanja optimizovanih formulacija čvrstih disperzija

Iz tri optimizovane formulacije čvrstih disperzija izvršeno je *in vitro* ispitivanje brzine rastvaranja karbamazepina, kao i ispitivanje permeabilnosti karbamazepina, primenom PAMPA testa. Diferencijalna skenirajuća kalorimetrija (DSC), infracrvena spektroskopija sa Furijevom transformacijom (FT-IR) i Ramanska spektroskopija su sprovedene nakon izrade, kao i nakon 24 meseca čuvanja uzoraka pod ambijentalnim uslovima (25 °C, 40 % RH), u cilju procene dugoročne stabilnosti čvrstih disperzija.

2. 2. 7. Procena permeabilnosti karbamazepina

Procena permeabilnosti karbamazepina iz odabranih formulacija i čistog karbamazepina izvršena je korišćenjem PAMPA testa.

Prilikom izvođenja PAMPA testa, kao nosač veštačke membrane i akceptorski panel korišćen je filtracioni panel sa 96 bazena, izrađen od hidrofilnog poliviniliden difluorida (PVDF) (Millipore, SAD). U bazene akceptorske ploče naneto je po 5 µl rastvora lecitina jajeta u dodekanu (1 %, m/V) i ostavljeno 2 h na sobnoj temperaturi, da rastvarač potpuno ispari. Na ovaj način je dno akceptorske ploče impregnirano lecitinom i formirana je veštačka membrana, koja u kontaktu sa rastvorom pufera formira multilamelarni lipidni dvosloj između pora filtera. Akceptorska ploča je postavljena na donorsku, u čije je bazene prethodno naneto po 300 µl suspenzije čistog karbamazepina i odabranih formulacija u fosfatnom puferu pH 5,5. Istovremeno je u bazene akceptorske ploče naneto po 300 µl fosfatnog pufera pH 5,5. Akceptorska ploča je prekrivena folijom, kako bi se sprečilo isparavanje rastvarača. Ispitivanje za svaki uzorak je vršeno u triplicatu, a rezultat je predstavljen kao srednja vrednost \pm SD. Nakon inkubacije od 2 h na sobnoj temperaturi, koncentracija karbamazepina u bazenima akceptorske ploče određivana je prethodno razvijenom i validiranim HPLC metodom [8,13].

Koeficijenti permeabilnosti (P_{app}) izračunati su primenom sledećih jednačina [15]:

$$T/\% = 100 \frac{A_R V_R}{A_{D0} V_D} \quad (6)$$

$$P_{app} = \frac{V_D V_R}{(V_D + V_R) St} \ln \frac{100 V_D}{100 V_D - T(V_D + V_R)} \quad (7)$$

gde su:

V_D i V_R – zapremine donorskog i akceptorskog rastvora (ml);

A_{D0} i A_R – HPLC površine pikova pripremljenog rastvora ispitivanog uzorka i akceptorskog rastvora;

S – površina membrane između komora (0,28 cm²);

t – vreme inkubacije (s).

2. 2. 8. Diferencijalna skenirajuća kalorimetrija (DSC)

DSC merenja izvršena su na Mettler–Toledo AG termalnom analizatoru (Mettler–Toledo AG, Analytical, Švajcarska). Precizno odmerena masa uzorka (2–5 mg) stavljena je u T-Zero® aluminijumske posude, koje su potom hermetički zatvarane, a merenja vršena na temperaturama od 20 do 200 °C, pri brzini zagrevanja od 10 °C/min, u struji azota, sa protokom od 100 ml/min.

2. 2. 9. Infracrvena spektroskopija sa Furijevom transformacijom (FT-IR)

FT-IR spektri u regionu od 600–4000 cm⁻¹, čistog karbamazepina i tri optimizovane formulacije, dobijeni su korišćenjem Shimadzu IR-Prestige-21 FT-IR spektrometra spojenog sa horizontalnim Golden Gate MKII jednorefleksnim ATR sistemom (Specac, 214 Kent, Velika Britanija) i opremljenog sa Zn-Se sočivom. Nakon odgovarajuće pripreme uzorka urađeno je šesnaest snimanja za svaki uzorak.

2. 2. 10. Ramanska spektroskopija

Merenje Ramanskih spektra je izvedeno korišćenjem JY T64000 Ramanskog spektrometra (Horiba Scientific, Nemačka) sa 1800/1800/1800 zarez/mm kombinacijom rešetki i Symphony detektorom hlađenim tečnim azotom. Sistem je postavljen u mikro-konfiguraciju sa objektivom x100. Ulazni slit je postavljen na 100 µm. Za ekscitaciju je korišćen čvrstotelni laser, talasne dužine 532 nm.

3. REZULTATI I DISKUSIJA

3. 1. *In vitro* procena brzine rastvaranja karbamazepina iz čvrstih disperzija

Rezultati *in vitro* brzine rastvaranja karbamazepina iz 16 izrađenih čvrstih disperzija, komercijalnih tableta i čiste supstance, prikazani su u tabeli 2 (i na slici S2., Prilog rada).

Tabela 2. Procenti rastvorenog karbamazepina iz čvrstih disperzija, komercijalnih tableta i čiste lekovite supstance, u funkciji vremena

Uzorak	Količina rastvorenog karbamazepina u funkciji vremena, %						
	10 min	20 min	30 min	45 min	60 min	90 min	120 min
F1	56,20±1,24	80,60±3,21	90,60±1,24	96,00±0,37	95,60±0,21	96,70±0,43	98,80±0,21
F2	67,70±1,06	85,40±1,74	92,00±1,21	96,80±0,65	98,30±0,23	98,70±0,37	98,20±0,09
F3	60,60±0,86	78,30±1,27	85,30±2,29	90,30±1,57	93,30±0,33	94,80±0,54	96,50±0,71
F4	62,50±1,94	85,04±0,68	93,62±0,71	98,26±1,02	99,30±0,09	99,61±0,23	99,81±0,15
F5	65,00±0,33	90,40±0,23	95,60±0,17	97,50±0,06	97,70±0,38	99,00±0,16	99,20±0,25
F6	31,00±2,21	49,20±3,21	62,80±3,24	83,10±1,16	83,50±1,53	94,50±0,34	93,90±0,11
F7	53,48±0,97	73,86±1,12	78,92±0,86	83,33±0,14	83,01±0,21	84,36±0,21	87,32±1,23
F8	48,37±1,46	76,99±2,23	82,92±2,96	89,71±0,32	90,53±0,45	92,65±0,23	94,87±0,87
F9	42,26±2,14	61,53±1,32	70,87±1,31	83,19±0,96	83,23±0,14	89,42±1,54	90,61±0,37
F10	63,28±1,32	79,26±0,78	87,40±0,65	91,11±0,32	92,14±0,85	94,77±1,09	96,23±1,23
F11	52,77±2,87	70,39±2,21	79,14±0,33	87,15±0,39	87,69±0,65	92,10±1,12	94,58±2,22
F12	60,60±0,86	78,30±1,27	85,30±2,29	90,30±1,57	93,30±0,33	94,80±0,54	96,50±0,71
F13	65,00±0,33	90,40±0,23	95,60±0,17	97,50±0,06	97,70±0,38	99,00±0,16	99,20±0,25
F14	52,77±2,87	70,39±2,21	79,14±0,33	87,15±0,39	87,69±0,65	92,10±1,12	94,58±2,22
F15	42,26±2,14	61,53±1,32	70,87±1,31	83,19±0,96	83,23±0,14	89,42±1,54	90,61±0,37
F16	62,50±1,94	85,04±0,68	93,62±0,71	98,26±1,02	99,30±0,09	99,61±0,23	99,81±0,15
Karbamazepin	4,91±0,09	26,42±0,87	41,56±0,24	41,89±0,11	48,85±0,98	53,00±0,21	59,41±1,04
Tablete*	13,99±1,02	22,52±1,21	30,36±0,76	38,08±0,34	46,45±1,98	50,98±2,36	55,63±0,47

*Komercijalne tablete karbamazepina sa trenutnim oslobađanjem lekovite supstance

Najveće razlike u procentu rastvorenog karbamazepina iz ispitivanih čvrstih disperzija primećene su posle 10 minuta (od 31,00 % do 67,70 %). Kod većine ispitivanih formulacija (F1 – F5, F8, F10, F12 – F14; Tabela 2.) nakon 30 minuta dolazi do oslobađanja više od 80% karbamazepina, što odgovara zahtevima Američke farmakopeje (USP 38/NF33) za preparate sa trenutnim oslobađanjem aktivne supstance. Može se smatrati da je povećanje brzine oslobađanja karbamazepina iz ispitivanih čvrstih disperzija posledica površinske aktivnosti korišćenih ekscipijenasa. Procenti oslobođenog karbamazepina nakon 30 minuta iz uzoraka F6, F9 i F16, znatno manji od 80%, ukazuju da udeli tj. međusobni odnosi karbamazepina i ekscipijenasa (*Gelucire*® 44/14 i *Soluplus*®) nisu odgovarajući, jer ne dovode do željenog oslobađanja aktivne supstance. I pored toga, procenti oslobođenog karbamazepina iz čvrstih disperzija su veći u poređenju sa čistom supstancom (41,56 %, nakon 30 min) i komercijalnim tabletama (30,36 %, nakon 30 min). Nakon 90 i 120 minuta se ne uočavaju značajne razlike u brzini rastvaranja karbamazepina (Tabela 2.), pa se vrednosti procenta oslobođenog karbamazepina nakon 60-og minuta nisu koristile kao izlazni parametri za modelovanje u eksperimentalnom dizajnu.

3. 2. Modelovanje uticaja ulaznih na izlazne parametre primenom metode dizajna smeše

Primenom metode D-optimalnog eksperimentalnog dizajna smeše, izvršen je izbor regresionog modela, koji prema statističkim parametrima najbolje opisuje vezu između ulaznih i izlaznih parametara. Na osnovu poređenja statističkih parametara (pomenutih u delu: Materijali), odabran je kubni model, koji je najviše odgovarao zahtevima za izlazni parametar R_1 (procenat rastvorenog karbamazepina nakon 10 minuta) (Tabela 3.). Prilikom primene regresionih modela isprobane su linearna i kvadratna funkcija, međutim na osnovu dobijenih profila brzine rastvaranja karbamazepina iz čvrstih disperzija nije ni bilo očekivano dobro uklapanje u ove modele, na šta ukazuju i niske vrednosti koeficijenta determinacije za ova dva modela (Tabela 3.).

Tabela 3. Prikaz statističkih parametara za izbor regresionog modela za R_1 (procenat rastvorenog karbamazepina nakon 10 minuta)
Table 3. Presentation of statistical parameters for selecting a regression model for R_1 (percentage of dissolved carbamazepine after 10 minutes)

Model	Standardna devijacija	R^2	Prilagođeni R^2	PRESS
Linearni	8,93	0,3365	0,2344	1402,84
Kvadratni	7,96	0,5941	0,3911	1814,92
Specijalni kubni	4,67	0,8743	0,7905	723,03
Kubni	1,59	0,9903	0,9757	1368,88

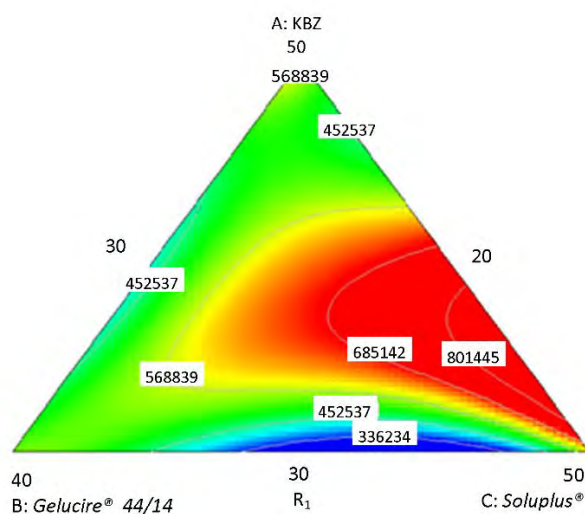
Nakon dobijanja regresionog modela vršeno je isključivanje parametara, koji nemaju statističku značajnost ($p > 0,05$). Za izlazni parametar R_1 (procenat oslobođenog karbamazepina nakon 10 minuta) isključen je koeficijent uz parametar AB(A-B), čiji je $p = 0,7204$. Uticaj svih ostalih parametara je bio statistički značajan. U tabeli S1 (Prilog) prikazana je statistička značajnost parametara pre i nakon isključivanja parametra AB(A-B) koji nema statistički značaj.

Nakon toga je dobijena jednačina, na osnovu koje je moguće za bilo koje vrednosti ulaznih parametara, a u okviru postavljenih graničnih vrednosti, predvideti procenat rastvorenog karbamazepina nakon 10 minuta. Statistički parametri ove jednačine su $p < 0,0001$ i $F = 87,06$, a ona glasi:

$$R_1 = 60,76A + 53,03B + 62,69C - 57,81AB + 39,90AC - 124,23BC + 639,92ABC - 235,24AC(A-C) + 132,67BC(B-C) \quad (8)$$

Na slici 1. prikazan je 2D trokomponentni dijagram, koji opisuje uticaj ulaznih parametara na R_1 . Na temena trouglova predstavljene su maksimalne vrednosti ispitivanih parametara, dok se na sredinama naspramnih stranica nalaze minimalne vrednosti. Crveni, žuti, zeleni, svetlo plavi i tamno plavi regioni predstavljaju regione u kojima su postignuti različiti procenti oslobođenog karbamazepina, od najvišeg (crveni) ka najnižem (tamno plavi).

Najveći procenat rastvorenog karbamazepina, nakon 10 minuta, dobija se sa udelom ove supstance od oko 40 % u formulaciji, dok je pri udelima karbamazepina od oko 30 % ili oko 50 % manji procenat rastvorene supstance (Slika 1.). Ovakava zavisnost uočava se i nakon 20, 30, 45 i 60 minuta. Povećanje brzine rastvaranja karbamazepina iz čvrstih disperzija koje sadrže Soluplus® i Gelucire® 44/14, verovatno je posledica boljeg kvašenja lekovite supstance, kao i njene solubilizacije ekscipijensima [16].



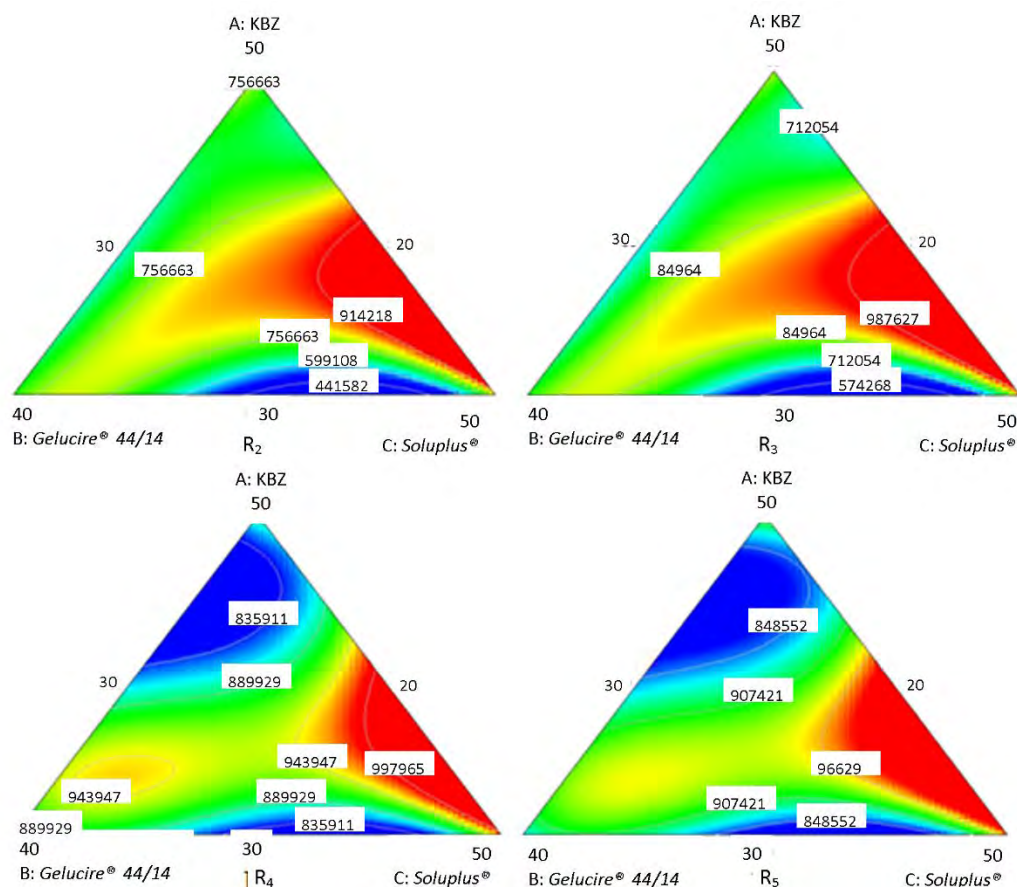
Slika 1. 2D trokomponentni dijagram koji opisuje uticaj ulaznih parametara na R_1 . Na temena trouglova predstavljene su maksimalne vrednosti ispitivanih parametara, dok se na sredinama naspramnih stranica nalaze minimalne vrednosti. Crveni, žuti, zeleni, svetlo plavi i tamno plavi regioni predstavljaju regione u kojima su postignuti različiti procenti oslobođenog karbamazepina, od najvišeg (crveni) ka najnižem (tamno plavi)
Figure 1. 2D ternary diagram which describes the effect of input parameters on R_1 . The maximum values of the tested parameters are presented on the triangle vertex, while the minimal values are presented in the center of the contrary sides. Red, yellow, green, light blue and dark blue regions represent regions where different percentages of released carbamazepine have been achieved, from the highest (red) to the lowest value (dark blue), respectively.

Za ostale izlazne parametre (R_2 - R_5) odabrani regresioni model bio je takođe kubni, a dobijene su jednačine, čije su vrednosti faktorskih efekata i njihovi statistički parametri prikazani u tabeli 4.

Tabela 4. Vrednosti faktorskih efekata i njihovi statistički parametri za izlazne parametre $R_2 - R_5$ Table 4. Values of factor effects, and their statistical parameters for output parameters $R_2 - R_5$

	R_2	R_3	R_4	R_5
A	+78,67	+85,30	+90,43	+93,41
B	+70,95	+79,57	+87,31	+87,81
C	+85,42	+93,88	+98,38	+99,41
AB	-50,59	-42,78	-16,71	-24,49
AC	+68,08	+54,49	+25,77	+21,22
BC	-146,39	-127,33	-44,88	-47,95
ABC	+573,90	+504,94	+130,63	+155,06
AB(A-B)	/	/	-88,81	-82,33
AC(A-C)	-281,97	-259,30	-99,20	-130,66
BC(B-C)	+261,15	+228,41	+71,52	+79,88
Statistički parametri odabranih (kubnih) modela				
p	0,0003	0,0003	0,0001	<0,0001
F	21,38	20,84	41,19	75,98

Na slici 2. prikazani su 2D trokomponentni dijagrami, koji opisuju uticaj ulaznih parametara na R_2 , R_3 , R_4 i R_5 (procenat rastvorenog karbamazepina nakon 20, 30, 45 i 60 minuta).

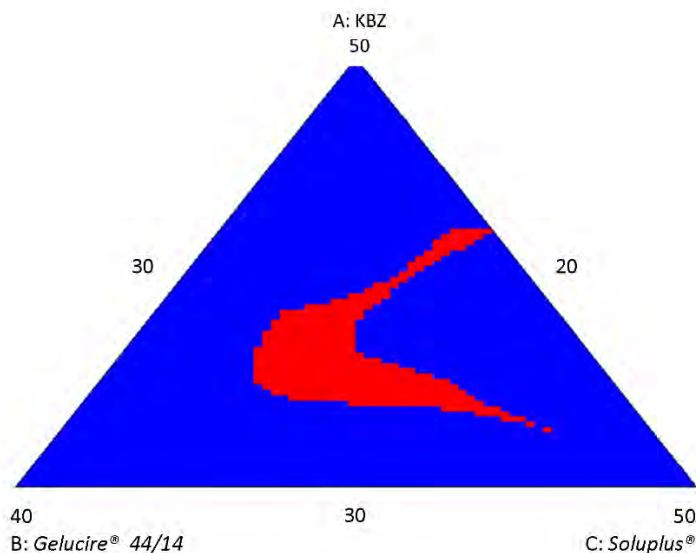


Slika 2. 2D trokomponentni dijagrami koji opisuju uticaj ulaznih parametara na R_2 (gore levo), R_3 (gore desno), R_4 (dole levo) i R_5 (dole desno). Na temena trouglova predstavljene su maksimalne vrednosti ispitivanih parametara, dok se na sredinama naspramnih stranica nalaze minimalne vrednosti. Crveni, žuti, zeleni, svetlo plavi i tamno plavi regioni predstavljaju regione u kojima su postignuti različiti procenti oslobođenog karbamazepina, od najvišeg (crveni) ka najnižem (tamno plavi)

Figure 2. 2D ternary diagram which describes the effect of input parameters on R_2 (up left), R_3 (up right), R_4 (down left) i R_5 (down right). The maximum values of the tested parameters are presented on the triangle vertex, while the minimal values are presented in the center of the contrary sides. Red, yellow, green, light blue and dark blue regions represent regions where different percentages of released carbamazepine have been achieved, from the highest (red) to the lowest value (dark blue), respectively

3. 3. Optimizacija formulacija čvrstih disperzija

Trokomponentni dijagram (Slika 3.) pokazuje oblast u kojoj se ukrštaju zadate vrednosti odgovora, postavljene tokom optimizacije. Kompiuterski program *Design Expert*® je u okviru ove oblasti predvideo 22 formulacije, čiji su sastavi (udeli komponenti) i predviđene vrednosti izlaznih parametara prikazani u tabeli 5.



Slika 3. 2D trokomponentni dijagram sa regionom (označenom crvenom bojom) u okviru koga se nalaze optimalne formulacije. Na temena trouglova predstavljene su maksimalne vrednosti ispitivanih parametara, dok se na sredinama naspramnih stranica nalaze minimalne vrednosti.

Figure 3. 2D ternary diagram with the region (marked in red) indicating optimal formulations. The maximum values of the tested parameters are presented on the triangle vertex, while the minimal values are presented in the center of the contrary sides.

Tabela 5. Formulacije čvrstih disperzija predložene kompiuterskim programom *Design Expert*® (sastav i vrednosti izlaznih parametara)

Table 5. Formulations of optimal solid dispersions proposed by computer program *Design Expert*® (the composition and values of the output parameters)

Oznaka formulacije	Ulazni parametri			Izlazni parametri				
	Sadržaj karbamazepina, %	Sadržaj Gelucire® 44/14, %	Sadržaj Soluplus®, %	R ₁	R ₂	R ₃	R ₄	R ₅
O1	33,92	26,24	39,84	62,80	78,63	87,07	93,35	94,56
O2	36,90	27,13	35,97	65,55	84,47	91,32	92,40	92,95
O3	39,15	24,59	36,26	65,67	84,39	90,69	90,59	90,96
O4	35,30	30,33	34,37	60,53	81,84	89,23	93,80	94,10
O5	38,66	25,11	36,23	66,08	84,72	91,12	90,97	91,41
O6	37,91	25,99	36,10	66,13	84,78	91,37	91,54	92,04
O7	33,56	25,39	41,05	62,44	77,39	86,16	93,52	94,91
O8	35,69	26,77	37,54	66,64	84,69	91,84	93,64	94,54
O9	40,94	21,62	37,44	63,68	84,90	90,49	92,46	92,49
O10	36,20	27,60	36,20	65,28	84,28	91,30	93,02	93,64
O11	34,52	29,84	35,64	61,16	81,79	89,37	93,85	94,41
O12	34,67	28,71	36,62	62,66	81,95	89,56	93,57	94,29
O13	36,87	26,85	36,28	66,15	84,89	91,71	92,57	93,18
O14	35,28	29,64	35,08	61,85	82,51	89,86	93,67	94,11
O15	36,27	29,03	34,70	62,27	82,55	89,72	92,81	93,15
O16	35,90	29,77	34,33	61,09	81,94	89,23	93,23	93,50
O17	37,22	26,81	35,97	65,75	84,58	91,35	92,11	92,65
O18	33,78	24,83	41,39	61,82	80,18	88,61	94,48	96,01
O19	35,49	29,28	35,23	62,45	82,80	90,08	93,49	93,96
O20	34,12	29,08	36,80	61,02	80,40	88,29	93,43	94,17
O21	41,56	21,32	37,12	61,05	82,32	88,01	91,67	91,45
O22	37,98	27,44	34,58	62,53	81,91	88,85	90,56	90,81

R₁, R₂, R₃, R₄, R₅: procenat rastvorenog karbamazepina nakon 10, 20, 30, 45, 60 minuta.

3. 4. Ispitivanja odabranih optimizovanih formulacija čvrstih disperzija

Radi procene uspešnosti predviđanja, iz različitih delova optimizacione oblasti odabrane su tri formulacije čvrstih disperzija (O2, O4 i O21; Tabela 5.), koje su izrađene na prethodno opisan način i iz kojih je ispitana *in vitro* brzina rastvaranja karbamazepina.

Predviđeni i eksperimentalno dobijeni procenti rastvorenog karbamazepina iz odabranih čvrstih disperzija prikazani su u tabeli 6. Na osnovu poređenja eksperimentalno dobijenih i predviđenih profila brzine rastvaranja karbamazepina iz izrađenih čvrstih disperzija i izračunatih vrednosti za faktore razlike f_1 i faktore sličnosti f_2 (Tabela 6.), uočava se veliko slaganje između predviđenih i dobijenih profila brzine rastvaranja lekovite supstance i zaključuje se da se ovi profili mogu smatrati sličnim, jer je $f_1 < 15$ i $f_2 > 50$ [14], kao i da nema statistički značajne razlike među njima.

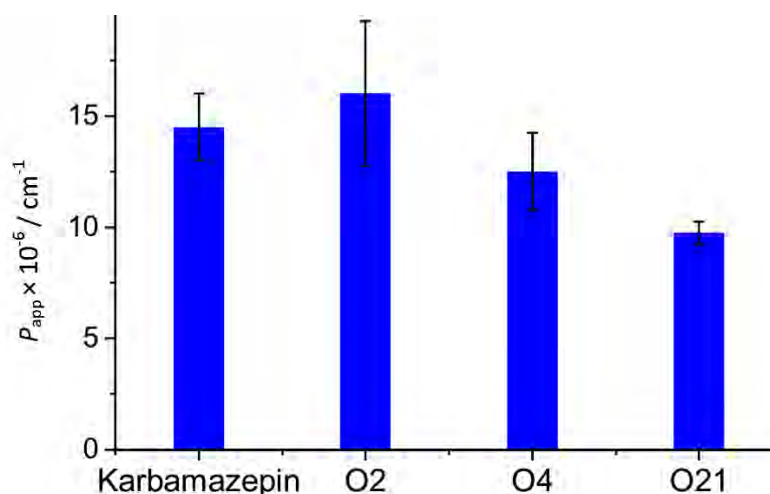
Tabela 6. Dobijeni i predviđeni sadržaj rastvorenog karbamazepina iz čvrstih disperzija, faktori razlike (f_1) i faktori sličnosti (f_2)

Table 6. Obtained and predicted percentages of dissolved carbamazepine from solid dispersions, the difference factors (f_1) and the similarity factors (f_2)

	Sadržaj rastvorenog karbamazepina, %					
	Formulacija O2		Formulacija O4		Formulacija O21	
	dobijeno	predviđeno	dobijeno	predviđeno	dobijeno	predviđeno
10	59,21	63,19	61,61	61,12	54,55	60,17
20	78,22	81,97	75,82	75,81	78,74	80,57
30	88,70	89,60	85,90	85,30	88,18	87,84
45	93,42	93,52	96,45	94,86	94,21	91,65
60	96,55	94,31	98,76	96,56	96,19	91,78
f_1	2,64		1,17		3,58	
f_2	88,12		96,02		83,93	

3. 5. Procena permeabilnosti karbamazepina

Rezultati ispitivanja permeabilnosti karbamazepina (PAMPA test) iz ispitivanih formulacija i čistog karbamazepina dati su na slici 4. Dobijena vrednost koeficijenta permeabilnosti za čist karbamazepin ($14,52 \pm 1,50 \times 10^{-6}$ cm/s) bila je u skladu sa prethodno dobijenim rezultatima u sličnim ispitivanjima [8, 13, 15]. Rezultati PAMPA testa pokazuju da je postignuto izvesno povećanje permeabilnosti karbamazepina iz formulacije O2 ($16,18 \pm 3,17 \times 10^{-6}$ cm/s), dok je permeabilnost neznatno smanjena u slučaju uzorka O4 ($12,41 \pm 1,88 \times 10^{-6}$ cm/s), ali ove razlike nisu statistički značajne ($p > 0,05$). Permeabilnost karbamazepina iz formulacije O21 je značajno smanjena ($9,71 \pm 0,61 \times 10^{-6}$ cm/s) ($p < 0,05$), što može biti posledica najnižeg udela *Gelucire*® 44/14 u ovoj formulaciji. Ovaj ekscipijens verovatno stupa u interakciju sa veštačkom membranom, pa se može pretpostaviti da se sa smanjenjem njegove koncentracije smanjuje i propustljivost membrane, a sa tim i permeabilnost karbamazepina iz navedenog uzoraka čvrste disperzije [17].



Slika 4. Rezultati PAMPA testa za prašak karbamazepina i tri odabrane optimizovane formulacije (O2, O4 i O21) (P_{app} - koeficijent permeabilnosti)

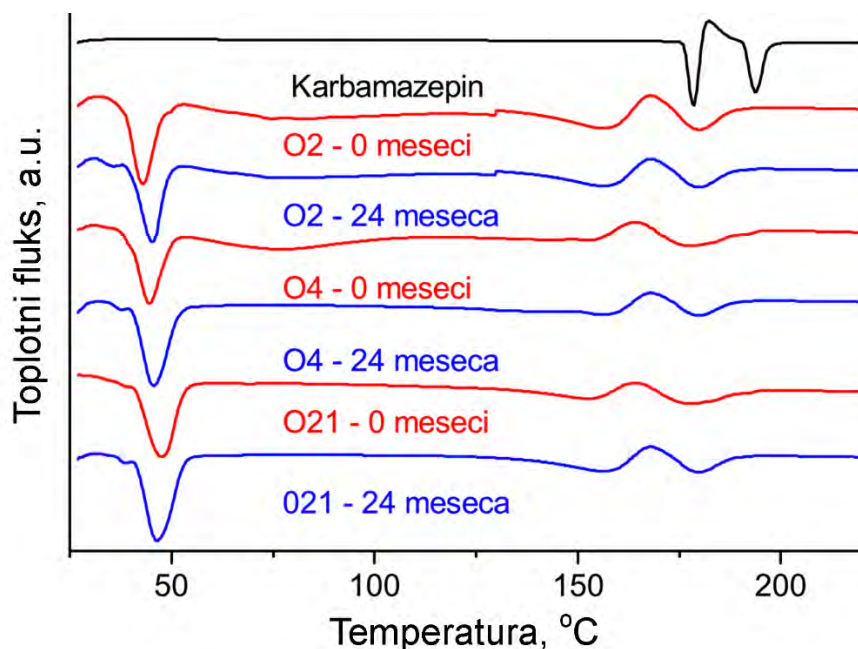
Figure 4. Results of the PAMPA test for carbamazepine powder and three selected optimized formulations (O2, O4 i O21) (P_{app} - permeability coefficient)

Rezultati ove studije idu u prilog osnovnoj pretpostavci da prilikom razvoja formulacija sa teško rastvorljivom lekovitom supstancom treba postići kompromis između brzine rastvaranja, sa jedne, i permeabilnosti, sa druge strane. Dobra rastvorljivost lekovite supstance u vodenoj sredini gastrointestinalnog trakta je skoro uvek preduslov za dobru

bioraspoloživost lekovite supstance nakon peroralne primene. Međutim, tokom izrade formulacija u kojima se povećava rastvorljivost lekovitih supstanci, može doći do promene permeabilnosti, odnosno uticaja na resorpciju [12]. Prilikom povećanja brzine rastvaranja lekovite supstance, najčešće dolazi do formiranja struktura koje su veće od molekula same lekovite supstance. Veličina čestica je važan faktor koji utiče na resorpciju lekovite supstance, naročito onih koje su teško rastvorljive u vodi ili biološkim tečnostima. Kao posledica formiranja struktura koje su veće od molekula same lekovite supstance, može nastati problem sa permeabilnošću aktivne supstance iz ovakvih formulacija. Takođe, primena površinski aktivnih materija za povećanje rastvorljivosti lipofilnih lekovitih supstanci, koje pokazuju visoku permeabilnost, kakav je i sam karbamazepin (BSK klasa II), usled solubilizacije lekovite supstance primenom površinski aktivne materije može doći do smanjenja slobodne frakcije lekovite supstance, što posledično vodi smanjenju permeabilnosti, što verovatno jeste još jedan od razloga za smanjenje permeabilnosti iz formulacije O21. Iz svega navedenog, može se smatrati da su formulacije čvrstih disperzija O2 i O4 prihvatljive, jer je postignuta ravnoteža između brzine rastvaranja i permeabilnosti karbamazepina [13,18].

3. 6. Diferencijalna skenirajuća kalorimetrija

Na DSC krivoj čistog karbamazepina (Slika 5), na osnovu karakterističnih pikova, može se zaključiti da je karbamazepin u polimorfnom obliku III, jedinom farmakološki aktivnom obliku [19-21]. Na to ukazuje endotermni pik na oko 178 °C, koji je posledica topljenja polimornog oblika III karbamazepina, a egzotermni pik na oko 181 °C predstavlja rekristalizaciju polimornog oblika III karbamazepina u polimorfni oblik I. Topljenje polimornog oblika I je verovatno uzrok pojave endoternog pika na 194 °C. Karakteristični pikovi topljenja polimornog oblika III karbamazepina u temperaturnom opsegu od 150 do 180 °C [7,19,20] su uočeni na DSC krivama svih ispitivanih formulacija, kako u trenutku izrade, tako i nakon 24 meseca čuvanja pod ambijentalnim uslovima. Uočavaju se na gotovo svim DSC krivama i endotermni pikovi topljenja polimornog oblika I, međutim rekristalizacioni egzotermni pikovi prelaska polimornog oblika III u polimorfni oblik I nisu uočeni na svim DSC krivama. Izostajanje egzotermnih pikova prelaska karbamazepina iz polimornog oblika III u polimorfni oblik I su verovatno posledica malog udela lekovite supstance u uzorku i prisustva ekscipijenasa u formulaciji. Takođe, na DSC krivama ispitivanih formulacija uočavaju se i endotermni pikovi topljenja u opsegu temperatura od 40 do 50 °C, koji su verovatno posledica topljenja *Gelucire*® 44/14, prisutnog u formulacijama. Rezultati DSC analize ukazuju da je karbamazepin u svim ispitivanim formulacijama prisutan u polimorfnom obliku III i da su uzorci stabilni tokom dvogodišnjeg čuvanja.



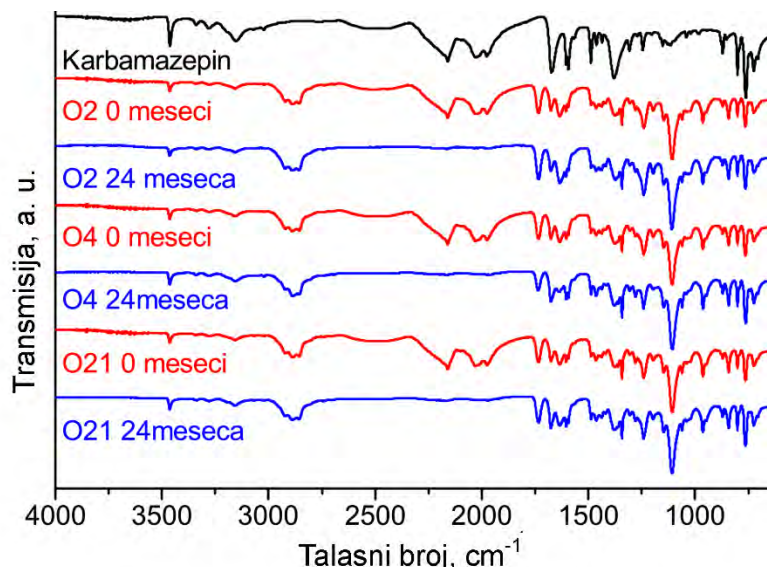
Slika 5. DSC krive karbamazepina i ispitivanih uzoraka O2, O4 i O21 nakon izrade i nakon 24 meseca

Figure 5. DSC curve of carbamazepine and investigated samples O2, O4 i O21 initially after preparation and after 24 months

3. 7. Infracrvena spektroskopija sa Furjeovom transformacijom

Na spektru čistog karbamazepina (Slika 6.) se uočavaju karakteristične trake na 3462 cm^{-1} (–NH valenciona vibracija), 1674 cm^{-1} (–CO–R vibracija), 1593 cm^{-1} i 1605 cm^{-1} (opseg za –C=C– i –C=O vibraciju i –NH deformaciju), što takođe ukazuje da je on u polimorfnom obliku III [22, 23]. U tri izrađene optimizovane formulacije se takođe uočavaju ove karakteristične trake, što ukazuje da nije došlo do interakcije između karbamazepina i ekscipijenasa i da je karbamazepin ostao u polimorfnom obliku III. Nakon čuvanja uzoraka 24 meseca pod ambijentalnim uslovima, takođe se uočavaju

karakteristične trake na spektru ovih formulacija. I ovi rezultati idu u prilog tome da je karbamazepin i nakon navedenog vremenskog perioda ostao u kristalnom polimorfnom obliku III.



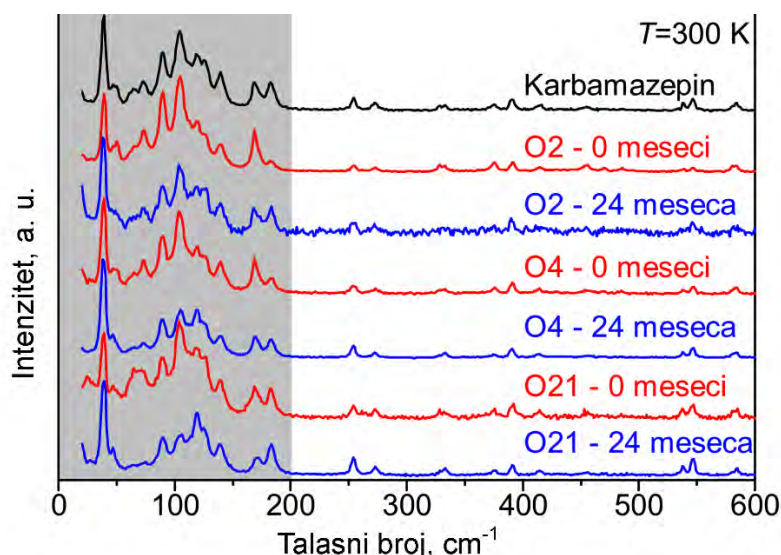
Slika 6. FT-IR spektri karbamazepina i ispitivanih uzoraka O2, O4 i O21 nakon izrade i nakon 24 meseca

Figure 6. FT-IR spectra of pure carbamazepine and investigated samples O2, O4 i O21 initially after preparation and after 24 months

3. 8. Ramanska spektroskopija

Na slici 7. prikazani su spektri Ramanovog rasejanja karbamazepina i tri odabrane optimizovane formulacije, nakon izrade i nakon 24 meseca čuvanja pod ambijentalnim uslovima.

U molekularnom kristalu, generalno, mogu se razlikovati dva spektralna opsega Ramanovog rasejanja, visoko energetske (konvencionalni) opseg, koji se sastoji od intramolekulskih vibracija i nisko energetske opseg (ispod 200 cm^{-1}) u kojem dominiraju intermolekulske vibracije (Slika 7) [24]. Iako visoko energetske opseg takođe može nositi informaciju vezanu za kristalnu strukturu, uočene promene između različitih polimorfnih oblika su obično male i često ograničene na varijacije u intenzitetu Ramanskih pikova. Istraživanje nisko energetske opsega pruža direktan uvid u kristalnu strukturu materijala [24]. U Ramanskim spektrima prisutni su svi karakteristični pikovi polimorfnog oblika III karbamazepina, sa naglaskom na pikove na oko 40, 91 i 141 cm^{-1} [25, 26]. Isti pikovi su prisutni i u uzorcima nakon 24 meseca, čime se potvrđuje očuvanje polimorfnog oblika III i stabilnost izrađenih formulacija nakon 24 meseca čuvanja. Varijacije u relativnim intenzitetima Ramanskih pikova posledica su različite orijentacije kristalita.



Slika 7. Ramanski spektri karbamazepina i ispitivanih uzoraka O2, O4 i O21 nakon izrade i nakon 24 meseca

Figure 7. Raman scattering spectra of carbamazepine and investigated samples O2, O4 i O21 initially after preparation and after 24 months

Rezultati ispitivanja, dobijeni primenom tri tehnike karakterizacije (DSC, FT-IR i Ramanska spektroskopija) su u saglasnosti i potvrđuju da je karbamazepin u uzorcima ostao u polimorfnom obliku III, kao i da su tri odabrane formulacije stabilne nakon 24 meseca čuvanja pod ambijentalnim uslovima.

4. ZAKLJUČAK

Primenom metode eksperimentalnog dizajna smeše, formulisane su čvrste disperzije variranjem udela karbamazepina, *Gelucire*® 44/14 i polimera *Soluplus*®. Rezultati ispitivanja *in vitro* brzine rastvaranja karbamazepina iz čvrstih disperzija su pokazali da je postignuto povećanje procenta rastvorenog karbamazepina iz čvrstih disperzija, u odnosu na čistu supstancu i komercijalne tablete sa trenutnim oslobađanjem. Najveće vrednosti procenta oslobođenog karbamazepina dobijene su pri udelima karbamazepina od oko 35 – 40 %, *Gelucire*® 44/14 od oko 25 – 30 % i *Soluplus*® od oko 35 – 40 %. Na osnovu dobijenih rezultata matematičke regresije, sa velikom tačnošću se može predvideti procenat rastvorenog karbamazepina, za bilo koju kombinaciju ulaznih parametara, u ispitvanom opsegu.

Poređenjem eksperimentalno dobijenih i predviđenih profila brzine rastvaranja karbamazepina iz tri izrađene optimizovane formulacije čvrstih disperzija, uočava se veliko slaganje ($f_1 < 15$; $f_2 > 50$).

Primenom PAMPA testa je pokazano da je u dve, od tri ispitivane optimizovane čvrste disperzije očuvana, odnosno blago povećana permeabilnost karbamazepina.

Rezultati ispitivanja uzoraka čvrstih disperzija nakon izrade, kao i nakon skladištenja 24 meseca, dobijeni primenom metoda DSC, FT-IR i Ramanske spektroskopije su potvrdili njihovu stabilnost i očuvanje karbamazepina u polimorfnom obliku III, jedinom farmakološki aktivnom obliku.

Zahvalnica: Ovaj rad je realizovan u okviru projekata TR34007 i ON171032, koje finansira Ministarstvo prosvete, nauke i tehnološkog razvoja Republike Srbije.

LITERATURA

- [1] Potta S, Minemi S, Nukala N, Peinado C, Lamprou DA, Urquhart A, Douroumis D. Development of solid lipid nanoparticles for enhanced solubility of poorly soluble drugs. *J Biomed Nanotechnol.* 2010; 6: 634–640.
- [2] Leuner C, Dressman J. Improving drug solubility for oral delivery using solid dispersions. *Eur J Pharm Biopharm.* 2000; 50: 47–60.
- [3] Damian F, Blaton N, Naesens L, Balzarini J, Kinget R, Augustijns P, Vanden Mooter G. Physicochemical characterization of solid dispersions of the antiviral agent UC-781 with polyethylene glycol 6000 and Gelucire 44/14. *Eur J Pharm Sci.* 2000; 10: 311–322.
- [4] Kalivoda A, Fischbach M, Kleinebudde P. Application of mixtures of polymeric carriers for dissolution enhancement of oxeglitazar using hotmelt extrusion. *Int J Pharmaceut.* 2012; 439: 145–156.
- [5] Serajuddin A. Solid dispersion of poorly water-soluble drugs: early promises, subsequent problems, and recent breakthroughs. *J Pharm Sci-US.* 1999; 88(10): 1058-1066.
- [6] Djuris J, Ioannis N, Ibric S, Djuric Z, Kachrimanis K. Effect of composition in the development of carbamazepine hot-melt extruded solid dispersions by application of mixture experimental design. *J Pharm Pharmacol.* 2014; 66 (2):232-243.
- [7] Krstić M, Ibrić S. Primena dizajna smeše u formulaciji i karakterizaciji čvrstih samo-nanoemulgujućih terapijskih sistema sa karbamazepinom. *Hem Ind.* 2016; 70(5): 525-537. (in Serbian)
- [8] Krstić M, Ražić S, Đekić Lj, Dobričić V, Momčilović M, Vasiljević D, Ibrić S. Application of a mixture experimental design in the optimization of the formulation of solid self-emulsifying drug delivery systems containing carbamazepine. *Lat Am J Pharm.* 2015; 34 (5): 885-894.
- [9] Dahan A, Miller MJ, Hoffman A, Amidon EG, Amidon LG. The solubility - permeability interplay in using cyclodextrins as pharmaceutical solubilizers: mechanistic modeling and application to progesterone. *J Pharm Sci-US.* 2010; 99(6): 2739-2749.
- [10] Kataoka M, Tsuneishi S, Maeda Y, Masaoka Y, Sakuma S, Yamashita S. A new *in vitro* system for evaluation of passive intestinal drug absorption: Establishment of a double artificial membrane permeation assay. *Eur J Pharm Biopharm.* 2014; 88(3): 840-846.
- [11] Kostewicz ES, Aarons L, Bergstrand M, Bolger MB, Galetin A, Hatley O, Jamei M, Lloyd R, Pepin X, Rostami-Hodjegan A, Sjögren E, Tannergren C, Turner DB, Wagner C, Weitschies W, Dressman J. PBPK models for the prediction of *in vivo* performance of oral dosage forms. *Eur J Pharm Sci.* 2014; 57: 300-321.
- [12] Dahan A, Miller JM. The solubility-permeability interplay and its implications in formulation design and development for poorly soluble drugs. *AAPS J.* 2012; 14(2): 244-251.
- [13] Krstić M, Popović M, Dobričić V, Ibrić S. Influence of Solid Drug Delivery System Formulation on Poorly Water-Soluble Drug Dissolution and Permeability. *Molecules.* 2015; 20: 14684-14698.
- [14] Moore JW, Flanner HH. Mathematical Comparison of curves with an emphasis on *in vitro* dissolution profiles. *Pharm Tech.* 1996; 20(6): 64-74.
- [15] Zhu C, Jiang L, Chen TM, Hwang KK. A comparative study of artificial membrane permeability assay for high-throughput profiling of drug absorption potential. *Eur J Med Chem.* 2002; 37: 399-407.
- [16] Shamma RN, Basha M. Soluplus®: A novel polymeric solubilizer for optimization of Carvedilol solid dispersion: Formulation design and effect of method of preparation. *Powder Technol.* 2013; 29(1): 161-165.
- [17] Porter C, Trevaskis N, Charman W. Nature Lipids and lipid-based formulations: optimizing the oral delivery of lipophilic drugs. *Nat Rev Drug Discov.* 2007; 6: 231-248.

- [18] Löbenberg R, Amidon GL. Modern bioavailability, bioequivalence and biopharmaceutics classification system. New scientific approaches to international regulatory standards. *Eur J Pharm Biopharm.* 2000; 50: 3-12.
- [19] Grzesiak A, Lang M, Kim K, Matzger A. Comparison of the four anhydrous polymorphs of carbamazepine and the crystal structure of form I. *J Pharm Sci-US.* 2003; 92: 2261-2271.
- [20] Yu L, Reutzel-Edens SM, Mitchell CA. Crystallization and Polymorphism of Conformationally Flexible Molecules: Problems, Patterns, and Strategies. *Org Process Res Dev.* 2000; 4(5): 396-402.
- [21] Krstić M, Ražić S, Vasiljević D, Spasojević Đ, Ibrić S. Application of experimental design in the examination of the dissolution rate of carbamazepine from formulations. Characterization of the optimal formulation by DSC, TGA, FT-IR and PXRD analysis. *J Serb Chem Soc.* 2015; 80(2): 209-222.
- [22] Rustichelli C, Gamberini G, Ferioli V, Gamberini MC, Ficarra R, Tommasini S. Solid-state study of polymorphic drugs: Carbamazepine. *J Pharm Biomed Anal.* 2000; 23(1): 41-54.
- [23] Kobayashi Y, Ito S, Itai S, Yamamoto K. Physicochemical properties and bioavailability of carbamazepine polymorphs and dihydrate. *Int J Pharm.* 2000; 193: 137-146.
- [24] Lazarević J, Uskoković-Marković S, Jelikić-Stankov M, Radonjić M, Tanasković D, Lazarević N, Popović Z. Intermolecular and low-frequency intramolecular Raman scattering study of racemic ibuprofen. *Spectrochim Acta A.* 2014; 126: 301-305.
- [25] Saikat R, Chamberlin B, Matzger A. Polymorph Discrimination Using Low Wavenumber Raman Spectroscopy. *Org Process Res Dev.* 2013;17(7): 976-980.
- [26] Krstić M, Djurić J, Petrović O, Lazarević N, Cvijic S, Ibrić S. Application of the melt granulation technique in development of lipid matrix tablets with immediate release of carbamazepine. *J Drug Deliv Sci Tech.* 2017; 39: 467-474.

SUMMARY

Solid dispersions with carbamazepine: optimization of formulation, characterization and examination of long-term stability

Marko Krstić¹, Igor Lukić², Alma Bušatlić³, Nenad Lazarević⁴, Dragana Vasiljević¹

¹Department of Pharmaceutical Technology and Cosmetology, University of Belgrade - Faculty of Pharmacy, Vojvode Stepe 450, 11221 Belgrade, Serbia

²ASV Beograd d.o.o., Kumodraška 380, 11221 Belgrade, Serbia

³Adoc d. o. o., Milorada Jovanovića 11, 11030 Belgrade, Serbia

⁴Center for Solid State Physics and New Materials, Institute of Physics Belgrade, University of Belgrade, Pregrevica 118, 11080 Belgrade, Serbia

(Scientific paper)

Solid dispersions are defined as dispersions of one or more active pharmaceutical ingredients in inert solid-state carriers. They are made with the aim to increase solubility and the dissolution rate of low solubility active pharmaceutical ingredients, with the subsequent increase in their bioavailability.

The aim of this study was the development and optimization of solid dispersion formulations with carbamazepine, using D-optimal experimental design, in order to increase the dissolution rate of the selected model drug. By using the method of experimental mixture design, solid dispersions were formulated by varying the ratio of carbamazepine (30-50 %), *Gelucire*® 44/14 (20-40 %) and *Soluplus*® polymer (30-50 %) (input parameters). Sixteen formulations were made and used for in vitro testing of the carbamazepine dissolution rate. The observed output parameters were the percentages of carbamazepine released after 10, 20, 30, 45, and 60 minutes. After the data analysis, three test formulations were chosen from different parts of the optimization area. They were prepared and the carbamazepine dissolution rate was determined, followed by stability assessment for 24 months under ambient conditions (25 °C, 40 % RH).

The highest dissolution rate of carbamazepine from solid dispersions (more than 80 % in 30 minutes) was achieved at the carbamazepine mass fraction of about 40 %, *Soluplus*® of about 45 % and *Gelucire*® 44/14 of about 25 %. Comparing the predicted and the experimental obtained release rate profiles of carbamazepine from the three prepared optimized formulations, a significant compliance of the results was observed ($f_1 < 15$; $f_2 > 50$). The application of the PAMPA (Parallel Artificial-Membrane Permeability Assay) test has shown that carbamazepine permeability was maintained and mildly increased in two out of the three tested optimized solid state formulations. Raman spectroscopy, FT-IR and DSC analyses showed that in the three optimized solid dispersions, after preparation and 24 months of storage, interactions between carbamazepine and the excipients were not present and that carbamazepine remained in the single pharmacologically active crystal polymorph form III.

Proper selection of solid dispersion proportions of carbamazepine, *Gelucire*® 44/14 and *Soluplus*® may significantly increase the dissolution rate of the active substance, and the method of experimental mixture design can be successfully used for optimization of these formulations.

Keywords: solid dispersions, carbamazepine, formulation optimization, experimental design, in vitro release, physical stability

Temperature-Dependent Raman Study of Nanostructured and Multifunctional Materials

Maja Šćepanović,* Mirjana Grujić-Brojčin, Nenad Lazarević, and Zoran V. Popović

The scope of this paper is temperature dependence of Raman spectra in several nanocrystalline materials and iron-based single-crystals. The Raman results presented and analyzed here are related to TiO_2 nanopowders (with dominant anatase and brookite phase) and $\text{Zn}_x\text{Cd}_{1-x}\text{Se}$ single layers measured at different temperatures. Temperature-dependent Raman spectra of iron-based sulphides and selenides (BaFe_2S_3 and BaFe_2Se_3), as well as alkali-doped iron selenides ($\text{K}_x\text{Fe}_{2-y}\text{Se}_2$ and $\text{K}_{0.8}\text{Fe}_{1.8}\text{Co}_{0.2}\text{Se}_2$) are also analyzed. A physical model, including thermal expansion as well as three- and four-phonon anharmonic effects, is used to quantitatively analyze temperature evolution of the characteristic Raman mode self-energies for the materials of interest. It is demonstrated how this model can be used as a tool for predicting the temperature of structural and phase transitions, with critical scrutiny of its limitations.

spin ladders, spin dimers, etc.).^[5] The temperature dependent Raman spectra of iron-based sulphides and selenides (BaFe_2S_3 and BaFe_2Se_3 , belonging to the family of the iron-based $S=2$ two-leg spin-ladder compounds),^[5] together with alkali-doped iron selenides (superconducting $\text{K}_x\text{Fe}_{2-y}\text{Se}_2$ and non-superconducting $\text{K}_{0.8}\text{Fe}_{1.8}\text{Co}_{0.2}\text{Se}_2$)^[6] are analyzed. A physical model, including thermal expansion, as well as three- and four-phonon anharmonic effects, is used to quantitatively analyze experimentally obtained temperature dependence of energy and linewidth of the Raman modes characteristic for investigated materials. We have shown that this simplified model could be successfully used to predict the temperature of microstructural phase transitions, but its limitations have also been indicated.

1. Introduction

Variable-temperature Raman scattering measurements provide great assistance in the analysis of structural, electronic, and magnetic properties, as well as phase transitions, in large number of materials currently in the focus of modern research in condensed matter physics. Two important classes of materials are in the scope of the present paper – nanomaterials and iron-based compounds. Temperature-dependent Raman spectra of nanomaterials is a significant source of information on their thermal stability and other properties (such as phase composition, nanocrystallite size distribution, strain, defects, and non-stoichiometry) strongly depended on the temperature and affecting the shape, shift, and linewidth of characteristic Raman modes.^[1–4] The obtained Raman results are related to titanium dioxide (TiO_2) nanopowders (with dominant anatase or brookite phase) and $\text{Zn}_x\text{Cd}_{1-x}\text{Se}$ single layers. In addition the influence of the antiferromagnetic order, ferromagnetism, and magnetic fluctuations on the Raman scattering spectra of several iron-based compounds measured in wide temperature range were also analyzed. These materials may have not only superconducting but also low-dimensional magnetic properties (forming spin chains,

2. Theoretical Background

Lattice vibrations are strongly related to crystalline, thermodynamical, and transport properties of materials, including phase stability at finite temperatures, lattice thermal conductivity, and superconducting critical temperature of phonon-mediated superconductors.^[7] In order to interpret experimental vibrational spectra some computational methods based on density functional theory have been developed. These methods use the first-principles calculations of phonons and other related properties, but it appears that their performance is always limited by chosen approximations and assumptions. The harmonic approximation, assuming independent phonons, is usually adopted in calculations of phonon properties at low temperatures; it is a method of choice when describing the phonon spectra of the metals and insulators, valid and useful for obtaining phonon dispersion curves and studying phase stability. However, harmonic approximation is not successful in describing phonon behavior at high temperatures, where phonon-phonon interactions must be considered, together with properties related to the lattice anharmonicity (thermal expansion, lattice thermal conductivity, temperature, and volume dependences of phonon frequencies). The anharmonic effects can be successfully treated by the many-body perturbation theory.^[8,9] However, this theory seems to be inadequate, when the cubic and higher-order anharmonic terms of the phonon energies are larger than the harmonic one, or when the harmonic solution shows dynamical instability. In order to overcome these limitations, some advanced methods have been

Dr. M. Šćepanović, Dr. M. Grujić-Brojčin, Dr. N. Lazarević,
Prof. Z. V. Popović
Center for Solid State Physics and New Materials
Institute of Physics
University of Belgrade
Pregrevica 118, 11080 Belgrade, Serbia
E-mail: maja@ipb.ac.rs

DOI: 10.1002/pssa.201800763

developed, such as the self-consistent phonon theory,^[10] or ab-initio molecular dynamics method,^[11,12] both treating anharmonic effects in solids nonperturbatively.^[7] However, all these calculations require significant computer resources, rapidly increasing with the size of the system. This may be the reason why the first-principles calculations of phonons are usually performed at low temperatures, and the results related to the temperature dependence of phonon properties are, to the best of our knowledge, still unavailable for materials studied here.

The analysis of experimentally obtained temperature dependence of phonon frequency and lifetime in the materials presented in this paper includes quasiharmonic and anharmonic contribution to the lattice potential, which both contribute to nonharmonic lattice dynamics. The phonon modes in the quasiharmonic model behave harmonically with infinite lifetimes, but their frequencies are influenced by the effects of lattice volume on the interatomic potential,^[13] whereas explicit anharmonicity originates from phonon-phonon interactions increasing with temperature.

Frequency shift and broadening of phonon mode can be described as real and imaginary part of phonon self-energy^[6,14,15]:

$$\Sigma_i(T) = \Delta_i(T) + i\Gamma_i(T) \quad (1)$$

where $\Delta_i(T)$ corresponds to the energy of i -th Raman mode and $\Gamma_i(T)$ to its linewidth, defined as inverse value of phonon lifetime τ . Temperature dependence of Raman shift can be defined by the real part of self-energy:

$$\omega_i(T) = \omega_{0,i} + \Delta_i(T) \quad (2)$$

where $\omega_{0,i}$ is temperature independent contribution to phonon mode energy. Temperature dependent term may be written as

$$\Delta_i(T) = \Delta_i^V + \Delta_i^A \quad (3)$$

The first term, Δ_i^V , corresponds to the frequency shift from the volume thermal expansion or quasiharmonicity, and can be expressed as

$$\Delta_i^V = -\omega_{0,i} \left(e^{-\gamma_i \int_0^T \alpha_V(T') dT'} - 1 \right) \quad (4)$$

with Grüneisen parameter γ_i of given mode and volume thermal expansion coefficient $\alpha_V(T)$ of investigated material.^[15] The Grüneisen model assumes that the Grüneisen parameter correlates the temperature dependence of vibrational frequencies with the unit cell volume. At constant pressure the Grüneisen constant is defined by

$$\gamma_i = \left. \frac{\partial \ln \omega_i}{\partial \ln V} \right|_P = - \frac{1}{\alpha_V} \left. \frac{\partial \ln \omega_i}{\partial T} \right|_P \quad (5)$$

where ω_i is the frequency of i -th vibrational mode, V the unit cell volume and α_V the volumetric thermal expansion given by

$$\alpha_V = \left. \frac{1}{V} \frac{\partial V}{\partial T} \right|_P \quad (6)$$



Maja Šćepanović received her PhD from the School of Electrical Engineering, University of Belgrade. She is employed as a Research Professor at the Center for Solid State Physics and New Materials, Institute of Physics Belgrade. She has contributed greatly to the understanding of a number of problems in the experimental study

and simulation of intense ns laser pulse-matter interaction, Raman, infrared and photoluminescence spectroscopy, and spectroscopic ellipsometry. In recent years, she has been primarily concerned with the experimental and theoretical studies, as well as development of numerical models, related to the investigation of nanostructured and iron-based related materials.



Mirjana Grujić-Brojčin, PhD (School of Electrical Engineering, University of Belgrade). Employed, as a Research Professor at the Center for Solid State Physics and New Materials, Institute of Physics Belgrade. She is engaged in experimental study and development of numerical models in Raman, infrared and photoluminescence

spectroscopy, and spectroscopic ellipsometry of nanomaterials. In recent years she has been involved in application of spectroscopic techniques in Cultural Heritage.



Nenad Lazarević is Research Associate professor employed at the Center for Solid State Physics and Materials, Institute of Physics, University of Belgrade. His main research interest is focused on optical spectroscopy of strongly correlated electron systems with particular emphasis on Raman spectroscopy. In the last years, his

activities were mostly focused on the iron-based superconductors and related materials. Other activities include work on devising new experimental setups for Raman spectroscopy.

Hence, when the temperature dependence of vibrational modes is known, the Grüneisen parameter (which varies significantly from one mode to the other) can be determined from the known thermal expansion (or vice-versa).

The second term, Δ_i^A , in the Equation (3) describes the frequency shift caused by the anharmonic phonon-phonon coupling, that is, the explicit anharmonicity or pure temperature

effect. The anharmonic decay of phonons includes the leading, three-phonon and four-phonon processes, cubic $\Delta_i^{(3)}$ and quartic $\Delta_i^{(4)}$ components of the anharmonicity term Δ_i^A and it should be determined for each Raman mode. The explicit anharmonicity for frequency shift may be simplified by the model proposed by Klemens^[16] and extended by Balkanski et al.^[17] where phonon-phonon interactions include only overtone processes (one optical phonon at the Γ point decays into two or three phonons of equal energy on the same branch), specifying the contributions of three-phonon and four-phonon processes to the frequency shift in the following form^[17]:

$$\Delta_i^A = \Delta_i^{(3)} + \Delta_i^{(4)} = C_i \left(1 + \frac{2}{e^{\frac{\hbar\omega_i}{2k_B T}} - 1} \right) + D_i \left(1 + \frac{3}{e^{\frac{\hbar\omega_i}{3k_B T}} - 1} + \frac{3}{\left(\frac{\hbar\omega_i}{e^{3k_B T} - 1} \right)^2} \right) \quad (7)$$

where C_i and D_i are so-called anharmonic constants. It should be noted that the parameters which exist in the simplified Klemens model are treated as independent, which is not quite physically correct. In general, the exact interdependence of these parameters is very hard to determine. In order to obtain the relationship between the parameters, when the anharmonic effect can be defined only by three phonon processes, the model of a damped oscillator is adopted,^[15] and phonon-phonon scattering contribution to energy of Raman mode is represented as:

$$\Delta_i^A = C_i \left(1 + \frac{4\lambda_{ph-ph,i}}{\frac{\hbar\omega_i}{e^{2k_B T} - 1}} \right) \quad (8)$$

with phonon-phonon interaction constant λ_{ph-ph} introduced as fitting parameter to represent phonon-phonon coupling strength.

Unlike the phonon energy, the phonon linewidth is not affected by the thermal expansion of crystal lattice. Two main contributions to the phonon linewidth are the anharmonic decay of the phonons and the perturbation of the crystal translational symmetry, due to the presence of impurities and defects. According to Klemens model, temperature dependence of Raman mode linewidth can be described by

$$\Gamma_i(T) = \Gamma_{0,i} + A_i \left(1 + \frac{2}{e^{\frac{\hbar\omega_i}{2k_B T}} - 1} \right) + B_i \left(1 + \frac{3}{e^{\frac{\hbar\omega_i}{3k_B T}} - 1} + \frac{3}{\left(e^{\frac{\hbar\omega_i}{3k_B T}} - 1 \right)^2} \right) \quad (9)$$

where $\Gamma_{0,i}$ is the temperature-independent linewidth, which originates mainly from the presence of impurities and defect (nonstoichiometry), whereas A_i and B_i are the three- and four-phonon anharmonic constants, respectively. According to the model of a damped oscillator, if four-phonon processes turned out to be negligible, Raman mode linewidth could be written as^[15]:

$$\Gamma_i(T) = \Gamma_{0,i} \left(1 + \frac{2\lambda_{ph-ph,i}}{\frac{\hbar\omega_i}{e^{2k_B T}} - 1} \right) \quad (10)$$

with $\Gamma_{0,i}$ as anharmonic constant, which could be related to the phonon-phonon interaction constant λ_{ph-ph} and the anharmonic parameter C_i from relation (8), given as^[15]:

$$C_i = \frac{\Gamma_{0,i}^2}{2\omega_{0,i}} \quad (11)$$

It should be noted that more general calculations, including asymmetric decay channels, result in a better agreement with experiment, especially in some semiconductors.^[15]

3. Temperature-Dependent Raman Spectra of Nanomaterials

The Raman scattering provides important information on the nature of the solid on a scale of few lattice constants. Therefore, this technique can be used to study the correlation between the change in vibrational properties on one, and structural and/or morphological changes in nanostructured material on the other side.

The Raman spectra of nanocrystalline materials are usually simulated by phenomenological phonon confinement model (PCM).^[18,19] In this model several independent factors, like phonon confinement, strain, non-homogeneity of the size distribution, defects, and variations in phonon relaxation with crystallite size decreasing, contribute to the changes in the position and linewidth of calculated Raman mode.^[18–21] Due to the crystallite size decrease, the phonons are confined and optical phonons over the entire Brillouin zone (BZ) contribute to the first-order Raman spectra. The Raman intensity $I(\omega)$ for crystallite size L , according to Richter et al.^[22] and Campbell and Fauchet,^[23] is presented as a superposition of weighted Lorentzian contributions over the whole BZ, by the equation^[3,4,18–23]:

$$I(\omega) = \sum_{i=1}^m \int_0^\infty \rho(L) dL \left(\int_{BZ} \frac{\exp\left(\frac{-q^2 L^2}{8\beta}\right) d^3 q}{[\omega - (\omega_i(q) + \Delta\omega_i(q, L, T))]^2 + \left(\frac{\Gamma_{0i}(T)}{2}\right)^2} \right) \quad (12)$$

where $\rho(L)$ defines crystallite size distribution, q is expressed in units of π/a_L (a_L – effective unit cell parameter), β – strength of confinement (varies from $\beta = 1$ in the Richter's confinement model to $\beta = 2\pi^2$ in the Campbell's confinement model, depending on the confinement boundary conditions in different nanomaterials), $\omega_i(q)$ – phonon dispersion, $\Gamma_{0i}(T)$ – the intrinsic linewidth of Raman mode dependent on temperature T , as well as nonstoichiometry, disorder, and defects state.

The change of the lattice parameters (lattice volume) with nanocrystallite size decrease is registered in nanomaterials due to effect of microstrain and may affect the Raman mode position. The influence of strain on Raman shift $\Delta\omega_i(q, T, L)$ of particular mode is included into PCM through the term given by^[4,20,24]:

$$\Delta\omega_i(q, T, L) = -\gamma_i\omega_i(q, T) \frac{V(L)}{V_0} \quad (13)$$

The unit cell volume variation of nanocrystallite size L can be written as

$$V(L) = V_0 \pm \Delta V(L) \quad (14)$$

where signs “+” and “−” correspond to tensile and compressive strain, respectively.

3.1. TiO₂ Based Nanomaterials

Titanium dioxide is material of great importance in modern materials science. It is probably the most characterised oxide in different areas, such as defect chemistry, phase transitions, surface structure, surface chemistry, optical properties, and electronic structure.^[2] Also, it is widely used nowadays, with a variety of achieved and potential applications: as a pigment, in photocatalysis, as electron transport layer in solar cells, as self-cleaning material, etc.^[25] Only three of TiO₂ several polymorphs (rutile, anatase, and brookite) are considered to be its naturally occurring phases. Although extensively studied during past decades, there are still some unresolved questions related to vibrational and thermal properties of these phases, especially those originated from their nanocrystalline structure.

3.1.1. Anatase Nanocrystalline Powders

The Raman spectroscopy of nanocrystalline anatase (the TiO₂ phase most commonly synthesized at ambient conditions), has been established as a very sensitive tool for detecting nanostructural changes in this material, associated with phonon confinement effect, non-stoichiometry, internal stress/surface tension effects and/or the anharmonicity effects due to temperature variations.^[1–4]

In this review we present our experimental results related to the temperature dependence of the most intense anatase E_g Raman mode, taken from laser-synthesized and commercial anatase nanopowder samples, published in our earlier papers.^[1,2] The interpretation of these results is slightly modified here, in accordance with recent experimental and theoretical findings related to the variation of nanostructural properties of anatase with temperature.^[26–30]

The results of a detailed study of the most intense E_g mode in the Raman spectra of anatase nanopowder synthesized by laser-induced pyrolysis, with crystallite size about 12.3 nm, are presented in the **Figure 1**. The spectra in the temperature range from 25 to 300 K were taken in closed cryostat coupled with Jobin Yvon U1000 macro-Raman system. Other spectra were obtained in the same Raman system, but under conditions of local heating of the sample due to laser radiation, with the temperature estimation based on the intensity ratio between the Stokes and anti-Stokes Raman spectra.^[1]

As can be seen from the Figure 1a, very good agreement between the experimental and calculated spectra of anatase

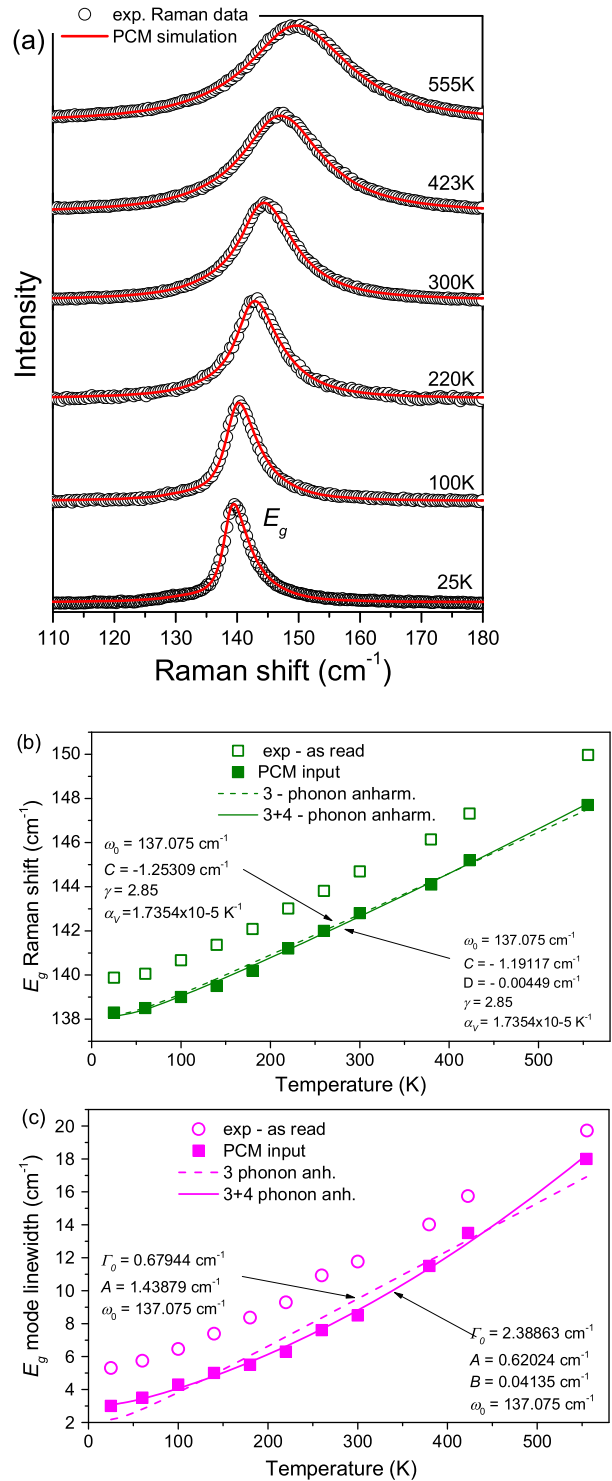


Figure 1. a) The Raman spectra of laser-synthesized TiO₂ nanopowder measured at different temperatures (circles) simulated by PCM (lines). Temperature dependence of the E_g Raman (b) shift and (c) linewidth fitted by three- (dashed lines) and four-phonon (full lines) anharmonic model with the corresponding parameters specified in the figures.

nanopowder has been obtained at all given temperatures, by using the PCM (Equation (12)) with anisotropic dispersion relations^[31] and temperature dependent parameters.^[1] It has also been demonstrated that the frequency shift (Figure 1b) and mode broadening (Figure 1c) of the E_g Raman mode were induced by both phonon confinement due to the nanocrystalline size and effect of heating. In order to analyze only heating effects on E_g Raman shift and linewidth, their as-read experimental values (shown with open symbols in the Figure 1b and c) have been corrected to exclude the effects of phonon confinement. Thereafter the corresponding temperature dependences of the E_g Raman shift and linewidth (closed symbols in Figures 1b and c) were fitted according to the Equations (7) and (9), respectively. The obtained results show that the contribution of explicit anharmonicity overpowers the effect of quasiharmonicity in the E_g frequency shift. Namely, the volume thermal expansion due to the heating, in combination with the positive value of Grüneisen parameter for E_g mode, should lead to a decreasing in E_g Raman frequency with temperature, contrary to experimental observation. It also has been shown that the curves (full line) corresponding to the contributions of both three- and four-phonon processes were better matched to the experimental results, than those calculated with the assumption of three-phonon processes only (dashed line). This effect is particularly pronounced in linewidth temperature dependence of E_g Raman mode.

Raman spectra of commercial anatase TiO_2 nanocrystals (Aldrich 637254, 99.7%) with a declared average crystallite size of about 5 nm were measured in the temperature range from 22 to 900 °C using Linkam TS 1500 heating stage coupled with Jobin Yvon T64000 micro-Raman system.^[2] The temperature dependences of Raman shift and broadening of the lowest frequency E_g mode were analyzed by using PCM and anharmonic model. Comparison between experimental spectra and those calculated by PCM (Equation (12)) at several chosen temperatures is shown in the Figure 2a. In this case PCM included not only the effects of phonon confinement and nonstoichiometry, but also the strain. Namely, recently published results have revealed that the strain in anatase particles varied with temperature^[26,27,29,30]: at some medium-high temperatures, the strain could be released, but at high temperatures, close to the transformations from anatase to rutile phase, the strain could strengthen again. Also, in situ x-ray diffraction study of the anatase microstructure evolution as a function of temperature has confirmed that anatase nanoparticle size increased with temperature. But it should be pointed out that the temperature at which the particles size begin to increase depends on their initial size,^[32] and that for smaller anatase nanoparticles the increase starts at higher temperature. This was the reason for modification of our previous calculations by including the strain in PCM, which led to the increase of calculated temperature at which the anatase nanoparticles begin to grow from previously estimated 500 °C to currently specified 600 °C.^[2] Different calculated results are the consequence of following assumption: the discrepancy of experimental temperature dependences of E_g Raman shift and linewidth from those predicted by anharmonic model (Equations (7) and (9)), observed at about 500 °C, originates from strain relaxation, and nanoparticle growth starts at higher temperatures (about 600 °C). Also, nanoparticles growth with temperature, estimated

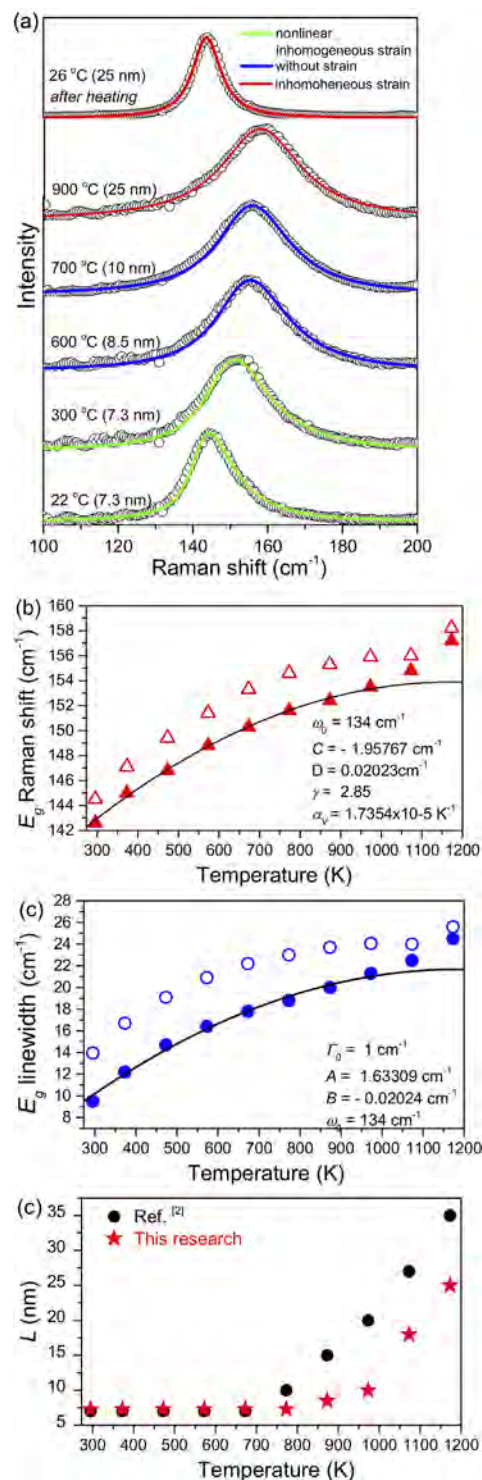


Figure 2. a) The Raman spectra of commercial anatase TiO_2 nanopowder measured at different temperatures (circles) simulated by PCM (lines). Temperature dependence of the E_g Raman (b) shift and (c) linewidth fitted by four-phonon anharmonic model (full lines) with the corresponding parameters specified in the figures. d) Nanocrystallite size L estimated by using PCM with (circles) and without (asterisks) included strain.

by using PCM with strain effect, is less steep than that obtained with strain effect neglected,^[2] which is much more consistent with the published XRD results for very small anatase nanoparticles.^[32] Note that we assume anatase nanocrystallites to obey a log-normal size distribution with average crystallite size of about 7 nm, previously estimated by the procedure based on the low frequency Raman scattering measurements.^[2]

3.1.2. Brookite Nanocrystalline Powders

Unlike the anatase phase, the variation of Raman spectra of TiO₂ brookite phase with temperature has not yet been reported, to the best of our knowledge. The Raman spectra of hydrothermally synthesized spindle-like brookite nanoparticles with mean crystallite size of ≈ 33 nm (according to XRD results^[33]) were measured in the temperature range from 80 to 860 K using Linkam THMS 600 heating stage coupled with Jobin Yvon T64000 micro-Raman system. The Raman spectra of brookite taken at several temperatures are shown in the **Figure 3a**. It can be seen that a great number of observed modes, characteristic for this orthorhombic structure (36 Raman active modes are expected according to symmetry considerations),^[34] broadens and shifts towards lower frequencies with the temperature increase. The temperature dependence of Raman shift (squares) and linewidth (circles) of the most intensive brookite A_{1g} mode, collected from experimental spectra is presented in the **Figure 3b**. The PCM has not been used to analyze the spectra of brookite nanopowder, because of relatively large mean crystallite size, as well as quite flat phonon dispersion curves theoretically predicted for this brookite Raman mode.^[35] Even the application of the anharmonic model in this analysis is not simple, due to lack of experimental and calculated data on the brookite thermal expansion coefficients, as well as the pressure dependence of brookite vibrational properties, needed for determination of mode Grüneisen parameter. Therefore, the value of volume thermal expansion coefficient for brookite is assumed in the range limited by expansion coefficients of anatase and rutile, as indicated by published experimental results related to polyhedral thermal expansion in these TiO₂ polymorphs.^[36] The value of Grüneisen parameter is taken as fitting parameter in the calculation of quasi-harmonic contribution to A_{1g} Raman shift according to Equations (4). The curves calculated as described above start to deviate from experimental temperature dependence of A_{1g} Raman shift on temperature already at 450 K, whereas the discrepancy of the values predicted according to Equation (9) from experimental linewidth appears above 600 K. The experimental A_{1g} linewidth at higher temperatures, narrower than predicted by the model, can be explained by the strain relaxation and increase of the brookite crystallite size with temperature. Note that gradual increase of brookite crystallite size due to thermal treatment of TiO₂ nanopowders has been documented in the literature.^[37] The comparison between brookite Raman spectra measured at 80 K, before and after heating the sample at 873 K (**Figure 3a**), indicates that some modes become better defined, narrower, and shifted to lower frequencies after the thermal treatment, thus supporting the assumptions of defect relaxation and partial consolidation of small particles into larger. On the other hand, the deviation of

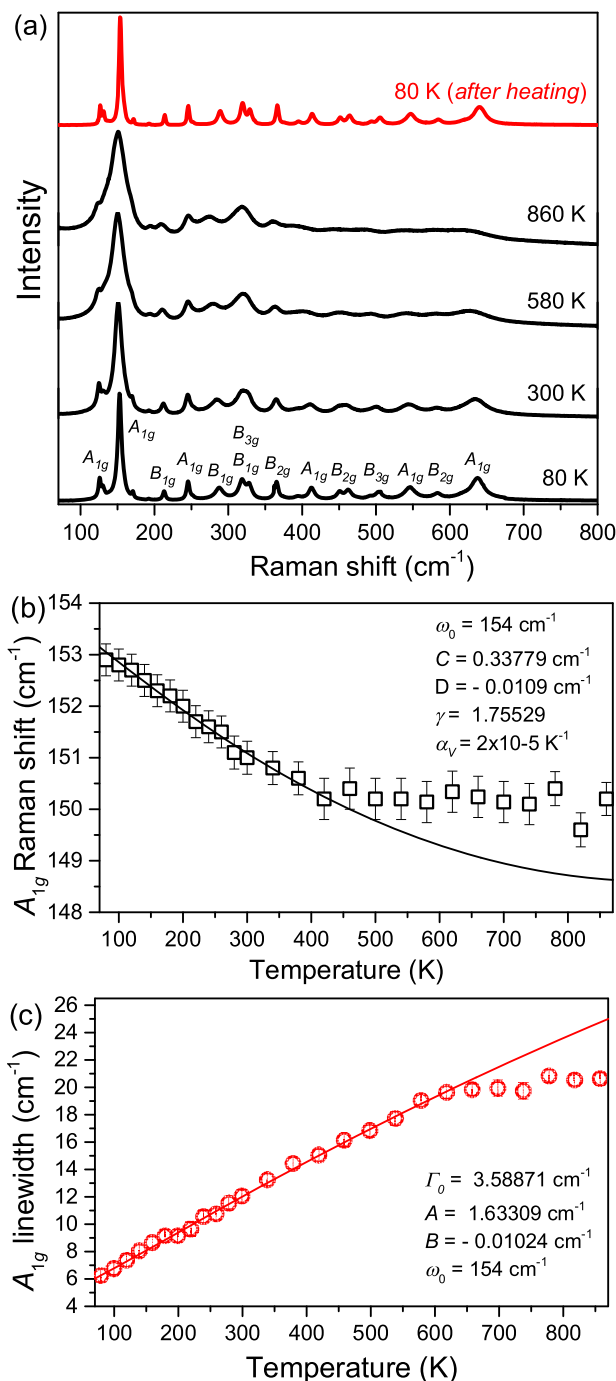


Figure 3. a) The Raman spectra of brookite TiO₂ nanopowder measured at different temperatures with characteristic modes assigned. Temperature dependence of the A_{1g} Raman mode (b) shift and (c) linewidth; experimental as read values (symbols) are fitted by four-phonon (full lines) anharmonic model with the corresponding parameters specified in the figures.

temperature dependence of A_{1g} Raman shift from those predicted by model, could be not only a consequence of microstructural changes in brookite nanopowder due to heating, but also a result of the changes in the thermal properties of

brookite with temperature. These changes are not taken into account because, despite some indications, precise data about these phenomena still are not available.

3.2. $\text{Zn}_x\text{Cd}_{1-x}\text{Se}$ Single Layers

The examination of vibrational properties of $\text{Zn}_{1-x}\text{Cd}_x\text{Se}$ is a matter of special interest due to structural phase transition observed in this material with variation of composition x and temperature.^[38] There are also the strong indications that vibration properties of thin layers are not identical to those for bulk $\text{Zn}_{1-x}\text{Cd}_x\text{Se}$ mixed crystal.^[39] The Raman spectra of microcrystalline $\text{Zn}_x\text{Cd}_{1-x}\text{Se}$ single layer (with composition $x = 0.59$ and thickness of 400 nm), prepared by thermal vacuum evaporation, through alloying of ultrathin ZnSe and CdSe films with equivalent thickness,^[40] were measured in the temperature range from 20 to 600 °C using Linkam THMS 600 heating stage coupled with Jobin Yvon T64000 micro-Raman system. Some of these spectra, obtained with 514.5 nm line of mixed Ar/Kr laser, are presented in the Figure 4a. The temperature dependences of Raman shift and linewidth of the most intensive Raman mode, ascribed to the scattering from 1LO phonons of the $\text{Zn}_x\text{Cd}_{1-x}\text{Se}$,^[38,41,42] are shown in the Figure 4b for chosen temperatures. We have decided to analyze temperature dependence of 1LO mode because of the change of the LO-phonon spectrum versus crystal composition, which has been described as one-mode type. On the other side, the TO-phonon dependence appeared to be much more complicated, with rather anomalous features in the line shape and mode frequency versus crystal composition, as well as the temperature, due to the anharmonic coupling between TO-mode and two-phonon states.^[42] To simulate this dependence by the model described in Section 2, values for thermal expansion coefficient and Grüneisen parameter have been taken from recently calculated pressure and temperature dependence of $\text{Zn}_{0.5}\text{Cd}_{0.5}\text{Se}$ thermodynamic properties.^[43] It is obvious that at the temperatures higher than 700 K, there are some discrepancies between experimentally obtained values and those predicted by the model, more pronounced for the mode frequencies. Such discrepancies are most probably the consequence of the change in the film composition at higher temperatures. Namely, it is well known that frequency of 1LO Raman mode of $\text{Zn}_x\text{Cd}_{1-x}\text{Se}$ increases with the increase in composition x , which arises here due to the evaporation of Cd at higher temperatures.^[41]

4. Temperature Dependence of Raman Spectra of Iron-Based Materials

The discovery of superconductivity in iron-based materials has attracted a great attention of the solid state community. During the last decade many new classes of iron-based materials with reach phase diagrams have been reported, featuring a variety of the (competing) phases,^[44] and their phonon properties have been extensively studied by using temperature-dependent Raman spectroscopy.^[5,6,45–64] In order to demonstrate the ability of inelastic light scattering to probe a number of structural and/or magnetic properties of iron-based materials, an overview of some published results is presented.^[5,6] The Raman scattering experiments shown here were performed in backscattering micro-Raman configuration using 514.5 nm line

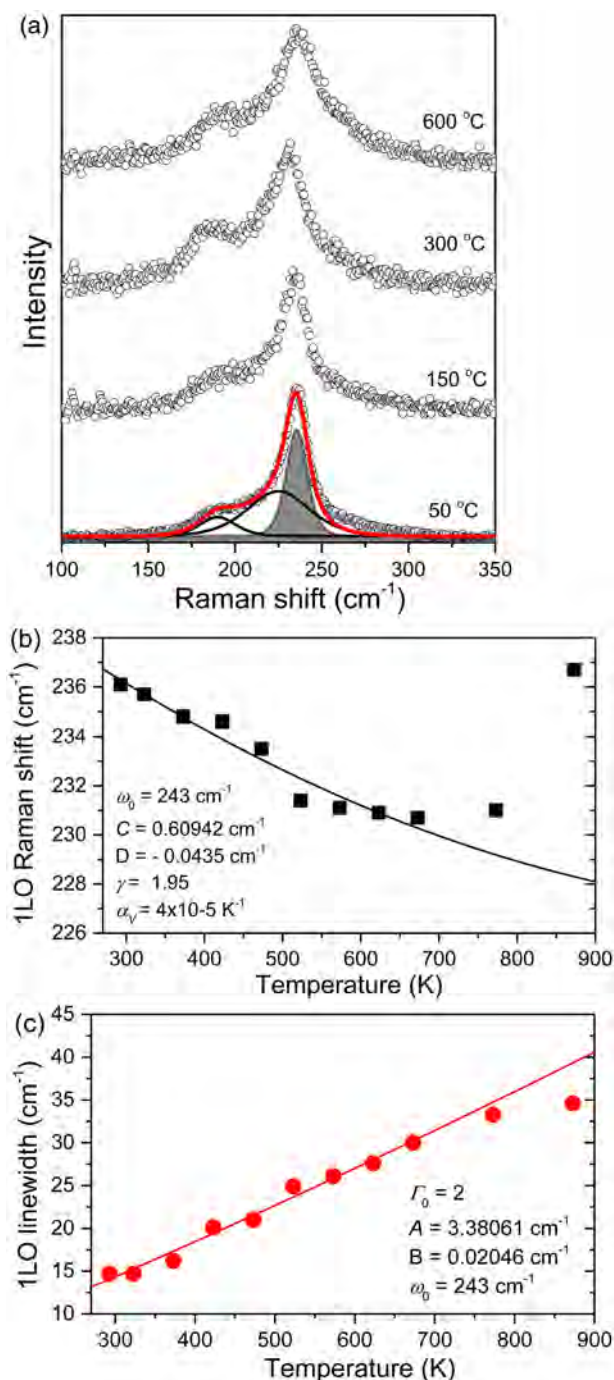


Figure 4. a) Experimental Raman spectra of $\text{Zn}_x\text{Cd}_{1-x}\text{Se}$ single layers measured at different temperatures; Lorentzian fit correspond to the 1LO mode of $\text{Zn}_x\text{Cd}_{1-x}\text{Se}$ is pointed out. Temperature dependence of the 1LO Raman mode (b) shift and (c) linewidth; symbols represent as-read experimental values, whereas full lines correspond to the results calculated by model described in the text with the parameters specified in the figures.

of an Ar^+/Kr^+ mixed laser. Low-temperature measurements were taken using KONTE CryoVac continuous flow cryostat coupled with JY T64000 or TriVista 557 Raman systems, whereas the Raman scattering measurements at higher

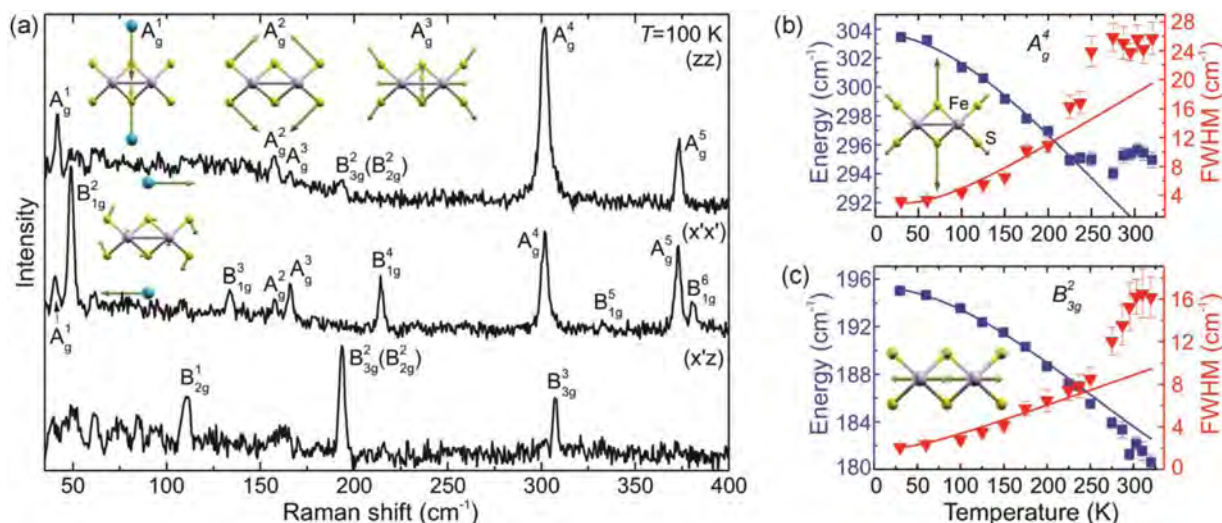


Figure 5. a) The polarized Raman scattering spectra of BaFe_2S_3 single crystal measured at 100 K. Insets: the normal modes of the A_1^1 , A_2^2 , A_3^3 , and B_{2g}^1 vibrations. $x = [110]$, $y = [\bar{1}\bar{1}0]$, and $z = [001]$. Experimental values (symbols) and calculated temperature dependence (solid lines) of the energies and broadenings of (b) A_g^4 and (c) B_{3g}^2 Raman modes of BaFe_2S_3 , with the normal modes of corresponding vibrations graphically represented in the insets. Reproduced with permission.^[5] Copyright 2015, American Physical Society.

temperatures were done using a Linkam THMS600 heating stage.

4.1. Temperature-Dependent Raman Spectra of BaFe_2S_3 and BaFe_2Se_3

The crystal structures of the BaFe_2S_3 and BaFe_2Se_3 , representatives of the iron-based $S=2$ two-leg spin-ladder compound

family, are isomorphic, but not isostructural.^[5] They can be described as alternate stacking of Fe-S(Se) layers and Ba cations along the crystallographic a axis (b axis), whereas in the Fe-S(Se) plane, only one-dimensional (1D) double chains of edge-shared $[\text{FeS(Se)}]_4$ tetrahedra propagate along these axes.

The BaFe_2S_3 is a quasi-one-dimensional semiconductor with orthorhombic crystal symmetry, with space group $Cmcm$ and $Z=4$. Based on the factor group analysis, the 18 Raman active modes are expected to be registered in the spectra of single-

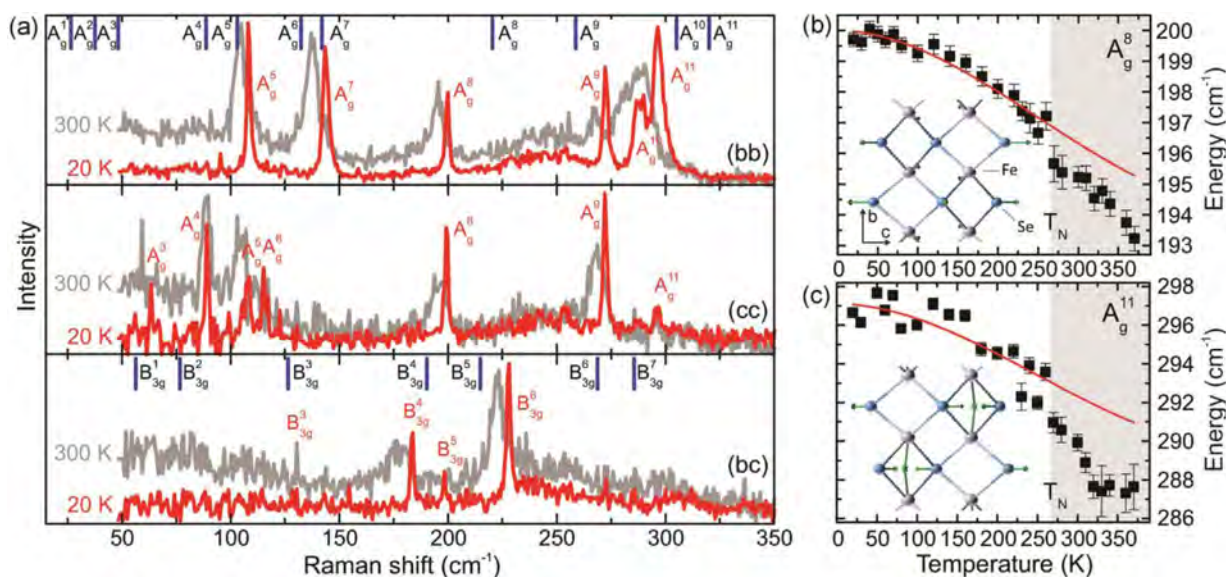


Figure 6. a) The $x(yy)\bar{x}$, $x(zz)\bar{x}$, and $x(yz)\bar{x}$ polarized Raman scattering spectra of BaFe_2Se_3 single crystals measured at room temperature and at 20 K. Vertical bars are calculated values of the A_g^8 and the B_{3g}^7 symmetry Raman active vibrations. Experimental values (symbols) and calculated temperature dependence (solid lines) of BaFe_2Se_3 (b) A_g^8 and (c) A_g^{11} Raman mode energies with normal modes of corresponding vibrations graphically represented in the insets. Reproduced with permission.^[5] Copyright 2015, American Physical Society.

crystal with (110) orientation.^[5] Most of these modes are observed in polarized Raman scattering spectra of BaFe₂S₃ investigated here (Figure 5a).

Experimental values and temperature dependence of the energy and broadening of A_g^4 and B_{3g}^2 Raman modes of BaFe₂S₃, calculated by Equations (3), (4), (8) and (10), are shown in the Figures 5b and c, respectively. The change in the slope of temperature dependence of these modes linewidth (energy), as well as deviations of simulated anharmonic behavior from experimental values, is observed at about 275 K. This could be related to the spin and charge, because of a hump in the inverse molar magnetic susceptibility, and a change of slope of the electrical resistivity temperature dependence, which have been observed in BaFe₂S₃ at similar temperature.

The antiferromagnetic ordering of spins within the ladder legs could change from short-range to the long-range state, without 3D antiferromagnetic spin ordering (the Néel state) of the whole BaFe₂S₃ crystal, followed by the change of electronic structure, which could explain the abrupt increase of the resistivity at this temperature. Note that 3D-antiferromagnetic phase transition is registered in many of iron-based spin-ladder materials at about 260 K.

The BaFe₂Se₃ also has an orthorhombic structure (*Pmna*) with unit cell consisting of four formula units containing 24 atoms. However, unlike the BaFe₂S₃, there is an alternation of the Fe–Fe distances along the chain direction in BaFe₂Se₃. The 36 Raman active modes are predicted in the BaFe₂Se₃ spectra by the factor

group analysis, but only modes of A_g and B_{3g} symmetry are observed in the spectra measured from the (100) plane of the sample (the crystallographic *a* axis is perpendicular to the plane of the single crystal), as shown in the Figure 6a.

The energies of A_g^8 and A_g^{11} Raman modes of BaFe₂Se₃ change abruptly at temperatures below $T_N=255$ K, when this compound becomes antiferromagnetically long-range ordered (Figure 6b and c, respectively). It appears that the spin-phonon (magnetoelastic) coupling is responsible for Raman mode energy change in the antiferromagnetic phase, due to significant local lattice distortion (Fe atom displacement along the *b* axis of ≈ 0.001 nm) driven by the magnetic order. Moreover, local displacements in the Fe atoms at T_N have a significant impact on the electronic structure due to rearrangement of electrons near the Fermi level, and, consequently, the change in the phonon energy and broadening.

4.2. Temperature-Dependent Raman Spectra of Superconducting $K_xFe_{2-y}Se_2$ and Non-Superconducting $K_{0.8}Fe_{1.8}Co_{0.2}Se_2$

According to the selection rules, two Raman modes in the spectra of $K_xFe_{2-y}Se_2$ can be ascribed to high symmetry (*I4/mmm*), whereas 18 phonon modes could originate from low-symmetry (*I4/m*) phase, out of which 16 has been observed in this phase-separated sample.^[6,50] Polarized Raman scattering

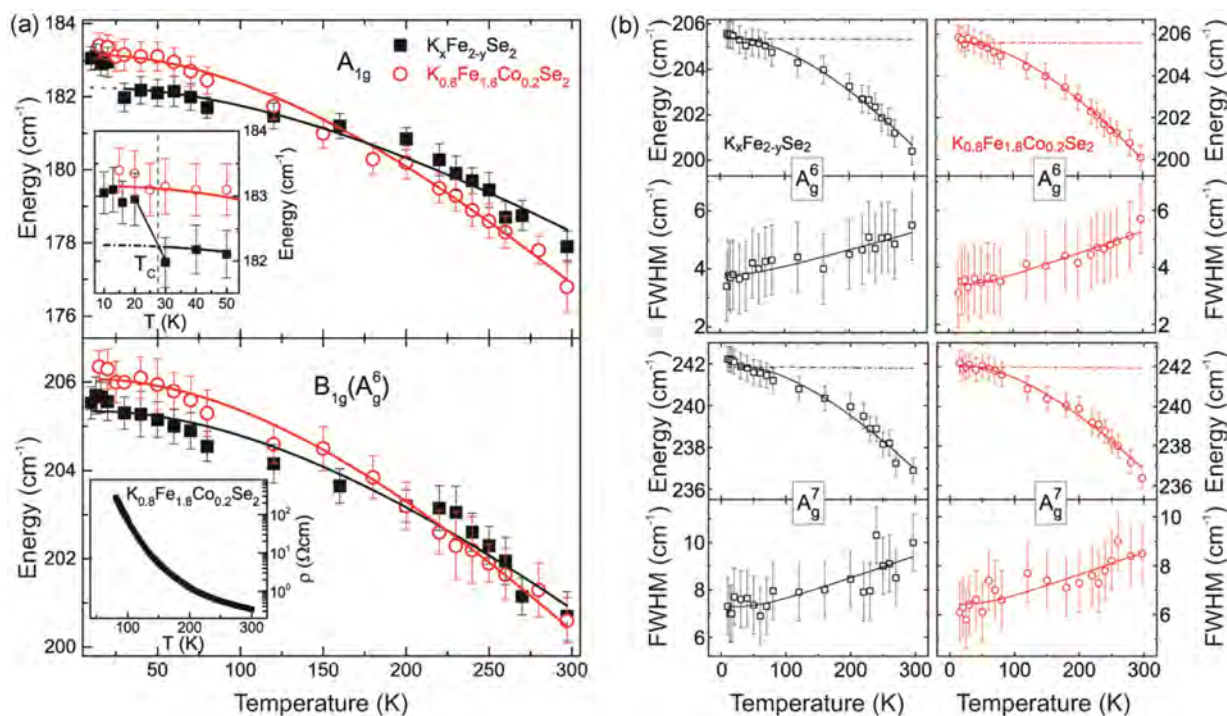


Figure 7. a) Temperature dependence of the energy for the A_{1g} and $B_{1g}(A_g^6)$ Raman modes of $K_xFe_{2-y}Se_2$ and $K_{0.8}Fe_{1.8}Co_{0.2}Se_2$ single crystals. Upper inset: Enlarged view of the dependence of the A_{1g} mode energy on temperature in a low-temperature region near T_C for $K_xFe_{2-y}Se_2$. Lower inset: the temperature dependence of the electrical resistivity for $K_{0.8}Fe_{1.8}Co_{0.2}Se_2$ shows the nonmetallic behaviour of this single crystal. b) Temperature dependence of energy and linewidth for some A_g modes of $K_xFe_{2-y}Se_2$ (left panel) and $K_{0.8}Fe_{1.8}Co_{0.2}Se_2$ (right panel). Solid lines take into account only the volume contribution to the phonon mode energy. Reproduced with permission.^[6] Copyright 2015, IOP Publishing.

spectra of $\text{K}_{0.8}\text{Fe}_{1.8}\text{Co}_{0.2}\text{Se}_2$ single crystals, measured from the (001) plane of the sample at various temperatures, have shown that the energies of Raman active phonons are close to the energies of the corresponding modes in $\text{K}_x\text{Fe}_{2-y}\text{Se}_2$. The same number of Raman modes observed in both compounds, with similar corresponding energies, suggests that phase separation is also present in $\text{K}_{0.8}\text{Fe}_{1.8}\text{Co}_{0.2}\text{Se}_2$, and that doping of a $\text{K}_x\text{Fe}_{2-y}\text{Se}_2$ single crystal with a small amount of Co does not have a significant impact on the phonon spectrum in the normal state.^[6]

The temperature dependences of A_{1g} and $B_{1g}(A_g^6)$ modes of $\text{K}_x\text{Fe}_{2-y}\text{Se}_2$ and $\text{K}_{0.8}\text{Fe}_{1.8}\text{Co}_{0.2}\text{Se}_2$ single crystals are shown in the Figure 7a. These dependences are analyzed using Equation (3) with Δ_i^V therm only, knowing that the calculated values of parameters C_i in the anharmonic term Δ_i^A are negligible. The temperature dependence of the $B_{1g}(A_g^6)$ mode energy in both samples in the whole temperature range under investigation is well described by the proposed model. However, A_{1g} mode energy is well fitted by this model only in the case of non-superconducting Co-doped sample, whereas an abrupt change in A_{1g} mode energy around T_C in the superconducting sample is observed. It may be concluded that the hardening of A_{1g} mode around T_C (observed for superconducting sample and absent for non-superconducting one; see the inset in the Figure 7a) is caused by the superconductivity induced phonon renormalization. Note that sudden change in the energy near T_C is registered only for the mode corresponding to vibration of high-symmetry ($I4/mmm$) phase in the superconducting $\text{K}_x\text{Fe}_{2-y}\text{Se}_2$ and could be related to the rearrangement of the electronic states to which this mode couples, as the superconducting gap opens.

On the other side, the temperature dependence of the Raman energy and linewidth of A_g^6 and A_g^7 modes (Figure 7b), registered in the spectra of $\text{K}_x\text{Fe}_{2-y}\text{Se}_2$ and $\text{K}_{0.8}\text{Fe}_{1.8}\text{Co}_{0.2}\text{Se}_2$ single crystals, and ascribed to non-superconducting low-symmetry phase ($I4/m$), are well described by the proposed lattice anharmonic model only with the contribution of the lattice thermal expansion.

5. Conclusion

The results presented in this paper have shown how temperature-dependent Raman scattering measurements could be used to analyze the variation of structural, morphological, compositional, electronic, and/or magnetic material properties with the temperature. It was demonstrated that physical model, including quasi-harmonic and anharmonic contributions, used to quantitatively analyze experimentally obtained temperature dependence of energy and linewidth of the characteristic Raman modes, could serve as predictive tool for determining the temperatures at which significant changes occur in studied materials. Temperature-dependent Raman spectra of nanomaterials have given information about their thermal stability and allowed tracking changes in phase composition, nanocrystallite size, strain and non-stoichiometry with temperature. In addition to thermal expansion and three-phonon anharmonic contribution, usually the four-phonon anharmonic contribution must be included in order to describe the temperature dependence of the shift and linewidth of Raman modes in nanomaterials.

However, it should be noted that, although this approach provides good fits to experimental Raman data of investigated nanomaterials, some results may not have a complete physical meaning, due to oversimplified approximations (too large cubic anharmonicity in comparison to the quartic, a negative fitting parameter for the quartic anharmonicity in some cases, which is unreasonable). However, if asymmetric phonon decays and four phonon processes turn out to be negligible, the Klemens model provides a reasonable fit to the Raman shift and linewidth of all studied phonons in iron-based single crystals, making this model very convenient for investigated iron-based materials. Thermal expansion and three-phonon anharmonic contributions are usually sufficient to describe temperature dependence of shift and linewidth of Raman modes characteristic for iron-based materials, whereas deviation of experimental values from those predicted by the model has indicated structural and phase transitions and has allowed determining the temperature at which they occurred. The influence of antiferromagnetic order, ferromagnetism, and magnetic fluctuations on the Raman scattering spectra of iron-based compounds depending on temperature can show, not only superconducting, but also a low-dimensional magnetic properties of these materials.

Acknowledgements

This work was financially supported by the Ministry of Education, Science and Technological Development, Republic of Serbia, under the Project No. III45018. We would like to express our very great appreciation to dr Diana Nesheva (Institute of Solid State Physics, Bulgarian Academy of Sciences), dr Cedomir Petrovic (Condensed Matter Physics & Materials Science Department Brookhaven National Laboratory), and dr Nataša Tomić (Institute of Physics, University of Belgrade), who provided us with valuable sample materials and participated in discussing experimental results. The assistance provided by dr Marko Opačić (Institute of Physics, University of Belgrade) is always greatly appreciated.

Conflict of Interest

The authors declare no conflict of interest.

Keywords

iron-based compounds, nanomaterials, quasi-harmonic and anharmonic effects, Raman spectra

Received: September 30, 2018

Revised: January 21, 2019

Published online:

- [1] M. J. Šćepanović, M. Grujić-Brojčin, Z. D. Dohčević-Mitrović, Z. V. Popović, *Appl. Phys. A* **2007**, 86, 365.
- [2] M. J. Šćepanović, M. Grujić-Brojčin, Z. D. Dohčević-Mitrović, Z. V. Popović, *Sci. Sinter.* **2009**, 41, 67.
- [3] M. Šćepanović, M. Grujić-Brojčin, Z. Dohčević-Mitrović, Z. V. Popović, *J. Phys. Conf. Ser.* **2010**, 253, 012015.
- [4] M. Grujić-Brojčin, M. J. Šćepanović, Z. D. Dohčević-Mitrović, Z. V. Popović, *Acta Phys. Pol. A* **2009**, 116, 51.

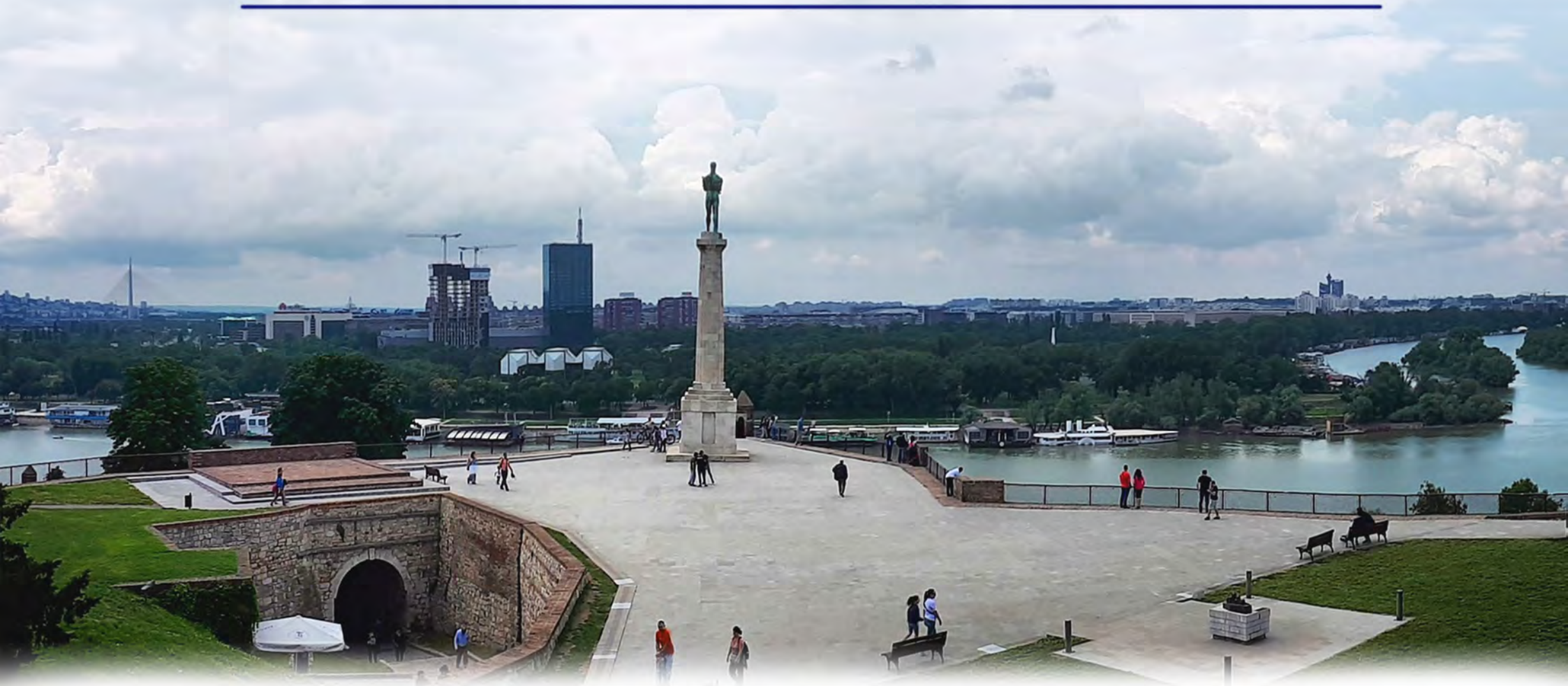
- [5] Z. V. Popović, M. Šćepanović, N. Lazarević, M. Opačić, M. M. Radonjić, D. Tanasković, H. Lei, C. Petrovic, *Phys. Rev. B* **2015**, 91, 064303.
- [6] M. Opačić, N. Lazarević, M. Šćepanović, H. Ryu, H. Lei, C. Petrovic, Z. V. Popović, *J. Phys. —Condens. Mat.* **2015**, 27, 485701.
- [7] T. Tadano, S. Tsuneyuki, *J. Phys. Soc. Jpn.* **2018**, 87, 041015.
- [8] A. A. Maradudin, R. F. Wallis, *Phys. Rev.* **1960**, 120, 442; A. A. Maradudin, P. A. Flinn, R. A. Coldwell-Horsfall, *Ann. Phys-New York* **1961**, 15, 337; A. A. Maradudin, P. A. Flinn, R. A. Coldwell-Horsfall, *Ann. Phys-New York* **1961**, 15, 360; A. A. Maradudin, I. P. Ipatova, *J. Math. Phys.* **1968**, 9, 525.
- [9] I. P. Ipatova, A. A. Maradudin, R. F. Wallis, *Phys. Rev.* **1967**, 155, 882.
- [10] I. Errea, M. Calandra, F. Mauri, *Phys. Rev. B* **2014**, 89, 064302.
- [11] T. Sun, D.-B. Zhang, R. M. Wentzcovitch, *Phys. Rev. B* **2014**, 89, 094109.
- [12] T. Lan, X. Tang, B. Fultz, *Phys. Rev. B* **2012**, 85, 094305; T. Lan, C. W. Li, O. Hellman, D. S. Kim, J. A. Munoz, H. Smith, D. L. Abernathy, B. Fultz, *Phys. Rev. B* **2015**, 92, 054304; T. Lan, Z. Zhu, *Adv. Cond. Matter Phys.* **2016**, 2714592.
- [13] Z. Zhao, J. Elwood, M. A. Carpenter, *J. Phys. Chem. C* **2015**, 119, 23094.
- [14] J. Menéndez, M. Cardona, *Phys. Rev. B* **1984**, 29, 2051.
- [15] H.-M. Eiter, P. Jaschke, R. Hackl, A. Bauer, M. Gangl, C. Pfleiderer, *Phys. Rev. B* **2014**, 90, 024411.
- [16] P. G. Klemens, *Phys. Rev.* **1966**, 148, 845.
- [17] M. Balkanski, R. F. Wallis, E. Haro, *Phys. Rev. B* **1983**, 28, 1928.
- [18] A. K. Arora, M. Rajalakshmi, T. R. Ravindran, V. Sivasubramanian, *J. Raman Spectrosc.* **2007**, 38, 604.
- [19] M. Fernandez-Garcia, A. Martinez-Arias, J. C. Hanson, J. A. Rodriguez, *Chem. Rev.* **2004**, 104, 4063.
- [20] J. E. Spanier, R. D. Robinson, F. Zhang, S.-W. Chan, I. P. Herman, *Phys. Rev. B* **2001**, 64, 245407.
- [21] S. Kelly, F. H. Pollak, M. Tomkiewicz, *J. Phys. Chem. B* **1997**, 101, 2730.
- [22] H. Richter, Z. P. Wang, L. Ley, *Solid State Commun.* **1981**, 39, 625.
- [23] I. I. Campbell, P. M. Fauchet, *Solid State Commun.* **1986**, 58, 739.
- [24] K.-R. Zhu, M.-S. Zhang, Q. Chen, Z. Yin, *Phys. Lett. A* **2005**, 340, 220.
- [25] A. C. Breeson, G. Sankar, G. K. Liang Goh, R. G. Palgrave, *Phys. Chem. Chem. Phys.* **2016**, 18, 24722.
- [26] H. M. Moghaddam, S. Nasirian, *Nanosci. Methods* **2012**, 1, 201.
- [27] B. Choudhury, A. Choudhury, *Int Nano Lett* **2013**, 3, 55.
- [28] W. Naffouti, T. B. Nasr, H. Meradji, N. Kamoun-Turki, *J. Electron. Mater.* **2016**, 45, 5096.
- [29] M. K. Hossain, M. F. Pervez, M. N. H. Mia, S. Tayyaba, M. J. Uddin, R. Ahamed, R. A. Khan, M. Hoq, M. A. Khan, F. Ahmed, *Mater. Sci. —Poland* **2017**, 35, 868.
- [30] A. Verma, A. K. Yadav, N. Khatun, S. Kumar, C.-M. Tseng, S. Biring, S. Sen, *J. Mater. Sci.: Mater. Electron* **2017**, 28, 19017.
- [31] M. Mikami, S. Nakamura, O. Kitao, H. Arakawa, *Phys. Rev. B* **2002**, 66, 1552131.
- [32] S. Patra, C. Davoisne, H. Bouyanfif, D. Foix, F. Sauvage, *Sci. Rep. —UK* **2016**, 5, 10928.
- [33] N. Tomić, M. Grujić-Brojčin, N. Finčur, B. Abramović, B. Simović, J. Krstić, B. Matović, M. Šćepanović, *Mater. Chem. Phys.* **2015**, 163, 518.
- [34] M. N. Iliev, V. G. Hadjiev, A. P. Litvinchuk, *Vib. Spectrosc.* **2013**, 64, 148.
- [35] E. Shojaei, M. Abbasnejad, M. Saeedian, M. R. Mohammadzadeh, *Phys. Rev. B* **2011**, 83, 174302.
- [36] E. P. Meagher, G. A. Lager, *Can. Mineral.* **1979**, 17, 77.
- [37] N. S. Allen, N. Mahdjoub, V. Vishnyakov, P. J. Kelly, R. J. Kriek, *Polym. Degrad. Stabil.* **2018**, 150, 31.
- [38] L. K. Vodopyanov, E. A. Vinogradov, V. S. Vinogradov, I. V. Kucherenko, B. N. Mavrin, N. N. Novikova, P. V. Shapkin, *phys. stat. sol. (c)* **2004**, 1, 3162.
- [39] L. K. Vodopyanov, *J. Alloy Compd.* **2004**, 371, 72.
- [40] D. Nesheva, Z. Aneva, M. J. Šćepanović, I. Bineva, Z. Levi, Z. V. Popović, B. Pejova, *J. Phys. Conf. Ser.* **2010**, 253, 012035.
- [41] D. Nesheva, Z. Aneva, M. J. Šćepanović, Z. Levi, I. Iordanova, Z. V. Popovic, *J. Phys. D: Appl. Phys.* **2011**, 44, 415305.
- [42] M. Y. Valakh, M. P. Lisitsa, G. S. Pekar, G. N. Polysskii, V. I. Sidorenko, A. M. Yaremko, *Phys. Stat. Sol. (b)* **1982**, 113, 635.
- [43] N. ul Aarifeen, A. Afaq, *Mater. Res. Express* **2017**, 4, 095901.
- [44] G. R. Stewart, *Rev. Mod. Phys.* **2011**, 83, 1589.
- [45] Z. V. Popović, M. Šćepanović, N. Lazarević, M. M. Radonjić, D. Tanasković, H. Lei, C. Petrovic, *Phys. Rev. B* **2014**, 89, 014301.
- [46] Z. V. Popović, N. Lazarević, S. Bogdanović, M. M. Radonjić, D. Tanasković, R. Hu, H. Lei, C. Petrovic, *Solid State Commun.* **2014**, 193, 51.
- [47] N. Lazarević, M. Radonjić, M. Šćepanović, H. Lei, D. Tanasković, C. Petrovic, Z. V. Popović, *Phys. Rev. B* **2013**, 87, 144305.
- [48] N. Lazarević, H. Lei, C. Petrovic, Z. V. Popović, *Phys. Rev. B* **2011**, 84, 214305.
- [49] N. Lazarević, M. M. Radonjić, D. Tanasković, R. Hu, C. Petrovic, Z. V. Popović, *J. Phys.: Condens. Matter* **2012**, 24, 255402.
- [50] N. Lazarević, M. Abeykoon, P. W. Stephens, H. Lei, E. S. Bozin, C. Petrovic, Z. V. Popović, *Phys. Rev. B* **2012**, 86, 054503.
- [51] R. Hu, H. Lei, C. Petrovic, *Solid State Commun.* **2014**, 193, 51.
- [52] M. R. Opačić, N. Ž. Lazarević, *J. Serb. Chem. Soc.* **2017**, 82, 1.
- [53] M. Opačić, N. Lazarević, D. Tanasković, M. M. Radonjić, A. Milosavljević, Y. Ma, C. Petrovic, Z. V. Popović, *Phys. Rev. B* **2017**, 96, 174303.
- [54] A. Baum, Ying Li, M. Tomić, N. Lazarević, D. Jost, F. Löffler, B. Muschler, T. Böhm, J.-H. Chu, I. R. Fisher, R. Valentí, I. I. Mazin, R. Hackl, *Phys. Rev. B* **2018**, 98, 075113.
- [55] A. Baum, A. Milosavljević, N. Lazarević, M. M. Radonjić, B. Nikolić, M. Mitschek, Z. Inanloo Maranloo, M. Šćepanović, M. Grujić-Brojčin, N. Grujić-Brojčin, M. Opel, Aifeng Wang, C. Petrovic, Z. V. Popović, R. Hackl, *Phys. Rev. B* **2018**, 97, 054306.
- [56] A. P. Litvinchuk, V. G. Hadjiev, M. N. Iliev, Bing Lv, A. M. Guloy, C. W. Chu, *Phys. Rev. B* **2008**, 78, 060503(R).
- [57] V. Gnezdilov, Y. G. Pashkevich, P. Lemmens, D. Wulferding, T. Shevtsova, A. Gusev, D. Chareev, A. Vasiliev, *Phys. Rev. B* **2013**, 87, 144508.
- [58] V. Gnezdilov, Yu. Pashkevich, P. Lemmens, A. Gusev, K. Lamonova, T. Shevtsova, I. Vitebskiy, O. Afanasiev, S. Gnatchenko, V. Tsurkan, J. Deisenhofer, A. Loidl, *Phys. Rev. B* **2011**, 83, 245127.
- [59] L. Chauvière, Y. Gallais, M. Cazayous, A. Sacuto, M. A. Méasson, D. Colson, A. Forget, *Phys. Rev. B* **2009**, 80, 094504.
- [60] Y. Gallais, A. Sacuto, M. Cazayous, P. Cheng, L. Fang, H. H. Wen, *Phys. Rev. B* **2008**, 78, 132509.
- [61] A. M. Zhang, K. Liu, J. H. Xiao, J. B. He, D. M. Wang, G. F. Chen, B. Normand, Q. M. Zhang, *Phys. Rev. B* **2012**, 85, 024518.
- [62] T.-L. Xia, D. Hou, S. C. Zhao, A. M. Zhang, G. F. Chen, J. L. Luo, N. L. Wang, J. H. Wei, Z.-Y. Lu, Q. M. Zhang, *Phys. Rev. B* **2009**, 79, 140510(R).
- [63] A. Ignatov, A. Kumar, P. Lubik, R. H. Yuan, W. T. Guo, N. L. Wang, K. Rabe, G. Blumberg, *Phys. Rev. B* **2012**, 86, 134107.
- [64] Y. J. Um, A. Subedi, P. Toulemonde, A. Y. Ganin, L. Boeri, M. Rahlenbeck, Y. Liu, C. T. Lin, S. J. E. Carlsson, A. Sulpice, M. J. Rosseinsky, B. Keimer, M. Le Tacon, *Phys. Rev. B* **2012**, 85, 064519.



<http://www.sfkm.ac.rs/>

The 20th Symposium on Condensed Matter Physics

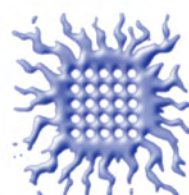
BOOK OF ABSTRACTS



University of Belgrade,
Faculty of Physics



Institute of Physics Belgrade



Vinca Institute
of Nuclear Sciences



Serbian Academy
of Sciences and Arts



Ministry of Education, Science and
Technological Development,
Republic of Serbia

Nematic Fluctuations In Iron Based Systems

A. Baum^{ab}, F. Kretzschmar^{ab}, D. Jost^{ab}, T. Böhm^{ab}, L. Peis^{ab},
U. Karahasanović^c, B. Muschler^{ab}, J. Schmalian^c, S. Caprara^d, M. Grilli^d,
C. Di Castro^d, J. G. Analytis^e, J.-H. Chu^e, I. R. Fisher^e, P. Gegenwart^f,
J. Maiwald^f, R. Hosseinian Ahangharnejhad^{ab}, P. Adelmann^c, T. Wolf^c,
N. Lazarević^g, Z. Popović^{gh} and R. Hackl^a

^aWalther Meissner Institut, Bayerische Akademie der Wissenschaften, Garching

^bFakultät für Physik E23, Technische Universität München

^cKarlsruhe Institute of Technology (KIT)

^dDepartment of Physics, University of Rome "Sapienza"

^eSIMES, SLAC National Accelerator Laboratory, and Geballe Laboratory for Advanced Materials
& Department of Applied Physics, Stanford University

^fExperimentalphysik VI, Universität Augsburg

^gCenter for Solid State Physics and New Materials, Institute of Physics, University of Belgrade

^hSerbian Academy of Sciences and Arts, Belgrade

Abstract. The origin and interplay of nematicity, magnetism, and superconductivity in iron based materials are still a subject of current research. The fluctuations which precede the ordered phases provide an additional probe for these phenomena. Using Raman spectroscopy we study fluctuations in $\text{Ba}(\text{Fe}_{1-x}\text{Co}_x)_2\text{As}_2$ ($x = 0-0.051$) as a function of temperature, symmetry, and doping. Our results provide evidence for critical spin fluctuations, suggesting a spin driven mechanism of the nematic and magnetic order. We discuss similarities with related systems such as EuFe_2As_2 and FeSe .

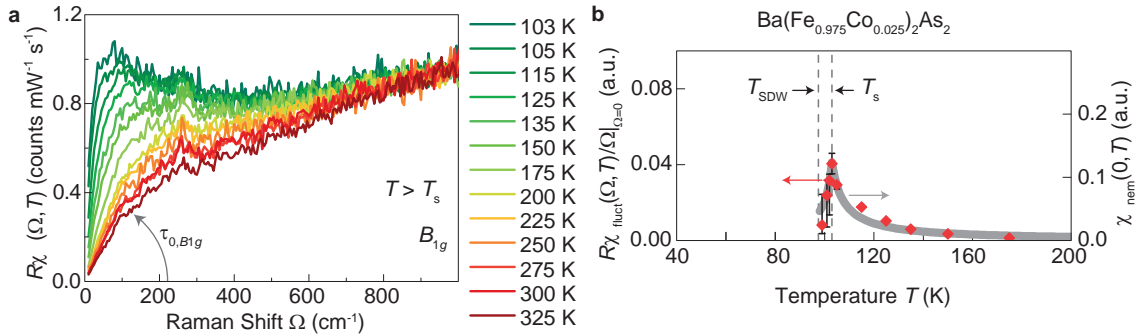


FIGURE 1. Fluctuations in $\text{Ba}(\text{Fe}_{0.975}\text{Co}_{0.025})_2\text{As}_2$. **a** Due to the response from fluctuations above the structural phase transition at $T_s \approx 103\text{ K}$ the spectral weight at low energies and the initial slope $\tau_{0,B1g}$ increase upon cooling. **b** The initial slope (red diamonds) exhibits a maximum at T_s , but the fluctuations only vanish at the magnetic ordering temperature T_{SDW} . The maximum is reflected in the temperature dependence of the electronic nematic susceptibility $\chi_{\text{nem}}^{\text{el}}$ (grey) when the fluctuations couple to the lattice.

REFERENCES

1. Kretzschmar *et al.*, *Nat. Phys.* **12**, 560-563 (2016)

The vibrational properties of CrI₃ single crystals

S. Djurdjic-Mijin,¹ A. Šolajić,¹ J. Pešić,¹ M. Šćepanović,¹ Y. Liu,² A. Baum,^{3,4} C. Petrovic,² N. Lazarević,¹ and Z. V. Popović^{1,5}

¹Center for Solid State Physics and New Materials, Institute of Physics Belgrade, University of Belgrade, Pregrevica 118, 11080 Belgrade, Serbia

²Condensed Matter Physics and Materials Science Department, Brookhaven National Laboratory, Upton, New York 11973-5000, USA

³Walther Meissner Institut, Bayerische Akademie der Wissenschaften, 85748 Garching, Germany

⁴Fakultät für Physik E23, Technische Universität München, 85748 Garching, Germany

⁵Serbian Academy of Sciences and Arts, Knez Mihailova 35, 11000 Belgrade, Serbia

Abstract. CrI₃ is a two-dimensional layered material and a ferromagnetic [1] with Curie temperature of 61K [1,2] and first order phase transition that occurs at 220K [3,4]. This class of materials has recently gained a lot of attention due to numerous potential applications. Here we represent our work consisting of both experimental and theoretical Raman scattering study of CrI₃ lattice dynamics. Based on our results we can distinguish two different phases for CrI₃ with monoclinic (*C2/m*) being the high-temperature and rhombohedral (*R3*) phase being the low-temperature phase. Abrupt changes to the spectra were found at the first order phase transition which was located at $T_s \approx 180$ K, lower than in previous studies. In contrast to the prior reports we found no sign of phase coexistence over temperature range exceeding 5 K [5].

REFERENCES

- [1] E. Navarro-Moratalla, B. Huang, G. Clark *et al.*, Layer dependent ferromagnetism in a van der Waals crystal down to the monolayer limit, *Nature (London)* **546**, 270 (2017).
- [2] J. F. Dillon, Jr. and C. E. Olson, Magnetization, resonance, and optical properties of the ferromagnet CrI₃, *J. Appl. Phys.* **36**, 1259 (1965).
- [3] M. A. McGuire, H. Dixit, V. R. Cooper, and B. C. Sales, Coupling of crystal structure and magnetism in the layered, ferromagnetic insulator CrI₃, *Chem. Mater.* **27**, 612 (2015).
- [4] D. T. Larson and E. Kaxiras, Raman Spectrum of CrI₃: An *ab initio* study, *Phys. Rev. B* **98**, 085406 (2018).
- [5] S. Djurdjic-Mijin, A. Šolajić, J. Pešić, M. Šćepanović, Y. Liu, A. Baum, C. Petrovic, N. Lazarević, and Z. V. Popović, Lattice dynamics and phase transition in CrI₃ single crystals, *Phys. Rev. B* **98**, 104307 (2018.)

Nanostructured BiFeO₃ thin films

B. Colson^a, V. Fuentes^a, Z. Konstantinovic^b, C. Frontera^a, D. Colson^c, A. Forget^c,
N. Lazarevic^b, M. Scepanovic^b, Z. V. Popovic^b, Ll. Balcells^a, B. Martinez^a, A. Pomar^a

^aICMAB-CSIC, Campus UAB, 08193 Bellaterra, Spain

^bCSSPNM, Institute of Physics Belgrade, University of Belgrade, Serbia

^cSPEC/IRASMIS/ DSM, CEA-Saclay, Gif-sur Yvette, France

Abstract. Well defined structures at nanometric scale of multiferroic materials present an increasing interest due to their unique physical properties and potential applications. Fabrication of artificial nanostructures requires sophisticated technology and has been recognized as a hard-attainable issue. For these reasons the fabrication of ordered nanostructures, via spontaneous self-organization, is a topic of major relevance. Complex oxide thin films are often elastically strained and this lattice strain can, in some cases, select preferential growth modes leading to the appearance of different self-organized morphologies. In this work we report on the controlled fabrication of a self-assembled network of nanostructures (pits and grooves) in highly epitaxial BiFeO₃ thin films. As previously shown in the case of manganite thin films [1-2], the remarkable degree of ordering is achieved using vicinal substrates with well-defined step-terrace morphology. Nanostructured BiFeO₃ thin films show mixed-phase morphology, exhibiting the giant ferroelectric polarization close to the theoretical limit. These particular microstructures open a huge playground for future applications in multiferroic nanomaterials.

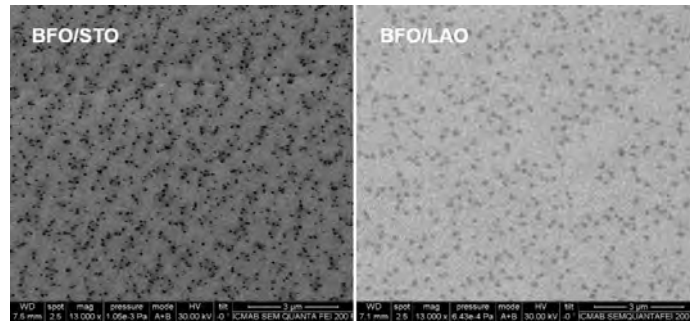


FIGURE 1. Scanning Electron Microscopy of nanostructured BiFeO₃ films grown on top of SrTiO₃ and LaAlO₃ substrates.

REFERENCES

1. Z. Konstantinovic et al., Small 5, 265 (2009)
2. Z. Konstantinovic et al., Nanoscale, 5, 1001 (2013).

Raman Spectroscopy Study of Primary Mesenchymal Stem Cells

J. J. Lazarević^a, T. Kukolj^b, U. Ralević^a, D. Bugarski^b, N. Lazarević^a, B. Bugarski^c, and Z.V. Popović^{a,d}

^a*Center for Solid State Physics and New Materials, Institute of Physics Belgrade, University of Belgrade, Pregrevica 118, Belgrade 11080, Serbia*

^b*Laboratory for Experimental Hematology and Stem Cells, Institute for Medical Research, University of Belgrade, Belgrade, Serbia*

^c*Department of Chemical Engineering, Faculty of Technology and Metallurgy, University of Belgrade, Karnegijeva 4, Belgrade 11060, Serbia*

^d*Serbian Academy of Science and Arts, Knez Mihailova 35, Belgrade 11000, Serbia*

Abstract. Cells possess specific dynamic biochemical structure and by analyzing (inter)molecular vibrations with Raman spectroscopy, correlation between biochemical composition to specific cell lineages is established, as well as to disorders of their physiologic state. In regenerative medicine and tissue engineering, mesenchymal stem cells, as adult stem cells, are of crucial importance, due to self-renewal, multi-lineage differentiation potential and undemanding isolation procedure. These cells are widespread in the adult organism and no ethical issues are related to their isolation. However, they need to be well characterized and purified before further application, having in mind their intrinsic heterogeneity. Raman spectroscopy was used for analyzing the influence of two most frequently used chemical fixatives, methanol and formaldehyde, on Raman spectra of primary mesenchymal stem cells isolated from periodontal ligament. Further, this vibrational spectroscopy technique was applied for probing differentiation status of these cells, after stimulating towards chondrogenic, adipogenic, and osteogenic lineages.

REFERENCES

1. Lazarević J.J., Kukolj T., Bugarski D., Lazarević N., Bugarski B., and Popović Z.V., *Spectrochim Acta A Mol Biomol Spectrosc.* **213**, 384-390 (2019).
2. Lazarević J.J., Ralević U., Kukolj T., Bugarski D., Lazarević N., Bugarski B., and Popović, Z.V., *Spectrochim Acta A Mol Biomol Spectrosc.* **216**, 173-178 (2019).

Frustrated Spin Order and Fluctuations in FeSe: A Raman Scattering Study

N. Lazarević^a, A. Baum^{b,c}, H. N. Ruiz^{d,e}, Yao Wang^{d,f,j}, T. Böhm^{b,c,k}, R. H. Ahanghamejhad^{b,c,l}, P. Adelmann^g, T. Wolf^g, Z. V. Popović^{a,h}, B. Moritz^d, T. P. Devereaux^{d,i}, R. Hackl^b

^aCenter for Solid State Physics and New Materials, Institute of Physics Belgrade, University of Belgrade, Pregrevica 118, 11080 Belgrade, Serbia.

^bWalther Meissner Institut, Bayerische Akademie der Wissenschaften, 85748 Garching, Germany.

^cFakultät für Physik E23, Technische Universität München, 85748 Garching, Germany.

^dStanford Institute for Materials and Energy Sciences, SLAC National Accelerator Laboratory, 2575 Sand Hill Road, Menlo Park, CA 94025, USA.

^eDepartment of Physics, Stanford University, Stanford, CA 94305, USA.

^fDepartment of Applied Physics, Stanford University, Stanford, CA 94305, USA.

^gKarlsruher Institut für Technologie, Institut für Festkörperphysik, 76021 Karlsruhe, Germany.

^hSerbian Academy of Sciences and Arts, Knez Mihailova 35, 11000 Belgrade, Serbia.

ⁱGeballe Laboratory for Advanced Materials, Stanford University, Stanford, CA 94305, USA.

^jPresent address: Lyman Laboratory 336, Harvard University, 17 Oxford St. Cambridge, 02138 MA, USA.

^kPresent address: TNG Technology Consulting GmbH, Beta-Straße, 85774 Unterföhring, Germany.

^lPresent address: School of Solar and Advanced Renewable Energy, Department of Physics and Astronomy, University of Toledo, Toledo, OH 43606, USA.

Abstract. FeSe is the simplest and yet the most controversial member of the iron based superconductors whose charge and spin dynamics may hold key information on the physics of high temperature superconductors. As opposed to the related iron pnictides and FeTe, no long range magnetic order is found down to lowest temperatures. Here, we present the results of the inelastic light scattering experiments on FeSe as a function of temperature and polarization. In agreement with numerical simulations of a spin-1 Heisenberg model, several peaks in all Raman active symmetries can be assigned to spin excitations. The dominating feature is a peak in B_{1g} symmetry around 500 cm⁻¹ which shows distinct temperature dependence. Further comparison of the simulations to neutron scattering data furnishes evidence for FeSe hosting nearly frustrated stripe order of local spins.

REFERENCES

1. A. Baum, H. N. Ruiz, N. Lazarević, Yao Wang, T. Böhm, R. Hosseinian Ahanghamejhad, P. Adelmann, T. Wolf, Z. V. Popović, B. Moritz, T. P. Devereaux & R. Hackl, *Communications Physics* **2**, 14 (2019).
2. H. Ruiz, Yao Wang, B. Moritz, A. Baum, R. Hackl & T. P. Devereaux, *Phys. Rev. B* **99**, 125130 (2019).

Lattice dynamics and phonon anomalies in FeS

A. Baum^{a,b}, A. Milosavljević^c, N. Lazarević^c, M.M. Radonjić^d, B. Nikolić^e, M. Mitschek^{a,b}, Z. Inanloo Maranloo^a, M. Šćepanović^c, M. Grujić – Brojčin^c, N. Stojilović^f, M. Opel^a, Aifeng Wang^g, C. Petrovic^g, Z.V. Popović^{c,h} and R. Hackl^a

^aWalther Meissner Institut, Bayerische Akademie der Wissenschaften, 85748 Garching, Germany

^bFakultät für Physik E23, Technische Universität München, 85748 Garching, Germany

^cCenter for Solid State Physics and New Materials, Institute of Physics Belgrade, University of Belgrade, Pregrevica 118, 11080 Belgrade, Serbia

^dScientific Computing Laboratory, Center for the Study of Complex Systems, Institute of Physics Belgrade, University of Belgrade, Pregrevica 118, 11080 Belgrade, Serbia

^eFaculty of Physics, University of Belgrade, Studentski trg 12, Belgrade, Serbia

^fDepartment of Physics and Astronomy, University of Wisconsin Oshkosh, Oshkosh, Wisconsin 54901, USA

^gCondensed Matter Physics and Materials Science Department, Brookhaven National Laboratory, Upton, New York 11973-5000, USA

^hSerbian Academy of Sciences and Arts, Knez Mihailova 35, 11000 Belgrade, Serbia

Abstract. Crystal structure, magnetic ordering and nematic phase are closely interrelated in the iron-based superconductors. Although isostructural and isoelectronic, properties of 11 chalcogenides, FeSe, FeTe and FeS, differ significantly. Whereas FeSe undergoes a nematic and structural phase transition at 90 K, together with superconductivity below 9 K, and no traces of long-range magnetic ordering, FeTe is not superconducting but exhibits magnetostructural phase transition at temperature of 67 K. The last member of the family, FeS, have a superconducting transition at 5 K, and remains tetragonal down to lowest temperatures.

Here, we present results of Raman scattering experiment on tetragonal FeS, and analysis of vibrational properties close to potential instabilities [1]. Besides A_{1g} and B_{1g} modes assignment, which is in a good agreement with DFT calculations, third peak within a gap of calculated phonon density of states can be identified as a result of second order scattering process. Both, selection rules for two-phonon processes, based on modified group projector technique and energy are in a good agreement with the experiment. A fourth mode, close to A_{1g} could originate from either defect-induced scattering or second order scattering as well. The temperature dependence of all four modes is governed by the contraction of the lattice, with anomalies at 50 K and below 20 K. The anomaly observed at 20 K has a correspondence with previously reported results of short-range magnetic ordering. The presence of two-phonon scattering indicates strong phonon-phonon scattering, which is likely to originate from an electron-phonon interaction being enhanced in comparison to other pnictides and chalcogenides.

REFERENCES

1. A. Baum, A. Milosavljević, N. Lazarević, M. M. Radonjić, B. Nikolić, M. Mitschek, Z. I. Maranloo, M. Šćepanović, M. Grujić-Brojčin, N. Stojilović, M. Opel, A. Wang, C. Petrovic, Z.V. Popović, and R. Hackl, Phonon anomalies in FeS, *Phys.Rev.B* **97**, 054306 (2018).

Lattice dynamics and phase transitions in $\text{Fe}_{3-x}\text{GeTe}_2$

A. Milosavljević^a, A. Šolajić^a, S. Djurdjić Mijin^a, J. Pešić^a, B. Višić^a, Y. Liu^b, C. Petrovic^b, N. Lazarević^a and Z. V. Popović^c

^aCenter for Solid State Physics and New Materials, Institute of Physics Belgrade, University of Belgrade, Pregrevica 118, 11080 Belgrade, Serbia

^bCondensed Matter Physics and Materials Science Department, Brookhaven National Laboratory, Upton, New York 11973-5000, USA

^cCenter for Solid State Physics and New Materials, Institute of Physics Belgrade, University of Belgrade, Pregrevica 118, 11080 Belgrade, Serbia and Serbian Academy of Sciences and Arts, Knez Mihailova 35, 11000 Belgrade, Serbia

Abstract. A new class of magnetic van der Waals bonded materials has recently become of great interest, as a suitable candidates for various applications. Whereas CrXTe_3 ($X = \text{Si, Ge, Sn}$) and CrX_3 ($X = \text{Cl, Br, I}$) classes maintain low phase transition temperatures even in a monolayer regime, $\text{Fe}_{3-x}\text{GeTe}_2$ has a high bulk transition temperature, between 220 and 230 K, making it a promising applicant.

Here we present DFT calculations of lattice dynamics and Raman spectroscopy measurements of the van der Waals bonded ferromagnet $\text{Fe}_{3-x}\text{GeTe}_2$ [1]. Four out of eight Raman active modes are observed and assigned, in agreement with numerical calculations. The energies and linewidths of the observed modes display an unconventional temperature dependence at about 150 and 220 K, followed by the nonmonotonic evolution of the Raman continuum. Whereas the former can be related to the magnetic phase transition, the origin of the latter anomaly remains an open question.

REFERENCES

1. A. Milosavljević, A. Šolajić, S. Djurdjić-Mijin, J. Pešić, B. Višić, Yu Liu, C. Petrovic, N. Lazarević, and Z. V. Popović. "Lattice dynamics and phase transitions in $\text{Fe}_{3-x}\text{GeTe}_2$." *Physical Review B* 99, no. 21 (2019): 214304.



**XVII INTERNATIONAL WORKSHOP ON
Vortex Matter in Superconductors**
Antwerp, Belgium
20-25 May, 2019

ABSTRACT BOOK



This conference is organized within the framework of

[EU-COST](#) Action CA16218:

*Nanoscale Coherent Hybrid Devices for Superconducting
Quantum Technologies*



**NANOSCALE COHERENT
HYBRID DEVICES
FOR SUPERCONDUCTING
QUANTUM TECHNOLOGIES**

Frustration and fluctuations in FeSe: A Raman scattering study

Nenad LAZAREVIĆ¹, Andreas BAUM^{2,3}, Harrison N RUIZ⁴, Yao WANG^{4,6,10}, Thomas BÖHM^{2,3,11}, R Hosseinian AHANGHAMEJHAD^{2,3,12}, Peter ADELMANN⁷, Thomas WOLF⁷, Zoran V POPOVIĆ^{1,8}, Brian MORITZ⁴, Thomas P DEVEREAUX^{4,9}, Rudi HACKL²

¹Center for Solid State Physics and New Materials, Institute of Physics Belgrade, University of Belgrade, Pregrevica 118, 11080 Belgrade, Serbia.

²Walther Meissner Institut, Bayerische Akademie der Wissenschaften, 85748 Garching, Germany.

³Fakultät für Physik E23, Technische Universität München, 85748 Garching, Germany.

⁴Stanford Institute for Materials and Energy Sciences, SLAC National Accelerator Laboratory, 2575 Sand Hill Road, Menlo Park, CA 94025, USA.

⁵Department of Physics, Stanford University, Stanford, CA 94305, USA.

⁶Department of Applied Physics, Stanford University, Stanford, CA 94305, USA.

⁷Karlsruher Institut für Technologie, Institut für Festkörperphysik, 76021 Karlsruhe, Germany.

⁸Serbian Academy of Sciences and Arts, Knez Mihailova 35, 11000 Belgrade, Serbia.

⁹Geballe Laboratory for Advanced Materials, Stanford University, Stanford, CA 94305, USA.

¹⁰Present address: Lyman Laboratory 336, Harvard University, 17 Oxford St. Cambridge, 02138 MA, USA.

¹¹Present address: TNG Technology Consulting GmbH, Beta-Straße, 85774 Unterföhring, Germany.

¹²Present address: School of Solar and Advanced Renewable Energy, Department of Physics and Astronomy, University of Toledo, Toledo, OH 43606, USA.

FeSe, the simplest of the iron based superconductors, is a puzzling material. As opposed to the related iron pnictides and FeTe, no long range magnetic order is found down to lowest temperatures. Here, we use Raman scattering as a function of temperature and polarization to probe charge and spin dynamics in FeSe. In agreement with numerical simulations of a spin-1 Heisenberg model several peaks in all Raman active symmetries can be assigned to spin excitations. The dominating feature is a peak in B_{1g} symmetry around 500 cm⁻¹ which shows distinct temperature dependence. Further comparison of the simulations to neutron scattering data furnishes evidence for FeSe hosting nearly frustrated stripe order of local spins.

References

- [1] A. Baum, H. N. Ruiz, N. Lazarević, Yao Wang, T. Böhm, R. Hosseinian Ahangharnejhad, P. Adelmann, T. Wolf, Z. V. Popović, B. Moritz, T. P. Devereaux & R. Hackl, *Communications Physics* **2**, 14 (2019).
- [2] H. Ruiz, Yao Wang, B. Moritz, A. Baum, R. Hackl & T. P. Devereaux, *Phys. Rev. B* **99**, 125130 (2019).

E-mail: nenad.lazarevic@ipb.ac.rs

Univerzitet u Beogradu

Elektrotehnički fakultet

Marko Opačić

**Razdvajanje faza na nanoskali u
superprovodnicima na bazi gvožđa
korišćenjem Ramanove spektroskopije**

Doktorska disertacija

Beograd, 2018.

University of Belgrade

School of Electrical Engineering

Marko Opačić

**Nanoscale phase separation in iron-based
superconductors investigated by Raman
spectroscopy**

Doctoral disertation

Belgrade, 2018.

Članovi komisije:

Akademik Zoran V. Popović, mentor

Naučni savetnik

Institut za fiziku Beograd, Univerzitet u Beogradu

Dr Milan Tadić, mentor

Redovni profesor

Elektrotehnički fakultet, Univerzitet u Beogradu

Dr Nenad Lazarević

Viši naučni saradnik

Institut za fiziku Beograd, Univerzitet u Beogradu

Dr Jelena Radovanović

Redovni profesor

Elektrotehnički fakultet, Univerzitet u Beogradu

Dr Vladimir Arsoski

Docent

Elektrotehnički fakultet, Univerzitet u Beogradu

Datum odbrane:

Disertaciju posvećujem porodici i prijateljima

Ova disertacija je u potpunosti urađena u Centru za fiziku čvrstog stanja i nove materijale Instituta za fiziku Beograd. Istraživanje je finansirano od strane Ministarstva prosvete, nauke i tehnološkog razvoja Republike Srbije, u okviru projekata III45018 i ON171017. Numeričke simulacije vršene su na superračunaru PARADOX koji se nalazi u okviru Laboratorije za primenu računara u nauci Instituta za fiziku Beograd. Uzorci su sintetisani u Brukhejven Nacionalnoj Laboratoriji, Apton, SAD.

Prvenstveno želim da se zahvalim akademiku Zoranu V. Popoviću, formalnom mentoru ovog rada, na pruženoj šansi za rad na ovoj temi, veoma korisnim savetima i primedbama, učenju dobroj naučnoj praksi i stvorenim uslovima za rad.

Suštinskom mentoru dr Nenadu Lazareviću dugujem zahvalnost na uvođenju u veoma interesantnu oblast proučavanja vibracionih osobina novih materijala. Pored toga, veoma sam mu zahvalan na stalnoj podršci i pomoći tokom merenja, obrade rezultata, pisanja radova i na kraju pisanja ove teze, kao i na odnosu koji je više od kolegijalnog.

Duboku zahvalnost izražavam i kolegama sa kojima sam blisko sarađivao tokom izrade ove teze: dr Maji Šćepanović na pomoći i savetima vezanim za eksperimentalna merenja, dr Darku Tanaskoviću na saradnji vezanoj za numeričke simulacije i veoma iscrpnim diskusijama tokom pisanja radova, prof. dr Čedomiru Petroviću na pripremi uzoraka, dr Milošu Radonjiću na DFT proračunima dinamike rešetke razmatranih materijala i MSc Ani Milosavljević na saradnji i pomoći.

Prijateljska i pozitivna atmosfera u okruženju u mnogome je doprinela kvalitetu mog rada. Za to su zaslužne kolege iz kancelarije: Dimitrije, Nataša i Bojan, kao i ostale kolege iz Centra.

U mom profesionalnom i ljudskom usavršavanju značajnu ulogu su imali moja pokojna učiteljica Stoja Nikolić kao i profesori Pete beogradske gimnazije mr Eugen Vedral i Ljiljana Svorcan, te im i na ovaj način iskazujem zahvalnost. Zahvaljujem i

svim ostalim profesorima Pete beogradske gimnazije i Elektrotehničkog fakulteta koji su eksplicitno ili implicitno doprineli ovom radu.

Konačno, želim da pomenem dvoje svojih bliskih prijatelja, Bojanu Milošević i Marka Mladenovića, te da im zahvalim na prijateljstvu i podršci svih ovih godina.

Na kraju, iako ne najmanje važno, zahvaljujem porodici na ljubavi, strpljenju i beskonačnoj podršci.

Razdvajanje faza u superprovodnicima na bazi gvožđa korišćenjem Ramanove spektroskopije

U okviru ovog rada izloženi su rezultati istraživanja vibracionih svojstava materijala iz grupe superprovodnika na bazi gvožđa i niskodimenzionalnih magnetnih materijala, metodom Ramanove spektroskopije. Ova spektroskopska tehnika omogućava i analizu uticaja strukturnih, elektronskih i magnetnih svojstava i njihovih promena na dinamiku rešetke kristalnih materijala. Eksperimentalni rezultati podržani su numeričkim proračunima dinamike kristalne rešetke.

U prvom delu istraživanja mereni su polarizovani ramanski spektri superprovodnog monokristala $K_xFe_{2-y}Se_2$ i nesuperprovodnog uzorka $K_{0.8}Fe_{1.8}Co_{0.2}Se_2$. U izmerenim spektrima oba materijala pojavljuju se fononski modovi koji potiču od metalne-superprovodne $I4/mmm$ faze i izolatorske $I4/m$ faze sa uređenim vakancijama gvožđa. Temperaturska analiza energije i poluširine vibracionih modova vršena je pomoću modela koji uzima u obzir toplotno širenje rešetke i anharmonijske efekte. Modovi koji potiču od izolatorske $I4/m$ faze mogu se dobro opisati ovim modelom. Nagli skok energije A_{1g} moda oko kritične temperature uočen je samo u superprovodnom uzorku. Ova renormalizacija pripisana je promeni elektronske strukture kristala $K_xFe_{2-y}Se_2$ pri ulasku u superprovodno stanje. Na osnovu amplitude fononske renormalizacije procenjeno je da konstanta elektron-fonon interakcije ima veoma malu vrednost.

Proučavanjem Ramanovih spektara monokristala $K_xFe_{2-y}Se_2$ dopiranih različitim koncentracijama kobalta praćena je evolucija faznog razdvajanja. Uočeno je da pri povećanju koncentracije kobalta iščezavaju fononi koji potiču od $I4/m$ faze, te u spektrima materijala sa visokim sadržajem kobalta preostaju samo dva moda iz visokosimetrične $I4/mmm$ faze. Pojava široke asimetrične strukture kod uzoraka sa srednjim koncentracijama kobalta pripisana je jakom kristalnom neuređenju u niskosimetričnoj fazi.

Krajnji član ovog niza, čist $K_xCo_{2-y}Se_2$ monokristal, proučavan je detaljnije. Prisustvo samo dva fononska moda, A_{1g} i B_{1g} simetrije, isključuje postojanje uređenih vakancija. Naši rezultati pokazuju da feromagnetni fazni prelaz pri $T_C = 74$ K ima značajan uticaj na ponašanje ramanskih modova. Iznad T_C temperaturska

zavisnost energije fonona konvencionalna, a ispod kritične temperature magnetnog prelaza oba moda imaju nagli porast energije, A_{1g} mod se sužava a B_{1g} mod značajno širi, što je objašnjeno uticajem spin-fonon i elektron-fonon interakcije. Velika širina ramanskih modova potiče od elektron-fononskog sprezanja pojačanog kristalnim neuređenjem i efektima spinskih fluktuacija.

U poslednjem delu istraživanja proučavana su fononska svojstva kvazijednodimenzionalnog magnetnog materijala $\text{TaFe}_{1.25}\text{Te}_3$. Na osnovu merenja u različitim polarizacijama i simetrijske analize izvršena je asignacija devet ramanski aktivnih modova. Jedina odstupanja temperaturske zavisnosti analiziranih modova od konvencionalnog ponašanja uočena su u neposrednoj blizini magnetnog prelaza, što je pripisano spinskim fluktuacijama. Dobijeni rezultati ukazuju da je magnetni fazni prelaz kontinualan i da elektron-fonon interakcija i gustina elektronskih stanja slabo zavise od temperature.

Ključne reči: superprovodnost, fononi, Ramanova spektroskopija, energija, poluširina

Naučna oblast: Elektrotehnika i računarstvo

Oblast istraživanja: Nanoelektronika i fotonika

UDK broj: 621.3

Nanoscale phase separation in iron-based superconductors investigated by Raman spectroscopy

In this work the results on vibrational properties of unconventional iron-based superconductors and low dimensional magnetic materials, by means of Raman spectroscopy, are given. This spectroscopic technique allows also an analysis of the impact of structural, electronic and magnetic properties and their changes on lattice dynamics of crystalline materials. Experimental results are supported by the numerical calculations of lattice dynamics.

In the first part of the research polarized Raman scattering spectra of superconducting $K_xFe_{2-y}Se_2$ and nonsuperconducting $K_{0.8}Fe_{1.8}Co_{0.2}Se_2$ single crystals were measured. In the obtained spectra of both materials there are phonon modes originating from metallic/superconducting $I4/mmm$ phase and insulating $I4/m$ phase with ordered Fe vacancies. Temperature analysis of energy and linewidth of the vibrational modes were done using the model which takes into account lattice thermal expansion and anharmonic effects. The modes from insulating $I4/m$ phase are well described by that model. A_{1g} model energy in the superconducting sample exhibits sudden jump. This renormalization was ascribed to the change of electronic structure in $K_xFe_{2-y}Se_2$ when entering the superconducting state. From the magnitude of phonon renormalization it was estimated that electron-phonon coupling constant is very small.

By investigating Raman spectra of $K_xFe_{2-y}Se_2$ single crystals doped with different Co concentrations, it was followed the evolution of phase separation in these samples. It was observed that with increasing cobalt content phonon modes originating from the $I4/m$ phase disappear, and in Raman spectra remain only two modes from the high symmetry $I4/mmm$ phase. The appearance of a broad asymmetric structure in the samples with intermediate cobalt concentration was ascribed to the strong crystalline disorder in the low symmetry phase.

End member of these sequence, $K_xCo_{2-y}Se_2$ single crystal, was investigated in detail. The presence of only two phonon modes, of A_{1g} and B_{1g} symmetry, excludes the possibility of ordered vacancies. Our results show that ferromagnetic phase transition around $T_C = 74$ K has significant impact on Raman mode behavior. Above

T_C temperature dependence of phonon energy and linewidth looks conventional, and below magnetic phase transition both modes exhibit sudden hardening, A_{1g} mode narrows and B_{1g} one significantly broadens, which is explained by the impact of spin-phonon and electron-phonon interaction. Large linewidth of Raman modes originates from the electron-phonon coupling enhanced by the crystal disorder and spin fluctuation effects.

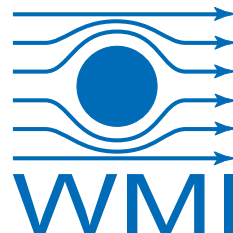
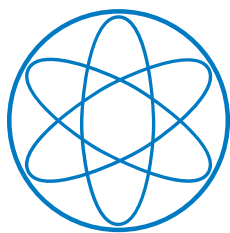
In the last part of the research phonon properties of quasi-one-dimensional magnetic material $\text{TaFe}_{1.25}\text{Te}_3$ were investigated. Based on spectroscopic measurements in different polarization and symmetry analysis, nine Raman active modes were assigned. The only deviations of phonon energy and linewidth from conventional behavior were observed in the vicinity of the magnetic phase transition, which is ascribed to the spin fluctuations. Our results suggest that magnetic phase transition in this single crystal is continuous, with electron-phonon interaction and density of electronic states weakly dependent on temperature.

Keywords: superconductivity, phonons, Raman spectroscopy, energy, linewidth

Scientific field: Electrical and Computer Engineering

Research area: Nanoelectronics and Photonics

UDC number: 621.3



Interrelation of lattice, charge, and spin degrees of freedom in iron based systems

Dissertation

Andreas Christoph Baum

September 2018

Fakultät für Physik

TECHNISCHE UNIVERSITÄT MÜNCHEN

TECHNISCHE UNIVERSITÄT MÜNCHEN

Fakultät für Physik

Lehrstuhl E23 für Technische Physik

Walther-Meißner-Institut für Tieftemperaturforschung
der Bayerischen Akademie der Wissenschaften

Interrelation of lattice, charge, and spin degrees of freedom in iron based systems

Andreas Christoph Baum

Vollständiger Abdruck der von der Fakultät für Physik der Technischen
Universität München zur Erlangung des akademischen Grades eines

Doktors der Naturwissenschaften

genehmigten Dissertation.

Vorsitzender: Prof. Dr. Wilhelm Zwerger

Prüfer der Dissertation: 1. Priv. Doz. Dr. Rudolf Hackl
2. Prof. Dr. Peter Böni

Die Dissertation wurde am 19.09.2018 bei der
Technischen Universität München eingereicht und durch
die Fakultät für Physik am 07.11.2018 angenommen.

Abstract

Magnetic order is a dominating phase in iron based pnictides and chalcogenides. Neither its origin nor its interplay with the neighbouring phases of nematic order and unconventional superconductivity are well understood yet. Raman spectroscopy allows access to the relevant excitations. This thesis focusses on the role of magnetism on lattice anomalies and the discrimination of localized and itinerant magnetic order. Simulations and experiments show that the magnetism in FeSe results from frustrated localized moments.

Kurzzusammenfassung

Magnetische Ordnung ist eine dominierende Phase in eisenbasierten Pniktiden und Chalcogeniden. Weder ihr Ursprung noch ihre Wechselwirkung mit den benachbarten Phasen der nematischen Ordnung und der unkonventionellen Supraleitung sind wohlverstanden. Raman-Spektroskopie erlaubt Zugang zu den relevanten Anregungen. Im Fokus dieser Arbeit stehen die Rolle des Magnetismus bei Gitteranomalien und die Unterscheidung von lokalisierter und itineranter magnetischer Ordnung. Simulationen und Experiment zeigen, dass der Magnetismus in FeSe von frustrierten lokalisierten Momenten stammt.

List of publications

- A. Baum, Y. Li, M. Tomić, N. Lazarević, D. Jost, F. Löffler, B. Muschler, T. Böhm, J.-H. Chu, I. R. Fisher, R. Valentí, I. I. Mazin, and R. Hackl. Interplay of lattice, electronic, and spin degrees of freedom in detwinned BaFe_2As_2 : A Raman scattering study. *Phys. Rev. B* **98**, 075113 (2018)
- A. Baum, A. Milosavljević, N. Lazarević, M. M. Radonjić, B. Nikolić, M. Mitschek, Z. I. Maranloo, M. Šćepanović, M. Grujić-Brojčin, N. Stojilović, M. Opel, A. Wang, C. Petrovic, Z. V. Popović, and R. Hackl. Phonon anomalies in FeS. *Phys. Rev. B* **97**, 054306 (2018)
- N. Chelwani, A. Baum, T. Böhm, M. Opel, F. Venturini, L. Tassini, A. Erb, H. Berger, L. Forró, and R. Hackl. Magnetic excitations and amplitude fluctuations in insulating cuprates. *Phys. Rev. B* **97**, 024407 (2018)
- T. Böhm, R. Hosseinian Ahangharnejhad, D. Jost, A. Baum, B. Muschler, F. Kretzschmar, P. Adelmann, T. Wolf, H.-H. Wen, J.-H. Chu, I. R. Fisher, and R. Hackl. Superconductivity and fluctuations in $\text{Ba}_{1-p}\text{K}_p\text{Fe}_2\text{As}_2$ and $\text{Ba}(\text{Fe}_{1-n}\text{Co}_n)_2\text{As}_2$. *physica status solidi (b)* **254**, 1600308 (2017)
- U. Ralević, N. Lazarević, A. Baum, H.-M. Eiter, R. Hackl, P. Giraldo-Gallo, I. R. Fisher, C. Petrovic, R. Gajić, and Z. V. Popović. Charge density wave modulation and gap measurements in CeTe_3 . *Phys. Rev. B* **94**, 165132 (2016)
- F. Kretzschmar, T. Böhm, U. Karahasanovic, B. Muschler, A. Baum, D. Jost, J. Schmalian, S. Caprara, M. Grilli, C. Di Castro, J. G. Analytis, J.-H. Chu, I. R. Fisher, and R. Hackl. Critical spin fluctuations and the origin of nematic order in $\text{Ba}(\text{Fe}_{1-x}\text{Co}_x)_2\text{As}_2$. *Nat. Phys.* **12**, 560 (2016)
- F. Kretzschmar, B. Muschler, T. Böhm, A. Baum, R. Hackl, H.-H. Wen, V. Tsurkan, J. Deisenhofer, and A. Loidl. Raman-Scattering Detection of

Nearly Degenerate s -Wave and d -Wave Pairing Channels in Iron-Based $\text{Ba}_{0.6}\text{K}_{0.4}\text{Fe}_2\text{As}_2$ and $\text{Rb}_{0.8}\text{Fe}_{1.6}\text{Se}_2$ Superconductors. *Phys. Rev. Lett.* **110**, 187002 (2013)

Submitted

- S. Djurdjić-Mijin, A. Šolajić, J. Pešić, M. Šćepanović, Y. Liu, A. Baum, C. Petrovic, N. Lazarević, and Z. V. Popović. Lattice dynamics and phase transition in CrI_3 single crystals (2018). [arXiv e-print 1807.03259v1](#)
accepted for publication in *Phys. Rev. B*
- A. Baum, H. N. Ruiz, N. Lazarević, Y. Wang, T. Böhm, R. Hosseinian Ahangharnejhad, P. Adelman, T. Wolf, Z. V. Popović, B. Moritz, T. P. Devereaux, and R. Hackl. Frustrated spin order and stripe fluctuations in FeSe (2018). [arXiv e-print 1709.08998v2](#)
accepted for publication in *Commun. Phys.*
- T. Böhm, F. Kretzschmar, A. Baum, M. Rehm, D. Jost, R. Hosseinian Ahangharnejhad, R. Thomale, C. Platt, T. A. Maier, W. Hanke, B. Moritz, T. P. Devereaux, D. J. Scalapino, S. Maiti, P. J. Hirschfeld, P. Adelman, T. Wolf, H.-H. Wen, and R. Hackl. Microscopic pairing fingerprint of the iron-based superconductor $\text{Ba}_{1-x}\text{K}_x\text{Fe}_2\text{As}_2$ (2017). [arXiv e-print 1703.07749](#)
accepted for publication in *npj Quantum Mater.*